SOLAR-TERRESTRIAL ENERGY PROGRAM:

Handbook of Ionospheric Models

Edited by:

R. W. Schunk

August, 1996

Acknowledgment

The publication of this handbook was supported, in part, by Utah State University and by SCOSTEP. We are indebted to Shawna Johnson for producing the camera-ready versions of the papers and for carefully proofing the manuscripts.

Copies can be obtained from:

R. W. Schunk
Center for Atmospheric and Space Sciences
Utah State University
Logan, UT 84322-4405

J. H. Allen
SCOSTEP Secretariat
NOAA/NGDC
325 Broadway
Boulder, Colorado 80303

PREFACE

One of the primary goals of the STEP program is to obtain a better quantitative understanding of the coupling mechanisms that are responsible for the transfer of mass and energy between the different regions of the solar-terrestrial system. In an effort to achieve this goal, coordinated experimental campaigns, involving aircraft, balloons, rockets, satellites, and ground-based radars and optical instruments, have been conducted on a world-wide basis. These diverse and comprehensive data sets should play a crucial role in elucidating the cause-effect relationships governing the different regions in the solar-terrestrial system. However, because the data are typically collected at different regions and times, physics-based models of the different solar-terrestrial regions can play an important role by providing a basis for interpreting and synthesizing the extensive data sets. Specifically, they can relate measurements made at different times and places by taking into account time delay effects.

Since many measurements pertain to the ionosphere, STEP Working Group 3.6 was established to promote the development of *Aeronomical Models of the Ionosphere*. The main goal of this effort was to identify physics-based ionospheric models that could be made available to the international community in some fashion, either via a collaboration with the model developers on specific model-data comparisons or via the acquisition of a specific model. This handbook was assembled in order to identify what ionospheric models exist, what physics and chemistry the models are based on, and how the models can be used. The models cover the D, E, and F-regions at low, middle, and high latitudes. There are global ionospheric models as well as models that describe the self-consistent coupling of the ionosphere to the mesosphere, thermosphere, plasmasphere, and electrodynamics.

The members of the coordinating committee of STEP Working Group 3.6 are: R. W. Schunk (USA, Chairman); D. Anderson (USA); D. Bilitza (USA); L. Bossy (Belgium); R. Y. Liu (China); S. A. Pulinets (USSR); S. Quegan (UK); C. E. Rasmussen (USA); K. Rawer (Germany); D. Rees (UK); R. G. Roble (USA); K. Serafimov (Bulgaria); E. Szuszczewicz (USA); J. Titheridge (New Zealand); P. Wilkerson (Australia).

R. W. Schunk
August, 1996

Solar-Terrestrial Energy Program: Handbook of Ionospheric Models

Table of Contents

Table of Contents (Continued)

D-Region Ion Chemistry Model

E. Turunen, H. Matveinen, J. Tolvanen and H. Ranta

Sodankylä Geophysical Observatory, FIN-99600 Sodankylä, Finland

1. Introduction

The D-region ion-chemistry model, Sodankylä Ion Chemistry (SIC) model, was developed as an alternative approach to those D-region ion chemistry models, which combine the more doubtful chemical reactions to effective parameters whose values are set against experimental data. A detailed chemical scheme, in a conceptually simple model, was built to be a tool for interpretation of D-region incoherent scatter experiments and cosmic radio noise absorption measurements, both of which form the basis of D-region research done at Sodankylä Geophysical Observatory. Although the present version of the model does not include all the reactions one could think of, it is designed so that adding reactions and new components is simple and can be done by any user of the model. The number of different ions in the first versions of the scheme was 35. The model was first applied by *Burns et al.* [1991] in a study of incoherent scatter measurements. A detailed description of the model is given by *Turunen et al.* [1992]. In the following, a shortened but self-contained description of the SIC-model is given. The description refers to the first versions of the model and published results. Presently, a major revision of the model is being made and the results of the revised model are not yet published.

SIC-model is a steady-state model which calculates ion and electron concentrations in ionospheric D- and lower E-regions. Local chemical equilibrium is calculated in the altitude range from 70 to 100 km at 1 km steps. Originally, the model was developed for applications during geophysically quiet conditions. Consequently, the solar radiation at a wavelength range of 5-134 nm and galactic cosmic rays were considered as ionization sources acting on five primary neutral components: N_2, O_2, O, NO, and $O_2(^1\Delta_g)$. At present however, the model is extended to include electron precipitation as an ionization source, as described by *Turunen et al.* [1992]. A similar extension was made to use the model during solar proton events, as in the application of the SIC-model by *Turunen* [1993].

The assumptions on which the model is based are:

1) The neutral atmosphere is described by the semi-empirical model MSIS-90 [*Hedin*, 1991].

2) The ionospheric D-region is sunlit. This restricts the range of the solar zenith angle to below about 95 degrees.

3) Ionization during quiet time is primarily caused by photoionization and galactic cosmic rays. Ionization by solar protons and precipitating electrons is calculated using measured particle energy deposition rates in air.

4) We neglect any transport effects. Photoequilibrium can be assumed since the chemical lifetimes of the ions are short with respect to transport processes.

5) The concentrations of neutral species are much higher than those of ions and thus assumed to be unaffected by ion chemistry.

(6) An overall charge neutrality prevails.

In addition to the above mentioned neutrals, Ar, He, and CO_2 are also included in photoionization calculations, because they absorb the solar radiation at the relevant wavelength range. To account for important ion-chemical reactions we also need to include H_2O, N, H, O_3, OH, NO_2, and HO_2, in the list of neutral components in the model.

2. Mathematical Formulation

Photoionization at altitude h, for solar zenith angle χ, is calculated using the following expression:

$$q_j(\chi,h)=\int_{\lambda} I_\infty(\lambda)\, e^{-\sum_k \sigma_k(\lambda)\int_h^\infty N_k Ch(h,\chi)dh}\, \eta_j(\lambda)\sigma_j(\lambda)n_j(h)d\lambda, \qquad (1)$$

where

$q_j(\chi,h)$ = photoionization rate for neutral component j,

$I_\infty(\lambda)$ = intensity of solar radiation outside the atmosphere,

$\sigma_k(\lambda)$ = absorption cross-section for neutral component k,

$Ch(h,\chi)$ = grazing incidence function,

$\eta_j(\lambda)$ = photoionization efficiency for neutral component j

and

$n_j(h)$ = concentration of neutral component j.

The exponential function in expression (1) describes the absorption of solar radiation at each wavelength. The grazing incidence function accounts for the Earth's curvature. The integral in the exponent is calculated numerically using expressions [*Rees*, 1989]:

$$\int_{h_o}^{\infty} n_j(h)\, Ch(h,\chi)dh=\int_{h_o}^{\infty} n_j(h)\left[1-\left(\frac{R+h_o}{R+h}\right)^2\sin^2\chi\right]^{-\frac{1}{2}}dh, \text{ for } \chi<90^\circ \qquad (2a)$$

$$\int_{h_o}^{\infty} n_j(h)\, Ch(h,\chi)dh=2\int_{h_{min}}^{\infty} n_j(h)\left[1-\left(\frac{R+h_{min}}{R+h}\right)^2\right]^{-\frac{1}{2}}dh-\int_{h_o}^{\infty} n_j(h)\left[1-\left(\frac{R+h_o}{R+h}\right)^2\sin^2\chi\right]^{-\frac{1}{2}}dh,$$
$$\text{for } \chi>90^\circ, \qquad (2b)$$

where

R = Earth radius

$h_{min}=\cos(\chi-90^\circ)(h_o+R)-R$ is the minimum height along the photon path.

Absorption cross-sections for N_2, O_2, O and He are from *Torr et al.* [1979]; for NO and Ar, the constants from the Tables of *Ohshio et al.* [1966] are used; and for CO_2, the data are from *McEwan and Phillips* [1975]. Photoionization efficiencies come from the same references as the absorption cross-sections. The absorption cross-sections and photoionization efficiencies are listed in Table 1.

A reference solar spectrum was collected from the spectrum by *Torr et al.* [1979] and from spectrum *R*74113 by *Heroux and Hinteregger* [1978]. The intensities for wavelengths 103.76 nm and 110.8 nm were taken from the paper of *Huffman et al.* [1971]. The *Ly*-α line for our reference spectrum was chosen from *Lean and Skumanich* [1983]. The intensities can be varied according to the chosen level of solar activity. The reference spectrum for the value $F_{10.7} = 68$ is also given in Table 1.

Heaps [1978] has derived a convenient parameterization of the empirical rate of ion pair production by cosmic rays, Q_σ, as a function of latitude, altitude and solar activity level. We use this parameterization as described by the following expressions (units $s^{-1}cm^{-3}$) :

$$Q_\sigma = \left(X_1 + X_2 \sin^4 \phi\right) \cdot 3 \cdot 10^{17(1-X_3)} \cdot M^{X_3} \text{ , for } M > 3 \cdot 10^{17} \text{ , } |\phi| < 53^\circ, \tag{3a}$$

where

$$X_1 = 1.74 \cdot 10^{-18} \text{ ,}$$
$$X_2 = 1.93 \cdot 10^{-17} \text{ (solar maximum),}$$
$$X_2 = 2.84 \cdot 10^{-17} \text{ (solar minimum),}$$
$$X_3 = 0.6 + 0.8 \cdot |\cos\phi| \text{ ,}$$
$$\text{M = number density of air } \left[\frac{1}{cm^3}\right] \text{ ,}$$

and

ϕ = latitude ;

$$Q_\sigma = \left(X_1 + X_2 \sin^4 \phi\right) \cdot M \text{ for } M < 3 \cdot 10^{17} \text{ , } |\phi| < 53^\circ; \tag{3b}$$

$$Q_\sigma = X_1 \cdot M \text{ for solar maximum, } |\phi| > 53^\circ \text{ ;} \tag{3c}$$

and

$$Q_\sigma = \left(X_1 + X_2\right) \cdot M \text{ for solar minimum, } |\phi| > 53^\circ \text{ ,} \tag{3d}$$

where

$$X_1 = 1.44 \cdot 10^{-17}$$

and

$$X_2 = 4.92 \cdot 10^{-18}.$$

This is initially taken to be effective for the major neutral components N_2 and O_2.

Table 1. The solar spectrum corresponding to the value $F_{10.7}$=68, absorption cross-sections and photoionization efficiencies.

Wave-length	Intens. 10^9	Abs. cross sect. (cm^{-2})							Ion. eff.							
(nm)	$cm^{-2}s^{-1}$	N_2	O_2	O	Ar	He	NO	O_2 ($^1\Delta^g$)	CO_2	N_2	O_2	O	Ar	He	NO	O_2 ($^1\Delta^g$)
5-10	0.3834	6.00e-19	1.18e-18	1.06e-18	0	2.10e-19	0	0	0	1.00	1.00	1.00	6.16	1.00	0	0
10-15	0.1346	2.32e-18	3.61e-18	3.53e-18	0	5.30e-19	0	0	0	1.00	1.00	1.00	3.50	1.00	0	0
15-20	1.8418	5.40e-18	7.27e-18	5.96e-18	0	1.02e-18	0	0	0	1.00	1.00	1.00	2.54	1.00	0	0
20-25	0.9235	8.15e-18	1.05e-17	7.55e-18	0	1.71e-18	0	0	0	1.00	1.00	1.00	0.22	1.00	0	0
25.63	0.2713	9.65e-18	1.28e-17	8.43e-18	0	2.16e-18	0	0	0	1.00	1.00	1.00	0	1.00	0	0
28.415	0.1	1.06e-17	1.48e-17	9.26e-18	0	2.67e-18	0	0	0	1.00	1.00	1.00	0	1.00	0	0
25-30	0.8405	1.01e-17	1.36e-17	8.78e-18	0	2.38e-18	0	0	0	1.00	1.00	1.00	0	1.00	0	0
30.331	0.235	1.16e-17	1.60e-17	9.70e-18	0	3.05e-18	0	0	0	1.00	1.00	1.00	0	1.00	0	0
30.378	6	1.16e-17	1.60e-17	9.72e-18	0	3.05e-18	0	0	0	1.00	1.00	1.00	0	1.00	0	0
30-35	0.8661	1.46e-17	1.72e-17	1.00e-17	0	3.65e-18	0	0	0	1.00	1.00	1.00	0	1.00	0	0
36.807	0.7394	1.80e-17	1.84e-17	1.08e-17	0	4.35e-18	0	0	0	1.00	1.00	1.00	0	1.00	0	0
35-40	0.2121	1.75e-17	1.87e-17	1.07e-17	0	4.25e-18	0	0	0	1.00	1.00	1.00	0	1.00	0	0
40-45	0.3926	2.11e-17	1.94e-17	1.12e-17	0	5.51e-18	0	0	0	1.00	1.00	1.00	0	1.00	0	0
46.522	0.18	2.18e-17	2.04e-17	1.13e-17	2.99e-17	6.53e-18	0	0	0	1.00	1.00	1.00	0.55	1.00	0	0
45-50	0.3063	2.18e-17	2.16e-17	1.16e-17	2.47e-17	7.09e-18	0	0	0	1.00	1.00	1.00	0.44	1.00	0	0
50-55	0.5085	2.45e-17	2.41e-17	1.19e-17	3.68e-17	7.20e-19	0	0	0	1.00	1.00	1.00	0.55	1.00	0	0
55.437	0.7992	2.47e-17	2.56e-17	1.21e-17	3.81e-17	0	0	0	0	1.00	1.00	1.00	0.57	0	0	0
58.433	1.58	2.32e-17	2.20e-17	1.22e-17	4.32e-17	0	2.31e-17	0	0	1.00	1.00	1.00	0.71	0	0.93	0
55-60	0.4843	2.24e-17	2.50e-17	1.19e-17	3.82e-17	0	0	0	0	1.00	1.00	1.00	0.67	0	0.37	0
60.976	0.45	2.31e-17	2.61e-17	1.22e-17	4.09e-17	0	2.37e-17	0	0	1.00	1.00	1.00	0.78	0	0.96	0
62.973	1.5	2.32e-17	2.58e-17	1.22e-17	4.26e-17	0	2.37e-17	0	0	1.00	1.00	1.00	0.81	0	0.96	0
60-65	0.1746	2.32e-17	2.60e-17	1.22e-17	3.93e-17	0	2.25e-17	0	0	1.00	1.00	1.00	0.79	0	0.96	0
65-70	0.2223	2.98e-17	2.63e-17	1.00e-17	3.75e-17	0	2.07e-17	0	0	0.84	0.84	1.00	0.81	0	0.94	0
70.336	0.3915	2.63e-17	2.50e-17	1.13e-17	3.63e-17	0	2.22e-17	0	0	0.88	0.92	1.00	0.88	0	0.82	0
70-75	0.1667	3.09e-17	2.91e-17	8.00e-18	3.51e-17	0	2.06e-17	0	0	0.75	0.82	1.00	0.85	0	0.78	0
76.515	0.1997	3.55e-17	2.20e-17	4.18e-18	3.34e-17	0	1.60e-17	0	0	0.67	0.39	1.00	0.78	0	0.57	0
77.041	0.2425	2.69e-17	2.52e-17	4.18e-18	3.41e-17	0	1.60e-17	0	0	0.68	0.39	1.00	0.78	0	0.57	0
78.936	0.7931	1.93e-17	2.67e-17	4.28e-18	0	0	1.71e-17	0	0	0.53	0.41	1.00	0	0	0.56	0
75-80	0.8728	3.07e-17	2.71e-17	4.23e-18	3.10e-17	0	1.89e-17	0	0	0.55	0.35	1.00	0.70	0	0.58	0
80-85	1.9311	1.50e-17	2.09e-17	4.38e-18	0	0	1.77e-17	0	0	0	0.29	1.00	0	0	0.54	0
85-90	4.4325	4.66e-17	9.85e-18	4.18e-18	0	0	2.71e-17	0	0	0	0.48	1.00	0	0	0.47	0
90-95	4.217	1.70e-17	1.55e-17	2.12e-18	0	0	3.38e-17	0	0	0	0.60	1.00	0	0	0.45	0
97.702	5.957	7.00e-19	4.00e-18	0	0	0	1.96e-17	0	0	0	0.63	0	0	0	0.55	0
95-100	1.785	3.62e-17	1.65e-17	0	0	0	1.99e-17	0	0	0	0.74	0	0	0	0.55	0
102.572	4.375	0	1.60e-18	0	0	0	1.94e-17	0	0	0	0.63	0	0	0	0.52	0
100-102.7	1.112	0	1.10e-18	0	0	0	2.08e-17	0	0	0	0.25	0	0	0	0.55	0
103.191	3.184	0	1.12e-18	0	0	0	1.38e-17	5.52e-18	0	0	0	0	0	0	0.62	1.00
103.761	1.63	0	1.08e-18	0	0	0	1.30e-17	5.14e-18	0	0	0	0	0	0	0.65	1.00
102.7-105	0.898	0	1.10e-18	0	0	0	1.16e-17	5.16e-18	0	0	0	0	0	0	0.66	1.00
105-110	2.8	0	9.50e-19	0	0	0	8.89e-18	4.81e-18	1.63e-17	0	0	0	0	0	0.79	1.00
110.8	0.24	0	5.00e-21	0	0	0	4.43e-18	3.32e-18	2.30e-17	0	0	0	0	0	0.82	1.00
110-111.8	0.232	0	3.90e-19	0	0	0	4.43e-18	3.40e-18	3.48e-17	0	0	0	0	0	0.82	1.00
111.8-115	0.438	0	0	0	0	0	3.49e-18	0	0	0	0	0	0	0	0.83	0
115-120	4.4	0	0	0	0	0	2.71e-18	0	0	0	0	0	0	0	0.86	0
121.568	232	6.00e-23	9.00e-21	0	0	0	2.40e-18	0	0	0	0	0	0	0	0.81	0
120-125	8	0	3.06e-19	0	0	0	2.21e-18	0	0	0	0	0	0	0	0.76	0
125-130	4.1	0	0	0	0	0	2.27e-18	0	0	0	0	0	0	0	0.52	0
130-135	12.4	0	2.90e-18	0	0	0	2.52e-18	0	0	0	0	0	0	0	0.23	0

Description of ionization by a given precipitating particle flux may be included using an empirically defined particle energy dissipation distribution function [*Rees*, 1963]. We use the following formulation, given by *Rees* [1989]:

The energy dissipation distribution function $\Lambda(s/R)$ is a function of a relative range of electrons s/R, where s is the atmospheric scattering depth calculated by integrating the atmospheric density ρ between the top of ionosphere and the altitude considered:

$$s = \int_{z}^{\infty} \rho(z)dz, \tag{4a}$$

and R is the range of electrons given by the expression (in units gcm^{-2}, for energy range 200 eV - 50 keV):

$$R(E) = 4.30 \cdot 10^{-7} + 5.36 \cdot 10^{-6} E^{1.67}. \tag{4b}$$

Figure 1 shows the energy dissipation distribution function for four different angular distributions of electrons. The function is normalized to conserve energy according to

$$\int_{-1}^{+1} \Lambda(s/R)\, d(s/R) = 1 \tag{5}$$

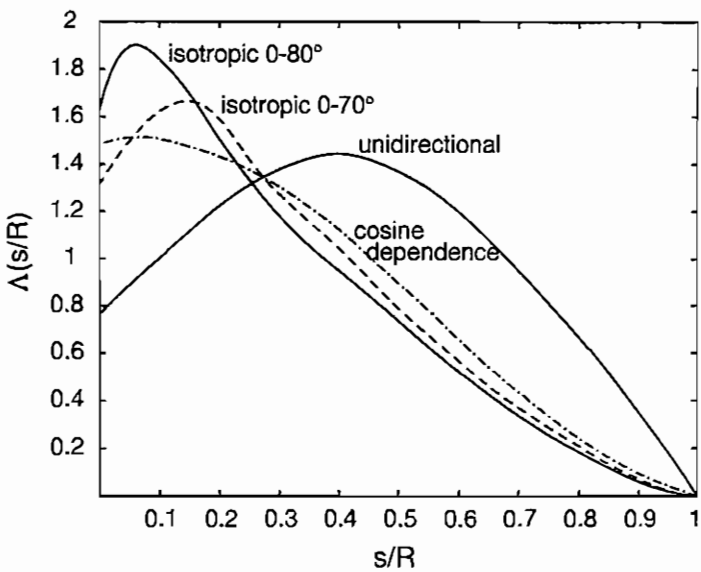

Figure 1. The normalized energy dissipation distribution function of electrons for four different angular distributions [*Rees*, 1989].

The energy ε, deposited by monoenergetic electrons at altitude z, is now given by the expression

$$\varepsilon(z,E) = q(z) \cdot \Delta\varepsilon_{ion} = F \cdot E \cdot \Lambda(s/R) \frac{p(z)}{R(E)} , \tag{6}$$

where q is the ionization rate, $\Delta\varepsilon_{ion}$ is the energy loss per ion-electron pair formation, and F is the flux of electrons. A commonly adopted value of 35 eV is taken for $\Delta\varepsilon_{ion}$. The ionization rate due to precipitation of monoenergetic electrons is now

$$q(z,E) = \frac{\varepsilon(z,E)}{\Delta\varepsilon_{ion}}. \tag{7}$$

When the ionization rate due to monoenergetic electrons is known, the ionization rate caused by precipitating electrons, having an arbitrary energy spectrum, may be calculated from the expression

$$q(z) = \int_0^\infty q(z,E)\, N(E)\, d(E), \tag{8}$$

where $N(E)$ is the differential energy spectrum of precipitating electrons.

In order to simplify the input of different energy spectra to the SIC-model, we parameterize the differential electron flux in exponential form, defined by two parameters j_o and E_o in the expression

$$N(E)dE = j_o\, e^{-E/E_o} dE. \tag{9}$$

Ionization rate is now calculated using expression (8), where the integration over solid angle is to be added. We assume an isotropic angular distribution between pitch angles 0° and 80°. At the auroral zone, the trigonometric term in the calculation of atmospheric depth, is negligible due to the direction of magnetic field, since the magnetic field direction is almost vertical.

The total ionization rate due to precipitating particles is then divided between the main ionizable constituents according to the relative magnitudes of the effective ionization cross sections and concentrations of the constituents. In order to get ion production rates suitable to be added to those by photoionization, in addition we must account for the branching ratios between direct and dissociative ionization processes. Denoting the ionization rate of air due to electron precipitation by q, we have the following expressions [*Jones*, 1974; *Rees*, 1989] for the production rates $p_e(X)$ of ions X:

$$p_e(N_2^+) = 0.76 \cdot q(N_2) ,$$

$$p_e(O_2^+) = 0.66 \cdot q(O_2) \tag{10}$$

and

$$p_e(O^+) = 0.33 \cdot q(O_2) + q(O),$$

where

$$q(N_2) = q\frac{0.92n(N_2)}{0.92n(N_2)+n(O_2)+0.56n(O)},$$

$$q(O_2) = q\frac{n(O_2)}{0.92n(N_2)+n(O_2)+0.56n(O)},$$

$$q(O) = q\frac{0.56n(O)}{0.92n(N_2)+n(O_2)+0.56n(O)}$$

and

n(X) = is the concentration of neutral component X.

Ionization by solar protons can be calculated following similar principles. The algorithm in the SIC-model is originally due to Reid, and was used (with different neutral atmosphere) by *Hargreaves et al.* [1987], in their study of the solar proton event of February, 1984.

The primary ions N_2^+, O_2^+, O^+, NO^+ and electron e^- react with neutral components forming more complex ions. The first version of the SIC-model included 24 positive and 11 negative ions altogether. These are introduced in Figures 2 and 3, showing the positive and negative ions, and their mutual reactions, respectively. The solid lines indicate ions and reactions in first versions of the SIC-model. These were used in all publications referred to in this report. The present version includes additions, which are indicated with dashed and/or dotted lines.

A complete reaction list, including also recombination, photodissociation and photodetachment processes, is given in Table 2. Updated reaction rate constants for the first version of the model are shown. Table 2 is a collection of information from several sources. The main contributions were taken from the works by *Chakrabarty et al.* [1978], *Dymek* [1980], *Wisemberg and Kockarts* [1980], *Torkar and Friedrich* [1983] and *Thomas and Bowman* [1985].

Our purpose is to calculate the equilibrium concentrations of the ions introduced in Figures 2 and 3, under the effect of all the reactions listed in Table 2 and the direct production processes described above. Additional assumptions used in the mathematical formulation of the model are the overall charge neutrality condition and an extremely low ionization degree. The neutral concentrations can thus be considered to be unaffected by the ion chemistry.

A change in the concentration n_i of the ion i can be described by the continuity equation. Let us denote the particle production rate by P_i and the loss rate by L_i. For a steady state condition, and neglecting the transport effects, the continuity equation simplifies to the form

$$P_i - n_i \cdot L_i = 0, \tag{11}$$

where

$$P_i = \sum_{\text{production processes } k} p_{ik} \tag{12a}$$

and

$$L_i = \sum_{\text{loss processes } k} l_{ik} \tag{12b}$$

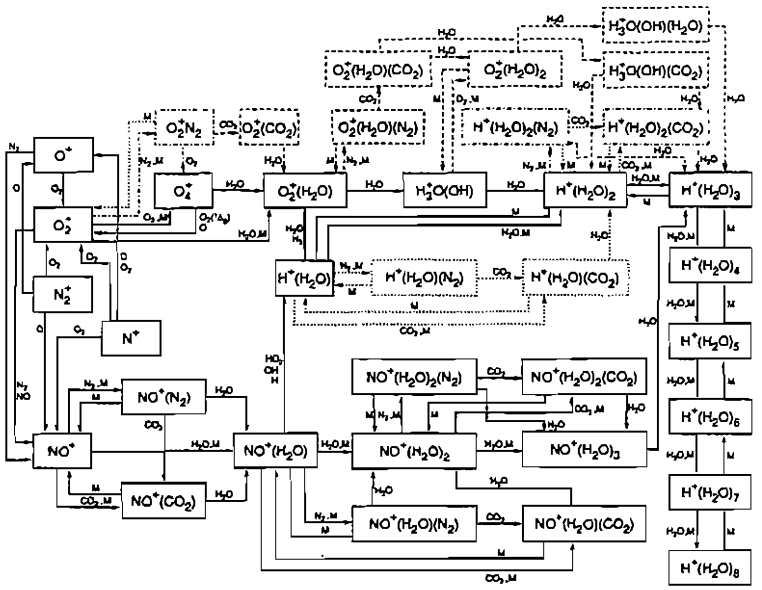

Figure 2. SIC-model positive ion reaction scheme. Ions and reactions in the first versions of the model are shown using solid lines. The present version includes additions, which are indicated with dashed and/or dotted lines.

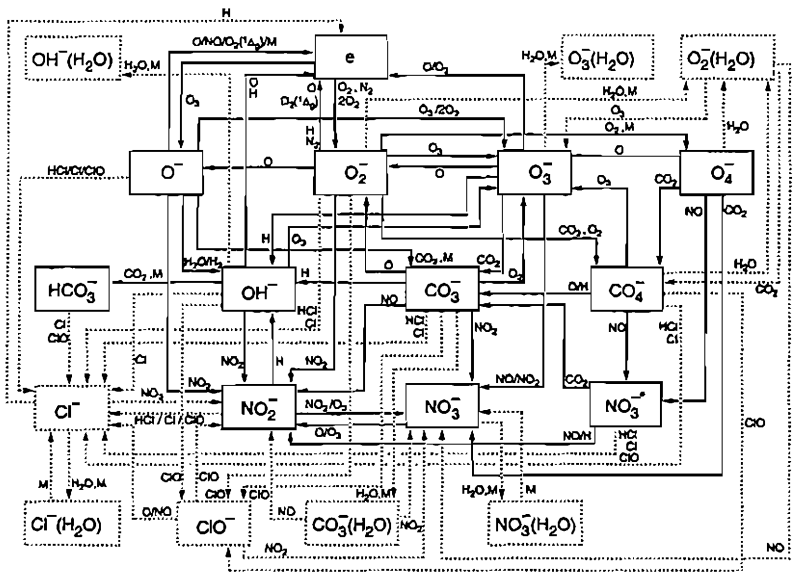

Figure 3. SIC-model negative ion reaction scheme. Ions and reactions in the first versions of the model are shown using solid lines. The present version includes additions, which are indicated with dashed and/or dotted lines.

Table 2. Ion-chemical reactions and reaction rates in the SIC-model. The units of the rate constants are s^{-1}, $cm^{-3}\ s^{-1}$ or $cm^{-6}\ s^{-1}$, as appropriate to the reaction shown.

Positive ion reactions	Rate coefficients	
$O^+ + O_2 \rightarrow O_2^+ + O$	$1.5\cdot10^{-11}$ (300/T)	/26/
$O^+ + N_2 \rightarrow NO^+ + N$	$1.2\cdot10^{-12}$ (300/T)	/26/
$O_2^+ + O_2 + M \rightarrow O_4^+ + M$	$4.0\cdot10^{-30}$ (300/T)$^{2.93}$	/5/
$O_2^+ + NO \rightarrow NO^+ + O_2$	$4.4\cdot10^{-10}$	/2/
$O_2^+ + N_2 \rightarrow NO^+ + NO$	$5\cdot10^{-16}$	/20/
$O_2^+ + H_2O + M \rightarrow O_2^+(H_2O) + M$	$2.8\cdot10^{-28}$	/2/
$O_4^+ + O \rightarrow O_2^+ + O_3$	$3\cdot10^{-10}$	/2/
$O_4^+ + O_2(^1\Delta_g) \rightarrow O_2^+ + 2O_2$	$> 10^{-10}$	/13/
$O_4^+ + H_2O \rightarrow O_2^+(H_2O) + O_2$	$1.7\cdot10^{-9}$	/31/
$N^+ + O_2 \rightarrow NO^+ + O$	$2.6\cdot10^{-10}$	/41/
$N^+ + O_2 \rightarrow O_2^+ + N$	$3.1\cdot10^{-10}$	/41/
$N^+ + O_2 \rightarrow O^+ + NO$	$3.0\cdot10^{-11}$	/42/
$N^+ + O \rightarrow O^+ + N$	$5\cdot10^{-13}$	/42/
$N_2^+ + O \rightarrow O^+ + N_2$	$9.8\cdot10^{-12}$ (300/T)$^{0.23}$	/11/
$N_2^+ + O_2 \rightarrow O_2^+ + N_2$	$5\cdot10^{-11}$ (300/T)$^{0.8}$	/26/
$N_2^+ + O \rightarrow NO^+ + N$	$1.4\cdot10^{-10}$ (300/T)$^{-0.4}$	/11/
$NO^+ + N_2 + M \rightarrow NO^+(N_2) + M$	$3.0\cdot10^{-31}$ (300/T)$^{4.3}$	/1/
$NO^+ + CO_2 + M \rightarrow NO^+(CO_2) + M$	$1.4\cdot10^{-29}$ (300/T)^{4}	/1/
$NO^+ + H_2O + M \rightarrow NO^+(H_2O) + M$	$1.8\cdot10^{-28}$ (308/T)$^{4.7}$	/21/
$NO^+(N_2) + M \rightarrow NO^+ + N_2 + M$	$1.5\cdot10^{-9}$ (300/T)$^{4.3}$ exp(-2093/T)	/1/
$NO^+(N_2) + CO_2 \rightarrow NO^+(CO_2) + N_2$	$1\cdot10^{-9}$	/27/
$NO^+(N_2) + H_2O \rightarrow NO^+(H_2O) + N_2$	$1\cdot10^{-9}$	/21/
$NO^+(CO_2) + M \rightarrow NO^+ + CO_2 + M$	$3.1\cdot10^{-4}T^{-4}\exp(-4590/T)$	/21/
$NO^+(CO_2) + H_2O \rightarrow NO^+(H_2O) + CO_2$	$1\cdot10^{-9}$	/21/
$NO^+(H_2O) + H_2O + M \rightarrow NO^+(H_2O)_2 + M$	$1\cdot10^{-27}$ (308/T)$^{4.7}$	/21/
$NO^+(H_2O) + N_2 + M \rightarrow NO^+(H_2O)(N_2) + M$	$2\cdot10^{-31}$ (300/T)$^{4.4}$	/21/
$NO^+(H_2O) + CO_2 + M \rightarrow NO^+(H_2O)(CO_2) + M$	$7\cdot10^{-30}$ (300/T)^{3}	/1/
$NO^+(H_2O)_2 + H_2O \rightarrow H^+(H_2O)_3 + HNO_2$	$7\cdot10^{-11}$	/21/
$NO^+(H_2O)(N_2) + M \rightarrow NO^+(H_2O) + N_2 + M$	$1.5\cdot10^{-6}T^{-5.4}\exp(-2150/T)$	/21/
$NO^+(H_2O)(N_2) + H_2O \rightarrow NO^+(H_2O)_2 + N_2$	$1\cdot10^{-9}$	/21/
$NO^+(H_2O)(N_2) + CO_2 \rightarrow NO^+(H_2O)(CO_2) + N_2$	$1\cdot10^{-9}$	/21/
$NO^+(H_2O)(CO_2) + M \rightarrow NO^+(H_2O)_2 + CO_2 + M$	$3.8\cdot10^{-6}$ (300/T)$^{5}\exp(-4025/T)$	/1/
$NO^+(H_2O)(CO_2) + H_2O \rightarrow NO^+(H_2O)_2 + CO_2$	$1\cdot10^{-9}$	/21/
$NO^+(H_2O)_2(N_2) + M \rightarrow NO^+(H_2O)_2 + N_2 + M$	$1.5\cdot10^{-6}T^{-5.4}\exp(-1800/T)$	/21/
$NO^+(H_2O)_2(N_2) + H_2O \rightarrow NO^+(H_2O)_3 + N_2$	$1.0\cdot10^{-9}$	/21/
$NO^+(H_2O)_2(N_2) + CO_2 \rightarrow NO^+(H_2O)_2(CO_2) + N_2$	$1\cdot10^{-9}$	/21/
$NO^+(H_2O)_2(CO_2) + M \rightarrow NO^+(H_2O)_2 + CO_2 + M$	$3.8\cdot10^{-6}$ (300/T)$^{5}\exp(-3335/T)$	/1/
$NO^+(H_2O)_2(CO_2) + H_2O \rightarrow NO^+(H_2O)_3 + CO_2$	$1\cdot10^{-9}$	/21/
$O_2^+(H_2O) + H_2O \rightarrow H_3O^+(OH) + O_2$	$9.0\cdot10^{-10}$	/31/
$O_2^+(H_2O) + H_2O \rightarrow H^+(H_2O) + OH + O_2$	$2.4\cdot10^{-10}$	/2/
$H_3O^+(OH) + H_2O \rightarrow H^+(H_2O)_2 + OH$	$2.0\cdot10^{-9}$	/2/
$H^+(H_2O) + H_2O + M \rightarrow H^+(H_2O)_2 + M$	$4.6\cdot10^{-27}$ (300/T)^{4}	/30/
$H^+(H_2O)_2 + M \rightarrow H^+(H_2O) + H_2O + M$	$2.5\cdot10^{-2}$ (300/T)$^{5}\exp(-15900/T)$	/30/
$H^+(H_2O)_2 + H_2O + M \rightarrow H^+(H_2O)_3 + M$	$8.6\cdot10^{-27}$ (300/T)$^{1.5}$	/30/
$H^+(H_2O)_3 + M \rightarrow H^+(H_2O)_2 + H_2O + M$	$1.2\cdot10^{-3}$ (300/T)$^{8.5}\exp(-9800/T)$	/30/
$H^+(H_2O)_3 + H_2O + M \rightarrow H^+(H_2O)_4 + M$	$3.6\cdot10^{-27}$ (300/T)$^{8.1}$	/30/
$H^+(H_2O)_4 + M \rightarrow H^+(H_2O)_3 + H_2O + M$	$1.5\cdot10^{-1}$ (300/T)$^{9.1}\exp(-9000/T)$	/30/
$H^+(H_2O)_4 + H_2O + M \rightarrow H^+(H_2O)_5 + M$	$4.6\cdot10^{-28}$ (300/T)^{14}	/30/
$H^+(H_2O)_5 + M \rightarrow H^+(H_2O)_4 + H_2O + M$	$1.7\cdot10^{-3}$ (300/T)$^{15}\exp(-6400/T)$	/30/
$H^+(H_2O)_5 + H_2O + M \rightarrow H^+(H_2O)_6 + M$	$5.8\cdot10^{-29}$ (300/T)$^{15.3}$	/30/
$H^+(H_2O)_6 + M \rightarrow H^+(H_2O)_5 + H_2O + M$	$4.0\cdot10^{-3}$ (300/T)$^{16.3}\exp(-5800/T)$	/30/
$H^+(H_2O)_6 + H_2O + M \rightarrow H^+(H_2O)_7 + M$	$9\cdot10^{-28}$ (300/T)$^{15.3}$	/30/
$H^+(H_2O)_7 + M \rightarrow H^+(H_2O)_6 + H_2O + M$	$1.3\cdot10^{-2}$ (300/T)$^{16.3}\exp(-5400/T)$	/30/
$H^+(H_2O)_7 + H_2O + M \rightarrow H^+(H_2O)_8 + M$	$9\cdot10^{-28}$ (300/T)^{4}	/21/
$H^+(H_2O)_8 + M \rightarrow H^+(H_2O)_7 + H_2O + M$	$2.3\cdot10^{10}T^{-5}\exp(-5000/T)$	/21/

Recombination of positive ions with electron	Rate coefficients	
$O^+ + e \rightarrow O$	$4.0\cdot10^{-12}$ (300/Te)$^{0.7}$	/29/
$O_2^+ + e \rightarrow O + O$	$1.6\cdot10^{-7}$ (300/Te)^{a} 0.35<a<0.7	/5/
$O_4^+ + e \rightarrow 2O_2$	$4.2\cdot10^{-6}$ (300/Te)$^{0.5}$	/32/
$N^+ + e \rightarrow N$	10^{-12}	/43/
$N_2^+ + e \rightarrow N + N$	$3.5\cdot10^{-7}$ (300/Te)$^{0.5}$	/17/
$NO^+ + e \rightarrow N + O$	$4.2\cdot10^{-7}$ (300/Te)^{a} 0.37<a<0.9	/5/
$NO^+(N_2) + e \rightarrow NO + N_2$	$1.4\cdot10^{-6}$ (300/Te)$^{0.4}$	/32/
$NO^+(CO_2) + e \rightarrow NO + CO_2$	$1.5\cdot10^{-6}$	/16/
$NO^+(H_2O) + e \rightarrow NO + N_2O$	$1.5\cdot10^{-5}$	/33/
$NO^+(H_2O)_2 + e \rightarrow NO + 2H_2O$	$2.0\cdot10^{-5}$	/33/
$NO^+(H_2O)_3 + e \rightarrow NO + 3H_2O$	$2.0\cdot10^{-5}$	/33/
$NO^+(H_2O)(N_2) + e \rightarrow NO + H_2O + N_2$	$3.0\cdot10^{-5}$	/14/
$NO^+(H_2O)(CO_2) + e \rightarrow NO + H_2O + CO_2$	$3.0\cdot10^{-6}$	/14/
$NO^+(H_2O)_2(N_2) + e \rightarrow NO + 2H_2O + N_2$	$3.0\cdot10^{-5}$	/14/
$NO^+(H_2O)_2(CO_2) + e \rightarrow NO + 2H_2O + CO_2$	$3.0\cdot10^{-6}$	/14/
$O_2^+(H_2O) + e \rightarrow O_2 + H_2O$	$2.0\cdot10^{-6}$	/33/
$H_3O^+(OH) + e \rightarrow$ neutrals	$1.5\cdot10^{-6}$	/33/
$H^+(H_2O) + e \rightarrow H + N_2O$	$6.3\cdot10^{-7}$ (300/Te)$^{0.5}$	/34/
$H^+(H_2O)_2 + e \rightarrow H + 2H_2O$	$2.5\cdot10^{-6}$ (300/Te)$^{0.1}$	/32/
$H^+(H_2O)_3 + e \rightarrow H + 3H_2O$	$3.0\cdot10^{-6}$ (300/Te)$^{0.1}$	/32/
$H^+(H_2O)_4 + e \rightarrow H + 4H_2O$	$3.6\cdot10^{-6}$	/33/
$H^+(H_2O)_5 + e \rightarrow N + 5H_2O$	$5.0\cdot10^{-6}$	/33/
$H^+(H_2O)_6 + e \rightarrow H + 6H_2O$	$5.0\cdot10^{-6}$	/32/
$H^+(H_2O)_7 + e \rightarrow H + 7H_2O$	$<8.0\cdot10^{-5}$	/34/
$H^+(H_2O)_8 + e \rightarrow N + 8H_2O$	$1.0\cdot10^{-5}$	/4/

Photodissociation of positive ions	Rate coefficients	
$O_2^+(H_2O) + h\nu \rightarrow O_2^+ + H_2O$	0.42	/23/

Negative ion reactions	Rate coefficients	
$O^- + M \rightarrow O + M + e$	$< 10^{-12}$	/2/
$O^- + O \rightarrow O_2 + e$	$1.9\cdot10^{-10}$	/2/
$O^- + NO \rightarrow NO_2^- + e$	$3.1\cdot10^{-10}$ (300/Te)$^{0.83}$	/36/
$O^- + O_2(^1\Delta_g) \rightarrow O_2 + e$	$3\cdot10^{-10}$	/2/
$O^- + O_3 \rightarrow O_3^- + O$	$8.0\cdot10^{-10}$	/2/
$O^- + 2O_2 \rightarrow O_3^- + O_2$	$1.4\cdot10^{-30}$	/18/
$O^- + H_2O \rightarrow OH^- + OH$	$6.0\cdot10^{-13}$	/2/
$O^- + CO_2 + M \rightarrow CO_3^- + M$	$2.0\cdot10^{-28}$	/2/
$O^- + NO_2 \rightarrow NO_2^- + O$	$1.0\cdot10^{-9}$	/2/
$O^- + H_2 \rightarrow OH^- + H$	$3.2\cdot10^{-11}$	/38/
$O_2^- + O \rightarrow O_2 + e$	$1.5\cdot10^{-10}$	/2/
$O_2^- + O_2(^1\Delta_g) \rightarrow 2O_2 + e$	$2\cdot10^{-10}$	/2/
$O_3^- + N_2 \rightarrow N_2 + O_2 + e$	$1.9\cdot10^{-12}$ (300/T)$^{-1.5}\exp(-4990/T)$	/15/

Table 2 (cont'd). Ion-chemical reactions and reaction rates in the SIC-model. The units of the rate constants are s^{-1}, $cm^{-3}\,s^{-1}$ or $cm^{-6}\,s^{-1}$, as appropriate to the reaction shown.

$O_2^- + H \rightarrow HO_2 + e$	$1.4\cdot10^{-9}$ /38/
$O_2^- + O \rightarrow O^- + O_2$	$1.5\cdot10^{-10}$ /2/
$O_2^- + O_3 \rightarrow O_3^- + O_2$	$7.8\cdot10^{-10}$ /36/
$O_2^- + O_2 + M \rightarrow O_4^- + M$	$3.4\cdot10^{-31}$ /2/
$O_2^- + CO_2 + O_2 \rightarrow CO_4^- + O_2$	$4.7\cdot10^{-29}$ /2/
$O_2^- + NO_2 \rightarrow NO_3^- + O_2$	$7\cdot10^{-10}$ /2/
$O_2^- + O \rightarrow 2O_2 + e$	$1\cdot10^{-10}$ /15/
$O_3^- + O_3 \rightarrow 3O_2 + e$	$1\cdot10^{-10}$ /1/
$O_3^- + O \rightarrow O_2^- + O_2$	$2.5\cdot10^{-10}$ /2/
$O_3^- + H \rightarrow OH^- + O_2$	$8.4\cdot10^{-10}$ /2/
$O_3^- + CO_2 \rightarrow CO_3^- + O_2$	$5.5\cdot10^{-10}$ /2/
$O_3^- + NO \rightarrow NO_3^- + O$	$2.6\cdot10^{-12}$ /2/
$O_3^- + NO_2 \rightarrow NO_3^- + O_2$	$2.8\cdot10^{-10}$ /2/
$O_4^- + O \rightarrow O_3^- + O_2$	$4\cdot10^{-10}$ /2/
$O_4^- + CO_2 \rightarrow CO_4^- + O_2$	$4.3\cdot10^{-10}$ /2/
$O_4^- + NO \rightarrow NO_3^- + O_2$	$2.5\cdot10^{-10}$ /2/
$OH^- + O \rightarrow HO_2 + e$	$2\cdot10^{-10}$ /2/
$OH^- + H \rightarrow H_2O + e$	$1.4\cdot10^{-9}$ /2/
$OH^- + O_3 \rightarrow O_2^- + OH$	$9\cdot10^{-10}$ /2/
$OH^- + NO_2 \rightarrow NO_2^- + OH$	$1.1\cdot10^{-9}$ /2/
$OH^- + CO_2 + M \rightarrow HCO_3^- + M$	$7.6\cdot10^{-28}$ /2/
$CO_3^- + O \rightarrow O_2^- + CO_2$	$1.1\cdot10^{-10}$ /2/
$CO_3^- + O_3 \rightarrow O_3^- + CO_2$	$6.0\cdot10^{-15}$ /2/
$CO_3^- + H \rightarrow OH^- + CO_2$	$1.7\cdot10^{-10}$ /2/
$CO_3^- + NO \rightarrow NO_2^- + CO_2$	$1.0\cdot10^{-10}$ /15/
$CO_3^- + NO_2 \rightarrow NO_3^- + CO_2$	$2\cdot10^{-10}$ /2/
$CO_4^- + O_3 \rightarrow O_3^- + O_2 + CO_2$	$1.3\cdot10^{-10}$ /2/
$CO_4^- + H \rightarrow CO_3^- + OH$	$2.3\cdot10^{-10}$ /2/
$CO_4^- + O \rightarrow CO_3^- + O_2$	$1.4\cdot10^{-10}$ /2/
$CO_4^- + NO \rightarrow NO_3^- + CO_2$	$4.8\cdot10^{-11}$ /2/
$NO_2^- + H \rightarrow OH^- + NO$	$3\cdot10^{-10}$ /2/
$NO_2^- + NO_2^- \rightarrow NO_3^- + NO$	$2\cdot10^{-13}$ /2/
$NO_2^- + O_3 \rightarrow NO_3^- + O_2$	$1.2\cdot10^{-10}$ /2/
$NO_3^- + O \rightarrow NO_2^- + O_2$	$< 1\cdot10^{-11}$ /2/
$NO_3^- + O_3 \rightarrow NO_2^- + 2O_2$	$1\cdot10^{-13}$ /2/
$NO_2^- + CO_2 \rightarrow CO_3^- + NO_2$	$1.0\cdot10^{-11}$ /2/
$NO_2^- + H \rightarrow NO_2^- + OH$	$7.2\cdot10^{-10}$ /2/
$NO_3^- + NO \rightarrow NO_2^- + NO_2$	$1.0\cdot10^{-12}$ /37/

Electron photodetachment of negative ions	Rate coefficients
$O^- + h\nu \rightarrow O + e$	1.4 /19/
$O_2^- + h\nu \rightarrow O_2 + e$	$3.8\cdot10^{-1}$ /19/
$O_3^- + h\nu \rightarrow O_3 + e$	$4.7\cdot10^{-7}$ /6/
$OH^- + h\nu \rightarrow OH + e$	1.1 /6/
$CO_3^- + h\nu \rightarrow CO_3 + e$	$2.2\cdot10^{-2}$ /16/
$NO_2^- + h\nu \rightarrow NO_2 + e$	$8.0\cdot10^{-4}$ /9/
$NO_3^- + h\nu \rightarrow NO_3 + e$	$5.2\cdot10^{-2}$ /24/

Photodissociation of negative ions	Rate coefficients
$O_2^- + h\nu \rightarrow O^- + O_2$	0.47 /8/
$O_4^- + h\nu \rightarrow O_2^- + O_3$	0.34 /8/
$CO_4^- + h\nu \rightarrow O^- + CO_3$	0.15 /16/
$CO_4^- + h\nu \rightarrow O_2^- + CO_2$	$6.2\cdot10^{-3}$ /6/

Electron attachment to neutrals	Rate coefficients
$O_3 + e \rightarrow O^- + O_2$	$9.1\cdot10^{-12}(300/Te)^{-1.66}$ /25/
$2O_2 + e \rightarrow O_2^- + O_2$	$4\cdot10^{-30}\exp(-193/Te)$ /28/
$O_2 + N_2 + e \rightarrow O_2^- + N_2$	$1\cdot10^{-31}(300/Te)\exp(-600/Te)$ /19/

Ion–ion recombination	Rate coefficients
$X^+ + Y^- \rightarrow$ neutrals	$6\cdot10^{-8}$ /22/
$NO_2^- + X^+ \rightarrow NO_2 + X$	$1.7\cdot10^{-7}$ /10/
$NO_2^- + X^+ \rightarrow NO_1 + X$	$3.4\cdot10^{-8}$ /10/
$NO^+ + NO_2^- \rightarrow$ neutrals	$6.8\cdot10^{-7}$ /39/
$O_2^+ + O_2^- + M \rightarrow 3O_2 + M$	$3\cdot10^{-25}(300/T)^{2.5}$ /29/
$O_2^+ + O_2^- \rightarrow 2O_2$	$6\cdot10^{-8}$ /40/

References:

1.	Adams and Megill, 1967
2.	Albritton, 1978
3.	Banks, 1988
4.	Biondi, 1973
5.	Böhringer and Arnold, 1982
6.	Cosby et al., 1976
7.	Dhandhukia and Johnsen, 1983
8.	DNA, 1972
9.	Dunkin et al., 1971
10.	Eisner and Hirsh, 1971
11.	McFarland et al., 1974
12.	Fehsenfeld et al., 1975
13.	Fehsenfeld et al., 1971
14.	Huang et al., 1978
15.	Lelevier and Braascomb, 1968
16.	Moseley et al., 1976
17.	Mul and McGowan, 1979
18.	Payzant and Kebarle, 1972
19.	Phelps, 1969
20.	Rees, 1989
21.	Reid, 1977
22.	Smith et al., 1976
23.	Smith et al., 1978
24.	Smith et al., 1979
25.	Stelman et al., 1977
26.	Swider and Narcisi, 1975
27.	Thomas, 1976
28.	Truby, 1972
29.	Whitten and Poppoff, 1971
30.	Lao et al., 1982
31.	Rakshit and Warneck, 1980
32.	Johnson, 1987
33.	Swider and Narcisi, 1983
34.	McGowan and Mitchell, 1984
35.	Ferguson et al., 1979
36.	Viggiano and Paulson, 1984
37.	Wisemberg and Kockarts, 1980
38.	Brasseur and DeRaes, 1986
39.	Smith and Church, 1977
40.	Smith et al., 1981
41.	Adams et al., 1980
42.	Rees, 1989
43.	Torbin and Friedrich, 1983

The charge neutrality condition reads:

$$N_e = \sum_{positive} n_i - \sum_{negative} n_i \tag{13}$$

In order to describe the chemical production terms p_{ik} and loss terms l_{ik} in expressions (12a) and (12b), let us consider a single reaction where ion C^+ is formed when the ion A^+ reacts with the neutral component B:

$$A^+ + B \rightarrow C^+ + D \ . \tag{14}$$

If the reaction rate constant of process (14) is denoted by k, the ion C^+ is produced with rate $p_{C^+14} = k[A^+][B]$ and the ion A^+ is lost at the same rate $l_{A^+14} = k[A^+][B]$. When assuming that the neutral concentrations are much larger than the ion concentrations, and are not affected by the changes in ion concentrations, it is practical to define a new reaction rate constant, where the usual rate constant is multiplied by the relevant neutral concentration. Thus, the production of ion C^+ and loss of ion A^+ can be described by the constants Π_{C^+} and Λ_{A^+} in expressions

$$p_{C+14} = \Pi_{C+14}\left[A^+\right] \tag{15a}$$

and

$$l_{A+14} = \Lambda_{A+14}\left[A^+\right]. \tag{15b}$$

If all the processes were linear in the unknown variables (the ion concentrations n_i), one could write equations (11) for each ion as a group of linear coupled equations expressed in matrix form as

$$B\vec{N} + \vec{Q} = \vec{0}, \tag{16}$$

where B is a 35x35 matrix having as its elements the terms Π and Λ which describe the production and loss rates of each ion. $\vec{N}$ is a vector containing the 35 unknown ion concentrations. $\vec{Q}$ is a vector which contains the constant production rates from expressions (1), (3) and (10).

Writing equation (16) in element form as

$$\begin{pmatrix} -\Lambda_1 & & & \\ & -\Lambda_2 & (\Pi) & \\ & & \ddots & \\ & (\Pi) & & -\Lambda_n \end{pmatrix} \begin{pmatrix} n_1 \\ n_2 \\ \vdots \\ n_n \end{pmatrix} + \begin{pmatrix} p_{11} + p_{12} \\ p_{21} + p_{22} \\ \vdots \\ p_{n1} + p_{n2} \end{pmatrix} = \vec{0} \ , \tag{17}$$

we can assign the contributions from different types of the involved processes to the elements in equation (17), as described in Table 3.

The diagonal elements Λ_i in the matrix in equation (17) are the sums of all the loss rates of ion i. The non-diagonal elements are seemingly single production rates in separate processes, but sometimes one ion may be formed from the same source ion through a few different reactions with different neutrals, in which case also the production rate could be a composite one.

Table 3. Location of production and loss terms in equation (17). Only two primary production processes are shown. Ionization by electron or proton flux contributes similarly as ionization by galactic cosmic rays.

Process type	Reaction	production rate of ion k (i → k)	loss rate of ion i	location		
				B		Q
				b_{ki}	b_{ii}	q_k
Photoionization	$A + h\nu \rightarrow A^+ + e^-$	p_{k1}				p_{k1}
Galactic cosmic rays	$A + E \rightarrow A^+ + e^-$	p_{k2}				p_{k2}
Positive ion reactions	$A^+ + M \rightarrow B^+ + N$	Π_{ki}	Λ_i	Π_{ki}	$-\Lambda_i$	—
Negative ion reactions	$A^- + M \rightarrow B^- + N$ $A^- + M \rightarrow AM + e^-$ $A^- + M \rightarrow A + M + e^-$	Π_{ki} — —	Λ_i Λ_i Λ_i	Π_{ki} = =	$-\Lambda_i$ $-\Lambda_i$ $-\Lambda_i$	— = =
Positive ion dissociation	$AM^+ + h\nu \rightarrow A^+ + M$	Π_{ki}	Λ_i	Π_{ki}	$-\Lambda_i$	—
Negative ion dissociation	$CM^- + h\nu \rightarrow C^- + M$	Π_{ki}	Λ_i	Π_{ki}	$-\Lambda_i$	—
Negative ion photodetachment	$B^- + h\nu \rightarrow B + e^-$	—	Λ_i	—	$-\Lambda_i$	—

Table 4. Processes which introduce non-linearity in equation (17).

Process type	Reaction	effect on elements	dependence introduced	
			B	Q
Positive ion recombination	$A^+ + e^- \rightarrow A$	$\Lambda_i \rightarrow \Lambda_i + \alpha_i N_e$	$B \rightarrow B(N)$	
Ion-ion recombination	$X^+ + X^- \rightarrow$ neutrals	$\Lambda_i \rightarrow \Lambda_i + \xi_{i\,pos} n_{pos}$ $\Lambda_i \rightarrow \Lambda_i + \eta_{i\,neg} n_{neg}$	$B \rightarrow B(N)$	
Electron attachment	$A + e^- \rightarrow A^-$	$q_i \rightarrow q_i + \gamma_i N_e$		$Q \rightarrow Q(N)$

If we express the electron concentration using the charge neutrality condition (13), equation (16) is missing the processes which make our set of simultaneous coupled equations nonlinear. These are the positive ion recombination with electron, recombination reactions between positive and negative ions and the negative ion formation by electron attachment to neutrals. The effect of these processes in equation (17) is described in Table 4.

The equilibrium condition, including all the processes described in Tables 3 and 4, can now be expressed in a simple form

$$\vec{F}(\vec{N}) = \vec{B}(\vec{N})\vec{N} + \vec{Q}(\vec{N}) = \vec{0}, \tag{18}$$

where the elements of the matrix B and vector $\vec{Q}$ are given by Tables 2, 3 and 4, together with information on neutral concentrations.

3. Numerical Solution Procedure

We solve equation (18) using the Newton-Raphson method [see e.g. *Press et al.*, 1986]. Let us denote, by vector $\vec{N}$, the solution of equation (18), and by $\vec{N}_o$, some initial guess of the solution. We may write

$$\vec{N} = \vec{N}_o + \vec{\delta}, \tag{19}$$

where $\vec{\delta}$ is the correction vector needed to bring $\vec{N}_o$ to be the real solution $\vec{N}$.

In the neighborhood of $\vec{N}_o$, each component f_i of function $\vec{F}$ may be written as a Taylor series expansion

$$f_i\left(\vec{N}_o + \vec{\delta}\right) = f_i\left(\vec{N}_o\right) + \sum_j \left(\frac{\partial f_i}{\partial N_j}\right)_{\vec{N}=\vec{N}_o} \cdot \delta_j + \ldots = 0 \tag{20}$$

If we suppose that the guess $\vec{N}_o$ is sufficiently near the solution $\vec{N}$, we may neglect the second and higher order terms in expression (18). Thus, we get a linear equation for each component of the correction vector $\vec{\delta}$ in the form

$$\sum_j \left(\frac{\partial f_i}{\partial N_j}\right)_{\vec{N}=\vec{N}_o} \cdot \delta_j = -f_i\left(\vec{N}_o\right). \tag{21}$$

From equation (18), the components f_i of the function $\vec{F}$ may be written in the form $f_i\left(\vec{N}\right) = \sum B_{ij}\left(\vec{N}\right) n_j + q_i\left(\vec{N}\right)$. The partial derivatives of the components f with respect to the ion concentrations n can then be expressed as

$$\left(\frac{\partial f_i}{\partial n_k}\right)_{\vec{N}=\vec{N}_o} = \left(\sum_j \frac{\partial B_{ij}\left(\vec{N}\right)}{\partial n_k} n_j + B_{ik}\left(\vec{N}\right) + \frac{\partial q_i\left(\vec{N}\right)}{\partial n_k}\right)_{\vec{N}=\vec{N}_o} \tag{22}$$

The partial derivatives (22) can be written in a simple explicit form by defining vectors $\vec{G}^+, \vec{G}^-$ and $\vec{G}^e$, which identify the positive and negative ions and their charges. The components of these vectors are given by expressions

$$q_i^+ = \begin{cases} 1, & for\ i \le 24 \\ 0, & for\ i \ge 25, \end{cases} \tag{23a}$$

$$q_i^- = \begin{cases} 0, & for\ i \le 24 \\ 1, & for\ i \ge 25, \end{cases} \tag{23b}$$

and

$$\vec{G}^e = \vec{G}^+ - \vec{G}^-. \tag{23c}$$

The total electron and ion concentrations are then $N_e = \vec{G}^e \cdot \vec{N}, N^+ = \vec{G}^+ \cdot \vec{N}$ and $N^- = \vec{G}^- \cdot \vec{N}$.

Using the coefficients defined in Tables 2, 3 and 4, the partial derivatives are given by the expression

$$\left(\frac{\partial f_i}{\partial n_k}\right)_{\vec{N}=\vec{N}_o} = \left(-\alpha_i g_k^e - \xi_i g_k^+ - \eta_i g_k^-\right)\left(\vec{N}_o\right)_i + B_{ik}\left(\vec{N}_o\right) + \gamma_i g_k^e. \qquad (24)$$

The linear group of equations (21) is solved using the singular value decomposition method, which makes it possible to check any improper behavior of the set of equations.

Once the equation for the correction vector $\vec{\delta}$ is solved, from expression (19) we have a new value $\vec{N}' = \vec{N}_o + \vec{\delta}$ for the guess of the unknown ion concentrations $\vec{N}$. If our initial guess $\vec{N}_o$ was good enough, the new guess $\vec{N}'$ is nearer to the solution $\vec{N}$. By solving again for a correction vector $\vec{\delta}'$, we form an iterative procedure which gives an approximation of the solution $\vec{N}$. The numerical accuracy of the solution could be controlled, for example, by the components of the vector $\vec{\delta}$, satisfying the condition $\sqrt{\sum_i \delta_i^2} < \varepsilon$, where ε is a number defining the desired numerical accuracy.

In practice, for the SIC-model procedure, we use the behavior of the components of the vector function $\vec{F}$ as the criterion to stop the iteration. If the iteration converges, the elements f_i give direct information about how good of a solution we have found for each equation. The initial guess for the solution must be sensible to make the iteration converge. Since the amount of important ion species rapidly decreases with increasing altitude, a trial solution is first formed for the lowest altitude, where all included ions are present. Having an initial solution for the lowest height, we solve the equations (18) and continue with the next height in a 1 km grid, always using the final solution of the previous height as the initial guess.

4. Model Inputs

As input to the neutral atmosphere model, MSIS-90, one gives time, location and information about solar and geomagnetic activity. The resulting neutral constituent concentrations are then used to calculate ion production rates and chemical reaction rates.

For those neutral constituents which are not covered by the MSIS-90 model $\left(NO, O_2\left({}^1\Delta_g\right), CO_2, H_2O, O_3, OH, NO_2, HO_2\right)$, fixed reference profiles may be selected. Also, fixed mixing ratios of $3 \cdot 10^{-4}$ and $1 \cdot 10^{-6}$ for CO_2 and H_2O, respectively, can be used. Some applications of the model may require that some of the above mentioned minor constituent profiles are kept fixed, while selected concentrations are varied. Examples of used reference minor constituent concentration profiles are given in Figure 4.

Calculation of photoionization needs two basic inputs: the zenith angle of the sun, which is calculated from time and location; and the solar spectrum, which can be varied from the reference spectrum to any desired form. The absorption cross sections and photoionization efficiencies in Table 1 represent fixed inputs to the calculation.

The spectrum of precipitating electrons can be given in a parameterized form of the differential energy spectrum, as in expression (9). Alternatively, a precise form of the spectrum can be given, e.g. in the form of fluxes at selected energy channels. Input of the proton flux is formulated to correspond measurements at predefined energy channels, as those used by the satellite GOES-7, for example. Ion production by galactic cosmic rays is presently hard coded in the program code of the model.

The basic parameters which control the calculation are the altitude range, step and the wanted relative accuracy of the results. Other control parameters are hard coded. The calculation of chemical equilibrium needs reaction rates which are formed from concentrations of the neutral constituents and a defined set of reaction rate constants. Individual reactions, as well as individual ions, can be added or removed. One should note that when a new ion is added to the scheme, usually new neutral components are also introduced. Thus their concentrations should be known. A trial solution for ion concentrations at the lowest altitude is needed for the numerical procedure.

The data which are needed as input to the model are seen in Figure 5, where a flow chart of the model is shown.

5. Model Outputs

The ion chemistry model gives altitude profiles of ion concentrations as direct output. From the ion concentrations, total positive and negative ion concentrations, electron concentration and mean ion mass are also calculated. We have mostly used the altitude range from 70 km to 100 km, with 1 km altitude steps, since this corresponds to the most common D-region measurements made by the EISCAT incoherent scatter radars. The radar data are suitable for direct comparisons of the model with experimental data.

The first check of the SIC-model was a comparison of a test phase version of the model with rocket measurements at mid-latitudes and with corresponding results from the model by *Thomas and Bowman* [1985]. Calculations were performed for solar zenith angle 65° and geographic location 50°*N*, 20°*E*, corresponding to the date 23 April 1974 and time 1500 UT. The date was selected just due to solar reference spectrum determination, and the location and time are a compromise between available information about important neutral minor species concentrations and the choice of northern mid-latitudes. The concentration of *NO* was taken from a profile presented by *Brasseur* [1984], and the one for $O_2(^1\Delta_g)$ from *Paulsen et al.* [1972]. The concentration of O_3 came from model CIRA-72, the concentration of H_2O was from the model by *Rodrigo et al.* [1986], and the concentrations of N, H, CO_2, OH, NO_2 and HO_2 originated from *DNA 3476* [DNA, 1972]. The main neutral components N_2, O_2, O, Ar and He, as well as the temperature, were taken to be described by the model MSIS-83, together with the *Alcayde* [1981] altitude extension below mesopause. The calculated ion concentrations are shown in Figures 6 and 7. These were compared with a rocket experiment determination of ion concentrations for low solar activity conditions by *Kopp et al.* [1984], and with the model calculations of negative ion concentrations at noon time by *Thomas and Bowman* [1985], which are shown in Figures 8a and 8b.

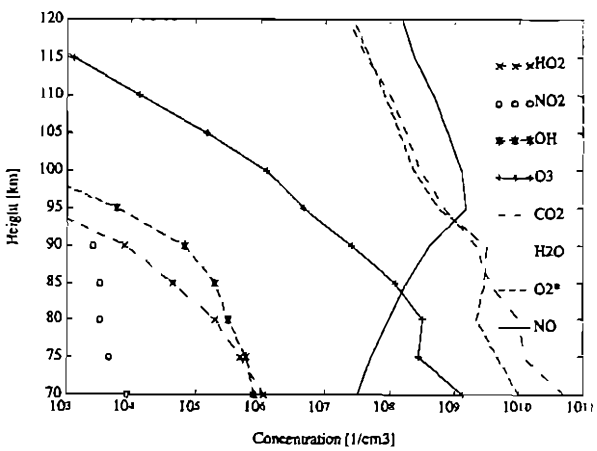

Figure 4. Selected example concentrations for neutral constituents not covered by MSIS-90 model.

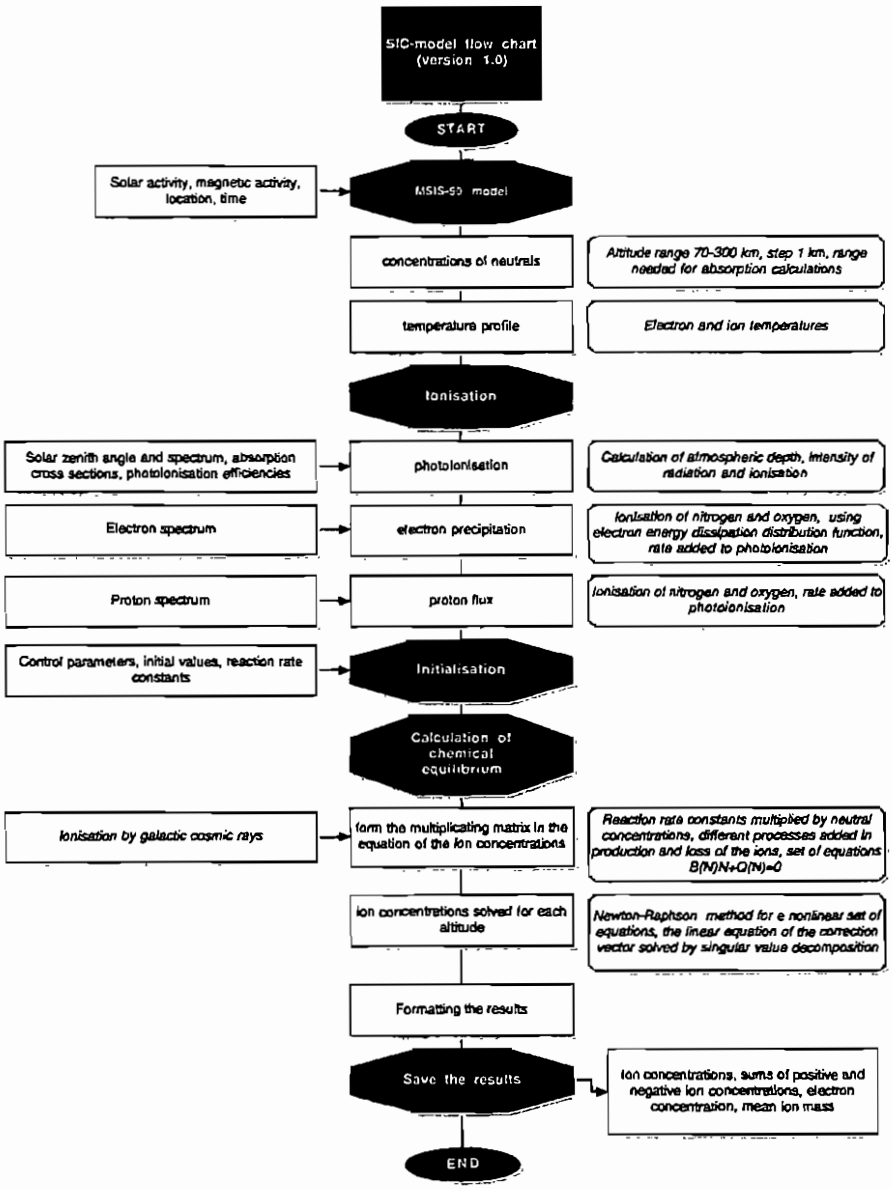

Figure 5. Flow chart of version 1.0 of the SIC-model. Additionally, the current version 2.1 contains a user friendly interface and possibility to add and remove reactions and components.

Comparison between Figures 6 and 8a shows that when counting for the difference between the zenith angles 65° and 28.1°, all the essential features of D-region ionic composition are present in the model results. The total electron density is increasing from a few hundreds per cubic centimeter at 80 km, to a few tens of thousands at 90 km, the SIC-model values being a bit smaller due to the higher zenith angle. The difference in the zenith angles also affects the O_2^+ concentrations, which for the SIC-model are much lower at the lowest heights. This is caused by less creation of $O_2(^1\Delta_g)$, which is the source of O_2^+ ions below 80 km. Above 90 km, the importance of $O_2(^1\Delta_g)$ is decreasing and direct ionization of O_2 takes over. The minimum in SIC-model values results from the used neutral concentrations, which for O_2 and $O_2(^1\Delta_g)$ were taken from different sources. The sharp ledge region, present at 84 km in the experimental results, is not so prominent in the SIC-model electron density profile. A clear sign of the ledge is seen in the NO^+ profile. One should note that in the neutral NO values, such a feature was not introduced. The sharp appearance of cluster ions is smoothed in the SIC-model and the different species start to appear at different heights. At lowest heights, the most abundant ion in the SIC-model is $H^+(H_2O)_4$. The ion $NO^+(H_2O)$ is the dominant cluster around 90 km. The concentrations of both species agree well with the experimental values at these heights, but at the region around 80 km and slightly above the NO^+, clusters dominate in the SIC-model as opposed to the experimental findings. The cluster ion concentrations are, however, so strongly dependent on water and nitric oxide concentrations, and temperature profiles, that this behavior can follow the assumed neutral structure.

Comparing Figures 7 and 8b, we see that for the negative ions, the main features are the same for both models. This should not be surprising since the negative ion chemistry in the model by Thomas and Bowman was taken as the starting point when creating the SIC-model. The neutral properties are treated differently, which should also be seen in the results. At the height of 70 km, the most abundant negative ion is HCO_3^-. Its concentration is around 100 per cubic centimeter in both models. Also the next abundant ions, CO_3^- and O_2^-, have the same concentration, i.e., around 10 per cubic centimeter. However, it appears that the for the ions O^-, NO_2^- and O_3^- the same values are achieved at higher heights in the SIC-model (the form of the profile being the same), and for the ions NO_3^- and CO_4^- there is a similar shift in the other direction. The greatest difference between the models is seen at the higher end of the negative ion region in the concentration of HCO_3^-, where there is a local maximum around 80 km in the Thomas and Bowman model. The reactions of HCO_3^- are different from those of the other ions in the sense that HCO_3^- is not producing other ions through any reactions. The ion is located in the end of a reaction chain and is formed from other negative ions through reactions with neutrals.

The first practical application of the SIC-model, after some checking and updating of the test version, was a comparison by *Burns et al.* [1991] with EISCAT incoherent scatter radar measurements during geomagnetically quiet time when one could assume the absence of electron precipitation. The details of the comparison are given in the work by *Burns et al.*, and we quote here only the main assumptions in the study and the results of applying the SIC-model. This study also included use of the Mitra-Rowe six-ion scheme [*Mitra and Rowe*, 1972], thus giving reliable background for evaluating the usefulness of the complicated 35-ion scheme. The electron density profiles measured by the EISCAT radar were used as constraints in a modeling effort to deduce the neutral nitric oxide profile. Both UHF and VHF radar measurements were used but the main emphasis was on the UHF data on 23rd of August, 1985. Electron density profiles, representative of quiet time, were carefully selected for three solar zenith angle values: 57.8°, 70.8° and 83.7°. First, the solar flux was adjusted so that a reasonable fit between model and experimental electron densities was achieved at E-region heights for zenith angle 57.8°. This meant multiplying the reference spectrum of the SIC-model (Table 1) by a factor 1.3 except for the *Lyman* $-\alpha$ flux, which was left untouched. Next, the initially assumed height profile of NO concentration was adjusted until a satisfactory fit at all altitudes was found. This NO concentration was then used in modeling the electron density profile at zenith angles

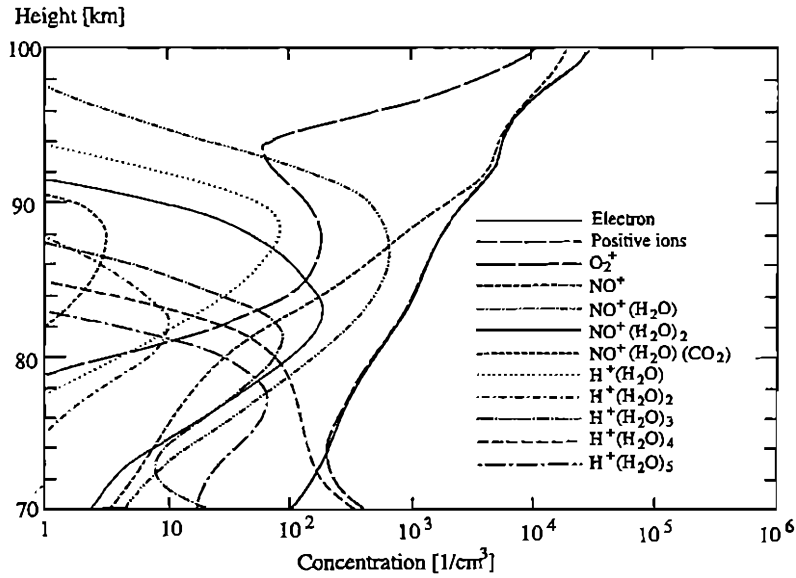

Figure 6. SIC-model positive ion concentrations for 50°N, 20°E on 23.04.1976 at 1500 UT.

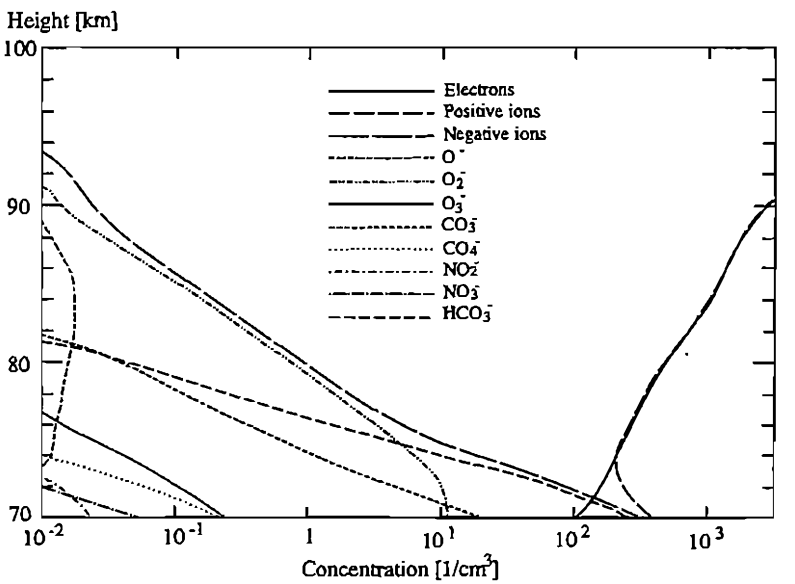

Figure 7. SIC-model negative ion concentrations for 50°N, 20°E on 23.04.1976 at 1500 UT.

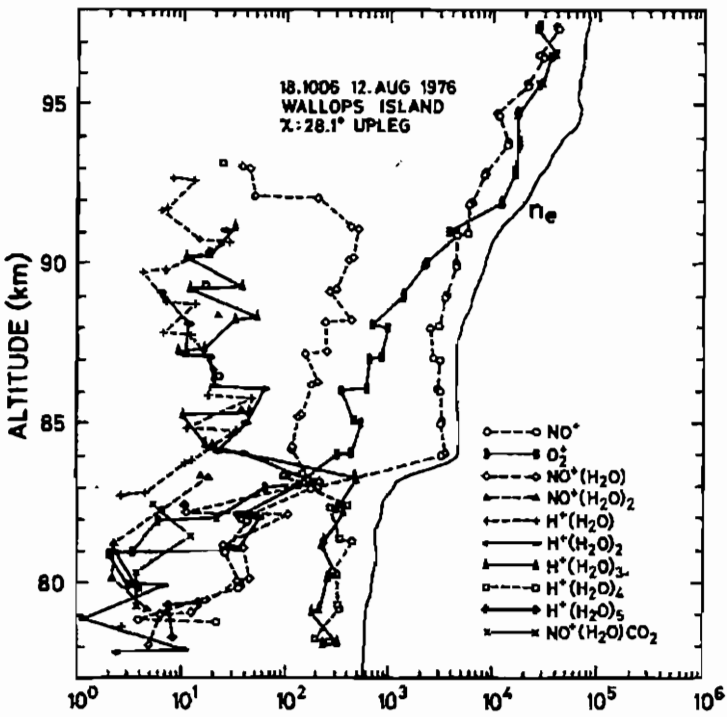

Figure 8a. D-region ion and electron concentrations at Wallops Island on 12 August 1976 (zenith angle 28.1°) [*Kopp et al.*, 1984].

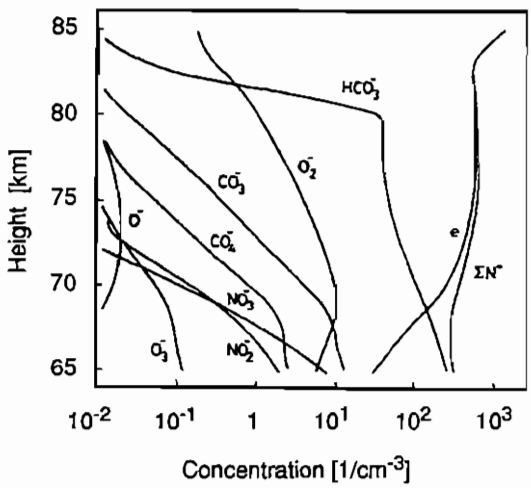

Figure 8b. Negative ion concentrations at noon in the model by *Thomas and Bowman* [1985].

70.8° and 83.7°. All the minor constituent concentrations were assumed to be constant for the range of solar zenith angles studied.

The final results for both models are shown in Figure 9. The adjustment of solar flux and NO concentration results in an increase in NO^+ concentration in the height interval concerned. Correspondingly, the O_2^+ concentration decreases because NO plays an important role in the loss of O_2^+. Other parameters, such as the effective loss rate, the negative ion to electron density ratio and the hydrated ion concentration, remain relatively unchanged. The electron density profiles from two independent model schemes agreed reasonably well with each other; see *Burns et al.* [1991]. Both models produced the experimentally-seen functional dependence on solar zenith angle. The deduced NO concentrations resemble those observed at geomagnetically disturbed times. This is explained by auroral activity in the post-midnight and morning sectors [*Burns et al.*, 1990, *Hargreaves and Devlin*, 1990] on 23 August, occurring just a few hours before the time period selected for this study. Since energetic particle precipitation into the thermosphere can enhance NO concentration [e.g. *Rusch and Barth*, 1975; *Swider and Narcisi*, 1977], and transport is known to be the dominant factor controlling the concentration of NO at D-region altitudes, as compared with the mean lifetime with respect to chemical processes [e.g. *McEwan and Phillips*, 1975], increased NO concentrations would be expected in the time scale which is relevant in our case. One should note that both models show the same feature in the resulting NO concentrations, after adjustments of solar flux and initial NO profile. The adjustments were done independently for the two models.

Comparison of SIC-model and experiment during high energy electron precipitation is shown in Figure 10. Fig. 10a shows the measured differential flux of electrons as function of electron energy [*Torkar et al.*, 1985]. The sounding rocket was launched from Andoya, Norway, at 03.25 UT on 28 November 1980. The given form of electron energy spectrum is fitted by an exponential form with two parameters just to simplify the input to the calculations. The parameterized form $0.8 \cdot 10^9 e^{-E/31keV}\ m^{-2}s^{-1}sr^{-1}keV^{-1}$ underestimates the flux at energies less than 30 keV, but fits well with the given form at higher energies. The ion production rates

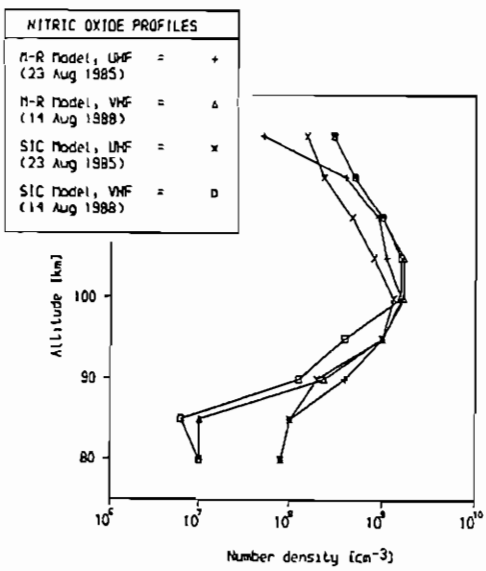

Figure 9. The deduced NO concentration above Tromsø, Norway, on 12 August 1985 and 14 August 1988, from two independent ion chemistry models.

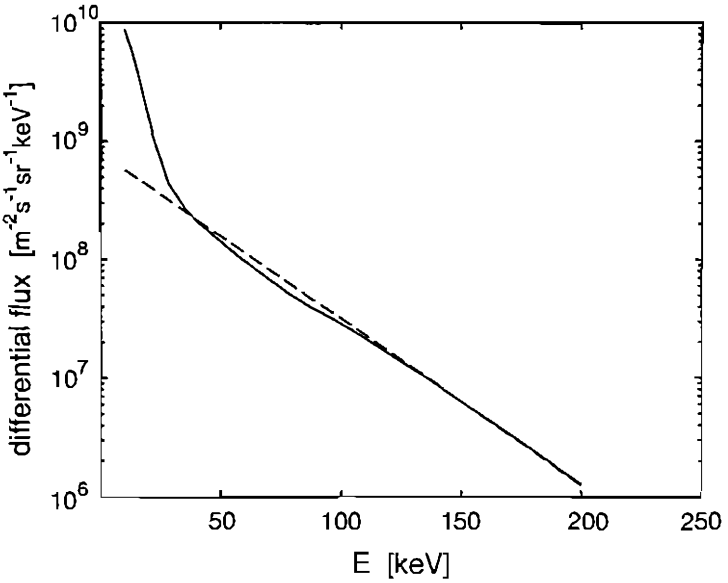

Figure 10a. Differential energy spectrum of electrons measured on 28 November 1980 at 0325 UT above Andoya, Norway (*Torkar et al.* 1985, solid line) and the exponential fit with two parameters ($0.8 \cdot 10^{9} e^{-E/31keV}$, dashed line), to be used as input to the SIC-model.

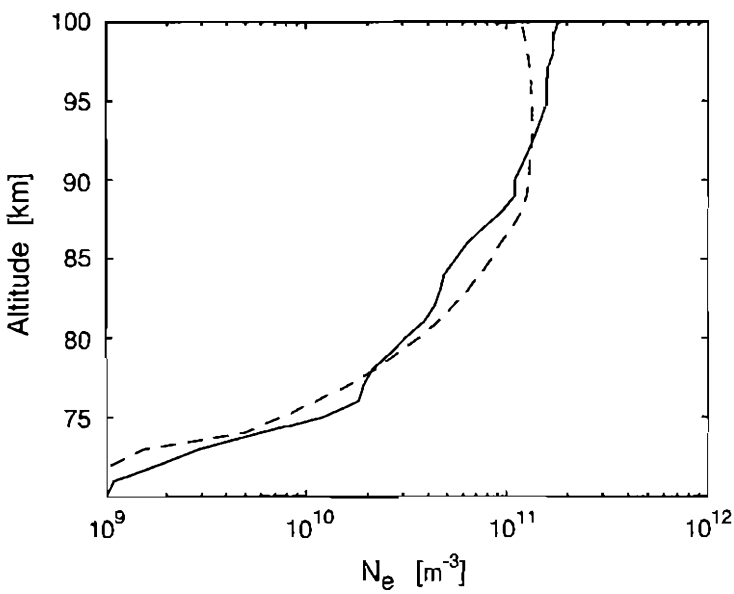

Figure 10b. The experimental electron density profile (*Torkar et al.*, 1982, solid line) on 28 November 1980 at 0325 UT above Andoya, Norway, corresponding to the differential energy spectrum of electrons in Figure 10a, together with the electron density profile given by the SIC-model (dashed line) for the parameterized form of the same energy spectrum.

were calculated according to the formulation described in section 2, using the fitted differential energy spectrum and assuming an isotropic electron flux over pitch angles from 0° to 80°. The electron density from the SIC-model is shown in Figure 10b as the dashed line. The experimental electron density profile, measured during the same rocket flight as for the differential energy spectrum of electrons, is shown as the solid line [*Torkar et al.*, 1982]. From Figure 10, we may conclude that the SIC-model gives a valid description of the electron density profile. The agreement between model and experiment appears excellent. At the altitudes approaching 100 km, the SIC-model gives lower values. This is consistent with the fact that the parameterization of electron energy spectra underestimates the flux at lower energies.

An example of the use of the SIC-model during a solar proton event was given by *Turunen* [1993] (for details, see the original paper). Ion production rates were first calculated from the GOES-7 satellite data. The measured incoherent scatter data were then used as constraints in a self-consistent calculation where temperature was adjusted to make the model fit the data. Note that the neutral density was also varied according to the temperature variation. Figure 11 shows the resulting neutral temperature profiles above Tromsø, Norway, for two selected times, 0005 UT and 0255 UT, on 14 August 1989. For comparison, a mean profile from lidar measurements at Andoya, Norway, during the night 14/15 August 1989 [*Hansen et al.*, 1991], as well as an extrapolated temperature profile from the MSIS-86 model, are also shown in Figure 11. The deduced mesopause temperatures closely match the lidar temperature average. Also, the sharp gradient above mesopause is present in the deduced temperatures. The gradients around mesopause even match those of the lidar temperature average. However, the altitudes of the mesopause are seen to differ by about two kilometers. One should note that the lidar and radar measurements were not co-located. The distance between Andoya and Tromsø is 129 km.

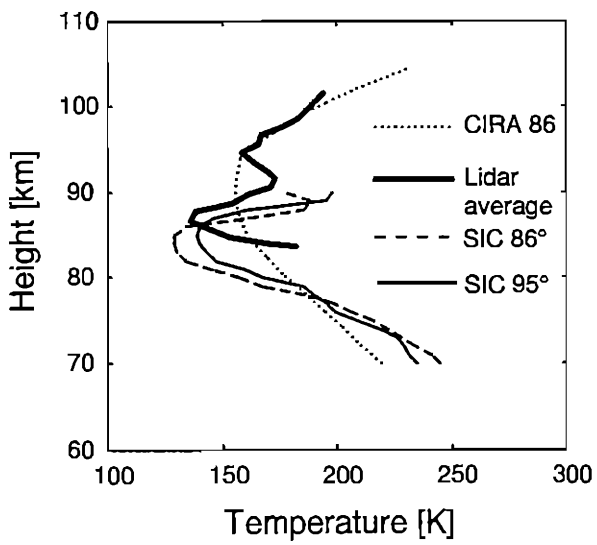

Figure 11. The deduced temperature profiles above Tromsø, Norway, at 0005 UT and 0255 UT (thin solid and dashed lines, respectively) on 14 August 1989, and an average profile (thick solid line) from lidar measurements at Andoya, Norway, during the night 14/15 August 1989. The extrapolated MSIS-86 model temperature profile, which was used as starting point in the calculations, is also shown (dotted line).

6. Uncertainties and Limitations

It is clear that a detailed ion chemical scheme with many reactions is subject to the uncertainties and inaccuracies in the reaction rate constants. Moreover, when the number of components is increased, the degrees of freedom in comparisons with experimental data are also increased. One could imagine that it would be possible to reproduce any experimental finding with a suitable combination of the uncertain input parameters. This should always be kept in mind when using models similar to the presented model.

There are some omissions in the physical principles which might restrict the use of the present model. First, it is a steady-state model. We cannot answer the question: What happens during transient phenomena, such as a sudden local high energy electron precipitation? The information available from the model is useful in comparisons over long time periods and for slowly varying events. In general, comparisons with momentary measurements are difficult since knowledge about neutral atmosphere is based on empirical, averaged models. Before using a time dependent code, we aim to at least include hard X-rays and scattered radiation at night as ionization sources, and heavier cluster ions, clusters of negative ions, and metallic ions as new ions in the model. Although the model gives altitude profiles of ion concentration as result, its mathematical nature is 0-dimensional. Transport phenomena are omitted. The chemistry of minor neutral constituents is not included in the model, but the neutral atmosphere is taken only as a static background. If the effect of particle fluxes is considered in detail, one should care about the dissociation of neutral minor constituents also. For investigations around sunset and sunrise times, the effects of neutral photochemistry should be included into the calculations.

The model was tested mainly in the altitude range from 70 km to 100 km. The altitude range could easily be expanded into the E-region if the odd nitrogen species were treated more carefully.

7. Model Availability

The early versions of the model were based on a FORTRAN code, which we do not support anymore. The present version of the model is coded in *Matlab* language, which makes the model user friendly, easy to adopt and easy to be tailored to specific needs. A new version for *Matlab 4.2* is currently being written, with emphasis on a user friendly interface to add and remove reactions. The code runs on computers which can run *Matlab*. The code is not optimized for speed, but this could be done by any user. The *Matlab 4.2* -version will be made available to anyone interested. The authors welcome also any collaboration in adding new ion components and reactions, and improving the model. Currently, we are also developing a time dependent code to be used in analysis of combined incoherent scatter radar and heating experiments in the D-region.

8. References

Adams, G. W. and L. R. Megill, *Planet. Space Sci., 15*, 111, 1967.
Albritton, D. L., *Atom. Data Nucl. Data Tables, 22*, 1 , 1978.
Adams, N. G., D. Smith, J. F. Faulson, *J. Chem. Phys., 72*, 288, 1980.
Alcayde, D., *Ann. Geophys., 37*, 515, 1981.
Bates, D. R., *Planet. Space Sci., 36*, 55, 1988.
Biondi, M. A., *Mol. Phys. 4*, 85, 1973.
Brasseur, G. and P. DeBaets, *J. Geophys. Res., 91*, 4025, 1986.

Brasseur, G. and S. Solomon, *Aeronomy of the Middle Atmosphere*, D. Reidel Publishing Company, Holland, 1984.
Burns, C. J., W. G. Howarth, and J. K. Hargreaves, *J. Atmos. Terr. Phys., 52*, 205, 1990.
Burns, C. J., E. Turunen, and H. Matveinen, *J. Atmos. Terr. Phys., 53*, 115, 1991.
Böhringer, H. and F. Arnold, *J. Chem. Phys., 77*, 5534, 1982.
Chakrabarty, D. K., P. Chakrabarty, and G. Witt, *J. Atmos. Terr. Phys., 40*, 437, 1978.
Cosby, P. C., J. H. Ling, and J. R. Peterson, *J. Chem. Phys., 65*, 5267, 1976.
Dhendhanoo, S. and R. Johnsen, *Planet. Space Sci., 31*, 933, 1983.
DNA, *Defense Nuclear Agency Reaction Rate Handbook*, General Electric, Santa Barbara, 1972.
Dunkin, D. B., F. C. Fehsenfeld, A. L. Schmeltekopf, and E. E. Ferguson, *J. Chem. Phys., 54*, 3817, 1971.
Dymek, M. K., *Low Latitude Aeronomical Processes*, ed. by A. P. Mitra, COSPAR Symp. Ser., 8, 115. Pergamon Press, Oxford and New York, 1980.
Eisner, P. N. and M. N. Hirsh , *Phys. Rev. Lett., 26*, 874, 1971.
Fehsenfeld, F. C., M. Mosesman, and E. E. Ferguson, *J. Chem. Phys., 55*, 2120, 1971.
Fehsenfeld, F. G., C. J. Howard, W. J. Harrop, and E. E. Ferguson, *J. Geophys. Res., 80*, 2229, 1975.
Ferguson, E., F. C. Fehsenfeld, and D. L. Albritton, *Gas Phase Ion Chemistry*, ed. by M.T. Bowers, Academic Press, *1*, 45, 1979.
Hansen, G., U-P. Hoppe, E. Turunen, and P. Pollari, *Radio Sci., 26*, 1153, 1991.
Hargreaves, J. K and T. Devlin, *J. Atmos. Terr. Phys., 52*, 193, 1990.
Hargreaves, J. K., H. Ranta, A. Ranta, E. Turunen and T. Turunen, *Planet. Space Sci., 35*, 947, 1987.
Heaps, M. G., *Planet. Space Sci., 26*, 513, 1978.
Hedin, A. E., *J. Geophys. Res., 96*, 1159, 1991.
Heroux, L. and H. E. Hinteregger, *J. Geophys. Res., 83*, 5305, 1978.
Huang, C.-M., M. Whitaker, M. A. Biondi, and R. Johnsen, *Phys. Rev., 18*, 64, 1978.
Huffman, R. E., D. E. Paulsen, and J. C. Larrabee, *J. Geophys. Res., 76*, 1028, 1971.
Johnsen, R., *Int. J. Mass. Spec. Ion Proc., 81* , 67, 1987
Jones, A. V., *Aurora*, D. Reidel Publishing Company, Dordrecht, Holland, 1974.
Kopp. E. and U. Herrmann, *Annales Geophysicae, 2*, 83, 1984.
Lau, J. K., S. Ikuta, and P. Kebarle, *J. Am. Chem. Soc., 104*, 1462, 1982
Lean, J. L. and A. Shumanich, *J. Geophys. Res., 88*, 5751, 1983.
Lelevier, R. E. and L. M. Branscomb, *J. Geophys. Res., 73*, 27, 1968.
McEwan, M. J. and L. F. Phillips, *Chemistry of the Atmosphere*, Edward Arnold Ltd., London, 1975.
McFarland, M., D. L. Albritton, F. C. Fehsenfeld, E. E. Ferguson, and A.L. Schmeltekopf, *J. Geophys. Res., 79*, 2925, 1974.
McGowan, J. Wm. and J. B. A. Mitchell, *Electron - Molecule Interactions and their Applications, ed.* by L. G. Christophoron, Academic Press, *2*, 65 1984.
Mitra, A. P. and J. N. Rowe, *J. Atmos. Terr. Phys., 34*, 795, 1972.
Moseley, J. T., P. C. Cosby, and J. R. Peterson , *J. Chem. Phys., 65*, 2512, 1976.
Mul, P. M. and J. W. McGowan, *Journal of Physics B*, 159, 1979.
Ohshio, M., R. Maeda , and H. Sakagami, *J. Radio Res. Lab., 13*, 245, 1966.
Paulsen, D. E., R. E. Huffman, and J. C. Larrabee, *Radio Science, 7*, 51, 1972.
Payzant, J. D. and P. J. Kebarle, *J. Chem. Phys., 56*, 3482, 1972.
Phelps, A. V., *Can. J. Chem., 47*, 1783, 1969.
Press, W. H., B. P. Flannery, S. A. Teukolsky, and W. T. Vetterling, *Numerical Recipes, The Art of Scientific Computing*, Cambridge University Press, New York, USA, 1986.
Rakshit, A. B. and P. Warneck, *J. Chem. Phys., 73*, 5074, 1980.
Rees, M. H., *Physics and Chemistry of the Upper Atmosphere*, Cambridge University Press, Cambridge, Great Britain, 1989.
Rees, M. H., *Planet. Space Sci., 11*, 1209, 1963.
Reid, G. C., *Planet. Space Sci., 25*, 275, 1977.

Rodrigo, R., J. J. Lopez-Moreno, M. Lopez-Puertas, F. Moreno, and A. Molina, *Planet. Space Sci., 34*, 723, 1986.
Rusch D. W. and C. A. Barth, *J. Geophys. Res., 80*, 3719, 1975.
Smith, D. and M. J. Church, *Planet. Space Sci., 25*, 433, 1977.
Smith, D., N. G. Adams, and M. J. Church, *Planet. Space Sci., 24*, 697, 1976.
Smith, G. P., L. C. Lee, P. C. Cosby, J. R. Peterson, and J. T. Moseley, *J. Chem. Phys., 68*, 3818, 1978.
Smith, G. P., L. C. Lee, and P. C. Cosby, *J. Chem. Phys., 71*, 4464, 1979.
Smith, D., N. G. Adams, and E. Alge, *Planet. Space Sci., 29*, 449, 1981.
Stelman, D., J. L. Moruzzi, and A. V. Phelps, *J. Chem. Phys., 56*, 4183, 1972.
Swider, W. and R. S. Narcisi, *J. Geophys. Res., 80*, 655, 1975.
Swider, W. and R. S. Narcisi, *J. Atmos. Terr. Phys., 45*, 493, 1983.
Thomas, L., *J. Atmos. Terr. Phys., 38*, 1345, 1976.
Thomas, L. and M.R. Bowman, *J. Atmos. Terr. Phys., 47*, 547, 1985.
Torkar, K. M. and M. Friedrich, *J. Atmos. Terr. Phys., 45*, 369, 1983.
Torkar, K. M., M. Friedrich, and W. Riedler, *Internal Report INW 8211*, Technical University Graz, 1982.
Torkar, K. M., A. Urban, J. Bjordal, J. Å. Lundblad, F. Søraas, L. G. Smith, A. Dumbs, B. Grandal, J. C. Ulwick, and R. P. Vancour, *J. Atmos. Terr. Phys., 47*, 61, 1985.
Torr, M. R., D. G. Torr, R. A. Ong, and H. E. Hinteregger, *Geophys. Res. Lett., 6*, 771, 1979.
Truby, F. K., *Phys. Rev. A, 6*, 671, 1972.
Turunen, E., *J. Atmos. Terr. Phys., 55*, 767-781, 1993.
Turunen, E., H. Matveinen and H. Ranta, Sodankylä Ion Chemistry (SIC) Model. *Sodankylä Geophysical Observatory Report No. 49*, Sodankylä, Finland, 1992.
Viggiano, A. A. and J. F. Paulson, *Swarms of Ions and Electrons in Gases*, eds. Lindinger, W., T. D. Mark, and F. Howorka, Springer, 218, 1984.
Whitten, R. C. and I. G. Poppoff, *Fundamentals of Aeronomy*, Wiley, New York, 1971.
Wisemberg, J. and G. Kockarts, *J. Geophys. Res., 85*, 4642, 1980.

Steady-State D-Region Model

W. Swider

Phillips Laboratory, Geophysics Directorate
29 Randolph Road
Hanscom AFB, MA 01731-3010

1. Introduction

The D-region has the most complex chemistry of any ionospheric region by far, and to this day, its chemistry has not been elucidated fully. Nevertheless, there has been success in modeling the D-region, especially the electron concentrations of the disturbed D-region. This achievement has been made possible largely because ion-ion recombination (neutralization) coefficients all appear to be near 10^{-7} cm^{-3} s^{-1} [*Smith et al.*, 1976] regardless of the type of ions involved. Hence, even though the negative ion chemistry is still unsatisfactory as to the concentrations of the various individual ions, the electron concentration can be determined with some confidence, as seen in Figure 1, where the model to be discussed is shown to match well the upleg data for a Solar Proton Event (SPE) or Polar Cap Absorption (PCA) event.

2. Mathematical Formulation

The formation of the model is purely a sequence of algebraic expressions which yield solutions, after sufficient iterations, for the electron concentration, [e] and all the individual ions currently in the model; 21 positive ions and 8 negative ions. Especially for disturbed events, but even for quiet conditions, D-region processes are sufficiently rapid, compared with the complexity of the chemistry, that steady-state conditions are appropriate, except during twilight.

Transport is ignored. Collision frequencies may easily be included for calculating the absorption of electromagnetic waves [*Swider and Chidsey*, 1977].

3. Numerical Solution Procedure

An iterative scheme was developed to solve for all species concentrations. Using initial concentrations for electrons, [e], and the positive ion sum, SP, the individual negative ion concentrations are first determined and summed, NSUM. Then the positive ions are individually calculated and summed, PSUM. A new

$$[e] = \{\text{previous } [e] + \text{PSUM}/(1+\lambda)\}/2 \qquad (1)$$

where λ = NSUM/previous [e], and a new

$$\text{SP} = \{\text{previous } [e] + \text{NSUM} + \text{PSUM}\}/2 \qquad (2)$$

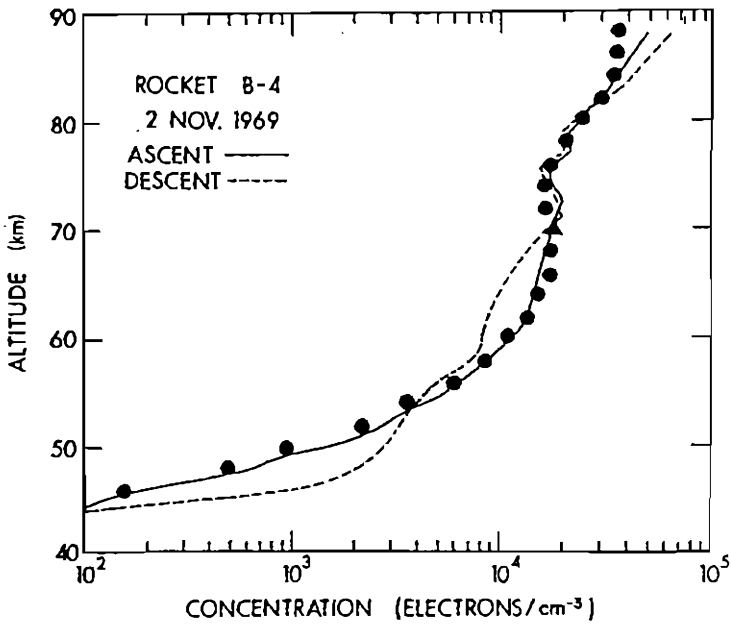

Figure 1. Measured and computed electron concentrations for Rocket B-4 launched at 2110 UT, 2 November 1969. The solar zenith angle was 83.2°.

are then determined. This sequence is repeated until PSUM equals NSUM + [e] within a specified precision. For the November, 1969, SPE, not more than nine iterations were required to reach ± 1% for altitudes 40-90 km.

Initial daytime concentrations were derived from $[e] = (q/\psi)^{1/2}$, where ψ, the effective recombination coefficient, is that derived from the November 2-5, 1969, SPE [*Swider and Dean*, 1975]. The values determined (in units of $cm^{-3}\ s^{-1}$) were 3.4×10^{-7} (85 km), 4.8×10^{-7} (80 km), 1.1×10^{-6} (75 km), 1.8×10^{-6} (70 km), 4×10^{-6} (65 km), 8.8×10^{-6} (60 km), 5.5×10^{-5} (55 km), 5.1×10^{-4} (50 km), and 3.5×10^{-2} (45 km).

Initial nighttime electron concentrations were derived from [*Swider et al.*, 1971]

$$[e] = \{(L(A)/2\alpha_D)^2 + q/\alpha_D\}^{1/2} - L(A)/2\alpha_D \qquad (3)$$

where α_D, the mean (ion-electron) recombination coefficient is $4 \times 10^{-7}\ cm^{-3}\ s^{-1}$, and where

$$L(A) = k_{61}[O_2]^2 + k_{62}[O_2]\ [N_2] \qquad (4)$$

is the loss rate (s^{-1}) for electrons through attachment to O_2 with k_{xx} a specific reaction rate.

Initial total positive ion concentrations were determined from

$$SP = \{q(5[O]/\alpha_D + [O_3]/\alpha_i)/(5[O] + [O_3])\}^{1/2} \qquad (5)$$

with α_i the mean ion-ion recombination coefficient, $6 \times 10^{-8}\ cm^{-3}\ s^{-1}$.

4. Model Inputs

The following neutral concentrations are required: O, O_2, O_3, $O_2(^1\Delta)$, N_2, CO_2, H_2O, NO and NO_2, T (temperature) and total neutral concentration, M. The relationships $[N_2] = 0.7808[M]$, $[O_2] = 0.2095[M]$, $CO_2 = 3 \times 10^{-4}[M]$ may be used. Values for total ionization production, q, must be provided. For quiet conditions in the daytime, q may be derived from the photoionization of NO by H Lyα, nominally [*Swider*, 1978]

$$q(NO^+) = 6 \times 10^{-7}[NO]\exp\{-10^{-20}[O_2]H\} \qquad (6)$$

where H is the scale height of the atmosphere.

Processes and rate coefficients are listed in Tables 1 and 2. Photodissociation rates were multiplied by unity for daytime and zero for nighttime. Choices for α_i and α_D were given above.

5. Model Outputs

Concentrations of electrons, 21 positive ions and 8 negative ions are determined to two significant figures. Also printed are q, λ, ψ, L(A), PSUM, NSUM + [e], initial [e], and initial SP.

6. Uncertainties and Limitations

The model has been fitted well to the November 1969 PCA event [*Swider and Foley*, 1978; *Swider*, 1988]. Indeed, for electron concentrations under disturbed conditions, the day and night empirical expressions given above for initial [e] may be sufficiently accurate [*Swider*, 1988]. For quiet conditions, the accuracy of the outputs is less certain, in part because D-region data for quiet conditions are also of low accuracy.

7. Availability of tbe Model

The model [*Swider and Foley*, 1978] may be ordered from the National Technical Information Service.

8. References

Smith, D., N. G. Adams, and M. J. Church, *Planet. Space Sci., 24*, 697-703, 1976.
Swider, W., *J. Geophys. Res., 83*, 4407-4410, 1978.
Swider, W., *PAGEOPH, 127*, 403-414, 1988.
Swider, W. and I. L. Chidsey, Jr., *J. Geophys. Res., 82*, 1617-1619, 1977.
Swider, W. and W. A. Dean, *J. Geophys. Res., 80*, 1815-1819, 1975.
Swider, W. and C. I. Foley, AFGL-TR-78-0155, 1978.
Swider, W., R. S. Narcisi, T. J. Keneshea, and J. C. Ulwick, *J. Geophys. Res., 76*, 4691-4694, 1971.

Table 1. Positive Ion Reactions. Units for photo-processes, two-body and three-body processes are sec^{-1}, cm^3/sec and cm^6/sec, respectively. The various process coefficients, $k = A(T/300)^B e^{D/T}$, are presented in the format A B D

										A	B	D
4	O4+	+	HV		=	O2+	+	O2		3.00E-01		
5	O2+.H2O	+	HV		=	O2+	+	H2O		6.00E-01		
6	O2+	+	NO		=	NO+	+	O2		4.50E-10		
7	O2+	+	O2	+ O2	=	O4+	+	O2		3.90E-30	-3.2	
8	O4+	+	O		=	O2+	+	O3		3.00E-10		
9	O4+	+	H2O		=	O2+H2O	+	O2		1.50E-09		
10	O2+H2O	+	H2O		=	H3O+OH	+	O2		1.00E-09		
11	O2+H2O	+	H2O		=	H3O+	+	OH	+ O2	2.00E-10		
12	H3O+OH	+	H2O		=	H5O2+	+	OH		1.40E-09		
13	H3O+	+	H2	+ N2	=	H3O+.N2	+	N2		1.40E-30	-2.0	
14	H3O+.N2	+	CO2		=	H3O+.CO2	+	N2		1.00E-09		
15	H3O+.Co2	+	H2O		=	H5O2+	+	CO2		1.00E-10		
16	H5O2+	+	CO2	+ M	=	H5O2+.CO2	+	M		3.00E-30		
17	H5O2+.CO2	+	H2O		=	H7O3+	+	CO2		1.00E-10		
18	H3O+	+	H2O	+ M	=	H5O2+	+	M		3.50E-27	-3.0	
19	H5O2+	+	H2O	+ M	=	H7O3+	+	M		2.20E-27	-3.0	
20	H7O3+	+	H2O	+ M	=	H9O4+	+	M		2.30E-27	-3.0	
21	NO+	+	CO2	+ N2	=	NO+CO2	+	N2		3.00E-29	-2.0	
22	NO+CO2	+	H2O		=	NO+H2O	+	CO2		5.00E-10		
23	NO+H2O	+	H2O	+ N2	=	NO+(H2O)2	+	N2		1.10E-27	-4.7	
24	NO+(H2O)2	+	H2O	+ N2	=	NO+(H2O)3	+	N2		1.50E-27	-4.7	
25	NO+(H2O)3	+	H2O		=	H7O3+	+	HNO2		7.00E-11		
26	NO+	+	E		=	N	+	O		4.00E-07	-1.0	
27	O2+	+	E		=	O	+	O		2.00E-07	-1.0	
28	O4+	+	E		=	O2	+	O2		2.00E-06		
29	O2+.H2O	+	E		=	O2	+	H2O		2.00E-06		
30	H3O+.OH	+	E		=	2H2O				2.00E-06		
31	H3O+	+	E		=	H2	+	OH		1.00E-06		
32	H5O2+	+	E		=	H2O	+	H2	+ OH	2.00E-06		
33	H7O3+	+	E		=	2H2O	+	H2	+ OH	4.00E-06		
34	H9O4+	+	E		=	3H2O	+	H2	+ OH	5.00E-06		
35	H3O+.N2	+	E		=	H	+	H2O	+ N2	2.00E-06		
36	H3O+.CO2	+	E		=	H	+	H2O	+ CO2	2.00E-06		
37	H5O2+.CO2	+	E		=	H	+	2H2O	+ CO2	3.20E-06		
38	NO+.CO2	+	E		=	NO	+	CO2		1.50E-06		
39	NO+H2O	+	E		=	NO	+	H2O		1.50E-06		
40	NO+(H2O)2	+	E		=	NO	+	2H2O		3.00E-06		
41	NO+(H2O)3	+	E		=	NO	+	3H2O		4.50E-06		
42	O4+	+	M		=	O2+	+	O2	+ M	3.30E-06	-4.0	-5.03E+03
43	NO+	+	M2	+ N2	=	NO+.N2	+	N2		2.00E-31	-4.4	
44	NO+.N2	+	CO2		=	NO+.CO2	+	N2		2.00E-09	0.0	
45	NO+.H2O	+	N2	+ N2	=	NO+H2ON2	+	N2		2.00E-31	-4.4	
46	NO+H2ON2	+	CO2		=	NO+H2OCO2	+	N2		2.00E-09	0.0	
47	NO+H2OCO2	+	H2O		=	NO+.2H2O	+	CO2		2.00E-09	0.0	
48	NO+.2H2O	+	N2	+ N2	=	NO+2H2ON2	+	N2		2.00E-31	-4.4	
49	NO+2H2ON2	+	CO2		=	NO+2H2OCO2	+	N2		2.00E-09	0.0	
50	NO+2H2OCO2	+	H2O		=	NO+.3H2O	+	CO2		2.00E-09	0.0	
51	NO+.N2	+	N2		=	NO+	+	N2	+ N2	1.00E-08	-4.4	-2.10E+03
52	H9O4+	+	M		=	H7O3+	+	H2O	+ M	1.20E-01	-4.0	-8.80E+03

Table 2. Negative Ion Reactions. Units and format are as for Table 1

									A	B	D
60	O2–	+	O3		=	O3–	+	O2		5.00E–10		
61	O2	+	E	+ O2	=	O2–	+	O2		1.40E–29	–1.0	–6.00E+02
62	O2	+	E	+ N2	=	O2–	+	N2		1.00E–31		
63	O2–	+	O		=	O3	+	E		1.50E–10		
64	O2–	+	O		=	O–	+	O2		1.50E–10		
65	O2–	+	O2(1Δ)		=	O2	+	O2	+ E	2.00E–10		
66	O2–	+	O2	+ O2	=	O4–	+	O2		3.50E–31	–1.0	
67	O4–	+	CO2		=	CO4–	+	O2		4.30E–10		
68	CO4–	+	O3		=	O3–	+	CO2	+ O2	1.30E–10		
69	CO4–	+	NO		=	NO3–	+	CO2		4.80E–11		
70	CO4–	+	O		=	CO3–	+	O2		1.50E–10		
71	O3–	+	O		=	O2–	+	O2		3.20E–10		
72	O3–	+	CO2		=	CO3–	+	O2		5.50E–10		
73	CO3–	+	O		=	O2–	+	CO2		1.10E–10		
74	CO3–	+	NO		=	NO2–	+	CO2		1.10E–11		
75	CO3–	+	NO2		=	NO3–	+	CO2		2.00E–10		
76	NO2–	+	O3		=	NO3–	+	O2		9.00E–11		
77	O–	+	O2	+ O2	=	O3–	+	O2		1.10E–30	–1.0	
78	O–	+	O		=	O2	+	E		2.00E–10		
79	O–	+	O2(1Δ)		=	O3	+	E		3.00E–10		
80	O–	+	O3		=	O3–	+	O		4.40E–10		
81	O–	+	O3		=	O2–	+	O2		4.40E–10		
91	O2–	+	HV		=	O2	+	E		6.60E–01		
92	O–	+	HV		=	O	+	E		2.80E+00		
93	CO4–	+	HV		=	CO2	+	O2	+ E	6.00E–01		
94	CO3–	+	HV		=	CO2	+	O–		4.00E–01		
95	NO2–	+	HV		=	NO2	+	E		6.00E–02		
96	NO3–	+	HV		=	NO2–	+	O		6.00E–02		
97	NO3–	+	HV		=	NO	+	O2	+ E	4.40E–03		

E-Region Time-Dependent Chemical Model

W. Swider

Phillips Laboratory, Geophysics Directorate
29 Randolph Road
Hanscom AFB, MA 01731-3010

1. Introduction

A modeling technique of *Keneshea* [1967] was applied by *Keneshea, Narcisi and Swider* [1970] to the E-region for detailed comparisons with ionic compositions measured at twilight (two at sunset and two at sunrise). The experiments were conducted under normal (quiet) conditions at mid-latitudes, near Eglin Air Force Base in Florida during April, 1967. This month was one of moderate solar activity with a mean sunspot number of 69.5.

2. Mathematical Formulation

The model was set up to simultaneously solve a set of coupled partial differential equations

$$\frac{\partial n_i}{\partial t} = Q_i - L_i \tag{1}$$

where n_i is the number density of the i species with Q_i and L_i the respective production and loss terms for that species, which terms commonly include other species concentrations.

Concentrations were calculated for: negative ions O^-, O_2^-, O_3^-, NO_2^-, NO_3^-, and CO_3^-; positive ions O^+, O_2^+, N_2^+ and NO^+; and electrons, e. In addition, differential equations were solved for the following neutral species: NO, N, NO_2, O, N_2O, O_3, CO_2, H_2, H, OH, HO_2, H_2O, H_2O_2, O_2, and N_2. However, in applying the code to the E-region, NO and N were held fixed. The major gases changed very little over the course of the run; about one day commencing at noon, when the solar zenith angle was 21.6°. The major species (O_2, N_2) changed imperceptibly over this period and negative ions were negligible. As we were not focusing on the chemistry of the minor neutrals, but rather on the major positive ions and electrons, we list only their relevant chemistry (Table 1), which has changed little over the intervening years.

Transport was ignored in this model. However, because one sunset observation was quite distorted, a special calculation was performed [*Keneshea and MacLeod*, 1970] which compared well with the data. This model variation included transport terms using the full continuity equation. The velocities required for the divergence term were derived from the measured neutral wind profiles for an earlier flight and used in a collision - geomagnetic equilibrium expression

$$v_i = \frac{1}{1+\rho_i^2}[\rho_i^2 \boldsymbol{u} + \rho_i\, \boldsymbol{u}\times\Gamma + (\boldsymbol{u}\cdot\Gamma)\Gamma], \tag{2}$$

where ρ_i is the ratio of neutral-ion collision frequency to gyrofrequency, Γ, a unit vector in the geomagnetic field direction, and $\boldsymbol{u}$ the neutral wind [*MacLeod*, 1966].

Table 1. E-Region Ionic Reactions and Their Coefficients ($cm^{-3}\ s^{-1}$)

1. $O_2^+ + e \rightarrow O + O$	$2.0 \times 10^{-7}\ (300/T)$
2. $NO^+ + e \rightarrow N + O$	$4.0 \times 10^{-7}\ (300/T)$
3. $N_2^+ + e \rightarrow N + N$	$2.8 \times 10^{-7}\ (300/T)$
4. $O^+ + O_2 \rightarrow O_2^+ + O$	2.0×10^{-11}
5. $O^+ + N_2 \rightarrow NO^+ + N$	1.0×10^{-12}
6. $N_2^+ + O \rightarrow O^+ + N_2$	1.0×10^{-12}
7. $N_2^+ + O \rightarrow NO^+ + N$	2.5×10^{-10}
8. $N_2^+ + O_2 \rightarrow O_2^+ + N_2$	5.0×10^{-11}
9. $O_2^+ + NO \rightarrow NO^+ + O_2$	6.0×10^{-10}
10. $O_2^+ + N \rightarrow NO^+ + O$	1.8×10^{-10}

3. Numerical Solution Procedure

The method of solution for the partial differential equations uses a fourth order Runge Kutta integration with a variable mesh. When a species enters its quasi-equilibrium state, its differential equation is removed from the set and its equilibrium equation is inserted into the simultaneous algebraic set which is solved by the method of successive substitutions. The overall solution is obtained by iteration between the differential and algebraic sets.

A numerical solution to this problem that requires the use of a high speed digital computer has been discussed [*Keneshea*, 1967]. The computer program resulting from that study, although it developed satisfactory solutions within a minimum of computer time, can be used only at E-region altitudes. One reason for this restriction is that the number density of NO^+ ions is always computed from the requirement of balance of charge (the sum of the positive ions equals the sum of the electrons and the negative ions). This method is applicable, however, only if NO^+ is the most abundant ion. Although this appears to be true in the E region, it will not be the case at lower altitudes, in the D-region. Because the system is solved on a digital computer, it is not possible to accurately determine the concentration of a minor species through conservation of charge. The required number density is located in the least significant bits of the computer word and, depending upon the amount of accumulated round-off error, the result could be erroneous.

4. Model Inputs

Solar fluxes and absorption cross sections were taken from *Watanabe and Hinteregger* [1962] above about 100A. Below this wavelength, the values listed by *Nicolet and Aiken*

[1960] for quiet solar conditions were adopted. The solar flux in the range 10-170A was increased by a factor of 4 over the values cited above in order to best match the data. The proper X-ray flux for the E-region is still of concern in more recent codes which aim to determine minor odd nitrogen species, particularly N and NO. An H Ly α flux of 4 ergs cm^{-2} sec^{-1} was adopted, and the ionization effects of the scattered H Ly α and H Ly β radiations were approximated by setting their fluxes at 1% and 0.4%, respectively, of their noontime height-dependent direct flux profiles. The paper by *Strobel et al.* [1980] should be consulted for a detailed analysis of nighttime ionization sources and their intensities. The declination of the sun was fixed at 8.62° for comparison with the specific experimental data; the noontime solar zenith angle, χ, being 21.63°. Atmospheric concentrations and temperatures were taken from the mean 1965 COSPAR International Reference Atmosphere (CIRA). All particles were assumed to have the same temperature distribution. In calculating the optical depth, appropriate CIRA concentrations were integrated along the various solar zenith angles. The nitric oxide concentrations essentially were a smooth version of *Barth's* [1966] results, but lower at 85 km, the lowest altitude of the calculation. Atomic nitrogen concentrations were effectively negligible, $[N] = 10^{-2}[NO]$. Both species were held constant throughout the time-dependent solutions of the charged constituents.

The specific nitric oxide concentrations used were, in units of 10^6 cm^{-3}; 3 (140 km); 5.4 (130 km); 11 (120 km); 25 (110 km); 34 (105 km); 40 (100 km); 38 (95 km); 25 (90 km); and 10 (85 km). Calculations were performed only at these altitudes. Nitric oxide plays two major roles. Firstly, it converts O_2^+ ions into NO^+ ions via the charge transfer reaction (#9 in Table 1). However, it is the product k_9 [NO] which is important. Thus, as k_9 is now about 25% lower than the value in Table 1, the [NO] used is effectively 4/3 the values cited. More significant is that near a solar zenith angle of 90°, the attenuation of H Ly α near 100-110 km is negligible and the main ionization source is therefore H Ly $\alpha + NO \rightarrow NO^+ + e$. If [NO] is enhanced, as often the case for the auroral region (discussed below), E-region concentrations, [e], at sunrise increase too, as $[e]^2$ is proportional (numerically) to [NO] [*Swider and Keneshea*, 1993].

5. Model Outputs

In the original paper [*Keneshea et al.*, 1970], the only outputs shown were the election concentrations and the NO^+ / O_2^+ ionic ratios beginning with a solar zenith angle of 40° (ignoring the startup period 21° to 40°) and continuing through the night and into the day up to noon (21.6°) for all nine of the altitudes considered. Here, in Figure 1, we show a different plot for [e] for the last period of the calculation, post-sunrise to about noon.

Figure 2 shows results [*Keneshea and MacLeod*, 1970] for one sunset which includes the use of the measured winds. Results agreed far better with the data (not shown here) than with the model without transport.

Finally, in Figure 3, the E-region model with factors of 10, 100, and 10^3 times greater levels of [NO] are compared [*Swider and Keneshea*, 1993] to EISCAT results for the high-latitude E-region during quiet conditions in winter. We contend that these results can be explained by the buildup of nitric oxide to concentrations as great as 10^9 cm^{-3} in the wintertime high-latitude E-region, when and where photodissociation of NO is negligible.

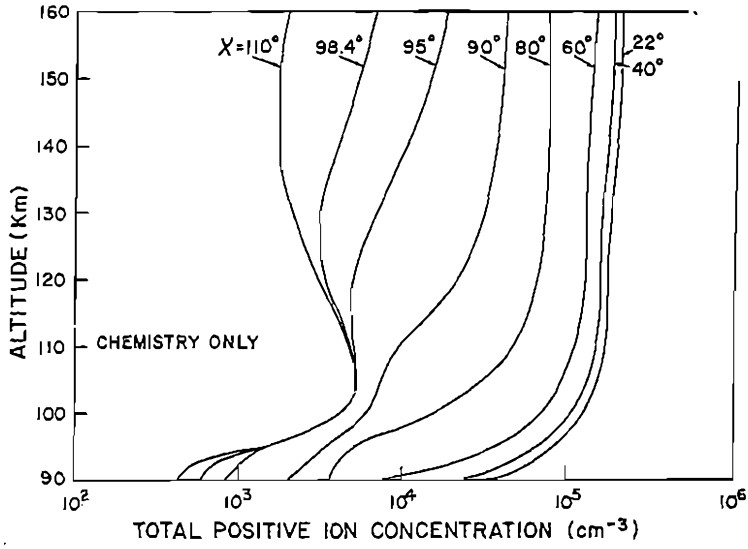

Figure 1. Total ion/electron concentrations for the quiet mid-latitude E-region [*Keneshea et al.*, 1970].

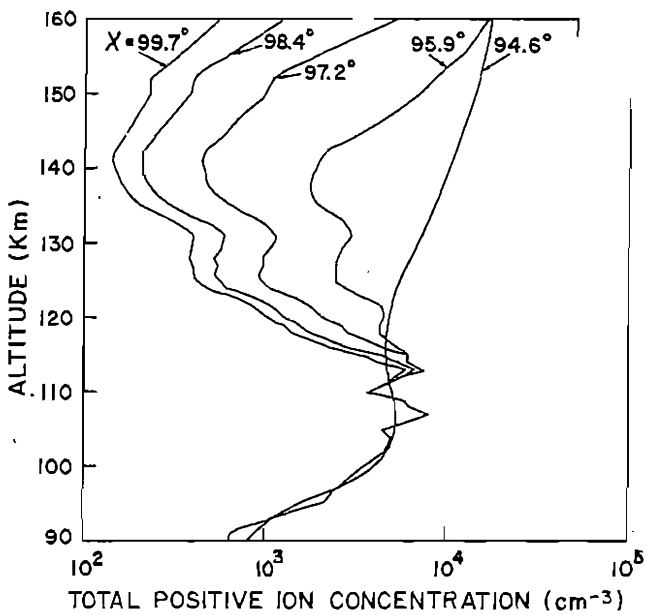

Figure 2. Model of a sunset E-region profile using the measured winds [*Keneshea and MacLeod*, 1970].

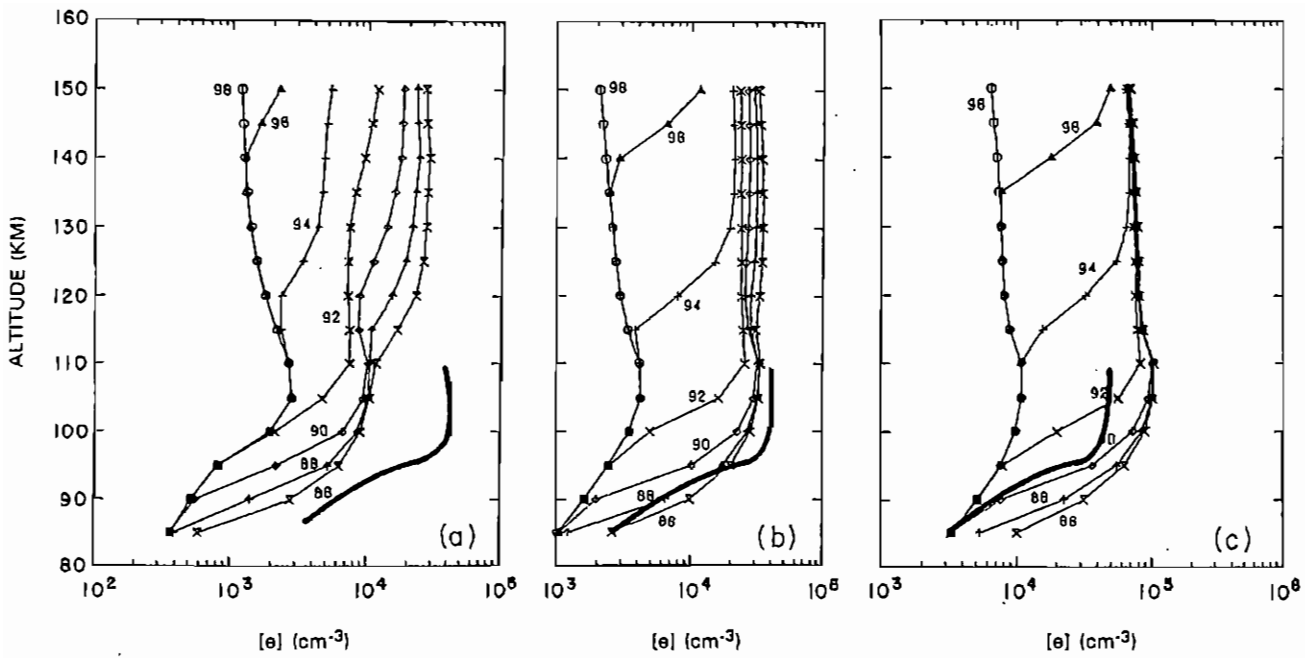

Figure 3. Sunrise E-region profiles [*Swider and Keneshea*, 1993] calculated using multiples of [NO] 10, 10^2, and 10^3 greater than for a quiet model [*Keneshea et al.*, 1970] for comparison to EISCAT data (thick curve).

6. Uncertainties and Limitations

It is our experience that [NO] appears generally to be greater in the E-region than many models assume. Thus some models yield $O_2^+ >> NO^+$ near 95-100 km, whereas the observational data, with perhaps one exception, does not support this result [*Swider*, 1994]. The values of [NO] used here are in the higher range of those determined from gamma-band data. However, these values have worked well. Again, our use of a somewhat higher X-ray flux appears justified by the model's good comparison with the observational ionic data. There have been suggestions that there is insufficient ionization produced near 95-100 km, implying a missing source of ionization. However, none have offered any specific details and our model agrees quite well with incoherent scatter data in the lower E-region [*Trost*, 1979].

7. Availability of the Model

A version of the model may be available (contact W. Swider), but it may not be worth running in view of the published outputs, and especially because others undoubtedly have codes much faster than the one discussed here. The original printout is available (W. Swider). The originator/writer of the code (T. J. Keneshea) has expanded it to include transport and IR emissions, but its availability through Visidyne Research, Inc., may be limited.

8. References

Barth, C. A., *Ann. Geophys., 22*, 198-207, 1966.
Keneshea, T. J., AFCRL-67-0221, 1967.
Keneshea, T. J. and M. A. MacLeod, *J. Atmos. Sci., 27*, 981-984, 1970.
Keneshea, T. J., R. S. Narcisi, and W. Swider, Jr., *J. Geophys. Res., 75*, 845-854, 1970.
MacLeod, M. A., *J. Atmos. Sci., 23*, 96-109, 1966.
Nicolet, M. and A. C. Aikin, *J. Geophys. Res., 65*, 1469-1483, 1960.
Stobel, D. F., C. B. Opal, and R. R. Meier, *Planet Space Sci., 28*, 1027-1033, 1980.
Swider, W. and T. J. Keneshea, *J. Geophys. Res., 98*, 1725-1728, 1993.
Swider, W., *EOS, 75*, 246, 1994.
Trost, T. F., *J. Geophys. Res., 84*, 2736-2742, 1979.
Watanabe, K. and H. E. Hinteregger, *J. Geophys. Res., 67*, 999-1006, 1962.

Mid-Latitude Ionospheric Model

C. Taïeb

CNET-CETP, 38-40 Avenue Général Leclerc,
F-92131 Issy-les Moulineaux, France

1. Introduction

The near earth environment is a gas made of neutral atoms and molecules and ionized particles with concentrations roughly concentric around the earth and a well-marked vertical structure. The ionized component is detectable from about 60 km with ion concentrations of 1 to 10 cm^{-3}. At the upper part, the frontier is less clearly defined. Above approximately 600 km, in a region called the protonosphere, the concentrations of the most important remaining H^+ and O^+ ions decrease smoothly toward less than 10^3 cm^{-3}.

Below 90 km, where the neutral atmospheric density is high enough to allow free electron attachment with neutral particles, thus creating negative ions, the region is called the D-Region.

The model has been worked out in the range 90 to 600 km that includes several regions E, F1, F2, characterized by different predominant chemical processes and by the ion-neutral collision frequencies (ν_{in}) to the ion gyrofrequencies ($\omega_i = e/m_iB$, where e and m_i are electron charge and ion mass, and B is the magnetic field intensity) ratio. While ω_i decreases slowly with altitude, ν_{in} changes much more rapidly so that a transition region exists at approximately 150 km where $\omega_i \approx \nu_{in}$.

In the range of altitudes 90-600 km, solar radiations from 50 A to 1250 A are completely absorbed by the neutral atmospheric particles, creating ionized particles. Energetic electrons precipitated in the atmosphere may also ionize the neutral particles, but it occurs very rarely at mid-latitude. Charged particles including electrons react chemically with the neutrals in which some of the ions lose their charge through several sorts of reactions. Internal and external forces also contribute to change the ion concentrations as a function of altitude. Due to the physical processes, production, recombination and transport, the vertical distribution of the concentrations reach a near equilibrium with a time constant depending on the altitude.

The existing earth magnetic field plays an important role for the ions vertical distribution. Its lines of force in the model are supposed to be generated by a dipole location at the center of the earth. In the range of altitude that we consider, they are very close to a straight line making an angle in the magnetic meridian plane with the horizontal line called dip angle (I).

Collision frequencies decrease upward like the neutral densities. Around 160 to 180 km, ν_{in} starts to be much smaller than ω_i. Consequently, below this transition altitude, the influence of the magnetic field is negligible and the ions are dragged by the neutral particles moving horizontally with no effect on the vertical structure of the ionization. Vertical gradients of the neutral atmosphere velocity sometimes exist due to gravity waves inducing an increase of ionization called Sporadic-E in a few km range. This phenomenon is not taken into account in the model. Above the transition altitude, the electrons, having a greater mobility than the ions, are free to move along the magnetic line of force under the action of several forces (electromagnetic force, gravity, neutral drag and plasma pressure). Ions are less mobile than the

electrons and, in order to respect the electrical neutrality, a polarization electric field is created to maintain electrons and ions close enough. Ambipolar diffusion of electrons and ions due to pressure gradients then moves the ions along the field line as does the external forces. The dipole model and the derived quantities I and B are obtained from *Chapman and Akasofou* [1972].

2. Mathematical Formulation

Differential equations for concentration and velocity functions, depending on time and altitude, can be written to obey the fundamental laws of physics: mass, movement and energy conservation. They are obtained by taking velocity moments of Boltzman's equation. Following *Schunk* [1974], they may be formulated for mass and movement as:

$$\frac{\partial n_i}{\partial t} + \nabla \cdot \left(n_i \vec{V}_i \right) = \frac{\delta n_i}{\delta t} \tag{1}$$

$$m_i n_i \frac{D_i \vec{V}_i}{Dt} + \nabla \cdot \vec{P}_i - m_i n_i \vec{G} - n_i e_i \left(\vec{E} + \vec{V}_i \times \vec{B} \right) = \frac{\delta \vec{M}_i}{\delta t} \tag{2}$$

where $\frac{D_i}{Dt} = \frac{\partial}{\partial t} + \vec{V}_i \cdot \nabla$

and n_i, m_i, $\vec{V}_i$ are concentration, mass and velocity vector of the ith ion. $\vec{P} = n_i k \vec{T}_i$ is the pressure vector, where k is the Boltzman constant and $\vec{T}_i$ the temperature vector. Pressure and temperature are scalar quantities in the mid-latitude ionosphere. $\vec{G}$ is the gravity force directed downward, $\vec{E}$ the polarization electric field and $\vec{V}_i \times \vec{B}$ the electromagnetic force.
The right hand side of equation (1) is:

$$\frac{\delta n_i}{\delta t} = Q_i - R_i n_i$$

where Q_i is the number of ion-pairs produced by the different sources, principally the solar radiations and R_i are recombination coefficients.

The friction force formulated in the right hand side of equation (2) is:

$$\frac{\delta \vec{M}_i}{\delta t} = \sum_j n_i m_i \nu_{ij} \left(\vec{V}_j - \vec{V}_i \right)$$

where i corresponds to the ith ion interacting with all other particles j, including neutrals.

The differential equation for the energy is not solved to calculate ion and electron temperatures. Instead we use an empirical formula and a model.

Equations (1) and (2) are vectorials and should be examined along the magnetic field line and perpendicular to it. Transportation of ionized particles perpendicularly to $\vec{B}$ is negligible because electrons circling around the line of force are tight to it. Forces capable of moving them in that direction are not intense enough, at mid-latitude, to change the spatial distribution of the particles perceptibly. Then it suffices to examine the equations parallel to $\vec{B}$ for continuity and

movement. It can be safely assumed that velocities change smoothly with altitude and time so that the inertial term can be ignored. Equation (2) becomes:

for each ion

$$\nabla \cdot n_i k T_i - m_i n_i g - n_i e_i E = m_i n_i \nu_{in} V_i \tag{3}$$

and for electrons

$$\nabla \cdot n_e k T_e - m_e n_e g - n_e e_e E = m_e n_e \nu_{en} V_e \tag{4}$$

Eliminating the polarization field E between equation (3) and equation (4) and taking account of $m_i >> m_e$ and $m_i \nu_{in} >> m_e \nu_{en}$, it can be obtained:

$$V_{id} = \frac{k \sin^2 I}{m_i \nu_{in}} \left[T_i \frac{1}{n_i} \frac{\partial n_i}{\partial z} + T_e \frac{1}{n_e} \frac{\partial n_e}{\partial z} + \frac{\partial (T_e + T_i)}{\partial z} + \frac{m_i g}{k} \right] \tag{5}$$

where I is the magnetic dip angle and V_{id} is the ion drift due to the ambipolar diffusion projected on the vertical axis.

From the perpendicular component of equation (2) it can be derived:

$$\nu_{in} \left(\vec{V}_i - \vec{V}_n \right) + \vec{\omega}_i \times \left(\vec{V}_i - \vec{V}_E \right) = 0 \tag{6}$$

where $\vec{V}_E = \frac{\vec{E} \times \vec{B}}{B^2}$ and $\vec{\omega}_i = \frac{e\vec{B}}{m_i}$

From equation (6), the ion velocity due to the neutral wind drag and the convection electric field along the magnetic field line is obtained. Its projection on the vertical axis is:

$$V_{iz} = -\frac{1}{1+a_i^2} V_x \sin I \cos I + \frac{a_i^2}{1+a_i^2} V_y + \frac{1}{1+a_i^2} \frac{E_y}{B} \cos I - \frac{a_i^2}{1+a_i^2} \frac{E_x}{B} \cos I \tag{7}$$

where $a_i = (\nu_{in}/\omega_i)$, V_x and V_y are respectively meridional and zonal wind, E_x and E_y are respectively meridional and zonal convection electric field. Above 160 km, a_i^2 being very small, only the contribution of the meridional neutral wind and the zonal electric field remains:

$$V_{iz} = V_{nx} \sin I \cos I + \frac{E_y}{B} \cos I$$

An eastward electric field and a southward neutral wind contribute to an upward drift of the ions.

The divergence term of equation (1) is then replaced by two terms: $\nabla \cdot \left(n_i V_{iz} \right)$ that involves only the first derivatives for concentration and velocity, and

$$\nabla\cdot\left(n_i V_{id}\right)=\frac{\partial}{\partial z}\left(\Phi\frac{\partial n_i}{\partial z}+\Phi\frac{T_e}{T_i}\frac{n_i}{n_e}\frac{\partial n_e}{\partial z}\right)+\frac{\partial}{\partial z}\left(\Psi\cdot n_i\right)$$

with $\Phi=-k\dfrac{T_i\sin^2 I}{m_i\nu_{in}}$ and $\Psi=\Phi\left[\dfrac{m_i g}{kT_i}+\dfrac{I}{T_i}\dfrac{\partial}{\partial z}\left(T_e+T_i\right)\right]$

which involves the second derivative for concentrations.

Then we have to solve for each ionized component, a single differential equation depending on the ion concentration, and its first and second derivative.

3. Numerical Solution Procedure

A spectral method [*Gottlieb and Orszag*, 1977] is adopted to solve a coupled system of second order and quadratic differential equations. The method is supposed to be less consuming, especially when developing it in two and three dimensions.

We seek an approximate solution to our problem in the form :

$$f=\sum_0^\infty a_i\varphi_i \tag{8}$$

where φ_i is a set of <<trial >> functions chosen mutually orthogonal for a scalar product $\langle f,\varphi\rangle=\int fg\rho dz$. Here ρ is a weighting function chosen beforehand. The a_i coefficients defined by the scalar product can be approximated [*Gottlieb and Orszag*, 1977] as :

$$a_i=\sum_0^n \alpha_k f\left(z_k\right)\varphi\left(z_k\right) \tag{9}$$

where α_k and z_k are, respectively, the weight and the Gauss' points for the particular scalar product [*Legras*, 1971]:

$$\langle fg\rangle=\int\frac{fg}{\sqrt{1-z^2}}dz.$$

According to (8) and (9), at a point y, f can be written as :

$$f(y)=\sum_i\sum_k\alpha_k f\left(z_k\right)\varphi_i\left(z_k\right)\varphi_i(y) \text{ or } f(y)=\sum_i\sum_k\beta_k\varphi_i\left(z_k\right)\varphi_i(y)$$

For the n Gauss' points it leads to:

$$f\left(z_j\right)=\sum_i\sum_k\beta_k\varphi_i\left(z_k\right)\varphi_i\left(z_j\right)$$

and writing $f\left(z_j\right)=f^j$, $\varphi_i\left(z_k\right)=\varphi_k{}^i$ and $\varphi_i\left(z_j\right)=\varphi_i{}^j$ we have: $f^j=\beta^k\varphi_k{}^i\varphi_i{}^j$.

which shows that a matrix is involved in this relation. The matrix A represents the change of coordinates of the f vector from the frame of φ_i to the frame of δ functions, $\delta(z-z_k)$.

The interpretation of A as an operator for changing the basis of a vector leads us to the building of <<derivative matrices>> which is equivalent in a certain sense to Gauss' points for the integration. Let us have a function f defined by (8) and its derivative $f' = \sum a_i \varphi_i'$ assuming that a_i coefficients decrease rapidly. It can be shown [*Gottlieb and Orszag*, 1977] that φ_i' can be defined on the φ_i basis,

$$\varphi_i' = \sum_k b_i{}^k \varphi_k .$$

Then φ_i' is related linearly to φ_k and consequently there is a matrix B so that: $\varphi_i' = B_i{}^k \varphi_k$.

According to linear algebra rules the matrix of the linear derivative mapping reads: $D = A^{-1}BA$. The operation of D to an n component vector as $f(z_k)$ gives the n components of the derivative $f'(z_k)$ with the same accuracy as the expansion of f on the φ basis. For instance we have used the following differential operator :

$$\frac{\partial}{\partial z} = \mathbf{D} \qquad \frac{\partial^2}{\partial z^2} = \mathbf{D} \circ \mathbf{D} = \mathbf{D}^2 \qquad \frac{\partial}{\partial z}\left(p(z)\frac{\partial}{\partial z}\right) = \mathbf{D} \circ \mathbf{p} \circ \mathbf{D}$$

where **p** is a diagonal matrix p(z)

For the time differentiating methods we choose the following implicit integration:

$$n_i(t+\Delta t) = n_i(t) + \Delta t \times Dn_i(t+\Delta t)$$

The altitudes, not equally spaced, are defined by the number of Gauss' points, n and a chosen scalar product, with the altitude boundaries given at 90 and 600 km. Many trials have shown that a polynomial function with n=30 coefficients gives correct ion concentrations for the least consuming cpu time. To summarize, after the calculation of all physical coefficients of a 4*n matrix we have to solve a system of 4*n linear equations at each instant when four ionized constituents are considered.

At the lower boundary of integration, 90 km, the concentration for each ion is put equal to 10^3 cm^{-3}. Changing this value by a factor of 10 has a small effect at the altitude steps above the second one of the profile. Above f_0F2 the concentration decreases exponentially according to $n_i = n_{i0}e^{\alpha_i z}$ where n_{i0} is the density at a particular bottom altitude z_0 and α_i is the slope equal to $1/n_i \partial n_i/\partial z$. The slope at the upper boundary is a guess value at the initial time t_0. At $t+\Delta t$, $t+2\Delta t$, ..., the boundary value is deduced from an extrapolation of three points below. The initial profile for each ion is obtained after 24 hours of 15 minute step time integration from t_0 to t_0+24, and the simulation starts at t_0 with any integration time step.

4. Model Inputs

Figure 1 is a block diagram showing the models that contribute to determine the coefficients of the differential equations.

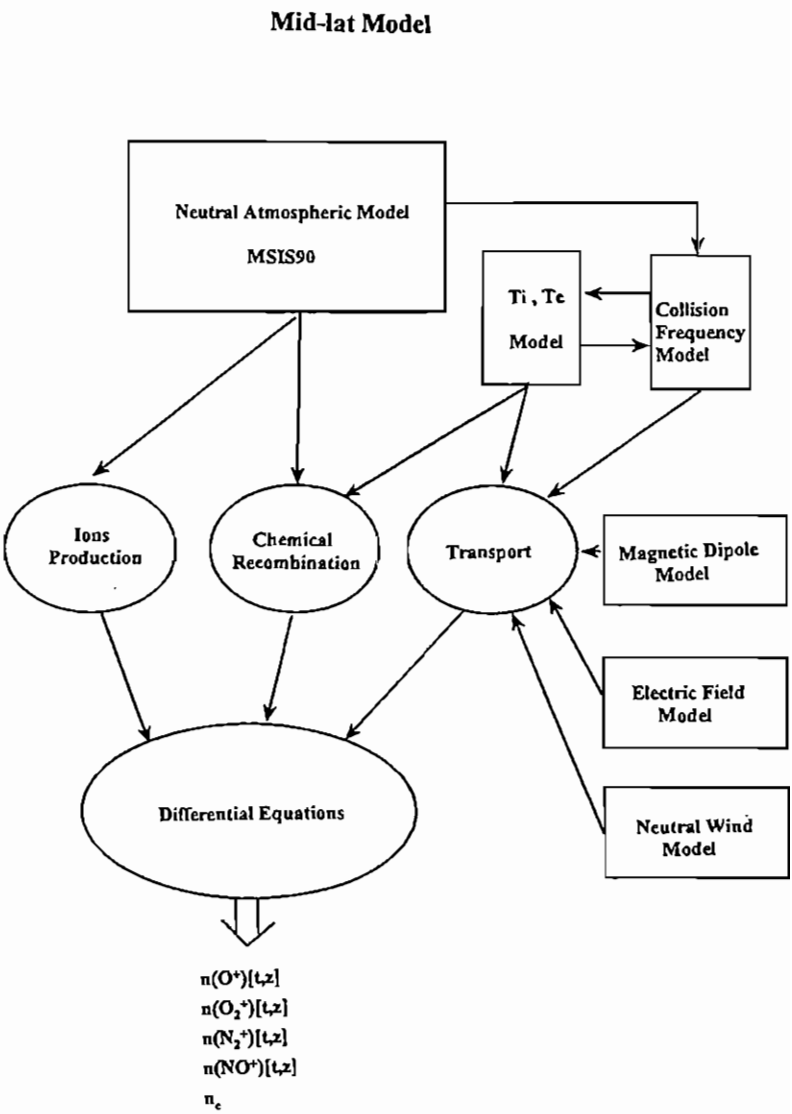

Figure 1. A schematic diagram of model inputs.

Neutral Atmospheric Model

The MSIS90 neutral atmospheric model [*Hedin et al.*, 1979 and *Hedin*, 1987] is used to get neutral concentrations for O, O_2, N_2, H and the exospheric temperature, as well as the neutral temperature, as a function of height. The NO density is given by the following empirical model [*Gérard and Taïeb*, 1986]:

$$[NO] = [A - (3.96*10^4) - (1.6*10^5)(z - 115)^2] * [1 + B\sin(\pi/9(t - 10.5))]$$

for $z \leq 115$ km

$$[NO] = [A\exp((115 - z)/30) - (3.96*10^4)] * [1 + B\sin((\pi/9(t-10.5))]$$

for $z \geq 115$ km. A and B are adjustable coefficient of the order $A = 10^8$ and $B = A/3$

Collision Frequency Model

The collision frequencies are calculated with the coefficients given by *Stubbe* [1968].

Production

Solar radiations in the range 30-1250 A interact with neutral particles of the atmosphere to produce O^+, O_2^+, N_2^+, NO^+, H^+. The interaction depends on absorption and ionization cross-sections [*Banks and Kockarts*, 1978; *Taïeb and Poinsard*, 1984] and solar fluxes Φ_∞ [*Heroux and Hinteregger*, 1978 and *Torr et al.*, 1979] for each elementary range of the solar radiations. The solar flux is statistically related to the solar 10.7 cm flux according to Hinteregger's formula [*Hinteregger*, 1970].

$$\Phi = \Phi_\infty (1 + 5.10^{-3} (F10.7 - 150))$$

The radiation absorption is proportional to $\sec\chi$, where χ is the solar zenith angle. When $\chi > 60°$, it is necessary to take account of the earth curvature, then the function relating the absorption to χ is more complicated than a secant law. According to *Swider and Gardner* [1969] and *Swider* [1964], different formulas are adopted for $60° < \chi < 90°$ and for $90° < \chi < 120°$.

The model assumes that the energy lost by solar radiations to extract an electron from a neutral particle is about 35 eV. Some of these free electrons have enough energy to secondarily ionize particles. This effect is taken in account in using a coefficient [*Lilensten et al.*, 1989] which depends on the solar zenith angle, the latitude, the solar activity and the altitude.

Chemical Reactions

Two sorts of reactions have to be considered:

1. *Recombinations*

$$O^+ + e \rightarrow O + h\nu \rightarrow \alpha_1 = 5.0*10^{-12}(250/T_e)^{0.7}$$

$$O_2^+ + e \rightarrow O + O \rightarrow \alpha_2 = 2.2*10^{-7}(300/T_e)$$

$$N_2^+ + e \rightarrow N + N \rightarrow \alpha_3 = 1.8*10^{-7}(300/T_e)^{1/3}$$

$NO^+ + e \rightarrow N + O \rightarrow \alpha_4 = 4.2*10^{-7}(300/T_e)$

2. *Charge Exchange*

$O^+ + N_2 \rightarrow O + N_2^+ \rightarrow \gamma_1 = 7.0*10^{-10}$

$O^+ + N_2 \rightarrow N + NO^+ \rightarrow \gamma_2 = 1.53*10^{-12} - 5.92*10^{-13}*T_i/300+8.6*10^{-14}(T_i/300)^2$ for $T_i < 1700°$

$\gamma_2 = 2.73*10^{-12} - 1.15*10^{-12}*T_i/300+1.44*10^{-13}*(T_i/300)^2$ for $T_i > 1700°$

$O^+ + O_2 \rightarrow O + O_2^+ \rightarrow \gamma_3 = 2.82*10^{-11} - 7.74*10^{-12}*T_i/300+1.07*10^{-12}*(T_i/300)^2 - 5.17*10^{-14}*(T_i/300)^3$

$O^+ + NO \rightarrow O + NO^+ \rightarrow \gamma_4 = 8.36*10^{-13} - 2.02*10^{-13}*(T_i/300)+6.95*10^{-14}*(T_i/300)^2$ for $T_i < 1500°$

$\gamma_4 = 5.33*10^{-13} - 1.64*10^{-14}*(T_i/300)+4.72*10^{-14}*(T_i/300)^2 - 7.05*10^{-16}$ for $1500 < T_i < 6000°$

$O_2^+ + NO \rightarrow O_2 + NO^+ \rightarrow \gamma_5 = 4.4*10^{-10}$

$O_2^+ + N_2 \rightarrow NO + NO^+ \rightarrow \gamma_6 = 2.0*10^{-16}$

$N_2^+ + O_2 \rightarrow NO + NO^+ \rightarrow \gamma_7 = 3.0*10^{-14}$

$N_2^+ + O \rightarrow N + NO^+ \rightarrow \gamma_8 = 1.4*10^{-10}*(300/T_i)^{0.44}$

$N_2^+ + O_2 \rightarrow N_2 + O_2^+ \rightarrow \gamma_9 = 7.0*10^{-11}$

$N_2^+ + NO \rightarrow N_2 + NO^+ \rightarrow \gamma_{10} = 3.3*10^{-10}$

$N_2^+ + O \rightarrow N_2 + O^+ \rightarrow \gamma_{11} = 1.0*10^{-12}*(300/T_i)^{0.23}$

where T_i and T_e are ion and electron temperatures.

Electron Temperature Model

Electron temperature is calculated with an empirical model due to *Pandey and Mahajan* [1981] which takes account of three physical processes, namely, the electron heating by photoelectrons, the electron cooling by heat transfer to ion and neutral particles and heat transport due to thermal conduction. Electron temperature is obtained as a function of electron density in the altitude range 200 to 300 km from two tables corresponding to different level of solar activity. Values of the tables are interpolated to get T_e at the desired altitude and electron density and solar activity. Assuming that thermal conduction is the most important physical process above 300 km, T_e is obtained with the following equations:

$$F_c = KdT_e/dz \sin I \quad \text{and} \quad K = 7.7*10^5 T_e^{5/2}$$

where F_c is the heat flux in $eV/cm^2/s$ and K is the thermal conduction of elcctrons in eV/cm/s/deg.

At altitudes less than 200 km T_e is calculated by a third order polynomial which coefficients are deduced when assuming that $T_e = T_n$ and $dT_e/dz = dT_n/dz$ at the lower boundary altitude and that T_e is the value obtained from the table at 200 km.

Ion Temperature Model

According to *Stubbe and Chandra* [1971] who pointed out the effect of the frictional heating by neutral wind, the ion temperature is related to neutral and electron temperatures as follows:

$$T_i = T_n + \frac{m_e \nu_{ie}}{\sum_n \frac{\mu^2_{in}}{m_n} \nu_{in}} (T_e - T_i) + \frac{\sum_n \mu^2_{in} \nu_{in}}{3k \sum_n \frac{\mu^2_{in}}{m_n} \nu_{in}} (\bar{V}_n - \bar{V}_i)^2$$

where $\mu_{in} = \frac{m_i m_n}{m_i + m_n}$,

m_e, m_i and m_n are electron, ion and neutral masses. $\bar{V}_n$ and $\bar{V}_i$ are neutral and ion velocity vectors; ν_{in} and k are respectively the ion-neutral collision frequency and the Boltzman constant. The ion-electron collision frequency is given by:

$$\nu_{ie} = 1.74 \cdot 10^{-3} \left(\frac{1000}{T_e} \right)^{3/2} n_e$$

where n_e is the electron concentration.

Neutral Wind Model

The meridional wind component is derived from several years of Saint-Santin measurements [*Bernard*, 1974; *Amayenc*, 1974] and a model based on the following relations is obtained, which corresponds for 100<z<180 km to tidal oscillations in the E region:

$$V_{nx}(z) = A_{12}(z) \cos \frac{2\pi}{12} (t - \varphi_{12}(z)) + A_{24}(z) \cos \frac{2\pi}{24} (t - \varphi_{24}(z))$$

for z > 180 km

$$V_{nx} = A_0 + A_8 \cos \frac{2\pi}{8} (t - \varphi_8) + A_{12} \cos \frac{2\pi}{12} (t - \varphi_{12}) + A_{24} \cos \frac{2\pi}{24} (t - \varphi_{24})$$

Below 180 km the neutral wind depends on the altitude. Above, V_{nx} is constant with altitude. All A's and φ's change with the season.

This model can be replaced by the global thermospheric wind HWM90 due to *Hedin et al.* [1991] which is included in the code.

Electric Field Model

Meridional and zonal electric fields perpendicular to the magnetic field lines are calculated from a model developed by *Richmond et al.* [1980]. This model was obtained on a world-wide basis of observations including several incoherent scatter sounders, one of which is Saint-Santin, and takes account of diurnal and seasonal variations.

At mid-latitude, usually, the intensity of the convection electric field is about 2mV/m during low magnetic activity and at most 5 to 10 mV/m for disturbed conditions. When this geophysical parameter reaches 20 mV/m, or much more as happens in the polar cap, the ionospheric plasma turns out to be anisotropic because ions are strongly accelerated horizontally. For such a situation, the code has to be modified. According to *Schunk et al.* [1975], an additional term is introduced in the ambipolar diffusion velocity and an effective ion temperature for some chemical reactions is determined. Inside the brackets of equation (5) the following term is added:

$$T_i \frac{1}{n_i k T_i} \frac{\partial \tau_{i\parallel}}{\partial z} ,$$

where $\tau_{i\parallel}$ is the stress tensor parallel to the field line. $\tau_{i\parallel}$ is given by *Schunk et al.* [1975]. Rate coefficients for charge exchange of O^+ with N_2, O_2 or NO depend on an effective temperature T_{eff} given by *Schunk et al.* [1975] where it is shown that: $T_{eff} = T_n + 0.329E^2_{\perp}$, $E_{\perp}$ is the convection electric field in mV/m and T_n is the neutral temperature. T_{eff} increases as the square of the field and the rate coefficient as the 4th power. With these modifications in the code, simulation can be applied to any field alignment located at high latitudes in the F-region of the ionosphere provided a convection electric model is given.

5. Output Model

The code calculates the density (cm^{-3}) of O^+, O_2^+, N_2^+, NO^+ and the electron density which is equal to their sum, as a function of altitude and time at any geographic location. The initial concentrations, at any time, are determined from a preliminary 24 hours integration or injected in the code from experimental results. Then profiles can be obtained with any time step, generally not less than 1 to 3 minutes, during many hours without limitation.

For example a simulation has been carried out at the Saint-Santin coordinates (44.2 °N, 2.15 °E) when the radar was operating. Two options were adopted for the simulation,

- Option 1: The electron and ion density profiles are obtained as described above with models for the convection electric field and the neutral wind.

- Option 2: The electric field and the neutral wind models are not used. Instead, V_{iz} is deduced from the radar measurements and injected in the code. The measured vertical ion velocity, V_i, is the sum of two terms, V_{id} and V_{iz}. Measuring temperatures and density, the diffusion velocity can be obtained and subtracted from V_i to get V_{iz}. Figure 2 shows profiles for Option 1 and 2, and measured electron densities between 250 and 350 km. The result of Option 2 is clearly closer to measurements [*Taïeb and Poinsard*, 1984a]. It shows that observed electron density profiles are highly dependent on short term neutral wind variations.

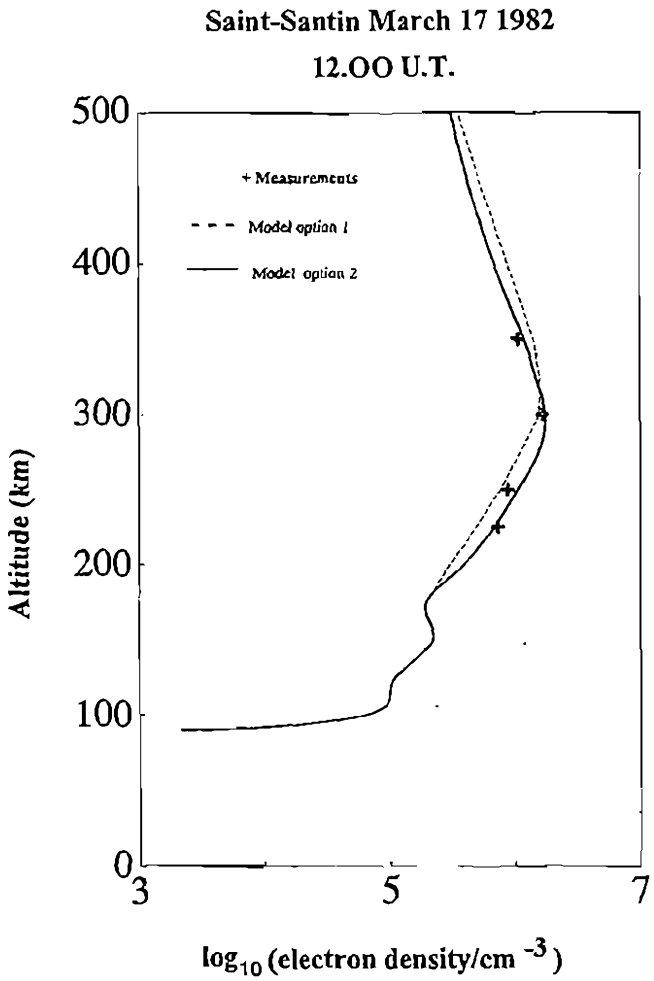

Figure 2. Calculated electron density profiles compared to incoherent scatter measurements.

The code has been running also at high latitudes with an experimental model, derived from EISCAT measurements, of the convection electric field covering the polar cap [*Taïeb*, 1991]. The simulation reproduces the main features of the experimental data (Figure 3), that is, a large decrease of the electron density in the invariant magnetic latitude range 68-72° and between 02.00-05.00 Magnetic Local Time. The calculation showed that the decrease is mainly due to a sharp rise of the ion temperature reaching a nominal value coinciding closely with the EISCAT measurements. Consequently, it is due to a recombination process.

6. Uncertainties and Limitations

Outputs are only concentrations of O^+, O_2^+, N_2^+, NO^+; ion velocities are implicit in the method. If vertical ion velocities and their vertical gradients are great enough, the resulting concentrations are not reliable because the inertial term in the momentum equations has been neglected.

7. References

Amayenc, P., *Radio Sci., 9*, 281, 1974

Bernard, R., *J. Atmos. Terr. Phys., 36*, 1105, 1974.

Banks, P. M., and G. Kockarts, *Aeronomy*, Academic Press, New York, London, 1973.

Chapman, S., and S.-I. Akasofou, *Solar Terrestrial Physics*, Oxford at the Clarendon Press, 1972

Gottlieb, D., and S. A. Orszag, Society for Industrial and Applied Mathematics.

Hedin, A. E., C. A. Reber, N. W. Spencer, and H. C. Brinton, *J. Geophys .Res., 84*, 1-9, 1979.

Hedin, A. E., *J. Geophys .Res., 92*, 4649-4662, 1987.

Hedin, A. E., M. A. Biondi, R. G. Burnside, G. Hernandez, R. M. Johnson, T. L. Killeen, C. Mazaudier, J. W. Meriwether, J. E. Salah, R. J. Sica, R. W. Smith, N. W. Spencer, V. B. Wickwar, T. S. Virdi, *J. Geophys .Res., 96*, 7657, 1991.

Heroux, L., and H. E. Hinteregger, *J. Geophys. Res., 83*, 5305, 1978.

Hinteregger, H. E., *Ann. Geophys., 26*, 547, 1970.

Legras, J., Méthodes et techniques de l'analyse numérique, Dunod

Lilensten, J., W. Kofman, J. Wisemberg, E. S. Oran, and C. R. Devore, *Ann. Geophysicae, 7*, 83-90, 1989.

Pandey, V. K., and K. K Mahajan, *Ind. J. Rad. Space Phys.*, 10, 85-94, 1981.

Richmond, A. D., M. Blanc, B. A. Emery, R. H. Wand, B. G. Fejer, and R. F. Woodman, *J. Geophys. Res., 45*, 4658-4664, 1980.

Schunk, R. W., *Planet. and Space Sci., 23*, 437-485, 1974.

Schunk, R. W., W. J. Raitt, and P. M. Banks, *J. Geophys. Res., 80*, 3121-3130, 1975.

Stubbe, P., *J. Atmos. Terr. Phys., 30*, 1968.

Stubbe, P., and S. Chandra, *Planet. and Space Sci., 19*, 731-737, 1971.

Taïeb, C., and P. Poinsard, *Ann. Geophysicae*, 2, 197-206, 1984a.

Taïeb, C., and P. Poinsard, *Ann. Geophysicae*, 2, 359-367, 1984b.

Taïeb, C., *J. Atmos. Terr. Phys., 53*, 135-151,1991.

Torr, D. G., M. R. Torr, H. C. Brinton, L. H. Brace, N. W. Spencer, A. E. Hedin, W. B. Hanson, J. H. Hoffman, A. O. Nier, J. C. G. Walker, and D. W. *J. Geophys. Res., 84*, 3360-3372,1979.

Swider, W., *Planet. Space Sci., 12*, 761, 1970.

Swider, W., and M. E. Gardner, *Appl. Opt., 8*, 725, 1969.

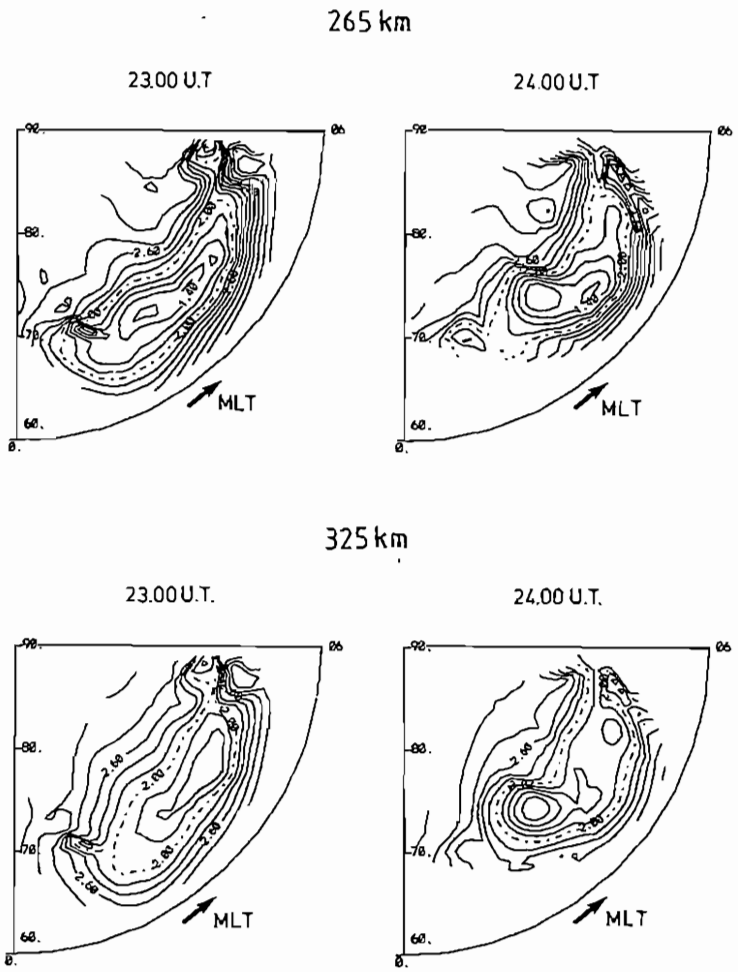

Figure 3. Plot contour, obtained from simulation, of electron density showing a minimum in few degrees range of latitude just like it is observed by the EISCAT radar. Densities, plotted between 60° and 90° geomagnetic latitude and from 00.00 to 06.00 MLT, are to be multiplied by 10^5 (cm^{-3})

8-Moment Fluid Models Of The Terrestrial High Latitude Ionosphere Between 100 And 3000 km

P. L. Blelly[1], A. Robineau[1], D. Lummerzheim[2],and J. Lilensten[3]

[1]CESR, CNRS/UPS, 9 Avenue du Colonel Roche, 31029 Toulouse, Cedex, FRANCE

[2]Geophysical Institute of Alaska, University of Alaska, Fairbanks, AK 99775-7320

[3]CEPHAG, 38492 S[t] Martin d'Hères, FRANCE

1. Introduction

The TRANSCAR Models set is composed of two one-dimensional time dependent fluid models of the ionosphere; one of them is based on an explicit numerical scheme (Flux Corrected Transport) and the other one on an implicit numerical scheme (Method of Lines). Both models describe the ionosphere between 100 and 3000 km, assuming it is composed of 6 ions (O_2^+, N_2^+, NO^+, O^+, H^+ and N^+) and electrons. The models solve the temporal evolution of the lower moments (concentration, velocity, temperature and heat flow) of the isotropic distribution function of each species. Furthermore, in the altitude range covered by the models, the motion is assumed to be organized along the magnetic field lines, allowing only the field-aligned projections of the vectorized parameters to be solved (velocity and heat flow). Nevertheless, the models include convection electric field effects like Joule heating. Related physical processes, such as field-aligned currents or thermospheric winds, are also taken into account. Furthermore, these models are associated with a kinetic transport model of energetic electrons which allows for precipitations of electrons originating from the magnetosphere and for photoelectrons resulting from the solar photons action on the neutral atmosphere to be taken into account. This kinetic model is based on a discrete ordinate method and provides ion production rates and electron heating source for the fluid models. The production rates are in balance with a scheme of energy-dependent chemical reactions included in the models, involving the six ions, their neutral parents and the electrons. The different thermal effects, such as conduction, diffusion, heating and cooling through collisions, are intrinsically contained in the set of equations. However, the energy transfer from the magnetosphere to the ionosphere is modeled by a downward electron heat flow and downward energetic electrons at the top of the ionosphere and are not self consistently generated by the model, but are imposed as boundary conditions.

2. Mathematical Formulation

2.1 Fluid Transport Description

The description chosen for the modeling corresponds to a 8-moment approximation [*Schunk*, 1977], and consistently solves for each species s (of mass m_s and charge e_s), the concentration n_s , the mean flow velocity u_s , the temperature T_s (assuming that the pressure tensor is isotropic), and the heat flow q_s. The set of equations is derived from Boltzmann's equation with the hypothesis that the distribution function f_s of each species can be obtained by an expansion of a Maxwellian distribution function f_{so} up to the third order (heat flow). This truncation procedure allows the system to close by expressing the higher moments as a function of the lower ones. The 8-moment distribution function is then expressed as:

$$f_s = f_{so}\left[1 - \frac{m_s}{k_b T_s p_s}\left(1 - \frac{m_s c_s^2}{5 k_b T_s}\right) q_s . c_s\right] \quad (1)$$

where

$$f_{so} = n_s \left(\frac{m_s}{2\pi k_b T_s}\right)^{3/2} \exp\left(-\frac{m_s c_s^2}{2 k_b T_s}\right) \quad (2)$$

and k_b is the Boltzman's constant, $p_s = n_s\, k_b\, T_s$ is the partial pressure, and c_s the thermal velocity (in the local frame) of the species s.

The validity of this expansion has been discussed by *Robineau et al.* [1996] and *Blelly et al.* [1996] and is correct for heavy ions and electrons in the altitude range covered by the models. The expansion is questionable for the light ion H^+ in the supersonic regime, but in this case, the thermal energy is mainly transported by the diffusion, the conduction (heat flow) being rather negligible.

Furthermore, as the ion movement in the ionosphere is essentially organized along the magnetic field and disconnected from the perpendicular motion, the problem reduces to one dimension by projecting the equations along the field direction. In such a description, $\mathbf{E} \times \mathbf{B}$ electric field effects can still be included in the energy equations through the collisions. Lastly, a dipolar coordinate system is used for the projection in order to account for the diverging effect of the magnetic flux tube.

2.1.1 Continuity Equations

The ionosphere mainly arises from the ionization of the major neutral components (O, N_2 and O_2) by EUV solar radiation and particle precipitations. The major ions resulting from direct excitation are molecular (N_2^+ and O_2^+) at low altitudes (below 200 km) and atomic (O^+) at high altitudes (above 200 km).

Besides this primary production, different processes are responsible for other ion production:

- N^+ ions are created by N_2 dissociative ionization,
- H^+ ions are essentially produced by charge exchange reactions between O^+ and H,
- NO^+ arises from chemical recombination with neutrals and is a major ion of the E-region although its neutral parent NO is a minor constituent of the atmosphere.

These production sources are balanced by chemical reactions involving ions, electrons and the neutral parents. Figure 1 summarizes the global chemistry scheme used in the model: the major neutral species are reported in grey circles and the ionized ones in white circles. The ions resulting from the ionization of their neutral parents are labeled with "$h\nu$" (photons) and "eV" (precipitating electrons); the other arrows represent chemical reactions and recombination, the reactant neutral is indicated above the arrow.

These chemical reactions are strongly dependent on the kinetic temperature of the different species involved in the reactions, and the rate coefficients for the 21 different chemical reactions

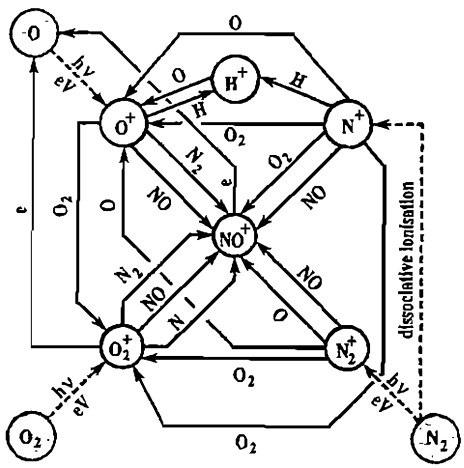

Figure 1. Synopsis of the photo-ionization and chemistry model. The reactant neutrals are mentioned above the arrows and the ionization processes are specified by "hν" (photoionization) and "eV" (precipitating electrons).

and 4 ionization rates included in the model are presented in Table 1; the numerical values are derived from *Schunk and Raitt* [1980], *Schunk* [1988], *Rees* [1989] and references herein. The effective temperature T_{eff} used in some reaction rates is a function of the ion and neutral reactant species temperatures and is discussed by *Mc Farland et al.* [1973, 1974] and *Diloy et al.* [1996].

Considering a specific ion s (O_2^+, N_2^+, NO^+, O^+, H^+ or N^+) and gathering the sources and sinks for this ion in production term P_s and loss term L_s, respectively, the continuity equation for this ion can be written as:

$$\frac{\partial n_s}{\partial t} + \frac{1}{A}\frac{\partial A n_s u_s}{\partial r} = P_s - L_s \tag{3}$$

where r represents the path along the field line. 'A' corresponds to the cross section of the magnetic tube perpendicularly to the field line.

The electron concentration can then be directly obtained from the charge neutrality hypothesis which leads to:

$$n_e = \sum_s n_s \tag{4}$$

2.1.2 Momentum Equations

The interest for an 8-moment description compared to the standard one has been evidenced by *Blelly and Schunk* [1993]. It essentially lies in the intrinsic property of the 8-moment to account for thermal diffusion effects [*Schunk*, 1977]. These effects are materialized in the momentum equation by the appearance of the heat flows in the momentum transfer through the collision terms. These terms are important above the F region, where significant enhancements in the ion and electron temperatures can be found, inducing significant temperature gradients and important heat flows. Thermal diffusion acts to drive the ions toward higher altitudes, where the temperatures are elevated [*Walker*, 1967; *Schunk and Walker*, 1969; 1970a,b; *Schunk*, 1977].

Writing u_s and q_s as the field-aligned projection of u_s and q_s, respectively, the general expression of the momentum equation for a species s projected along the magnetic field line can then be written as:

$$\frac{\partial u_s}{\partial t} + u_s \frac{\partial u_s}{\partial r} + \frac{1}{m_s n_s} \frac{\partial}{\partial r}(n_s k_b T_s) - \frac{e_s}{m_s} E_e - g \sin I = \frac{\delta u_s}{\delta t} \tag{5}$$

In equation (5), g stands for the gravity acceleration, I for the dip angle of the magnetic field and E_e for the polarization electrostatic field. Due to their light mass, the momentum equation for the electron gas can be modified and divided into two contributions. In that equation, the electrostatic force balances the electron pressure gradient, leading to an explicit expression for the electrostatic field. Moreover, a condition for ambipolar flow can be written which may account for a possible field-aligned current $J_{//}$, assumed to be transported by the thermal electrons. The resulting system becomes:

$$\begin{cases} e_e E_e = \dfrac{1}{n_e} \dfrac{\partial}{\partial r}(n_e k_b T_e) & \text{polarization electric field} \quad (6) \\ n_e u_e = \sum\limits_s n_s u_s - \dfrac{J_{//}}{e_e} & \text{ambipolar flow} \quad (7) \end{cases}$$

$\frac{\delta u_s}{\delta t}$ represent the momentum transfer through collisions which expresses:

$$\frac{\delta u_s}{\delta t} = \sum_t \nu_{st}(u_t - u_s)\phi_{st} + \frac{3}{5}\sum_t \nu_{st} \frac{1}{k_b(m_s T_t + m_t T_s)} \left\{ m_t \frac{q_s}{n_s} - m_s \frac{q_t}{n_t} \right\} \tag{8}$$

where the sum is done over all the other charged and neutral species considered in the models; ν_{st} is the momentum collision frequency between the species s and t. The correction factors ϕ_{st} has been introduced as a correction of the collisional terms in case of large differential drift velocity between the various species.

Furthermore the molecular ions, important in the low altitude range where the collisions are prominent, are assumed to have the same mean velocity. The corresponding transport equation is then obtained by the mean of the different momentum equations of the three ions O_2^+, N_2^+ and NO^+, and is not shown here.

2.1.3 Energy Equations

The choice for a 8-moment approximation is interesting for the energy transport equations since there is one equation for the temporal evolution of the thermal energy ($k_b T_s$) and one for the field aligned component of the flux of thermal energy (q_s).

Such a description allows to account for various energetic couplings of the ionosphere: with the atmosphere through the frictional heating, with the sun through the thermalization of the photoelectrons and with the magnetosphere through the energy transfer by thermalization of the precipitating electrons and the energy input by a downward electron heat flow.

Considering a species s, the transport equations for T_s and q_s can be expressed:

$$k_b \frac{\partial T_s}{\partial t} + u_s k_b \frac{\partial T_s}{\partial r} + \frac{2}{3n_s} \frac{1}{A} \frac{\partial A q_s}{\partial r} = k_b \frac{\delta T_s}{\delta t} + \frac{2}{3n_s} (L_s - Q_s) \tag{9}$$

$$\frac{\partial q_s}{\partial t} + u_s \frac{\partial q_s}{\partial r} + \frac{16}{5} q_s \frac{\partial u_s}{\partial r} + \frac{21}{5} u_s q_s \frac{1}{A} \frac{\partial A}{\partial r} + \frac{5}{2} n_s k_b^2 T_s \frac{\partial T_s}{\partial r} = \frac{\delta q_s}{\delta t} - \frac{2}{5} n_s k_b T_s m_s \frac{\delta u_s}{\delta t} \tag{10}$$

where:

$$\frac{\delta T_s}{\delta t} = \frac{2}{3} \sum_t \frac{m_s \nu_{st}}{m_s + m_t} \left\{ 3(T_t - T_s) \psi_{st} + \frac{m_t}{k_b} (u_t - u_s)^2 \phi_{st} \right\} \tag{11}$$

$$\frac{\delta q_s}{\delta t} = \sum_t \nu_{st} \left[-D_{st}^{(1)} q_s + D_{st}^{(4)} \frac{n_s m_s}{n_t m_t} q_t + n_s k_b T_s \frac{5m_s + 2m_t}{2(m_s + m_t)} (u_t - u_s) \right] - \frac{4}{5} \nu_{ss} q_s \tag{12}$$

ψ_{st} is a correction factor to account for large differential flow velocities between different species. $D_{st}^{(1)}$ and $D_{st}^{(4)}$ in equation (12) are mass dependent coefficients which are related to the kind of collisions encountered by the species s and t. Their expressions are given by *Schunk* [1977].

The differential velocity terms in the collisions related to the heat flow transport equations account for thermoelectric and diffusion-thermal effects. In the region where the collisions are important, the heat flow transport equation reduces to an explicit formulation of the heat flow which is composed of two terms. The first one is the classical Fourier's law and expresses the energy transport through the plasma by conduction resulting from the collisions. The second one expresses the energy transport by diffusion of a species through the others (diffusion thermal effects) and may be important in two cases:

- when the species is a minor one (e.g. H^+), the diffusion may prevail over the conduction [*Conrad and Schunk*, 1979] and the phenomenon may be emphasized by a supersonic outflow [*Blelly and Schunk*, 1993];

- when field-aligned currents are present, the electron heat flow is strongly altered by the differential drift between the ions and the electrons [*Schunk*, 1975].

In equation (9), the terms Q_s and L_s refer to energy sources and losses, respectively. These terms differ significantly for ions and electrons.

For the ions, the losses given by equation (11) are the only ones taken into account. However, a specific source of heating is included which is connected to the $\mathbf{E} \times \mathbf{B}$ drift. The $\mathbf{E} \times \mathbf{B}$ drift imposes a horizontal motion of the plasma through the neutral atmosphere, inducing heating of the ions through the friction on the neutral components. The amount of heating is given by:

$$Q_s = \frac{n_s e_s^2}{m_s} \frac{\nu_s E_\perp^2}{\nu_s^2 + \Omega_s^2} \tag{13}$$

where $E_\perp$ is the convection electric field amplitude, B is the magnetic field strength, $\Omega_s = (e_s B)/m_s$ is the gyrofrequency of the species s and ν_s is a global collision frequency for the species s, given by the expression:

$$\nu_s = \sum_t \frac{m_s}{m_s + m_t} \nu_{st} \tag{14}$$

For the electrons, the problem is slightly different because of their small mass. The frictional heating is negligible for that species and the main heating source is the energy deposition from the suprathermal electrons resulting from either photoionization or precipitation.

Besides this heating, specific losses must be included as they can be important in the F region. These losses correspond to inelastic collision processes which are not described by the 8-moment approximation as it only accounts for elastic processes. The electron gas collides with the neutral atmosphere and can then excite the rotational or vibrational states of the molecular species N_2 and O_2, the atomic oxygen to the ^1D state, or the fine structure levels of O. Expressions of these processes are given by *Schunk and Nagy* [1978].

The molecular ions, N_2^+, O_2^+, and NO^+ are assumed to be in thermal equilibrium with each other. This assumption is justified as these ions contribute to the plasma only in the lower ionosphere, where large collision frequencies cause the local energy deposition to prevail over energy transport. As a consequence, the heat flow carried by the molecular ions is negligible for the energy exchange processes and is omitted from the transport equations. The temporal evolution of the temperature of the molecular ions is obtained from the mean of the energy equations, analogous to the consideration for the momentum equations.

2.2 The Kinetic Transport of Energetic Electrons

In the terrestrial ionosphere, precipitating electrons or primary photoelectrons move along the magnetic field lines, producing heating, excitation and ionization. During an ionization process, the incident electron - called "primary electron" in case of precipitating source, and "primary photoelectron" in case of solar ionization - is scattered mostly forward, whereas the extracted electron - called "secondary electron"- may be scattered into any direction [*Opal et al.*, 1971]. In the following, it is assumed that there is no angular scattering during an excitation process, and no energy redistribution in an elastic collision [*Strickland et al.*, 1976].

The kinetic transport equation describes the angular and energy redistributions of the electrons, which govern the evolution of a steady-state electron flux from the top of the ionosphere to the low E-region. This equation can be approximated in a relatively simple way: first, we assume that electrons are predominantly transported along magnetic field lines, and that the atmosphere is stratified perpendicularly to these field lines. This approximation is justified at middle and high latitudes. Secondly, the motion of the electrons is represented by the motion of their centers of gyration along the magnetic field. The effect of ionospheric horizontal electric fields on the energetic electrons is small and is neglected. The acceleration of the electrons is assumed to have taken place above the modeled altitude range, and local field aligned potential drops and the mirror force from the converging geomagnetic field are neglected. With these assumptions, the transport equation for energetic electrons can be written [*Oran and Strickland*, 1978] as:

$$\mu \frac{\partial I(\tau,\mu,E)}{\partial \tau(z,E)} = -I(\tau,\mu,E) + sf(\tau,\mu,E) + \frac{n_e(z)}{\sum_k n_k(z)\,\sigma_k^T(E)} \frac{\partial\,(L(E)\,I(\tau,\mu,E))}{\partial E}$$

$$+ \sum_l \left\{ \frac{n_l(z)\,\sigma_l^T(E)}{\sum_k n_k(z)\,\sigma_k^T(E)} \int_{-1}^{1} d\mu \int_{E}^{E_{max}} dE' R^l(E',\mu' \rightarrow E,\mu) I(\tau,\mu',E') \right\} \tag{15}$$

$I(\tau, \mu, E)$: Electron stationary flux ($cm^{-2}\ s^{-1}\ eV^{-1}\ sr^{-1}$)

E, E' : Energies (eV) of scattered and incident electrons

μ, μ' : Cosines of scattered and incident electron pitch-angles

$\tau(z, E)$: Electron scattering depth, defined by: $d\tau(z,E) = -\sum_k \sigma_k^T(E) n_k(z) dz$

$\sigma_k^T(E)$ = Total elastic and inelastic collision cross section for the neutral species k, for an electron at energy E

$n_k(z)$: Density of the neutral species k (N_2, O_2, O, H, He)

$n_e(z)$: Electron density

R^l : Redistribution function describing the degradation from a state (E', μ') to a state (E, μ) for the neutral species l(N_2, O_2, O, H, He)

$$R^l(E',\mu' \rightarrow E,\mu) = \frac{\sum_p \sigma_p^l(E',\mu' \rightarrow E,\mu)}{\sigma_l^T(E)} \qquad (16)$$

In this formula, the summation is done over every elastic and inelastic process p. The differential cross sections $\sigma_p^l(E',\mu' \rightarrow E,\mu)$ in units of $cm^2\ eV^{-1}\ (2\pi sr)^{-1}$ are deduced from the cross sections as described in *Lummerzheim and Lilensten* [1994].

The left-hand part of the equation $\mu \frac{\partial I(\tau,\mu,E)}{\partial \tau(z,E)}$ is the variation of the steady-state electron flux $I(\tau, \mu, E)$ with the scattering depth.

The second term on the right-hand side of the equation is the source function. It may be the precipitated flux at the "top" of the ionosphere (considered at about 600 km), or it may be initialized at every altitude as the primary photoelectron flux (in units of $cm^{-2}\ s^{-1}\ eV^{-1}\ sr^{-1}$) caused by solar EUV:

$$sf(\tau,\mu,E) = \frac{1}{4\pi \sum_k n_k(z)\ \sigma_k^T(E)} q_{k,i}(z,W) \qquad (17)$$

$$q_{k,i}(z,W) = n_k(z)\ \sigma_{k,i}^{ion}(E)\ \Phi_\infty(E) \exp\left(-\sum_m \sigma_m(E) \int_z^{+\infty} n_m(s) ds \right) \qquad (18)$$

$q_{k,i}$: primary electron production ($cm^{-3}\ s^{-1}\ eV^{-1}$)

W : difference between the energy E and the ionization threshold for species k, at the i^{th} state

$\sigma_{k,i}^{ion}$: ionization cross section for species k, at the i^{th} state

Φ_∞ : solar flux on the top of the ionosphere [*Torr and Torr*, 1985]

$\sigma_m(E)$: absorption cross section of the neutral species m for one photon at energy E

The integration is done along s, the line of sight to the sun. To obtain the primary photo-production along a vertical column, we use the Chapman function.

The loss function $L(E)$ appearing in the third term is assumed to be a continuous energy loss to the thermal electrons. We assume that the primary electrons are not deflected in this process. The function $L(E)$ is [*Swartz and Nisbet*, 1972]:

$$L(E) = \frac{3.37\ 10^{-12}}{E^{0.94} n_e^{0.03}} \left(\frac{E - E_e}{E - 0.53 E_e} \right)^{2.36} \tag{19}$$

E_e is the thermal energy, in eV, equal to $8.61\ 10^{-5} T_e$, where T_e is the electron temperature in Kelvin.

The last term in the transport equation represents the electron production due to degradation of higher-energy fluxes (collisions between electrons and neutral particles) [*Mantas* , 1973; *Oran and Strickland*, 1978; *Stamnes*, 1981]. The collisions between secondary electrons are neglected.

The numerical procedure for solving equation (15) and references concerning the cross section inputs are described in detail in *Lilensten et al.* [1989], and *Lummerzheim and Lilensten* [1994], and will not be re-explained here. The results of this code have been successfully compared with other numerical procedures, laboratory experiments and auroral observations [*Lummerzheim and Lilensten*, 1994]. The output of this kinetic model provides ionization and heating sources for the fluid model. The parameters calculated by the kinetic model include:

- the ion production P_m and the secondary electron production P_s :

$$P_m(z) = 2\pi n_m(z) \int_{-1}^{1} d\mu \int_{E_{min}}^{E_{max}} dE\ \sigma_m^{ion}(E)\ I(z,E,\mu) \tag{20}$$

$$P_s(z) = \sum_m P_m \tag{21}$$

where n_m is the density of the neutral species m, and $\sigma_m^{ion}(E)$ is the ionization cross section.

- the thermal electron gas heating rate [*Schunk and Nagy*, 1978]:

$$Q_e(z) = \int_0^{E_t} \left(E - \frac{3}{2} kT_e \right) P_e dE + \int_{E_t}^{+\infty} -\frac{dE}{dx} \hat{I}(z,E) dE + \left(E_t - \frac{3}{2} kT_e \right) \left(-\frac{dE}{dx} \hat{I}(z,E_t) \right) \tag{22}$$

where:

$$\hat{I}(z,E) = \int_{-1}^{1} I(z,E,\mu) d\mu \tag{23}$$

P_e represents the production rate of electrons (primaries and secondaries), and E_t is the energy at which the stationary and the thermal flux are equal. The expression $-(dE/dx)$ is the rate at which an electron with energy E looses its energy to the ambient gas, and is equal to the loss function $L(E)$ (equation 19). In this heating rate equation, the first part on the right hand side is negligible, since E_t is smaller than 1 eV. The second term represents the losses from the stationary flux to the thermal electrons at all energies, and the third term is a "surface" term, corresponding to the losses taking place between E_t and the thermal energy.

3. Numerical Solution Procedure

For the fluid representation (equation 1-14), two different time-dependent numerical methods have been chosen for the modeling of the ionosphere between 100 and 3000 km. Concerning the kinetic part (equation 15-23), one specific numerical scheme has been used to cover the range between 100 and 1000 km.

3.1 Method of Lines

The standard routines of the partial differential equations solver MOLCH of the International Mathematical and Statistical Library (IMSL), [*Sewell*, 1982; *Sincovec and Madsen*, 1975] are used here. The method of lines consists of a spatial approximation of the solution by cubic splines developed on a base of Hermite polynomials with time-dependent coefficients. Assuming that the discretization grid of the problem is composed of N points and that M parameters ρ_j are solved, each parameter can be written as:

$$\rho_j(x,t) = \sum_{i=1}^{N} (a_i^j(t)\Phi_i(x) + b_i^j(t)\Psi_i(x)),\ 1 \le j \le M \qquad (24)$$

where Φ_i and Ψ_i are the Hermite polynomials of degree 3.

The initial system of equations of the parameters of interest (density, velocity, temperature and heat flow) becomes a differential system of first order in time on the coefficients $a_i^j(t)$ and $b_i^j(t)$, closed by Dirichlet or Neumann boundary conditions. This system is then integrated in time with an implicit Gear method of first order [*Byrne et al.*, 1977].

3.2 Flux Corrected Transport Method

The flux corrected transport technique [FCT; *Boris and Book*, 1976] has been developed for fluid mechanics applications and is basically devoted to shock propagation. It is a finite volume conservative technique based on a second order Goudounov explicit scheme. In normal flows, it is stabilized up to fourth order using a numerical antidiffusive stage (which makes the scheme non-centered). When steep gradients are present, the scheme is degraded to first order accuracy with a stabilization procedure which consists of a diffusive numerical flux. It is able to solve conservative equations including transport terms or local source terms.

3.3 Discrete Ordinate Method

The transport equation for energetic electrons can be separated into two distinct tasks: the energy degradation that electrons experience in inelastic collisions, and the scattering and transport. In the energy degradation routine, the source term of equation (15) is evaluated on a discrete energy grid with the constraint of energy conservation. The method used here was initially proposed by *Swartz* [1985]. Since electrons never gain energy in a collision, the degradation source term can be evaluated at a given energy after the transport equation has been solved for all higher energies.

Once the source term is known, the transport equation (15) is formally equivalent to the equation of radiative transfer. Well tested numerical procedures are available to solve this equation. In our model we adopt the discrete ordinate method (DISORT). This algorithm is based on ideas by *Chandrasekhar* [1960]. The numerical implementation was developed and tested by *Stamnes et al.* [1988], and *Wiscombe* [1977]. This code is particularly well suited for the strongly peaked phase functions that occur in scattering of high energy electrons.

3.4 Boundary Conditions in the Fluid and Kinetic Transport Models Coupling

These two models are dynamically coupled: the fluid code provides the electron concentration and temperature to the kinetic code, and the kinetic code provides the ionization and the electron heating rates to the fluid code.

Energetic exchanges between the ionosphere and magnetosphere are accounted for at the upper limit as energy inputs from the magnetosphere to the electron gas and are imposed, in the fluid part, as a condition on the downward electron heat flow, i.e. a heat transfer to the thermal electron gas by conduction. Moreover, the number flux and mean energy of precipitating electrons are imposed to the kinetic part, corresponding to suprathermal energy exchanges.

On the other hand, the ion gases are supposed to transfer thermal energy to the magnetosphere, so that their heat flow is imposed to be upward at the upper limit in the fluid part.

At the lower limit, no explicit boundary conditions are imposed in the fluid part, but are rather implicitly defined by the collisions with the neutrals which impose ion production/loss balance and thermal equilibrium.

The different couplings of the present models are summarized in figure 2.

For the numerical procedure, the spatial grid is non uniformly spaced according to the increasing scale heights between 100 and 3000 km. The grid step is necessarily small (~1 km) at the lower altitudes to numerically solve the collision dominated ionosphere in the E-region, and rapidly increases (~80 km) in the topside ionosphere to solve the collisionless plasma transport.

4. Models Inputs

The fluid models, as well as the kinetic model need boundary conditions to materialize the different couplings which are present at auroral latitudes.

4.1 Solar EUV

The photoelectron fluxes are dependent on the solar flux, which in turn is interpolated between solar maximum and minimum using the $F_{10.7}$ index.

4.2 Neutral atmosphere

Both fluid and kinetic parts require vertical profiles of the major neutral components in order to compute ionization rates, and elastic and inelastic collisions. These components are obtained from the empirical model MSIS-90 [*Hedin*, 1991]. This model includes the solar cycle dependence ($F_{10.7}$ index) and geomagnetic activity (Ap index). Furthermore, as NO^+ is a major species in the E region and is mainly produced from chemical reaction involving its neutral parent NO, one needs an estimation of the nitric oxide concentration in the atmosphere and a knowledge of its diurnal evolution. The nitric oxide is a minor species around 100 km and arises from chemical reactions; then, its concentration and flux are numerically solved at the same level as the ionized species.

Moreover, thermospheric wind effects are included using the MSIS-Wind Model [*Hedin et al.*, 1991] and the FTH model better suited for high latitudes comparisons [*Fauliot et al.*, 1993].

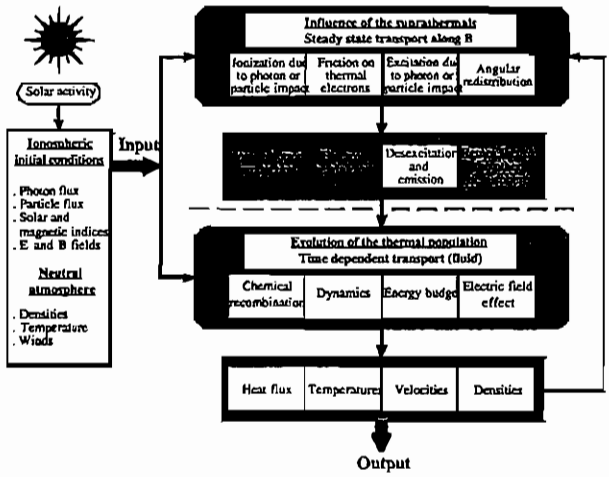

Figure 2. Scheme of the resolution showing the inputs, the couplings between the two transport modules and the outputs of the model. The dashed line separates the kinetic transport module from the fluid one.

4.3 Magnetosphere Coupling

4.3.1 Auroral precipitations.

In the auroral regions, electron precipitation is an important source of both ion production and electron gas heating. Depending on the location, different sources of precipitations originating from the magnetosphere are encountered, which are characterized by various energy levels. The *Hardy et al.* [1987] statistical model is used in the modeling because it covers a wide range of electron energy levels starting at 50 eV. Moreover, the latitudinal coverage of the model is large enough for auroral and polar studies. For the simulations, the precipitating electrons are assumed to have a Maxwellian energy distribution, with characteristics (energy flux and mean energy) obtained from the *Hardy et al.* [1987] model. However, any spectral density shape can be imposed, since it is a direct input to the kinetic part.

4.3.2 Energy input.

Besides the connections between photoelectrons and precipitating electron fluxes, which are in the kinetic part, and the thermal electron gas, which is contained in the fluid description, a thermal energy transfer from the magnetosphere to the ionosphere has to be imposed to the fluid part and is materialized by a downward electron heat flow. Presently, the values are taken from a special analysis of the EISCAT data [*Blelly and Alcaydé*, 1994], which provides the temporal evolution of the downward electron heat flow at the EISCAT latitude.

4.3.3 Convection Electric Field.

The convection electric field is imposed on the model. This field can be freely specified or taken from ionospheric observations. A version of our model that uses a convection electric field from the statistical model of *Senior et al.* [1990] is in preparation.

4.3.4 Field-Aligned Currents.

Any departure from the ambipolar flow hypothesis can be imposed to the code by imposing a field-aligned current. This current is supposed to be transported by the thermal electrons.

5. Models Outputs

The TRANSCAR models yield the evolution with time of the vertical profiles of concentration, velocity and temperature for the six ions and the electrons, and the vertical profiles of heat flow for O^+, H^+, N^+ ions and the electrons. Depending on the choice, the results may be concerned with a fixed geographic location (evolution connected to the variation of the local time) or with a fixed magnetic tube (evolution due to the variation of the location resulting from the convection and the associated variation of the local time).

5.1 Results

Figure 3a shows an output of the model for the location of EISCAT in May at 07:00 UT during high solar activity ($F_{10.7} > 200$) and without convection electric field. The E and F regions are well determined with a transition from molecular to atomic ions ensured by NO^+. The transition altitude from NO^+ to O^+ (altitude where both ions have the same concentration) lays at 180 km in that simulation, and the F peaks reaches 6 10^{11} m^{-3}. Above the F-region, N^+ reaches 5% of O^+ in accordance with previous measurements and numerical studies. Figure 3b shows, for the same time, the effect of a convection electric field of 100 mVm^{-1} amplitude (constant with altitude) on the ion concentrations above 150 km. The strong electric field amplitude induces a frictional heating which affects the reaction rates through T_{eff} and significantly alters the composition of the ionosphere. In that case, the transition altitude between NO^+ and O^+ reaches 320 km, while the F peak is reduced to 1.5 10^{11} m^{-3} (reduction factor of 4).

Figure 4a presents the vertical profiles of O^+ and molecular ions temperatures. They are identical in the altitude range where the balance is done between cooling on the neutrals (at low altitude) and heating on the electrons (at higher altitude). Figure 4b presents the effects of the frictional heating on the O^+ ion and the molecular ions temperatures. The friction results from collisions of the ions with the neutral components. As the collisions are more effective for the molecular species than for the atomic ones, their temperatures can differ from about 1000 K in the F-region.

6. Uncertainties and Limitations

A former version of this model, which does not include the energetic electron transport model and was limited to two ion species and electrons, has been compared to EISCAT-VHF data both in steady state configuration [*Robineau et al.*, 1996] and in dynamical response to external perturbation [*Blelly et al.*, 1996]. Figure 5 shows the comparison between the two models of solution of the fluid equations (ML and FCT) and the EISCAT-VHF data for a winter period. Temperatures, concentration and ion velocity are quantitatively reproduced in that simulation with minimum inputs: electron heat flow at the upper altitude, and convection electric field in the F-region. They showed their ability to well reproduce the main features of the ionosphere above the F-region in static, as well as in dynamic state. Moreover, figure 5 shows that both methods (FCT: dot-dashed line, ML: full line) give comparable results in the altitude range probed by the radar. The differences observed at higher altitudes are mainly due to boundary conditions which are not imposed in the same way in the two techniques.

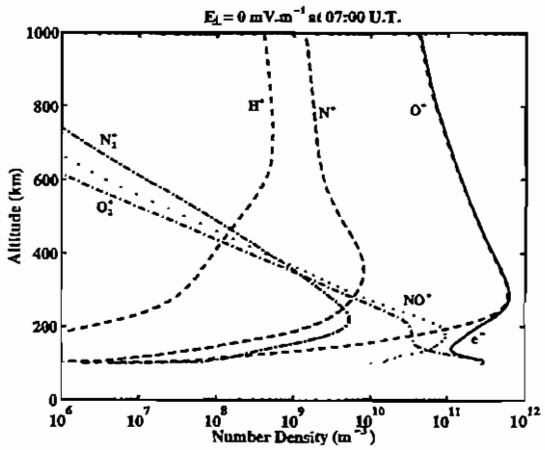

Figure 3. Vertical ionospheric concentration structure at 07:00 UT for a quiet ionosphere (a); with a convection electric field of 100 mV m^{-1} amplitude (b). The electrons are plotted with full line, the atomic ions with dashed lines, NO^+ with dotted line and other molecular ions with dot-dashed lines.

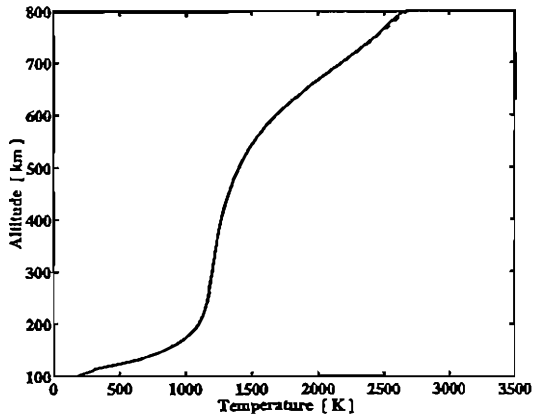

a

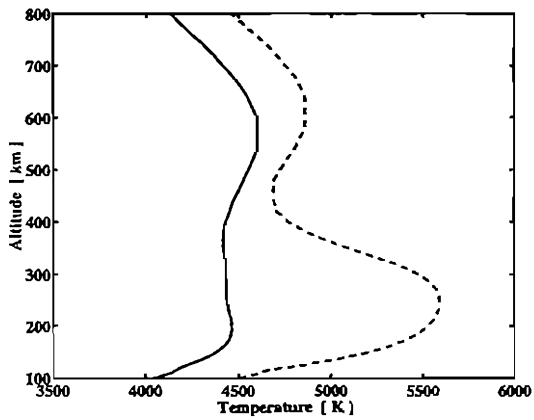

b

Figure 4. Vertical profiles of O^+ ion (full line) and molecular ions (dashed line) temperatures at 07:00 UT for a quiet ionosphere (a); with a convection electric field of 100 mV m^{-1} amplitude (b).

Nevertheless, the differences are negligible even in the dynamic configuration. Further comparisons for these new models in the E-region are on the way.

A basic limitation is imposed by the expansion presented in equation (1), which implicitly assumes that the terms in the expansion are small. *Robineau et al.* [1996] and *Blelly et al.* [1996] have shown that for a quiet or a perturbed ionosphere, electrons and heavy ions (O^+) verify the conditions of the expansion, while for light ions (H^+) in a supersonic outflow configuration, the conditions are less reliable at high altitudes (above 3000 km).

The kinetic part has been tested and compared to problems with analytic solutions, laboratory measurements, and auroral observations [*Lummerzheim and Lilensten*, 1994]: it has reproduced the laboratory observations of electron penetration into N_2 gas by *Barret and Hays* [1976], and auroral emission ratio measurements by *Gattinger et al.* [1991]. The numerical procedure developed introduces an error which is estimated to be less than 5% to the results.

7. Availability of the Model

These codes have been developed to run on a workstation, despite their large size. The program developers are willing to collaborate with interested scientists on any specific problems either theoretical or experimental (comparison with data), which are adapted to a one-dimensional study.

The results are stored on direct files, each record corresponding to a specific time. Besides the direct output of the models, these files contain vertical distribution of some parameters which may be of interest. So, the neutral atmosphere composition (N_2, O_2, NO, O, H, N), temperature and the three components of the neutral wind are included. Production rates for N_2^+, O_2^+, O^+, H^+, N^+ and heating rates for the electron gas are also provided.

Each record starts with a header which provides information on the models inputs at the corresponding time: $F_{10.7}$ and Ap indices, energy flux and mean energy of the precipitating electrons [*Hardy et al.*, 1985] and ions [*Hardy et al.*, 1991], convection electric field components; the field-aligned current can be determined from equation 7. Furthermore, location parameters such as geographic and magnetic coordinates are also included, as well as the solar zenith angle and the magnetic local time.

A matlab routine is available to analyze these direct access files, which provides temporal displays of the main parameters and allows vertical plot of any one of the parameters contained in these files [*Alcaydé et al.*, 1994].

8. References

Alcaydé, D., P.-L. Blelly, and J. Lilensten, GIVEME: General Ionosphere Visualization and Extraction from a Model for the EISCAT Svalbard Radar, *EISCAT Technical Note*, 9452, 1994.

Barret, J. L. and P. B. Hays, Spatial distribution of energy deposited in nitrogen by electrons, *J. Chem. Phys.*, *64*, 743, 1976.

Blelly, P. L. and R. W. Schunk, A comparative study of the time-dependent standard 8-, 13- and 16-moment transport formulations of the polar wind, *Ann. Geophys.*, *11*, 443-469, 1993.

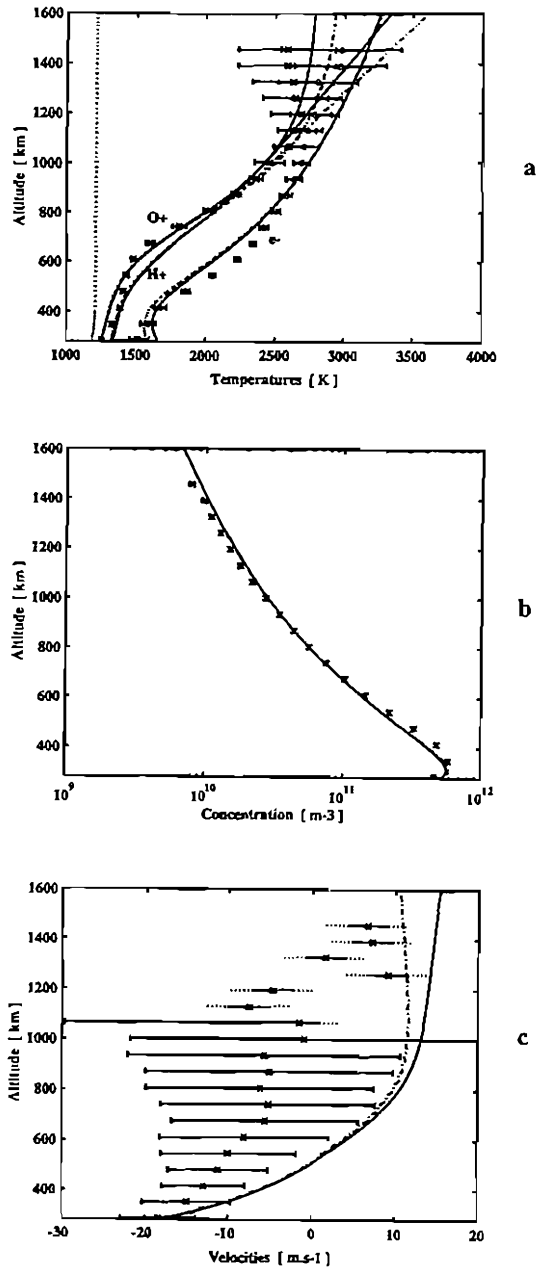

Figure 5. 920212 experiment: vertical profiles of raw data (cross) with error bars and noon steady state O^+, H^+ ions and electrons from ML (solid lines) and FCT (dot-dashed lines) models: ions and electron temperature (a); O^+ ions concentration (b); O^+ ions velocity (c).

Blelly, P. L., A. Robineau, and D. Alcaydé, Numerical modeling of sporadic ion outflow events above EISCAT, *J. Atmos. Terr. Phys., 58*, 273-285, 1996.

Blelly, P. L. and D. Alcaydé, Electron heat flow in the auroral ionosphere inferred from EISCAT-VHF observations, *J. Geophys. Res., 99*, 13181-13188, 1994.

Boris, J. P., Flux-corrected transport modules for generalized continuity equations, *NRL Memorandum Report 3237*, Naval Research Laboratory, Washington, DC, 1976.

Byrne, G. D., A. C. Hindermarsh, K. R. Jackson, and H. G. Brown, A comparison of two ODE codes: Gear and Episode, *Computers and Chemical Engineering, 1*, 133-147, 1977.

Chandrasekhar, S., *Radiative Transfer*, 393 pp., Dover Publications, New York, 1960.

Conrad, J. R. and R. W. Schunk, Diffusion and heat flow equations with allowance for large temperature differences between the interacting species, *J. Geophys. Res., 84*, 811-822, 1979.

Diloy P.-Y., A. Robineau, J. Lilensten, P.-L. Blelly, and J. Fontanari, A numerical model of ionosphere, including the E-region above EISCAT, *Ann. Geophys., 14*, 191-200, 1996.

Fauliot, V., G. Thuiller, M. Hersé, Observations of the F-region horizontal and vertical winds in the auroral zone, *Ann. Geophys., 11*, 17-28, 1993.

Gattinger, R. L., A. Vallance Jones, J. H. Hecht, D. J. Strickland, and J. Kelly, Comparison of ground-based optical observations of N_2 second positive to N_2^+ first negative emission ratios with electron precipitation energies inferred from the Sondre Stromfjord radar, *96*, 11341-11351, 1991.

Hardy, D. A., M. S. Gussenhoven, R. Raistrick, and W. J. McNeil, Statistical and functional representations of the pattern of auroral energy flux, number flux, and conductivity, *J. Geophys. Res., 92*, 12275-12294, 1987.

Hardy, D. A., W. J. McNeil, M. S. Gussenhoven, and D. Brautigam, A statistical model of auroral ion precipitation 2. Functional representation of the average patterns, *J. Geophys. Res., 96*, 5539-5547, 1991.

Hedin, A. E., Extension of the MSIS thermosphere model into the middle and lower atmosphere, *J. Geophys. Res., 96*, 1159-1172, 1991.

Hedin, A. E., M. A. Biondi, R. G. Burnside, G. Hernandez, R. M. Johnson, T. L. Killeen, C. Mazaudier, J. W. Meriwether, J. E. Salah, R. J. Sica, R. W. Smith, N. W. Spencer, V. B. Wickwar, and T. S. Virdi, Revised global model of thermosphere winds using satellite and ground-based observations, *J. Geophys. Res., 96*, 7657-7688, 1991.

Lilensten, J., W. Kofman, J. Wisemberg, E. S. Oran, and C. R. DeVore, Ionization efficiency due to primary and secondary photoelectrons: A numerical model, *Ann. Geophys., 7*, 83-90, 1989.

Lummerzheim, D., and J. Lilensten, Electron transport and energy degradation in the ionosphere: evaluation of the numerical solution, comparison with laboratory experiments and auroral observations, *Ann. Geophys.*, in press, 1994.

McFarland, M., D. Albritton, F. C. Fehsenfeld, E. E. Ferguson, and A. L. Schmeltekopf, Flow-drift technique for ion mobility and ion-molecule reaction rate constant measurements, 2, Positive ion reactions of N^+, O^+ and N_2^+ with O_2 and O^+ with N_2 from thermal to 2eV, *J. Chem. Phys., 59*, 6620-6628, 1973.

McFarland, M., D. L. Albritton, F. C. Fehsenfeld, E. E. Ferguson, and A. L. Schmeltekopf, Energy dependence and branching ratio of the $N_2^+ + O$ reaction, *J. Geophys. Res., 79*, 2925-2926, 1974.

Mantas, G. P., Electron collision processes in the ionosphere, Aeronomy report no. 54, Aeronomy Laboratory, Dept. of Electrical Engineering, Univ. of Illinois, Urbana, Illinois, 1973.

Opal, C. B., W. K. Peterson, and E. C. Beaty, Measurement of secondary-electron spectra produced by electron impact ionization of a number of simple gases, *J. of Chem. Physics, 55*, 4100-4106, 1971.

Oran, E. S., and D. J. Strickland, Photoelectron flux in the earth's ionosphere, *Planet. Space Sci., 26*, 1161-1177, 1978.

Rees, M. H., *Physics and Chemistry of the Upper Atmosphere*, Cambridge University Press, New York, 1989.

Robineau, A., P. L. Blelly, and J. Fontanari, Time-dependent models of the auroral ionosphere above EISCAT. *J. Atmos. Terr. Phys., 58*, 257-271, 1996.

Schunk, R. W., and J. C. G. Walker, Thermal diffusion in the topside ionosphere for mixtures which include multiply-charged ions, *Planet. Space Sci., 17*, 853-868, 1969.

Schunk, R. W., and J. C. G. Walker, Thermal diffusion in the F_2-region of the ionosphere, *Planet. Space Sci., 18*, 535-557, 1970a.

Schunk, R. W., and J. C. G. Walker, Minor ion diffusion in the F_2-region of the ionosphere, *Planet. Space Sci., 18*, 1319-1334, 1970b.

Schunk, R. W., W. J. Raitt, and P. M. Banks, Effect of electric fields on the daytime high-latitude E and F regions, *J. Geophys. Res., 80*, 3121-3130, 1975.

Schunk, R. W., Transport equations for aeronomy, *Planet. Space Sci., 23*, 437-485, 1975.

Schunk, R. W., Mathematical structure of transport equations for multispecies flows, *Rev. Geophys. Space Phys., 15*, 429-445, 1977.

Schunk, R. W., and A. F. Nagy, Electron temperature in the F-region of the ionosphere, *Rev. Geophys. Space. Phys., 16*, 355-399, 1978.

Schunk, R. W. and W. J. Raitt, Atomic nitrogen and oxygen ions in the daytime high-latitude F region, *J. Geophys. Res., 85*, 1255-1272, 1980.

Schunk, R. W., A mathematical model of the middle and high latitude ionosphere, *Pure Appl. Geophys., 127*, 255-303, 1988.

Senior, C., D. Fontaine, G. Caudal, D. Alcaydé, and J. Fontanari, Convection electric fields and electrostatic potential over $61° < \Lambda < 72°$ invariant latitude observed with the European incoherent scatter facility, 2. Statistical results, *Ann. Geophys., 8*, 257-272, 1990.

Sewell G., IMSL software for differential equations in one space variable, *IMSL Technical Report Series*, no. 8202, 1982.

Sincovec, R. F., and N. K. Madsen, Software for nonlinear partial differential equations. *ACM Transactions on Mathematical Software, 1*, 232-260, 1975.

Stammes, K., On the two-stream approach to electron transport and thermalization, *J. Geophys. Res., 86*, 2405-2410, 1981.

Stammes, K., S. C. Tsay, W. J. Wiscombe, and K. Jayaweera, Numerically stable algorithm for Discrete-Ordinate-Method radiative transfer in a multiple scattering and emitting layered media, *Applied Optics, 27*, 2502, 1988.

Strickland, D. J., D. L. Book, T. P. Coffey, and J. A. Fedder, Transport equation technique for the deposition of auroral electrons, *J. Geophys. Res., 81*, 2755-2764, 1976.

Swartz, W. E., Optimization of electron energy degradation calculation, *J. Geophys. Res., 90*, 6587-6593, 1985.

Swartz, W. E., and J. S. Nisbet, Revised calculations of the F-region ambient electron heating by photoelectrons, *J. Geophys. Res., 77*, 6259-6277, 1972.

Torr, M. R., and D. G., Torr, Ionization frequencies for solar cycle 21: Revised, *J. Geophys. Res., 90*, 6675-6678, 1985.

Walker, J. C. G., Thermal diffusion in the topside ionosphere, *Planet. Space Sci., 15*, 1151-1156, 1967.

Wiscombe, W. J., The delta-M method: Rapid, yet accurate radiative flux calculations for strongly asymmetric phase functions, *J. Atmos. Sci., 34*, 1408, 1977.

Table 1. Chemical reaction rates taken from *Rees* [1988] and *Schunk* [1988] and references herein.

Reaction	Rate coefficients k_n and α_n ($cm^3 \cdot s^{-1}$); P_N($cm^{-3} \cdot s^{-1}$)
$O^+ + N_2 \xrightarrow{k_1} NO^+ + N$	$k_1 = \begin{cases} 1.533\ 10^{-12} - 5.92\ 10^{-13}\left(\frac{T_{eff}}{300}\right) + 8.6\ 10^{-14}\left(\frac{T_{eff}}{300}\right)^2 & 300 \le T_{eff} \le 1700\ K \\ 2.73\ 10^{-12} - 1.155\ 10^{-12}\left(\frac{T_{eff}}{300}\right) + 1.483\ 10^{-13}\left(\frac{T_{eff}}{300}\right)^2 & 1700 < T_{eff} \le 6000\ K \end{cases}$
$O^+ + O_2 \xrightarrow{k_2} O_2^+ + O$	$k_2 = 2.82\ 10^{-11} - 7.74\ 10^{-12}\left(\frac{T_{eff}}{300}\right) + 1.073\ 10^{-12}\left(\frac{T_{eff}}{300}\right)^2 - 5.17\ 10^{-14}\left(\frac{T_{eff}}{300}\right)^3 + 9.65\ 10^{-16}\left(\frac{T_{eff}}{300}\right)^4$ $300 \le T_{eff} \le 6000\ K$
$O^+ + NO \xrightarrow{k_3} NO^+ + O$	$k_3 = \begin{cases} 8.36\ 10^{-13} - 2.02\ 10^{-13}\left(\frac{T_{eff}}{300}\right) + 6.95\ 10^{-14}\left(\frac{T_{eff}}{300}\right)^2 & 300 \le T_{eff} \le 1500\ K \\ 5.33\ 10^{-13} - 1.64\ 10^{-14}\left(\frac{T_{eff}}{300}\right) + 4.72\ 10^{-14}\left(\frac{T_{eff}}{300}\right)^2 - 7.05\ 10^{-16}\left(\frac{T_{eff}}{300}\right)^3 & 1500 \le T_{eff} \le 6000\ K \end{cases}$
$O^+ + H \xrightarrow{k_4} H^+ + O$	$k_4 = 2.5\ 10^{-11}\sqrt{T_n + \frac{T_{O^+}}{16}} + 1.2\ 10^{-4}\left[v(O^+) - v_n\right]^2$
$O_2^+ + N_2 \xrightarrow{k_5} NO^+ + NO$	$k_5 = 5.0\ 10^{-16}$
$O_2^+ + N \xrightarrow{k_6} NO^+ + O$	$k_6 = 1.2\ 10^{-10}$
$O_2^+ + NO \xrightarrow{k_7} NO^+ + O_2$	$k_7 = 4.5\ 10^{-10}$
$O_2^+ + e \xrightarrow{\alpha_1} O + O$	$\alpha_1 = 1.6\ 10^{-7}\left(\frac{300}{T_e}\right)^{0.55}$
$N_2^+ + O_2 \xrightarrow{k_8} O_2^+ + N_2$	$k_8 = 5.0\ 10^{-11}\left(\frac{300}{T_{eff}}\right)$

Table 1. (Continued)

Reaction	Rate coefficients k_n and α_n ($cm^3 \cdot s^{-1}$); $P_N(cm^{-3} \cdot s^{-1})$
$N_2^+ + O \xrightarrow{k_9} O^+ + N_2$	$k_9 = \begin{cases} 1.0\ 10^{-11}\left(\frac{300}{T_{eff}}\right)^{0.23} & T_{eff} \le 1500\ K \\ 3.6\ 10^{-12}\left(\frac{300}{T_{eff}}\right)^{-0.41} & T_{eff} > 1500\ K \end{cases}$
$N_2^+ + O \xrightarrow{k_{10}} NO^+ + N$	$k_{10} = \begin{cases} 1.4\ 10^{-10}\left(\frac{300}{T_{eff}}\right)^{0.44} & T_{eff} \le 1500\ K \\ 5.2\ 10^{-11}\left(\frac{300}{T_{eff}}\right)^{-0.2} & T_{eff} > 1500\ K \end{cases}$
$N_2^+ + NO \xrightarrow{k_{11}} NO^+ + N_2$	$k_{11} = 3.3\ 10^{-10}$
$N_2^+ + e \xrightarrow{\alpha_2} N + N$	$\alpha_2 = 1.8\ 10^{-7}\left(\frac{300}{T_e}\right)^{0.39}$
$N^+ + O_2 \xrightarrow{k_{12}} NO^+ + O$	$k_{12} = 2.6\ 10^{-10}$
$N^+ + O_2 \xrightarrow{k_{13}} O_2^+ + N$	$k_{13} = 3.1\ 10^{-10}$
$N^+ + O_2 \xrightarrow{k_{14}} O^+ + NO$	$k_{14} = 3.7\ 10^{-11}$
$N^+ + NO \xrightarrow{k_{15}} NO^+ + N$	$k_{15} = 2.0\ 10^{-11}$
$N^+ + H \xrightarrow{k_{16}} H^+ + N$	$k_{16} = 3.6\ 10^{-12}$
$N^+ + O \xrightarrow{k_{17}} O^+ + N$	$k_{17} = 5.0\ 10^{-13}$
$NO^+ + e \xrightarrow{\alpha_3} N + O$	$\alpha_3 = 4.2\ 10^{-7}\left(\frac{300}{T_e}\right)^{0.85}$
$H^+ + O \xrightarrow{k_{18}} O^+ + H$	$k_{18} = 2.2\ 10^{-11}\sqrt{T_{H^+} + \frac{T_n}{16}} + 1.2\ 10^{-4}\left[v(H^+) - v_n\right]^2$

The Graz Ionospheric Flux Tube Simulation Model

G. Kirchengast

Institut für Meteorologie und Geophysik, Universität Graz,
Halbärthgasse 1, A-8010 Graz, Austria

1. Introduction

The Graz Ionospheric Flux Tube Simulation (GIFTS) model is a mathematical model of the ionospheric F-region at mid- and high-latitudes. It is based on a set of hydrodynamic transport equations which is a suitably adapted form of the so-called 13-moment approximation [cf. *Schunk*, 1977]. The model can be applied along magnetic field lines at arbitrary non-equatorial sites encompassing the height range between 150 km and 600 km. It yields the field-aligned time-dependent evolution of the electron density, n_e, the field-aligned ion velocity, v_i, and the ion and electron temperatures, T_i and T_e, respectively, in a self-consistent way. The number densities of the major ion species (O^+, NO^+, O_2^+, N_2^+) are simultaneously deduced, assuming photochemical equilibrium with respect to the molecular species. Optionally, a coupled system of meridional and zonal neutral wind equations is self-consistently included. This, in addition, yields the evolution of the meridional, u_n, and zonal, v_n, wind velocities in the thermosphere.

The GIFTS model takes account of the relevant physical processes of the mid- and high-latitude F-region, including production of the plasma and of heat due to EUV irradiance and electron precipitation, chemistry of metastable and stable ions, neutral winds (forced by horizontal pressure gradients, Coriolis deflection, viscosity, advection, and ion drag when self-consistently treated), field-aligned diffusion, thermal and frictional heat transfer between ions, electrons and neutrals, electron heat conduction and heating due to field-aligned currents, and plasma advection due to $\mathbf{E} \times \mathbf{B}$ drift. Model runs can be performed with high spatial and temporal resolution (e.g., 1 km and 1 min) in reasonable computing times and experience shows that realistic results can be obtained for a wide range of geophysical conditions.

Originally, the GIFTS model was developed as a plasma density and transport model yielding n_e and v_i as described by [*Kirchengast et al.*, 1992], i.e., ion and electron temperatures were required as input. As a next step, an ion energy equation was included; a detailed description of the model at this stage is given by [*Kirchengast*, 1992]. Recently, an appropriate electron energy equation was added which enabled the model to handle the whole set of fundamental ionospheric parameters (n_e, v_i, T_i, T_e) self-consistently. One-to-one comparisons of model results with incoherent scatter data described by *Kirchengast et al.* [1995 and 1996] indicate the reliability and usefulness of the model at this stage. Neutral wind equations also were recently included as an option which allows better account for ionosphere-thermosphere momentum coupling in some high-latitude studies. A report giving a complete up-to-date description of the GIFTS model is in preparation and will be available upon request from the author. Details not given in the more concise description below are found there.

2. Mathematical Formulation

The GIFTS model is based on a system of transport equations which describes, for a partially ionized gas containing ions, electrons and neutrals, the spatial and temporal evolution of density, drift velocity, temperature, stress and heat flow on an equal footing. *Schunk* [1977] gives an instructive review on equation systems like this so-called 13-moment approximation which are obtained by taking velocity moments of Boltzmann's equation.

Our adapted form of the general 13-moment approximation is tailored to describe the high- and mid-latitude F-region in a realistic, but not fully rigorous, manner leading to a model efficient even in case of high-resolution applications. Specifically, we express stress and heat flow explicitly in terms of the lower order moments density, drift and temperature [cf. *Schunk*, 1988]. This reduces the general set of differential equations to one containing the three lowest order moments only, i.e., one closed at the 5-moment level, usually termed a set of continuity, momentum and energy equations. We solve appropriate versions of these conservation equations yielding, in our case, the self-consistent evolution of the parameter set (n_e, v_i, T_i, T_e, optionally u_n, v_n). Simultaneously, any desired derivable quantities are computed, e.g., ion densities, parallel and perpendicular ion temperatures, electron heat flow, or single terms of equations.

2.1 Model Geometry.

The GIFTS model provides magnetic field-aligned time-dependent solutions at arbitrary sites at mid- and high-latitudes. Figure 1 sketches the model geometry adopted for this purpose. It is described in detail by *Kirchengast et al.* [1992] and *Kirchengast* [1992], and only a brief outline relevant to the understanding of the mathematical-numerical formulation shall be given below.

The geometry is based on the concept of straight, non-divergent field-aligned flux tubes well approximating the highly inclined and weakly arched non-equatorial F-region flux tubes. The site (i.e., specific field line) has to be chosen *a priori*, either by prescribing an ionospheric volume of origin (height h_0, latitude φ_0, longitude λ_0) through which the model fits a local Cartesian coordinate system based on the local IGRF (International Geomagnetic Reference Field) field line, or by prescribing the geographic footpoint location of a field line and its inclination, I, and declination, D. The latter method is convenient when simulating, e.g., a field-aligned incoherent scatter radar beam, since antenna position and azimuth and elevation of the beam can directly be fed into the model. In either case, the model automatically sets up its geometry, i.e., computes throughout the F-region all grid point coordinates (h_i, φ_i, λ_i) needed for the numerical computations.

If simulations involving $\mathbf{E} \times \mathbf{B}$ drift are performed at high latitudes, so-called Help Flux Tubes (HFTs) can be set up in addition to the Main Flux Tube (MFT). This enables an estimation of horizontal gradients in the plasma, i.e., the parametric inclusion of horizontal plasma advection in the basically field-aligned model. HFTs also enable the estimation of horizontal heat advection in the ion energy balance. Furthermore, they enable, for the neutral wind equations, the computation of the horizontal pressure gradient force, the driving force of neutral winds (using a neutral density and temperature model), and the parametric inclusion of horizontal advection forcing.

2.2 Plasma Density and Transport Equations.

The continuity equation of the electrons, involving that of the ions, is used in conjunction with the momentum equation of the ions, involving that of the electrons, in order to describe the spatial and temporal evolution of electron density, n_e, and field-aligned ion velocity, v_i. Based on the diffusion approximation, a well established approach for describing concentration and transport of ionization in the F-region, the properly derived set of equations reads in our case

$$\frac{\partial n_e}{\partial t} + \nabla_{\parallel} \cdot (n_e \mathbf{v}_{\parallel}) + \mathbf{v}_{\perp} \cdot \nabla_{\perp} n_e = q_e - L_e, \qquad (1)$$

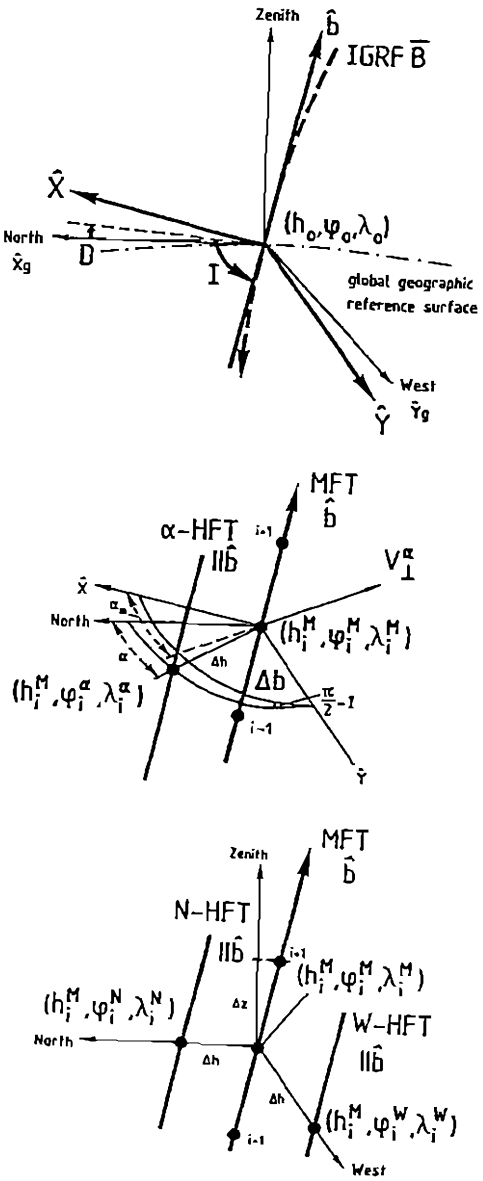

Figure 1. Model geometry. Upper panel: basic geometry; middle panel: one Help Flux Tube (α-HFT) case - direction of $\vec{E}$ fields temporally constant; lower panel: two Help Flux Tubes (N-HFT & W-HFT) case - arbitrary variable $\vec{E}$ fields. After *Kirchengast et al.* [1992].

$$\mathbf{v}_{\parallel} = \mathbf{v}_{n\parallel} - D_a\left[\frac{\nabla_{\parallel} n_e}{n_e} + \frac{-\langle m_i\rangle \mathbf{g}_{\parallel} + 2k_B(\nabla_{\parallel} T_p + \omega\nabla_{\parallel} T_n + \omega^*\nabla_{\parallel} T_i) + n_e^{-1}\nabla_{\parallel}(\bar{\tau}_i:\mathbf{BB})}{k_B(T_i + T_e)}\right], \tag{2}$$

$$D_a = \frac{k_B(T_i + T_e)}{\langle m_i\nu_i\rangle(1-\Delta_{in})}, \langle m_i\nu_i\rangle = \frac{1}{n_e}\sum_i(n_i m_i \sum_n \nu_{in}), \langle m_i\rangle = \frac{1}{n_e}\sum_i n_i m_i, T_p = \frac{T_i + T_e}{2},$$

$$\mathbf{v}_{\perp} = \frac{\mathbf{E}\times\mathbf{B}}{B^2} \quad , \tag{3}$$

where the subscripts e, i, and n, apply to electrons, ions, and neutrals, respectively, the subscripts $\parallel$ and $\perp$ refer to the directions parallel and perpendicular to the magnetic field, n denotes number density, $\mathbf{v}$ drift velocity, T temperature, $\bar{\tau}_i$ the ion stress tensor, q_e is the electron production rate, L_e their chemical loss rate, m_i is the mass of ion species i, ν_{in} the momentum transfer collision frequency of ion i with the neutrals n, $\mathbf{g}$ is the acceleration of gravity, $\mathbf{B}$ the magnetic induction (further referred to as "field"), $\mathbf{E}$ the electric field, k_B is Boltzmann's constant, ω and ω^* are thermal diffusion coefficients, Δ_{in} is an ordinary diffusion correction factor, D_a is the ambipolar diffusion coefficient, the brackets, $\langle ... \rangle$, denote density-weighted averages, and T_p is the plasma temperature.

Relying on the basic principles of charge neutrality, conservation and polarization, Eqs. (1) – (3) are implicitly associated with the identities $\mathbf{v}_{\parallel} = \mathbf{v}_{i\parallel} = \mathbf{v}_{e\parallel} + \mathbf{j}_{\parallel}/en_e$, where $\mathbf{j}_{\parallel} = en_e(\mathbf{v}_{i\parallel} - \mathbf{v}_{e\parallel})$ is the field-aligned current density with e the elementary charge, and $\mathbf{v}_{\perp} = \mathbf{v}_{i\perp} = \mathbf{v}_{e\perp}$. Note that, instead of $\mathbf{v}_{e\parallel}$, $\mathbf{v}_{i\parallel} = \mathbf{v}_{\parallel}$ appears in the field-parallel transport term of Eq. (1). This is justified since $\nabla(\mathbf{j}_{\parallel}/e) = 0$ is valid throughout the F-region where space charges are absent. $\mathbf{v}_{\perp}$ and $\mathbf{j}_{\parallel}$, usually height-independent functions of time at a given site, are inputs to the model.

The inclusion of the field-perpendicular transport term of Eq. (1), $\mathbf{v}_{\perp}\cdot\nabla_{\perp} n_e$, in a field-aligned model requires an appropriate formulation of the perpendicular gradient, $\nabla_{\perp} n_e$. *Kirchengast et al.* [1992] describe, in detail, a semi-parametric treatment successfully doing this formulation within the GIFTS model. Briefly, one or two Help Flux Tubes (cf. Fig. 1) are used for a parametric estimation of the (geographically) horizontal part of $\nabla_{\perp} n_e$ while the field-aligned part is rigorously included in the field-aligned diffusion equation. In case of $\mathbf{E}\times\mathbf{B}$ drift, in order to obtain realistic horizontal plasma advection with this method, it is of course necessary that all model input quantities relevant to this advection exhibit a realistic horizontal structure by themselves.

Equation (2) gives the ion drift in its classical form as the sum of neutral wind induced drift and diffusion velocity. It is evident that, for diffusive equilibrium, the local plasma scale height is established by the ratio of the thermal energy to the sum of the forces due to gravity, temperature gradients and a gradient in stress. The contribution of stress is not straightforward to see; it generally acts to reduce the scale height [*Schunk et al.*, 1975]. Diffusion in the F-region is generally governed by the O^+ ions so that density-weighted averaging of ion mass and the mass-collision frequency product in Eq. (2) is not strictly needed. However, preferably during nighttimes in case of weak air drag, molecular ion diffusion can play a role at heights below about 200 km. The averaging is included for such regimes and since we refrained from the expense of a rigorous treatment of the coupled equations of the major ions. The quantities Δ_{in}, ω, and ω^*, which depend on height and the ratio T_i/T_n (ω also weakly depends on n_e), are formulated based on results of *Conrad and Schunk* [1979]. Under normal ionospheric conditions, however, the ordinary diffusion correction and thermal diffusion exert only small to negligible effects.

$v_{n\parallel}$ and $g_\parallel$ are expressed in our geometry (Fig. 1) as $v_{n\parallel} = -u_{ng} \cos I \cos D + v_{ng} \cos I \sin D + w_{ng} \sin I$ and $g_\parallel = -g \sin I$, respectively, where u_{ng}, v_{ng}, and w_{ng} are the geographically northward, westward, and upward components of the neutral wind. Concerning the stress tensor $\bar{\tau}_i$, which reflects a pressure/temperature anisotropy in the plasma, its element associated with the **B** direction, $(\bar{\tau}_i:\mathbf{BB})$, is significant in case of considerable $\mathbf{E} \times \mathbf{B}$ drifts. Based on expressions given by *Schunk* [1975; 1988], we formulated this term as

$$\bar{\tau}_i:\mathbf{BB} = \tau_{i\parallel} = -\frac{\langle m_i \rangle}{3} n_e \left(Q_i \frac{E_{eff}^2}{B^2} \right), \quad Q_i = \frac{R_i}{S_i + 0.6 \nu_{ii}} \tag{4}$$

where R_i and S_i, contained in the dimensionless factor Q_i, are mass and cross-section weighted ion-neutral collision frequencies, whereby we set the cross-section ratios to 0.8 for non-resonant and to 0.5 for resonant interactions, ν_{ii} is the ion self collision frequency. $\mathbf{E}_{eff} = \mathbf{E} + \mathbf{v}_n \times \mathbf{B}$ is an effective electric field accounting properly for the relative ion-neutral perpendicular drift causing the stress in the plasma.

When solving the equations above, we assume the neutral atmosphere and ionosphere to consist of their major species (O, N_2, O_2) and (O^+, NO^+, O_2^+, N_2^+, n_e), respectively. Thus, various collision frequencies, both resonant and non-resonant, are needed. The necessary non-resonant ones are taken from *Schunk* [1988], and the resonant ones from *Figueroa and Hernández* [1988]. The latter conveniently include the effect of relative ion-neutral drifts in terms of a series expansion [cf. *Kirchengast et al.*, 1992]. The O^+–O collision frequency is enhanced by 40% in the model following indications of several studies [e.g., *Burnside et al.*, 1987] on the accuracy of the present theoretical values.

2.3 Plasma Production and Loss.

The free thermal electrons and ions representing the ionosphere are produced at high latitudes by solar extreme ultraviolet (EUV) irradiance and by the precipitation of non-thermal electrons and ions into the upper atmosphere. After a certain lifetime during which they may have undergone chemical transforms and transport, they are removed through recombination processes, unless they flowed away.

2.3.1 Production.

The local ion production rate due to solar EUV radiation, q_i, is given in the form

$$q_i(h,\varphi,\lambda,t) = n_n \sum_s \sigma_i^{(i)s} \Phi_\infty^s e^{-\tau^s}, \tag{5}$$

$$\tau^s = \sum_n \sigma_n^{(a)s} n_n H_n Ch(X_n,\chi), \tag{6}$$

where the superscript s denotes the s-th ionizing solar EUV wavelength band, $\sigma_n^{(a)s}$ and $\sigma_i^{(i)s}$ are the absorption and ionization cross sections, respectively. Φ_∞^s is the solar photon flux incident at the top of the atmosphere, τ^s is the optical depth, $H_n = k_B T_n / m_n g$ is the neutral scale height, and $Ch(X_n, \chi)$ is the Chapman grazing incidence function, where X_n stands for $(R_E + h)/H_n$ with the earth's radius R_E, and χ is the solar zenith angle.

The atmospheric constituents absorb solar EUV, leading essentially to the reactions

$$\begin{array}{lcl} O + h\nu & \rightarrow & O^+(4S) + e^- \\ & \searrow & O^+(2D) + e^- \\ & \searrow & O^+(2P) + e^- \\ N_2 + h\nu & \rightarrow & N_2^+ + e^- \\ O_2 + h\nu & \rightarrow & O_2^+ + e^- \quad , \end{array} \tag{7}$$

whereby the five corresponding ion production rates are calculated as outlined below.

The 37 wavelength scheme introduced by *M. Torr et al.* [1979] is applied to divide the solar EUV spectrum into discrete intervals between 5 and 105 nm and the cross sections $\sigma_n^{(a)s}$ and $\sigma_j^{(i)s}$ are adopted from this work. Thereby, the $\sigma_{O^+(4P)}^{(i)s}$ are subsumed in the $\sigma_{O^+(4S)}^{(i)s}$ and the $\sigma_{O^+(2P^*)}^{(i)s}$ in the $\sigma_{O^+(2D)}^{(i)s}$, since the $O^+(4P)$ and $O^+(2P^*)$ states are known to relax very rapidly in essentially this way [*Dalgarno and McElroy*, 1965]. Φ_∞^s is computed using the EUV flux model SERF3 from *Tobiska* [1991], which gives Φ_∞^s as a function of the solar $F_{10.7}$ flux (and other indices) for a day specified. For the large zenith angles ($\chi > 60°$), which frequently occur at high latitudes, the approximate expressions after *Smith and Smith* [1972] are used to evaluate the Chapman function $Ch(\chi_n, \chi)$.

Concerning impact ionization, electron impact can be significant in the F-region. We adopt a model constructed by *Brown and Daniell* [private communication, 1991] which yields the local production rates for incident electrons with mean energies > 500 eV for the same five ions as accounted for in the reaction scheme (7) above. For the following, the impact production rates shall simply be thought subsumed in the photoionization rates q_i of Eq. (5).

2.3.2 *Chemistry of the metastable ions.*

We do not include the chemistry of metastable ions in the stable one (Table 1), but rather consider it as contributing to the production side of the stable ions. This is justified, since the metastable ions $O^+(2P)$ and $O^+(2D)$ are much more rapidly converted into the stable ions $O^+(4S)$ (= O^+ ground state), N_2^+ and O_2^+, than the stable chemistry itself works [cf. *Torr and Torr*, 1982; *D. Torr et al.*, 1979].

Within this approach, described in detail by *Kirchengast et al.* [1992] including tables on the relevant chemistry, we use the concept of conversion fractions. For the radiative decay and quenching of the metastable $O^+(2P)$ ions these are defined according to the $O^+(2P)$ chemistry. The $O^+(2D)$ decay is handled with constant conversion factors, although known to be rather complicated in reality [cf. *Torr and Torr*, 1982]. This is done since some rate coefficients of the $O^+(2D)$ chemistry are still uncertain today. Roughly, the fraction of $O^+(2D)$ converted into N_2^+ is known to vary between 25% and 75%, dependent on geophysical conditions, the complementary rest being converted to $O^+(4S)$. Accordingly, we set the conversion factors of $O^+(2D)$ into $O^+(4S)$ and N_2^+ to between 0.25 and 0.75 in our model studies.

Through these conversions, the five ion production rates generated by the reaction scheme (7) in conjunction with the corresponding electron impact ionization are conveniently reduced to three "effective" production rates for the stable ions $O^+(4S)$ (further referred to simply as "O^+"), N_2^+ and O_2^+. These are used as inputs for the (stable) ion chemistry described below.

Table 1. Ion Chemistry

Reaction	Rate coefficient [m^3s^{-1}]
$O^+ + N_2 \xrightarrow{\gamma_1} NO^+ + N$	$\gamma_1 = \frac{1}{n(N_2)} \sum_{i=0}^{8} \gamma_{1i} n_i(N_2)$
$O^+ + O_2 \xrightarrow{\gamma_2} O_2^+ + O$	$\gamma_2 = \gamma_{20} f(T_n)$
$N_2^+ + O \xrightarrow{\gamma_3} NO^+ + N$	$\gamma_3 = \gamma_{30}$
$NO^+ + e^- \xrightarrow{\alpha_1} N + O$	$\alpha_1 = 4.2 \times 10^{-13} \left(\frac{300}{T_e}\right)^{0.85}$
$N_2^+ + e^- \xrightarrow{\alpha_2} N + N$	$\alpha_2 = 1.8 \times 10^{-13} \left(\frac{300}{T_e}\right)^{0.39}$
$O_2^+ + e^- \xrightarrow{\alpha_3} O + O$	$\alpha_3 = 1.6 \times 10^{-13} \left(\frac{300}{T_e}\right)^{0.55}$

References for the rate coefficients and expressions for γ_{10}, γ_{20}, and γ_{30} are given in *Kirchengast et al.* [1992].

2.3.3 Ion chemistry and electron loss.

The ion chemistry, leading finally to the charged particles loss via recombination, is assumed to consist of the six reactions depicted in Table 1. This rather simple reaction scheme can essentially describe the F-region behavior as worked out, e.g., by *Strobel and McElroy* [1970] for the F_2-region and mainly by *D. Torr et al.* [1979] for the F_1-region.

The reaction scheme of Table 1 is discussed in detail by *Kirchengast et al.* [1992] and the rate coefficients γ_{10}, γ_{20}, and γ_{30}, whose main feature is a pronounced temperature dependence, denote the ones used and described there. γ_1 and γ_2 have been modified since then. We include now the influence of vibrational excitation of N_2 and O_2 on γ_1 and γ_2, based on results of *Pavlov* [1988 a, b; 1989], *Pavlov and Namgaladze* [1988], *Vlaskov and Henriksen* [1985]. Briefly, γ_1 is evaluated assuming a Boltzmann distribution of $n(N_2)$ over the vibrational levels i, $n_i(N_2) = n(N_2)(1-\exp(-E_v/T_v))\exp(-iE_v/T_v)$, with $E_v = 3353$ K. The vibrational temperature T_v is approximated by $T_v = T_n + \Delta T$(solar activity, n_e, T_e, electron impact) with the function $\Delta T(...)$ roughly accounting for the dependence of T_v on geophysical conditions. The rate coefficients for levels $i \geq 1$ are computed following *Pavlov* [1988a], for level $i = 0$ the original γ_{10} is used. The influence of vibrational excitation of O_2 on γ_2 is expressed by applying a correction factor $f(T_n) = \exp(-1.032 \times 10^{-3} T_n + 0.374)$ following *Pavlov* [1989].

In order to solve the continuity Eq. (1), our model needs the ion chemistry in terms of the electrons. Assuming photochemical equilibrium with respect to the molecular ions and relying on quasi-neutrality ($n_e = n(O^+) + n(NO^+) + n(O_2^+) + n(N_2^+)$), we find an appropriate photochemical balance directly for the electrons in the convenient form

$$q_e - L_e = q_{O^+} - \frac{(\beta_1 + \beta_2)}{\left(1 + \frac{\beta_1}{\alpha_1 n_e} + \frac{\beta_2}{\alpha_3 n_e}\right)} \left[n_e - \frac{q_{N_2^+}}{\beta_3 + \alpha_2 n_e} \left(1 + \frac{\beta_3}{\alpha_1 n_e}\right) - \frac{q_{O_2^+}}{\alpha_3 n_e} \right] , \qquad (8)$$

where

$$q_e = q_{O^+} + q_{N_2^+} + q_{O_2^+},\ \beta_1 = \gamma_1 n(N_2),\ \beta_2 = \gamma_2 n(O_2),\ \beta_3 = \gamma_3 n(O)\ . \tag{9}$$

As illustrated by Eqs. (8)–(9) and Table 1, the chemistry is quite sensitive to the ambient geophysical conditions, especially via the various dependencies of the competing rate coefficients. Note also that Eq. (8) contains several commonly-used more simple electron loss descriptions [cf. *Kirchengast*, 1992], e.g., the F_2-region loss $L_e = (\beta_1 + \beta_2)n_e$ (limit $\beta_1 \ll \alpha_1 n_e$, $\beta_2 \ll \alpha_3 n_e$, $n_e \approx n(O^+)$).

Along with Eq. (8), we derive expressions for the ion number densities. We obtain

$$n(N_2^+) = \frac{q_{N_2^+}}{\beta_3 + \alpha_2 n_e} \tag{10}$$

$$n(O^+) = \frac{n_e - n(N_2^+)\left(1 + \dfrac{\beta_3}{\alpha_1 n_e}\right) - \dfrac{q_{O_2^+}}{\alpha_3 n_e}}{1 + \dfrac{\beta_1}{\alpha_1 n_e} + \dfrac{\beta_2}{\alpha_3 n_e}} \tag{11}$$

$$n(NO^+) = \frac{\beta_1}{\alpha_1 n_e} n(O^+) + \frac{\beta_3}{\alpha_1 n_e} n(N_2^+) \tag{12}$$

$$n(O_2^+) = \frac{\beta_2}{\alpha_3 n_e} n(O^+) + \frac{q_{O_2^+}}{\alpha_3 n_e} \tag{13}$$

Equations (10)–(13) are used in order to determine the ion density profiles once the n_e profile is computed at a given time.

2.4 Ion Energy Equation.

Throughout our region of interest, below about 500 km, the ion energy equation is dominated by collisional coupling of the ions to the neutrals and electrons, which significantly simplifies its general 13-moment formulation. In particular, to a good approximation, the higher-order influences of heating due to divergent heat flows and viscous heating due to stress combined with velocity gradients/shears are negligible in this regime. Thus, the basic formulation of the ion energy equation for our model reads

$$\frac{D_i\left(\frac{3}{2} p_i\right)}{Dt} + \frac{5}{2} p_i \nabla \cdot \mathbf{v}_i = \frac{\delta E_i}{\delta t}, \tag{14}$$

$$\frac{\delta E_i}{\delta t} = \rho_i \sum_n \frac{\nu_{in}}{m_i + m_n}\left[3k_B(T_n - T_i)\Psi_{in} + m_n(\mathbf{v}_i - \mathbf{v}_n)^2 \Phi_{in}\right] + 3k_B n_i \nu_{ie}(T_e - T_i).$$

At the left hand side of Eq. (14), which contains inertial, advective and adiabatic heating, $p_i = n_i k_B T_i$ is the ion pressure, and $(D_i/Dt) = (\partial/\partial t) + \mathbf{v}_i \cdot \nabla$ denotes the convective derivative of

ion species i. At the right hand side, denoted by $(\delta E_i/\delta t)$, which represents heating due to collisional coupling to the ambient neutrals and electrons, $\rho_i = m_i n_i$ is ion mass density, Ψ_{in} and Φ_{in} are velocity dependent correction factors for heat and momentum transfer.

Equation (14) is solved for the temperature of the O^+ ions, which well represents the common temperature of all ions, T_i, since the temperature differences between the ion species are small [*Schunk et al.*, 1975]. The collisional processes (right hand side) dominate Eq. (14) while the non-collisional ones (left hand side) are generally unimportant, but can be non-negligible at heights above about 400 km when phenomena varying at scales of 100 km or smaller are modeled. The dominance of $(\delta E_i/\delta t)$,allows a simplified and numerically convenient treatment of the energy balance. The self-consistent solution of Eq. (14) is carried out for the balance

$$\frac{\partial\left(\frac{3}{2}p_i\right)}{\partial t} = \frac{\delta E_i}{\delta t}$$

while advective heating, $v_i \cdot \nabla$ $((3/2)p_i)$, and adiabatic heating, $(5/2)p_i \nabla \cdot v_i$ are not self-consistently included, but merely in a simultaneous manner [*Kirchengast*, 1992]. Although this is not a rigorous account for the latter minor processes, it allows a good estimation of their relevance to a given modeling problem with small scale variations involved.

The necessary collision frequencies are, as for the plasma density and transport equations, taken from *Schunk* [1988] in case of the non-resonant ones. In case of collisions of ions with their parent neutrals, the O^+–O collision in our case, the factors Ψ_{in} and Φ_{in} depart from unity for pronounced relative ion-neutral drifts and we adopt a separate treatment. We do not directly include the rather complicated expressions for Ψ_{in} and Φ_{in} [cf. *Schunk*, 1977] in this case, but follow the work of *Figueroa and Hernández* [1988]. They conveniently express the entire Joule heating term, the first term of $(\delta E_i/\delta t)$ comprising ion-neutral heat exchange and frictional heating, as a series expansion with respect to the relative ion-neutral drift. When, in case of pronounced relative drifts, the ion temperature anisotropy is of interest, $T_{i\parallel}$ and $T_{i\perp}$ are readily computed taking the stress contribution $\tau_{i\parallel}/n_i k_B$ (cf. Eq. (4)) into account. *Kirchengast* [1992] describes the handling of T_i in detail.

2.5 Electron Energy Equation.

The energy equation of the electrons for the mid- and high-latitude F-region takes a more complicated form than that of the ions, although the general formulation, holding for the thermal balance of an arbitrary species, is identical. This is because heating by a divergent heat flow, inelastic collisions, and external heat sources play a role for the electrons. Heating involving stress is, as for the ions, negligible, however, and the relevant flows are tied to the direction of the magnetic field lines. Accounting for the relevant processes, we use the electron energy equation in the form

$$\frac{3}{2}\frac{p_e}{T_e}\frac{DT_e}{Dt} + p_e \nabla_{\parallel} \cdot v_e + \nabla_{\parallel} \cdot q_e = \frac{\delta E_e}{\delta t} + \sum Q_e - \sum L_e \quad , \tag{15}$$

where

$$p_e = n_e k_B T_e \qquad v_e = v_{i\parallel} - j_{\parallel}/en_e \qquad q_e = -\lambda_e \nabla_{\parallel} T_e - \beta_e j_{\parallel}. \tag{16}$$

At the left-hand side of Eq. (15), which contains inertial, advective, adiabatic and divergent-heat-flow heating, p_e is the electron pressure, $(D/Dt) = (\partial/\partial t) + v_e \cdot \nabla_{\parallel}$ is a convective

derivative, v_e is the electron drift primarily induced by the field-aligned current density $j_{||}$ (the ambipolar contribution $v_{i||}$ is normally not relevant), and q_e is the electron heat flow generated by temperature gradients, $\nabla_{||}T_e$, λ_e being the thermal conductivity; and by $j_{||}$, β_e being the thermoelectric coefficient. Expressions of *Schunk and Walker* [1970] are used to specify λ_e and β_e, the collision frequencies involved are taken from *Schunk* [1988]. Note that significant contributions of the $j_{||}$ terms to the energy balance are confined to the auroral region [*Schunk et al.*, 1987].

At the right-hand side, which represents collisional heat exchange terms, $(\delta E_e/\delta t)$ denotes heating/cooling via elastic collisions with neutrals and ions as well as Joule heating by $j_{||}$ and frictional heating by neutrals (a minor term), ΣQ_e denotes heating by solar EUV-produced photoelectrons and auroral electron precipitation, and ΣL_e denotes inelastic cooling processes.

For elastic collisions, the model takes account of heat exchange with the neutrals N_2 and O and the ions O^+, NO^+, and O_2^+, expressions are taken from *Schunk and Nagy* [1978]. For Joule heating, $j_{||}^2/\sigma_e$, the electrical conductivity σ_e is expressed after *Schunk and Walker* [1970], the collision frequencies involved are from *Schunk* [1988]. Frictional heating is expressed after *Schunk and Nagy* [1978].

Heating by EUV-produced photoelectrons is expressed by integrating the product of photoelectron flux and photo- to thermal-electron energy loss rate over the appropriate energy range [*Schunk and Nagy*, 1978]. The photoelectron flux is specified using a model of *Richards* [private communication, 1993; see also *Richards and Torr*, 1984], the energy loss rate using the expression of *Swartz et al.* [1971]. For the heating by precipitating auroral electrons a model constructed by *Brown and Daniell* [private communication, 1991] is adopted.

Concerning cooling via inelastic collisions, account is taken of cooling due to vibrational and rotational excitation of N_2 and O_2, respectively, excitation of the fine structure levels of the O ground state, and electronic excitation of O to the ^{1}D state. The fine structure cooling rate is expressed after *Hoegy* [1976], the other inelastic cooling rates are taken from *Schunk and Nagy* [1978]. A report is in preparation describes the handling of T_e, and that of the neutral wind introduced below, in detail.

2.6 Neutral Wind Equations

The neutral wind in the thermosphere blows, to a good approximation, horizontally, since the atmosphere is almost vertically stratified. Therefore, its evolution can be described by coupled equations of a meridional and zonal wind component, respectively. An appropriate form for the thermosphere at F-region heights, which we used for our model, reads in vector notation

$$\frac{D\mathbf{v}_n}{Dt} + 2\Omega_C \times \mathbf{v}_n + \frac{1}{\bar{\rho}_n}\nabla_h \bar{p}_n - \frac{1}{\bar{\rho}_n}\nabla_z(\bar{\eta}_n \nabla_z \cdot \mathbf{v}_n) = \bar{\nu}_{ni}(\mathbf{v}_i - \mathbf{v}_n) \qquad (17)$$

where

$$\mathbf{v}_n = u_n\hat{x} + v_n\hat{y}, \qquad \Omega_C \times \mathbf{v}_n = \Omega_C \sin\varphi(-v_n\hat{x} + u_n\hat{y}), \qquad \nabla_h = \nabla_x\hat{x} + \nabla_y\hat{y},$$

$$\bar{\rho}_n = \sum_n m_n n_n,\ \bar{p}_n = \left(\sum_n n_n\right)k_B T_n,\ \bar{\eta}_n = \frac{1}{\sum_n n_n}\sum_n n_n \eta_n,\ \bar{\nu}_{ni} = \frac{1}{\sum_n n_n}\sum_i n_i\left(\sum_n \frac{m_i}{m_n}\nu_{in}\right) .$$

$\mathbf{v}_n$ denotes the horizontal neutral wind vector comprising a meridional (northward unit vector $\hat{x}$) and a zonal (westward unit vector $\hat{y}$) component, u_n and v_n, respectively. $(D/Dt) = (\partial/\partial t) + \mathbf{v}_n \cdot \nabla_h$ is a convective derivative, Ω_C is the Earth's Coriolis vector (φ is latitude), $\bar{\rho}_n$ is the total

neutral mass density, $\bar{\rho}_n$ is the total pressure, $\bar{\eta}_n$ is the mean viscosity coefficient, and $\bar{\nu}_{ni}$ is the mean neutral-ion collision frequency. The neutral constituents involved are O, N_2, and O_2.

The terms in Eq. (17), from left to right, denote convective (inertial and advective) forcing, Coriolis forcing, horizontal pressure gradient forcing (which is the driving force), viscous forcing, and collisional drag by the ionosphere, each term playing a non-negligible role in the balance during some time of a day [e.g., *Killeen and Roble*, 1984; 1986]. Equation (17), separated into the two scalar equations for u_n and v_n, which are coupled by the Coriolis force, is self-consistently solved along with the ionospheric equations. The advection term, $(\mathbf{v}_n \cdot \nabla_h)\mathbf{v}_n$, is included in the same parameterized manner (invoking Help Flux Tubes) as was the plasma advection term in the continuity equation. Generally, advection is small, especially at high latitudes [cf., *Rüster and Dudeney*, 1972; *Killeen and Roble*, 1984; 1986].

The driving force term, $(1/\bar{\rho}_n)\nabla_h \bar{p}_n$, is computed using the neutral temperature and densities of the DTM-78 model of *Barlier et al.* [1978]. Note, however, that everywhere else in the model we use MSISE-90 [*Hedin*, 1991] to specify n_n and T_n. This separate treatment of the driving force is performed since the MSIS parameters, although quite reasonable individually, appear to be unreasonable at heights below about 250 km when combined into the $(1/\bar{\rho}_n)\nabla_h \bar{p}_n$ expression.

The viscosity coefficients η_n are taken from *Rees* [1989]. The viscous forcing, negligible at lower heights, is increasingly important with increasing height due to its $1/\bar{\rho}_n$ dependence. The collision frequencies ν_{in} for computing $\bar{\nu}_{ni}$ are from *Schunk* [1988] and *Figueroa and Hernández* [1988] (cf. section on plasma density and transport above). Ion drag is particularly important for constraining the thermospheric wind speed during the daytime when the ionization is high due to the direct solar EUV irradiance.

3. Numerical Solution Procedure

The transport equations are first rearranged into a format appropriate for numerical solution with respect to their governing parameters n_e, v_i, T_i, T_e, u_n, and v_n. Each equation can be rewritten into the general form of a time-dependent, parabolic, nonlinear, partial differential equation of second order in the field-aligned coordinate, b (upward unit vector $\hat{b}$), which reads

$$\frac{\partial X_i}{\partial t} = A_3(\mathbf{r},t,X_i,X_n)\frac{\partial^2 X_i}{\partial b^2} + A_2(\mathbf{r},t,X_i,X_n)\frac{\partial X_i}{\partial b} + A_1(\mathbf{r},t,X_i,X_n)X_i + A_0(\mathbf{r},t,X_i,X_n), \quad (18)$$

where X_i denotes the governing parameter of the equation considered (e.g. n_e), and X_n stands for the governing parameters of the other equations of the coupled system (e.g. T_i and T_e). The coefficients $A_0, \ldots, A_3$ are complicated expressions to be computed at the geographic location $\mathbf{r}$ of each numerical volume element at each time t. They generally depend on the model inputs as well as on X_i and the X_n's. Their dependence on X_i brings nonlinearity into play, their dependence on the X_n's coupling.

The nonlinearities and couplings have to be carefully handled to allow Eq. (18) to be considered linear, which is necessary for its efficient solution, and to get a numerically stable and accurate solution of the whole system of equations. We achieve this by using, where necessary and appropriate, linear prediction of a parameter over a time step, a few predictor-corrector iterations, a cross-over time stepping for different equations, and an individual selection of each time step as a function of actual variations in critical parameters. For the numerical solution, an implicit discretization scheme with space-centered spatial derivatives and forward time derivatives is applied to Eq. (18), considering it to be linear. This converts it into a

set of algebraic equations with tridiagonal coefficient matrix which is solved for X_i by a standard method [cf. *Kirchengast et al.*, 1992].

In our model, the equations for n_e and T_e are of the general form of Eq. (18), and the equations for u_n and v_n are of this form but linear (except for the parameterized advection term). For n_e, the form is achieved by putting the explicitly formulated momentum equation, Eq. (2), into the continuity equation, Eq. (1). For T_e, the Eqs. (16), expressing electron pressure, drift and heat flow, are set into the electron energy equation, Eq. (15), and a variable transform, $\theta_e = T_e^{7/2}$, is introduced to formulate the equation for θ_e (i.e. $X_i = \theta_e$). The latter transform is performed for reasons of numerical stability. For u_n and v_n, the vector equation, Eq. (17), is split into the scalar equations of these two components, which are arranged according to Eq. (18).

Boundary conditions are needed at the lower (about 150 km) and upper (about 600 km) boundaries for these equations. Lower boundary: For n_e not only the commonly-used photochemical equilibrium is adopted, but the full n_e equation subject to a special discretization [*Kirchengast*, 1992]. For T_e, local heating and cooling rates are equated. For u_n and v_n, viscosity and advection are neglected and the time derivative discretized in the respective equations. Upper boundary: For n_e, an electron flux balance derived from an integration of the continuity equation is adopted including a parameter to specify interhemispheric electron flow through the boundary [*Kirchengast et al.*, 1992]. For T_e, either the electron heat flux or, directly, the temperature has to be specified. For u_n and v_n, the field-aligned gradients of these parameters are assumed to have reached zero at the boundary.

Our equation for T_i, Eq. (14), corresponds to a quite simplified form of Eq. (18) as it has zero spatial derivatives (since advective and adiabatic heating are not self-consistently treated). This allows, after time discretization, to explicitly formulate it with respect to T_i, so that, stepping forward in time, it can be solved along with the implicit equations [*Kirchengast*, 1992]. v_i, finally, which is explicitly given by the algebraic equation, Eq. (2), is readily computed once the profiles of the other parameters have been obtained at a given time [cf., *Kirchengast et al.*, 1992]. The same holds true for the ion densities O^+, NO^+, O_2^+, and N_2^+, which are obtained based on Eqs. (10)–(13).

In summary, the numerical integration procedure of our model works as follows. Beginning with simple initial profiles for n_e, T_i, T_e, and u_n and v_n (Chapman profile for n_e, etc.), steady state solutions are sought and found fairly rapidly at local noon of a chosen starting day. Then, stepping forward in time, field-aligned profiles are computed for subsequent times, yielding the time-dependent evolution. Time-dependent convergence is achieved within a few hours after start time.

For an arbitrary time step Δt, advancing time from t to $t + \Delta t$, first an appropriate value for Δt is selected within the limits 10 sec to 10 min. The selection is based on both physical arguments and extensive tests and depends on the actual variations of parameters like n_e, T_e, and the $\mathbf{E} \times \mathbf{B}$ drift, as well as on specific disturbances included, e.g., gravity waves. With Δt determined, inputs and solution profiles for u_n and v_n, as well as T_i and T_e, are computed at time $t + \Delta t/2$. Next, n_e is computed at time $t + \Delta t$ and, finally, v_i and the ion densities and any other desired quantity are computed, nominally at time $t + \Delta t/2$. At any stage, information on parameters already known at the previous or actual time layers is invoked.

The nominal vertical step used is 1 km, the nominal horizontal step 5 km (Main to Help Flux Tube spacing). When Help Flux Tubes are invoked, the computations are equally performed for each flux tube in order to enable the necessary cross-tube estimations at any time, the results for the Main Flux Tube being the nominal output. As mentioned earlier, the neutral wind equations are used optionally, so they can be excluded from the self-consistent solution. For flexibility, also the electron energy equation can be excluded. When the model runs in such a mode, the governing parameters of equations excluded (e.g. u_n and v_n) are, of course,

required as input. Concerning typical performance, a model run for one day, including some event lasting several hours and needing a time resolution of about 1 min, takes several minutes on an Alpha-processor based DEC/VMS computer.

4. Model Inputs

Various inputs are required for the thermosphere and external influences in order to be able to solve the equation set of the GIFTS model. Most convenient are global input models as they allow, without specific changes, the application of the GIFTS model to arbitrary mid- and high-latitude sites. In any case, the inputs have to be available for a given site considered. Note that experimental data can add on-site input information, which is particularly useful when performing one-to-one comparisons of GIFTS results to measurements [cf. *Kirchengast et al.*, 1992]. Below, the inputs adopted are briefly summarized.

4.1 Neutral Atmosphere.

The neutral temperature T_n, and the number densities $n(O)$, $n(N_2)$ and $n(O_2)$ are, except for the driving force term of the neutral wind equations, taken from the global empirical atmospheric model MSISE-90 described by *Hedin* [1991]. This model is, at present, probably the most elaborate empirical model available on neutral temperature and composition. For the neutral wind driving force term, the global empirical thermospheric model DTM-78, described by *Barlier et al.* [1978], is adopted (cf. the section on the neutral wind equations above).

4.2 Neutral Wind.

Wind input is needed when the GIFTS model option to self-consistently include the neutral wind equations is disabled. In this case, the neutral wind components, u_n and v_n, are taken from the global empirical neutral wind model HWM-90 described by *Hedin et al.* [1991]. This global model provides in a convenient form height and time dependent thermospheric wind patterns. Generally, we use the HWM-90 in a modified way, improving its reasonableness by including on- or near-site wind information from other sources like measured data [e.g., *Kirchengast et al.*, 1992; *Leitinger et al.*, 1994].

4.3 Electron Temperature, Upper-boundary Heat Flux, and $j_{||}$-pattern.

Input for T_e is required when the GIFTS model is run in the mode not including the electron energy equation self-consistently. In this case, either on-site data are used for specifying T_e [cf. *Kirchengast et al.*, 1992] or some model, e.g., a simple one after *Clark et al.* [1970] or the International Reference Ionosphere (IRI) [*Bilitza*, 1992]. In the usual case of including the T_e equation, the time-dependent electron heat flux or temperature, $q_{eU}(t)$ or $T_{eU}(t)$, is needed at the upper boundary at a given site. Such a $q_{eU}(t)$- or $T_{eU}(t)$-profile is either derived from data or models. Similarly, the field-aligned current $\mathbf{j}_{||}$, when considered non-zero, is specified as a $\mathbf{j}_{||}(t)$-profile for a given site, and reasonable profiles are adopted based on data or models.

4.4 **B** Field and **E** Field.

The required parameters of the **B** field, inclination, declination and magnitude, are derived from the global International Geomagnetic Reference Field (IGRF) model [see, e.g., *Bilitza*, 1992]. Concerning the **E** field, it is directly related to the perpendicular convection velocity, $\mathbf{v}_\perp$, via Eq. (3). We supply $\mathbf{v}_\perp$ at a given site as a time-dependent function, based, e.g., on incoherent scatter data [cf. *Kirchengast et al.*, 1992]. In general, such a $\mathbf{v}_\perp(t)$-profile can be considered to be singled out for a given site from a whole convection pattern.

4.5 Solar EUV Radiation.

Solar EUV leads to photoionization and electron heating. The EUV flux model SERF3 described by *Tobiska* [1991] is used as EUV input for computing photoionization. The concept of photoelectron production frequencies [*Richards and Torr*, 1984] and EUV fluxes given by *M. Torr et al.* [1979] are involved in the photoelectron flux model of *Richards* [private communication, 1993] used for computing electron heating.

4.6 Particle Precipitation.

For specifying impact ionization and heating of ionospheric electrons due to precipitating auroral electrons, we adopt a model developed by *Brown and Daniell* [private communication, 1991]. This model is designed for rapid numerical evaluation of ionization and heating rates and is based on detailed calculations on the deposition of auroral electrons [*Strickland et al.*, 1976]. The average energy and the energy flux of the incident electrons are needed as a time-dependent input to this model. Currently, these quantities are obtained using the empirical model of *Spiro et al.* [1982]. Alternatively, the more convenient empirical model described by *Hardy et al.* [1987] could be invoked.

5. Model Outputs

The GIFTS model yields its output parameters as time-dependent field-aligned distributions at a chosen simulation site. The output nominally covers the altitude range from 160 km to 600 km and the simulation runs from noon of a selected starting day to a selected termination day and time. The basic output parameters are n_e, v_i, T_i, T_e, and u_n, and v_n. When required for a specific study, additional parameters are output, like the densities of the ion species O^+, NO^+, O_2^+, and N_2^+, anisotropic ion temperatures, and the magnitude of (about forty, presently) individual terms or other quantities of the equations involved. Furthermore, post-processing routines are used for computing any derivable quantity desired, e.g., moments of the space-time distribution of the parameters (e.g. N_mF_2, h_mF_2) or derivatives of them ($(\partial n_e v_i/\partial b)$, $(\partial T_e/\partial t)$, etc.).

The field of recent and potential applications of the GIFTS model can be divided into three areas: (i) climatological modeling for a wide range of geophysical conditions, (ii) high-resolution simulations of various phenomena, and (iii), invoking synthetization concepts, time-dependent three-dimensional modeling. (i) and (ii) can be performed at any high- or mid-latitude site (e.g., at an appropriate observing station, allowing model-data comparison), (iii) is useful for mid-latitude regions, where the ionosphere co-rotates with the Earth. In what follows, examples of model results in each of the three areas are presented.

5.1 Climatological Modeling.

Simulating climatology with the GIFTS model means to obtain the evolution of the output parameters at a given site for a given time range, typically a day, subject to average conditions prevailing (i.e., no specific "weather"-phenomena are at work). These average conditions include input conditions (actual EUV irradiance, particle precipitation, $\mathbf{E} \times \mathbf{B}$ drift, etc.) and geophysical conditions (actual season, solar and geomagnetic activity), whereby, in general, the former conditions depend on the latter. The model runs can naturally be performed for a whole range of conditions like different seasons and solar activities.

An exemplary climatological result of simulations performed at the European Incoherent Scatter (EISCAT) radar site near Tromsø, Norway, is shown in Figure 2. GIFTS results on n_e, v_i, T_i, and T_e are compared with EISCAT data, the latter being low-pass filtered in time (periods < 180 min excluded) to represent background behavior. The model was geometrically set up

along the field-aligned EISCAT radar beam so that Figure 2 corresponds to a genuine one-to-one comparison. The morning time interval shown contains background ionosphere results computed for a work by *Kirchengast et al.* [1995], which includes the study of a pronounced Traveling Ionospheric Disturbance observed by EISCAT in this interval.

Geophysical conditions on this day were late summer season, high solar activity ($F_{10.7}$(day) = 195, $F_{10.7}$(81-day av.) = 161) and quiet magnetic activity (Ap = 7 for 0-12 UT). Input conditions included neutral wind input based on the HWM-90 model (i.e. the wind equations were not self-consistently treated), the $\mathbf{E} \times \mathbf{B}$ drift considered zero (as the EISCAT $v_\perp$-data suggested it to be weak), and an upper boundary profile $T_{eU}(t)$ (at 600 km) estimated from the EISCAT data.

Figure 2 indicates that the GIFTS model has the capability to predict the climatological behavior of the ionosphere fairly well in all the fundamental parameters computed. Simulations performed for a variety of other days subject to different conditions, including cases with the neutral wind equations self-consistently treated, support this indication in that generally good agreement was found when comparing the results with measured data.

5.2 High-Resolution Simulations.

When medium to small scale phenomena at spatial scales from 1000 km down to about 10 km and temporal scales from a few hours down to about 1 min are studied with the GIFTS model, we term this high-resolution simulations. A variety of high-latitude phenomena occur at these scales, including Traveling Ionospheric Disturbances (TIDs) caused by Atmospheric Gravity Waves (AGWs), $\mathbf{E} \times \mathbf{B}$ drift and field-aligned current variations triggered by magnetospheric processes, and particle precipitation fluctuations associated with auroral arcs. Such phenomena can be observed by powerful ionospheric measurement facilities, e.g., incoherent scatter radars like EISCAT. High-resolution studies with models like the GIFTS model are particularly suited to support the interpretation of such observations and the elucidation of the physics involved.

An example is illustrated by Figures 3 and 4, which depict results of a study of the AGW-TID relationship at the site of the EISCAT radar [*Kirchengast et al.*, 1996]. A TID with a period of about 60 min, observed with EISCAT in the parameters n_e, v_i, T_i, and T_e, was simulated with the GIFTS model. The analysis for obtaining the observed TID from the basic EISCAT data is described by *Hocke et al.* [1996]. The TID was presumed to be caused by an AGW (of the same period), relying on modeling and data analysis experience with high-latitude "TIDs" from various mechanisms (AGWs, $\mathbf{E} \times \mathbf{B}$ drift variations, etc.). A model based on the work of *Clark et al.* [1970; 1971] was adopted for the AGW and was superposed on the neutral background models [cf. *Kirchengast*, 1996]. Such an AGW-disturbed thermosphere was coupled to the GIFTS model and the free AGW parameters, wind-disturbance amplitude at the lower boundary (160 km) and horizontal wave vector in our case, were tuned to fit the observed TID with the simulated TID. A detailed description of this "inverse modeling" procedure is given by *Kirchengast et al.* [1995].

We found that the GIFTS-TID showed quantitative consistency with the EISCAT-TID in all parameters only for a quite specific model-AGW (free parameters constrained to: southward propagation, horiz. wavelength 1000 km, amplitude 5 ms^{-1} at 160 km). For this 'best-fit'-case, the TID-amplitude profiles of all parameters are shown in Fig. 3, (a) – (d), the TID-phase profiles (with respect to the v_i-phase profile) in Fig. 4 (a). In all these panels, the model results are shown in one-to-one comparison to the data illustrating that the agreement is fairly good. In turn, there is no room for doubt that also the causative AGW underlying this 'best-fit'-TID is close to reality. The modeling performed is thus a powerful means of retrieving comprehensive AGW information from incoherent scatter data. Fig. 3, (e) – (f), and Fig. 4 (b) illustrate this model-AGW information associated with the 'best-fit'-TID. This kind of simulations of the AGW-TID relationship is valuable, further, in improving our theoretical insight into this

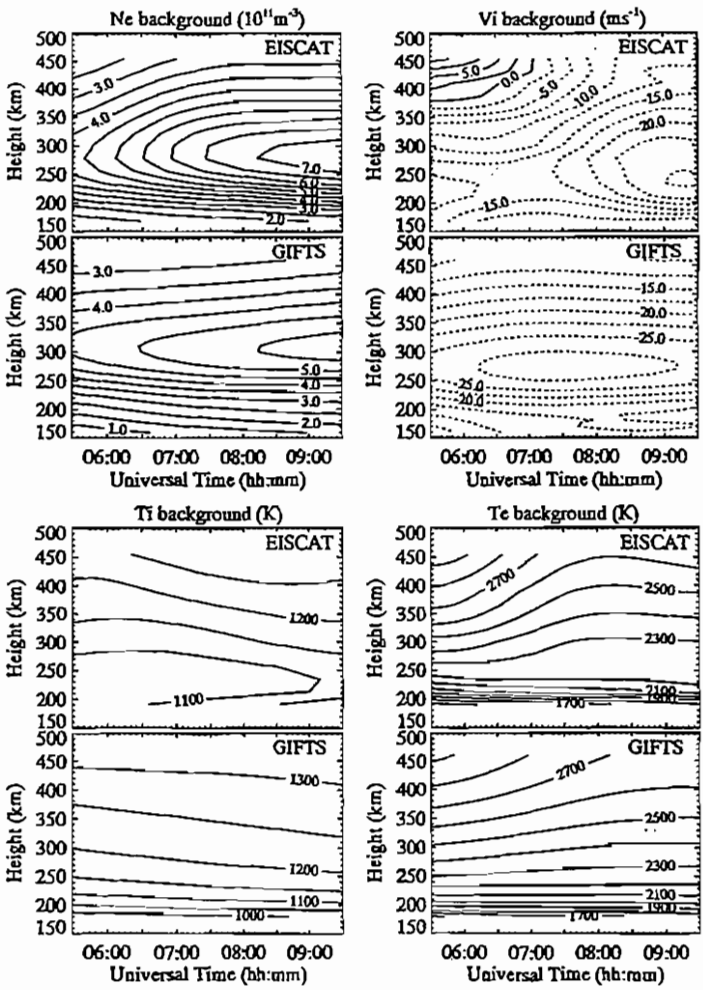

Figure 2. One-to-one comparison of climatological GIFTS model results to EISCAT data for a morning time interval of 31 August 1988 (EISCAT location [geogr.]: 59.6° N lat., 19.2° E long., LT ~ UT + 1.25 hrs). Contour plots of electron density, (upward) field-aligned ion drift, ion temperature, and electron temperature are shown. After *Kirchengast et al.* [1995].

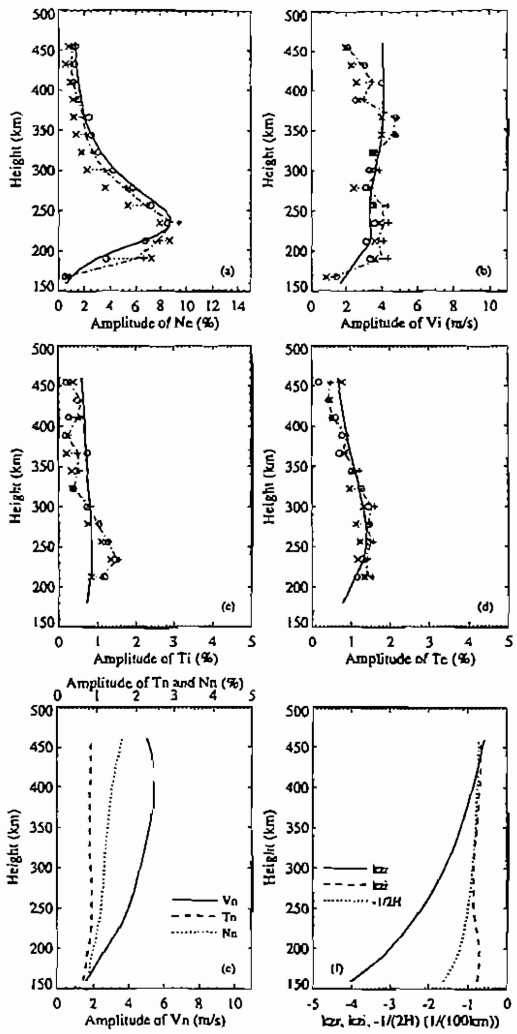

Figure 3. Panels (a) - (d) show amplitude profiles of TID signatures in the parameters n_e, v_i, T_i, and T_e (absolute v_i signature, other parameters relative to background) for a TID event observed with EISCAT on 6 September 1988 from ~ 14:30 - 18:30 UT. In each of the four panels, the mean model TID amplitude (heavy solid profile) is compared to the mean observed one (dashed-dotted profile). In order to illustrate that especially the observed amplitude exhibits some variation around its mean profile during the event, profiles of three subsequent event-subintervals are added in this case (denoted by the symbols o, +, x). Panel (e) shows the amplitude profiles of the corresponding AGW disturbance in v_n (field-aligned wind disturbance), T_n, and n_n (absolute v_n disturbance, other parameters relative to background), and panel (f) the real, k_{zr}, and imaginary, k_{zi}, part of the vertical AGW wave number together with the factor $-1/(2 \times$ Scale height) (cf. *Kirchengast et al.* [1996]).

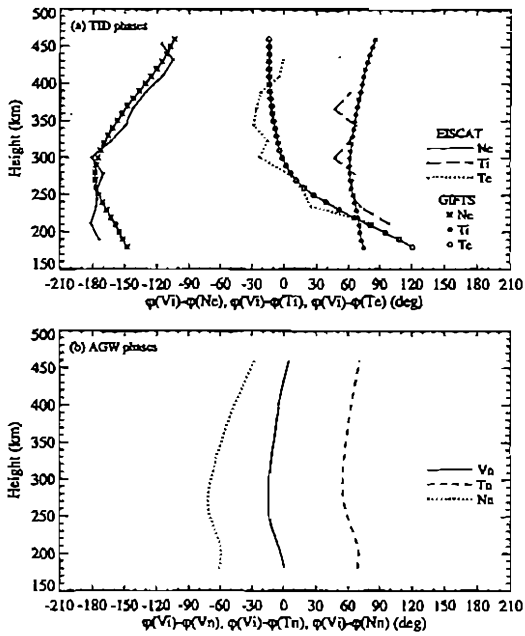

Figure 4. Phase profiles illustrating the relative phase relationships among the TID parameters (upper panel) and the parameters of the corresponding AGW (lower panel) for the TID event considered of 6 September 1988. The phases are shown with respect to the v_i-phase (i.e., the observed phases referenced to the observed v_i, the simulated to the simulated v_i). The upper panel compares the simulated TID phase profiles (connected symbols) with the observed ones (bold dots connected with lines), the lower panel shows the corresponding AGW phase profiles (bold lines) in the same frame (cf. *Kirchengast et al.* [1996]).

complex phenomenon as it permits the detailed inspection of the physical processes at work. Such a detailed elucidation of the AGW-TID physics was recently performed, with the aid of the GIFTS model, by *Kirchengast* [1996].

5.3 Time-Dependent Three-Dimensional Modeling

At mid-latitudes, the $\mathbf{E} \times \mathbf{B}$ drift is, in general, negligible and the ionosphere co-rotates with the Earth. In this regime, modeling results obtained with the GIFTS model along local field lines at a sample of geographically distributed sites can be synthesized into a more-dimensional picture. Properly done, this leads to time-dependent three-dimensional (t-d 3-d) distributions for a desired output parameter (e.g. n_e), which can be useful for purposes like comprehensive model validation, ray tracing of electromagnetic waves and ionospheric tomography investigations.

Recently, a t-d 3-d model of the electron density over Europe was constructed based on GIFTS computations for a grid of corresponding sites. Interpolating the field-aligned GIFTS profiles to the vertical, the results were synthesized into 'data-boxes' with a 10 km height spacing from 150 km to 550 km, a 3° latitude spacing from 30° to 60°, a 5° longitude spacing from –15° to 45°, and 30 min time steps from 0 UT to 24 UT. Such a 'data-box' was computed for all seasons at each low ($F_{10.7}$ = 80) and high ($F_{10.7}$ = 200) solar activity, the magnetic activity represented by Ap = 10. Input conditions for the computations included electron

temperature from a simple but reasonable model after *Clark et al.* [1970] and neutral wind as described by *Leitinger et al.* [1994] (i.e., the equations for T_e and the neutral wind were not self-consistently treated).

Figures 5 and 6 show a comparison between vertical Total Electron Content (TEC) constructed essentially from the t-d 3-d model and TEC from an empirical model [see for details, *Leitinger et al.*, 1994]. The exemplary results shown for a summer and a fall day for both low and high solar activity illustrate that the simulated TEC is in reasonable agreement with the empirical TEC. The general features like the TEC increase with decreasing latitude, the change of the local time shape from more flat to more sinusoidal from summer to fall, and the increase of the total level of ionization from low to high solar activity are well seen in the simulated TEC. Details point to the quantitative limitations involved, like the hump in TEC early in the morning in summer (Fig. 5 (a) and 6 (a)), which is probably caused by unreasonable neutral wind input during this time, and the absolute TEC level too low at high solar activity in fall (Fig. 6 (c)), which could be caused by underestimated EUV fluxes or uncertainties in the chemistry of the ions. Other features like the morning increase of TEC being sharper than its evening decrease (e.g. Fig. 6 (c)) are more realistic in the simulated than in the empirical TEC. According to validation efforts as the ones illustrated, the GIFTS model appears to be a useful tool for constructing reasonable t-d 3-d models of mid-latitude regions.

6. Uncertainties and Limitations

Model uncertainties and limitations can be divided into rooting in geometrical constraints, physical insufficiencies, and inaccurate inputs.

6.1 Geometry.

The GIFTS model is a field-aligned F-region model, with horizontal **E**×**B** drift parameterized, applicable at mid- and high-latitude sites. Thus, its spatial range is limited to the non-equatorial F-region and, in the plasma convection regime at high-latitudes, to fixed sites excluding the ability of modeling dynamic three-dimensional phenomena there.

6.2 Physics.

Comparison of GIFTS model results with observations and experience gained with other models based on similar physics [e.g., *Schunk*, 1988] indicate that no relevant physical processes have been overlooked or are inappropriately treated. Quantitative uncertainties exist in the physical description, however, and improvements are needed. Most required in this respect is a reliable scheme for the $O^+(2D)$ chemistry, an improved treatment of vibrationally excited N_2 and O_2 concerning both O^+ loss and electron cooling rates, and an accurate definitive value for the O^+-O collision frequency [cf. *Kirchengast et al.*, 1992].

6.3 Inputs.

The model inputs are the most relevant limitation for realistic simulation results (cf. the review on F-region models by *Sojka*, [1989], especially the conclusion section). Even when the best available empirical input models are used, relative deviations of some tens-of-percent or more may readily occur in comparisons of simulations with genuine data. The most serious quantitative uncertainties are typically caused by particle precipitation and **E**×**B** drift, both highly variable high-latitude phenomena, the neutral wind, and the electron heat and particle flux at the upper model boundary. For lack of a reliable model, precipitating soft electrons (mean energies < 500 eV) are currently not input to the GIFTS model, although this can be an important source of ionization and electron heating in the high-latitude F-region. At the present stage, the best

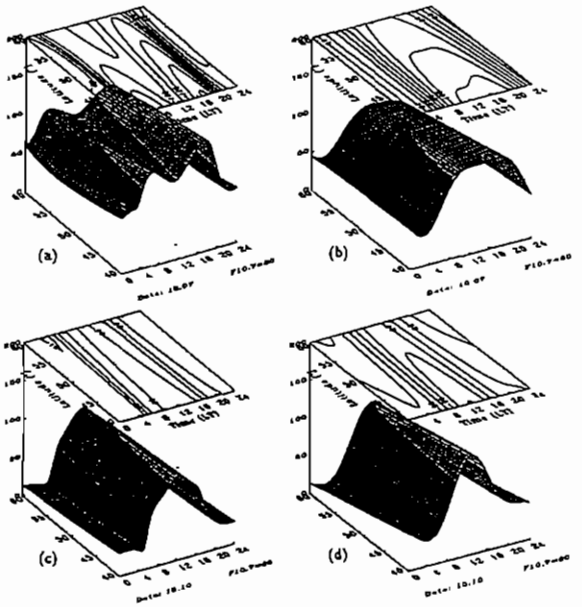

Figure 5. Total Electron Content (TEC) in units of $10^{15}m^{-2}$ as a function of latitude and local time for low solar activity. Simulated TEC (left hand panels) is compared to empirical TEC (right hand panels) for summer (upper panels) and fall (lower panels).

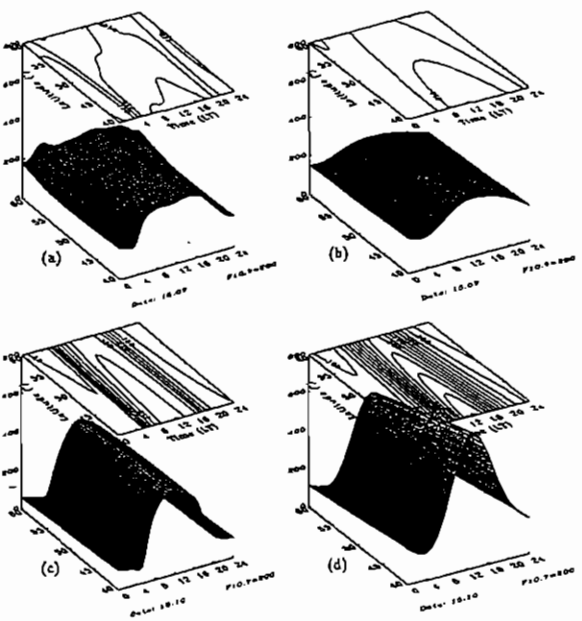

Figure 6. Total Electron Content (TEC) in units of $10^{15}m^{-2}$ as a function of latitude and local time for high solar activity. Simulated TEC (left hand panels) is compared to empirical TEC (right hand panels) for summer (upper panels) and fall (lower panels).

simulation results are obtained when using as much input as available from appropriate observations.

7. Availability of Model

The GIFTS model is programmed in FORTRAN and nominally runs on DEC/VAX platforms. It consists of a large bundle of subroutine modules and a driver module (main program) which can be tailored to various outputs. Since the FORTRAN code in the modules is nearly uncommented, the model is not user-friendly. However, the model developer (the author) is willing to collaborate with interested colleagues on studies utilizing the model as well as on model extensions, the personal time available depending on other current projects. In accordance with the ethical standards of the author, collaboration deliberately supporting military-oriented research is impossible.

8. References

Barlier, F., C. Berger, J. L. Falin, G. Kockarts, and G. Thuillier, *Ann. Géophys., 34*, 9-24, 1978.

Bilitza, D., *Planet. Space Sci., 40*, 541-579, 1992.

Burnside, R. G., C. A. Tepley, and V. B. Wickwar, *Ann. Geophys., 5A*, 343-349, 1987.

Clark, R. M., K. C. Yeh, and C. H. Liu, *Techn. Rep. No. 39*, Ionosphere Radio Lab., Univ. Ill. Urbana Campaign, U.S.A., 1970.

Clark, R. M., K. C. Yeh, and C. H. Liu, *J. Atmos. Terr. Phys., 33*, 1567-1576, 1971.

Conrad, J. R., and R. W. Schunk, *J. Geophys. Res., 84*, 811-822, 1979.

Dalgarno, A. and M. B. McElroy, *Planet. Space Sci., 13*, 947-957, 1965.

Figueroa, D. and R. Hernández, *J. Atmos. Terr. Phys., 50*, 447-454, 1988.

Hardy, D. A., M. S. Gussenhoven, R. Raistrick, and W. J. McNeil, *J. Geophys. Res., 92*, 12275-12294, 1987.

Hedin, A. E., *J. Geophys. Res., 96*, 1159-1172, 1991.

Hedin, A. E., M. A. Biondi, R. G. Burnside, G. Hernandez, R. M. Johnson, T. L. Killeen, C. Mazaudier, J. W. Meriwether, J. E. Salah, R. J. Sica, R. W. Smith, N. W. Spencer, V. B. Wickwar, and T. S. Virdi, *J. Geophys. Res., 96*, 7657-7688, 1991.

Hocke, K., K. Schlegel, and G. Kirchengast, *J. Atmos. Terr. Phys., 58*, 245-255, 1996.

Hoegy, W. R., *Geophys. Res. Lett., 3*, 541-544, 1976.

Killeen, T. L. and R. G. Roble, *J. Geophys. Res., 89*, 7509-7522, 1984.

Killeen, T. L. and R. G. Roble, *J. Geophys. Res., 91*, 11291-11307, 1986.

Kirchengast, G., Ph.D. thesis, *Wiss. Ber. No. 1*, Inst. Meteorol. Geophys., Univ. Graz, Austria, 1992.

Kirchengast, G., *J. Geophys. Res., 101*, 13353-13368, 1996.

Kirchengast, G., K. Hocke, and K. Schlegel, *Radio Sci., 30*, 1551-1567, 1995.

Kirchengast, G., K. Hocke, and K. Schlegel, *J. Atmos. Terr. Phys., 58*, 233-243, 1996.

Kirchengast, G., R. Leitinger, and K. Schlegel, *Ann. Geophys., 10*, 577-596, 1992.

Leitinger, R., E. Feichter, G. Kirchengast, and W. Rothleitner, *Proc. Beacon Sat. Sympos. '94*, Aberystwyth Wales, U.K., 254-257, 1994.

Pavlov, A. V., *Pure and Appl. Geophys., 127*, 529-544, 1988a.

Pavlov, A. V., *Geomagn. Aeron., 28*, 371-375, 1988b.

Pavlov, A. V., *Geomagn. Aeron., 29*, 717-722, 1989.

Pavlov, A. V. and A. A. Namgaladze, *Geomagn. Aeron., 28*, 607-620, 1988.

Rees, M. H., *Physics and Chemistry of the Upper Atmosphere*, Cambridge Univ. Press, Cambridge, 125-126, 1989.

Richards, P. G. and D. G. Torr, *J. Geophys. Res., 89*, 5625-5635, 1984.

Rüster, R. and J. R. Dudeney, *J. Atmos. Terr. Phys., 34*, 1075-1083, 1972.

Schunk, R. W., *Planet. Space Sci., 23*, 437-485, 1975.

Schunk, R. W., *Rev. Geophys. Space Phys., 15*, 429-445, 1977.
Schunk, R. W., *Pure and Appl. Geophys., 127*, 255-303, 1988.
Schunk, R. W. and A. F. Nagy, *Rev. Geophys. Space Phys., 16*, 355-399, 1978.
Schunk, R. W. and J. C. G. Walker, *Planet. Space Sci., 18*, 1535-1550, 1970.
Schunk, R. W., W. J. Raitt, and P. M. Banks, *J. Geophys. Res., 80*, 3121-3130, 1975.
Schunk, R. W., J. J. Sojka, and M. D. Bowline, *J. Geophys. Res., 92*, 6013-6022, 1987.
Smith, F. L. and C. Smith, *J. Geophys. Res., 77*, 3592-3597, 1972.
Sojka, J. J., *Rev. Geophys., 27*, 371-403, 1989.
Spiro, R. W., P. H. Reiff, and L. J. Maher, Jr., *J. Geophys. Res., 87*, 8215-8227, 1982.
Strickland, D. J., D. L. Block, T. P. Coffey, and J. A. Fedder, *J. Geophys. Res., 81*, 2755-2764, 1976.
Strobel, D. F. and M. B. McElroy, *Planet. Space Sci., 18*, 1181-1202, 1970.
Swartz, W. E., J. S. Nisbet, and A. E. S. Green, *J. Geophys. Res., 76*, 8425-8426, 1971.
Tobiska, W. K., *J. Atmos. Terr. Phys., 53*, 1005-1018, 1991.
Torr, M. R. and D. G. Torr, *Rev. Geophys. Space Phys., 20*, 91-144, 1982.
Torr, D. G., M. R. Torr, H. C. Brinton, L. H. Brace, N. W. Spencer, A. E. Hedin, W. B. Hanson, J. H. Hoffman, A. O. Nier, J. C. G. Walker, and D. W. Rusch, *J. Geophys. Res., 84*, 3360-3372, 1979.
Torr, M. R., D. G. Torr, R. A. Ong, and H. E. Hinteregger, *Geophys. Res. Lett., 6*, 771-774, 1979.
Vlaskov, V. A. and K. Henriksen, *Planet. Space Sci., 33*, 141-145, 1985.

UAF Eulerian Model of the Polar Ionosphere

S. A. Maurits and B. J. Watkins

Geophysical Institute
University of Alaska Fairbanks
Fairbanks, AK 99775-7320

1. Introduction

The UAF ionospheric model is a 3-D time-dependent model that covers the ionospheric region poleward from 50 degrees geographic latitude over the altitude range of 80-500 km. The model has been developed recently at the University of Alaska, Fairbanks. It is a first principles theoretical model that self-consistently solves equations of continuity, equations of motion, and equation of energy balance to establish the 3-D distribution of electrons, seven ion species ($O^+(^4S)$, $O^+(^2D)$, $O^+(^2P)$, NO^+, O_2^+, N_2^+, N^+), and the minor neutral species NO and $N(^4S)$, $N(^2D)$, which are important for the ionization balance in the lower ionosphere. The densities of major thermospheric components and neutral winds are taken from VSH/MSIS models. The model accounts for about 40 photochemical processes, including night sources of ionization and auroral precipitation, variations of EUV radiation over the course of the solar activity cycle together with the associated neutral composition changes, the sheared drag of neutral thermospheric winds, electrodynamic drifts in the crossed electric and magnetic fields, and the field-aligned ambipolar diffusion. The vertical transport mechanism for the long-living neutral species NO and $N(^4S)$ is molecular and eddy diffusion. The model also solves the equation of energy balance for isotropic electron and ion temperatures including thermal conduction by electrons, and Joule heating effects.

The model uses a quasi-hydrodynamic approach that results in a system of the first five velocity moments of the Boltzmann equation. Empirical relations are used for the stress tensor and the heat flow vector that truncates the chain of equations and makes the system mathematically closed. Since the model is applicable to a limited polar region of the Earth, the curvature is neglected and the system of equations is solved on the Cartesian grid with the stereographic projection of all geographic coordinates. All inputs which are known in the geomagnetic frame are included by point by point transformations accounting for the offset of the geographic and geomagnetic poles. The model frame co-rotates with the Earth as a purely Eulerian regular grid with a scalable resolution. The workstation version of the model has achieved 100×100 *km* horizontal resolution, while the supercomputer version has virtually no memory limitations and is expected to have a resolution up to a few tens of kilometers. The numerical algorithm maintains stability for variable time steps in the range from seconds up to 10-15 minutes or longer; this allows a flexible time coverage of the processes with different time scales. This highly effective algorithm together with the uniform spatial coverage of the regular model grid significantly saves computational resources and allows the realization of the supercomputer-scale model on a low-cost workstation platform with a useful resolution.

The model output realistically represents the seasonal changes and the large scale features of the polar ionosphere such as the sunlit region that is extended into the dusk sector due to the co-rotation of the long-living O^+ ions; the polar cap tongue of ionization, auroral oval, polar hole, and ionospheric troughs of different origins. Numerical experiments with a fast changing convection field (variation of B_y-component of IMF) successfully demonstrates destruction of

homogeneous polar cap structures and creation of separated "patches" of ionized plasma of several hundred kilometers in characteristic diameter. The model has been applied to the simulations of weather-scale variations in the ionosphere using model inputs appropriate to specific geophysical situations. These results are presented in section 5 (Model Outputs).

2. Mathematical Formulation

2.1 Equation of Continuity in Lagrangian and Eulerian Frames

The first basic governing equation of the model is the equation of continuity. The model solves this for all included species in a form that depends upon the particular species life-time. The most general form of continuity equation or equation of mass conservation of a particular species is

$$\frac{\partial n}{\partial t}+\nabla\cdot(n\mathbf{v})=-L(n)+P \qquad (1)$$

where n is the concentration, $\mathbf{v}$ is the velocity, L are local sinks, and P are local sources of species in question. Physically this equation establishes that the changes of concentration in time are equal to the difference of local sources and sinks, if they exist, plus influx or outflow due to the transport term $\nabla\cdot(n\mathbf{v})$. The relative importance of the equation terms vary with the species life-time. The characteristic time scale of the model is its variable time step, that is typically set at several hundreds of seconds. For short-living model components, their photochemical life-time is much smaller than the life-time by transport processes, only local sinks and sources are important and the equation (1) is reduced to the algebraic relation (2), where the loss term $L(n)$ is re-defined by $L(n)=\ell\cdot n$

$$\mathrm{P}-\ell\cdot\mathrm{n}=0 \qquad (2)$$

This approach is implemented in the model for the metastable state of atomic nitrogen $N(^2D)$ and for all ion species except the major ion of the ionospheric F-region $O^+(^4S)$.

The current version of the model includes neither horizontal nor vertical transport of the molecular ions NO^+ and O_2^+. This assumption is valid for the high electron concentrations, but it is an obvious over-simplification for the low night-time electron density in the $F1$- and E-regions of the ionosphere. The life-time of these ions depends on the fast recombination processes that have reaction rates of about $10^{-7}\ cm^{-2}\ sec^{-3}$. For electron densities as high as $10^5\ cm^{-3}$ the chemical life-time is short ($100\ sec$) compared to the transport effectiveness (horizontal drifts typically range up to about a km/sec). However, the lower night electron density ($10^3\ cm^{-3}$) results in a significant increase of the life-time to the level comparable to the life-time of O^+ ion. In the future versions of the model the transport processes for NO^+ and O_2^+ will be included to improve the calculated values, particularly in the regions where the electron concentration is lower.

The long-living species of the model are $O^+(^4S)$, NO, and $N(^4S)$. For the neutral components NO and $N(^4S)$, that are important for the ionization balance in the lower ionosphere, vertical transport by molecular and eddy diffusion is utilized since the vertical wind contribution is small, while the transport by horizontal winds is not included in the current version. The diffusion flux of the neutral species n_n in the vertical direction is

$$\phi_n = -D_a\left(\frac{\partial n_n}{\partial z} + \frac{n_n}{T}\frac{\partial T}{\partial z} + \frac{n_n}{H_n}\right) - K\left(\frac{\partial n_n}{\partial z} + \frac{n_n}{T}\frac{\partial T}{\partial z} + \frac{n_n}{H}\right) \tag{3}$$

where D_a is the molecular diffusion and K is the eddy diffusion coefficients (the second term in the equation (3) is important up to *120 km*); H_n is the scale height of species n_n ($H_n = kT_n/gm_n$); and H is the scale height of the background neutral gas mixture ($H = kT_n/\overline{gm}$), where k is the Boltzmann constant, T_n is the temperature of neutrals, g is the gravitational acceleration and m_n, $\overline{m}$ is the mass of molecule of n-species and the averaged mass of the gas mixture molecule, respectively.

After substitution of ϕ_n into the continuity equation (1) and neglecting horizontal divergent terms, we obtain a parabolic partial differential equation of second order (4) to be solved numerically (see the next section for discussion of the numerical algorithms)

$$\frac{\partial n_n}{\partial t} = A\frac{\partial^2 n_n}{\partial z^2} + B\frac{\partial n_n}{\partial z} + C\cdot n_n + E \tag{4}$$

where $A = D_a + K$; $E = P_n$; and preserving vertical wind term w for generality

$$B = \frac{\partial}{\partial z}(D_a + K) + \frac{D_a + K}{T}\frac{\partial T}{\partial z} + \left(\frac{D_a}{H_n} + \frac{K}{H}\right) - w$$

$$C = \frac{\partial}{\partial z}\left(\frac{D_a + K}{T}\frac{\partial T}{\partial z}\right) + \frac{\partial}{\partial z}\left(\frac{D_a}{H_n} + \frac{K}{H}\right) - L_n$$

The major vertical transfer mechanism for the ionized component $O^+(^4S)$ is ambipolar diffusion along the magnetic field line with some contribution from the vertical drift. Taking into account the dip angle I of the magnetic field line one can obtain for the vertical component of the flux

$$\phi_i = -D_a \sin^2 I\cdot\left(\frac{\partial n_i}{\partial z} + \frac{n_i}{T_p}\frac{\partial T_p}{\partial z} + \frac{n_i}{H_i}\right) + w_i\cdot n_i \tag{5}$$

where w_i is the vertical drift velocity; n_i is the density; D_a is ambipolar diffusion coefficient, $T_p = (T_i + T_e)/2$ is the plasma temperature; and H_i is the height scale of $O^+(^4S)$.

Contrary to the case for the neutral species, the horizontal flux divergence terms are presented in the equation of continuity for $O^+(^4S)$. After substituting expression (5) and neglecting $\partial w/\partial z$ term, in the Cartesian frame the equation becomes

$$\frac{\partial n_i}{\partial t} = A\frac{\partial^2 n_i}{\partial z^2} + B\frac{\partial n_i}{\partial z} - \frac{\partial}{\partial x}\left(n_i \vartheta_x^i\right) - \frac{\partial}{\partial y}\left(n_i \vartheta_y^i\right) + C\cdot n_i + E \tag{6}$$

where ϑ_x^i, ϑ_y^i are x- and y-components of the ion drift velocities, n_i is the $O^+(^4S)$ density; $A = D_a \sin^2 I$; $E = P$ and the other parameters as follows

$$B = \sin I\left(\frac{\partial D_a}{\partial z} + \frac{D_a}{T_p}\frac{\partial T_p}{\partial z} + \frac{D_a}{H_i}\right) - w_i\ ; \quad C = \sin I \cdot \frac{\partial}{\partial z}\left(\frac{D_a}{T_p}\frac{\partial T_p}{\partial z} + \frac{D_a}{H_i}\right) - L_i$$

Equation (6) differs from the equation (4) by the presence of horizontal divergence terms that correspond to the advective motion. The transition to the frame moving with the velocity ϑ_x^i, ϑ_y^i (Lagrangian frame) eliminates these terms and significantly simplifies the equation reducing it to the one-dimensional case. This concept of convecting flux tubes with the vertical plasma transfer by the ambipolar diffusion inside them is implemented in Lagrangian ionospheric models. Historically, Lagrangian models were the first polar ionospheric models that simulated the large-scale and meso-scale features of the polar ionosphere [e.g., *Sojka et al.*, 1993, and references therein] and for a long time the Lagrangian frame was the only approach implemented in large-scale polar ionosphere modeling. However, the Lagrangian approach has inherent limitations. Recently, a Eulerian description of the global ionosphere in the NCAR TIGCM model [*Roble and Ridley*, 1987] had revived interest to the Eulerian approach in the ionospheric models.

The default assumption for the concept of flux tube convecting as a whole in the Lagrangian frame is the absence of any vertical shears in the drift velocities ϑ_x^i, ϑ_y^i. Otherwise, in the general 3-D case the height-variable advection pattern would destroy the vertical continuity of the flux tube. In the terrestrial thermosphere, the assumption of absence of vertical shears in the ion motion is valid only for the *F2*-region heights, where the ion motion is dominated by the height-independent E×B-drift. In the lower ionospheric regions, starting from the lower *F1*-layer and especially in the E-layer, there is considerable shear since the transition from E×B-driven ion motion to the collisionally dominated drag by neutral winds takes place in this altitude range, 100-200 km [*Roble*, 1992]. The role of the neutral wind and its own height-dependence is quite important there (for instance, formation of sporadic E-layers). The Lagrangian approach cannot easily account for these effects and it has, therefore, become common practice in Lagrangian models to ignore them by assuming the *F*-region plasma drifts map down uniformly through the entire ionosphere.

By contrast, the Eulerian approach is the most general computational treatment of the multi-dimensional plasmas. Its implementation does not require any limiting assumptions. The Eulerian frame rests in the Earth's geographic coordinate system and, therefore, accounts explicitly for all types of plasma motion. It readily allows for the effect of wind shear. The Eulerian frame also preserves the regularity and the even coverage of its grid. This latter advantage is especially important for high-resolution modeling, including the multi-grid applications.

In the Eulerian frame, the basic time step has no other limitations except those imposed by the variability of the inputs and the time scale of appropriate processes. It has allowed us to implement new approaches in the numerical algorithms to avoid excessive computational time while preserving the numerical stability. The time steps may be varied over a wide range, usually from a few tens of minutes to tens of seconds.

The Eulerian grid comprises a stable and well-defined 3-D computational domain. This is important for real-time high-resolution predictive applications when the ranges and the time-variations of the model input parameters (e.g., E-field structure, particle precipitation) are unknown before the model run and may vary greatly during a model simulation. Further, we anticipate future use of massively parallel computing platforms where we suggest the Eulerian formulation is well suited. In parallel computing environment, the local finite difference

representations can be effectively partitioned in distributed memory with minimal inter-node exchange.

The disadvantage of the Eulerian approach is the additional mathematical complexities that are introduced, plus the corresponding numerical challenge in solving the mixed diffusive-advective partial differential equations in 3-D. The method essentially requires the specification of the time-dependent boundary condition. Another disadvantage is the considerably greater demand for computer memory, however this is no longer a limitation with modern computing resources.

2.2 Equation of Motion

The 3-D fields of neutral wind and ion drift are essential for solving the equation of continuity (6). The UAF model uses the neutral composition and neutral wind from the combined empirical thermospheric models MSIS and VSH [*Killeen et al.*, 1987] based on the NCAR TIGCM runs, while the ion drift velocities are calculated in the model. The governing equation of ion motion is derived from the general equation of momentum conservation, the second velocity moment of the Boltzmann equation. This relation equates the acceleration of a unit mass parcel in the corotating Earth coordinate system to the sum of all affecting forces

$$\frac{\partial \mathbf{v}_j}{\partial t}+\mathbf{v}_j\cdot\nabla\mathbf{v}_j+2\Omega\times\mathbf{v}+\frac{1}{\rho_j}\nabla\cdot P=g+\frac{1}{\rho_j}(\mathbf{J}\times\mathbf{B})+\frac{A_j}{\rho_j} \tag{7}$$

where the two first terms represent the convective derivative along the trajectory of a unit mass parcel ($D\mathbf{v}_j/Dt = \partial\mathbf{v}_j/\partial t + \mathbf{v}_j\cdot\nabla\mathbf{v}_j$); the third term is the Coriolis acceleration (centripetal acceleration term is negligible at the heights of interest); P is the pressure tensor, the divergence of which gives the pressure gradient and viscous forces; g is the acceleration of gravity; $\mathbf{J}$ is current density and the whole term $(\mathbf{J}\times\mathbf{B})/\rho_j$ is acceleration due to ion drag. The last term is the collision term ($\mathbf{A}_j = \Sigma\mathbf{A}_{jk}$) that describes the dynamic effects of friction between species with different transport velocities [*Banks and Kockarts*, 1973].

Applying the general equation (7) for ion motion, we can neglect the Coriolis force and viscosity in the first approximation [*Rees*, 1989]. At F-region heights the dominant term is $\mathbf{E}\times\mathbf{B}$-drift. At the lower altitudes (E-region) strong collisional ion-neutral coupling prevails. The current $\mathbf{J}$ can be expressed in terms of ion velocity and density $\mathbf{J}=en_i\mathbf{v}_i$. Introducing the Lorentz force, for ion motions we obtain

$$\frac{D\mathbf{v}_i}{Dt}+\frac{1}{\rho_i}\nabla p_i-g-\frac{e}{m_i}\left(E+\frac{1}{c}\mathbf{v}_i\times B\right)=\sum_k \upsilon_{in}^k(\mathbf{v}_n-\mathbf{v}_i) \tag{8}$$

Relaxation times (tens of seconds) for ion response to the variations of electric field configuration [*Rees*, 1989] are much smaller than the typical model time step (hundreds of seconds) that leaves the relaxation processes beyond the model scope. The steady state condition for the ion motion perpendicular to $\mathbf{B}$ is the equality of the Lorentz force and the neutral wind drag force (we neglect the partial pressure force of the ions and introduce the total ion-neutral collision frequency $\upsilon_{in} = \sum_k \upsilon_{in}^k$)

$$\mathbf{v}_{i\perp} = \mathbf{v}_n+\frac{e}{\upsilon_{in}m_i}\left(\mathbf{E}_\perp+\frac{1}{c}\mathbf{v}_{i\perp}\times\mathbf{B}\right) \tag{9}$$

Note that the second term in equation (9) is small in the *E*- and *F1*-regions (up to about 150-180 km); this corresponds to strong collisional coupling where $\nu_{i\perp} \cong \nu_n$. By contrast, at the *F2*-region heights the second term dominates and the ion motion is predominantly determined by the Lorentz force. Assuming the neutral wind velocity is known as well as the electric and magnetic field components, the vector equation (9) gives rise to the system of three equations for three unknown components of ion drift velocity. Introducing the gyrofrequency $\omega_{ic} = eB/cm_i$; the ratio of the gyrofrequency to the collisional frequency $\gamma_i = \omega_{ic}/\nu_{in}$; and neglecting the vertical wind component compared to the horizontal components, one can obtain a solution to the system (9) for the general orientation of the magnetic field vector

$$u_i = \left(1+\gamma_i^2\right)^{-1}\left[\left(u+\gamma_i\frac{E_y}{B}\right)-\gamma_i\frac{B_z}{B}\left(\vartheta+\gamma_i\frac{E_x}{B}\right)\right]$$

$$\vartheta_i = \left(1-\gamma_i^2\right)^{-1}\left[\left(\vartheta+\gamma_i\frac{E_x}{B}\right)+\gamma_i\frac{B_z}{B}\left(u+\gamma_i\frac{E_y}{B}\right)\right] \qquad (10)$$

$$w_i = \left(1+\gamma_i^2\right)^{-1}\left[\left(\vartheta+\gamma_i\frac{E_x}{B}\right)\frac{\gamma_i B_y}{B}-\left(u+\gamma_i\frac{E_y}{B}\right)\frac{\gamma_i B_x}{B}\right]$$

where ϑ_i, u_i, w_i and ϑ, u, w are meridional, zonal, and vertical components of the ion drift and neutral wind, respectively; and E_x, E_y and B_x, B_y, B_z are meridional, zonal, and vertical components of the electric and magnetic field, respectively. Note, that the relations $\mathbf{B}\cdot\mathbf{E}_\perp = 0$ and $\mathbf{B}\cdot\mathbf{v}_{i\perp} = 0$ were used in the derivation.

In the collisionally coupled lower thermosphere $\gamma_i \ll 1$ and $u_i \cong u$, $\vartheta_i \cong \vartheta$, $w_i \cong w$ holds true, that corresponds to a vector relation $\mathbf{v}_i \cong \mathbf{v}_n$, while at the higher altitudes $\mathbf{E}\times\mathbf{B}$-drift components prevail. Dipole approximation for the magnetic field significantly simplifies equation (10), since B_y=0 in the dipole field.

In the current version of the model, the diamagnetic drifts due to horizontal gradients of ion density (associated with polar ionospheric structures such as auroral oval) are not accounted for, since the ion partial pressure force is not included. The importance of these drifts for the distribution of ion density is a subject for future investigations.

2.3 Equations of Energy Balance for Electrons and Ions

The general energy balance equation in terms of a heat flow vector $\mathbf{q}$ and stress tensor P in the presence of local energy sources (Q) and sinks (L) can be written as follows:

$$\frac{N}{2}k\frac{D(nT)}{Dt} = -\frac{5}{2}nkT\nabla\cdot\mathbf{v} - \nabla\cdot\mathbf{q} - \mathrm{P}:\nabla\mathbf{v} + Q - L \qquad (11)$$

where $D(nT)/Dt = \partial(nT)/\partial t + \mathbf{v}\cdot\nabla(nT)$ is the substantial derivative taken along the trajectory of motion of a gas parcel moving with the velocity $\mathbf{v}$; here N is the number of degrees of freedom (N=3 for mono-atomic gas, N=5 for di-atomic molecules), k is the Boltzmann constant, T is the gas kinetic temperature, and n is number density. For the processes of heat advection ($\mathbf{v}\cdot\nabla(nkT)$), the effect of scalar pressure variations resulting in cooling or heating due to expansion or

compression ($-5/2nkT\nabla\cdot\mathbf{v}$), the divergence of the heat flow vector ($-\nabla\cdot\mathbf{q}$), and viscous heating due to stress in the fluid ($-P:\nabla\mathbf{v}$) together with the local energy sources (Q) and sinks (L) are included in this general form of the energy balance equation.

Two higher order velocity moments of the distribution function (the heat flow vector $\mathbf{q}$ and the pressure tensor P) are presented in equation (11). To truncate the system of equations for the velocity moments, these quantities can be expressed in terms of scalar values such as temperature, velocity components, pressure, coefficients of thermal conductivity and viscosity, and thermo-electric coefficient. Viscous heating is important only for the major neutral species. The heat flow vector ($\mathbf{q}$) is a sum of two terms; first the heat flux due to thermal conduction from heat flux due to temperature gradients (term $-\lambda\nabla T$), and second for charged species, the heat carried by electrical currents (thermo-electric term, $-\beta\mathbf{J}$)

$$\mathbf{q} = -\lambda\nabla T - \beta\mathbf{J} = -\frac{5k^2nT}{2m\upsilon}\nabla T - \frac{5kT}{2|e|}\mathbf{J} \tag{12}$$

where $|e|$ is the electron charge and υ is the total collision frequency of the species of interest.

Generally speaking, equation (11) is applicable to neutrals, ions (assuming the same temperature for different ion species), and electrons. However, the equation of energy balance is solved in the model only for ion and electron temperatures (T_i and T_e), while the neutral temperature (T_n) is derived from the background thermospheric model.

The energy balance equation for the ionospheric electron gas in the altitude range of interest 80-500 km can be simplified [*Rees*, 1989] by assuming the dominance of the local sources and the vertical energy transport compared to the horizontal transport by advection, by adiabatic heating and cooling, and by thermal conduction, and neglecting the viscous heating or cooling effect as well as the heating effect of exothermic chemical reactions. One can then re-write the general energy balance equation for electrons in the following form

$$\frac{3}{2}k\left[\frac{\partial(n_eT_e)}{\partial t} + \mathbf{v}_e\cdot\nabla(n_eT_e)\right] = -\frac{5}{2}kT_en_e\nabla\cdot\mathbf{v}_e - \nabla\cdot\mathbf{q} + Q_e - L_e \tag{13}$$

where Q_e is the electron heat sources (mainly heating by Coulomb collisions with suprathermal electrons), and L_e represents electron heat sinks (cooling by elastic and inelastic collisions with neutrals).

Since the horizontal energy transfer is negligible, the only important direction is vertical. Height profiles of electron temperature can be determined for each latitude-longitude grid cell without accounting for horizontal energy transport. Therefore, the task of determination of the electron temperature field is essentially a 1-D problem to be solved at multiple points on a 2-D grid. Further simplification can be made by neglecting the thermo-electric transport terms compared to thermal conduction, and also by neglecting relaxation processes. The latter assumption is valid since the model time steps (typically tens of seconds and up) is much longer than the characteristic times of auroral electron penetration into the thermosphere and heating of the ambient electron gas [*Rees*, 1989]. The final form of the equation is

$$\sin^2 I\frac{\partial}{\partial z}\left(\lambda_e\frac{\partial T_e}{\partial z}\right) + Q_e - L_e = 0 \tag{14}$$

This second order ordinary differential equation can be solved by standard numerical procedures, for example by the method of relaxation of parameters Q_e (electron heat sources) and L_e (electron heat sinks). The model accounts for local heating by supra-thermal photoelectrons and precipitating energetic auroral electrons, while the local cooling processes result from both inelastic and elastic collisions with the major neutral species. Inelastic collisions include the respective N_2 and O_2 vibrational and rotational excitations, excitation of fine structure levels of atomic oxygen, and excitation of its $O(^1D)$ electron state. Electron elastic collisions with the major thermospheric neutrals (O, O_2, N_2) and the dominating ions (O^+, O_2^+, N_2^+) are considered. Parameterizations of all mentioned processes are available in the literature [e.g., *Schunk*, 1988].

The small temperature differences between each ion species are neglected in the model. The ion energy balance equation is derived under the same assumptions as the electron case, the vertical transport is dominant, and the thermo-electric term contribution in the heat flow vector is negligible compared to the thermal conductivity term at all heights. However, for the ion energy equation, further simplifications are possible [*Banks*, 1967]. The mass dependent ion thermal conductivity coefficient is only a small fraction of the electron coefficient. By contrast with the equation for electron energy balance, the ion thermal conductivity is only relevant at high altitudes (more than 500 km). Relaxation times for the ion temperature (usually, seconds at 300 km altitude and a few tens of seconds at 450-500 km) is longer than the relaxation time of electron temperature, but still may be shorter than the model time step. Assuming a steady state condition, the ion energy equation balance reduces to algebraic equality of sources and losses terms

$$Q_i - L_i = 0 \tag{15}$$

The major local heating sources for ions are the frictional heating by perpendicular electric fields (Joule heating) and the heating due to Coulomb collisions with electrons. Exothermic chemical reactions also contribute to the ion heating, but this source is small in the polar region compared with the Joule heating and heating by electrons. The major ion cooling processes are elastic non-resonant ion-neutral collisions with the polarization interactions and sinks due to the charge exchange reactions, or resonant charge transfer, e.g. $O^+ + O \rightarrow O + O^+$. The parameterizations for both sinks and sources are well described in the literature [*Banks and Kockarts*, 1973; *Schunk*, 1988].

2.4 Photochemical Scheme

Production and loss terms in the equations of continuity are mainly the sources and sinks due to photochemical transformations. The model accounts for about forty processes that are summarized in Table 1. The chemistry of odd nitrogen family ($N(^4S)$, $N(^2D)$, NO) is included (*R1-R11*) in addition to the traditional set of reactions of ionospheric importance (*R22-R36*) that govern the ion species O^+, NO^+, O_2^+, N_2^+, N^+. Three electron states of atomic oxygen ion $O^+(^4S,^2D,^2P)$ are considered in reactions *R12-R21*.

3. Numerical Solution

3.1 Equations of Continuity

Two types of the continuity equations, the diffusive type (4) and the mixed advective-diffusive type (6) will be considered in this section. First, we focus our consideration on

Table 1.
List of Photochemical Reactions and Processes
(reaction rates are in $cm^{-2}\ s^{-1}$ unless otherwise specified)

(R1) $N_2 + e^* \longrightarrow 2N(^2D,^4S) + e$	k_1
(R2) $N_2 + h\nu(\lambda \leq 1270\text{Å}) \longrightarrow 2N(^2D,^4S)$	ρ_2
(R3) $N(^4S) + O_2 \longrightarrow NO + O + 1.4eV$	$4.4\times10^{-12}exp(-3220/T_n)$
(R4) $N(^2D) + O \xrightarrow{}_2 NO + O(^1D) + 1.84eV$	5.0×10^{-12}
(R5) $N(^4S) + NO \longrightarrow N_2 + O + 2.68eV$	3.4×10^{-11}
(R6) $N(^2D) + O \longrightarrow N(^4S) + O + 2.38eV$	4.5×10^{-13}
(R7) $N(^2D) + e \longrightarrow N(^4S) + e + 2.38eV$	$6.0\times10^{-10}(T_e/300)^{1/2}$
(R8) $N(^2D) + NO \longrightarrow N_2 + O + 5.63eV$	7.0×10^{-1}
(R9) $N(^2D) \longrightarrow N(^4S) + h\nu$	$1.06\times10^{-5}sec^{-1}$
(R10) $NO + h\nu(\lambda \leq 1910\text{Å}) \longrightarrow N(^4S) + O$	$\rho_{4.10}$
(R11) $NO + h\nu(\text{H-Ly-}\alpha,\lambda=1216\text{-Å}) \longrightarrow \begin{cases} NO^+ + e \\ N(^4S) + O \end{cases}$	$\rho_{4.11}$
(R12) $O + h\nu(\lambda \leq 911,733,666\text{Å}) \longrightarrow O^+(^4S,^2D,^2P) + e$	$\rho_{4.12}$
(R13) $O + e(E \geq 13.61,16.92,18.61eV) \longrightarrow O^+(^4S,^2D,^2P) + 2e$	$k_{4.13}$
(R14) $O^+(^2P) \longrightarrow \begin{cases} h\nu(\lambda=7320\text{Å}) + O^+(^2D),\ f(^2D)=0.781 \\ h\nu(\lambda=2470\text{Å}) + O^+(^4S),\ f(^4S)=0.219 \end{cases}$	$0.22\ sec^{-1}$
(R15) $O^+(^2D) + N_2 \longrightarrow N_2^+ + O + 1.4eV$	8×10^{-10}
(R16) $O^+(^2D) + O \longrightarrow O^+(^4S) + O + 3.3eV$	$<3\times10^{-11}$
(R17) $O^+(^2D) + O_2 \longrightarrow O_2^+ + O + 4.8eV$	1×10^{-9}
(R18) $O^+(^2D) + e \longrightarrow O^+(^4S) + e + 3.31eV$	$7.8 \times 10^{-8}(300/T_e)^{1/2}$
(R19) $O^+(^2P) + N_2 \longrightarrow N_2^+ + O + 3.03eV$	$4.8\pm1.4\times10^{-10}$
(R20) $O^+(^2P) + O \longrightarrow O^+(^4S) + O + 5.00eV$	$5.2\pm2.5\times10^{-11}$
(R21) $O^+(^2P) + e \longrightarrow \begin{cases} O^+(^4S) + e + 5.00eV \\ O^+(^2D) + e + 3.31eV \end{cases}$	$4.7\times10^{-8}(300/T_e)^{1/2}$ $1.5\times10^{-7}(300/T_e)^{1/2}$
(R22,24) $O_2 + h\nu,e^* \longrightarrow \begin{cases} O^+ + O + e \\ O_2^+ + e \end{cases}$	ρ_{22}: k_{24}
(R23,25) $N_2 + h\nu,e^* \longrightarrow \begin{cases} N^+ + N + e \\ N_2^+ + e \end{cases}$	ρ_{23}: k_{25}

Table 1 (Continued)

(R26) $N_2^+ + O \longrightarrow NO^+ + N(^2D) + 0.70eV$	$\begin{cases} 1.4\times10^{-10}(T_R/300)^{-0.44}, & T_R<1500K^\circ \\ 5.2\times10^{-11}(T_R/300)^{0.2}, & T_R\geq1500K^\circ \end{cases}$
(R27) $N_2^+ + O_2 \longrightarrow O_2^+ + N + 3.53eV$	$5.1\times10^{-11}(T_R/300)^{-0.8}$
(R28) $N_2^+ + e \longrightarrow \begin{cases} N(^2D) + N(^4S) + 3.44eV, f(^2D)=0.9 \\ N(^4S) + N(^4S) + 5.82eV, f(^4S)=1.1 \end{cases}$	$1.8\times10^{-7}(T_e/300)^{-0.39}$
(R29) $O^+ + O_2 \longrightarrow O_2^+ + O + 1.56eV$	
(R30) $O^+ + N_2 \longrightarrow NO^+ + N(^4S) + 1.09eV$	
(R31) $O_2^+ + NO \longrightarrow NO^+ + O_2 + 2.81eV,$	4.4×10^{-10}
(R32) $O_2^+ + N(^4S) \longrightarrow \begin{cases} NO^+ + O(^3P) + 4.21eV, \\ NO^+ + O(^1D) + 2.25eV, \\ NO^+ + O(^1S) + 0.04eV, \end{cases}$	1.8×10^{-10}
(R33) $O_2^+ + e \longrightarrow \begin{cases} 2O(^3P) + 6.95eV, f(^3P)=0.15 \\ O(^1D) + O(^3P) + 4.98eV \end{cases}$	$\begin{cases} 1.6\times10^{-7}(300/T_e)^{0.55}, & T_e\geq1200K \\ 2.7\times10^{-7}(300/T_e)^{0.70}, & T_e<1200K \end{cases}$
(R34) $NO^+ + e \longrightarrow \begin{cases} N(^4S) + O + 2.75eV, f(^4S)=0.2 \\ N(^2D) + O + 0.38eV, f(^2D)=0.8 \end{cases}$	$4.2\times10^{-7}(300/T_e)^{0.85}$
(R35) $N^+ + O \longrightarrow O^+ + N + 0.93eV$	1.0×10^{-12}
(R36) $N^+ + O_2 \longrightarrow \begin{cases} NO^+ + O + 6.70eV, \\ O_2^+ + N(^4S) + 2.47eV, \end{cases}$	2.0×10^{-10} 4.0×10^{-10}

R1	*Zipf and McLaughlin*, [1978]; *Strickland and Meier*, [1982]
R2,R3,R5	*Richards et al.*, [1981]; *JPL*, [1981]
R4,R6,R7	*Frederick and Rusch*, [1977]; *Rusch and Sharp*, [1981];
R8	*Black et al.*, [1969]
R9	*Garstang*, [1956]
R10	*Nicolet*, [1979]; *Nicolet and Cielslik*, [1980]
R11	*Watanabe*, [1967]
R12-14;R 22-25	*Kirby-Docken et al.*, [1979] (cross sections, quantum yeilds)
R15	*Rowe et al.*, [1980]; *Johnsen and Biondi*, [1980]
R16,17	*D.G. Torr and M.R. Torr*, [1979]
R18,21	*Henry et al.*, [1969]; *M.R. Torr et al.*, [1980]
R19,20	*Rusch et al.*, [1977]; *M.R. Torr and D.G. Torr*, 1982
R26	*McFarland et al.*,[1974]; *Torr et al.*,[1977]; *Schunk and Raitt*, [1980]
R27,31,36	*Lindinger et al.*, [1974]; *Huntress and Anicicoh*, [1976]
R29,30	*Albritton et al.*,[1977]; *St.-Maurice and Torr*, [1978]
R32,35	*Torr et al.*, [1976]; *Torr*, [1985]
R28,33,34	*Mehr and Biondi*, [1969]; *Torr et al.*, [1979], *Schunk and Raitt*,[1980]

equation (4), the methods of its numerical solution, the initial and boundary conditions for different species, and the solution convergence and accuracy. We than proceed to the equation (6) to show how it can be numerically reduced to the combination of a purely advective equation that allows a simple numerical solution in explicit form, and purely diffusive equation that can be numerically treated the same way as equation (4).

The equation of continuity (4) is a parabolic type partial differential equation (PDE). An implicit Crank-Nicolson solution scheme has been used with an initial condition and two boundary conditions. The scheme is unconditionally stable and is accurate to the second order in both time and space steps. Assuming that $\tilde{n}$ and n define the density at the time step $\ell+1$ and ℓ respectively, the finite-difference relations at each of $k=2,...,K-1$ height cells are

$$\frac{\tilde{n}_k - n_k}{\Delta t} = A(k,\ell+1)\frac{\tilde{n}_{k+1} - 2\tilde{n}_k + \tilde{n}_{k+1}}{(\Delta z)^2} + B(k,\ell+1)\frac{\tilde{n}_{k+1} - \tilde{n}_{k-1}}{2\Delta z} + C(k,\ell)\tilde{n}_k + E(k,\ell+1,n_k) \quad (16)$$

After collection of terms, this gives rise to a tridiagonal system of $(K-2)$ linear algebraic equations for K variables $\tilde{n}_k$ $(k=1,...,K)$

$$a_k\tilde{n}_{k+1} + b_k\tilde{n}_k + c_k\tilde{n}_{k-1} = d_k \quad (17)$$

where the linear coefficients a_k, b_k, c_k, d_k are functions of terms A, B, C, D and time and height steps Δt, Δz.

Two boundary conditions for determination of $\tilde{n}_1$ and $\tilde{n}_k$ close the tridiagonal system and then allow the application the standard sweeping algorithm for a solution. The upper boundary condition for the neutral species of interest ($N(^4S)$, NO) is a diffusive equilibrium or specified flux through the upper boundary at 500 km. For O^+ ions, the vertical flux ($n_i w_i$) due to non-zero vertical drift w_i is considered. For the lower boundary at 80 km all species except NO are in photochemical equilibrium. The condition of the local minimum in the height profile $d[NO]/dz = 0$ is applicable to the NO density distribution at 80 km.

Note that the terms $C(k,\ell)$ and $E(k,\ell+1,n_k)$, which include photochemical sinks and sources, are calculated using the combination of densities (n_k) from the previous time step ℓ and the current production rates at the time step $\ell+1$. This simplification is made to avoid nonlinearity problems. The validity of our approach has been checked by evaluating the convergence of the solution to diurnal periodicity. Tests have demonstrated that iterations are not necessary for all practical purposes if the model time step does not exceed the characteristic time of the variations of photochemical sources. Thus, the practical limitation on the model time step is that variations in chemical sinks and sources must be small within one time advance. For example, model time steps up to 15-20 minutes are appropriate when the inputs are slowly varying parameters such as solar radiation.

A reasonable choice for the initial condition will accelerate the convergence of the model to a realistic simulation of diurnal variations. However, any arbitrary initial conditions are satisfactory. The 3-D fields of densities, winds, and drifts generated by the VSH model are also used as the initial conditions. The initial condition for NO density is a parameterization in terms of the major thermospheric components and temperature derived by *Mitra* [1968]. The convergence to the diurnally periodic solution can usually be achieved within several model hours for O^+ ions and within a few model days for the odd nitrogen group.

The mixed advection-diffusion equation (6) for the O^+ ion density belongs to the class of multi-dimensional PDE, and several numerical methods for its solution are feasible [e.g., *Potter*, 1977; *Ozisik*, 1994]; we use a modification of the Alternating Direction Implicit (ADI) method. In the general multi-dimensional case, the finite-difference expression gives rise to a linear system with a $N^n \times N^n$ matrix (here N is the number of cells, and n is the number of dimensions), which is much more complex than a tridiagonal $N \times N$ matrix (17). Although this $N^n \times N^n$ matrix is still sparse, its inversion is not a simple task. However, properties of tridiagonal matrices can still be usefully employed in such multi-dimensional problems by recognizing that the general matrix may be represented as a sum of certain tridiagonal matrices. To preserve this tridiagonal simplicity of the system matrix, the intermediate time sub-steps with the corresponding intermediate solutions are introduced. The implicit finite-difference scheme similar to one given by expression (16) is subsequently used three times, once for each dimension, each time advancing the solution by one sub-step in time. However, only the terms that correspond to the current dimension are treated as variables. The terms of other dimensions are calculated using the density from the previous time step or sub-step. This consideration resulted in three tridiagonal systems to be solved. Note, these three finite-difference expressions being added to each other result in a net expression that is exactly the same as one from the general case and the terms with intermediate solutions cancel.

This method is applicable to the 3-D diffusion equation that belongs to the class of parabolic PDE. In our case, equation (6) represents the system in which diffusion is significant only in the vertical direction. The horizontal terms are of advective origin and the equation is not purely parabolic in all three coordinates. Thus, the described ADI method is not strictly applicable in our case without modifications. However, the basic idea, to distinguish between the dimensions in time and to introduce intermediate time sub-steps with corresponding intermediate solutions, is appropriate.

Let us distinguish the vertical and horizontal directions. The former is dominated by the diffusion processes, while the latter is influenced mainly by advection. The life-time of O^+ ions (an hour or more) is long enough to neglect the processes of creation and losses and consider the horizontal motion as an advection of the passive substance in the external flow field. Further, there is no need to separate between two horizontal directions since the corresponding equation of advection can be solved in two dimensions simultaneously. Let's introduce the intermediate density n^* that resulted from the advective re-distribution of density n (corresponding to the time step ℓ) during the time step $\ell+1$. We omit the ion index i here, reserving it for the cells numbering in the x-direction, while the j-index will be used for the y-direction, and k-index for the vertical direction. Then, the explicit upwind finite-difference relation corresponding to the processes of 2-D advection is

$$\frac{n^*-n}{\Delta t} = -\frac{(n\vartheta_x)_{i+1}-(n\vartheta_x)_i}{\Delta x}\left(\text{or } -\frac{(n\vartheta_x)_i-(n\vartheta_x)_{i-1}}{\Delta x}, \text{if } \vartheta_x^i \ge 0\right) \qquad (18)$$

$$-\frac{(n\vartheta_y)_{j+1}-(n\vartheta_y)_j}{\Delta y}\left(\text{or } -\frac{(n\vartheta_y)_j-(n\vartheta_y)_{j-1}}{\Delta y}, \text{if } \vartheta_y^j \ge 0\right)$$

where Δx and Δy are the spatial steps, and ϑ_x and ϑ_y are the ion drift velocities in the x,y-directions, respectively. The velocities are solutions to the system (10), recalculated from the meridional and zonal components into the Cartesian frame of the model. Since the explicit

representation was used, equation (18) is an algebraic equation that readily can be solved for n^* on the entire horizontal mesh as soon as the boundary conditions are specified.

Several choices of the time-dependent boundary conditions have been tested. First, the updated O^+ density can be derived from the VSH model. Second, using the fact that the plasma flux through the boundary at the latitudinal circle of 50 degrees is predominantly outflow, the "open" or the "transparent" boundary can be chosen. The density can be calculated at the boundary assuming that the wind and density behind the boundary are the same as at the boundary. In other words, the incoming flux into the boundary cell from the domain is the same as the flux outgoing through that particular cell. This second option of the "open" boundary is more computationally feasible. In any case, the major plasma flows are located well inside the domain while the influence of the boundary is limited to a few neighboring cells.

Having the 3-D field of the O^+ ion density updated by advection, we can proceed to the remaining vertical direction. Using the implicit Crank-Nicolson scheme for the finite-difference representation of the diffusion and chemistry terms, we obtain a system of $(K\text{-}2)$-equations $(k=2,...,K\text{-}1)$ to be solved for the final distribution of O^+ ion density at the current time step

$$\frac{\tilde{n}_k - n_k^*}{\Delta t} = A(k,\ell+1)\frac{\tilde{n}_{k+1} - 2\tilde{n}_k + \tilde{n}_{k-1}}{(\Delta z)^2} + B(k,\ell+1)\frac{\tilde{n}_{k+1} - \tilde{n}_{k-1}}{2\Delta z} + C(k,\ell)\tilde{n}_k + E(k,\ell+1,n_k) \quad (19)$$

This system is similar to system (16) and the discussed methods of its inversion by the sweeping algorithm are applicable here as well. Note that the intermediate density n^* vanishes if (18) and (19) are added to each other, and the resulting equation is exactly the finite-difference form of (6) with the mixed implicit (diffusion and chemistry) and explicit (advection) representation.

Since the explicit methods are involved, for the numerical stability of the solution, the time step must satisfy the 2-D Courant-Lewy-Friedrichs condition

$$\Delta t_S \le \frac{\max(\Delta x, \Delta y)}{\sqrt{2(\vartheta_x^2 + \vartheta_y^2)}} \quad (20)$$

In the worst case scenario (for horizontal high spatial resolution and large convection velocities of 1 km/sec and up), this limit has an order of a few tens of seconds or less. Usually, it is about one minute for the resolution of 100×100 km. In any case, it is out of the range of the model time steps. To resolve this contradiction, the time sub-steps inside the model's basic time-step are introduced and the subsequent calculation of several intermediate densities n*, n**, n***, ... are performed. These intermediate densities can be considered as the different stages of the advective density re-distribution, the approach similar to the ADI method where consideration of "partial" diffusion in one direction and the correspondent intermediate density expansions finally creates the complete picture.

In practical terms, the code determines the duration of time sub-steps not longer than the 90% of a Courant-Lewy-Friedrichs limit, and consequently a number of time sub-steps to cover the entire time advance specified in the model. For instance, if the basic time step is ten minutes and the mesh resolution is chosen as 100×100 km, this leads up to 8-10 sub-steps for the higher convection velocities appropriate to geomagnetically disturbed periods, 4-6 sub-steps for the moderate conditions, and 2-3 sub-steps for the quiet periods. Higher resolution will require even more sub-steps.

The explicit method of the advection calculations (18) is very fast compared to the inversion of the tridiagonal system (17, 19). Even repetitive calculations of the advective redistribution of density do not significantly degrade the code performance, since the matrix inversion is still performed only once during the model time step. This is one of the reasons for the computational effectiveness of our implementation of the Eulerian algorithm.

3.2 Numerical Treatment of the Equations of Energy Balance for Electrons and Ions

In the previous section, it was shown that the determination of electron and ion temperatures over the model height range can be reduced to a 1-D ordinary differential equation for T_e, and to the algebraic relation in case of T_i. Equation (14) for T_e is solved at each model time step by the standard relaxation method from the Fortran package of *Press et al.* [1992]. Parameterization of electron heating by photoelectrons and precipitating particles from the TIGCM model are adopted, as well as the parameterization of the upper boundary condition in the form of a heat flux [*Roble and Ridley*, 1987]. The lower boundary condition is $T_e=T_n$. The ion temperature T_i is available from the algebraic relation for the ion energy balance (15).

4. Model Inputs

The model flow-chart in Figure 1 represents the model input, its internal structure, and the output. The chart includes a number of time-dependent inputs that are generated by various empirical and theoretical models to be utilized in the simulations. The responses of these models to the variable geophysical conditions depend upon a number of geophysical indexes that represent this variability. These geophysical indices are the basic initial inputs to our model. Besides the location either in the geographic or geomagnetic coordinates, the local (LT) or universal (UT) time, and season (usually, as a day number in a year), these indices are solar activity index $F_{10.7}$, interchangeable indices of geomagnetic activity A_p, K_p, or AE [*Rostoker*, 1992], and Interplanetary Magnetic Field (IMF) components B_y and B_z. The index-controllable inputs and the models which generate these inputs will be briefly discussed in this section.

4.1 Model Coordinates.

The model frame co-rotates with the Earth and the basic coordinates of the model are, therefore, geographic coordinates. Since the model covers only a limited polar region of the Earth, the curvature can be neglected and simple Cartesian geometry is applicable. A stereographic projection is used to map the geographic longitude and latitude to the Cartesian frame, while the radial distance is mapped as the vertical coordinate (see Figure 2, upper panel). This technique preserves the azimuth angles and does not introduce substantial distortion to latitudinal coordinates up to about 45 degrees of latitude. For example, near the latitude of 60 degrees, the accumulated angular distortion is 0.35 degree. Thus, distortions are negligible in the auroral zone and polar cap, regions of the most interest for this model.

The primary region of interest for the model coverage is poleward from 50 degrees of geographic latitude. However, calculations are performed in the broader domain (Figure 2, lower panel) to account for boundary effects, particularly when strong electric fields penetrate below 50 degree of geographic latitude that takes place in the Western Hemisphere due to the geomagnetic pole shift.

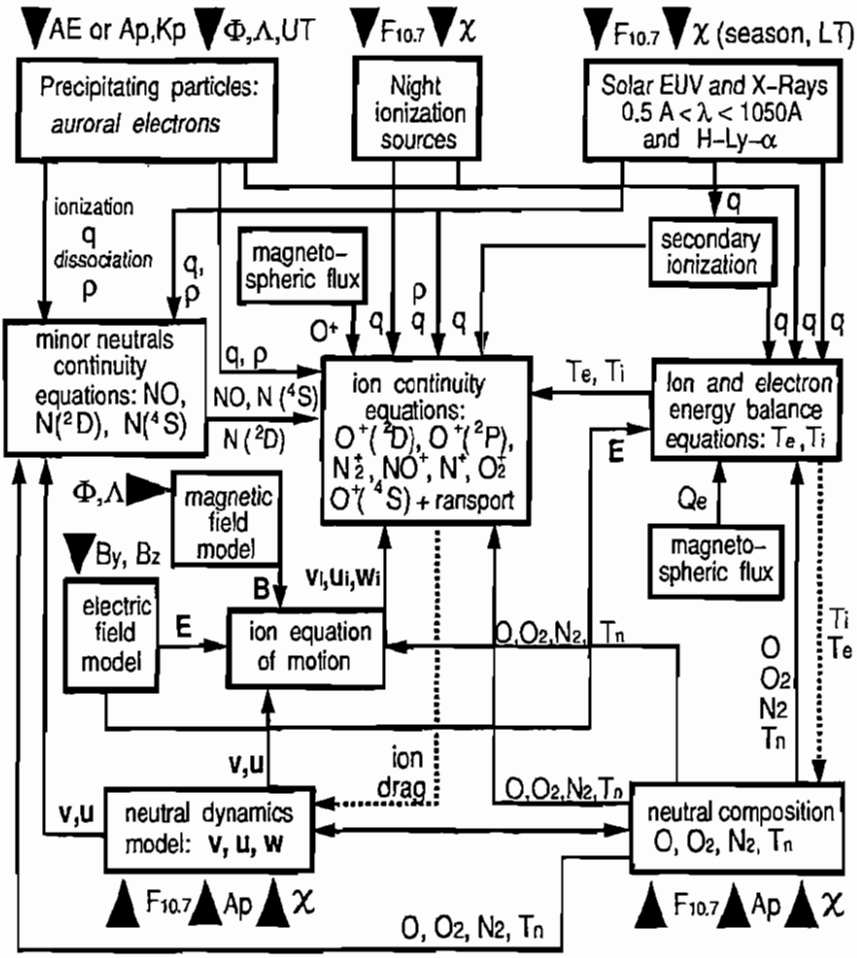

Figure 1. Schematic diagram of the polar ionosphere model. The inputs represented by the short thick arrows are season, the Universal Time (UT), and local time (LT) for the current location, the level of solar activity (index $F_{10.7}$), and level of geomagnetic activity (interchangeable indices AE, Kp, and Ap). Particles precipitation characteristics depend upon current location in the geomagnetic coordinates Φ, Λ, and the UT-dependent auroral oval position. The output of empirical electric field model depends on IMF (Interplanetary Magnetic Field) parameters B_z, B_y, and the cross-cap potential, that is a function of geomagnetic activity level. Dashed arrows correspond to the coupling that physically exists, but is not accounted for in the model. Model outputs are the 3-D distributions of electron density; densities of seven major ions $O^+(^4S)$, $O^+(^2D)$, $O+(^2P, NO^+, O_2^+, N_2^+$, and N^+; horizontal ion velocities v_i, u_i; and densities of the odd-nitrogen family $N(^4S)$, $N(^2D)$, and NO.

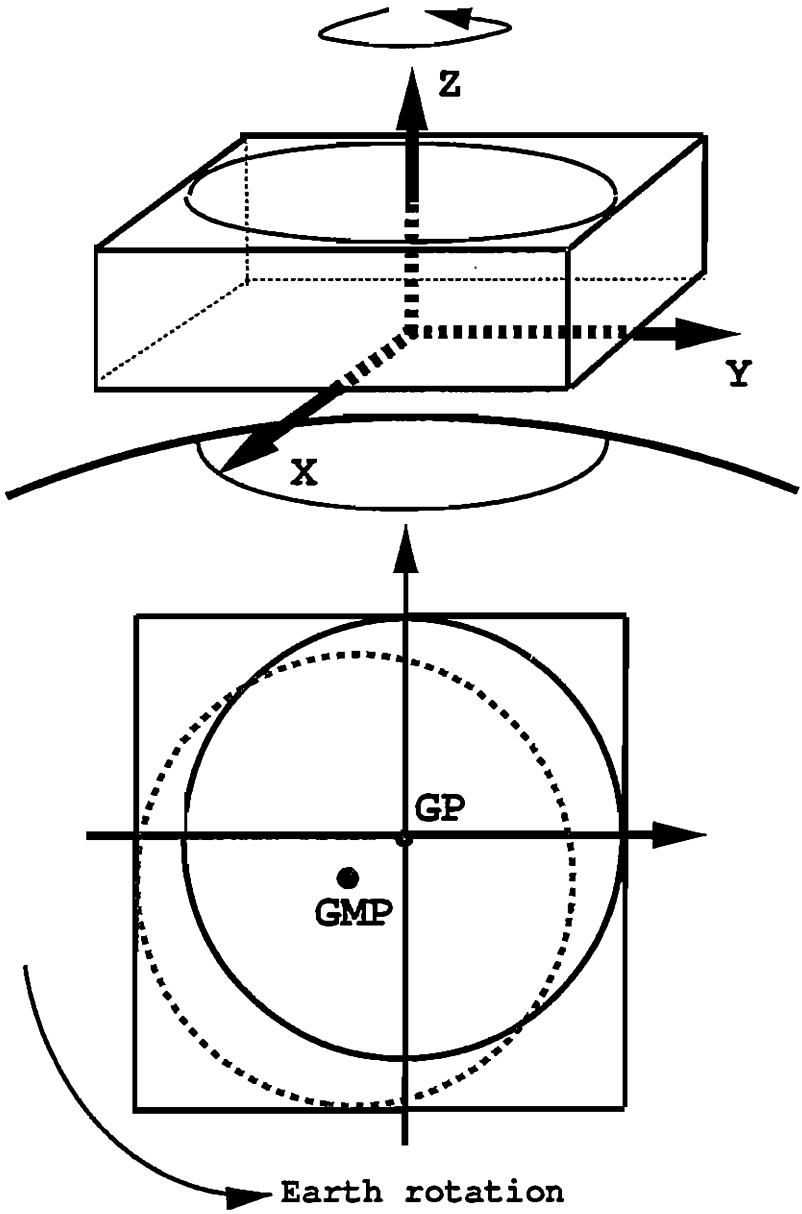

Figure 2. Orientation of the model Cartesian frame. Magnetic and geographic poles (GMP, GP) and the latitudinal circle of 50 degrees in both systems are schematically demonstrated. Orientation of x,y-axis is along geographic meridians of 90E and 180E, respectively.

Several model inputs are specified in the geomagnetic system, for instance the potential pattern of the magnetospheric electric field. Point-by-point transformation is used to convert the scalar fields specified in one system to another [*Baker and Wing*, 1989], and finally to the Cartesian frame. The Cartesian components of the electric field vector can be then calculated by numerical application of the gradient procedure. The vector values specified in terms of the geographic zonal and meridional components are recalculated into x,y-component in the Cartesian frame by the following expressions

$$\begin{aligned} \vartheta_x &= Sign(\vartheta)\cos(\lambda+\beta)\sqrt{\vartheta^2+u^2} \\ \vartheta_y &= Sign(\vartheta)\sin(\lambda+\beta)\sqrt{\vartheta^2+u^2} \end{aligned} \qquad (21)$$

where

$$\beta = \begin{cases} -\tan^{-1}(u/\vartheta), & \vartheta \neq 0 \\ \frac{\pi}{2}\cdot Sign(u), & \vartheta = 0 \end{cases} ; \quad Sign(x) \text{ is re-defined as } \quad Sign(x) = \begin{cases} -1, & x \leq 0 \\ +1, & x > 0 \end{cases} ;$$

and λ is the geographic longitude; ϑ, u are meridional and zonal components of a vector, respectively, and ϑ_x, ϑ_y are the x- and y-components of a vector in the Cartesian frame.

4.2 Neutral Thermosphere

We use a combination of two models to determine background thermospheric parameters (MSIS [*Hedin*, 1991] and VSH [*Killeen et al.*, 1987]). These models generate the time-dependent 3-D fields of necessary data, including the major component densities, neutral winds and temperatures, corresponding to the geophysical situation specified from the set of basic geophysical indices. In addition to the neutral thermospheric data, the VSH model yields some ionospheric parameters that can be used as the boundary and the initial conditions.

4.3 Ionization Sources

Calculation of photoionization and photodissociation rates are based on the recent EUV spectrum parameterization by *Tobiska and Barth* [1990], and the cross sections, branching ratios, and quantum yields from the comprehensive review by *Kirby-Docken et al.* [1979]. Secondary ionization by photoelectrons is accounted for in accordance with the parameterization of solutions to photoelectron transport equation by the season, solar activity, height, and local time [*Lilensten et al.*, 1989]. This parameterization simulates the sharp peaks (factor of 2-4) in the secondary ionization efficiency typical of the *F1*- and *E*-regions of the ionosphere. Nocturnal ionization sources by strong helium and hydrogen EUV-lines (*H Lyman-α, H Lyman-β*; and *HeI, HeII*) resonantly scattered on the geocorona are also included [*Strobel et al.*, 1974, 1980].

A corpuscular ionization profile is calculated by the range method [*Rees*, 1963; 1989] starting from the electron energies of 1 keV. The contribution by the low energy tail of precipitating spectrum is calculated by the convolution of the number flux in several energy ranges and the ionization profiles by a unit mono-energetic flux. These profiles are obtained as a two stream solution of the electron transport equation by *Banks et al.* [1974]. A Maxwellian spectral distribution of precipitating electrons is assumed. In the current version of the model, the number flux and characteristic energy at a given location corresponding to a specified level of magnetic activity are obtained from the statistical precipitation model derived by *Hardy et al.*

[1985, 1987]. For high resolution simulations in the future versions of our model, we plan to use auroral imagers data as a precipitation model input.

4.4 Magnetospheric Electric Field

This input plays a crucial role in polar ionospheric modeling since it determines both the governing dynamic processes in the upper ionosphere and the major Joule heating source. However, only statistically averaged patterns are currently available and the mesoscale variability is not well known at this time. The electric field pattern has a strong dependence on the IMF orientation. The effect of the IMF By-component is to introduce an asymmetric distortion of convection structures that may change the configuration of the polar cap flow. The southward orientation of B_z-component ($B_z < 0$) generates a two cell vortex-like pattern with the anti-sunward flow in the polar cap. Several electric field models have been formulated predominantly for the southward orientation of B_z [e.g., *Heelis*, 1982, 1984; *Heppner and Maynard*, 1987; *Rich and Maynard*, 1989].

Earlier investigations [e.g., *Heelis et al.*, 1986; *Knipp et al.*, 1991] have demonstrated that the northward orientation of B_z ($B_z > 0$) significantly decreases the cross-cap potential and the intensity of convection, and yields either an irregular pattern or multi-cell convection structure with combination of sunward and anti-sunward flows in the polar cap. *Rich and Hairston* [1994] and *Weimer* [1995] have introduced the most comprehensive electric field models to date, which include patterns for the general orientation of B_z and B_y IMF components including $B_z > 0$.

Our ionospheric model has been tested with "two-cell" electric field models that correspond to the numerical representation of potential patterns for $B_z < 0$ [*Heelis*, 1982; *Heppner and Maynard*, 1987; *Rich and Maynard*, 1989]. The ionospheric model has been recently updated to utilize the convection pattern formulated by *Weimer* [1995]. This electric field model can be readily used for numerical simulations, since it provides a digital representation of potential for arbitrary orientation of IMF via a number of sets of spherical harmonics coefficients that vary for the different values of the tangential component of IMF ($B_t = (B_z{}^2 + B_y{}^2)^{1/2}$), and/or for the value of magnetic dipole tilt. The latter variable represents large-scale seasonal changes, while the former can be considered as a measure of geomagnetic activity [*Shue and Weimer*, 1994]. Bilinear interpolation between sixteen angular sectors of IMF orientation and four B_t ranges provides a continuous transition between the potential patterns for different values and orientations of IMF.

4.5 Magnetic Field

The realistic distribution of the main magnetic field is used in the model. The magnetic inclination, declination, and radial components are calculated by the NASA MAGSAT Fortran package in accordance with the spherical harmonics representation of the International Magnetic Field Reference Model (IGRF80) for a specified magnetic epoch.

5. Model Outputs

5.1 The Model Operational Modes

The model output is the time-dependent 3-D distribution of the density of electrons, seven ion species ($O^+(^4S)$, $O^+(^2D)$, $O^+(^2P)$, NO^+, O_2^+, N_2^+, N^+), isotropic ion and electron temperatures, and the ion drift velocity. The results are considered valid inside the circle of 50

degrees geographic latitude, although the calculations are performed in a somewhat broader domain. The altitude coverage is 80-500 km. The densities of the minor neutral species NO and $N(^4S)$, $N(^2D)$, which are important for the ionization balance in the lower ionosphere, are also self-consistently calculated.

Depending on the choice of inputs, the model is capable of several modes of simulations. First, the climatology-scale simulations use statistical models of large-scale electric field and auroral precipitation. The second mode of operation applies to case studies when the particular patterns of these inputs are available, either as a time-series of precipitation data (e.g. from the auroral images), or coupled with measurements of the electric field or assimilative reconstructions by the AMIE-technique [*Richmond and Kamide*, 1988]. A third approach is a simulation of the ionospheric variability in response to time-series of varying geophysical indices such as IMF components, K_p, etc., using variable ionospheric inputs from the indices-driven statistical models.

5.2 Climatology-Scale Studies

This type of model study is designed to investigate the predominant large-scale behavior of the ionosphere in response to particular static or slowly varying geophysical conditions. There are three major cycles that determine the ionospheric climatology. These are the 11 year solar activity cycle (this governs the intensity of EUV ionizing radiation), seasonal effects, and the diurnal effect of the rotation that includes rotation of the geomagnetic pole around the geographic pole. Superposed on these slowly varying effects are the more variable geophysical changes resulting, for example, from the size of the convection system and auroral precipitation pattern. Changes in IMF orientation generally distorts the large-scale E-field pattern and auroral precipitation patterns. The variety of effects is so abundant that, for the climatological simulations, most inputs are usually kept fixed to simplify the picture and to trace the effects of limited number of input parameters.

A sample of this approach is represented in Figure 3, which illustrates contours of calculated electron density at 350 km altitude, together with the ion drift velocity vectors. This case applies to winter conditions, average solar activity ($F_{10.7}$ = 150), moderately-disturbed magnetic activity (K_p = 4o to 5+), and fixed IMF components ($B_z < 0$; and $B_y = 0$). As usual, the coordinates are geographic latitude (down to 50 degrees) and local time. The effects of rotation of the convection system around the geographic pole are represented in the four panels, each for different universal times.

The terminator is fixed in this frame in the upper third of a panel. The most polar location for the winter solstice is the polar circle or 67 degrees of latitude. The two cell vortex-like convection system rotates together with the geomagnetic pole preserving its orientation parallel to the day-night meridian. The "throat" of convection pattern, consequently, is distant from theterminator (0600 UT), approaches it at the dawn sector (1200 UT), reaches the most inside position in the sunlit region (1800 UT), and crosses it again (0000 UT) on the way out, this time at the dusk sector. Consequently, the ionospheric features follow this scenario. The tongue of ionization is not well pronounced at 0600 UT, starts to appear by 1200 UT, is most developed by 1800 UT, and begins to fade at 0000 UT. The pictures are not symmetric at 1200 UT and 0000 UT even though the convection system is at the same distance from the terminator. The region of abundant day-side ionization is tilted toward the dusk sector due to co-rotation of the long-living O^+ ions. This supply of enhanced plasma to maintain the anti-solar flow lasts well after the terminator is crossed at dusk by the convection system.

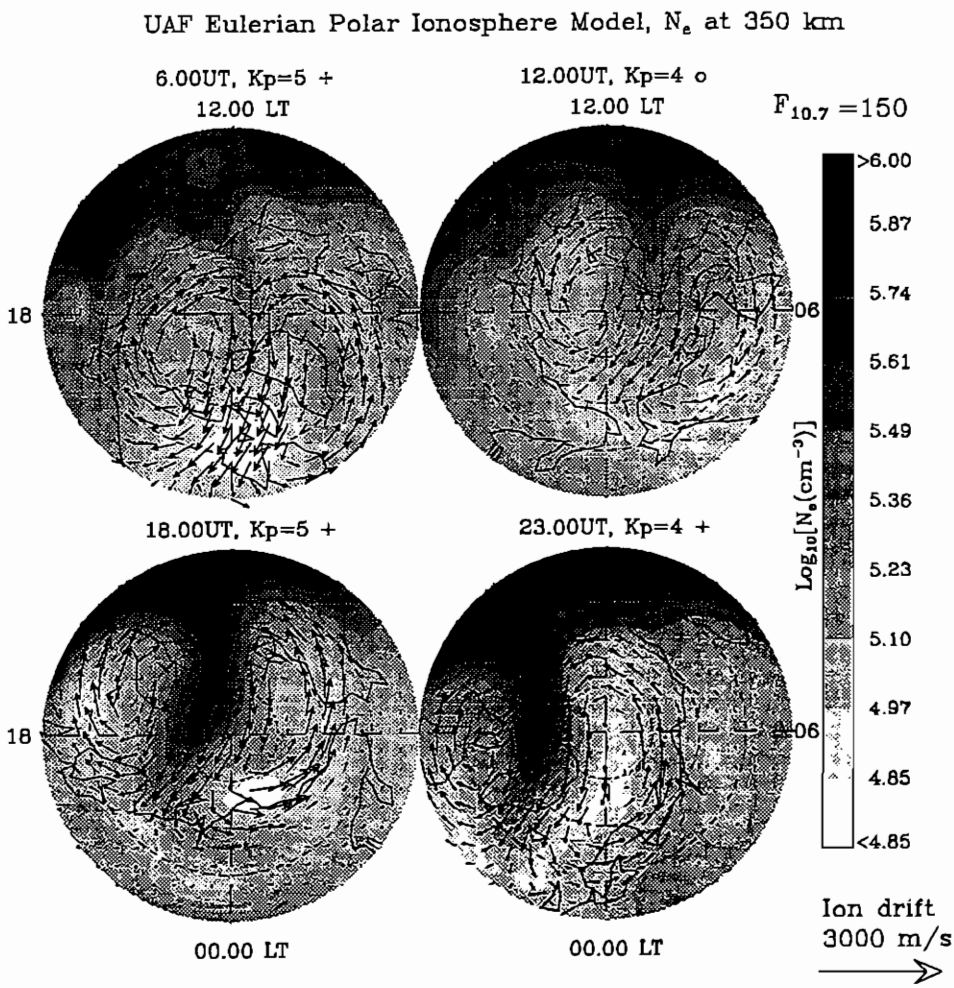

Figure 3. The ion drift velocity vectors and electron density contours in the geographic latitude-local time frame, for winter conditions, moderately-disturbed geomagnetic activity. Rotation of the geomagnetic pole results in different ionospheric response at different universal times (see text).

The appearance of ionospheric troughs is connected with the sunward flows and also follows the convection pattern displacements. The biggest shift of the equatorial edge of the main or mid-latitude trough to the night-side takes place at 0600 UT when the convection system is shifted toward the night-side itself. Later, at 1200 UT, the trough shapes up to a more regular oval-like structure and moves toward the general day-side direction. By 1800 UT, the strong plasma flow from the day-side separates the trough into three isolated features, dawn and dusk day-side troughs and the main night-side trough. On this plot, the polar hole, the region of depleted ionization engulfed by the elongated continuation of the tongue of ionization, has appeared. By 0000 UT, all three troughs merge together and again move toward the night-side.

5.3 High Resolution Simulations

The workstation-based version of the model has a horizontal resolution not better than 100×100 km due to the limited computational resources. This version of model is, therefore, capable of simulations of only meso-scale phenomena (100-1000 km structures).

An application of this mode is the study of the formation of polar cap "patches" of ionization shown in Figure 4. In response to change in the IMF B_y component, the polar cap convective flow of plasma may be disrupted causing localized plasma density enhancements within the polar cap. In this particular example, B_y was rapidly changed from -12γ to +12γ each hour. It is evident that the fast change of convection pattern results in the "patch" formation that rapidly evolves in time.

Future upgrades to our model, when it is converted to a supercomputer environment, will permit studies of smaller scale structures.

5.4 Reconstruction of Geophysical Conditions for Particular Periods and Simulation of Ionospheric Responses

The polar ionosphere is a system with a present state that depends on the prior time-sequence of input parameters. To trace the influence of inputs such as the convective electric field and auroral precipitation, it is necessary to reproduce their particular development in the time preceding the period of interest. The electric field model by *Weimer* [1995] is adopted as a standard source of electric field in the UAF ionospheric model and requires IMF B_z and B_y components as inputs. Comparison of simulated ionospheric response of a real geophysical case study is instructive for understanding the ability of our model to describe the real ionosphere.

Two examples of such studies are represented on Figure 5. The first period that is useful is February 19, 1990, because it is a period of continuous Sondrestrom Incoherent Scatter Radar measurements. Other modeling efforts have also been devoted to this period [*Valladares et al.*, 1994; *Decker et al.*, 1994]. Our modeling with the dynamically IMF-driven electric field input has achieved excellent agreement with the data for the time period preceding 1400 UT. The modeled ionospheric response has a significant variability that closely resembles the measured dependencies.

The upper panel of Figure 5 shows a discrepancy of about 2 MHz in f_oF_2 values between the data and our model results that begins at about 1400 UT at Sondrestrom and about half an hour later at Thule. The Sondrestrom ISR measurements [*Valladares et al.*, 1994] show that the localized plasma jet, with a velocity exceeding 2 km/sec, emerged near Sondrestrom at approximately the same time and later moved polarward to Thule within about 30 minutes. Local depletions of the plasma density are explainable by the enhanced recombination of the

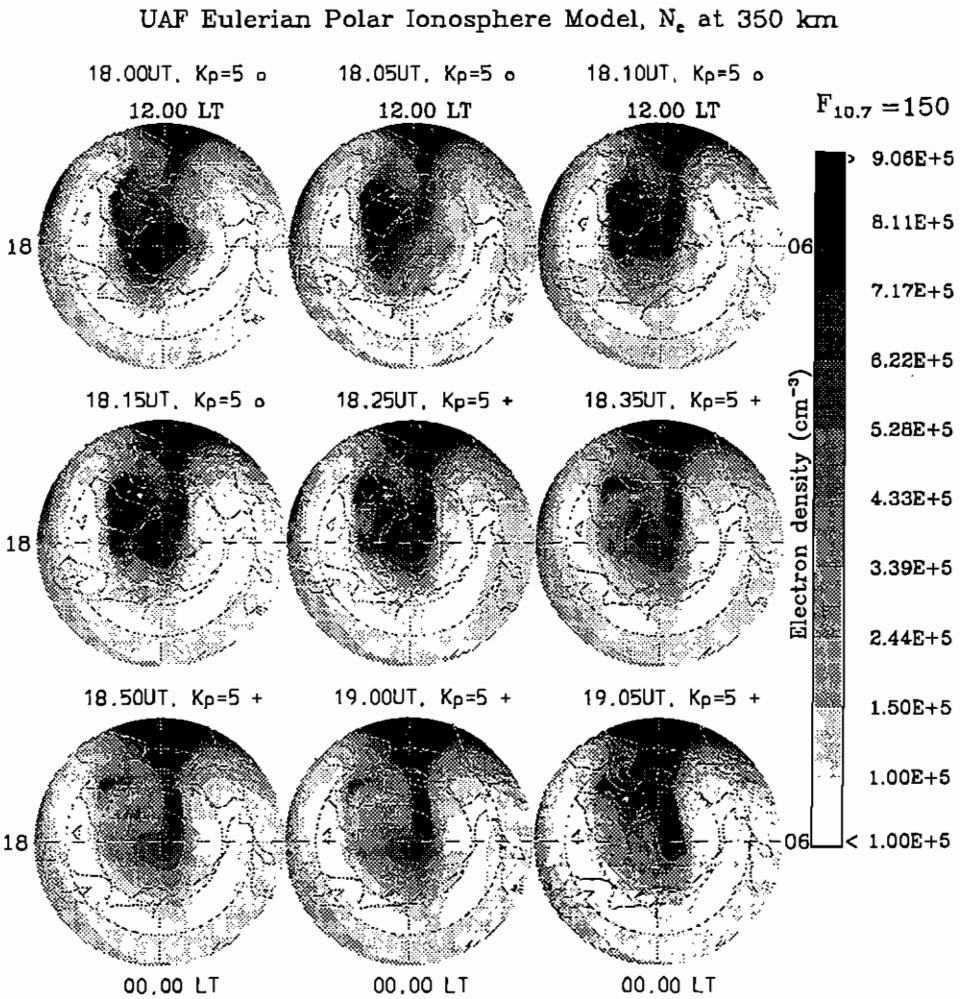

Figure 4. Ionospheric response upon a rapid change of the IMF B_y component from -12 nT (1800 UT) to +12 nT (1805 UT). Changes in the convection pattern result in development of new tongue of ionization, while the existing structures continue their convective motion, decaying into the separated patches. By 1905 UT, B_y had changed to -12 nT again, generating a new "patcherization" cycle.

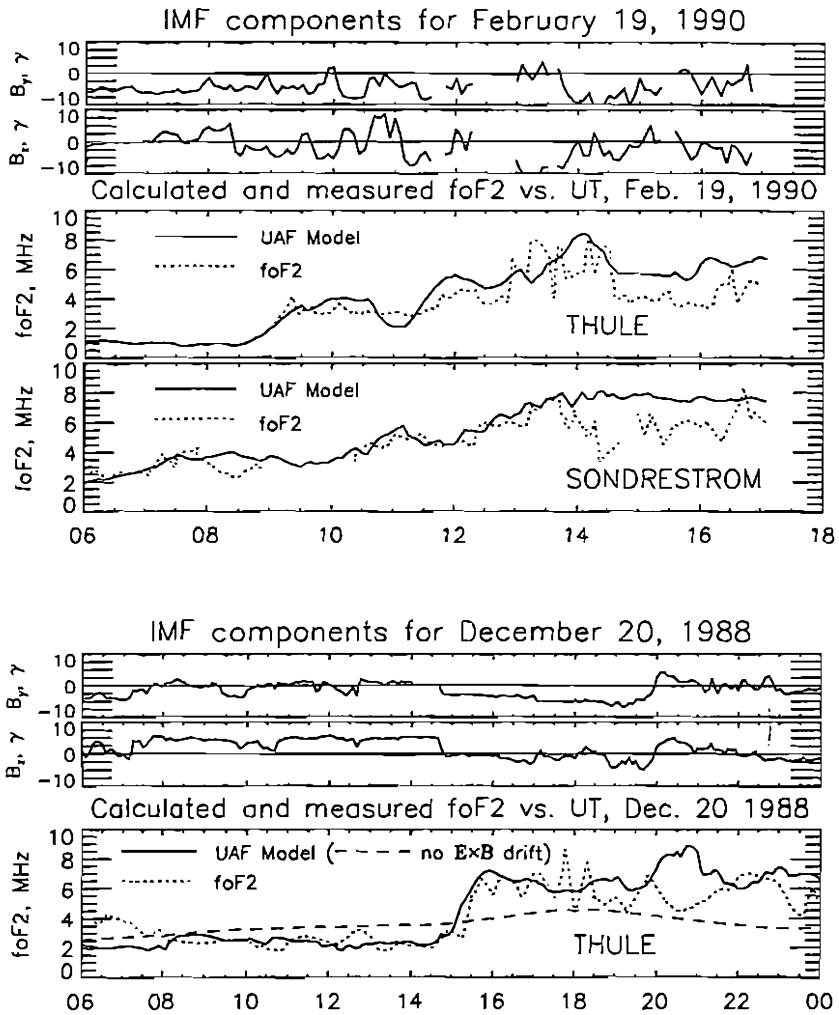

Figure 5. Comparisons of the model runs performed with the reproduction of geophysical time-history of particular periods and the digisonde measurements for the polar cap locations show a good overall agreement and a realistic variability of calculated parameters. See text for detailed discussion of particular periods..

Joule-heated plasma. This local disturbance in the real E-field structure is not represented in the E-field input to our model, and therefore a discrepancy of model and data at this time is not unreasonable.

The second modeled period is December 20, 1988 (the bottom panel of Figure 5). The distinct feature of this day is a strong northward (positive) orientation of B_z from 0700 UT to 1500 UT, then a fast reversal took place and B_z orientation changed to the southward direction (negative). The first regime corresponds to the period of weak convection, while the second regime generates intensive convective motion in the polar cap. An abrupt transition from one convection regime to another is evident from the digisonde measurements for this period by *Buchau and Reinisch* [1991], that are plotted as a dotted curve, while the dashed curve represents the model run without an account of the horizontal transport, i.e., the simulation of local production and loss including only transport mechanism by the vertical diffusion. Smooth variations of critical ionospheric frequency f_oF_2 near the locally created ambient ionization level are abruptly replaced by the fluctuations that correspond to the horizontal transport of the patch-like plasma structures over the measurement site (Thule). The ionospheric response simulated with our model follows this data trend rather closely, demonstrating a remarkably good overall agreement for the transition time and the magnitude of f_oF_2 changes.

It is evident that for experimental periods when the real E-field structures are well represented by the statistical model (e.g., *Weimer,* 1995), we use this model input, then the modeled electron density data are an excellent representation of real data. However, when localized E-field structures result in significant departures from the statistical E-field model, our modeled data do not accurately reflect real data. This reinforces the point that results of ionospheric models are critically dependent on their E-field inputs.

6. Model Uncertainties And Limitations

The main goal of the first version of this model was investigation of the polar ionospheric modeling in the Eulerian frame, its advantages, and the possible shortcomings. There are several model uncertainties that reflect the inadequacies of the input data (e.g., solar flux, electric fields, auroral ionization).

The crucial inputs for the polar ionosphere modeling are the auroral precipitation data and the convection electric field pattern. Statistical precipitation models are suitable for the climatic studies but can not be successfully implemented for weather-scale modeling. However, satellite auroral images are capable of providing "snapshots" of real precipitation with the spatial resolution exceeding the capabilities of current ionospheric models.

A serious limitation of our model is the current lack of high resolution time-dependent E-field and precipitation data that are used as model inputs.. Unfortunately, only the climatic-scale statistical models of electric field are now available. A promising approach for specific case studies is the electric field reconstruction by the AMIE-technique [*Richmond and Kamide,* 1988]. The method allows determination of the electric field evolution with the considerable temporal and spatial resolution over periods of a few days. The first arrays of such data recently became available in the CEDAR database [*Knipp et al.*, 1994].

Finally, better data for the upper O^+ boundary condition is desirable. The O^+ profile is very sensitive to the upper boundary condition and the density value near the profile main peak varies within considerable range for relatively small differences in the boundary flux. An

appropriate ion flux into or out from the magnetosphere is necessary to achieve a closer agreement with the data [*Min and Watkins*, 1995].

7. Model Availability

The Fortran code of the model consists of about 70 subroutines and has about 25,000 source lines. The model has a post-processor package capable of visualization and animation of the model runs include: animation of the model runs (animation of the model simulation of geomagnetic storm March 20-21, 1990, with AMIE-reconstruction of electric field as an input is available on-line at WWW-page http://www.arsc.edu/general/Visualizations.html). Both the code and the post-processor package are currently undergoing developments and are far from being user-friendly at this time. However, we plan to prepare a version for the CEDAR database for implementation on upper-end workstations. This version will be capable of resolution up to 200×200 km and will provide a user with selectable output.

A supercomputer version of the code is currently under the preparation in the Arctic Regional Supercomputing Center in UAF. The authors are willing to collaborate with interested parties in both theoretical studies with the model, especially testing of different ionospheric inputs, and the model-data comparisons.

Acknowledgments. This work was supported by the National Science Foundation under grant ATM-9213969. The IMF data from IMP8 and ISEE3 were provided by the National Space Science Data Center.

8. References

Albritton, D.L., I. Dotan, W. Lindinger, M. McFarland, J. Tellinghuisen, and F.C. Fehsenfeld, *J. Chem. Phys., 66*, 410, 1977.

Baker, K. B., S. Wing, *J. Geophys. Res., 94*, No.A7, 9139-9143, 1989.

Banks, P.M., *J. Geophys. Res., 72*, 3365-3385, 1967.

Banks, P.M., and G. Kockarts, *Aeronomy*, Academic Press, New York, 1973.

Banks P.M., C.R. Chappel, and A.F. Nagy, *J. Geophys. Res., 79*, 1459, 1974.

Buchau, J., and B. Reinisch, *Adv. Space Res., 11*, (10)29, 1991.

Black, G., T.G. Slanger, G.A. St.John, and R.A. Young, *J. Chem. Phys., 51*, 116, 1969.

Decker, D. T., C. E. Valladares, R. Sheehan, Su. Basu, D. N. Anderson, and R. A. Heelis, *Radio Sci., 29*, 149, 1994.

Frederick, J.E. and D.W. Rusch, *J. Geophys. Res., 82*, 3509, 1977.

Garstang, R.H., in *The Airglow and Aurora*, edited by E.B. Armstrong and A. Dalgarno, p.324, Pergamon, New York, 1956.

Hardy, D.A., M.S. Gussenhoven, and E. Holeman, *J. Geophys. Res., 90*, 4229-4248, 1985.

Hardy, D.A., M.S. Gussenhoven, R. Raistrick, and W.J. McNeil, *J. Geophys. Res., 92*, 12,275-12294, 1987.

Hedin, A.E., *J. Geophys. Res., 96*, A2, 1159-1172, 1991.

Heelis, R.A., J.K. Lowel, and R.W. Spiro, *J. Geophys. Res., 87*, 6339, 1982.

Heelis, R.A., *J. Geophys. Res., 89*, 2873-2880, 1984.

Heelis, R.A., P.H. Reif, J.D. Winningham, and J.D. Benson, *J. Geophys. Res., 91*, A5,5817-5830, 1986.

Henry, R.J.W., P.G. Burke, and A.L. Sinfailam, *Phys.Rev., 178*, 218, 1969.

Heppner, J.R., and N.C.Maynard, *J. Geophys. Res., 92*, 4467-4489, 1987.

Huntress, W.T., Jr., and V.G. Anicicoh, *Geophys. Res. Lett., 3*, 317, 1976. Jet Propulsion Laboratory (JPL), Chemical Kinetic and Photochemical Data for Use in Stratospheric Modeling, JPL 81-3, p. 124, NASA Panel for Data Evaluation, Jet Propulsion Laboratory, Pasadena, Calif., 1981.

Johnsen, R., and M.A. Biondi, *Geophys. Res. Lett., 7*, 401, 1980.

Killeen, T.L., R.G. Roble, and N.W. Spencer, *Adv.Space.Res., 7*, 207-215, 1987.

Kirby-Docken, K., E.R. Constantinides, S. Babeu, M. Oppenheimer, *Atomic Data Nucl. Data Tables, 23*, 63, 1979.

Knipp D.J., A.D. Richmond, B. Emery, N.U. Crooker, O. de la Beaujardiere, D. Evans, H. Kroehl, *Geophys. Res. Lett., 18*, No.4, 721-724, 1991.

Knipp D.J., B. A. Emery, A. D. Richmond, and W. F. Roberts, Abstracts of AGU Fall Meeting, 498, 1994.

Lindinger, W., F.C. Fehsenfeld, A.L. Schmeltekopf, and E.E. Ferguson, *J. Geophys. Res., 79*, 4753, 1974.

Lilensten J., W. Kofman, J. Wisemberg, E.S. Oran, and C.R. Devore, *Ann. Geoph., 7*, 83-90, 1989.

McFarland, M., D.L. Albritton, F.C. Fehsenfeld, E.E. Ferguson, and A.L. Schmeltekopf, *J. Geophys. Res., 79*, 2925, 1974.

Mehr, F.J., and M. Biondi, *Phys. Rev., 181*, 264, 1969.

Min, Q.-L., B.J.Watkins, *J. Geophys. Res., 100*, 251, 1995.

Mitra, A.P., *J. Atmos. Terr. Phys., 30*, 1065-1114, 1968.

Nicolet, M., *Geophys. Res. Lett., 6*, 866, 1979.

Nicolet, M., and S. Cielslik, *Planet. Space Sci., 28*, 105, 1980.

Ozisik, M.N., *Finite Difference Methods in Heat Transfer*, CRC Press, Boca Raton-Ann Arbor-London-Tokyo, 1994.

Potter, D., *Computational Physics*, John Wiley & Sons, Chichester-New York-Toronto, 1977.

Press, W.H., S.A. Teukolsky, W.T. Vetterling, B.P. Flannery, *Numerical Recipes in Fortran, The Art of Scientific Computing*, Cambridge Univesity Press, Cambridge, 1992.

Rees, M.H., *Planet. Space Sci., 11*, 1209, 1963.

Rees, M.H., *Physics and Chemistry of the Upper Atmosphere*, Cambridge Univesity Press, Cambridge, 1989.

Rich, F.J, and N.C. Maynard, *J. Geophys. Res., 94*, A4, 3687-3701, 1989.

Rich, F.J, and M. Hairston, *J. Geophys. Res., 99*, A3, 3827-3844, 1994.

Richards, P.G, M.R. Torr, and D.G. Torr, *Planet. Space Sci., 30*, 515, 1982.

Richmond, A. D., and Y. Kamide, *J. Geophys. Res., 93*, A6, 5741-5759, 1988.

Roble R.G., *Planet. Space Sci., 40*, No.2/3, 217-297, 1992.

Roble R.G., and E.C. Ridley, *Ann. Geophys, ser. A, 5*, No.6, 369-382, 1987.

Rostoker, G., *J. Geophys. Res., 96*, No. A4, 5853-5857, 1991.

Rowe, B.R., D.W. Fahey, F.C. Fehsenfeld, and D.L. Albritton, *J. Chem. Phys., 73*, 194, 1980.

Rusch, D.W., and W.E. Sharp, *J. Geophys. Res., 86*, 10,111, 1981.

Rusch, D.W., D.G. Torr, P.B. Hays, and J.C.G. Walker, D.G., *J. Geophys. Res., 82*, 719, 1977.

Schunk, R.W., *PAGEOPH, 127*, Nos.2/3, 255-303, 1988.

Schunk, R.W., and W.J. Raitt, *J. Geophys. Res., 85*, 1255, 1980.

Sojka, J.J, *Adv. Space Res., 12*, No.6, (6)51-(6)58, 1992.

Sojka, J.J, M.D. Bowline, R.W. Schunk, et al., *Geophys. Res. Lett., 20*, No.17, 1783-1786, 1993.

St.-Maurice, J.P., and D.G. Torr, *J. Geophys. Res., 83*, 969, 1978.

Strickland, D.G., and R.R. Meier, *NRL Memo. Rep., 5004*, 1-40, 1982.

Strobel, D.F., T.R. Young, R.R. Meier, T.P. Coffey, A.W. Ali, *J. Geophys. Res., 79*, No.22, 3171-3185, 1974.
Strobel, D.F., C.B. Opal, and R.R. Meier, *Planet. Space Sci., 28*, 1027-1033, 1980.
Shue, J.-H., and D.R. Weimer, *J. Geophys. Res., 99*, A1, 401-415, 1994.
Tobiska W.K., C.A. Barth, *J. Geophys. Res., 95*, A6, 8243-8251, 1990.
Torr, D.G., in *The Photochemistry of the Atmospheres*, 165-286, Academic, Orlando, Flo., 1985.
Torr, D.G., and M.R. Torr, *J. Atmos. Terr. Phys., 41*, 797, 1979.
Torr, D.G., M.R. Torr, J.C.G. Walker, and A.O. Nier, *J. Geophys. Res., 81*, 5578, 1976.
Torr, D.G., N. Orsini, M.T. Torr, W.B. Hanson, J.H. Hoffman, J.C.G. Walker, *J. Geophys. Res., 82*, 1631, 1977.
Torr, D.G., M.R. Torr, H.C. Brinton, L.H. Brace, N.W. Spencer, A.E. Hedin, W.B. Hanson, J.H. Hoffman, A.O. Nier, J.C.G. Walker, and D.W. Rusch, *J. Geophys. Res., 84*, 3360, 1979.
Torr, M.R., and D.G.Torr, *Rev. Geophys., 20*, 91, 1982.
Torr, M.R., P.G. Richards, and D.G.Torr, *J. Geophys. Res., 85*, 6819, 1980.
Torr, M.R., D.G. Torr, and H.E. Hinterregger, *J. Geophys. Res., 85*, 6063, 1980.
Torr, M.R., D.G. Torr, and P. Richards, *Planet. Space Sci., 28*, 581, 1980.
Valladares, C. E., S. Basu, J. Buchau, E. Friis-Christensen, *Radio Sci., 29*, 167, 1994.
Watanabe, K., *Appl. Opt., 6*, 391, 1967.
Weimer, D.R., *J. Geophys. Res., 100*, 19,595, 1995.
Zipf, E.C., and R.W. McLaughlin, *Planet. Space Sci., 26*, 449, 1978.

High-Latitude Model

J. Wu

China Research Institute of Radiowave Propagation,
P.O. Box 138, Xinxiang 453003,
Henan Province, China

C. Taïeb

CNET-CETP, 38-40 Avenue Général Leclerc,
F-92131 Issy-les Moulineaux, France

1. Introduction

The physics of the ionospheric environment at high latitude is much more complicated than at mid-latitude because the impact of the solar wind has more consequences due to the lines of force configuration of the magnetic field. The now familiar picture of the magnetosphere, first published by *Axford and Hines* [1961], shows that field lines, at latitudes of the polar cap, are open toward the antisolar direction or reconnect, far in the equatorial plane, into the opposite high latitude region. The pressure of the solar plasma on the lines of force which are locked to the surface of the Earth when it rotates, gives the picture of the magnetosphere. The interaction of the solar wind with the Earth's magnetic field polarizes the magnetosphere creating a large scale convection electric field that induces a movement of the plasma perpendicular to the field lines.

Magnetic storms tightly related to the solar activity are frequent, induce sharp changes of the electric field pattern, and often create precipitations of ions and electrons. Considering any line of force, the pressure of the frozen-in plasma at a rather large distance from the F-region is insufficient to balance the pressure of the ionospheric plasma source. Ions of the topside ionosphere, mostly H^+ and O^+, for which gravitational energy is nearly balanced by thermal energy, may thus escape from the ionosphere in a supersonic or not supersonic field-aligned flow. This was first stated by *Axford* [1968] and *Banks and Holzer* [1968], whose calculations indicated that dynamic expansion of the ionospheric plasma might be present along open field lines resulting in a supersonic outward flow. Later, it was realized that supersonic flow might also take place along field lines issuing from auroral and subauroral regions [*Banks et al.*, 1971].

The plasma, made of ions and neutral particles, is a gas sufficiently dense to be collision dominated until at least 1500 to 2000 km altitude and this allows use of the fluid hydrodynamic equations to study the ions' escape. The term exchange should be used rather than escape, as flows are observed in and out of the ionosphere. The model we propose has been worked out, for the altitude range from 300 km in the F-region to 2000 km where fluid hydrodynamic is still a characteristic of the plasma, to study ions exchange between the ionosphere and magnetosphere.

The main features of the neutral atmosphere are like those at mid-latitudes, although the diurnal and seasonal variations are somehow different for the concentration of its components, the temperature and dynamics. The MSIS model [*Hedin et al.*, 1977a; 1977b; 1979], which describes the neutral atmosphere, is based on measurements from mass spectrometer borne on satellites and from several incoherent scatter radars. For most of them, the measurements are limited in altitude and the relative concentration of O and H above 600 km are not reliable [*Wu*

and Taïeb, 1993]. Rather frequently, high values of the convection electric field accelerate the ions with the consequence of creating an anisotropy of the plasma and increasing their temperature along the field line up to 6000° K or more.

2. Mathematical Formulation

Differential equations for concentrations, velocities and temperatures functions, depending on time and altitude, are solved following *Schunk* [1974]. They are:

- Mass Conservation Equation

$$\frac{\partial n_i}{\partial t} + \nabla \cdot \left(n_i \bar{V}_i \right) = \frac{\delta n_i}{\delta t} \tag{1}$$

- Momentum Conservation Equation

$$m_i n_i \frac{D_i \bar{V}_i}{Dt} + \nabla \cdot \bar{P}_i - m_i n_i \bar{G} - n_i e_i \left(\bar{E} + \bar{V}_i \times \bar{B} \right) = \frac{\delta \bar{M}_i}{\delta t} \tag{2}$$

- Energy Equation

$$\frac{D_i \left(\frac{3}{2} p_i \right)}{Dt} + \frac{3}{2} p_i \left(\nabla \cdot \bar{V}_i \right) + \nabla \cdot \bar{q}_i + \bar{P}_i : \nabla \bar{V}_i = \frac{\delta E_i}{\delta t}$$

with

$$\frac{D_i}{Dt} = \frac{\partial}{\partial t} + \bar{V}_i \cdot \nabla$$

$$\frac{\delta n_i}{\delta t} = B_i - A_i n_i$$

$$\frac{\delta \bar{M}_i}{\delta t} = \sum_j n_i m_i V_{ij} \left(\bar{V}_j - \bar{V}_i \right) \Phi_{ij}$$

$$\frac{\delta E_i}{\delta t} = \sum_j \frac{n_i m_i \nu_{ij}}{m_i + m_j} \left[3k \left(\bar{T}_j - \bar{T}_i \right) \Psi_{ij} + m_j \left(\bar{V}_i - \bar{V}_j \right)^2 \Phi_{ij} \right]$$

Mass, concentration, charge, and velocity vector are m_i, n_i, e_i, $\bar{V}_i$, respectively. $\bar{P}_i$ is the pressure tensor, $\bar{P}_i = \bar{\tau}_i + p_i \bar{I}$, where $\bar{\tau}_i$ is the stress tensor, $p_i = n_i k \bar{T}_i$, the scalar pressure, k is the Boltzman's constant and $\bar{I}$, the unit tensor. $\bar{G}, \bar{E}, \bar{B}$ and $\bar{q}$ are gravity, electric field, magnetic field and heat flux vectors, respectively. Φ_{ij} and Ψ_{ij} are correction functions depending on velocity and temperature. ν_{ij} is the collision frequency between i and j species, which can be another ion, an electron, or a neutral particle. B_i represents the ion-electron pairs produced by solar radiation and charge transfer between ions. A_i is the loss by chemical reactions.

Each of the vectorial equations (1) and (2) can be developed into two equations, parallel and perpendicular to the magnetic field line. So we have :

$$V_i = V_{i\parallel} + V_{i\perp} \text{ and } \nabla = \frac{\partial}{\partial s}\bar{b} + \nabla_\perp,$$

where s is the distance along the magnetic field line, and $\bar{b}$, the unit vector, is positive upward. Parallel to the line to the field, equation (1) becomes:

$$\frac{\partial n_i}{\partial t} + \frac{1}{S}\frac{\partial (S n_i V_{i\parallel})}{\partial s} + \nabla_\perp \cdot (n_i V_{i\perp}) = \frac{\delta n_i}{dt} \tag{3}$$

$S = A_0/r^3$ is the cross section of the tube of force, A_0 is the cross section at the lower boundary and r is the radial distance. Equation (2) becomes:

$$m_i n_i \left[\frac{\partial}{\partial t} + V_{i\perp}\cdot\nabla_\perp + V_{i\parallel}\frac{\partial}{\partial s}\right] V_{i\parallel} + \frac{\partial p_i}{\partial s} - n_i m_i G_\parallel - n_i e_i E_\parallel = \frac{\delta M_{i\parallel}}{\delta t} \tag{4}$$

and perpendicular to it

$$\begin{aligned} &m_i n_i \left[\frac{\partial}{\partial t} + V_{i\perp}\cdot\nabla_\perp + V_{i\parallel}\frac{\partial}{\partial s}\right] V_{i\perp} + \nabla_\perp p_i - m_i n_i G_\perp \\ &-n_i e_i (E_\perp + V_{i\perp}\times B) = \frac{\delta M_{i\perp}}{\delta t} \end{aligned} \tag{5}$$

The horizontal variation of the concentrations is negligible compared to the altitude variation and the term $\nabla_\perp \cdot (n_i V_{i\perp})$ in Equation (3) is negligible. Also, in Equation (4) the term $V_{i\perp}\cdot\nabla_\perp V_{i\parallel}$, which is the perpendicular gradient of the velocity, can be neglected. Using the electron momentum equation with each ion momentum equation, it can be shown that the polarization electric field, $E_\parallel$, is equal to the partial pressure of the electron gas. Then we have:

$$\frac{\partial n_i}{\partial t} + \frac{\partial (n_i V_{i\parallel})}{\partial s} + n_i V_{i\parallel}\frac{1}{S}\frac{\partial S}{\partial s} = \frac{\delta n_i}{\delta t} \tag{6}$$

and

$$m_i n_i \frac{\partial V_{i\parallel}}{\partial t} + m_i n_i V_{i\parallel}\frac{\partial V_{i\parallel}}{\partial s} + \frac{\partial p_i}{\partial s} - m_i n_i G_\parallel + \frac{n_i}{n_e}\frac{\partial p_e}{\partial s} = \frac{\delta M_{i\parallel}}{\delta t} \tag{7}$$

Considering that the ion gyrofrequency is $\omega_i = \frac{e_i}{m_i}B_i$, Equation (5) can be written as:

$$\begin{aligned} &m_i n_i \left[\frac{\partial}{\partial t} + V_{i\perp}\cdot\nabla_\perp + V_{i\parallel}\frac{\partial}{\partial s}\right] V_{i\perp} + \nabla_\perp p_i - m_i n_i G_\perp \\ &-m_i n_i \left(\frac{e_i E_\perp}{m_i} + V_{i\perp}\times\omega_i\right) = \frac{\delta M_{i\perp}}{\delta t} \end{aligned} \tag{8}$$

In the F-region and above, ω_i is about 30 s^{-1} for O^+. The time constant τ for the variation of $V_{i\perp}$ is much greater than $1/\omega_i$ according to,

$$\frac{1}{\tau} = \left|\frac{1}{V_{i\perp}}\right|\left|\frac{\partial V_{i\perp}}{\partial t}\right| << \omega_i.$$

Acceleration perpendicular to $\bar{B}$ can be neglected since the lines of force are equipotential. In addition, it is supposed that the ion density and the ion temperature do not change horizontally, so that we can neglect $\nabla_\perp p_i$. The right hand side of equation (8) can be ignored because $\sum_j \nu_{ij} << \omega_i$.

Then the perpendicular momentum equation is:

$$\frac{e_i}{m_i} E_\perp + V_{i\perp} \times \omega_i = 0 \tag{9}$$

The equation for the vertical velocity is:

$$V_z = V_{i\parallel} \sin I + V_{im} \cos I$$

where I is the magnetic dip angle and V_{im} is the meridional component of $V_{i\perp}$. $V_{i\parallel}$ is the solution of equation (7) and $V_{i\perp}$ is the solution of equation (9).

Writing $u_i = V_{i\parallel} \sin I$ and $\partial z = \partial s * \sin I$, the momentum and continuity equations become:

$$\begin{aligned} &\frac{\partial u_i}{\partial t} + u_i \frac{\partial u_i}{\partial z} + \frac{1}{m_i n_i}\frac{\partial p_i}{\partial z}\sin^2 I + g\sin^2 I + \frac{1}{m_i n_e}\frac{\partial p_e}{\partial z}\sin^2 I \\ &= \sum_j \nu_{ij}\left(u_j - u_i\right) \end{aligned} \tag{10}$$

and

$$\frac{\partial n_i}{\partial t} + \frac{\partial\left(n_i u_i\right)}{\partial z} + n_i u_i \frac{1}{S}\frac{\partial S}{\partial z} = \frac{\delta n_i}{\delta t} \tag{11}$$

By multiplying equation (10) by n_i, equation (11) by u_i, and adding the resulting equations, they can be solved with respect to the new variable, $F_i = u_i n_i$, so that:

$$\begin{aligned} &\frac{\partial F_i}{\partial t} + \frac{\partial}{\partial z}\left(u_i F_i\right) + F_i u_i \frac{1}{S}\frac{\partial S}{\partial z} - u_i \frac{\delta n_i}{\delta t} + \sin^2 I\left[\frac{1}{m_i}\frac{\partial p_i}{\partial z} + \frac{n_i}{n_e}\frac{1}{m_i}\frac{\partial p_e}{\partial z} + n_i g\right] \\ &= -\sum_j \nu_{ij}\left(\frac{n_i}{n_j}F_j - F_i\right)\Phi_{ij} \end{aligned} \tag{12}$$

Equations (11) and (12) can be written as:

$$\frac{\partial n_i}{\partial t} + \frac{\partial}{\partial z}\left(u_i n_i\right) + A_i n_i = B_i \tag{13}$$

$$\frac{\partial F_i}{\partial t} + \frac{\partial}{\partial z}\left(u_i F_i\right) + C_i F_i = D_i \tag{14}$$

where A_i and B_i are, respectively, the loss frequency and the production, and where C_i and D_i are:

$$C_i = A_i - \sum_j \nu_{ij}\Phi_{ij}$$

$$D_i = -\sum_j \nu_{ij}\frac{n_i}{n_j}F_j\Phi_{ij} + u_i B_i - \sin^2 I\left[\frac{1}{m_i}\frac{\partial p_i}{\partial z} + \frac{n_i}{n_e}\frac{1}{m_i}\frac{\partial p_e}{\partial z} n_i g\right]$$

3. Numerical Solution Procedure

We have to solve differential equations (13) and (14), which are non-linearly coupled with partial derivatives, where i = 1 for O^+ and i = 2 for H^+. The variables n_i and F_i are chosen in order to get the same form for the continuity and momentum equations which make the numerical method easier to handle. A finite difference method is used following *Young et al.* [1980a, b].

The following equations are introduced into equations (13) and (14):

$$f\left(z_{k+1/2}\right) = \frac{\theta}{2}f\left(z_k, t_{l+1}\right) + \frac{1-\theta}{2}f\left(z_k, t_l\right) + \frac{\theta}{2}f\left(z_{k+1}, t_{l+1}\right) + \frac{1-\theta}{2}f\left(z_{k+1}, t_l\right)$$

and

$$\left(\frac{\partial f}{\partial z}\right)_{k+1/2} = \theta\frac{f\left(z_{k+1}, t_{l+1}\right) - f\left(z_k, t_{l+1}\right)}{z_{k+1} - z_k} = (1-\theta)\frac{f\left(z_{k+1}, t_l\right) - f\left(z_k, t_l\right)}{z_{k+1} - z_k}$$

The function f represents either the concentration or the flux, both depending on time and altitude. The derivative $\partial f/\partial z$ is changed into the time derivative in replacing z by t in equations (13) and (14). θ is a parameter defined in the [0,1] interval and is set equal to 0, 1/2 or 1, according to the adopted explicit Crank-Nicholson and Learsonen method. Schematically, the elementary space-time block is represented by:

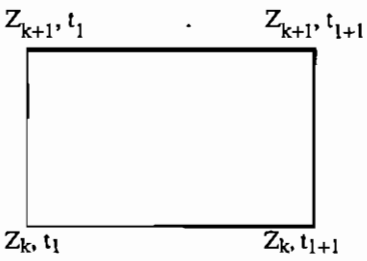

At the two left corners of the rectangle, n_i and F_i are known for the two ions from initial conditions, while the same variables at the upper right corner are calculated by solving four algebraic equations with four unknowns.

To correctly solve the equations, the time step is made dependent on C_i and A_i according to:

$$dt =<< \min\left|\frac{1}{C_i}\right| \text{ and } dt << \min\left|\frac{1}{A_i}\right|$$

Knowing order of magnitude values for C_i and A_i from EISCAT measurements, the time steps are typically:

$dt < 0.2$ s for H^+
$dt < 2.0$ s for O^+

The coefficients A_i, B_i, C_i, D_i change slowly, and a larger time step (10 s) ahead of the numerical integration is adopted.

The chosen altitude ranging from 300 to 1600 km is flexible.

4. Model Inputs

The code has been worked out with the idea of obtaining EISCAT measurements for initial concentrations, velocities, temperatures profiles and boundary conditions. The full time of integration is the same as the duration of the experiment, or a part of it. In this time interval, the temperatures are interpolated from measurements and used in the equations at each instant because, at the present state, the code does not solve the energy equations which is planned in the near future. Geographic coordinates, dip angle, date, geophysical parameters for the neutral atmospheric model (daily Ap index, daily F10.7 and $\overline{F10.7}$ flux) and initial times are given.

4.1 Neutral Atmospheric Model

The MSIS model [*Hedin et al.*, 1979] is used.

4.2 Collision Frequencies

C_i and D_i depend on collision frequencies that include momentum transfer between ions and neutrals and between ions. They also depend on correction functions. They are given by *Barakat et al.* [1987] and *Taïeb and Wu* [1991].

4.3 Production

The calculation of the production due to solar radiation is described in the Mid-latitude Ionospheric Model. There is also ion production due to the following charge exchange:

$$O^+ + H \rightarrow O + H^+ \qquad k_3$$
$$H^+ + O \rightarrow H + O^+ \qquad k_4$$

with

$$k_2 = 2.510^{-11}[T_n + T_1/16 + 1.210^{-8}(\bar{V}_1 - \bar{V}_n)^2]^{1/2}$$
$$k_2 = 2.210^{-11}[T_2 + T_n/16 + 1.210^{-8}(\bar{V}_2 - \bar{V}_n)^2]^{1/2}$$

where T_1 and T_2 are O^+ and H^+ temperatures, respectively, and are supposed equal. T_n is the neutral atmospheric temperature, $\bar{V}_1$ and $\bar{V}_2$ are velocity vectors for O^+ and H^+, and $\bar{V}_n$ is the neutral velocity vector. Then,

$$B_1 = q_1 + k_4[O]n_2$$

$$B_2 = q_2 + k_3[H]n_1$$

where [O] and [H] are oxygen and hydrogen concentrations. n_1 and n_2 are O^+ and H^+ concentrations, respectively, and q_1 and q_2 are solar radiation productions .

4.4 Chemical Reactions

Ions are recombined through two processes:

a - dissociation:

$$O^+ + e \rightarrow O + h\nu \qquad \alpha_1$$
$$H^+ + e \rightarrow H + h\upsilon \qquad \alpha_2$$
$$\alpha_1 = 5.\,010^{-12}\,(250/Te)^{0.7}$$
$$\alpha_1 = 2.410^{-10}\,(1/Te)^{0.7}$$

b - charge transfer:

$$O^+ + N_2 \rightarrow NO^+ + N \qquad k_1$$
$$O^+ + O_2 \rightarrow O_2^+ + O \qquad k_2$$

with

$$k_1 = 1.53310^{-12} - 5.9210^{-13}(T_1/300.) + 8.610^{-14}(T_1/300.)^2$$
$$\text{for} \quad 300. < T_i \leq 1700°\,K$$

$$k_1 = 2.7310^{-12} - 1.15510^{-12}(T_1/300.) + 1.48310^{-13}(T_1/300.)^2$$
$$\text{for} \quad 1700. < T_i \leq 6000.^\circ K$$

$$k_2 = 2.8210^{-11} - 7.7410^{-12}(T_1/300.) + 1.07310^{-12}(T_1/300.)^2$$
$$- 5.1710^{-14}(T_1/300.)^3 + 9.6510^{-16}(T_1/300.)^4$$

Then:

$$A_1 = k_1[N_2] + k_2[O_2] + \alpha_1 n_e + \frac{u_i}{S}\frac{\partial S}{\partial z}$$

$$A_1 = k_4[O] + \alpha_2 n_e + \frac{u_i}{S}\frac{\partial S}{\partial z}$$

4.5 Convection Electric Field

The electric field vector has a particular value for the line of force considered. With the rotation of the Earth, the line intersects different equipotentials of the convection electric field and, of course, the intensity and direction of the electric field changes with time. Tristatic EISCAT radar provides the values, but any semi-empirical model can be substituted.

4.6 Neutral Wind Model

The neutral wind model is the global thermospheric wind HWM90 due to *Hedin et al.* [1991].

5. Model Outputs

Outputs of the model are profiles of concentrations, velocities and fluxes for O^+ and H^+ at chosen time intervals. They are also time variation of concentrations, velocities and fluxes at different altitudes. Results showing variations of concentrations and fluxes for the ions during about six hours of observations between July 31, 1988, at 2200 hours UT; and August 1, 1988, at 0400 UT, is given in the figure. More results have been published by *Wu* [1990], and *Taïeb and Wu* [1991], where discrepancies between measurements and calculations are discussed.

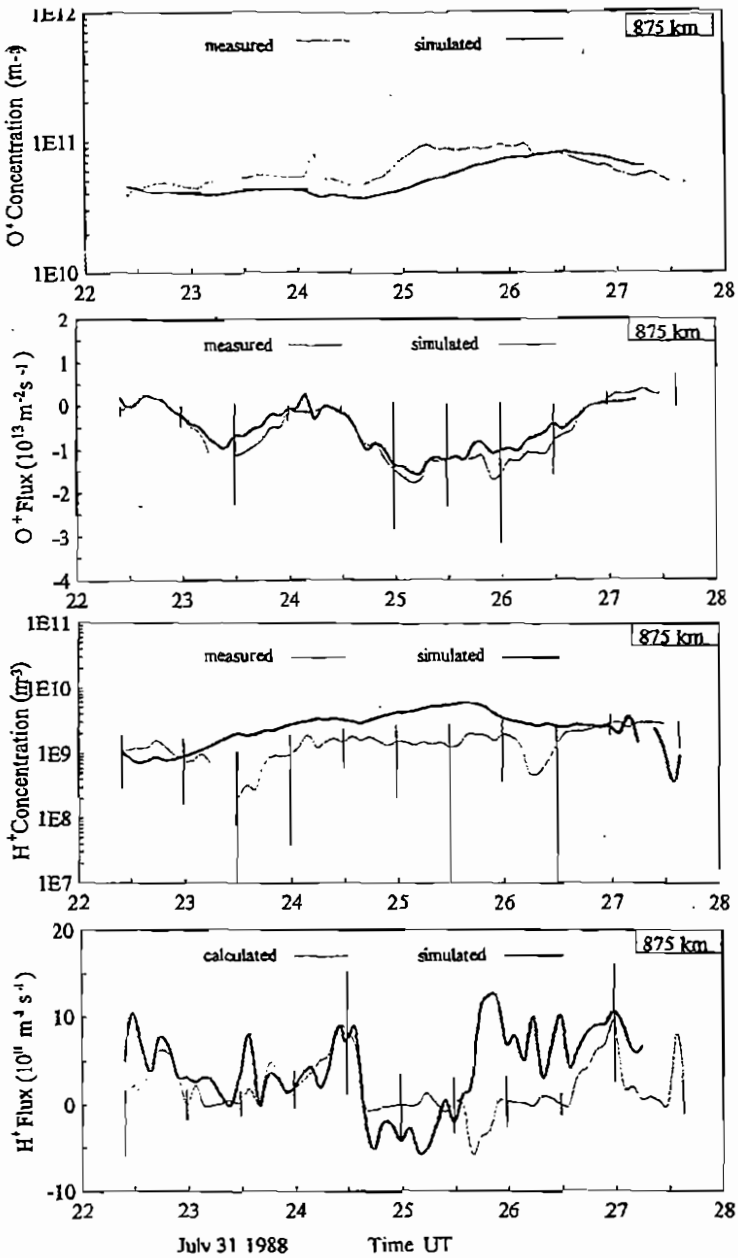

This figure represents one of the comparative EISCAT measurement-simulation results. Differences in the ion concentrations are due to the underestimations of MSIS H and to a lesser extent O concentrations.

6. Uncertainties and Limitations

Limitations are due to the physical assumptions.

7. Availability of Model

For the moment the code is not available until the energy equations are included with other ion species (O^+, NO^+, N_2^+, N^+) in order to describe the plasma from 150 to 1600 km.

8. References

Axford, W. I., *J. Geophys. Res., 73*, 6855-6859, 1968

Axford, W. I. and C. O. Hines, *Can. J. Phys., 39*, 1433-1464, 1961.

Banks P. M., A. E. Nagy, and W. I. Axford, *Planet. Space Sci., 19*, 1053-1067, 1971.

Banks P. M. and T. E. Holzer, *J. Geophys. Res., 73*, 6846-6853, 1968.

Banks P. M., and Kockarts G., *Aeronomy*, Academic Press, New York, London, 1973.

Barakat, A. R., R. W. Schunk, T. E. Moore, and J. H. Waite, Jr., *J. Geophys. Res., 92*, 12255-12266, 1987.

Chapman, S., and S.-I. Akasofou, *Solar Terrestrial Physics*, Oxford at the Clarendon Press, 1972

Hedin, A. E., J. E. Salah, J. V. Evans, C. A. Reber, G. P. Newton, N. W. Spencer, D. C. Kayser, D. Alcaydé, P. Bauer, L. Cogger, and J. P. McClure, *J. Geophys. Res., 82*, 2139-2147, 1977a.

Hedin, A. E., P. Bauer, H. G. Mayr, G. R. Carigan, L. H. Brace, H. C. Brinton, A. D. Parks, and D. T. Pels, *J. Geophys. Res., 82*, 3183-3189, 1977b.

Hedin, A. E., C. A. Reber, N. W. Spencer, and H. C. Brinton, *J. Geophys Res., 84*, 1-9, 1979.

Hedin, A. E., M. A. Biondi, R. G. Burnside, G. Hernandez, R. M. Johnson, T. L. Killeen, C. Mazaudier, J. W. Meriwether, J. E. Salah, R. J. Sica, R. W. Smith, N. W. Spencer, V. B. Wickwar, and T. S. Virdi, *J. Geophys Res., 96*, 7657, 1991.

Schunk, R. W., *Planet. and Space Sci., 23*, 437-485, 1974.

Taïeb, C., and J. Wu, *Ann. Geophysicae, 9, 804-820, 1991.*

Wu, J., *Thèse U. Pierre ete Marie Curie, Paris VI*, 30 Octobre 1990.

Wu, J., and C. Taïeb, *Ann. Geophysicae, 11*, 485-493, 1993.

Young, E. R., P. G. Richards, and D. G. Torr, *J. Comput. Phys., 38*, 141-156, 1980a.

Young, E. R., D. G. Torr, P. G. Richards, and A. E. Nagy, *Planet. Space Sci., 28*, 881-893, 1980b.

Global Theoretical Ionospheric Model (GTIM)

David N. Anderson
Ionospheric Effects Division, Phillips Laboratory, Hanscom AFB, MA

Dwight T. Decker and Cesar E. Valladares
Institute for Space Research, Boston College, Newton, MA

1. Introduction

This paper describes the Phillips Laboratory Global Theoretical Ionospheric Model (GTIM) which has been developed over the last two years. In addition to describing the model and its development, a brief discussion will be provided on the physical processes which are included and how this theoretical model has been used to generate a computationally-fast parameterized global ionospheric model. Finally, some examples of the usefulness of such a parameterized model will be described.

While empirical models such as the International Reference Ionosphere (IRI) model [*Rawer and Bilitza*, 1989] are useful in describing the "climatology" of ionospheric regions and their "average" behavior, they do not provide insight into what factors influence the day-to-day, geomagnetic storm-related, solar or seasonal variability of ionospheric parameters. In addition, empirical models being based on observations are limited to those regions where observations are made. Models developed from ground-based measurements lack the ocean area coverage, while satellite sensor-based models suffer from a mixture of latitude, altitude and local time effects which must be separated and binned accordingly.

Theoretical models, on the other hand, have the advantage of flexibility. They can be used to study the sensitivity of ionospheric parameters to changes in various input parameters such as solar or precipitating particle production rates, changes in transport mechanisms such as neutral winds and $\mathbf{E} \times \mathbf{B}$ drifts, or dependence on variations in neutral atmospheric constituents caused by geomagnetic storms. To the degree that we can realistically specify the input parameters, current state-of-the-art ionospheric models can reliably model electron and ion densities. Studies which compare calculated and observed electron density profiles that elaborate on this point will be discussed.

Another advantage of theoretical models is the ease with which they can be coupled to other theoretical models. It is well understood, for example, that there exists strong collisional coupling between the ionospheric plasma motion at high latitudes and the motion of the neutral atmosphere where the strong plasma transport velocities are due to $\mathbf{E} \times \mathbf{B}$ drifts of magnetospheric origin. At low latitudes, strong electrodynamic coupling exists between the ionospheric plasma and nighttime neutral winds via the F-region dynamo process. Understanding the interplay between the ionized and non-ionized portions of the atmosphere requires coupling at the first principles level.

2. Physical Processes

The important processes which determine the ambient ionized plasma distribution in the Earth's atmosphere can be generally grouped into three categories - production, loss and transport. The word "ambient" is used because the discussion is limited to the modeling of the large scale (tens of kilometers) thermal ionospheric population and not small scale features. Whether or not transport is an important process will depend on the lifetime of the ion and electron pairs. If the plasma can be transported over significant distances, either horizontally or vertically, within this lifetime then obviously transport plays a role.

The two primary sources for production of ionization is solar ultraviolet radiation and energetic particle precipitation which occurs primarily at the higher latitudes. Higher energy solar photons (shorter wavelengths) can penetrate deeper into the neutral atmosphere before they lose a significant amount of their energy. The respective wavelength limits for ionization of N_2, O and O_2 are 796A, 911A, and 1027A [*Rishbeth*, 1969]. If the flux of solar radiation is given by Φ, and σ is the cross-section for ionizing the neutral particles, then the ionizing production rate per unit volume, q, is given by

$$q = \Phi n \sigma \eta \tag{1}$$

where n is the density of the neutral species and η is the ionizing efficiency. The units are ion-electron pairs/cm^3-sec, since for each ion produced an electron is also produced. Without going through the specific steps, equation (1) is generalized to include all wavelengths and the attenuation of the solar flux as it traverses the neutral atmosphere giving the total production rate for a single neutral species,

$$q(h,\chi) = \Phi \eta \sigma n(h) \exp(-\tau(h,\chi)) \tag{2}$$

where $\tau\,(h, \chi) = \int \sigma\, n \sec \chi\, dh$. *Rishbeth* [1969] gives an excellent review of the specific derivations which have been omitted here.

At high latitudes, sufficiently energetic precipitating particles can also ionize the neutral atmosphere. Magnetospheric processes are responsible for the energizing process where the particles are mainly energetic electrons and protons. In an analogous manner to the derivation of the production rate by solar radiation, the production rate by energetic particles is given by

$$P(h) = \Sigma n(h) \int d\mu \int \Phi(h,E,\mu) \eta(E,\mu) dE \tag{3}$$

where Φ is the flux of precipitating electron or ions at energy E, at altitude, h, and μ is the particle's pitch angle [*Vallance-Jones*, 1974].

Another production source in the low and midlatitude nighttime region comes from scattered LY α radiation at 1216Å. Because the energy of these photons is below the ionization potential of atomic oxygen, this radiation can only ionize NO and contributes to maintaining the nighttime ionospheric E region, and not the F region.

Loss of ionization in the Earth's atmosphere can take place by one of two processes: dissociative recombination where an electron recombines with a molecular ion, or radiative recombination where an electron combines with an atomic ion. In the E region of the ionosphere where NO^+ and O_2^+ are the major ions, dissociative recombination is the major loss process

$$NO^+ + e \rightarrow N + O^*$$
$$O_2^+ + e \rightarrow O + O^*$$

where the O^* means the atomic oxygen is left in an excited state which subsequently emits a photon as it transitions to the ground-state. In the F-region where O^+ is the dominant ion, one would think that the primary loss rate would be radiative recombination

$$O^+ + e \rightarrow O + h\nu$$

However, this reaction is much slower than dissociative recombination because it is harder to satisfy both conservation of energy and momentum, simultaneously, since there is only one product of the reaction, namely atomic oxygen. Since this reaction is slow, O^+ ions are lost primarily by ion-atom interchange

$$O^+ + N_2 \rightarrow NO^+ + N$$
$$O^+ + O_2 \rightarrow O_2^+ + O$$

and subsequent dissociative recombination of NO^+ and O_2^+. Because the rate-limiting reaction is ion-atom interchange, the loss rate of O^+ in the F-region is governed by this reaction. Atomic oxygen becomes the dominant neutral species above about 150 km and because the loss of O^+ ions depends on the neutral N_2 and O_2 densities which are decreasing with increasing altitude, the major ion is O^+ and its lifetime becomes longer and longer at the higher altitudes. It turns out that above 150 km altitude, transport processes become important in redistributing the O^+ ions before they are lost through ion-atom interchange.

Ionospheric plasma transport mechanisms fall into two general categories, transport due to non-electromagnetic forces and those due to electromagnetic forces. *Kendall and Pickering* [1967] have shown that the principal non-electromagnetic forces in the ionospheric *F* region above ~ 150 km include (1) collisions with neutral particles, (2) forces due to gravity, and (3) plasma pressure gradient forces. In addition, because the ion-neutral collision frequency is less than the ion gyro-frequency around the magnetic field lines above this altitude, it is shown that only the component of these non-electromagnetic forces parallel to B are effective in producing plasma motion along the magnetic field lines. Electromagnetic forces, on the other hand, cause plasma motion perpendicular to B. This electric field, E, may be generated in the ionospheric *E*-region or *F*-region through dynamo action or in the magnetosphere. The magnetic field lines can be considered equipotentials so that an electric field generated in the *E* region say, will affect *F*-region plasma causing both ions and electrons to drift in the same direction with an $\mathbf{E} \times \mathbf{B}/B^2$ drift velocity. At high latitudes, the interaction of the Interplanetary Magnetic Field (IMF) imbedded in the solar wind with the Earth's geomagnetic field generates an electric field which maps down to the high latitude ionospheric *F* region. Depending on the direction of the IMF ($B_z > 0$ or $B_z < 0$), there exists characteristic patterns, which produce $\mathbf{E} \times \mathbf{B}$ plasma drift velocities

from 200 m/sec to 2 km/sec. These drift velocities are responsible for generating a wide variety of high latitude plasma density distributions which will be discussed in the next section.

While electric fields cause plasma motion perpendicular to B, neutral winds produce plasma motion parallel to B. The primary effect of these winds is to alter the height of the F layer, Hmax, and consequently the F-region peak density, Nmax. The winds themselves are generated through neutral pressure gradients and collisions with charged particles, so it is clear that the neutral atmosphere and the ionosphere form a tightly coupled system, where variations in one system will cause variations in the other. To completely study the interactions and physical mechanisms affecting both systems requires solving the coupled set of equations which describe the neutral atmospheric and ionospheric densities and motions [*Roble et al.*, 1988; *Rees et al.*, 1988]. In the next section, the equations which calculate global ionospheric densities and transport velocities are presented and their solution is briefly discussed. The section then concentrates on how ionospheric modeling studies have validated the physical processes which account for ionospheric observations in the low, mid and high latitude regions. Figure 1 presents a schematic diagram of the physical processes affecting the plasma distributions at low latitudes.

3. Theoretical Model

The Phillips Laboratory Global Theoretical Ionospheric Model (GTIM) determines the F region O^+ ion density by numerically solving the time dependent ion (O^+) continuity equation given by (4).

$$\frac{\partial N_i}{\partial t} + \nabla \cdot (N_i \overline{V}_i) = P_i - L_i \tag{4}$$

Here N_i is the ion density; V_i, the ion velocity, P_i, the production rate, and L_i, the ion loss rate. To solve (4) requires transforming the independent variables from a spherical r, θ, ϕ coordinate system to one which defines directions parallel and perpendicular to **B**. After some rearrangement, (1) takes the form

$$\frac{\partial N_i}{\partial t} + \overline{V}_{i\perp} \cdot \nabla N_i = P_i - L_i - \nabla \cdot (N_i \overline{V}_{i\parallel}) - N_i \nabla \cdot \overline{V}_{i\perp} \tag{5}$$

The left-hand side of (5) gives the time rate of change of ion density in a reference frame which drifts with the $Vi_\perp$ convection velocity, where $Vi_\perp = \mathbf{E} \times \mathbf{B}/B2$. The production rate includes production by photoionization, photoelectron impact ionization, particle precipitation, and nocturnal photoionization. The loss rate occurs by charge exchange with N_2 and O_2. The remaining quantity needed for the right-hand side of the equation is $V_{i\parallel}$, the velocity parallel to the magnetic field. An expression for $V_{i\parallel}$ [*Moffett*, 1979] is derived by combining the ion and electron momentum equations. It is within the momentum equations that the effects of gravity, pressure, the ambipolar electric field and the neutral wind are included in the model.

Substitution of the expression for $V_{i\parallel}$ into equation (5) gives a linear diffusion equation for the O^+ density. To solve this parabolic partial differential equation, the finite differencing

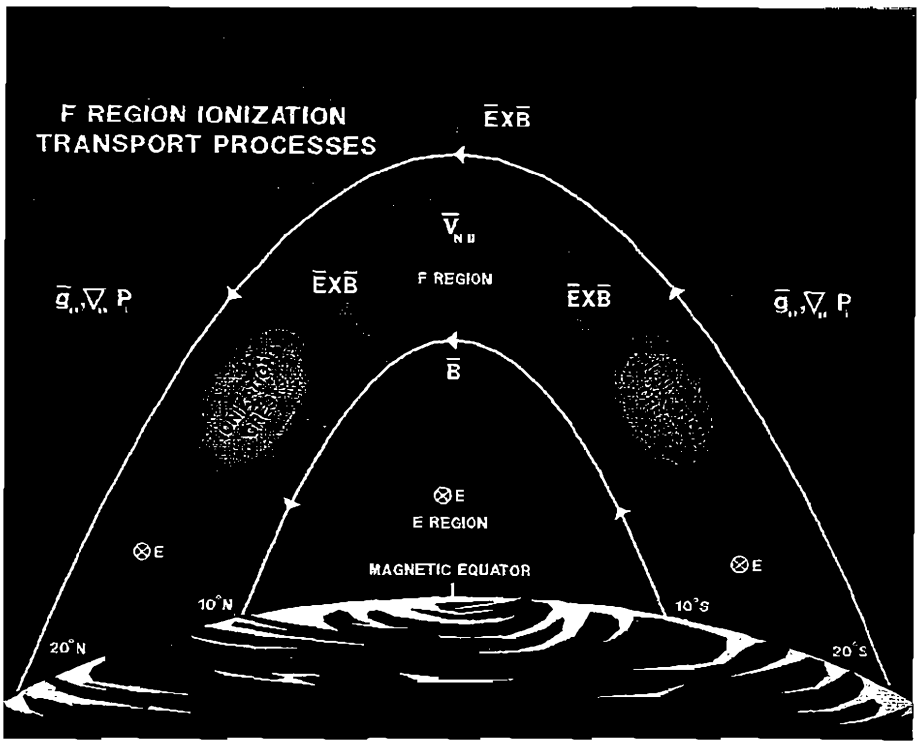

Figure 1. Schematic diagram of physical processes which transport ionization parallel and perpendicular to B at low latitudes.

scheme of Crank and Nicolson is used to produce a set of linear algebraic equations which are then solved using standard techniques for inverting a tridiagonal matrix. By applying this technique along a given magnetic field line, the O^+ density is determined along that field line as a function of time. Solving such an equation naturally requires that both initial and boundary conditions be specified. For the initial condition, we can specify any O^+ profile along the field line that is desired. Normally, we use a generic profile appropriate for the initial time of the particular simulation. For the lower boundary condition at both ends of the fieldline (100 km), we use the local approximation to provide the O^+ density. Finally, by going through this procedure for many field lines, a global picture of the O^+ density can be produced. A detailed description of the derivation and numerical solution of (5) can be found in the works by *Anderson* [1973] and *Moffett* [1979].

GTIM determines the N_2^+, O_2^+, NO^+, and O^+ ion densities in low- and midlatitude *E* regions by numerically solving the steady-state local approximation of the four coupled ion continuity equations given by (6).

$$P_i = L_i \qquad (6)$$

Here P_i is the production rate for the i^{th} ion and L_i is the ion loss rate. As for the *F* region, production includes photoionization, photoelectron impact ionization, and nocturnal photoionization. An additional source, as contrasted to the single species *F* region calculation, is that of chemical reactions involving the various neutrals and ions of the lower thermosphere. However, *E* region production by particle precipitation is not included, and thus the high latitude *E* region is not included in the present GTIM.

1. Neutral atmospheric densities of N_2, O_2, and O and the neutral temperature, as a function of altitude, location, time, solar activity, and magnetic activity are obtained from the mass spectrometer/incoherent scatter (MSIS-86) neutral atmosphere model [*Hedin*, 1987].

2. The horizontal neutral wind, as a function of location and time, is obtained from one of three available wind models. The empirical model HWM-87 [*Hedin et al.*, 1988], the empirical model HWM-90 [*Hedin et al.*, 1991], and the theoretical model VSH [*Killeen et al.*, 1987].

3. The ion and electron temperatures as a function of altitude and time are based on the analytic functions of *Strobel and McElroy* [1970] which in turn were derived from incoherent scatter radar measurements made at Millstone Hill during solar minimum. Another temperature that is needed is the effective temperature that is used in evaluating the ion loss rate. We use the simple expression due to *Schunk et al.* [1975] which contains an explicit dependence on the square of the magnetospheric electric field.

4. For the *F* region, Solar extreme ultraviolet (EUV) fluxes are derived from the reference spectrum SC#21REFW and the associated F10.7 algorithms of *Hinteregger et al.* [1981]. This detailed spectrum is averaged into 11 energy intervals before being used in calculating the photoproduction of O^+. For the *E* region, this detailed spectrum is used directly in calculating the photoionization rate.

5. In the *F* region, the production of O^+ from photoelectron impact ionization is based on the work of *Richards and Torr* [1988], where they parameterized the results of electron transport calculations of ionization rates. The rates are given as a fraction of the photoionization rate. For the *E* region, the impact ionization rate is determined directly from its definition by using a photoelectron flux calculated using the continuous slowing down (CSD) approximation [*Jasperse*, 1982].

6. The characteristics of the auroral electron precipitation are obtained from the statistical patterns of electron integral energy flux and average energy as measured by DMSP satellites [*Hardy et al.*, 1987].

7. The nighttime scattered EUV photons are assumed to consist of three lines at 834Å, 584Å, and 304Å. The intensities are based on *Knudsen et al.* [1977] and *Chakrabarti et al.* [1984]. The nocturnal ionization rates are calculated by assuming that these photons are incident at the top of the ionosphere.

8. Several $\mathbf{E} \times \mathbf{B}$ convection patterns are implemented for use in the model [*Heelis et al.*, 1982; *Heppner and Maynard*, 1987; *Hairston and Heelis*, 1990]. The inputs that specify a particular convection pattern vary depending on which one is being used.

4. Low and High Latitude Theoretical Studies

To illustrate how well theoretically-calculated electron density distributions compare with observations, two studies which have appeared in the open literature will be briefly summarized. It has already been demonstrated by a number of past investigations that the climatological features of the low latitude ionosphere F-region can be satisfactorily modeled if realistic, climatological $\mathbf{E} \times \mathbf{B}$ drift patterns are incorporated. The question arises, if both the drifts and the density profiles are measured together, over a particular 24 hour period, how well do the calculated profiles agree with the observations. This would establish that the theoretical model is, in fact, including realistic input parameters and that vertical drift is the primary transport mechanism in the equatorial region. Such a simultaneous data set has been obtained at Jicamarca for the period 30 Sept. – 3 Oct. 1970 [*Preble et al.*, 1994]. Figure 2 displays contours of measured electron density for the 1-2 Oct. period and the measured vertical drifts at Jicamarca. Note that the enhanced upward drift velocity after sunset between 1800 and 2000 hrs LT leads directly to the increase in Hmax from 450 km at 1800 LT to 600 km at 2000 LT. Downward drift velocity beginning at 2000 LT causes Hmax to decrease sharply from 600 km to 300 km by 2300 LT. In modeling this three day period, the time-dependent O^+ continuity equation was solved assuming an MSIS neutral atmosphere [*Hedin et al.*, 1987], a NASA wind model [*Hedin*, 1988], and the rate coefficients given by *Schunk* [1988]. Figure 3 displays contours of calculated electron density at the magnetic equator as a function of altitude and local time. In comparing the two contour plots, the agreement is excellent. The morning and afternoon peaks in density are reproduced, the increase in Hmax after sunset is accounted for and the increase in Nmax as the F layer is descending between 2000 and 2400 LT is matched. Figure 4 provides a comparison of the calculated and observed profiles at four local times. The noontime profile is very broad because the upward drift transports O^+ ions from the region of maximum solar production (~ 150-200 km altitude) to higher altitudes where the loss rate is lower. This observed profile shape is matched almost exactly by the calculated profile. Figure 5 displays the comparison between observed and calculated Nmax and Hmax values over the entire 24 hour period.

In the high latitude region, above 50° mag. latitude, $\mathbf{E} \times \mathbf{B}$ drift again plays a significant transport role, but in this case transport is horizontal rather than vertical. Magnetospherically imposed electric fields cause substantial (300 m/sec - 2000 m/sec) drift velocities to the *F*-region plasma, carrying charged particles thousands of kilometers in their lifetime. This means that the plasma trajectories can (1) cross sunrise and sunset terminators, (2) stagnate in one local time region because their drift just balances the corotation velocity of the magnetic field lines they reside on, or (3) cross the entire polar cap before recombination occurs. In addition, a new ionization source is imposed due to the precipitation of energetic particles in the auroral cusp and polar cap regions. The significance of this ionization source depends on the length of time the convecting flux tubes spend in this precipitation region. Figure 6 illustrates the two-cell convection pattern which is characteristic of $B_z < 0$ conditions.

Recently, GTIM has been used to successfully model two high latitude/polar cap features: 1) polar cap patches of enhanced *F*-region plasma densities [*Sojka et al.*, 1993; *Decker et al.* 1994; *Valladares et al.*, 1996], and 2) boundary blobs [*Anderson et al.*, 1996] which are observed as latitudinally-narrow, enhanced electron density features located near the equatorward edge of the auroral boundary normally occurring between 1500 and 2400 MLT. A variety of observations have established that during IMF $Bz < 0$ (southward) conditions, patches

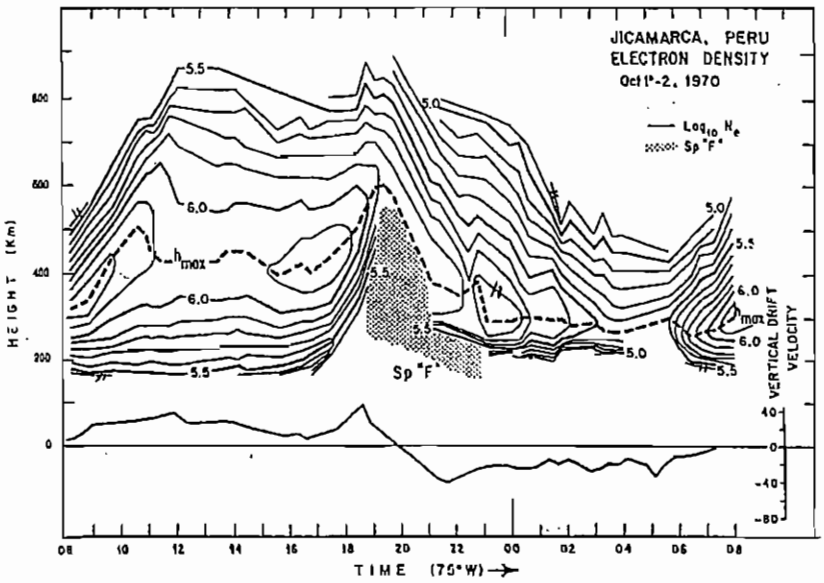

Figure 2. Contours of electron densities as a function of altitude and latitude measured by the Jicamarca radar on 1-2 Oct., 1970.

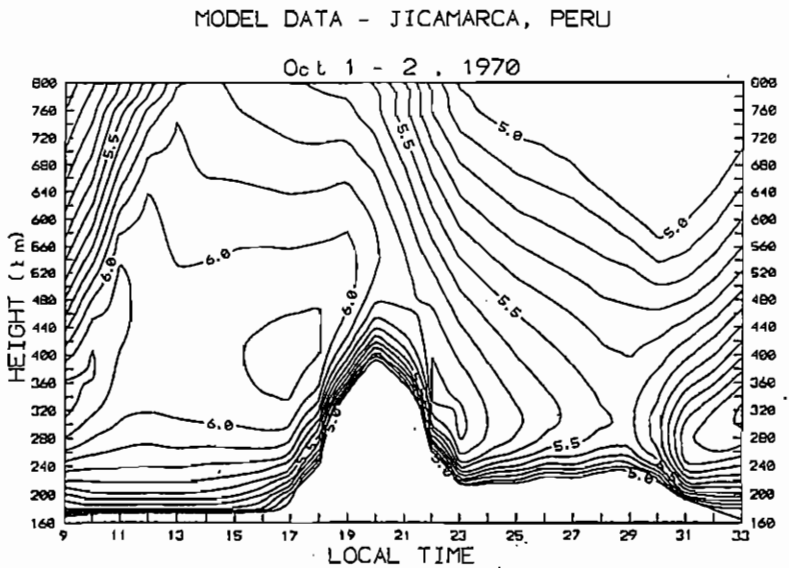

Figure 3. Contours of electron density calculated by GTIM over Jicamarca incorporating the vertical E × B drift measured on 1-2 Oct., 1970.

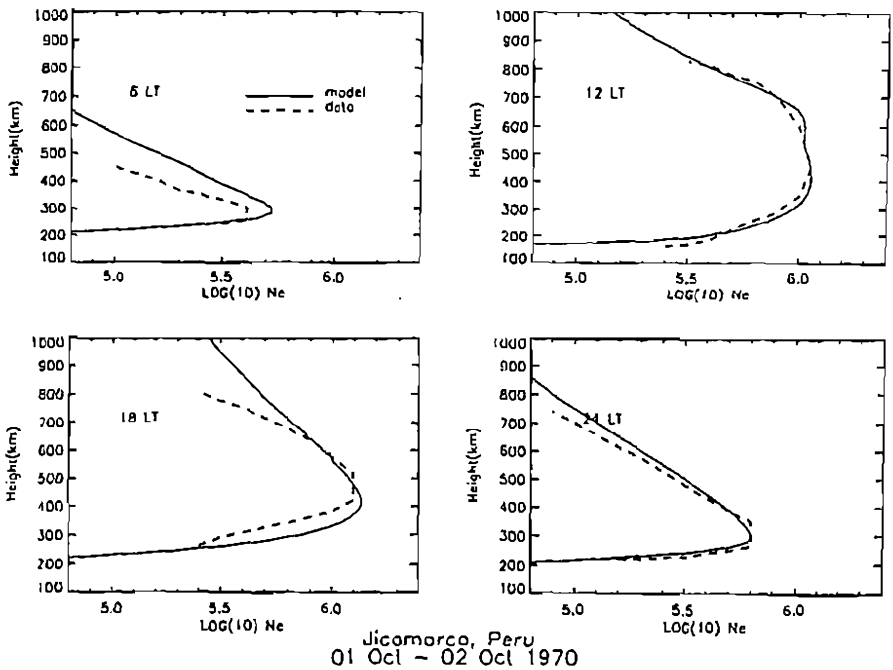

Figure 4. Comparisons between calculated and observed electron density profiles at 06, 12, 18, and 24 LT at Jicamarca.

of enhanced ionization drift across the polar cap in an anti-sunward direction with a typical horizontal extent of about 500 km. In modeling these patches [*Sojka et al.*, 1993], one approach was to introduce a time variation in the high latitude convection pattern, specifically the IMF By component. The Hairston-Heelis convection pattern was chosen with a cross-polar cap potential of 80 kv and an IMF By value which changes from +8 gamma to -8 gamma, held constant of 1 1/2 hours and then switched back to +8 gammas. Figure 7 displays the By > 0 pattern and color-coded contours of Nmax values at 1700 UT just before switching to -8 gamma. The effect of changing the convection pattern at 1700 UT can be seen in the Nmax snapshot at 1830 UT shown in Figure 8a. At 1830 UT, the convection switches back to its initial pattern and the resulting patches are seen in Figure 8b at 1930 UT.

The formation of boundary blobs are a natural evolution after patches are formed. Figure 9a,b display color-coded contours of Nmax at 2030 and 2130 UT, respectively, 2 and 3 hours after the switch back to the initial pattern. Note along the auroral boundary between 2300 and 1500 MLT the latitudinally-narrow, local time extended region of enhanced ionization. This enhancement results when the circular-shaped patch is caught up in the dusk cell and reconfigured by the pattern's sunward flow at the equatorward edge of the auroral region. Figure 10a,b represent snapshots of electron density contours as a function of altitude and latitude at 2230 and 1630 MLT, respectively. The narrow latitude extent, the altitude extension and factors of 4 to 8 enhancements over the background densities all replicate observed boundary blob features.

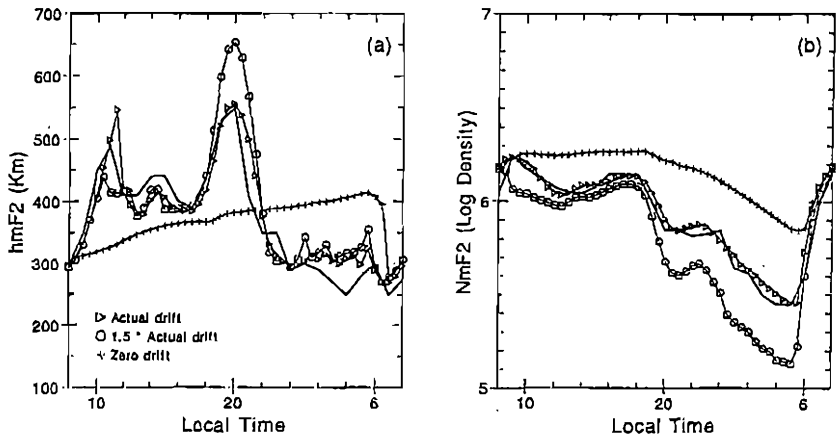

Figure 5. Comparisons between calculated and observed Nmax and Hmax values at Jicamarca and the comparison when the observed drift is multiplied by 0 and 1.5. Measured Nmax and Hmax are shown as the heavy, solid line.

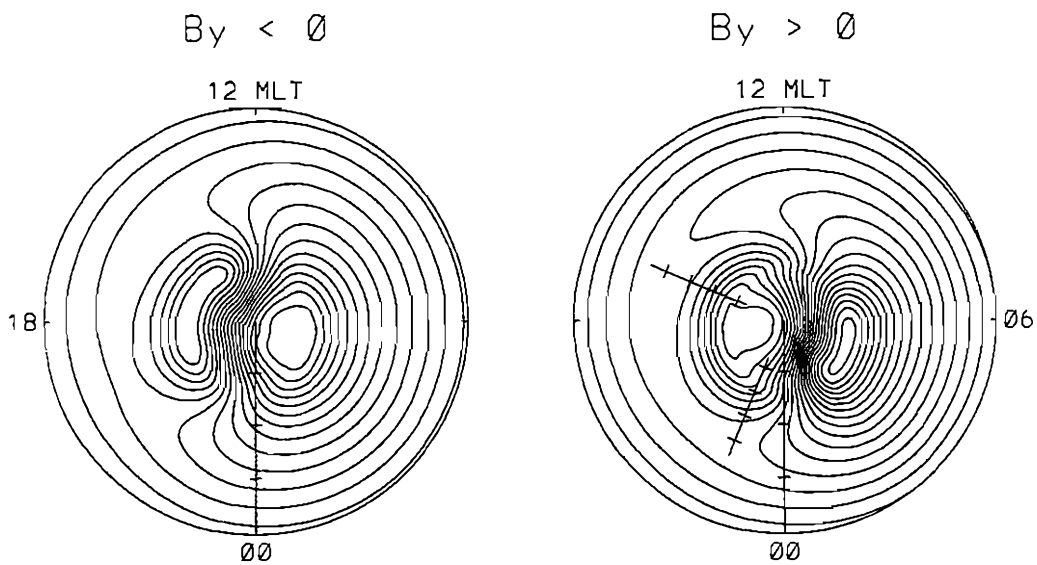

Figure 6. The Hairston-Heelis two cell convection pattern when $B_y < 0$ and $B_y > 0$ including the corotation potential.

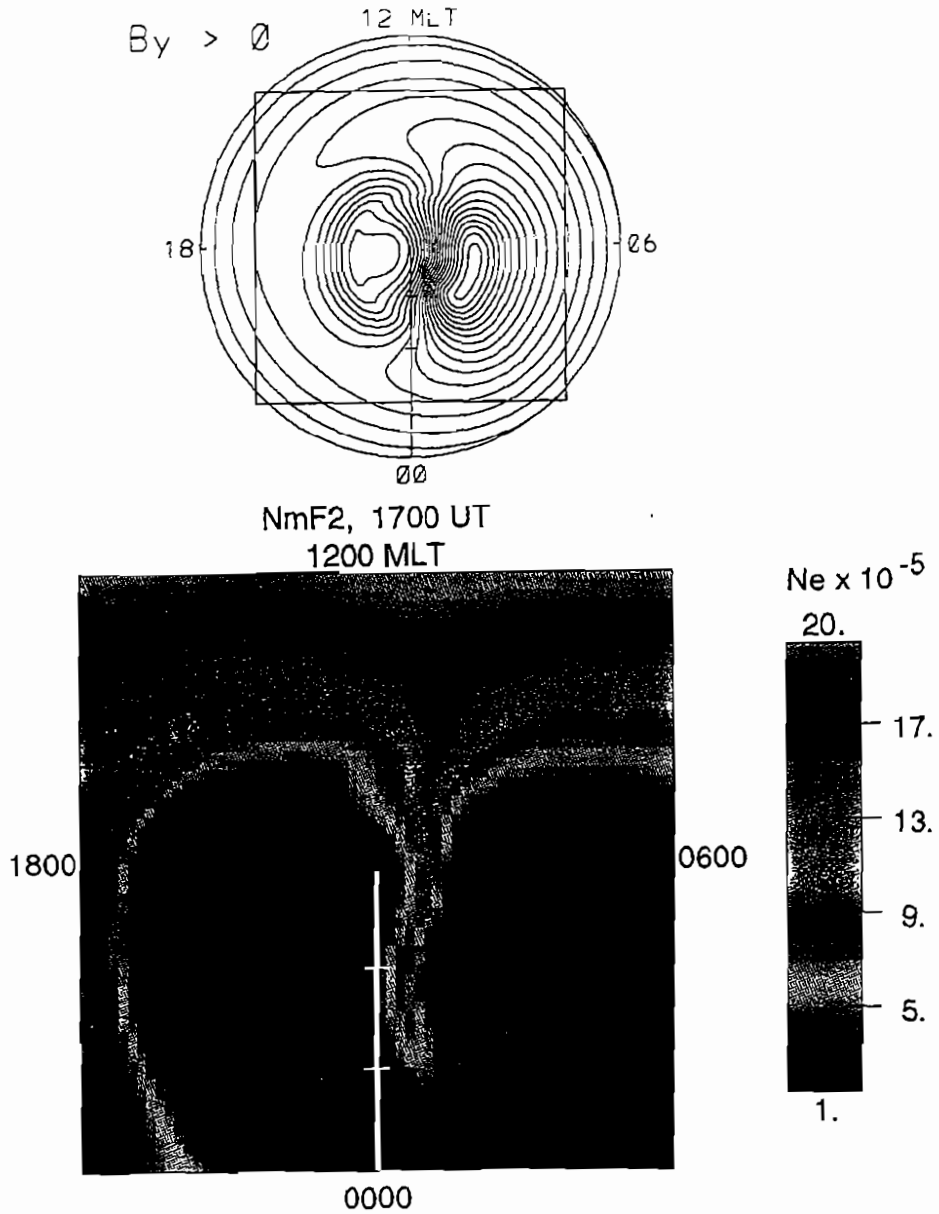

Figure 7. Hairston-Heelis convection pattern for $B_y > 0$ and color-coded contours of Nmax at 1700 UT as a function of CGMLAT and CGMLT. See text for details.

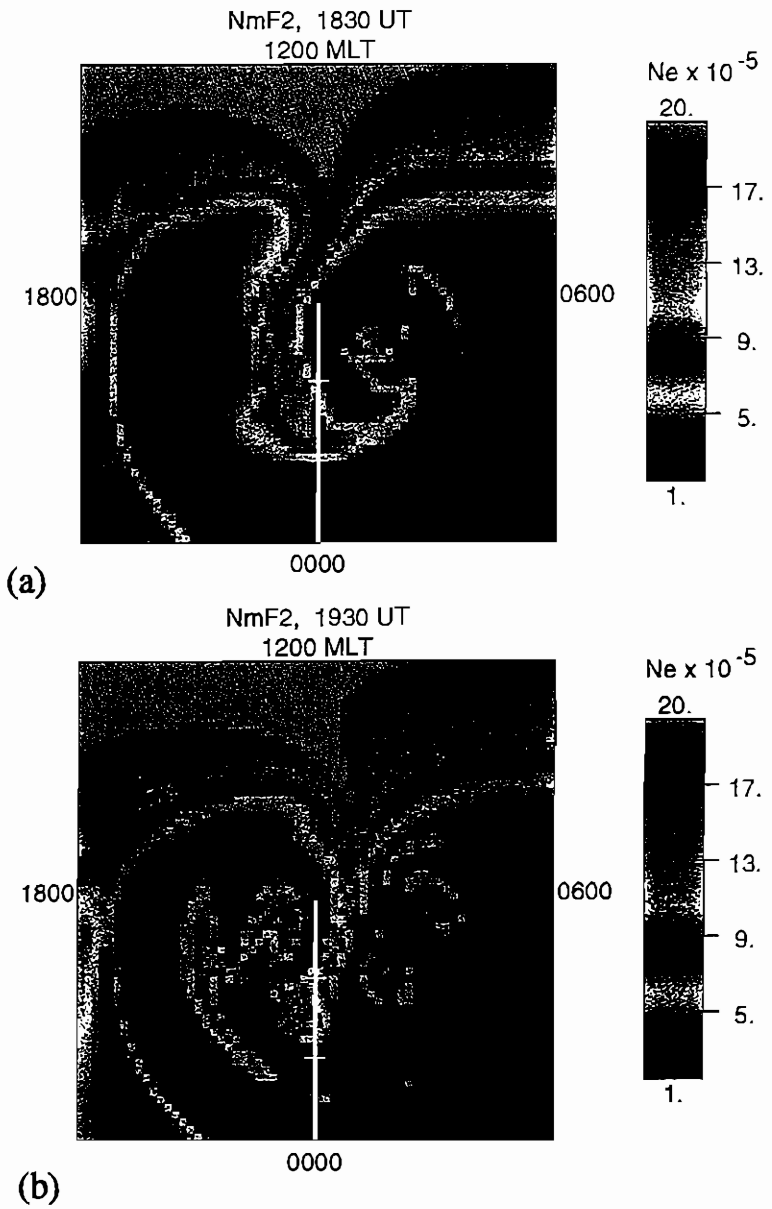

Figure 8. Color-coded contours of Nmax at 1830 UT (a) and 1930 UT (b). See text for details.

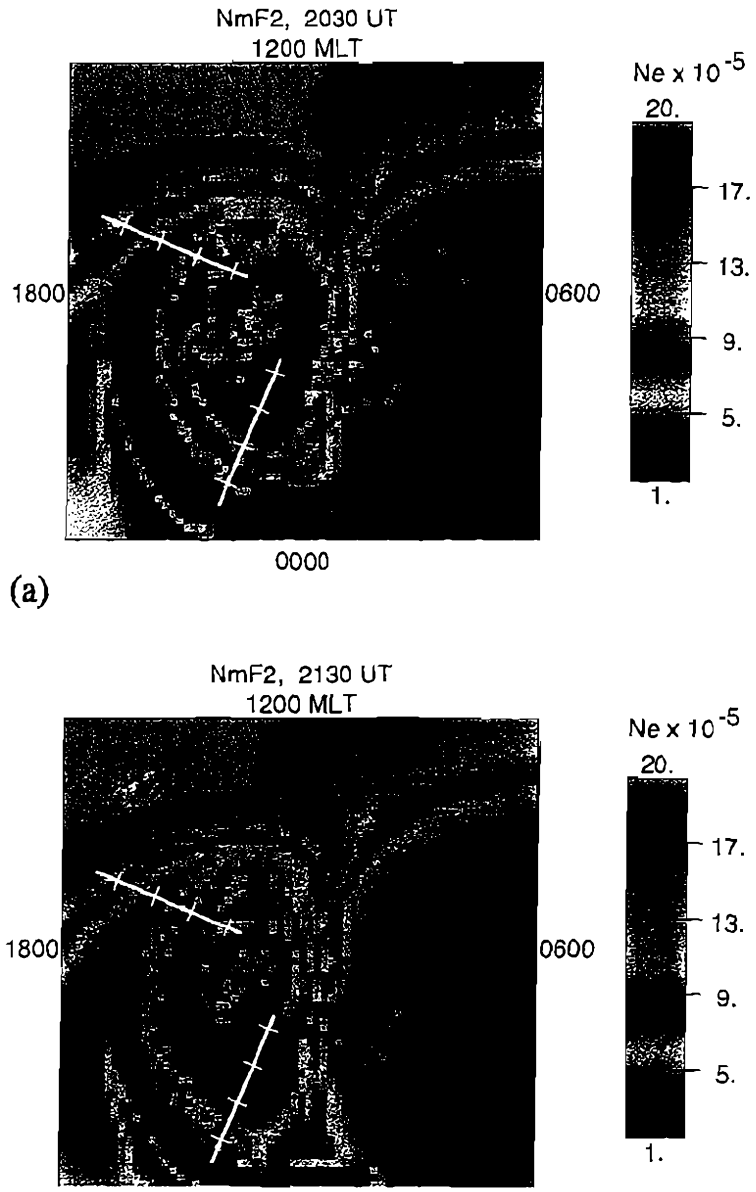

Figure 9. Color-coded contours of Nmax at 2030 UT (a) and 2130 UT (b) where white lines represent cuts at 2230 and 1630 MLT. See text for details.

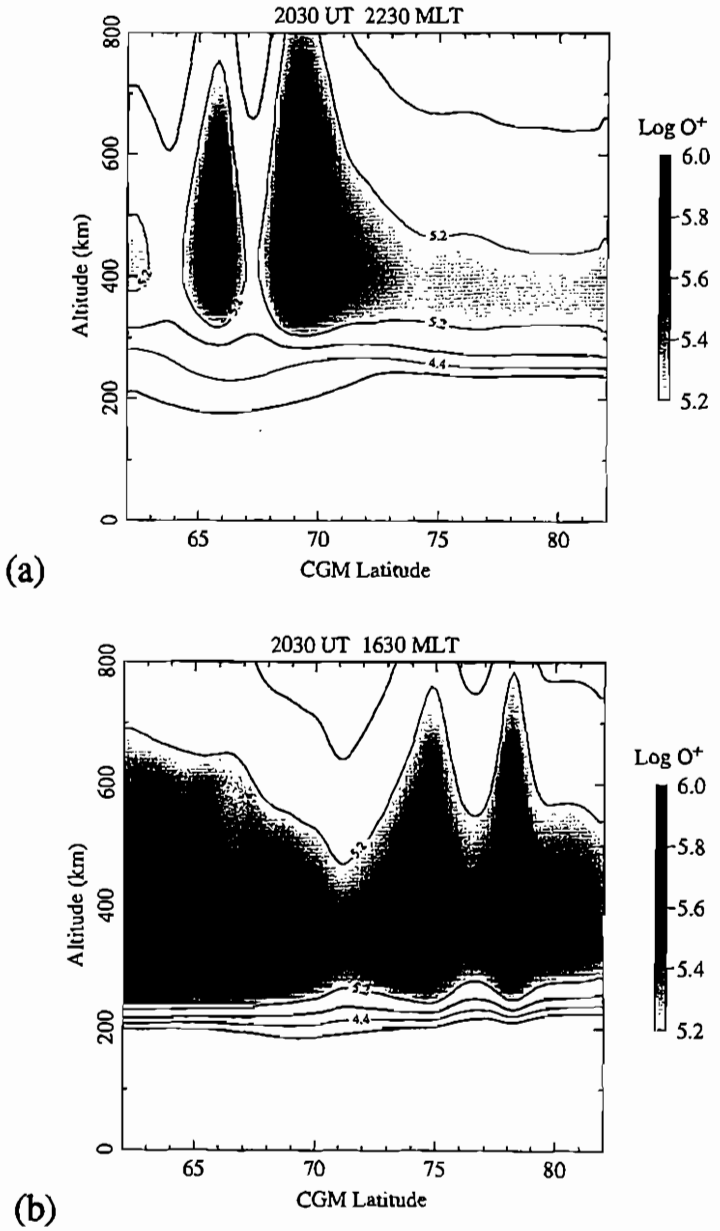

Figure 10. Electron density contours as a function of altitude and latitude at 2230 MLT (a) and 1630 MLT (b). See text for details.

5. Semi-Empirical, Parameterized Models

There are a number of empirical climatological ionospheric models which are based on a large set of observed ionospheric parameters such as peak density and altitude of the E region, NmE and hmE, and peak density and altitude of the F region, Nmax and Hmax. The most well-known are the International Reference Ionosphere (IRI) [*Rawer and Bilitza*, 1989], the Bent model [*Bent*, 1973], and the Chiu model [*Chiu*, 1975]. Both IRI and Bent models incorporate either the CCIR or URSI coefficients which specify Nmax, Hmax, NmE, and hmE. The Chiu model uses its own peak density and altitude databases, and then applies specific profile shapes depending on latitude and local time. The primary advantage of the empirical models is that they are computationally fast. The main disadvantage is they may not be very realistic in providing electron density profiles in those regions where observations are sparse or lacking. These include equatorial, polar cap and ocean area regions. *Rush et al.* [1984] recalculated the CCIR coefficients by combining theoretically-generated Nmax and Hmax values over the ocean areas with the previously-obtained empirical values over the rest of the globe. This new set is known as the URSI coefficients.

In an effort to improve the realism in the equatorial region and increase the computational speed, *Anderson et al.* [1987] developed a semi-empirical low latitude, ionospheric model (SLIM), which calculated F-region O^+ density profiles from 180 to 1000 km between $\pm 25^\circ$ dip latitude. In the development of SLIM, the low latitude portion of GTIM was used to theoretically calculate electron density profiles over the 24 hour day under a variety of solar and seasonal conditions. These theoretically-generated profiles were then fit by a Chapman function assuming four Chapman parameters, Hmax, Nmax, a bottomside and a topside scale height parameter. For every two degrees latitude and every hour local time, a different set of these four coefficient were found which would reproduce the theoretically-generated profile. Because the profiles are based on first principle calculations, the realism is retained while the computational speed is achieved by assuming Chapman-like profile shapes with appropriate coefficients. In order to provide this improvement to users of the Chiu model, a Fully-Analytic Ionospheric Mode (FAIM) was developed [*Anderson et al.*, 1989]. This model altered the low latitude portion of the Chiu model so that it reproduced SLIM profiles and slightly modified the Hmax Chiu values at mid-latitudes.

Using this same philosophy of parameterizing theoretically-calculated ion density profiles in order to achieve a computationally fast, global ionospheric model, the Air Force has recently developed a Parameterized Realtime Ionospheric Specification Model (PRISM) which is operational at the Air Force 50th Weather Squadron (50WS), Falcon Air Force Base, Colorado Springs, Colorado. PRISM consists of two segments, a Parameterized Ionospheric Model (PIM) database of Empirical Orthonormal Functions (EOFs) and a segment which incorporates near-realtime data from ground-based and satellite-based sensors available at the 50WS. Again, GTIM and GTIM-like equations were used to generate the global set of electron density profiles for 54 different sets of conditions - 3 solar activity periods, 3 seasons, 2 IMF By conditions and 3 Kp values. Figure 11a,b present contour plots of Nmax as a function of geographic latitude and longitude for a 00 UT high latitude snapshot and a 12 UT low latitude snapshot, respectively. In Figure 11a, the high latitude ionization trough and tongue of ionization in the polar cap region are evident, while in Figure 11b the crests in ionization known as the equatorial anomaly are prominent.

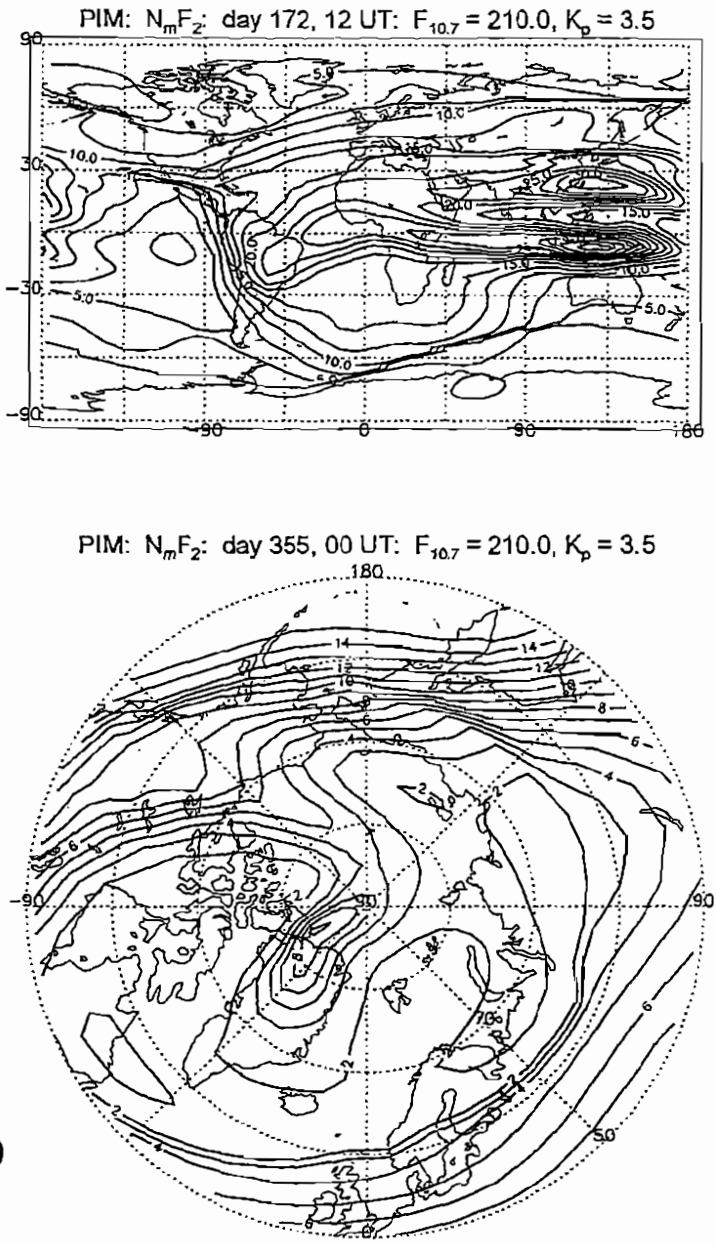

Figure 11. PIM contours of Nmax at high latitudes giving a snapshot at 00 UT as a function of geographic latitude and local time (a) and low latitudes at 12 UT as a function of geographic latitude and longitude (b).

PRISM has the capability of adjusting PIM to any and all realtime ionospheric data which is available at the 50WS. This data includes both ground-based bottom-side profiles from a network of 27 digital ionospheric sounders and *in situ* ionospheric measurements from the suite of sensors on the Defense Meteorological Satellite Program (DMSP) satellites in sun-synchronous orbits at 840 km. PRISM produces ion and electron density profiles from 90 to 1600 km, every 2° latitude from 90° N to 90° S geographic latitude and every 5° longitude from 0° to 360°, over the 24 hour UT day. In addition, it specifies the auroral oval boundary and the location and depth of the high latitude ionospheric trough.

6. Ionospheric Models for the User Community

There are a number of specific areas dealing with ionospheric structure, specification and radio wave effects where the availability and use of global ionospheric models is critical. Independent of which type of model is chosen, it must be as realistic as possible in providing the ionospheric specification. As examples, the specific areas might include tomography, radio wave propagation (both reflected and transionospheric), range and range rate error analysis, coupling studies between the ionosphere, thermosphere and magnetosphere, small scale irregularity growth rate calculations and determination of global UV-to-visible airglow radiances.

Significant progress in using radio tomographic techniques to remotely-sense ionospheric density structures and electron density profiles has taken place. In this scheme, a chain of ground-based receivers measures the total electron content (TEC) to a satellite-borne transmitter orbiting overhead. When the receivers are placed sufficiently far apart to study large-scale (hundreds of km) ionospheric features and diffraction effects can be neglected, *Kunitsyn and Tereshenko* [1992] have suggested the name Ray Radio Tomography (RRT) be applied. A number of studies [e.g., *Raymond et al.*, 1990] have shown that it is possible to invert the TEC values to obtain vertical density profiles over the latitude region spanned by the TEC measurements.

Computationally fast, semi-empirical models are ideal for verifying the accuracy of the inversion algorithm process. The model would first be used to generate the set of TEC values each receiver would "measure" as the satellite traverses overhead. Next, these TEC values would be used as inputs to the tomographic inversion algorithm which would calculate electron density profiles along the latitude covered by the hypothetical chain of receivers. A comparison of these profiles with those produced by the computationally fast ionospheric model would provide the degree of accuracy achievable.

Being able to realistically raytrace signals through the ionospheric medium depends critically on the ability to specify the electron density distribution in a computationally fast manner. This is especially true using three-dimensional raytracing programs. Until recently, climatological models using CCIR and URSI coefficients to specify Nmax and Hmax such as IONCAP [*Teters et al.*, 1983] have been the only computationally fast models available. The recent development of physically-based, semi-empirical or parameterized models now allows realistic ionospheric models to be adjusted in near-realtime and incorporated in state-of-the-art ray tracing programs for both HF and transionospheric propagation. The flexibility of these models can also be utilized to study the sensitivity of propagation modes to variations in specific

regions of the ionosphere. This approach has been adopted using PIM to study various aspects of observed OTH equatorial clutter to determine where the clutter originates.

In an ongoing study, PIM is being used to provide an ionospheric specification for a 3-D raytrace study investigating OTH equatorial spread Doppler clutter problems. Figure 12 shows an example of raytracing at a frequency of 20 Mhz through a PIM ionospheric cross section along a southerly great circle, over a distance of 12,000 km. The origin of the raytracing is the OTH radar in Bangor, Maine. The ionosphere cross section for 00 UT (1900 LT along the great circle) shows the strongly increased Hmax at the geomagnetic equator, and resulting "detached" or "whispering gallery" mode, skipping the second hop ground reflection. Analysis of a time sequence of such raytracing through a very realistic model has been instrumental in explaining OTH spread echo observations.

In the area of ionosphere-thermosphere-magnetosphere coupling, the availability of a realistic, parameterized ionospheric model is necessary in calculating the generation of magnetospherically-driven electric fields, how they penetrate to low latitudes and the ring current shielding effects which subsequently occur [*Spiro et al.*, 1988]. The important ionospheric parameters for these calculations are flux-tube-integrated Pedersen conductivities which implies the need for a global ionospheric specification capability. One can even imagine that a simple feedback adjustment to the parameterized ionospheric model based on the calculated electric fields would be possible.

In the equatorial region, the post-sunset enhancement in upward $\mathbf{E} \times \mathbf{B}$ drift, pictured in the bottom portion of Figure 5, raises the F layer above 500 km altitude. Under these conditions,

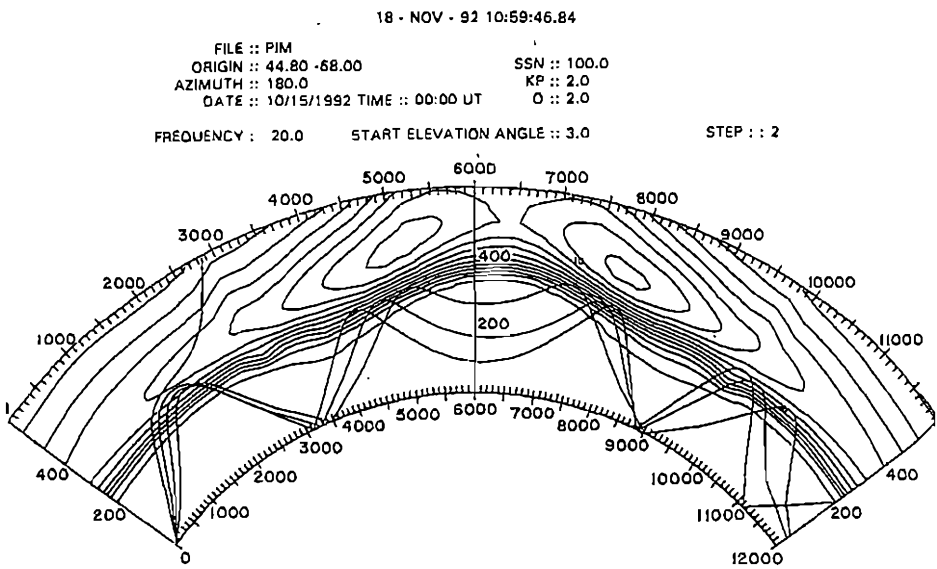

Figure 12. The propagation of radio waves through a PIM ionosphere simulating the Jones-Stephenson 3-D raytracing from the OTH-B radar site in Bangor, Maine.

the growth of small scale plasma density irregularities can occur (represented by the stippled area) within time scales of tens of minutes. Two instability growth rate mechanisms, Rayleigh-Taylor and gradient drift, are very sensitive to the flux tube-integrated quantities such as Pedersen conductivity, electron content and plasma recombination loss rates [*Kelley*, 1989]. Computationally fast ionospheric models would be very useful in carrying out sensitivity studies to investigate the various physical processes which tend to increase or decrease the plasma instability growth rates.

7. Summary

This paper has briefly described the fundamental physical processes which are important in determining electron and ion density distributions within the ionospheric F-region and a specific theoretical model which has been developed to calculate these distributions, globally. We have also presented examples where the model output has been compared with observations in order to validate the realism of the model. This effort at model validation is an ongoing process through specific workshops associated with the NSF CEDAR (Coupling Energetics and Dynamics of Atmospheric Regions) program. For the past five years, the PRIMO (Problems Related to Ionospheric Modeling and Observations) workshop has concentrated on comparing ionospheric observations, primarily ground-based radar measurements, with model results. The effort has succeeded in providing model developers the opportunity to standardize model inputs and to assure themselves that similarly-structured models are producing very similar results. A number of models described in this issue have been involved with and benefited from the PRIMO workshops.

Finally, physically-based, computationally-fast, semi-empirical models described earlier can be used to improve the realism of the climatological models. Because of the lack of equatorial as well as high latitude/polar cap observations, the IRI model does not reproduce many of the features which are known to exist, such as the high latitude "tongue" of ionization pictured in Figure 11a or the equatorial anomaly persistence after sunset pictured in Figure 11b. At the IRI Low Latitude Workshop held in New Delhi, India in January, 1995, a paper by Anderson et al. was presented which described how PIM parameters Nmax, Hmax, and the bottomside and topside half thicknesses could be incorporated into the current version of IRI90 so that users of IRI could obtain PIM-like profiles. This "PIM option" will be developed shortly and should become available to IRI users by 1997. It will be a global option and would include both high and low latitude features not currently existent in IRI90.

8. References

Anderson, D. N., *Planet. Space Sci., 21*, 409, 1973.
Anderson, D. N., M. Mendillo and B. Herniter, *J. Atmos. Terr. Phys., 22*, 292-306, 1987.
Anderson D. N., J. M. Forbes and M. Codescu, *J. Geophys. Res., 94*, 1520-1524, 1989.
Anderson, D. N., D. T. Decker, C. E. Valladares, *Geophys. Res. Lett., 23*, 579-582, 1996.
Bent, R. B., S. K. Llewellyn, AFGL-TR-73-0657 (Report), 1973.
Chakrabarti, S., R. Kimble, and S. Bowyer, *J. Geophys. Res., 89*, 5660, 1984.
Chiu, Y. T., *J. Atmos. Terr. Phys., 37*, 1563-1570, 1975.

Decker, D. T., C. E. Valladares, R. Sheehan, Su. Basu, D. N. Anderson, and R. A. Heelis, *Radio Sci., 29*, 249-268, 1994.

Hairston, M. R. and R. A. Heelis, *J. Geophys. Res., 95*, 2333, 1990.

Hardy, D. A., M. S. Gussenhoven, R. R. Raistrick and W. J. McNeil, *J. Geophys. Res., 92*, 12275, 1987.

Hedin, A. E., *J. Geophys. Res., 92*, 4649, 1987.

Hedin, A. E., N. W. Spencer and T. L. Killeen, *J. Geophys. Res., 93*, 9959, 1988.

Hedin, A. E., M. A. Biondi, R. G. Burnside, G. Hernandez, R. M. Johnson, T. L. Killeen, C. Mazaudier, J. W. Meriwether, J. E. Salah, R. J. Sica, R. W. Smith, N. W. Spencer, V. B. Wickwar, and T. S. Virdi, *J. Geophys. Res., 96*, 7657, 1991.

Heelis, R. A., J. K. Lowell, and R. W. Spiro, *J. Geophys. Res., 87*, 6339, 1982.

Heppner, J. P. and N. C. Maynard, *J. Geophys. Res., 92*, 4467, 1982.

Hinteregger, H. E., K. Fukui, and B. R. Gilson, *Geophys. Res. Lett., 8*, 1147, 1981.

Jasperse, J. R., *Physics of Space Plasmas* (ed. T. S. Chang, B. Coppi, and J. R. Jasperse), pp. 53-84, Sci. Publ., Cambridge, Mass., 1982.

Kelley, M. C., *The Earth's Ionospheric Plasma Physics and Electrodynamics*, pp. 487, Academic, San Diego, CA, 1989.

Kendall, P. C., and W. M. Pickering, *Planet. Space Sci., 15*, 825, 1967.

Killeen, T. L., R. G. Roble, and N. W. Spencer, *Adv. Space Res., 7*, 10207, 1987.

Knudsen, W. C., P. M. Banks, J. D. Winningham, and D. M. Klumpar, *J. Geophys. Res., 82*, 4784, 1977.

Kunitsyn, V. E., and E. D. Tereshchenko, *IEEE Antennas and Propagation, 34*, 22-32, 1992.

Moffett, R. J., *Fundaments of Cosmic Physics, 4*, 313-391, 1979.

Preble, A. J., D. N. Anderson, B. G. Fejer, and P. H. Doherty, *Radio Sci., 29*, 857, 1994.

Rawer, R. and D. Bilitza, *J. Atmos. Terr. Phys., 51*, 781-790, 1989.

Raymond, T. D., J. A. Austen, S. J. Franke, C. H. Liu, J. A. Klobuchar, and J. Stalker, *Radio Sci., 25*, 771-789, 1990.

Rees, D., T. J. Fuller-Rowell, S. Quegan, R. J. Moffett, and G. J. Bailey, *J. Atmos. Terr. Phys., 56*, 903-930, 1988.

Richards, P. G. and D. G. Torr, *J. Geophys. Res., 93*, 4060, 1988.

Rishbeth, H. and O. K. Garriott, *Introduction to Ionospheric Physics*, Academic Press, New York, 1969.

Roble, R. G., E. C. Ridley, A. D. Richmond, and R. E. Dickinson, *Geophys. Res., Lett., 15*, 1325-1328, 1988.

Rush, C. M., M. Pokempner, D. N. Anderson, J. Perry, F. G. Stewart, and R. Reasoner, *Radio Sci., 19*, 1083-1097, 1984.

Schunk, R. W., W. J. Raitt, and P. M. Banks, *J. Geophys. Res., 80*, 3121, 1975.

Schunk, R. W., *PAGEOPH, 127*, 255-303, 1988.

Sojka, J. J., M. D. Bowline, R. W. Schunk, D. T. Decker, C. E. Valladares, R. Sheehan, D. N. Anderson, and R. A. Heelis, *Geophys. Res. Lett., 20*, 1783-1786, 1993.

Spiro, R. W., R. A. Wolf, and B. G. Fejer, *Ann. Geophys., 6*, 39-50, 1988.

Strobel, D. F. and M. B. McElroy, *Planet. Space Sci., 18*, 1181-1202, 1970.

Teters, L. R., J. L. Loyd, G. W. Haydon, and D. C. Lucas, *Ionospheric Communications Analysis and Prediction Program Users Manual*, NTIA Rept. No. 83-127, 1983.

Valladares, C. E., D. T. Decker, R. Sheehan, and D. N. Anderson, *Radio Sci.*, in press, 1996.

Vallance-Jones, A., *Aurora*, D. Reidel, Dordrecht, Holland, 1974.

Weber, E. J., J. Buchau, J. G. Moore, J. R. Sharber, R. C. Livingston, J. D. Winningham, and B. W. Reinisch, *J. Geophys. Res., 88*, 1683-1694, 1984.

USU Model of the Global Ionosphere

R. W. Schunk and J. J. Sojka

Center for Atmospheric and Space Sciences
Utah State University
Logan, UT 84322-4405

1. Introduction

The USU model of the global ionosphere describes the three-dimensional time-dependent evolution of the global ionosphere at altitudes between 90 and 1000 km. The model is a first-principles numerical model that calculates density distributions for the electrons and six ion species (NO^+, O_2^+, N_2^+, O^+, N^+, He^+) as a function of latitude, longitude, and altitude on a prespecified spatial grid. The model also calculates the isotropic electron temperature and the ion temperatures both parallel and perpendicular to the geomagnetic field on the same spatial grid. The model outputs the global density and temperature distributions at specified times. In its current configuration, the model takes account of numerous chemical and physical processes, including field-aligned diffusion, cross-field electrodynamic drifts, thermospheric winds, polar wind escape, energy-dependent chemical reactions, neutral composition changes, ion production due to EUV radiation and auroral electron precipitation, thermal conduction, diffusion-thermal heat flow, and a host of local heating and cooling mechanisms. The model also takes account of the offset between the geomagnetic and geographic poles.

2. Model History

The ionospheric model was initially developed as a mid-latitude, multi-ion (NO^+, O_2^+, N_2^+, and O^+) model by *Schunk and Walker* [1973]. The time-dependent ion continuity and momentum equations were solved as a function of altitude for a corotating plasma flux tube including diurnal variations and the relevant *E* and *F* region processes. This model was extended to include high latitude effects due to convection electric fields and particle precipitation by *Schunk et al.* [1975, 1976]. A simplified ion energy equation was also added, which was based on the assumption that local heating and cooling processes dominate (valid below 500 km). A further extension of the model to include the minor ions N^+ and He^+, an updated photochemical scheme, and the MSIS atmospheric model is described in *Schunk and Raitt* [1980].

Sojka et al. [1981a, b] added empirical models for the plasma convection and particle precipitation inputs so that three-dimensional density and temperature distributions could be calculated in the high latitude domain. Then, *Schunk and Sojka* [1982] extended the ion energy formulation to include thermal conduction and diffusion-thermal heat flow so that rigorous ion temperatures could be calculated throughout the *E* and *F* regions. The adopted ion energy equation and conductivities are those given by *Conrad and Schunk* [1979]. Subsequently, *Schunk et al.* [1986] added the electron energy equation so that self-consistent electron temperatures could be calculated. This energy equation and the associated heating and cooling rates were taken from *Schunk and Nagy* [1978], while the thermal conductivities were taken from *Schunk and Walker* [1970]. *Sojka and Schunk* [1985] incorporated the *Sterling et al.*

[1969] model of the equatorial ionosphere, and then conducted the first, time-dependent, three-dimensional, numerical simulation of the global ionosphere.

3. Mathematical Formulation

The USU model of the global ionosphere is based on an Euler-Lagrange hybrid numerical scheme. For the mid-high latitude region, the ion continuity, momentum, and energy equations are solved as a function of altitude using a fixed spatial grid, while for the equatorial region the ion equations are solved along the magnetic field (**B**) from one hemisphere to the conjugate hemisphere on a fixed spatial grid. In all latitudinal domains, the plasma flux tubes are allowed to convect through a moving neutral atmosphere in a direction perpendicular to **B** due to magnetospheric, corotational, and dynamo electric fields (Figure 1). The three-dimensional nature of the model is obtained by following many flux tubes of plasma while keeping track of their positions at all times. This approach has an advantage over a purely Eulerian scheme, which requires fixed grid points in latitude and longitude, because more flux tubes can be placed in the high latitude regions where sharp horizontal gradients are expected, such as near the auroral oval and main trough.

3.1 Diffusion Equations

The ion continuity and momentum equations are solved in the diffusion approximation, which is valid for subsonic ambipolar flow. For ion species i, these equations can be expressed as:

$$\frac{D_i n_i}{Dt} + \nabla_{\parallel} \cdot (n_i \mathbf{u}_{i\parallel}) = P_i - L_i n_i \tag{1}$$

$$\mathbf{u}_{i\parallel} = \mathbf{u}_{n\parallel} - D_i \left[\frac{1}{n_i} \nabla_{\parallel} n_i + \frac{(\nabla \cdot \bar{\tau}_i)_{\parallel}}{n_i k T_i} - \frac{m_i \mathbf{G}_{\parallel}}{k T_i} + \frac{1}{T_i} \nabla_{\parallel} (T_e + T_i) + \frac{(T_e / T_i)}{n_e} \nabla_{\parallel} n_e \right] \tag{2}$$

where

$$D_i = k T_i / (m_i \sum_n \nu_{in}) \tag{3}$$

$$\frac{D_i}{Dt} = \frac{\partial}{\partial t} + \mathbf{u}_{i\perp} \cdot \nabla \tag{4}$$

and where n_i is the ion density, m_i the ion mass, T_i the ion temperature, $\mathbf{u}_i$ the ion drift velocity, τ_i the ion stress tensor, P_i the ion production rate, L_i the ion loss frequency, n_e the electron density, T_e the electron temperature, $\mathbf{u}_n$ the neutral drift velocity, ν_{in} the ion-neutral momentum transfer collision frequency, **G** is gravitational acceleration, k is Boltzmann's constant, t is time, and ∇ is the spatial gradient. The $\parallel$ and $\perp$ subscripts refer to the directions parallel and perpendicular to the geomagnetic field (**B**), respectively. Note that the convective derivative (4) is used for convecting flux tubes of plasma.

The ion stress tensor accounts for the fact that the ion temperature parallel to **B** can be different from that perpendicular to **B**. Such a situation can occur whenever there is a substantial ion-neutral relative drift. If vertical plasma gradients are more important than horizontal gradients, then only the tensor element associated with the **B** direction is important.

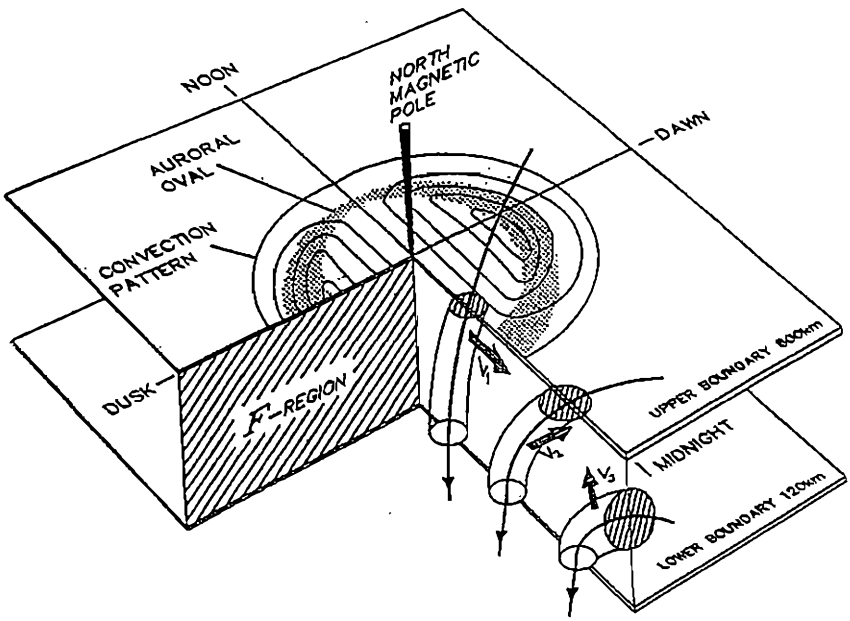

Figure 1. A schematic view of the F-region ionosphere bounded below (100 km) and above (1000 km) extending from the north pole to the magnetic equator. The imposed magnetospheric electric fields and auroral oval are shown as contoured lines and shaded regions, respectively. A midnight cross section reveals the direction of motion of a high latitude (V_1), mid-latitude (V_2), and equatorial (V_3) plasma flux tube. From *Sojka* [1989].

Schunk [1975] calculated this element for the case where the various neutral species have displaced Maxwellian velocity distributions with a common temperature and common drift velocity,

$$\tau_{i\|} = \frac{R_i}{S_i + 0.6\nu_{ii}} n_i m_i \left[(u_i - u_n)_\|^2 - \frac{1}{3}(\mathbf{u}_i - \mathbf{u}_n)^2 \right] \tag{5}$$

where

$$R_i = \sum_n \frac{m_n \nu_{in}}{m_i + m_n} \left[1 - \frac{3}{4} \frac{Q_{in}^{(2)}}{Q_{in}^{(1)}} \right] \tag{6}$$

$$S_i = \sum_n \frac{m_i \nu_{in}}{m_i + m_n} \left[1 + \frac{3}{4} \frac{m_n}{m_i} \frac{Q_{in}^{(2)}}{Q_{in}^{(1)}} \right] \tag{7}$$

and where m_n is the neutral mass, $Q_{in}^{(2)} / Q_{in}^{(1)}$ is a ratio of collision cross-sections, and ν_{ii} is the ion-ion collision frequency.

In the model, four ions are assumed to be major ions (NO^+, O_2^+, N_2^+, O^+) and two are assumed to be minor ions (N^+, He^+), where an ion is minor if its density is much less than the electron density. The major ion equations are solved simultaneously at each time step, and then the minor ion equations are solved. For all the ions except N_2^+, the complete diffusion formulation is used. For N_2^+ chemical equilibrium is assumed at all altitudes because its chemical lifetime is very short throughout the day and night. With this assumption $n(N_2^+) = P(N_2^+)/L(N_2^+)$.

The electron density and drift velocity are obtained from charge neutrality and charge conservation, respectively,

$$n_e = \Sigma_i n_i \tag{8}$$

$$\mathbf{J} = \Sigma_i e_i n_i \mathbf{u}_i - e n_e \mathbf{u}_e \tag{9}$$

where e_i is the ion charge and $\mathbf{J}$ is the field-aligned current density. Note that in Equations (8) and (9) the sum is only over the major ions.

Various Coulomb collision frequencies and both resonant and non-resonant ion-neutral collision frequencies are needed. These collision frequencies and the associated cross-section ratios are listed in *Schunk* [1988] and are not repeated here. In the model, account was taken of ion collisions with six neutrals (N_2, O_2, O, N, He, H).

3.2 Chemical Reaction Scheme

For the *E* and *F* regions of the ionosphere, the important photoionization processes are:

$$N_2 + h\upsilon \rightarrow N_2^+ + e \tag{10a}$$

$$\rightarrow N^+ + N + e \tag{10b}$$

$$O_2 + h\upsilon \rightarrow O_2^+ + e \tag{11}$$

$$O + h\upsilon \rightarrow O^+ + e \tag{12}$$

$$N + h\upsilon \rightarrow N^+ + e \tag{13}$$

$$He + h\upsilon \rightarrow He^+ + e \tag{14}$$

The calculation of the resulting photoionization rates requires a knowledge of the solar spectrum and the absorption and ionization cross sections for the neutral gases. The values adopted were obtained from *Torr and Torr* [1985], in which the solar spectrum was divided into 37 wavelength intervals. However, the solar fluxes are scaled with $F_{10.7}$ in order to account for solar cycle effects. The ionospheric model also includes a nocturnal ionization source due to resonantly scattered solar radiation, recombination radiation, and starlight [*Strobel et al.*, 1980; *Rasmussen et al.*, 1988].

The ions shown in Equations (10)-(14) are also produced by impact of precipitating auroral electrons on the ambient neutrals. The auroral production rates used in the ionospheric model are based on the electron deposition code originally developed by *Strickland et al.* [1976]. R. E. Daniell of Computational Physics Incorporated (CPI) ran a recent version of this code for numerous cases and then supplied us with the resulting sets of production rate profiles. He considered 27 geophysical cases, covering 3 levels of solar activity, 3 seasons, and 3 levels of geomagnetic activity. For each of the 27 geophysical situations, he considered 5 auroral spectra with different energy fluxes and characteristic energies. For the 135 cases, production rate profiles were obtained for N_2^+, O_2^+ and O^+, and we use these profiles to obtain production rates as plasma flux tubes convect through the auroral oval and encounter changing auroral conditions.

After the ions and electrons are created by either photoionization or auroral precipitation, they undergo numerous chemical reactions. The ones contained in the ionospheric model are shown in Table 1. The rate coefficients for the first three reactions have a complicated temperature dependence and are given in *Schunk* [1988], as are the references for the reaction rates. In addition to the reactions in Table 1, the metastable reaction of $O^+(^2D)$ with N_2 is indirectly taken into account as follows. When atomic oxygen is photoionized, both $O^+(^4S)$ and $O^+(^2D)$ are produced. The $O^+(^2D)$ ions then interact with N_2 to form N_2^+, and the fraction that is converted into N_2^+ varies from 25 to 75 percent, depending on the season. In the ionospheric model, the appropriate fraction of $O^+(^2D)$ ions produced is converted into N_2^+ and the rest remain as O^+ ions.

3.3 Ion Energy Equation

The complete ion energy equation is fairly complicated. However, for ionospheric applications several simplifications are possible because collisional coupling dominates at low altitudes and because vertical plasma gradients are much more important than horizontal gradients. Therefore, to a good approximation, the ion energy equation can be expressed as:

$$\frac{3}{2} n_i k \frac{\partial T_i}{\partial t} + \nabla \cdot \mathbf{q}_i = \sum_l \frac{n_i m_i \nu_{il}}{m_i + m_l} \left[3k(T_l - T_i) + m_l (\mathbf{u}_i - \mathbf{u}_l)^2 \right] \tag{15}$$

TABLE 1. CHEMICAL REACTION SCHEME

Reaction	Rate Coefficients, $cm^3\ s^{-1}$
$O^+ + N_2 \rightarrow NO^+ + O$	k_1
$O^+ + O_2 \rightarrow O_2^+ + O$	k_2
$O^+ + NO \rightarrow NO^+ + O$	k_3
$O_2^+ + N_2 \rightarrow NO^+ + NO$	5×10^{-16}
$O_2^+ + NO \rightarrow NO^+ + O_2$	4.4×10^{-10}
$O_2^+ + N \rightarrow NO^+ + O$	1.2×10^{-10}
$O_2^+ + e \rightarrow O + O$	$1.6 \times 10^{-7}\ (300/T_e)^{0.55}$
$N_2^+ + O \rightarrow NO^+ + N$	$1.4 \times 10^{-10}\ (300/T)^{0.44}$; $T \leq 1500°$ K
	$5.2 \times 10^{-11}\ (T/300)^{0.2}$; $T > 1500°$ K
$N_2^+ + O \rightarrow O^+ + N_2$	$1 \times 10^{-11}\ (300/T)^{0.23}$; $T \leq 1500°$ K
$N_2^+ + O_2 \rightarrow O_2^+ + N_2$	$5 \times 10^{-11}\ (300/T)$
$N_2^+ + NO \rightarrow NO^+ + N_2$	3.3×10^{-10}
$N_2^+ + e \rightarrow N + N$	$1.8 \times 10^{-7}\ (300/T_e)^{0.39}$
$NO^+ + e \rightarrow N + O$	$4.2 \times 10^{-7}\ (300/T_e)^{0.85}$
$He^+ + N_2 \rightarrow N^+ + N + He$	1×10^{-9}
$N^+ + O_2 \rightarrow NO^+ + O$	2×10^{-10}
$N^+ + O_2 \rightarrow O_2^+ + N$	4×10^{-10}
$N^+ + NO \rightarrow NO^+ + N$	2×10^{-11}

where the summation is over the electrons and all neutral species. The small temperature difference between the different ion species is ignored in our ionospheric model.

For the ion heat flow vector, $\mathbf{q}_i$, we adopted the expression derived by *Conrad and Schunk* [1979], which includes both thermal conduction and diffusion-thermal heat flow. This expression, which was derived for a collision-dominated, partially-ionized, three-component plasma in thermal nonequilibrium, is appropriate at F region altitudes where the dominant species are electrons, O^+ and neutral atomic oxygen. In the magnetic field direction, this expression takes the form:

$$\mathbf{q}_{i\parallel} = -K'_{ni}\nabla_\parallel T_i - K_{in}\nabla_\parallel T_n + R_{in}(\mathbf{u}_i - \mathbf{u}_n)_\parallel \tag{16}$$

where K'_{ni} and K_{in} are thermal conductivities and R_{in} is the diffusion-thermal coefficient; these expressions are given in *Conrad and Schunk* [1979]. Note that ion heat flow is important only in the upper F-region where O^+ dominates. Also note that an ion heat flow occurs in response to an ion temperature gradient, a neutral temperature gradient, and a relative ion-neutral drift (diffusion-thermal heat flow).

3.4 Electron Energy Equation

Like the ion energy equation, the complete electron energy equation is fairly complicated. A few simplifications are possible, but not as many as for the ion energy equation. A form that is appropriate at *E* and *F* region altitudes is:

$$\frac{3}{2}n_e k\frac{\partial T_e}{\partial t} = -n_e kT_e(\nabla\cdot\mathbf{u}_e) - \frac{3}{2}n_e k\mathbf{u}_e\cdot\nabla T_e - \nabla\cdot\mathbf{q}_e + \frac{\delta E_e}{\delta t} + Q_e - L_e \qquad (17)$$

where Q_e represents heat sources, L_e inelastic cooling processes, and $\delta E_e/\delta t$ represents coupling via elastic collisions with the various neutral and ion species. In the ionospheric model, account is taken of electron cooling via inelastic collisions due to N_2 and O_2 vibrational excitation, N_2 and O_2 rotational excitation, excitation of O to the ^1D state, and excitation of the fine structure levels of O. For elastic collisional coupling, account is taken of electron interactions with five neutrals (N_2, O_2, O, He, H) and four ions (NO^+, O_2^+, O^+, He^+). The main electron heating processes included in the model are due to photoelectrons and precipitating auroral electrons. The mathematical expressions for all of the heating and cooling processes are given by *Schunk* [1988] and are not repeated here.

The electron drift velocity terms in Equation (17) are important only on auroral field-lines where the Birkeland currents flow. Hence, in this equation it is convenient to relate $\mathbf{u}_e$ to the field-aligned current $\mathbf{J}$,

$$\mathbf{J}_{e\parallel} = -en_e\mathbf{u}_{e\parallel} \qquad (18)$$

The electron heat flow vector in Equation (17) is then related to both the field-aligned current and the electron temperature gradient,

$$\mathbf{q}_{e\parallel} = -\beta_e\mathbf{J}_{e\parallel} - \mathrm{K}^e\nabla_{\parallel}T_e \qquad (19)$$

where β_e is a thermoelectric coefficient and K^e is the electron thermal conductivity. The expressions adopted are those derived by *Schunk and Walker* [1970].

3.5 Numerical Solution

Because there are different time scales that govern the ion densities and temperatures, it is not necessary to solve all of the equations simultaneously at each time step. Also, the minor ion diffusion equations do not have to be solved simultaneously with the major ion diffusion equations. The procedure adopted at equatorial latitudes is described by *Sterling et al.* [1969] and is not repeated here. The procedure adopted at mid and high latitudes is as follows. At each time step, the diffusion equations for the major ions (NO^+, O_2^+, N_2^+, O^+) are solved. Next, the minor ion (N^+, He^+) diffusion equations are solved, and then the ion and electron thermal conduction equations.

When the diffusion Equation (2) is substituted into the continuity Equation (1), the equations governing the major ions NO^+, O_2^+ and O^+ take the form:

$$\frac{D_i n_i}{Dt} = A_{1i}(z,t)\frac{\partial^2 n_i}{\partial z^2} + A_{2i}\left(z,t,n_e,\frac{\partial n_e}{\partial z}\right)\frac{\partial n_i}{\partial z} + A_{3i}\left(z,t,n_e,\frac{\partial n_e}{\partial z},\frac{\partial^2 n_e}{\partial z^2}\right)n_i + A_{4i}(z,t,n_j) \qquad (20)$$

where the subscript j corresponds to another major ion species. The equation for N_2^+ is that appropriate for chemical equilibrium:

$$n(N_2^+) = P(N_2^+) / L(N_2^+) \tag{21}$$

The equations for NO^+, O_2^+, and O^+ form a set of coupled, nonlinear, second order, parabolic partial differential equations, while the equation for N_2^+ is merely a nonlinear algebraic equation but is coupled to the other major ion equations. The four equations are solved by first expanding all of the coupling and nonlinear terms in a Talyor series in time and then by using a finite difference scheme in combination with a completely implicit numerical technique [c.f. *Schunk*, 1988].

The equations governing the densities of the minor ions are also obtained by substituting their momentum equations into their continuity equations. However, since the major ion densities and the electron density are known prior to a solution for the minor ion densities, the minor ion equations are linear and of the form:

$$\frac{\partial n_j}{\partial t} = B_{1j}(z,t)\frac{\partial^2 n_j}{\partial z^2} + B_{2j}(z,t)\frac{\partial n_j}{\partial z} + B_{3j}(z,t)n_j + B_{4j}(z,t) \tag{22}$$

where the subscript j corresponds to a minor ion species and where the B-coefficients depend on the major ions and electrons. These equations are solved using finite differences and a completely implicit numerical technique.

Equations for the electron and ion temperatures are obtained by substituting the appropriate heat flow equations into the associated energy equations. This results in two coupled, nonlinear, second order, parabolic partial differential equations for T_e and T_i. However, before applying numerical techniques, it is convenient to introduce a change of variables for both T_e and T_i, $\theta = T^{7/2}$. With this change of variables, the temperature equations take the form:

$$\frac{D\theta}{Dt} = A_1(z,t)\frac{\partial^2\theta}{\partial z^2} + A_2(\theta,z,t)\frac{\partial\theta}{\partial z} + A_3(\theta,z,t)\theta + A_4(\theta,z,t). \tag{23}$$

To solve these equations, the terms that are nonlinear in θ are linearized in time, and then finite differences and completely implicit numerical techniques are used.

Boundary conditions are needed at both the upper (1000 km) and lower (90 km) boundaries. At the lower boundary, the densities are obtained by equating local production and loss terms. Likewise, the temperatures are obtained by equating local heating and cooling processes. At the upper boundary, downward ion and electron heat fluxes are specified for the solution of the temperature equations. The boundary conditions for the density equations allow for thermal expansion and contraction (i.e., scale height changes), but do not allow escape to the magnetosphere.

3.6 Trajectory Following

As noted earlier, in the mid and high latitude domains, the transport equations are solved as a function of altitude for convecting flux tubes of plasma. The paths that the flux tubes follow are determined by magnetospheric electric fields, and in practical applications empirical models

must be used because the electric fields are needed over the entire high-latitude region at all times. Even when the electric field pattern is provided, decisions have to be made with regard to how many trajectories to select, how many plasma flux tubes to follow, and where the flux tubes should be placed initially. Also, account must be taken of the fact that as the flux tubes convect in response to the imposed magnetospheric electric field pattern, their spatial distribution will become non-uniform because the various trajectories have different lengths and because the magnitude of the electric field varies around each trajectory differently.

An example of how the flux tube locations vary is shown in Figure 2. Initially, a spatial grid with cells that are 5° in latitude and 1 hour in MLT is created for the region poleward of 40° latitude. One plasma flux tube is placed at the center of each of the 120 cells (bottom panel). Subsequently, the flux tubes convect in response to the corotational and magnetospheric electric fields. In the case shown in Figure 2, a *Volland* [1978] symmetric two-cell convection pattern is used. As time evolves, the distribution of flux tubes becomes nonuniform. In the latest version of our model, flux tubes are added and removed from spatial cells as time proceeds in order to maintain a more uniform distribution. The resulting flux tube distribution is shown in the middle panel after 1 day and in the top panel after 3 days. For this case, the maximum number of flux tubes that exist at a given time is less than 400. However, for some of our high resolution studies, we follow several thousand plasma flux tubes.

4. Model Inputs

The USU model, like all ionospheric models, requires both magnetospheric and thermospheric inputs in order to account for ionospheric coupling to these regions. The inputs need to be time-dependent and global. Currently, various empirical (i.e., statistical) models are available for almost all of the required inputs and these are briefly discussed in the following subsections.

4.1 Coordinate Systems

There are two main coordinate systems used in the ionospheric model, namely geomagnetic and geographic. Most of our previous model studies were based on a tilted offset dipole magnetic system because relatively simple transformations exist to convert from this frame to geographic. More recently, the IGRF magnetic field model has been used, and it provides the inclination, declination, and magnitude of the magnetic field.

4.2 Neutral Atmosphere

The USU ionospheric model requires a global distribution of the neutral densities (N_2, O_2, O) and temperature at altitudes between 100-1000 km. These input parameters are obtained from the MSIS-90 atmospheric model [*Hedin*, 1991]. This empirical model yields the atmospheric parameters for different solar cycle, seasonal, and geomagnetic activity levels. It also contains diurnal and longitudinal variations.

4.3 Neutral Wind

In most of our early work with the USU ionospheric model, we used a modified form of the analytical thermospheric wind pattern given by *Murphy et al.* [1976]. More recently, we adopted the MSIS-Wind model constructed by *Hedin et al.* [1991]. This empirical model provides global distributions of the zonal and meridional wind components. As with the

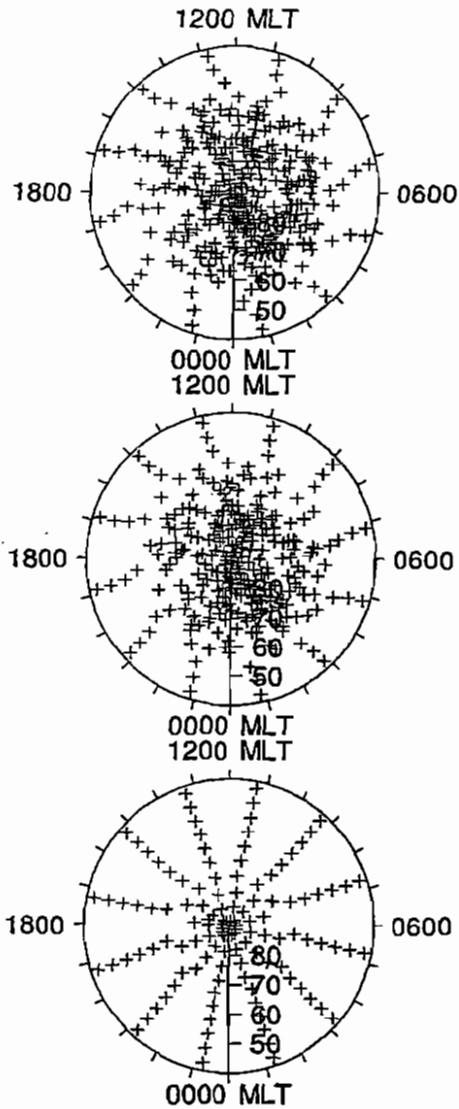

Figure 2. Flux tube locations at the start of the simulation (bottom panel), after 1 day (middle panel), and after 3 days (top panel) for Kp = 1.

atmospheric model, the wind model takes account of solar cycle, seasonal, geomagnetic activity, diurnal, and longitudinal variations.

4.4 Magnetospheric Electric Field

At high latitudes, the plasma convection pattern induced by magnetospheric electric fields is crucial in determining the ionospheric densities and temperatures. Because of its importance, several empirical models of the convection electric field have been developed over the years. The models have been based on both radar data and satellite electric field data [*Volland*, 1978; *Foster*, 1983; *Heelis et al.*, 1981; *Heelis*, 1984; *Heppner and Maynard*, 1987]. For the current version of the USU ionospheric model, we adopted the *Heppner and Maynard* [1987] electric field model. This model provides magnetospheric electrostatic potential distributions over the polar regions as a function of Kp for southward IMF ($B_z < 0$) and both negative and positive B_y values.

4.5 Auroral Precipitation

Particle precipitation in the auroral oval acts as an ionization source, a source of bulk heating for the electron gas, and a thermal conduction source through our upper boundary. As with the electric field, several empirical models are available that describe the precipitating electron energy flux and characteristic energy [*Feldstein and Starkov*, 1967; *Spiro et al.*, 1982; *Wallis and Budzinski*, 1981; *Hardy et al.*, 1985]. Most of our recent ionospheric model studies are based on the *Hardy et al.* [1985] empirical model, which is the most comprehensive precipitation model constructed to date. As the plasma flux tubes move through the auroral oval, the characteristic energy and energy flux values obtained from the *Hardy et al.* [1985] model are used to calculate ion production rates, the bulk electron heating rate, and the thermal conduction flux through the upper boundary.

4.6 Equatorial Electric Field

Dynamo electric fields, generated via the thermospheric wind, are extremely important for determining equatorial electron densities. Until recently, the best empirical model of equatorial electric fields was the one developed by *Richmond et al.* [1980], which was the one used in several of our ionospheric studies. Recently, however, B. Fejer and colleagues constructed a sophisticated empirical model of equatorial electric fields including longitudinal variations, and the ionospheric modeling results obtained with these electric fields have been impressive [*Preble et al.*, 1994]. Therefore, the Fejer equatorial electric field model is now used as an input to the USU ionospheric model.

4.7 Topside Heat Flow

Escaping photoelectrons and auroral electrons lose energy to the thermal electrons at high altitudes as they traverse the ionospheric plasma. The transferred energy is then conducted down to the lower ionosphere and enters as a topside (1000 km) boundary condition in the USU ionospheric model. The procedures for calculating the boundary heat flow values is identical to that described by *Schunk et al.* [1986].

5. Model Outputs

The ionospheric model yields density distributions for the electrons and six ion species (NO^+, O_2^+, N_2^+, O^+, N^+, He^+) as a function of latitude, longitude, and altitude on a

prespecified spatial grid at selected times. The model also outputs the isotropic electron temperature and the ion temperatures both parallel and perpendicular to the geomagnetic field on the same spatial grid and at the same times. The model also calculates auxiliary parameters, such as N_mF_2, h_mF_2, h_mE, N_mE, topside plasma scale heights, and NO^+/O^+ transition heights.

There are three basic modes of operation for the USU ionospheric model, including climatology studies, storm simulations, and high-resolution weather modeling. Examples of model outputs for all three modes are given in the following subsections.

5.1 Climatology Studies

For climatology modeling, the magnetospheric convection and precipitation patterns and the equatorial electric field distribution are usually held fixed during the ionospheric simulation (i.e., they do not vary with universal time). However, a diurnal variation still occurs because the input convection and precipitation patterns are ordered with respect to the magnetic frame and it rotates about the geographic pole. In the magnetic frame, the rotation appears as a motion of the terminator toward and then away from the magnetic pole. An example of results from a climatology simulation is shown in Figure 3, where contours of N_mF_2 are plotted versus magnetic latitude and MLT. The calculations are for solar maximum ($F_{10.7}$ = 170), June solstice, quiet geomagnetic activity (K_p = 2, Ap = 12) and southward interplanetary magnetic field ($B_z < 0$, $B_y = 0$) conditions. The left panel shows a global snapshot at 0300 UT, while the right panel is for 1500 UT. In the summer (northern) hemisphere, the densities at high latitudes are fairly uniform and the auroral oval is not very apparent owing to the fact that the bulk of the high latitude ionosphere is sunlit in summer and the auroral ionization source is weak during quiet geomagnetic activity. In the winter hemisphere, on the other hand, there is a large density variation at high latitudes. Clearly evident are ionization enhancements in the auroral region and a mid-latitude electron density trough that is situated just equatorward of the auroral oval. Note that the main trough covers all longitudes at 1500 UT, a feature that is common in the Southern Hemisphere in winter. The lower N_mF_2 values in the winter hemisphere occur because the bulk of the high-latitude region is in darkness and the auroral oval is more apparent because the weak auroral ionization source does not have to compete with ionization due to solar EUV radiation.

In the equatorial ionosphere, Appleton ionization peaks are clearly visible at night, but not during the day. The lack of Appleton peaks during the day can be traced to the adopted equatorial electric field pattern. For this study, the electric field values given by *Richmond et al.* [1980] were adopted. However, this model appears to inaccurately specify the phase of the upward $\mathbf{E} \times \mathbf{B}$ drift because the Appleton anomaly can be present during the day. Note the slight asymmetry in the Appleton peaks at 1500 UT, which is a consequence of both the neutral wind and the favorable magnetic field geometry at this UT.

5.2 Geomagnetic Storms

For geomagnetic storm modeling, large-scale convection and precipitation patterns are again used as inputs to the ionospheric model but the patterns vary with time. During a geomagnetic storm, the extent of the auroral oval, the intensity of auroral precipitation, and the plasma convection pattern vary significantly. One of our early storm simulations was for an idealized situation in which the storm growth phase was 1 hour, the main phase was 1.5 hours, and the decay phase was 3 hours [*Sojka and Schunk*, 1983, 1984]. In this simulation the convection pattern changed from a symmetric two-cell pattern with a 20 kV cross-tail potential to an asymmetric two-cell pattern with enhanced plasma flow in the dusk sector and a total cross-tail potential of 90 kV.

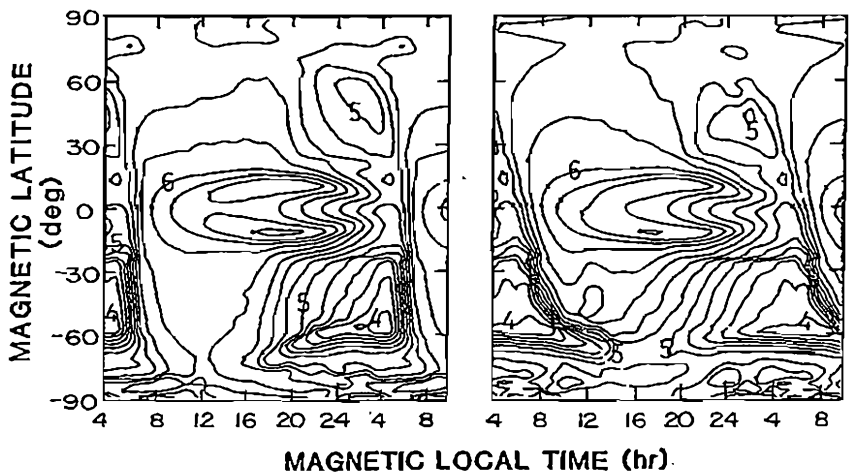

Figure 3. Contours of N_mF_2 in a magnetic latitude-MLT coordinate system at 0300 UT (left panel) and 1500 UT (right panel). The contours are labeled in $\log_{10}$ [N_mF_2 (cm^{-3})] and the contour interval is 0.2. From *Sojka and Schunk* [1985].

Figure 4 shows the ionospheric response to this idealized magnetic storm. Shown in this figure is the O^+ density over the polar region at 160 km (bottom) and 300 km (top) for eight times during the storm study. Each of the eight panels shows a "snapshot" in which the O^+ density has been contoured on a logarithmic scale and coded to denote the absolute density ranges. A comparison of the panels in Figure 4 reveals a very important result, i.e., the ionospheric response time to a magnetic storm is a strong function of altitude. The lower F region responds on a time scale of only minutes to the storm associated changes in the auroral precipitating electron flux, owing to the dominance of chemical processes over transport processes. At higher altitudes, in the vicinity of h_mF_2, the chemistry is balanced by both plasma diffusion along field lines and horizontal plasma convection, which acts to prolong the effect of the storm for many hours after it has ceased. The peak density responds only slowly to increased precipitation and may not reach its maximum enhanced value until over an hour after the storm main precipitation has passed. In the topside ionosphere, the density variations are not correlated with the morphology of the storm auroral precipitation or the temporal variation of the storm electric field pattern. Time delays of up to 3 or 4 hours occur at high altitudes for "peak" densities to be reached after a storm, and the subsequent recovery is on the order of 5 hours.

During the storm there were significant changes in the ion temperature, ion composition, and molecular/atomic ion transition height. The stormtime asymmetric convection pattern produced an ion temperature hot spot at the location of the dusk convection cell owing to increased ion-neutral frictional heating. In this hot spot there were significantly enhanced NO^+ densities, and hence, increased molecular/atomic ion transition heights. During the storm recovery phase, the decay of the enhanced NO^+ densities closely followed the decrease in the plasma convection speed. During the storm, elevated ion temperatures also appeared at high altitudes in the midnight-dawn auroral oval region. These elevated ion temperatures were a consequence of the storm-enhanced topside O^+ densities, which provided better thermal coupling to the hot electrons. This region also contained reduced molecular/atomic ion transition heights. These elevated ion temperatures and reduced transition heights persisted for several hours after the storm main phase ended.

5.3 High-Resolution Simulations

When studying mesoscale ionospheric features (100-1000 km), such as sun-aligned arcs, plasma patches, and convection vortices, a high-resolution spatial grid is embedded in our large-scale grid in order to obtain better resolution in the region containing the mesoscale feature [*Crain et al.*, 1993; *Sojka et al.*, 1993; *Schunk et al.*, 1994]. Such a grid was used in a recent study of plasma patch formation [*Sojka et al.*, 1993], with the goal being to determine whether or not patches form as a result of IMF B_y variations. This work required a very fine spatial grid (37×39 points) in the polar cap in order to resolve patch features, as shown in Figure 5a. In the simulation, we assumed the IMF was southward, adopted a Heppner-Maynard 2-cell convection pattern for B_y negative, and then calculated ionospheric densities for diurnally reproducible conditions in winter. Subsequently, the convection was changed and the effect on the densities was observed. The "A" convection pattern was used initially to obtain the diurnally reproducible densities, and then at 2100 UT the pattern was changed to the "DE" pattern and one-half hour later it was changed back to the "A" pattern. Both of these convection patterns are for B_y negative, but for the "A" pattern the antisunward convection is fairly uniform at about 500 m/s (Figure 5a). In contrast, the "DE" pattern displays a sharp asymmetry in the polar cap with enhanced convection (1 km/s) in the dusk sector and reduced convection (< 200 m/s) in the dawn sector.

When the diurnally reproducible densities were obtained with the "A" pattern, a fairly uniform tongue of ionization extended across the polar cap from the dayside to the nightside (not

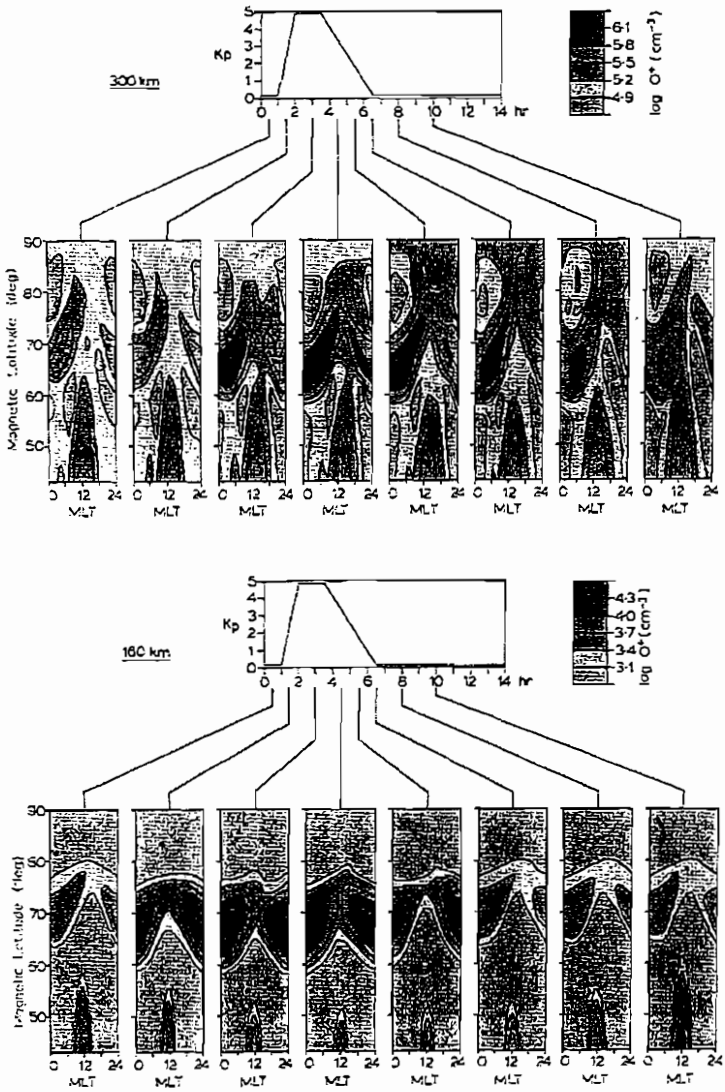

Figure 4. O^+ density contours as a function of magnetic latitude and MLT for selected times at an altitude of 160 km (bottom panel) and 300 km (top panel). Note that the density contours cover two orders of magnitude in the bottom panel. From *Sojka and Schunk* [1983].

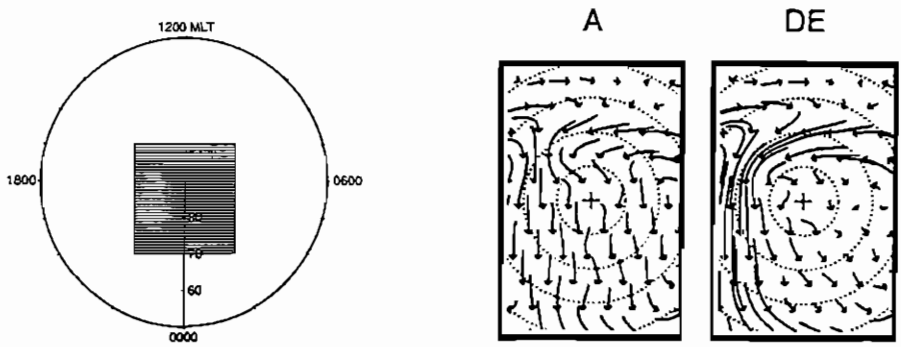

Figure 5a. A segment of the spatial grid used in the high-resolution plasma patch simulation (left dial). The flow directions in the grid segment for the Heppner-Maynard "A" and "DE" convection patterns (right side). From *Sojka et al.* [1993].

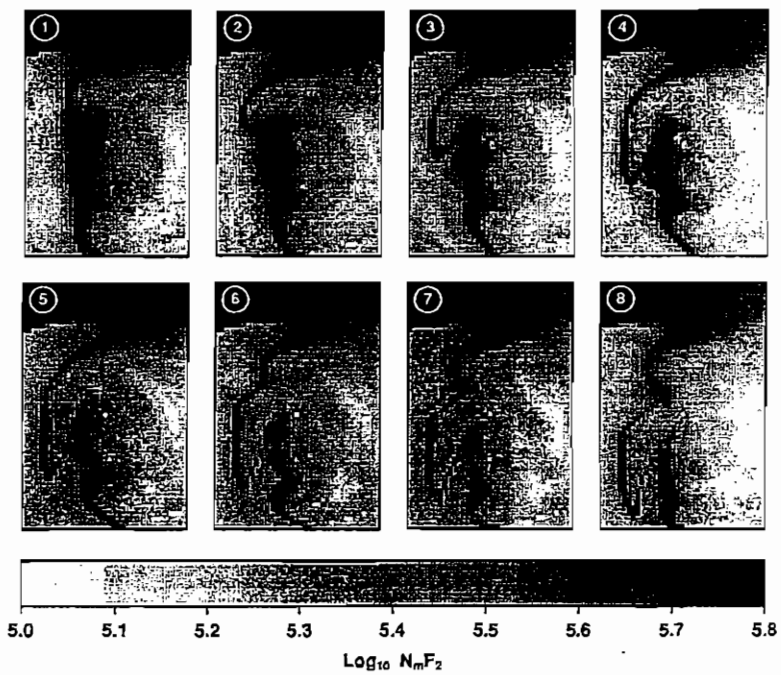

Figure 5b. N_mF_2 distributions at selected times during the plasma patch simulation. N_mF_2 is shown only in the spatial grid of Figure 5a. The panels labeled 1 to 8 correspond to successive snapshots starting at 2100 UT and separated by 7.5 minutes. Prior to Panel 1, the "A" convection pattern existed, for panels 1-4 the "DE" pattern existed, and for panels 5-8 the "A" pattern existed. From *Sojka et al.* [1993].

shown). However, after the convection pattern changes to the "DE" pattern at 2100 UT (Figure 5b, panel 1), a segment of the tongue breaks off, forming a plasma patch, which then convects across the dark polar cap toward midnight. At 2130 UT (Panel 5), the convection pattern reverts back to the "A" pattern and a new uniform tongue of ionization starts to form near noon. However, the detached plasma patch from the original tongue continues to convect across the dark polar cap. From this and other simulations, we conclude that plasma patches can easily be created as a result of time-varying magnetospheric electric fields.

6. Model Uncertainties And Limitations

Over the years, we have conducted numerous model/data comparisons in an effort to validate the chemical and physical processes contained in the model. The validations were relevant to *E*-region, *F*-region, and topside ionospheric features as well as to high-, mid, and low latitude domains in both the northern and southern hemispheres. Data from the AE-C, DMSP F2 and F4, and NOAA satellites were used in some of the comparisons [*Sojka et al.*, 1981, 1982, 1985, 1991]. In other model/data comparisons, data from the Chatanika, Sondre Strom, Millstone Hill and Arecibo incoherent scatter radars were used [*Sojka et al.*, 1983; *Murdin et al.*, 1984; *Rasmussen et al.*, 1986, 1988a, b; *Sica et al.*, 1988]. Also, data from a large number of ionosondes were used in several studies [*Berkey et al.*, 1987; *Sojka et al.*, 1988, 1990; *Wilkinson et al.*, 1988; *Sica et al.*, 1990; *Szuszczewicz et al.*, 1992]. In some of the model/data comparisons, extensive multi-year data sets from a single site were used, while in other comparisons, simultaneous data from multiple sites spread around the world were used. The specific details of the various model/data comparisons are given in a recent review by *Sojka* [1989]. The main conclusions from all of these comparisons are as follows:

1. To a large extent, the reliability of the calculated ionospheric parameters depends on the accuracy to which the global inputs can be specified. The ionospheric model is most sensitive to the magnetospheric electric field and particle precipitation inputs at high latitudes, the thermospheric winds at mid-latitudes, and the equatorial (dynamo) electric fields at low latitudes.
2. The topside plasma scale heights can be significantly affected by the downward electron heat flux through the upper boundary, but this input is virtually unknown on a global scale.
3. Steep spatial gradients can lead to plasma instabilities and scintillations, but the ionospheric model does not take instabilities into account.
4. A supercomputer is needed for global simulations.

7. Model Availability

The ionospheric model is in the form of a large FORTRAN code, but the model is not user-friendly and must be run on a supercomputer. However, the model developers are willing to collaborate with interested scientists on both purely theoretical studies or model-data comparisons. Sufficient computer resources exist at USU for such collaborative efforts.

8. References

Berkey, F. T., et. al., Polar Res., 48, 278, 1987.
Conrad, J. R. and R. W. Schunk, J. Geophys. Res., 84, 811-822, 1979.
Crain, D. J., J. J. Sojka, R. W. Schunk, and L. Zhu, J. Geophys. Res., 98, 6151-6162, 1993.

Feldstein, Y. I. and G. V. Starkov, Planet Space Sci., 15, 209-229, 1967.
Foster, J. C., J. Geophys. Res., 88, 981-987, 1983.
Hardy, D. A., M. S. Gussenhoven and E. Holeman, J. Geophys. Res., 90, 4229-4248, 1985.
Hedin, A. E., J. Geophys. Res., 96, 1159-1172, 1991.
Hedin, A. E., et al., J. Geophys. Res., 96, 7657-7688, 1991.
Heelis, R. A., J. Geophys. Res., 89, 2873-2880, 1984.
Heelis, R. A., J. K. Lowell and R. W. Spiro, J. Geophys. Res., 87, 6339-6345, 1982.
Heppner, J. R. and N. C. Maynard, J. Geophys. Res., 92, 4467-4489, 1987.
Murdin, J., J. J. Sojka, and R. W. Schunk, Planet. Space Sci., 32, 47-61, 1984.
Murphy, J. A., G. J. Bailey, and R. J. Moffett, J. Atmos. Terr. Phys., 38, 351-364, 1976.
Preble, A. J., D. N. Anderson, B. G. Fejer, and P. H. Doherty, Radio Sci., 29, 857-866, 1994.
Rasmussen, C. E., R. W. Schunk, and V. B. Wickwar, J. Geophys. Res., 93, 9831-9840, 1988b.
Rasmussen, C. E., et al., J. Geophys. Res., 91, 6986-6998, 1986.
Rasmussen, C. E., et al., J. Geophys. Res., 93, 1922-1932, 1988a.
Richmond, A. D., et al., J. Geophys. Res., 85, 4658-4664, 1980.
Schunk, R. W., PAGEOPH, 127, 255-303, 1988.
Schunk, R. W., Planet. Space Sci., 23, 437-485, 1975.
Schunk, R. W. and A. F. Nagy, Rev. Geophys. Space Phys., 16, 355-399, 1978.
Schunk, R. W. and W. J. Raitt, J. Geophys. Res., 85, 1255-1272, 1980.
Schunk, R. W. and J. J. Sojka, J. Geophys. Res., 87, 5169-5183, 1982.
Schunk, R. W. and J. C. G. Walker, Planet. Space Sci., 18, 1535-1550, 1970.
Schunk, R. W. and J. C. G. Walker, Planet. Space Sci., 21, 1875-1896, 1973.
Schunk, R. W., W. J. Raitt, and P. M. Banks, J. Geophys. Res., 80, 3121-3130, 1975.
Schunk, R. W., P. M. Banks, and W. J. Raitt, J. Geophys. Res., 81, 3271-3282, 1976.
Schunk, R. W., J. J. Sojka, and M. D. Bowline, J. Geophys. Res., 91, 12041-12054, 1986.
Schunk, R. W., L. Zhu, and J. J. Sojka, Geophys. Res. Lett., 21, 1759-1762, 1994.
Sica, R. J., R. W. Schunk, and C. E. Rasmussen, J. Atmos. Terr. Phys., 50, 141-152, 1988.
Sica, R. J., R. W. Schunk, and P. J. Wilkinson, J. Geophys. Res., 95, 8271-8279, 1990.
Sojka, J. J., Rev. Geophys., 27, 371-403, 1989.
Sojka, J. J. and R. W. Schunk, J. Geophys. Res., 88, 2112-2122, 1983.
Sojka, J. J. and R. W. Schunk, J. Geophys. Res., 89, 2348-2358, 1984.
Sojka, J. J. and R. W. Schunk, J. Geophys. Res., 90, 5285-5298, 1985.
Sojka, J. J., W. J. Raitt, and R. W. Schunk, J. Geophys. Res., 86, 609-621, 1981a.
Sojka, J. J., W. J. Raitt, and R. W. Schunk, J. Geophys. Res., 86, 2206-2216, 1981b.
Sojka, J. J., R. W. Schunk, and J. A. Whalen, J. Geophys. Res., 95, 15275-15280, 1990.
Sojka, J. J., R. W. Schunk, and G. L. Wrenn, J. Atmos. Terr. Phys., 50, 1027-1039, 1988.
Sojka, J. J., W. J. Raitt, R. W. Schunk, F. L. Rich, and R. C. Sagalyn, J. Geophys. Res., 87, 1711-1718, 1982.
Sojka, J. J., R. W. Schunk, J. V. Evans, J. M. Holt, and R. H. Wand, J. Geophys. Res., 88, 7783-7793, 1983.
Sojka, J. J., J. W. Raitt, R. W. Schunk, J. L. Parrish, and F. J. Rich, Planet. Space Sci., 33, 1375-1382, 1985.
Sojka, J. J., R. W. Schunk, W. R. Hoegy, and J. M. Grebowsky, Adv. Space Res., 11, 39-42, 1991.
Sojka, J. J., et. al., Geophys. Res. Lett., 20, 1783-1786, 1993.
Spiro, R. W., P. H. Reiff and L. H. Maher, J. Geophys. Res., 87, 8215-8227, 1982.
Sterling, D. L., W. B. Hanson, R. J. Moffett, and R. G. Baxter, Radio Sci., 4, 1005-1023, 1969.
Strickland, D. J., D. L. Book, T. P. Coffey and J. A. Fedder, J. Geophys. Res., 81, 2755, 1976.

Strobel, D. F., C. B. Opal and R. R. Meier, Planet. Space Sci., 28, 1027-1033, 1980.
Szuszczewicz, E., et al., Adv. Space Res., 12, 105-115, 1992.
Torr, M. R. and D. G. Torr, J. Geophys. Res., 90, 6675, 1985.
Volland, H., J. Geophys. Res., 83, 2695-2699, 1978.
Wallis, P. D. and E. E. Budzinski, J. Geophys. Res., 86, 125-137, 1981.

A Low-Latitude Ionosphere-Plasmasphere Model

G. J. Bailey and N. Balan

School of Mathematics and Statistics, Applied Mathematics Section,
The University of Sheffield, The Hicks Building, Sheffield S3 7RH, United Kingdom

1. Introduction

Mathematical models have played an important role in the development of our present-day understanding of the physical and chemical processes taking place within the Earth's upper atmosphere. Since the early 1970s, many mathematical models, both simple and comprehensive, have been developed and applied to a wide variety of problems. Simple models are constructed from much-simplified theory and are commonly used in studies of specific idealized problems. Comprehensive models, on the other hand, are designed to reproduce the real situation as far as possible. The systems of mathematical equations, which describe the known physical and chemical processes, are highly non-linear and special numerical techniques are required for their solution. In contrast to simple models, extensive computation is required. Comprehensive models are extremely versatile with wide-ranging application; the model described in the present paper is of this type.

In most theoretical studies of the Earth's ionosphere and plasmasphere, a mathematical model which incorporates an axial-centered dipole representation for the geomagnetic field has been used [e.g., *Young et al.*, 1980; *Bailey and Sellek*, 1990]. Although these models are adequate for most applications, they cannot be used in a self-consistent way to study longitudinal differences in the distribution of ionization which are caused by the longitudinal differences in the configuration of the geomagnetic field. A more realistic representation of the geomagnetic field is included in the model of *Anderson* [1973a, b]. In the Anderson model, the geomagnetic field is represented by the cross product of the gradients of two scalar potentials expressed in terms of tilted dipole coordinates with coefficients obtained from a spherical harmonic expansion of the geomagnetic scalar potential [*Stern*, 1967]. In the model to be described in the present paper, the geomagnetic field is represented by an eccentric dipole, the magnetic field being defined by the first eight non-zero terms of the usual spherical harmonic expansion of the geomagnetic scalar potential with coefficients taken from IGRF 1985 [*Barraclough*, 1987]. The magnetic field model can be adapted to an axial-centered or tilted-centered dipole by truncating the spherical harmonic expansion after the first or third non-zero terms, respectively (see Section 2).

Although the model of the present paper is described in the context of the low-latitude region, the model is also applicable to higher latitudes provided the magnetic field lines are closed [e.g., *Rippeth et al.*, 1991; *Balmforth et al.*, 1994]. In the model, time-dependent equations of continuity, momentum, and energy balance are solved along closed magnetic field lines between altitudes of around 130 km (geographic) in conjugate hemispheres to give values for the concentrations, field-aligned velocities, temperatures of the O^+, H^+, He^+, N_2^+, O_2^+ and NO^+ ions, and the electrons.

The low-latitude ionosphere is characterized by a trough in the latitudinal distribution of ionization at the magnetic equator with crests at about $\pm 17^\circ$ magnetic latitude. This feature is known as the Equatorial Anomaly or the Appleton Anomaly. The anomaly results from the daytime east-west electric field at equatorial latitudes, which gives rise to an upward $\mathbf{E} \times \mathbf{B}$ drift. This upward drift drives the plasma across the magnetic field lines to higher altitudes. The plasma then diffuses downwards along the magnetic field lines under the influence of gravity

and pressure gradient forces. The net result is the formation of a plasma 'fountain,' centered at the magnetic equator, which transfers plasma from the equatorial region to higher latitudes. The fountain rises to several hundred kilometers at the magnetic equator. The latitudinal extent of the fountain and the equatorial anomaly can exceed $\pm 30°$ [*Balan and Bailey*, 1995].

The equatorial anomaly has been reviewed by several authors, e.g., *Rajaram* [1977], *Moffett* [1979], *Anderson* [1981], *Walker* [1981], and *Stening* [1992]. Particular features of the anomaly are that the crest-to-trough ratio of the anomaly (about 1.5 in peak electron density) and the latitudinal locations of the crests increase with increasing upward $\mathbf{E} \times \mathbf{B}$ drift and that the asymmetries in the anomaly about the magnetic equator are a consequence of F-region neutral winds [*Balan et al.*, 1995]. There is strong longitudinal variation in the equatorial anomaly [*Walker*, 1981]. Recently, *Su et al.* [1995] have modeled the longitudinal variation in the equatorial anomaly and have shown that the longitudinal variation of the north-south asymmetries are due to the longitudinal differences in the asymmetry of the neutral wind in the magnetic meridian. These differences arise from the longitudinal differences in the offset of the magnetic and geographic equators and in the magnetic declination angle.

2. The Magnetic Field

At low and mid-latitudes, the Earth's magnetic field can be represented, to a good approximation, by a dipole. In the simplest approximation, i.e., the axial-centered dipole approximation, the magnetic and geographic coordinate axes coincide. A more accurate representation of the Earth's magnetic field can be obtained by tilting the dipole. The 'best fit' between the tilted dipole (TD) approximation and the Earth's magnetic field is obtained by taking a dipole whose axis cuts the surface of the Earth at about 79° N, 71° W and 79° S, 109° E [*Fraser-Smith*, 1987]. A still more accurate representation can be obtained by displacing the dipole from the Earth's center by a distance of about 500 km in the direction 21° N, 147° E. This gives the eccentric dipole (ED) approximation. The ED axis cuts the surface of the Earth at about 82° N, 90° W and 75° S, 119° E [*Fraser-Smith*, 1987].

As the currents which produce the Earth's magnetic field, **B**, do not flow across the Earth's surface the field is 'curl free' at the surface and so may be obtained from a scalar potential γ, where $\mathbf{B} = -\text{grad}\,\gamma$. Also, since div $\mathbf{B} = 0$, γ satisfies Laplace's equation and may be expressed in terms of a spherical harmonic expansion of the form

$$\gamma = a \sum_{n=1}^{\infty} \sum_{m=0}^{n} \left(\frac{a}{r}\right)^{n+1} P_n^m(\cos\theta)(g_n^m \cos m\phi + h_n^m \sin m\phi) \tag{1}$$

where (r, θ, ϕ) denotes the location of a point in geographic coordinates with origin at the center of the Earth, r is the radial distance, θ is the colatitude (measured from the north polar axis), ϕ is the longitude measured eastward from the Greenwich meridian, a is the radius of the earth, P_n^m are associated Legendre functions (in Schmidt-normalized form), and g_n^m and h_n^m are Gauss coefficients [*Chapman and Bartels*, 1940]. Formulation (1) is used in the International Geomagnetic Reference Field (IGRF) [*Barraclough*, 1987]. Developments to IGRF since 1985 are described in a recent publication by its Working Group [*IAGA Division V Working Group 8*, 1992]. The axial-centered dipole approximation is given by

$$\gamma = a\left(\frac{a}{r}\right)^2 g_1^0 \cos\theta \tag{2}$$

and the tilted dipole approximation by

$$\gamma = a\left(\frac{a}{r}\right)^2 [g_1^0 \cos\theta + (g_1^1 \cos\phi + h_1^1 \sin\phi)\sin\theta] \tag{3}$$

The eccentric dipole approximation is defined by the first eight non-zero Gauss coefficients and is described in the following sections.

2.1 Transformations Between the Geographic and TD Coordinates

Let the position of a point P be denoted by (r, θ, ϕ) in geographic coordinates and (r, θ', ϕ') in tilted-dipole (TD) coordinates, where r is the same radial coordinate as in the geographic system, θ' is the colatitude measured from the north TD pole, and ϕ' is the longitude measured eastward from the meridian half-plane bounded by the dipole axis and containing the south geographic pole (see Figure 1). Also, let the coordinates of the north TD pole be denoted by (a, θ_n, ϕ_n) and the TD declination, i.e. the angle between geographic north and the north TD pole (taken to be positive when the TD pole is to the east of geographic north), by ψ. Then, since transformation between the geographic and TD coordinates requires only a rotation, it can be obtained by applying the sine and cosine rules to the spherical triangle defined by the point P, the north geographic pole N, and the north TD pole B (see Figure 2). The sine rule gives

$$\frac{\sin\theta'}{\sin(\phi - \phi_n)} = \frac{\sin\theta}{\sin(180^\circ - \phi')} = \frac{\sin\theta_n}{\sin(-\psi)} \tag{4}$$

and the cosine rule

$$\cos\theta_n = \cos\theta\cos\theta' + \sin\theta\sin\theta'\cos(-\psi) \tag{5}$$

$$\cos\theta' = \cos\theta_n\cos\theta + \sin\theta_n\sin\theta\cos(\phi - \phi_n) \tag{6}$$

$$\cos\theta = \cos\theta_n\cos\theta' + \sin\theta_n\sin\theta'\cos(180^\circ - \phi') \tag{7}$$

From these equations there follows

$$\theta' = \cos^{-1}[\cos\theta_n\cos\theta + \sin\theta_n\sin\theta\cos(\phi - \phi_n)] \tag{8}$$

$$\phi' = \cos^{-1}[-(\cos\theta - \cos\theta_n\cos\theta')/(\sin\theta_n\sin\theta')] \tag{9}$$

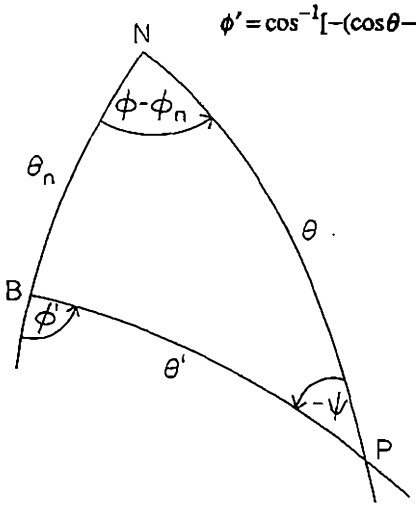

Figure 1. The spherical triangle used for the transformations between the geographic and TD coordinates; N denotes the north geographic pole, B the north TD pole (a, θ_n, ϕ_n), and P is a general point with geographic coordinates (r, θ, ϕ).

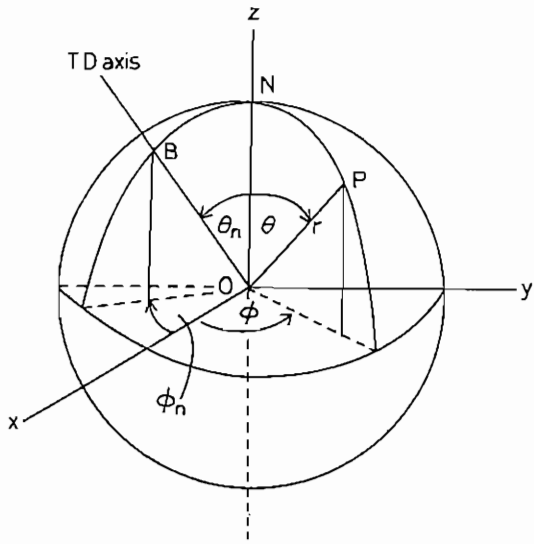

Figure 2. The geographically based spherical polar coordinate system (r, θ, ϕ) that is used as a reference for the TD coordinate system. In the associated Cartesian system (x, y, z), the positive x axis points toward the Greenwich meridian (0° longitude), the positive y axis points towards 90°E longitude, and the z axis points northward. The coincident origins for the two systems are located at the center of the Earth, O. Only the northern part of the TD axis is shown; it intersection B with the Earth's surface is the north TD pole (a, θ_n, ϕ_n), N is the north geographic pole, and P is a general point.

$$\phi' = \sin^{-1}[\sin\theta \sin(\phi - \phi_n) / \sin\theta'] \tag{10}$$

$$\psi = \cos^{-1}[(\cos\theta_n - \cos\theta\cos\theta')/(\sin\theta\sin\theta')] \tag{11}$$

$$\psi = \sin^{-1}[-\sin\theta_n \sin(\phi - \phi_n) / \sin\theta'] \tag{12}$$

Two equations are needed for ϕ' and ψ in order to avoid the ambiguity in angle when an inverse sine or cosine is evaluated. The inverse transformation from TD to geographic coordinates also follows from equations (4)–(7), i.e.

$$\theta = \cos^{-1}[\cos\theta_n \cos\theta' - \sin\theta_n \sin\theta' \cos\phi'] \tag{13}$$

$$\phi = \phi_n + \cos^{-1}[(\cos\theta' - \cos\theta_n \cos\theta)/(\sin\theta_n \sin\theta)] \tag{14}$$

$$\phi = \phi_n + \sin^{-1}[\sin\theta' \sin\phi' / \sin\theta] \tag{15}$$

The scalar potential for the TD field in terms of the dipole coordinates is given by

$$\gamma = -B_o a \left(\frac{a}{r}\right)^2 \cos\theta' \tag{16}$$

where B_o is given be equation (17). By combining equations (6) and (16) and then comparing with equation (3) there follows

$$B_o^2 = (g_1^0)^2 + (g_1^1)^2 + (h_1^1)^2 \tag{17}$$

$$\cos\theta_n = -g_1^0 / B_o \tag{18}$$

$$\tan\phi_n = h_1^1 / g_1^1 \tag{19}$$

Substitution of the IGRF 1985 Gauss coefficients (see Table 1) into equations (17)–(19) gives $B_o = 30438$ nT, $\theta_n = 11°$ and $\phi_n = -71°$.

Table 1. The first eight Gauss coefficients of IGRF 1985 (nT)

n	m	g_n^m	h_n^m
1	0	-29877	
1	1	-1903	5497
2	0	-2073	
2	1	3045	-2191
2	2	1691	-309

2.2 Transformations Between the TD and ED Coordinates

The eccentric dipole has the same moment as the tilted dipole and the same orientation of its axis, but is located away from the center of the Earth. The 'best' eccentric dipole approximation is obtained by minimizing the second order terms of the spherical harmonic expansion (1) [*Chapman and Bartels*, 1940]. In terms of the geographic Cartesian coordinates (x, y, z), the dipole is then located at the point (x_o, y_o, z_o), where

$$x_o = a(L_1 - g_1^1 E) / (3B_o^2) \tag{20}$$

$$y_o = a(L_2 - h_1^1 E) / (3B_o^2) \tag{21}$$

$$z_o = a(L_0 - g_1^0 E) / (3B_o^2) \tag{22}$$

and

$$L_0 = 2g_1^0 g_2^0 + \sqrt{3}(g_1^1 g_2^1 + h_1^1 h_2^1) \tag{23}$$

$$L_1 = -g_1^1 g_2^0 + \sqrt{3}(g_1^0 g_2^1 + g_1^1 g_2^2 + h_1^1 h_2^2) \tag{24}$$

$$L_2 = -h_1^1 g_2^0 + \sqrt{3}(g_1^0 h_2^1 - h_1^1 g_2^2 + g_1^1 h_2^2) \tag{25}$$

$$E = (L_0 g_1^0 + L_1 g_1^1 + L_2 h_1^1) / (4B_o^2) \tag{26}$$

and, in terms of geographic polar coordinates (d, θ, ϕ), by

$$d = (x_o^2 + y_o^2 + z_o^2)^{\frac{1}{2}} \tag{27}$$

$$\theta_o = \cos^{-1}(z_o / d) \tag{28}$$

$$\phi_o = \tan^{-1}(y_o / x_o) \tag{29}$$

Substitution of the IGRF 1985 Gauss coefficients into equations (20)–(22) gives $x_o = -392$ km, $y_o = 258$ km, and $z_o = 179$ km. The displacement of the dipole is $d = 502$ km and the direction of displacement is $\theta_o = 69°$, $\phi_o = 147°$.

The transformation between TD and ED coordinate axes involves only a translation, the directions of the Cartesian axes being the same. Thus, the equations relating the TD and ED coordinates are

$$x' = r\sin\theta'\cos\phi' = X + x'_o = R\sin\Theta\cos\Phi + x'_o \tag{30}$$

$$y' = r\sin\theta'\sin\phi' = Y + y'_o = R\sin\Theta\sin\Phi + y'_o \tag{31}$$

$$z' = r\cos\theta' = Z + z'_o = R\cos\Theta + z'_o \tag{32}$$

where the position of a point is given by (r, θ', ϕ') in TD polar coordinates, (x', y', z') in TD Cartesian coordinates, (R, Θ, Φ) in ED polar coordinates, and (X, Y, Z) in ED Cartesian coordinates. The location of the eccentric dipole, (x'_o, y'_o, z'_o), in terms of the TD coordinates (d, θ'_o, ϕ'_o), is given by

$$x'_o = d\sin\theta'_o\cos\phi'_o \tag{33}$$

$$y'_o = d\sin\theta'_o\sin\phi'_o \tag{34}$$

$$z'_o = d\cos\theta'_o \tag{35}$$

From equations (30)–(32) there follows

$$R = [(r\sin\theta'\cos\phi' - x'_o)^2 + (r\sin\theta'\sin\phi - y'_o)^2 + (r\cos\theta' - z'_o)^2]^{\frac{1}{2}} \tag{36}$$

$$\Theta = \tan^{-1}\left[\frac{[(r\sin\theta'\cos\phi' - x'_o)^2 + (r\sin\theta'\sin\phi' - y'_o)^2]^{\frac{1}{2}}}{r\cos\theta' - z'_o}\right] \tag{37}$$

$$\Phi = \tan^{-1}\left[\frac{r\sin\theta'\sin\phi' - y'_o}{r\sin\theta'\cos\phi - x'_o}\right] \tag{38}$$

and

$$r = [(R\sin\Theta\cos\Phi + x'_o)^2 + (R\sin\Theta\sin\Phi + y'_o)^2 + (R\cos\Theta + z'_o)^2]^{\frac{1}{2}} \tag{39}$$

$$\theta' = \tan^{-1}\left[\frac{[(R\sin\Theta\cos\Phi + x_o')^2 + (R\sin\Theta\sin\Phi + y_o')^2]^{\frac{1}{2}}}{R\cos\Theta + z_o'}\right] \tag{40}$$

$$\phi' = \tan^{-1}\left[\frac{R\sin\Theta\sin\Phi + y_o'}{R\sin\Theta\cos\Phi + x_o'}\right] \tag{41}$$

2.3 The Magnetic Field Vector

The magnetic field components B_r, B_θ, B_ϕ are determined from

$$\mathbf{B} = -\text{grad}\,\gamma \tag{42}$$

where γ is given, in terms of ED coordinates, by

$$\gamma = -B_o a\left(\frac{a}{R}\right)^2\cos\Theta \tag{43}$$

see equation (16). Thus, in ED coordinates the magnetic field is given by

$$B_R = -2B_o\left(\frac{a}{R}\right)^3\cos\Theta \tag{44}$$

$$B_\Theta = -B_o\left(\frac{a}{R}\right)^3\sin\Theta \tag{45}$$

$$B_\Phi = 0 \tag{46}$$

where

$$B = |\mathbf{B}| = B_o\left(\frac{a}{R}\right)^3(1+3\cos^2\Theta)^{\frac{1}{2}} \tag{47}$$

In order to determine the components B_r, B_θ, B_ϕ of the ED field in geographic coordinates the components B_X, B_Y, B_Z in ED Cartesian coordinates are first determined. As the transformation between the ED and TD coordinate systems involves only a translation, the directions of the TD and ED Cartesian axes are the same. Thus,

$$B_{x'} = B_X = B_R\sin\Theta\cos\Phi + B_\Theta\cos\Theta\cos\Phi \tag{48}$$

$$B_{y'} = B_Y = B_R\sin\Theta\sin\Phi + B_\Theta\cos\Theta\sin\Phi \tag{49}$$

$$B_{z'} = B_Z = B_R\cos\Theta - B_\Theta\sin\Theta \tag{50}$$

and

$$B_{r'} = B_{x'}\sin\theta'\cos\phi' + B_{y'}\sin\theta'\sin\phi' + B_{z'}\cos\theta' \tag{51}$$

$$B_{\theta'} = B_{x'}\cos\theta'\cos\phi' + B_{y'}\cos\theta'\sin\phi' - B_{z'}\sin\theta' \tag{52}$$

$$B_{\phi'} = -B_{x'}\sin\phi' + B_{y'}\cos\phi' \tag{53}$$

The final step is to determine the components in terms of the geographic coordinates. Since only a rotation is involved in transforming between the TD and geographic systems, the radial components are the same. The θ and ϕ components are determined by considering the spherical triangle on the Earth's surface shown in Figure 1. They are given by

$$B_r = B_{r'} \tag{54}$$

$$B_\theta = B_{\theta'}\cos\psi + B_{\phi'}\sin\psi \tag{55}$$

$$B_\phi = -B_{\theta'}\sin\psi + B_{\phi'}\cos\psi \tag{56}$$

Two important angles required by the model are the magnetic dip angle, I, and the magnetic declination angle, D. The magnetic dip angle is the angle the magnetic field lines make with the horizontal and is defined to be positive in the northern hemisphere and negative in the southern hemisphere. The magnetic declination angle is the angle between the magnetic field lines and geographic north in a horizontal plane and is defined to be positive in the eastward direction and negative in the westward direction. Thus,

$$\tan I = -\frac{B_r}{(B_\theta^2 + B_\phi^2)^{\frac{1}{2}}} \tag{57}$$

and

$$\tan D = -\frac{B_\phi}{B_\theta} \tag{58}$$

In the special case of a tilted-dipole representation, the magnetic field components are given by

$$B_r = -2B_o\left(\frac{a}{r}\right)^3\cos\theta' \tag{59}$$

$$B_\theta = -B_o\left(\frac{a}{r}\right)^3\sin\theta'\cos\psi \tag{60}$$

$$B_\phi = B_o\left(\frac{a}{r}\right)^3\sin\theta'\sin\psi \tag{61}$$

and ψ is the magnetic declination angle.

3. The Mathematical Formulation

The motion of the thermal plasma can be thought of as ambipolar diffusion parallel to the magnetic field with an additional $\mathbf{E}\times\mathbf{B}$ drift perpendicular to the magnetic field [*Kendall and Pickering*, 1967]. The $\mathbf{E}\times\mathbf{B}$ drift is such that all charged particles associated with a particular

magnetic flux tube are moved into a new magnetic flux tube. To avoid the notion of magnetic flux tubes moving, the terminology 'tubes of plasma' is used [*Murphy et al.*, 1980]. A tube of plasma has the same shape as a magnetic flux tube and is determined by specifying the amount of magnetic flux passing through it, or, equivalently, since the cross-sectional area is inversely proportional to the magnetic induction (see equation 47), by specifying the cross-sectional area at a particular altitude and L value. From this definition, as a tube of plasma moves to a new L value under $\mathbf{E} \times \mathbf{B}$ drift, the magnetic flux passing through it remains constant (follows from the condition div $\mathbf{B} = 0$). This necessitates a change in volume of the tube arising from the change in cross-sectional area. In this way, the $\mathbf{E} \times \mathbf{B}$ drift causes a compression or expansion of the plasma without any local changes in the magnetic field. The total content of charged particles within a tube of plasma can only change when there is a net production or loss within the tube or when there is a flow of plasma across the ends of the tube.

3.1 Ion Continuity Equations

The continuity equation for the ith ion ($i = O^+, H^+, He^+, N_2^+, O_2^+, NO^+$) is

$$\frac{dN_i}{dt} + \frac{1}{A}\frac{\partial A N_i v_i''}{\partial s} = P_i - \beta_i N_i - N_i \mathrm{div}\, \mathbf{v}_{em} \tag{62}$$

where

N_i = ion concentration,
t = time,
A = cross-sectional area of tube of plasma,
v_i'' = ion field-aligned velocity,
s = distance along magnetic field line (positive in the direction North to South),
P_i = ion production rate,
β_i = ion loss rate coefficient,
$\mathbf{v}_{em}$ = $\mathbf{E} \times \mathbf{B}$ drift velocity additional to corotation,

and

$$\frac{dN_i}{dt} = \frac{\partial N_i}{\partial t} + \mathbf{v}_{em} \cdot \mathrm{grad}\, N_i \tag{63}$$

The total time-derivative defined by equation (63) has been introduced because in the solution procedure a coordinate frame moving with an $\mathbf{E} \times \mathbf{B}$ drive velocity $\mathbf{v}_{em}$, additional to corotation, is considered. For a dipole magnetic field the cross-sectional-area A is inversely proportional to the magnetic field strength B (see equation 47).

If the meridional and zonal components of $\mathbf{v}_{em}$ in the ED coordinate frame are denoted by $\mathbf{v}^{\perp}$ and $\mathbf{v}^{\Phi}$, respectively, then

$$\mathbf{v}_{em} = \mathbf{v}^{\perp} + \mathbf{v}^{\Phi} \tag{64}$$

$$\mathbf{v}^{\perp} = |\mathbf{v}^{\perp}| = v_{eq}^{\perp} \frac{\sin^3 \Theta}{(1+3\cos^2\Theta)^{0.5}} \tag{65}$$

$$\mathbf{v}^{\Phi} = |\mathbf{v}^{\Phi}| = v_{eq}^{\Phi} \sin^3 \Theta \tag{66}$$

and

$$div\ \mathbf{v}_{em} = \frac{6v_{eq}^{\perp} \sin^2\Theta(1+\cos^2\Theta)}{R_{eq}(1+3\ \cos^2\Theta)^2} \tag{67}$$

where

$v_{eq}^{\perp}$ = equatorial value of $v^{\perp}$,
v_{eq}^{Φ} = equatorial value of v^{Φ},
R_{eq} = equatorial radial distance of magnetic field line.

In the model, ionization is produced by photoionization of the neutral gases by solar EUV radiation and by chemical reactions with the neutral gases. The solar EUV production of H^+ and NO^+ are not included, as they are negligible in comparison with the production from chemical processes. Ionization is lost through chemical reactions with the neutral gases. The chemical reactions and their rate coefficients are given in Table 2.

The production rate p_i of the ith ion by photoionization of the ith neutral gas is calculated from

$$p_i = \sum_{\lambda} \Phi(\lambda)\sigma_i(\lambda)n_i \exp\left(-\sum_j \sigma_j(\lambda)n_j H_j Ch_j(\chi)\right) \tag{68}$$

where

$\Phi(\lambda)$ = intensity of solar EUV flux radiation,
$\sigma_i(\lambda)$ = photoionization cross-section of the ith neutral gas,
n_i = concentration of the ith neutral gas,
$\sigma_j(\lambda)$ = photoabsorption cross-section of the jth neutral gas,
n_j = concentration of the jth neutral gas,
H_j = scale height of the jth neutral gas,
$Ch_j(\chi)$ = Chapman function of the jth neutral gas.

The summation $\sum_{\lambda}$ is over the wavelength range of the ionizing radiation and the summation $\sum_j$ is over the absorbing gases O, O_2 and N_2. The photoionization and photoabsorption cross-sections $\sigma_i(\lambda)$ and $\sigma_j(\lambda)$, respectively, are taken from *Torr and Torr* [1982] and are listed in Table 3. The solar EUV fluxes and the concentrations of the neutral gases are model inputs and are described in Section 5.

3.2 Ion Momentum Equations

In the formulation of the ion momentum equations the terms $\partial v_i/\partial t$ and $v_i(\partial v_i/\partial s)$ are neglected since at low latitudes and, in general, at mid-latitudes, the changes in plasma density are accompanied by relatively slow plasma flows [*Banks and Kockarts*, 1973]. Two formulations of the ion momentum equation are given, since a formulation of the thermal diffusion terms for more than three major ions has still to be developed. The first formulation (equation 69) is used for the O^+, H^+ and He^+ ions and includes the thermal diffusion terms derived by *Quegan et al.* [1981] for a fully-ionized plasma consisting of three major ions and electrons. The second formulation (equation 70) does not include the thermal diffusion terms and is used for the molecular ions N_2^+, O_2^+ and NO^+. Neglect of thermal diffusion in the molecular ions is justified since, in general, the molecular ions are in abundance only in the E

Table 2. Chemical reaction rates (cm^3s^{-1})

Reaction	Rate	Reference
$O^+ + N_2 \rightarrow NO^+ + N$	$1.533 \times 10^{-12} - 5.920 \times 10^{-13}\frac{T(O^+)}{300}$	
	$+8.600 \times 10^{-14}\left(\frac{T(O^+)}{300}\right)^2$	
	$300\ K \leq T(O^+) \leq 1700\ K$	*Torr and Torr* [1979]
	$2.730 \times 10^{-12} - 1.155 \times 10^{-12}\frac{T(O^+)}{300}$	
	$+1.483 \times 10^{-13}\left(\frac{T(O^+)}{300}\right)^2$	
	$1700\ K < T(O^+)$	*Torr and Torr* [1979]
$O^+ + O_2 \rightarrow O_2^+ + O$	$2.82 \times 10^{-11} - 7.74 \times 10^{-12}\frac{T(O^+)}{300}$	
	$+1.073 \times 10^{-12}\left(\frac{T(O^+)}{300}\right)^2$	
	$-5.17 \times 10^{-14}\left(\frac{T(O^+)}{300}\right)^3$	
	$+9.65 \times 10^{-16}\left(\frac{T(O^+)}{300}\right)^4$	*Torr and Torr* [1979]
$O^+ + H \rightarrow H^+ + O$	$2.5 \times 10^{-11}\ T_n^{0.5}$	*Raitt et al.* [1975]
$H^+ + O \rightarrow O^+ + H$	$\frac{8}{9} \times 2.5 \times 10^{-11}\ T^{0.5}(H^+)$	*Raitt et al.* [1975]
$He^+ + N_2 \rightarrow He + N_2^+$		
$\rightarrow He + N^+ + N$	1.2×10^{-9}	*Ferguson* [1973]
$He^+ + O_2 \rightarrow He + O^+ + O$	1.1×10^{-9}	*Ferguson* [1973]
$N_2^+ + O \rightarrow NO^+ + N$	$1.4 \times 10^{-10}\left(\frac{300}{T(O^+)}\right)^{0.44}$	*Torr and Torr* [1979]
$O_2^+ + e \rightarrow O + O$	$1.6 \times 10^{-7}\left(\frac{300}{T_e}\right)^{0.55}$	*Torr and Torr* [1979]
$O_2^+ + NO \rightarrow NO^+ + O_2$	4.4×10^{-10}	*Torr and Torr* [1979]
$NO^+ + e \rightarrow N + O$	$4.2 \times 10^{-7}\left(\frac{300}{T_e}\right)^{0.85}$	*Torr and Torr* [1979]

Table 3. Photoionization and photoabsorption cross-sections (10^{-18} cm^2)

		Photoionization				Photoabsorption		
	Wavelength Å	O	He	N_2	O_2	O	N_2	O_2
1	50–100	1.06	0.21	0.60	1.18	1.06	0.60	1.18
2	100–150	3.53	0.53	2.32	3.61	3.53	2.32	3.61
3	150–200	5.96	1.02	5.40	7.27	5.96	5.40	7.27
4	200–250	7.55	1.71	8.15	10.50	7.55	8.15	10.50
5	256.3	8.43	2.16	9.65	12.80	8.43	9.65	12.80
6	284.15	9.26	2.67	10.60	14.80	9.26	10.60	14.80
7	250–300	8.78	2.38	10.08	13.65	8.78	10.08	13.65
8	303.81	9.70	3.05	11.58	15.98	9.70	11.58	15.98
9	303.78	9.78	3.05	11.60	16.00	9.72	11.60	16.00
10	300–350	10.03	3.65	14.60	17.19	10.03	14.60	17.19
11	368.07	10.84	4.35	18.00	18.40	10.84	18.00	18.40
12	350–400	10.70	4.25	17.51	18.17	10.70	17.51	18.17
13	400–450	11.21	5.51	21.07	19.39	11.21	21.07	19.39
14	465.12	11.25	6.53	21.80	20.40	11.25	21.80	20.40
15	450–500	11.64	7.09	21.85	21.59	11.64	21.85	21.59
16	500–550	11.91	0.72	24.53	24.06	11.91	24.53	24.06
17	554.37	12.13	0.00	24.69	25.59	12.13	24.69	25.59
18	584.33	12.17	0.00	23.20	22.00	12.17	23.20	22.00
19	550–600	11.90	0.00	22.38	25.04	11.90	22.38	25.04
20	609.76	12.23	0.00	23.10	26.10	12.23	23.10	26.10
21	629.73	12.22	0.00	23.20	25.80	12.22	23.20	25.80
22	600–650	12.21	0.00	23.22	25.94	12.21	23.22	26.02
23	650–700	10.04	0.00	25.06	22.05	10.04	29.75	26.27
24	703.31	11.35	0.00	23.00	23.00	11.35	26.30	25.00
25	700–750	8.00	0.00	23.20	23.81	8.00	30.94	29.05
26	765.15	4.18	0.00	23.77	8.59	4.18	35.36	21.98
27	770.41	4.18	0.00	18.39	9.69	4.18	26.88	25.18
28	789.36	4.28	0.00	10.18	11.05	4.28	19.26	26.66
29	750–800	4.23	0.00	16.75	9.39	4.23	30.71	27.09
30	800–850	4.38	0.00	0.00	6.12	4.38	15.05	20.87
31	850–900	4.18	0.00	0.00	4.69	4.18	46.63	9.85
32	900–950	2.12	0.00	0.00	9.34	2.12	16.99	15.54
33	977.62	0.00	0.00	0.00	2.50	0.00	0.70	4.00
34	950–1000	0.00	0.00	0.00	12.22	0.00	36.16	16.53
35	1025.72	0.00	0.00	0.00	1.00	0.00	0.00	1.60
36	1031.91	0.00	0.00	0.00	0.00	0.00	0.00	1.00
37	1000–1050	0.00	0.00	0.00	0.27	0.00	0.00	1.10

and F regions where their distributions are dominated by chemical production (including production from photoionization of the neutral gases) and loss processes.

The momentum equation for the ith ion ($i = O^+, H^+, He^+$) is

$$
\begin{aligned}
0 = & -g\sin I - \frac{kT_i}{m_i N_i}\frac{\partial N_i}{\partial s} - \frac{kT_e}{m_i N_e}\frac{\partial N_e}{\partial s} - \frac{k}{m_i}\frac{\partial (T_e + T_i)}{\partial s} \\
& - \frac{k}{m_i}\beta_i \frac{\partial T_i}{\partial s} + \frac{k}{m_i}\beta_{ij}^* \frac{\partial T_j}{\partial s} + \frac{k}{m_i}\beta_{ik}^* \frac{\partial T_k}{\partial s} \\
& - [\nu_{ij}(1-\Delta_{ij}) - R_{ijk} + R_{ikj}](v_i'' - v_j'') \\
& - [\nu_{ik}(1-\Delta_{ik}) - R_{ikj} + R_{ijk}](v_i'' - v_k'') \\
& - \sum_m \nu_{im}(v_i'' - v_m'') - \sum_n \nu_{in}(v_i'' - u_\theta \cos D \cos I + u_\phi \sin D \cos I)
\end{aligned}
\tag{69}
$$

where

g = acceleration due to gravity,
k = Boltzmann's constant,
m_i = ion mass,
T_i = ion temperature,
T_e = electron temperature,
N_e = electron concentration,
ν_{im} = collision frequency for momentum transfer between the ith ion and the mth molecular ion,
ν_{in} = collision frequency for momentum transfer between the ith ion and the nth neutral gas,
u_θ = meridional component, in the geographic coordinate frame, of the neutral air wind velocity (positive in the direction North to South),
u_ϕ = zonal component, in the geographic coordinate frame, of the neutral air wind velocity (positive in the direction West to East),

The summation $\sum_m$ is over the molecular ions and the summation $\sum_n$ is over the neutral gases. The quantities β_i, β_{ij}^* and β_{ik}^* are thermal diffusion coefficients and the quantities Δ_{ij}, Δ_{ik}, R_{ijk}, and R_{ikj} are correction factors for the ith ion diffusion coefficient (see Section 3.3). Assignment of the subscripts i, j, and k is as follows: when $i = O^+$ then $j = H^+$ and $k = He^+$, when $i = H^+$ then $j = O^+$ and $k = He^+$, and when $i = He^+$ then $j = O^+$ and $k = H^+$. The collision frequencies for momentum transfer between the different ion species are determined from equation (71) and the collision frequencies for momentum transfer between the ions and the neutrals are given in Table 4.

Table 4. Collision frequencies for momentum transfer between the ions and neutrals (s^{-1})

O^+ collision frequencies	
ν_{O+O}	$4.45 \times 10^{-11} n(O) T^{0.5} (1.04 - 0.067 \log_{10} T)^2, \quad T = (T(O^+) + T_n)/2$
ν_{O+O_2}	$6.64 \times 10^{-10} n(O_2)$
ν_{O+N_2}	$6.82 \times 10^{-10} n(N_2)$
H^+ collision frequencies	
ν_{H+O}	$6.61 \times 10^{-11} n(O) T^{0.5} (H^+)(1 - 0.047 \log_{10} T(H^+))^2$
ν_{H+O_2}	$3.20 \times 10^{-9} n(O_2)$
ν_{H+N_2}	$3.36 \times 10^{-9} n(N_2)$
He^+ collision frequencies	
ν_{He+O}	$1.01 \times 10^{-9} n(O)$
ν_{He+O_2}	$1.53 \times 10^{-9} n(O_2)$
ν_{He+N_2}	$1.60 \times 10^{-9} n(N_2)$
N_2^+ collision frequencies	
ν_{N+O}	$2.58 \times 10^{-10} n(O)$
$\nu_{N_2^+O_2}$	$4.49 \times 10^{-10} n(O_2)$
$\nu_{N_2^+N_2}$	$5.14 \times 10^{-11} n(N_2) T^{0.5} (1 - 0.069 \log_{10} T)^2, \quad T = (T(N_2^+) + T_n)/2$
O_2^+ collision frequencies	
$\nu_{O_2^+O}$	$2.31 \times 10^{-10} n(O)$
$\nu_{O_2^+O_2}$	$2.59 \times 10^{-11} n(O_2) T^{0.5} (1 - 0.073 \log_{10} T)^2, \quad T = (T(O_2^+) + T_n)/2$
$\nu_{O_2^+N_2}$	$4.13 \times 10^{-10} n(N_2)$
NO^+ collision frequencies	
ν_{NO+O}	$2.44 \times 10^{-10} n(O)$
ν_{NO+O_2}	$4.27 \times 10^{-10} n(O_2)$
ν_{NO+N_2}	$4.34 \times 10^{-10} n(N_2)$

The momentum equation for the ith molecular ion ($i = N_2^+, O_2^+, NO^+$) is

$$0 = -g\sin I - \frac{kT_i}{m_i N_i}\frac{\partial N_i}{\partial s} - \frac{kT_e}{m_i N_e}\frac{\partial N_e}{\partial s} - \frac{k}{m_i}\frac{\partial (T_e + T_i)}{\partial s} - \sum_{j\neq i} \nu_{ij}(v_i'' - v_j'') - \sum_n \nu_{in}(v_i'' - u_\theta \cos D\cos I + u_\phi \sin D\cos I) \tag{70}$$

where the summation $\sum_{j\neq i}$ is over all the ions except the ith.

3.3 Thermal Diffusion Terms and Ion-Ion Collision Frequencies

The collision frequency for momentum transfer between the ions s and t (in cgs units) is given by [*Quegan et al.*, 1981]

$$\nu_{st} = 1.27\frac{A_{st}^{0.5}}{A_s T_{st}^{1.5}} n_t \tag{71}$$

where

n_t = concentration,
A_s = mass in a.m.u.,
$A_{st} = \dfrac{A_s A_t}{A_s + A_t}$ = reduced mass in a.m.u.,
$T_{st} = \dfrac{m_s T_t + m_t T_s}{m_s + m_t}$ = reduced temperature,
m_s = mass.

The thermal diffusion coefficients and correction factors required by the ion momentum equation (69) are determined from the expressions [*Quegan et al.*, 1981]

$$\beta_s = \frac{15}{8(1-\xi)}\frac{kT_s}{m_s \nu_s'} Y_{stu} \tag{72}$$

$$\beta_{st}^* = \frac{15}{8(1-\xi)}\frac{m_s}{m_t}\frac{kT_t}{m_t \nu_t'} Z_{stu} \tag{73}$$

$$\Delta_{st} = \frac{2}{5}\left(C_{st}\beta_s + \frac{n_s}{n_t} C_{ts}\beta_{st}^*\right) \tag{74}$$

$$R_{stu} = \frac{2}{5}\frac{m_t}{m_s}\nu_{tu} C_{tu}\beta_{st}^* \tag{75}$$

where

$$\xi = \xi_{st} + \xi_{tu} + \xi_{us} + \frac{\nu'_{st}\nu'_{tu}\nu'_{us} + \nu'_{ts}\nu'_{ut}\nu'_{su}}{\nu'_s\nu'_t\nu'_u} \tag{76}$$

$$\xi_{st} = \frac{\nu'_{st}\nu'_{ts}}{\nu'_s\nu'_t} = \xi_{ts} \tag{77}$$

$$\nu'_s = \nu_{ss} + \frac{5}{4}\nu_{st}\left[D^{(1)}_{st} + \frac{3}{2}\frac{A_{st}T_s}{A_sT_{st}}\right] + \frac{5}{4}\nu_{su}\left[D^{(1)}_{su} + \frac{3}{2}\frac{A_{su}T_s}{A_sT_{su}}\right] \tag{78}$$

$$\nu'_{st} = \frac{5}{4}\nu_{st}\left[D^{(4)}_{st} + \frac{3}{2}\frac{A_{st}T_s}{A_sT_{st}}\right] \tag{79}$$

$$D^{(1)}_{st} = 3\left(\frac{A_{st}T_t}{A_tT_{st}}\right)^2 - B^{(1)}_{st} - \frac{1}{5}B^{(3)}_{st} + \frac{A_{st}}{A_s + A_t}\frac{T_t}{T_{st}}\left[\frac{8}{5} - \frac{3}{2}\frac{T_s}{T_{st}}\right] \tag{80}$$

$$D^{(4)}_{st} = 3\left(\frac{A_{st}T_s}{A_sT_{st}}\right)^2 + B^{(2)}_{st} - \frac{1}{5}B^{(3)}_{st} - \frac{A_{st}}{A_s + A_t}\frac{T_s}{T_{st}}\left[\frac{8}{5}\frac{A_t}{A_s} + \frac{3}{2}\frac{T_t}{T_{st}}\right] \tag{81}$$

$$B^{(1)}_{st} = -\frac{1}{5}\frac{A^2_{st}}{A_s(A_s + A_t)}\frac{T_t - T_s}{T_{st}}\left[4 + 3\frac{A_s}{A_t}\frac{T_t}{T_{st}}\right] \tag{82}$$

$$B^{(2)}_{st} = \frac{1}{5}\frac{A^2_{st}}{A_s(A_s + A_t)}\frac{T_t - T_s}{T_{st}}\left[4 - 3\frac{T_s}{T_{st}}\right] \tag{83}$$

$$B^{(3)}_{st} = \left(\frac{A_{st}}{A_s}\right)^2\left[1 + 3\left(\frac{A_{st}}{A_t}\right)^2\left(\frac{T_t - T_s}{T_{st}}\right)^2\right] \tag{84}$$

$$C_{st} = \frac{5}{2} - \frac{A_{st}}{A_t}\left[\frac{5}{2}\frac{T_t}{T_{st}} + \frac{A_tT_{st}}{A_sT_s} - \frac{T_t - T_s}{T_s}y_{st}\right] \tag{85}$$

$$y_{st} = \frac{A_{st}}{A_s}\left[4 - 5\frac{T_s}{T_{st}} - 3\frac{A_{st}}{A_t}\frac{T_t - T_s}{T_{st}}\right] \tag{86}$$

$$Y_{stu} = \phi_{st}W_{tsu} + \phi_{su}W_{ust} = Y_{sut} \tag{87}$$

$$Z_{stu} = \phi_{st}W_{stu} - \phi_{su}X_{stu} = \phi_{st}W_{stu} + \phi_{su}X_{uts} \tag{88}$$

$$W_{stu} = 1 - \xi_{su} - V_{stu} \tag{89}$$

$$V_{stu} = \frac{\nu'_{st}}{\nu'_s} + \frac{\nu'_{su}\nu'_{ut}}{\nu'_s\nu'_u} \tag{90}$$

$$X_{stu} = V_{stu} - V_{uts} = -X_{uts} \tag{91}$$

$$\phi_{st} = \frac{\nu_{st}\mu_{st}}{kT_{st}} \tag{92}$$

$$\mu_{st} = \frac{m_s m_t}{m_s + m_t} \tag{93}$$

3.4 Electron Equations

For the electrons, it is assumed that charge neutrality is preserved, i.e.

$$N_e = \sum_i N_i \tag{94}$$

and that there are no field-aligned currents, i.e.

$$N_e v''_e = \sum_i N_i v''_i \tag{95}$$

where v''_e denotes the field-aligned electron velocity and $\sum_i$ denotes summation over the ions.

3.5 Energy Balance Equations

The energy balance equation for the ith constituent ($i = O^+, H^+, He^+, e$, where e denotes electrons) is

$$\frac{3}{2}kN_i\left(\frac{dT_i}{dt} + v''_i\frac{\partial T_i}{\partial s}\right) = Q_i - kN_iT_i\left(\frac{1}{A}\frac{\partial A v''_i}{\partial s} + div\, \mathbf{v}_{em}\right) + \frac{1}{A}\frac{\partial}{\partial s}\left(A\kappa_i\frac{\partial T_i}{\partial s}\right) + F_{in} \tag{96}$$

where

Q_i = collisional heating rate,
κ_i = thermal conductivity,
F_{in} = frictional heating,

and

$$\frac{dT_i}{dt} = \frac{\partial T_i}{\partial t} + \mathbf{v}_{em} \cdot \text{grad}\, T_i \tag{97}$$

Energy balance equations for the molecular ions are not included in the model, as their temperature is taken to be that of the O^+ ions.

The term F_{in} gives the frictional heating due to the relative motion between the ith ion and neutral gases and is given by

$$F_{in} = \sum_n \frac{m_i m_n}{m_i + m_n} \nu_{in} N_i \{(v_i'' - u_\theta \cos D \cos I + u_\phi \sin D \cos I)^2 + (v^\perp - u_\theta \sin D \sin I + u_\phi \cos D \sin I)^2 + (v^\Phi)^2\} \quad (98)$$

where m_n denotes the mass of the nth neutral constituent and the summation Σ is over the neutral constituents. The frictional heating term F_{en}, due to relative motion between the electrons and neutrals, is not included in the energy balance equation as it is negligible when compared with the other terms of the equation.

The thermal conductivities κ_i and κ_e (eV cm^{-1}s^{-1}K^{-1}) of the ith ion and electrons, respectively, are evaluated from the expressions

$$\kappa_i = \frac{4.6 \times 10^4 N_i}{A_i^{0.5} N_e} T_i^{2.5} \quad (99)$$

[*Banks and Kockarts*, 1973], where A_i is the ion mass in a.m.u., and

$$\kappa_e = \frac{7.7 \times 10^5 T_e^{2.5}}{\left[1 + \frac{3.22 \times 10^4 T_e^2}{N_e} [q(O)n(O) + q(N_2)n(N_2) + q(O_2)n(O_2)]\right]} \quad (100)$$

where

$$q(O) = 1.1 \times 10^{-16}(1 + 5.7 \times 10^{-4} T_e)$$

$$q(N_2) = 2.82 \times 10^{-17} T_e^{1/2}(1 - 1.21 \times 10^{-4} T_e)$$

$$q(O_2) = 2.2 \times 10^{-16}(1 + 3.6 \times 10^{-2} T_e^{0.5})$$

[*Schunk and Nagy*, 1978]; $n(O)$, $n(N_2)$ and $n(O_2)$ are the concentrations of the atmospheric constituents O, N_2 and O_2, respectively.

The heating rates Q_i ($i = O^+, H^+, He^+$) are determined from

$$Q_i = Q_{ie} + \sum_{j \neq i} Q_{ij} + Q_{in}^{el} + Q_{in} \quad (101)$$

and the heating rate Q_e from

$$Q_e = Q_{ph.e} + \sum_j Q_{ej} + Q_{en}^{rot} + Q_{en}^{vib} + Q_{en}^{f} \quad (102)$$

where $\sum_j$ denotes summation over the ions and $\sum_{j\neq i}$ denotes summation over the ions except for the ith. The terms Q_{in} and Q_{in}^{el} are given in Table 5, the terms Q_{en}^{rot}, Q_{en}^{vib} and Q_{en}^{f} in Table 6, and the terms Q_{ie}, Q_{ei} ($=-Q_{ie}$) and Q_{ij} (eV cm^{-3}s^{-1}) are evaluated from the expressions

$$Q_{ie} = 7.7\times10^{-6} N_e N_i \frac{(T_e - T_i)}{A_i T_e^{1.5}} \tag{103}$$

and

$$Q_{ij} = \frac{3.3\times10^{-4} N_i N_j (T_i - T_j)}{A_i A_j \left[\frac{T_i}{A_i} + \frac{T_j}{A_j}\right]^{1.5}} \tag{104}$$

[*Banks and Kockarts*, 1973], respectively.

Table 5. Ion collisional heating rates (eV cm^{-3}s^{-1})

O^+ heating rates		
$Q_{O^+n}^{el}$	Elastic collisions with neutrals	$[2.1\times10^{-15}n(O)(T(O^+)+T_n)^{0.5} + 3.3\times10^{-14}n(H)$ $+6.6\times10^{-14}n(N_2) + 5.8\times10^{-14}n(O_2)$ $+2.8\times10^{-14}n(He)]N(O^+)(T_n - T(O^+))$
Q_{O+H}	Inelastic collisions with neutral H	$3.8\times10^{-15}T_n^{0.5}n(H)N(O^+)$ $\times\left(\frac{8n(O)N(H^+)}{9n(H)N(O^+)}T_n^{0.5}T^{0.5}(H^+) - T(O^+)\right)$
H^+ heating rates		
$Q_{H^+n}^{el}$	Elastic collisions with neutrals	$[1.4\times10^{-14}n(H)(T(H^+)+T_n)^{0.5} + 3.5\times10^{-14}n(O)$ $+3.1\times10^{-14}n(N_2) + 2.8\times10^{-14}n(O_2)$ $+5.5\times10^{-14}n(He)]N(H^+)(T_n - T(H^+))$
Q_{H+O}	Inelastic collisions with neutral O	$3.4\times10^{-15}T^{0.5}(H^+)n(O)N(H^+)$ $\times\left(\frac{9n(H)N(O^+)}{8n(O)N(H^+)}T_n^{1.5}T^{-0.5}(H^+) - T(H^+)\right)$
He^+ heating rates		
$Q_{He^+n}^{el}$	Elastic collisions with neutrals	$[4.0\times10^{-15}n(He)(T(He^+)+T_n)^{0.5} + 5.7\times10^{-14}n(O)$ $+5.3\times10^{-14}n(N_2) + 4.5\times10^{-14}n(O_2)$ $+1.0\times10^{-13}n(H)]N(He^+)(T_n - T(He^+))$

Table 6. Electron collisional heating rates (eV $cm^{-3}s^{-1}$)

Electron heating rates		
Q_{en}^{rot}	rotational	$[7.0 \times 10^{-14} n(O_2) + 2.8 \times 10^{-14} n(N_2)] N_e (T_n - T_e) T_e^{-0.5}$
Q_{en}^{vib}	vibrational	$-5.196 \times 10^{-13} N_e n(O_2) \exp\left(f \frac{T_e - 700}{700\ T_e}\right)$ $\times \left[1 - \exp\left(-2770 \frac{T_e - T_n}{2000\ T_e}\right)\right]$ $-2.99 \times 10^{-12} N_e n(N_2) \exp\left(g \frac{T_e - 2000}{2000\ T_e}\right)$ $\times \left[1 - \exp\left(-h \frac{T_e - T_n}{T_e T_n}\right)\right]$ $f = 3300 - 839\ \sin[1.91 \times 10^{-4}(T_e - 2700)]$ $g = 1.06 \times 10^4 + 7.51 \times 10^3 \tanh[1.1 \times 10^{-3}(T_e - 1800)]$ $h = 3300 + 1.233(T_e - 1000) - 2.056 \times 10^{-4}(T_e - 1000)(T_e - 4000)$
Q_{en}^{f}	Fine structure	$-8.629 \times 10^{-6} \frac{N_e n(O)}{Z} \sum_{i=1}^{3} A_i C_i T_e^{(B_i - 0.5)}$ $\times \left\{ \epsilon (E_{xi} - D_{xi}) + 5.91 \times 10^{-9} (T_e - T_n) \right.$ $\left. \times \left[(1 + B_i) D_{xi} + \left(\frac{E_i}{T_e} + 1 + B_i \right) E_{xi} \right] \right\}$ $Z = 5 + 3\ \exp\left(-\frac{228}{T_1}\right) + \exp\left(-\frac{326}{T_0}\right)$ $T_0 = T_n \quad T_1 = T_n$

$\epsilon_1 = 0.02$	$\epsilon_2 = 0.028$	$\epsilon_3 = 0.008$
$A_1 = 7.883 \times 10^{-6}$	$A_2 = 9.466 \times 10^{-6}$	$A_3 = 1.037 \times 10^{-8}$
$B_1 = 1.021$	$B_2 = 0.8458$	$B_3 = 1.633$
$C_1 = 1.009$	$C_2 = 0.9444$	$C_3 = 1.466$
$E_1 = 228$	$E_2 = 326$	$E_3 = 98$

$D_{x1} = \exp\left(-\frac{228}{T_1}\right) \quad D_{x2} = \exp\left(-\frac{326}{T_0}\right) \quad D_{x3} = \exp\left(-\frac{326}{T_0}\right)$

$E_{x1} = \exp\left(-\frac{228}{T_e}\right) \quad E_{x2} = \exp\left(-\frac{326}{T_e}\right)$

$E_{x3} = \exp\left(-\frac{98}{T_e} - \frac{228}{T_1}\right)$

The term $Q_{ph.e}$ denotes the heating rate of the electron gas by energetic photoelectrons. These photoelectrons are produced by photoionization of the neutral gases and lose energy by collisions with the ambient electrons, ions, and neutral gases. Below about 300 km altitude, most of the energy is lost locally, but above this altitude the energetic photoelectrons are able to escape along the magnetic field lines to heat the ambient electron gas at the higher altitudes and, if the photoelectrons are sufficiently energetic, the conjugate hemisphere. The electron heating rate is found from the model developed by Richards and coworkers [*Young et al.*, 1980; *Torr et al.*, 1990]. This model uses the two-stream approximation method of *Nagy and Banks* [1970] and includes interhemispheric transport of photoelectrons.

4. Solution of Equations

4.1 Transformation to Dipole Coordinates

In Section 3, the model equations have been formulated for a dipole magnetic field line in terms of the physical coordinates L, s, and t, where $L = R_{eq}/a$, s is distance along the magnetic field line, and t the time. These coordinates, however, are not orthogonal and to work with such coordinates when v_{em}, the $\mathbf{E} \times \mathbf{B}$ drift velocity additional to corotation, is non-zero introduces unnecessary detailed mathematics. To facilitate the solution of the model equations, therefore, the (L, s, t) coordinates are transformed into the coordinates (p, q, t), where

$$p = \frac{R}{a \sin^2 \Theta} \tag{105}$$

and

$$q = \frac{a^2 \cos\Theta}{R^2} \tag{106}$$

[*Kendall*, 1962]. Two important properties of this transformation are that the p coordinate is constant along a dipole magnetic field line ($p = L$) and, for a fixed magnetic longitude, the paths of constant q are orthogonal to the field line. Also, for a dipole magnetic field line,

$$R = R_{eq} \sin^2 \Theta \tag{107}$$

and

$$\frac{\partial}{\partial s} = -\frac{(1+3\cos^2\Theta)^{0.5}}{a}\left(\frac{a}{R}\right)^3 \frac{\partial}{\partial q} = \eta \frac{\partial}{\partial q} \tag{108}$$

[*Bailey and Sellek*, 1990].

Applying this transformation of coordinates to the continuity, momentum, and energy balance equations (equations 62, 69, 70, and 96) and rearranging gives equations of the form

$$\frac{dN_i}{dt} = P_i - \alpha_i N_i - \eta^2 \frac{\partial}{\partial q}\left(\frac{N_i v_i''}{\eta}\right) \tag{109}$$

$$N_i v_i'' = -\eta R_i \frac{\partial N_i}{\partial q} - S_i N_i \tag{110}$$

$$\frac{3}{2} k N_i \left(\frac{dT_i}{dt} + v_i'' \eta \frac{\partial T_i}{\partial q} \right) = Q_i - k N_i T_i \left[\eta^2 \frac{\partial}{\partial q} \left(\frac{v_i''}{\eta} \right) + div\, v_{em} \right] + \eta^2 \frac{\partial}{\partial q} \left(k_i \frac{\partial T_i}{\partial q} \right) + F_{in} \tag{111}$$

where

$$\alpha_i = \beta_i + \text{div}\, v_{em} \tag{112}$$

and where, for $i = O^+$, H^+ and He^+,

$$R_i = \frac{\frac{k}{m_i} \left(T_i + T_e \frac{N_i}{N_e} \right)}{\left[\nu_{ij}(1-\Delta_{ij}) + \nu_{ik}(1-\Delta_{ik}) + \sum_m \nu_{im} + \sum_n \nu_{in} \right]} \tag{113}$$

$$\begin{aligned} S_i = \Bigg[& g \sin I + \frac{kT_e}{m_i N_e} \sum_{j \neq i} \frac{\partial N_j}{\partial s} + \frac{k}{m_i} \frac{\partial (T_e + T_i)}{\partial s} \\ & + \frac{k}{m_i} \beta_i \frac{\partial T_i}{\partial s} - \frac{k}{m_i} \beta_{ij}^* \frac{\partial T_j}{\partial s} - \frac{k}{m_i} \beta_{ik}^* \frac{\partial T_k}{\partial s} \\ & - [\nu_{ij}(1-\Delta_{ij}) - R_{ijk} + R_{ikj}] v_j'' \\ & - [\nu_{ik}(1-\Delta_{ik}) - R_{ikj} + R_{ijk}] v_k'' \\ & - \sum_m \nu_{im} v_m'' - \sum_n \nu_{in} (u_\theta \cos D \cos I + u_\phi \sin D \cos I) \Bigg] \\ & / \left[\nu_{ij}(1-\Delta_{ij}) + \nu_{ik}(1-\Delta_{ik}) + \sum_m \nu_{im} + \sum_n \nu_{in} \right] \end{aligned} \tag{114}$$

and, for $i = N_2^+$, O_2^+, and NO^+

$$R_i = \frac{\frac{k}{m_i} \left(T_i + T_e \frac{N_i}{N_e} \right)}{\left[\sum_{j \neq i} \nu_{ij} + \sum_n \nu_{in} \right]} \tag{115}$$

$$S_i = \left[g \sin I + \frac{kT_e}{m_i N_e} \sum_{j \neq i} \frac{\partial N_j}{\partial s} + \frac{k}{m_i} \frac{\partial (T_e + T_i)}{\partial s} \right.$$

$$\left. - \sum_{j \neq i} \nu_{ij} v_j'' - \sum_n \nu_{in} (u_\theta \cos D \cos I + u_\phi \sin D \cos I) \right] \tag{116}$$

$$/ \left[\sum_{j \neq i} \nu_{ij} + \sum_n \nu_{in} \right]$$

4.2 Finite Difference Equations

Equations (109)–(111) are solved numerically by an implicit finite-difference method. In the description of the finite-difference equations, the subscript for a particle species has been dropped, the subscript k is used to denote the kth point along the magnetic field line, and the superscript j, the jth time-step, e.g. a_k^j. If the superscript is omitted, e.g. a_k, then the quantity is evaluated at the time step $j + 1$, i.e. $a_k \equiv a_k^{j+1}$. Since the values of q remain fixed throughout the calculation procedure, the increments d_k, where

$$d_k = q_{k+1} - q_k \tag{117}$$

also remain fixed.

For each ion, the continuity and momentum equations (equations 109 and 110, respectively) are first combined to form a diffusion equation and then converted to a finite-difference equation. Let the flux term in the equation (109) at the point q_k be denoted by ϕ_k. Then,

$$\phi_k = \frac{N_k v_k''}{\eta_k} \tag{118}$$

and so, by using central differences, there follows the finite-difference representations

$$\left(\frac{dN}{dt} \right)_k = P_k - \alpha_k N_k - \eta_k^2 \frac{\left(\phi_{k+\frac{1}{2}} - \phi_{k-\frac{1}{2}} \right)}{\frac{1}{2}(d_{k-1} + d_k)} \tag{119}$$

and

$$\phi_{k+\frac{1}{2}} = -\frac{1}{2} \left(\frac{S_k N_k}{\eta_k} + \frac{S_{k+1} N_{k+1}}{\eta_{k+1}} \right) - \frac{1}{2} (R_k + R_{k+1}) \frac{(N_{k+1} - N_k)}{d_k} \tag{120}$$

for equations (109) and (110), respectively. By substituting for $\phi_{k+\frac{1}{2}}$ and $\phi_{k-\frac{1}{2}}$ into equation (120), there follows the finite-difference representation

$$\frac{N_k - N_k^j}{\Delta t} = P_k - \alpha_k N_k + \frac{\eta_k^2}{(d_{k-1}+d_k)}\left[\left(\frac{S_k N_k}{\eta_k} + \frac{S_{k+1}N_{k+1}}{\eta_{k+1}}\right)\right.$$
$$+ (R_k + R_{k+1})\frac{(N_{k+1}-N_k)}{d_k} - \left(\frac{S_{k-1}N_{k-1}}{\eta_{k-1}} + \frac{S_k N_k}{\eta_k}\right) \qquad (121)$$
$$\left. - (R_{k-1} + R_k)\frac{(N_k - N_{k-1})}{d_{k-1}}\right]$$

for the *i*th-ion diffusion equation.

The finite-difference representation of the energy balance equation (equation 111) is obtained by first expressing it in the form

$$\frac{3}{2}kN_k\frac{T_k - T_k^j}{\Delta t} = Q_k - kN_k T_k^j\left[\eta_k^2\frac{\partial}{\partial q}\left(\frac{\nu_k''}{n_k}\right) + div\,\mathbf{v}_{em}\right]$$
$$+ \eta_k^2\frac{(\psi_k - \psi_{k-1})}{d_{k-1}} + F_k \qquad (122)$$
$$- \frac{3}{2}kN_k\nu_k''\eta_k\frac{(T_k - T_{k-1})}{d_{k-1}}$$

where

$$\psi_k = \kappa_k\frac{(T_{k+1} - T_k)}{d_k} \qquad (123)$$

and then eliminating ψ_k and ψ_{k-1} to give

$$\frac{3}{2}kN_k\frac{T_k - T_k^j}{\Delta t} = Q_k - kN_k T_k^j\left[\eta_k^2\frac{\partial}{\partial q}\left(\frac{\nu_k''}{\eta_k}\right) + div\,\mathbf{v}_{em}\right]$$
$$+ \frac{\eta_k^2}{d_{k-1}}\left[\frac{\kappa_k}{d_k}(T_{k+1} - T_k) - \frac{\kappa_{k-1}}{d_{k-1}}(T_k - T_{k-1})\right] + F_k \qquad (124)$$
$$- \frac{3}{2}kN_k\nu_k''\eta_k\frac{(T_k - T_{k-1})}{d_{k-1}}$$

Application of equations (121) and (124) to each point along the magnetic field line provide tri-diagonal systems of algebraic equations from which the ion concentrations and the ion and electron temperatures are determined. At the base altitudes, the ion concentrations are obtained from the chemical equilibrium condition

$$N_i = \frac{P_i}{\beta_i} \qquad (125)$$

$i = O^+, H^+, He^+, N_2^+, O_2^+, NO^+$, and the ion and electron temperatures from the condition

$$Q_i = 0 \tag{126}$$

$i = O^+, H^+, He^+, e$, see equation (101).

The tri-diagonal systems of equations for the ion concentrations are solved in the order O^+, H^+, He^+, N_2^+, O_2^+ and NO^+, and for the temperatures in the order electrons, O^+, H^+, and He^+. The temperatures of the molecular ions are taken to be equal to the temperature of the O^+ ions. The field-aligned fluxes are determined from equation (121).

The procedure for determining the distribution of points along the magnetic field line is first to determine the highest magnetic field line reached by the tube of plasma during the model calculations and then to distribute the points in equal increments Δx along that magnetic field line, where

$$x = \begin{cases} \dfrac{\sinh(\Gamma q)}{\sinh(\Gamma q_n)}, & \text{northern hemisphere} \\ \dfrac{\sinh(\Gamma q)}{\sinh(\Gamma q_s)}, & \text{southern hemisphere} \end{cases} \tag{127}$$

and where Γ is a point distribution parameter, q_n is the value of q at the lower boundary in the northern hemisphere, and q_s is the value of q at the lower boundary in the southern hemisphere; the lower boundary in each hemisphere is taken to be at geographic altitude 130 km. The number of points taken along the highest magnetic field line depends upon its L value. The authors generally use 201 points with $\Gamma = 6$ for low-latitude L-values and 401 points with $\Gamma = 3$ at mid-latitude L-values. Numerical experiment has shown that reasonable accuracy is obtained when the points are distributed so that the altitude increments at F-region altitudes are about 5 km. The distribution of points is not changed in the calculation procedure, i.e. the values of q remain unchanged. However, as the plasma $\mathbf{E} \times \mathbf{B}$ drifts vertically it will be associated with different magnetic field lines. Thus, to keep the base altitudes in each hemisphere near to the initial base altitudes (geographic), points may have to be added or removed to either or both ends of the field line. When points are added to the field line, as a result of an upward $\mathbf{E} \times \mathbf{B}$ drift, the concentrations and temperatures at the additional points are given values determined from equations (125) and (126), respectively, and the field-aligned velocities are taken to be zero.

4.3 Solution Procedure

The tube of plasma associated with a particular magnetic field line drifts with vertical $\mathbf{E} \times \mathbf{B}$ drift velocity so that at later times it is associated with different magnetic field lines. Thus, in order to provide reasonable 24-hour coverage of the model values within a specified altitude and latitude region, the model equations have to be solved along many tubes of plasma (see Figures 3 and 4). In recent studies, 114 tubes of plasma have been used. Of these, 65 are distributed so that they have intervals of 50 km for apex altitudes between 200 and 3000 km, 100 km for apex altitudes between 3000 and 3500 km, and 500 km for apex altitudes between 3500 and 5000 km (these altitudes refer to the apex altitudes of the tubes of plasma at the commencement of the calculations). Figure 3 is a schematic of the local time variation of the apex altitude of several tubes of plasma under $\mathbf{E} \times \mathbf{B}$ drift, the solid curves denote the variations when the apex altitude lies within the altitude region 200 to 2000 km, the region used for the results presented in Section 6, and the large-dashed curves denote the variations when the apex altitude is above 2000 km. The remaining 49 tubes of plasma have apex altitude 150 km and are introduced at 15-minute time intervals between 08:00 to 20:00 LT to provide model values in the region left

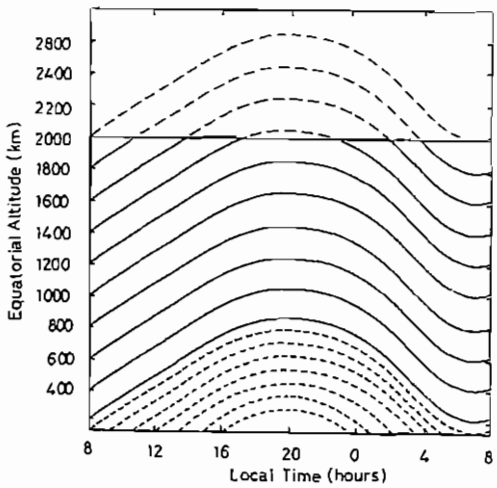

Figure 3. A schematic of the local time variation of the apex altitude of several tubes of plasma: ——— within the region of study; — — — —, above the region of study; - - - - - -, for tubes of plasma with initial apex altitude 150 km.

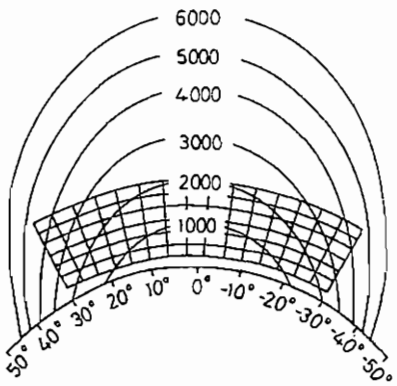

Figure 4. A schematic of the distribution of dipole magnetic field lines in the Earth's upper atmosphere; the gridded section denotes the region of study.

void by the drifting plasma (see the small-dashed curves of Figure 3). It should be noted that the tube of plasma with apex altitude 150 km at 08:00 LT drifts to an apex altitude of about 800 km within one day's calculations during medium solar activity. Figure 4 is schematic of the distribution of dipole magnetic field lines in the Earth's upper atmosphere; the gridded section denotes the region used for the results presented in Section 6. It has been found that the above distribution of the tubes of plasma provides a reasonably detailed 24-hour coverage of model values within the region 200 to 2000 km altitude and $\pm 30^{\circ}$ latitude.

The model calculations are carried out in two parts. In the first part, altitude profiles are produced that are close to dynamic equilibrium, i.e., there are only small day-to-day changes in the modeled values when there are not day-to-day changes in the atmospheric parameter values. These profiles are independent of the initial conditions. At low latitudes, the volume of the tube of plasma is small and only two or three calculation days (a calculation day is a 24-hour period of calculations) are required for the modeled thermal plasma to reach dynamic equilibrium. At mid-latitudes, on the other hand, many calculation days are required due to the large volume of the tube of plasma and the depletion effects of magnetic storms on the plasmasphere [*Bailey et al.*, 1978]. In the second part, the model calculations are carried out for a further 24-hour period of local time to provide model values for study (see Section 6).

For each tube of plasma, the model calculations are commenced at 12:00 LT with altitude distributions for the ion concentrations constructed from chemical and diffusive equilibrium conditions and ion field-aligned fluxes set equal to zero. The altitude distributions for the ion and electron temperatures are constructed from the neutral gas temperature using a simple empirical relationship. The time increment, Δt, is 900 seconds and there are no day-to-day changes in the atmospheric parameter values.

For the tubes of plasma with initial apex altitude of 150 km, the calculations are carried out without $\mathbf{E} \times \mathbf{B}$ drift velocity for 32 hours of local time, i.e., until 20:00 LT on calculation day 2, with the model values at each time step on and after 08:00 LT (on calculation day 1) being stored in data files. For the higher apex-altitude tubes of plasma, the calculations are carried out for 44 hours in local time, i.e., until 08:00 LT on calculation day 2; the results at this time step, for each tube of plasma, are also stored in data files. The first 20 hours of calculation for these tubes of plasma, i.e., until 08:00 LT on iteration day 1, are carried out without $\mathbf{E} \times \mathbf{B}$ drift velocity; between 08:00 LT on calculation day 1 and 08:00 LT on calculation day 2, the $\mathbf{E} \times \mathbf{B}$ drift velocity is included in the model calculations. Local time 08:00 is used in the model calculations since a substantial period of time elapses before the $\mathbf{E} \times \mathbf{B}$ drift is downward and the tube of plasma descends. If the calculations commenced with a downward $\mathbf{E} \times \mathbf{B}$ drift velocity, the low-altitude tubes of plasma would descend below the lower L-shell of the model calculations and a different calculation procedure would be needed.

A further 24-hour period of calculation is then carried out for each tube of plasma commencing with the altitude profiles produced and stored in data files in the manner described in the previous paragraph. For these calculations, the $\mathbf{E} \times \mathbf{B}$ drift velocity is also included in the model calculations for the tubes of plasma that have an initial apex altitude of 150 km. Also, for the tubes of plasma that have an initial apex altitude of 150 km, but which commence after 08:00 LT, the calculations cease when the apex altitude of the tube of plasma drifts below 150 km. The model values from this final 24-hour period of calculations are then regridded, using interpolation techniques, for each required atmospheric and ionospheric parameter to form regular 3-dimensional arrays of data with mesh size 30 minutes in time, 20 km in altitude, and 2° in latitude. All the figures shown in Section 6 have been constructed from these arrays using a computer graphics package.

5. Model Inputs

Several model inputs, viz magnetic field, photoionization and photoabsorption cross sections, collision frequencies, chemical reaction rates, and heating and cooling rates, have been described in Sections 2 and 3. In this section, the remaining model inputs are described. It should be borne in mind that the model inputs, including those described in Sections 2 and 3, are modified as and when improved values becomes available and may be changed to accommodate the application of the model.

5.1 Solar EUV Fluxes

The ions are produced by photoionization of the neutral gases by solar EUV radiation. The solar EUV fluxes are computed from the EUV94 solar EUV flux model, EUV94 is the latest of a series of solar EUV flux models developed by W. K. Tobiska. In these models, daily values of Lyman-α (1,216 Å), He I EW (10,830 Å), $F10.7$ and the 81-day running mean-values of $F10.7$ are used to calculate the solar EUV fluxes for the 37 wavelength groups and discrete lines that are in widespread use [*Tobiska*, 1991]. Variations with $F10.7$ of the various solar EUV fluxes obtained from the EUV91 model have been investigated by *Balan et al.* [1993, 1994a], who found, in particular, that the fluxes at all wavelengths increase linearly with $F10.7$ for values of $F10.7$ less than about 200 and for higher values of $F10.7$ the integrated solar EUV fluxes increase at a very much reduced rate. Recently, *Balan et al.* [1994b] have reproduced the observed non-linear variation of the ionospheric electron content with $F10.7$.

Recent modeling studies of He^+ give concentrations lower than observed. *Bailey and Sellek* [1990] and *Heelis et al.* [1990], using solar EUV fluxes based on the SC21REFW and F79050N reference spectra, needed to increase the photoionization rate of He^+ by the factor 2.5 to obtain agreement in their modeled values of He^+ and values observed by DE-2. Using the EUVAC solar EUV flux model, *Richards et al.* [1994] and *Craven et al.* [1995] obtained agreement between their modeled values of He^+ and values taken from the AE database by increasing the photoionization rate of He^+ by the factor 1.9. Reasons for the differences in the modeled and observed values of He^+ have still to be determined. In the present version of the model, the photoionization rate of He^+ is increased by the factor 2.5.

5.2 Neutral Atmosphere and Winds

The concentration of the atmospheric constituents O, O_2, N_2, H and He, and the neutral gas temperature, T_n, are calculated from the MSIS-86 model thermosphere [*Hedin*, 1987]. The constituent NO is not included in the MSIS-86 model and so its concentration, $n(NO)$, is calculated from the expression

$$n(NO) = 0.4 \exp\left(-\frac{3700}{T_n}\right) n(O_2) + 5.0 \times 10^{-7} n(O) \tag{128}$$

[*Mitra*, 1968].

The neutral wind velocities are obtained from the HWM90 thermospheric wind model [*Hedin*, 1991]. This model is based on satellite and ground-based observations and gives meridional and zonal wind velocities as a function of altitude, latitude, longitude and solar activity for all times of day. In the model, the wind velocity in the magnetic meridian is particularly important as it determines the height of the F layer which, in turn, controls the field-aligned distribution of plasma. This component of the neutral wind velocity is given by

$$u = u_\theta \cos D - u_\phi \sin D \tag{129}$$

where D is the magnetic declination angle and u_θ and u_ϕ are positive in the southward and eastward directions, respectively.

5.3 Plasma Drift Velocity

The $\mathbf{E} \times \mathbf{B}$ drift velocity has been measured routinely only at the two equatorial stations, Jicamarca (70° W) and Trivandrum (75° E) [*Fejer et al.*, 1991; *Namboothiri et al.*, 1989]. The drifts have large day-to-day, seasonal and solar cycle variations. A prominent feature of the vertical $\mathbf{E} \times \mathbf{B}$ drift velocity is the prereversal enhancement during evening hours. This feature is caused by conductivity gradients in the E and F regions [*Crain et al.*, 1993]. The longitudinal variations of the prereversal enhancement and the reversal time of the $\mathbf{E} \times \mathbf{B}$ drift velocity have been modeled for the South American longitude zone by *Batista et al.* [1986]. These authors found that the longitudinal variations are caused by the longitudinal variation of the magnetic declination angle.

There is observational and theoretical evidence that the vertical $\mathbf{E} \times \mathbf{B}$ drift velocity varies with altitude. In *Pingree and Fejer* [1987] it is shown that the vertical drift velocity over Jicamarca varies almost linearly with altitude in the F region and that the time variation, when extrapolated to higher altitudes, closely resembles the diurnal variation of the vertical drift velocity observed at F-region altitudes over Arecibo. From theoretical considerations, *Murphy and Heelis* [1986] showed that to neglect the altitude gradients of the equatorial plasma drifts, even though they are usually very small, would be inconsistent with a curl-free low-latitude electric field.

In the model the equatorial vertical $\mathbf{E} \times \mathbf{B}$ drift velocity, $v_{eq}^{\perp}$, is obtained from measurements made at Jicamarca by *Fejer et al.* [1991], and Arecibo by *Fejer* [1993]. A Jicamarca drift pattern is used for magnetic field lines with an apex altitude less than 600 km and an Arecibo drift pattern, scaled to the equatorial crossing altitude (see equation 65), when the apex altitude is greater than 2000 km; linear interpolation of the Jicamarca and Arecibo values is used at the intermediate apex altitudes. It should be borne in mind that there is considerable uncertainty in the altitude and longitudinal variations of the $\mathbf{E} \times \mathbf{B}$ drift velocity and so different variations may need to be tried in modeling studies of observational data. Figure 5 shows the equatorial drift patterns used for the model calculations described in Section 6 at 600 and 2000 km altitude; the zonal $\mathbf{E} \times \mathbf{B}$ drift velocity is taken to be zero.

6. Model Outputs

Figures 6–9 illustrate the model outputs. The outputs have been obtained from model calculations carried out for the longitude of Jicamarca (77° W) under magnetically quiet ($Ap = 4$) equinoctial conditions (day 264) at medium solar activity ($F10.7 = 145$, $F10.7A = 164$).

In Figures 6 and 7, latitude plots are shown of Nmax (peak electron concentration) and TEC (total ionospheric content, the electron content in a column of cross-sectional area 1 cm^2 between 200 and 2000 km altitude), respectively, at 14:00 and 24:00 LT from model calculations which include an eccentric dipole (ED) representation and a tilted dipole (TD) representation for the geomagnetic field. It is near 14:00 LT that Nmax has its daytime maximum, while the plots for 24:00 LT are representative of nighttime conditions. As the figures show, the model results are in qualitative agreement for both magnetic field models. The model values of Nmax reproduce the classical equatorial anomaly. However, in contrast to the observations [*Rajaram*, 1977; *Walker et al.*, 1994], the anomaly (crest-to-trough ratio) in TEC is weak. An explanation of the discrepancy in the modeled and observed values of TEC has been put forward by *Balan and Bailey* [1995].

The main effects at 24:00 LT, arising from using an ED magnetic field, is to increase the crest value of Nmax in each hemisphere by 15-20%, the increase in the northern hemisphere being greater than in the southern hemisphere, and to increase Nmax by about 20% at latitudes greater than 20° in the southern hemisphere. At 14:00 LT, the effects are small with the most noticeable difference being a 5% decrease in the crest value of Nmax in the northern hemisphere. The effects on TEC of using an ED magnetic field are much smaller than those on Nmax. At

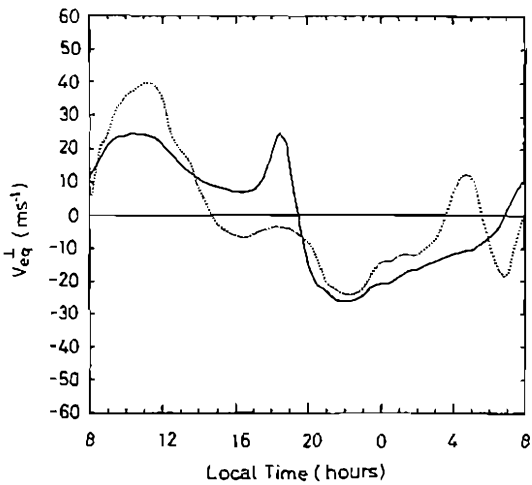

Figure 5. Diurnal variations of the equatorial vertical $\mathbf{E} \times \mathbf{B}$ drift velocity (————, 600 km altitude; ·····, 2000 km altitude.)

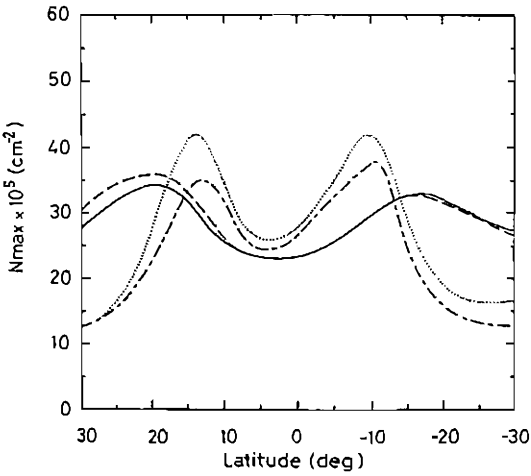

Figure 6. Latitudinal variation of Nmax for an ED magnetic field (————, 14:00 LT; ····· 24:00 LT) and a TD magnetic field (— — — —, 14:00 LT; — - — - —, 24:00 LT).

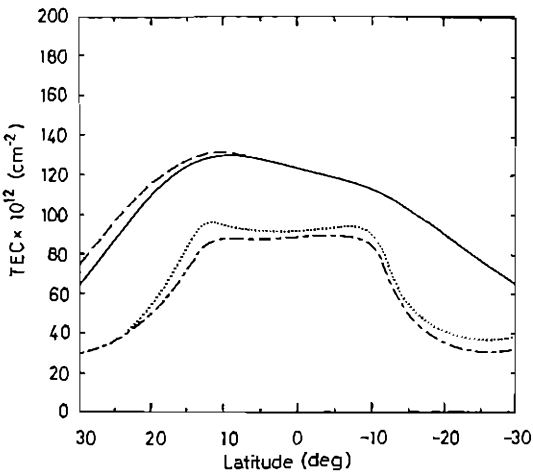

Figure 7. Latitudinal variation of TEC for an ED magnetic field (————— , 14:00 LT; ·····, 24:00 LT) and a TD magnetic field (— — — — , 14:00 LT; — - — - — , 24:00 LT).

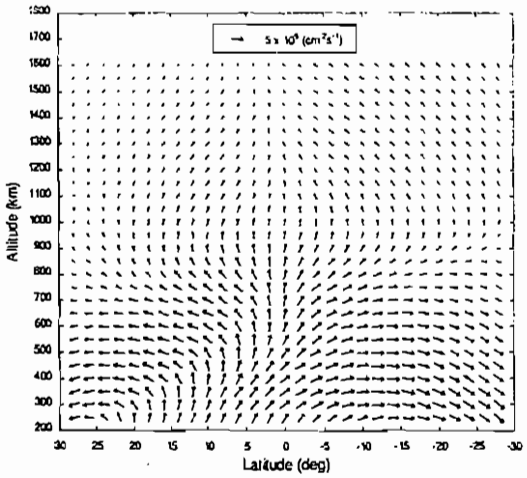

Figure 8a. Vector plasma fluxes at 14:00 LT.

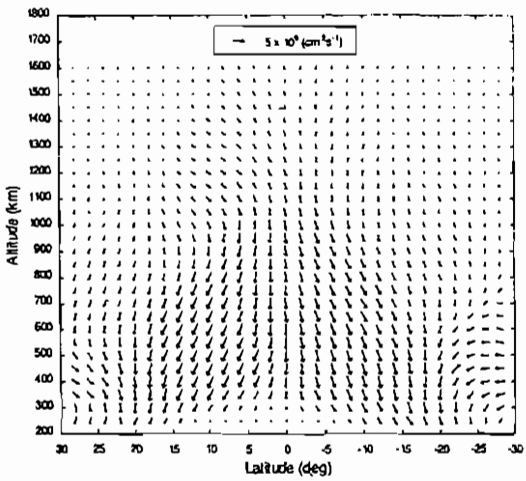

Figure 8b. Vector plasma fluxes at 20:00 LT.

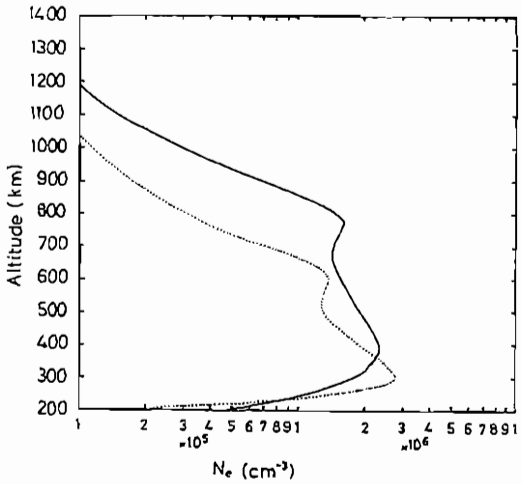

Figure 9. Altitude profiles of electron concentration (————— , 14:00 LT; ·····, 24:00 LT).

14:00 LT, there is a decrease in the northern hemisphere which increases with increasing latitude, while at 24:00 LT there is increase in both hemispheres. The differences in Nmax and TEC for the two magnetic field models arise principally from the changes to the neutral air wind in the magnetic meridian (see equation 129).

As the difference in the model results for the two magnetic field models are generally small, the remaining results presented in this section are from calculations in which the ED magnetic field has been used.

In Figures 8a and 8b are shown the modeled plasma fluxes at 14:00 and 20:00 LT, respectively. Figure 8a clearly shows the plasma fountain. As described in Section 1, the plasma fountain is generated by the vertical $\mathbf{E} \times \mathbf{B}$ drift and is modulated by the neutral wind. During daytime, the fountain rises to about 700 km altitude at the equator and extends to more than 30° latitude on either side of the equator. Outside the reach of the fountain, there is plasma flow towards the equator from both sides of the equator. Such flows have been detected by the DMSP F8 satellite near 840 km altitude [*Greenspan et al.*, 1994].

At the time of reversal of the $\mathbf{E} \times \mathbf{B}$ drift (19:30 LT, see Figure 5), the plasma in the region occupied by the fountain tries to diffuse downward along the magnetic field lines. However, the diffusion lasts for only a very short period of time because the drift quickly becomes large and downward. The effect of the large downward drift is illustrated in Figure 8b which shows that the plasma flow at 20:00 LT behaves somewhat like a reverse fountain [*Balan and Bailey*, 1995]. In this figure, the dots at the higher latitudes and altitudes denote that the modeled plasma fluxes have a magnitude less than 5×10^6 cm^{-2}s^{-1}.

As mentioned above and shown in Figure 8a, the plasma fountain is confined to a particular region in altitude and latitude and that, outside the region, plasma flows toward the equator from both hemispheres. The upward flow of plasma outside the fountain region can cause convergence of plasma above the F-region peak close to the equator. This convergence of plasma can lead to the formation of an additional layer, the F3-layer (see Figure 9). Model calculations indicate that the F3-layer has latitudinal coverage of about ±10° and a local-time coverage of more than 15 hours (11:00-02:00 LT) at the equator. Model calculations show that the F3-layer can become stronger than the F2-layer for a short period of time near noon just before the drift starts to decrease [*Balan and Bailey*, 1995]. Experimental evidence for the F3-layer being stronger than the F2-layer has been observed in ionograms recorded at Fortaleza, Brazil [*Balan et al.*, 1996].

In the publications describing our early studies of the plasma fountain, we called this additional layer the 'G-Layer.' However, more recent studies have shown that the layer arises from the dynamics of the F-layer at low latitudes. The layer should, therefore, be called the 'F3 layer.' This naming is consistent with the well-established nomenclature of using capital letters to denote different regions of the ionosphere, e.g., D, E, and F, and using the region letter followed by a number to denote distinct ionized layers within the region, e.g., F1 and F2.

A detailed modeling study of the observed plasma temperatures at Jicamarca has yet to be carried out. However, the plasma temperatures obtained from the present model calculations are in reasonable accord with the observations made at Jicamarca by *McClure* [1969]. More recently, in a paper by *Su et al.* [1995], it has been shown that for the December solstice of 1981 (solar maximum), that the model gives electron temperatures at about 600 km altitude in good agreement with the observations made by the Hinotori satellite.

7. Availability of Model

The model is not user-friendly and collaboration, in the first instance, is required between the user and the principal developer (GJB). The principal developer would be happy to make the model codes available to interested groups and to discuss collaborations with them. The model codes are written in FORTRAN and have been developed for use on a high-performance pc. However, it is straightforward to modify the code for use on workstations and mainframes.

Acknowledgments. The authors would like to thank W. K. Tobiska of the Jet Propulsion Laboratory, for providing the model code of the solar EUV flux model, to P. G. Richards of the Computer Science Department and the Center for Space Plasma and Aeronomic Research, University of Alabama in Huntsville, for providing the model code of the photoelectron heating rate, and to R. J. Moffett, University of Sheffield, for his assistance and useful discussions. The development of the model has been supported by grants from PPARC (formerly SERC).

References

Anderson, D. N., *Planet. Space Sci., 21*, 409-419, 1973a.
Anderson, D. N., *Planet. Space Sci., 21*, 421-442, 1973b.
Anderson, D. N., *J. Atmos. Terr. Phys., 43*, 753-762, 1981.
Bailey, G. J., R. J. Moffett, and J. A. Murphy, *Planet. Space Sci., 26*, 753-765, 1978.
Bailey, G. J. and R. Sellek, *Ann. Geophys., 8*, 171-190, 1990.
Bailey, G. J., R. Sellek, and Y. Rippeth, *Ann. Geophys., 11*, 263-272, 1993.
Balan, N. and G. J. Bailey, *J. Geophys. Res., 100*, 21421-21432, 1995.
Balan, N., G. J. Bailey, and B. Jayachandran, *Planet. Space Sci., 41*, 141-145, 1993.
Balan, N., G. J. Bailey, B. Jenkins, P. B. Rao, and R. J. Moffett, *J. Geophys. Res., 99*, 2243-2253, 1994a.
Balan, N., G. J. Bailey, and R. J. Moffett, *J. Geophys. Res., 99*, 17,467-17,475, 1994b.
Balan, N., G. J. Bailey, R. J. Moffett, Y. Z. Su, and J. E. Titheridge, *J. Atmos. Terr. Phys., 57*, 279-292, 1995.
Balan, N., G. J. Bailey, M. A. Abdu, K. I. Oyama, P. G. Richards, J. MacDougall, and I. S. Bastista, *J. Geophys. Res.*, in press, 1996.
Balmforth, H. F., R. J. Moffett, A. J. Smith, and G. J. Bailey, *Ann. Geophys., 12*, 296-303, 1994.
Banks, P. M. and G. Kockarts, *Aeronomy*, Academic Press, New York, 1973.
Barraclough, D., *Phys. Earth Planet. Int., 48*, 279-292, 1987.
Batista, I. S., M. A. Abdu, and J. A. Bittencourt, *J. Geophys. Res., 91*, 12,055-12,064, 1986.
Chapman, S. and J. Bartels, *Geomagnetism*, Vol. 2, Oxford University Press, London, 1940.
Crain, D. J., R. A. Heelis, and G. J. Bailey, *J. Geophys. Res., 98*, 6033-6037, 1993.

Craven, P. D., R. H. Comfort, P. G. Richards, and J. Grebowsky, *J. Geophys. Res.*, *100*, 257-268, 1995.
Fejer, B. G., *J. Geophys. Res.*, *98*, 13,645-13,652, 1993.
Fejer, B. G., E. R. de Paula, S. A. Gonzalez, and R. F. Woodman, *J. Geophys. Res.*, *96*, 13,901-13,906, 1991.
Fraser-Smith, A. C., *Rev. Geophys.*, *25*, 1-16, 1987.
Greenspan, M. E., W. J. Burke, F. J. Rich, W. J. Hughes, R. A. Heelis, *J. Geophys. Res.*, *99*, 3817-3826, 1994.
Hanson, W. B. and R. J. Moffett, *J. Geophys. Res.*, *71*, 5559-5572, 1966.
Hedin, A. E., *J. Geophys. Res.*, *92*, 4649-4662, 1987.
Hedin, A. E., M. A. Biondi, R. G. Burnside, G. Hernandez, R. M. Johnson, T. L. Killeen, C. Mazaudier, J. W. Meriwether, J. E. Salah, R. J. Sica, R. W. Smith, N. W. Spencer, V. B. Wickwar, and T. S. Virdi, *J. Geophys. Res.*, *96*, 7657-7688, 1991.
Kendall, P. C., *J. Atmos. Terr. Phys.*, *24*, 805-811, 1962.
Kendall, P. C., and W. M. Pickering, *J. Atmos. Terr. Phys.*, *15*, 825-833, 1967.
McClure, J. P., *J. Geophys. Res.*, *74*, 279-291, 1969.
Mitra, A. P., *J. Atmos. Terr. Phys.*, *30*, 1065-1114, 1968.
Moffett, R. J., *Fund. Cosmic Phys.*, *4*, 313-391, 1979.
Murphy, J. A. and R. A. Heelis, *Planet. Space Sci.*, *34*, 645-652, 1986.
Murphy, J. A., G. J. Bailey, and R. J. Moffett, *J. Geophys. Res.*, *85*, 1979-1986, 1980.
Nagy, A. F. and P. M. Banks, *J. Geophys. Res.*, *75*, 6260-6271, 1970.
Namboothiri, S. P., N. Balan, and P. B. Rao, *J. Geophys. Res.*, *94*, 12,055-12,060, 1989.
Pingree, J. E. and B. G. Fejer, *J. Geophys. Res.*, *92*, 4763-4766, 1987.
Rajaram, G., *J. Atmos. Terr. Phys.*, *39*, 1125-1144, 1977.
Richards, P. G., J. A. Fennelly, and D. G. Torr, *J. Geophys. Res.*, *99*, 8981-8992, 1994.
Rippeth, Y., R. J. Moffett, and G. J. Bailey, *J. Atmos. Terr. Phys.*, *53*, 551-555, 1991.
Schunk, R. W. and A. F. Nagy, *Rev. Geophys. Space Res.*, *16*, 355-399, 1978.
Stening, R. J., *J. Atmos. Terr. Phys.*, *54*, 1387-1412, 1992.
Su, Y. Z., K. I. Oyama, G. J. Bailey, T. Takahashi, and S. Watanabe, *J. Geophys. Res.*, *100*, 14,591-14,604, 1995.
Tobiska, W. K., *J. Atmos. Terr. Phys.*, *53*, 1005-1018, 1991.
Torr, M. R., and D. G. Torr, *Rev. Geophys. Space Phys.*, *20*, 91-144, 1982.
Torr, M. R., D. G. Torr, P. G. Richards, and S. P. Yung, *J. Geophys. Res.*, *95*, 21,147–21,168, 1990.
Walker, G. O., *J. Atmos. Terr. Phys.*, *43*, 463-471, 1981.
Walker, G. O., J. H. K. Ma, and E. Golton, *Ann. Geophys.*, *12*, 195-209, 1994.
Young, E. R., D. G. Torr, P. G. Richards, and A. F. Nagy, *Planet. Space Sci.*, *28*, 881-893, 1980.

The Field Line Interhemispheric Plasma Model

P. G. Richards and D. G. Torr

Center for Space Plasma and Aeronomic Research
University of Alabama
Huntsville, Alabama 35899

1. Introduction

The field line interhemispheric plasma (FLIP) model is a first-principles, 1-D, time-dependent chemical and physical, model of the ionosphere, plasmasphere, and thermosphere. This model couples the local ionosphere to the overlying plasmasphere and conjugate ionosphere by solving the ion continuity and momentum, ion and electron energy, and photoelectron equations along entire magnetic flux tubes. The output from the interhemispheric solutions consists of densities and fluxes of H^+, O^+, He^+, N^+ as well as the electron and ion temperatures. In addition, continuity and momentum equations are solved to provide the densities of minor neutral species ($N(^2D)$, $N(^4S)$, NO) and the first 6 vibrational levels of N_2 in both hemispheres. A large number of other minor ion and neutral densities are calculated from chemical equilibrium between 80 and 600 km in the northern and southern hemispheres. Other outputs from the model include particle and heat fluxes, electron heating and cooling rates, photoelectron fluxes, chemical production and loss rates, and most significant airglow emission rates. A 3-D version of the model is obtained by simulating several hundred corotating flux tubes.

2. Model Formulation

The FLIP model has been developed over a period of more than 15 years. Early progress was reported by *Young et al.* [1980a,b], but major recent developments have made those papers obsolete. The most comprehensive description of the model was given by *Torr et al.* [1990]. The He^+ chemical and physical processes have been discussed by *Newberry et al.* [1989] while the N^+ solution procedure has been discussed by *Craven et al.* [1994]. The main component of the FLIP model calculates the plasma densities and temperatures along entire magnetic flux tubes from 80 km in the northern hemisphere through the plasmasphere to 80 km in the southern hemisphere. A tilted dipole approximation is used for the Earth's magnetic field.

After the field line grid, neutral atmosphere densities and temperatures, and photoproduction rates have been established, the solution of the transport equations proceeds in the following order. First, the photoelectron transport equations are solved to provide electron heating rates and secondary ion production rates. Then the energy equations are solved to provide plasma temperatures (T_e and T_i) for the calculation of the major ion densities (O^+, H^+). Finally, the minor ion equations are solved to obtain densities for N^+ and He^+. After all the interhemispheric solutions have been determined, diffusion equations are solved on separate vertical grids in both hemispheres to obtain the densities of the minor neutral species $N(^2D)$, $N(^4S)$, NO, and vibrationally excited N_2. The vertical grids extend from 80 km to about 500 km in each hemisphere. Finally, altitude profiles of most airglow emission rates and densities of minor ion species (including vibrationally excited N_2^+) are generated for each hemisphere on both field line and vertical spatial grids. Although all the above solutions are available, considerable computation time and space can often be saved by switching off some of the solutions for the minor ion and neutral densities when they are not of prime interest.

The equations solved for the major ion densities are the continuity and momentum equations as formulated for the topside ionosphere by *Schunk* [1975] and *St.-Maurice and Schunk* [1976]. Collisions between ions and neutrals have been included in order to extend the equations into the *E* and *F* regions. The ion continuity equation for the major ions is given by

$$\partial N_i/\partial t = Q_i - L_i N_i - \nabla \bullet f_i \tag{1}$$

where N_i is the concentration of the i^{th} major ion, Q_i and L_i are its production and loss frequency, respectively, and $f_i = N_i U_i$ is the ion flux. U_i is the ion velocity which is obtained from the momentum equation for the major ions and is given by

$$U_i = \frac{\upsilon_{ij}}{\upsilon} U_j - D_i \left(\frac{\nabla N_i}{N_i} - \frac{m_i G}{kT_i} + \frac{\nabla T_i}{T_i} + \frac{T_e \nabla N_e}{T_i N_e} + \frac{\nabla T_e}{T_i} + \frac{N_j}{N_i + N_j} \left(\alpha_{ij} \frac{\nabla T_i}{T_i} - \alpha_{ij}^{*} \frac{\nabla T_j}{T_i} \right) \right) + \frac{\upsilon_{in}}{\upsilon} U_n \tag{2}$$

where the subscripts i and j refer to either O^+ or H^+, n for neutrals, and e refers to electrons. Similar equations are used for He^+ and N^+ but they are treated as minor ions. υ_{ij} is the collision frequency of ion i with ion j and υ is the sum of the collision frequencies of ion i with all other ions. U_n is the field aligned component of the neutral wind velocity and D_i is the ordinary diffusion coefficient. α_{ij} and α_{ij}^{*} are thermal diffusion coefficients. The expressions for υ_{ij}, υ, D_i, α_{ij} and α_{ij}^{*} are taken from *St.-Maurice and Schunk* [1976] and *Schunk and Nagy* [1980]. The electron density (N_e) is assumed to be equal to the sum of the ion densities. G is the acceleration due to gravity.

The method of solution of the continuity and momentum equations has been described by *Torr et al.* [1990]. A variable spatial grid is set up along the magnetic field line. There are approximately 200 grid points distributed in such a way as to give a grid spacing of less than 10 km in the ionosphere and less than one scale height of H^+ in the plasmasphere. The coupled partial differential equations for O^+ and H^+ are solved simultaneously using a Newton iterative procedure so that no linearization in density is required. In very early versions of the FLIP model, the entire plasmasphere was covered in one spatial step to avoid numerical instabilities at high altitudes [*Young et al.*, 1980a,b]. However, powerful modern computers have eliminated the numerical problems and the plasmasphere has been treated on an equal footing with the ionosphere for the past 10 years.

The electron and ion temperatures are obtained by solving the energy equations [*Schunk and Nagy*, 1978] on the same spatial grid as the ion continuity and momentum equations. The thermal electron energy equation is

$$\frac{3}{2} N_e k \frac{\partial T_e}{\partial t} = -N_e k T_e \nabla \cdot U_e - \frac{3}{2} N_e k v_e \cdot \nabla T_e - \nabla \cdot q_e + Q_e - L_e \tag{3}$$

where k is Boltzmann's constant, U_e is the electron velocity, q_e is the electron thermal heat flux, Q_e is the thermal electron heating rate, and L_e is the sum of the electron cooling rates.

The FLIP model includes heat sources due to photoelectron thermalization and the electron quenching of metastable species [$N(^2D)$, $O^+(^2P)$, $O^+(^2D)$]. The heat source due to electron quenching of $N(^2D)$ is the most important of the metastable sources and it also has a measurable effect on the photoelectron flux below 3 eV [*Richards*, 1986]. It is the most important metastable heat source between about 250 and 350 km altitude, but electron quenching of $O^+(^2D)$ and $O^+(^2P)$, is more important at higher altitudes. The thermal electron cooling rates to

ions and neutrals are from *Schunk and Nagy* [1978]. The thermal heat flux $q_e = -\lambda_e \nabla T_e$ where λ_e is the thermal conductivity coefficient of *Spitzer* [1963]. The ion energy equation is given by

$$\frac{3}{2}N_i k\frac{\partial T_i}{\partial t} = -N_i kT_i \nabla\cdot U_i - \frac{3}{2}N_i k v_i \cdot \nabla T_i - \nabla\cdot q_i + Q_i - L_i \qquad (4)$$

where U_i is the ion velocity, q_i is the ion thermal heat flux taken from *St.-Maurice and Schunk* [1976], Q_i is the thermal ion heating rate which results from Coulomb interactions with thermal electrons, and L_i is the sum of the ion cooling rates to the neutral gas. The expressions for the ion heating and cooling rates are from *Schunk and Nagy* [1978].

The non-linear electron and ion energy equations are solved simultaneously for T_e and T_i using the same Newton iterative procedure that is used for the ion continuity and momentum equations.

The photoelectron fluxes are obtained using the 2-stream formulation of *Nagy and Banks* [1970] which has been extended to encompass the entire field line on the same spatial grid as the ion continuity and momentum equations. The 2-stream model folds the photoelectron flux into an upward moving stream and a downward moving stream. The 2-stream photoelectron equations are given by

$$B\frac{d}{ds}\left(\frac{\phi^{\pm}}{B}\right) = \mp T_2\phi^{\pm} \pm T_1\phi^{\mp} \pm \frac{q}{2u} \pm \frac{q^{\pm}}{2u} \qquad (5)$$

where $\phi^{\pm} = \phi^{\pm}(E,s)$ are the upward (+) and downward (–) moving fluxes at energy E and position s, $q(E,s)$ is the primary photoelectron production rate, $q^{\pm}(E,s)$ are the production rates from energy degradation of higher energy electrons, μ is the average cosine of the pitch angle, and B is the magnetic field strength. T_1 and T_2 are coefficients that provide the collisional interaction between the upward and downward streams [*Nagy and Banks*, 1970].

In the FLIP model, the equations are solved along entire magnetic flux tubes on the same grid as the continuity, momentum and energy equations. The energy range from 1 to 100 eV is divided into discrete energy cells ranging from 1 eV at low energies to 5 eV at 100 eV. The solution of the 2-stream equations proceeds from high energies to low energies. Electrons that have lost energy are deposited into the appropriate lower energy cells by the method developed by *Swartz* [1983]. A number of modifications have been made to the basic 2-stream model to improve the accuracy of the fluxes and also the efficiency of the solution procedure. The improved photoelectron model uses the concept of photoelectron production frequencies as well as variable energy and spatial grids. The photoelectron solution procedure is the same as the solution procedure for auroral electron precipitation which has been described in detail by *Richards and Torr* [1990]. That paper also provides a summary of the electron impact cross sections that are used in the model. Further details of the physics of photoelectron fluxes can be found in *Richards and Torr* [1988]. Primary photoelectron production rates from solar EUV radiation are obtained from our EUVAC solar flux model [*Richards et al.*, 1994a].

Apart from the interhemispheric solutions, the FLIP model solves continuity and momentum equations for the minor neutral species NO, $N(^2D)$, $N(^4S)$ and the first six vibrational levels of N_2. These species play important roles in the chemistry and energetics of the ionosphere. Electron quenching of $N(^2D)$ provides an important energy source for thermal electrons [*Richards*, 1986] while vibrationally excited N_2 increases the loss rate of O^+ through the reaction $O^+ + N_2 \rightarrow NO^+ + N$ [*Richards et al.*, 1986; *Richards and Torr*, 1986]. However,

the importance of N_2^* has not yet been firmly established. In recent studies of ionospheric behavior during magnetically quiet and disturbed periods at Millstone Hill and Hobart during 1990, the FLIP model was able to reproduce the observed daytime densities extremely well without the need for N_2^* [*Richards et al.*, 1994b,c].

The FLIP model incorporates an extensive set of chemical reactions for more than 20 ion and neutral species. The reaction rates have been published by *Torr et al.* [1990, 1994]. The electron impact cross sections are extremely important for calculating airglow emission rates and secondary ion production rates. These have been published by *Richards and Torr* [1990]

3. Model Inputs

The philosophy behind the FLIP model has been to minimize the number of adjustable 'fudge' factors. Thus, most inputs to the model (reaction rates, cross sections, etc.) are hard wired and not changed unless there is compelling laboratory or aeronomic evidence for the change. In order to simulate the ionosphere, the FLIP model requires three key inputs: the neutral atmosphere, either the meridional component of the neutral wind or *hmF2* (which is converted into a wind), and the solar EUV flux.

The neutral densities and temperatures are provided by the mass spectrometer and incoherent scatter (MSIS-86) model [*Hedin*, 1987]. The state of the neutral atmosphere is established by inputting the daily or 3-hour Ap magnetic activity indices as well as the daily (F10.7) and 81-day average (F10.7A) solar activity indices. During magnetically quiet periods, the MSIS-86 model neutral densities are thought to be very reliable. However, the densities are much less reliable during magnetic storms because of the difficulty of characterizing the highly variable nature of storm response.

Methods of determining winds from the *F*-region peak height have been developed by *Richards and Torr* [1985a], *Miller et al.*, [1986], and *Richards* [1991]. Whenever h_mF_2 measurements are available they are used by the FLIP model to derive equivalent neutral winds using the method of *Richards* [1991], otherwise the winds are supplied by the HWM90 model of *Hedin et al.* [1991]. The winds from HWM90 generally do not allow ionospheric models to reproduce the measured h_mF_2 accurately enough for many applications because the winds are extremely variable from day-to-day. In the method of *Richards* [1991], the measured h_mF_2 is used by the model to calculate an equivalent neutral wind which is continually updated at each time step to ensure close agreement between the modeled and measured h_mF_2. The FLIP model also has the capability to use h_mF_2 from the International Reference Ionosphere empirical model [*Bilitza et al.*, 1993] as an alternative to the HWM90 wind model if wind measurements are not available. When using winds (but not h_mF_2) the magnitude of the O^+-O collision frequency is an important consideration. The aeronomy community has recently adopted a collision frequency that is a factor of 1.7 larger than the one previously used [*Burnside et al.*, 1987]. This larger frequency is the appropriate one to use with the HWM90 model because the radar winds on which the HWM90 model is partially based were derived with the larger frequency.

Recently, we have developed a new solar EUV flux model called EUVAC [*Richards et al.*, 1994a] which is based on the F74113 measured solar EUV reference spectrum and the relative variations of the EUV flux observed by the Atmosphere Explorer E satellite. EUVAC is now the standard EUV flux model but any other solar spectra can be input to FLIP provided it is first binned into the standard 37 wavelength bins. The F74113 reference spectrum was chosen as the solar minimum standard because it was widely used in the highly successful derivation of chemical reaction rates using the Atmosphere Explorer satellite data. Many reaction rates which

were first derived using the Atmosphere Explorer data have since been confirmed in the laboratory. The standard solar minimum spectrum is scaled with solar activity using the AE-E solar flux measurements between 1977 and 1980. This is the only suitable set of solar cycle EUV flux measurements at the present time. The EUVAC model produces 50-575 Å integrated fluxes that agree well with the most reliable rocket measurements. It also reproduces the shape of the measured photoelectron fluxes quite well.

The most recent enhancement to our overall modeling capability has been the development of a new algorithm which allows any time-dependent ionospheric model to reproduce the measured N_mF_2 . The measured h_mF_2 and N_mF_2 are input to the model which then reproduces the full measured electron density altitude profiles with a minimum of effort [*Richards et al.*, 1994d]. In this method, the entire model electron density profile undergoes a small adjustment at each time step so that the model N_mF_2 agrees with the measured N_mF_2 to within a few percent. At the same time, the model h_mF_2 is constrained to the observed value using the algorithm of *Richards* [1991]. Although the FLIP model is generally run using the standard inputs for comparisons with measurements, there are many applications that require more accurate electron densities; for example, when studying the airglow emission rates or when studying the ionospheric energy balance. For those studies that require accurate electron densities only as ancillary information, the new algorithm is invaluable.

We have developed an efficient 2-stream auroral electron model to study the deposition of auroral energy and the dependence of auroral emission rates on characteristic energy. This model incorporates the concept of average energy loss to reduce the computation time [*Richards and Torr*, 1990]. Our simple 2-stream auroral model produces integrated emission rates that are in excellent agreement with the much more complex multi stream model of *Strickland et al.* [1983]. The auroral model has been incorporated into the FLIP model and is being used to study the ratios of various auroral emissions with the aim of being able to deduce the auroral energy input [*Germany et al.* 1994a]. We are also investigating the relationship between auroral emissions and ionospheric conductivities in order to provide magnetospheric modelers with ionospheric conductivities from auroral imaging [*Germany et al.*, 1994b].

4. Model Outputs

The output from the FLIP model consists of densities and fluxes of O^+, H^+, N^+, He^+, electron and ion temperatures, heat fluxes, and photoelectron fluxes along complete interhemispheric flux tubes. The model also calculates the densities and emissions of numerous minor species in both hemispheres. Production and loss rates can be obtained for each species solved. The model typically uses time steps ranging from 5 minutes to half an hour depending on the rate of change of ionospheric conditions. Short time steps are normally desirable near sunrise and sunset when there are rapid changes in production and loss rates, but longer time steps are acceptable during the day and at night.

Sample outputs from the FLIP model are shown in Figures 1 and 2. Figure 1 shows altitude versus time contour plots of the electron density over Millstone Hill (43N, 71W) in December of 1991. The top panel compares the measured densities with the model densities when the model uses measurements of both h_mF_2 and N_mF_2 as inputs to force closer agreement with data at the $F2$ peak. Figure 1 shows that the model then fills in the full altitude profiles of the F-region extremely well. The bottom panel shows a comparison of the model density with the measured densities when the HWM90 model winds are used as an input. There is no longer good agreement as the peak height and density of the $F2$ layer are both too low.

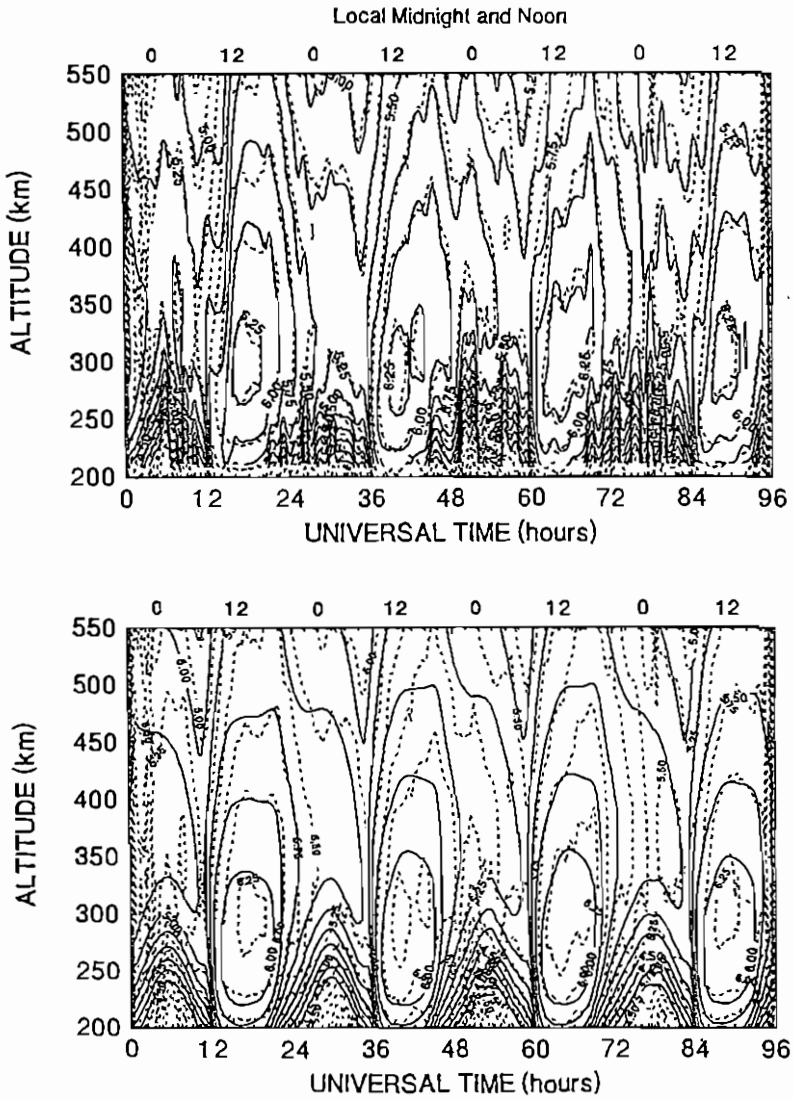

Figure 1. Comparison of the measured electron density at Millstone Hill (dashed lines) with calculated electron density (solid lines) for the LTCS6 period 8-11 December 1991. The contours represent log_{10} of the density which is in units of cm^{-3}. (a) The FLIP model employed the new N_mF_2 normalization algorithm and obtained the neutral wind from h_mF_2. (b) The FLIP model did not employ the new N_mF_2 normalization algorithm and HWM90 was used to provide the neutral wind.

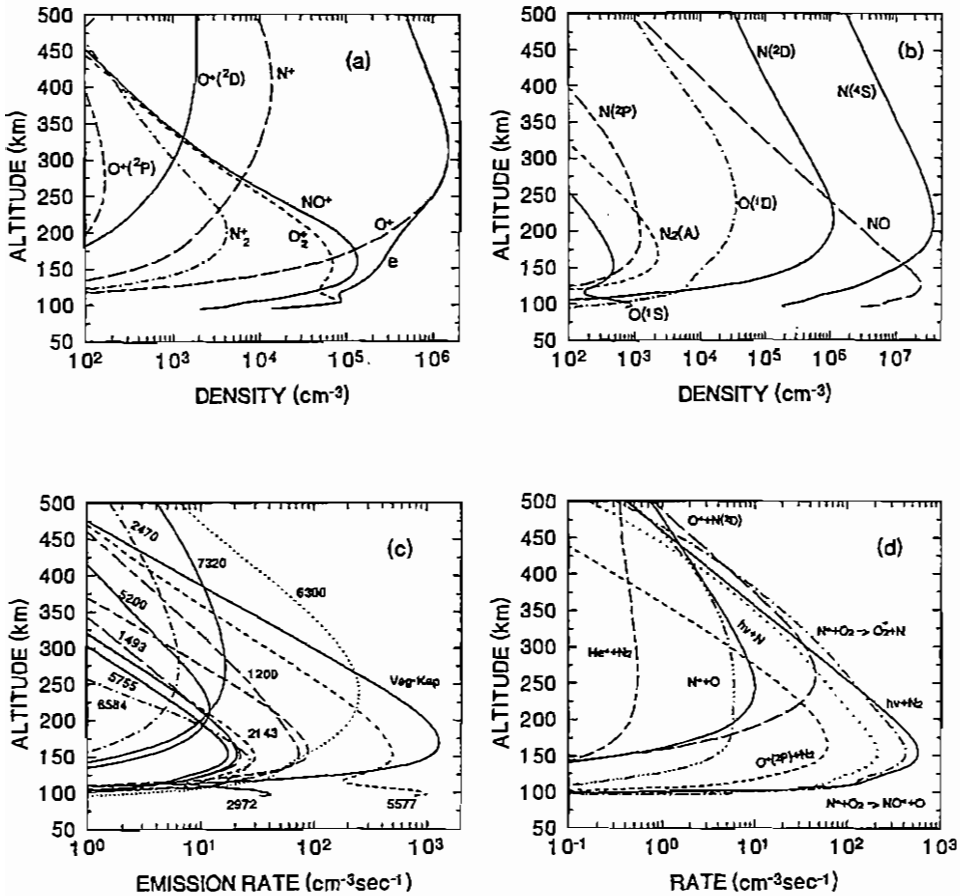

Figure 2. Sample altitude profiles of ion densities (2a), minor neutral densities (2b), airglow emission rates (2c), and N^+ production and loss rates (2d) for Hobart (42S, 147E) at solar maximum and equinox.

Similar contour plots can be obtained for all the other densities, temperatures, and emission rates that are output from the FLIP model. Sample altitude profiles of the FLIP output for solar maximum and equinox are shown in Figure 2a-d. Figure 2a shows altitude profiles of all the key ions except He^+ and H^+ which only become important at higher altitudes. Figure 2b shows the densities of the main minor neutral species that are output from the model while Figure 2c shows a selection of the main airglow emission rates. Finally, Figure 2d shows altitude profiles of the production and loss rates for N^+. Production and loss rates are available for all the ion and neutral species.

Other important outputs are photoelectron flux spectra (1-100 eV), electron heating and cooling rates, plasmaspheric heat and particle fluxes, electron and ion temperatures, major ion velocities, and the magnetic meridional component of the neutral wind. Photoionization fluxes and cross sections and electron impact cross sections can also be output.

5. Uncertainties and Limitations

One limitation of the FLIP model at the moment is the neglect of convection electric fields which are important at equatorial latitudes as well as auroral latitudes. We are currently in the process of developing the capability to include convection electric fields. However, it should be noted that these electric fields are not well known and the high latitude region in particular is highly variable. Thus, quantitative modeling of these regions is very difficult even when electric fields are included. The FLIP model is most accurate at midlatitudes for L values between about 1.3 and 5 under magnetically quiet conditions.

One problem in modeling the plasmasphere is knowing the appropriate initial ion densities in the flux tube. This introduces uncertainty in the calculated densities and temperatures in the ionosphere as well as the plasmasphere because the plasmasphere acts as an important reservoir of particles and energy for the ionosphere. This is not a large problem if magnetically quiet conditions prevail for several days, for then the flux tubes will be close to full. If, however, there has been a recent magnetic storm the flux tubes may have been partially or completely emptied and be in a state of recovery. The initial ion content of the flux tube will be very uncertain as a result. In addition, since the FLIP model is a low speed formulation (the inertial terms in the momentum equation have been neglected), it is not appropriate for the first day or so of refilling and the density distributions will not be physically meaningful at this time. Nonetheless, the refilling fluxes are likely to be reasonable because they are determined primarily by the conditions in the topside ionosphere [*Geisler*, 1967; *Richards and Torr*, 1985b]. As yet, there is no definite way of knowing the initial ion distributions in a flux tube following a magnetic storm. The FLIP model has a user specified parameter for setting the initial densities in the plasmasphere.

Until recently, the largest uncertainty for ionospheric modeling has been the neutral wind. The applicability of neutral wind models is limited because there is a large amount of day-to-day variability in the winds. When measurements of h_mF_2 are available, the wind uncertainty can be greatly reduced by using the methods of *Miller et al.* [1986] or *Richards* [1991] to determine the neutral winds.

Most first principles models have a problem modeling the nighttime *F*-region ionosphere. FLIP model peak electron densities are often a factor of 3 or more lower that the measurements at Millstone Hill (43N, 73W). However, there does not seem to be the same problem at Hobart (42S, 147E) in 1990 [*Richards et al.*, 1994d]. More reliable nighttime densities can be obtained

using the new N_mF_2 normalization algorithm whenever h_mF_2 and N_mF_2 are available. This is useful, for example, for studies of the nightglow and ionospheric energetics.

There are also problems in the *E*-region where most models give O_2^+ as the major ion but measurements show NO^+ to be the major ion. The problem, which can be seen in Figure 2a near 100 km, has been discussed in detail by *Buonsanto et al.* [1994].

6. Availability of Model

A VAX version of the FLIP model is available upon request from Phil Richards (richards@cs.uah.edu) who will install the model on your machine and ensure that it is running correctly. The model is set up to run from DEC command language (DCL) files which are well documented. There is also an interface that leads the user through the process of setting up the required parameters for the simulation. The user needs some familiarity with the VMS operating system, DCL, and a basic knowledge of the ionosphere. The model is currently being used by several scientists and graduate students nationally and internationally. Running the FLIP model is a little more complicated than running the IRI model.

The typical operating mode is to simulate one or more days of ionospheric behavior for each run. A run starts at midday local time and continues for 36 hours. Results prior to the first midnight are discarded to allow time for the model to iterate away from the rough initial conditions. A full up version of the model with all switches on requires about 10 minutes of CPU on a VAX Alpha machine for the 36 hour simulation. Between 10,000 and 20,000 VAX blocks of disk storage is needed to comfortably run the model as each run generates several thousand blocks of data.

Acknowledgments. This work was supported by NSF grants ATM-9018165, ATM-9017201, and ATM-9202887; and NASA grant NAGW-996 at The University of Alabama in Huntsville. Computational resources and data from the CEDAR data base were obtained from the National Center for Atmospheric Research which is sponsored by the National Science Foundation.

7. References

Bilitza, D., K. Rawer, L. Bossy, and T. Gulyaeva, *Adv. Space Res., 13*, #3, 3, 1993.

Buonsanto, M. J., P. G. Richards, W. K. Tobiska, S. C. Solomon, Y.-K. Tung, and J. A. Fennelly, submitted to *J. Geophys. Res., 99*, December, 1994.

Burnside, R. G., C. A. Tepley, and V.B. Wickwar, *Ann. Geophys.*, Ser. A, *5* (6), 343, 1987.

Craven, P. D., R. H. Comfort, P. G. Richards, and J. Grebowsky, *J. Geophys. Res., 100*, 257, 1994.

Geisler, J. E., *J. Geophys. Res., 72*, 81, 1967.

Germany, G., M. R. Torr, D. G. Torr, and P. G. Richards, *J. Geophys. Res., 99*, 383, 1994.

Germany, G., D. G. Torr, P. G. Richards, and M. R. Torr, *J. Geophys. Res., 99*, 23,297, 1994.

Hedin, A. E., *J. Geophys. Res., 92*, 4649, 1987.

Hedin, A. E., M. A. Biondi, R. G. Burnside, G. Hernandez, R. M. Johnson, T. L. Killeen, C. Mazaudier, J. W. Meriwether, J. E. Salah, R. J. Sica, R. W. Smith, N. W. Spencer, V. B. Wickwar, and T. S. Virdi, *J. Geophys. Res., 96*, 7657, 1991.

Miller, K. L., D. G. Torr, and P. G. Richards, *J. Geophys. Res., 91*, 4531, 1986.

Nagy, A. F., and P. M. Banks, *J. Geophys. Res., 75*, 6260, 1970.

Newberry, I. T., R. H. Comfort, and P. G. Richards, *J. Geophys. Res., 94*, 15,265, 1989.
Richards, P. G., and D. G. Torr, in *Proceedings of the Thermosphere Dynamics Workshop II* (edited by H. G. Mayr and N. J. Miller), NASA Conference Publication 2398, 369, 1985a.
Richards, P. G., and D. G. Torr, *J. Geophys. Res., 90*, 5261, 1985b.
Richards, P. G., *Planet. Space Sci., 34*, 689, 1986.
Richards, P. G., and D. G. Torr, *J. Geophys. Res., 91*, 11,331, 1986.
Richards, P. G., D. G. Torr, and W. A. Abdou, *J. Geophys. Res., 91*, 304, 1986.
Richards, P. G., and D. G. Torr, *J. Geophys. Res., 93*, 4060, 1988.
Richards, P. G., and D. G. Torr, *J. Geophys. Res., 95*, 10337-10344, 1990.
Richards, P. G., *J. Geophys. Res., 96*, 17,839, 1991.
Richards, P. G., J. A. Fennelly, and D. G. Torr, *J. Geophys. Res, 99*, 8981, 1994a.
Richards, P. G., D. G. Torr, B. W. Reinisch, R. R. Gamache, and P. J. Wilkinson, *J. Geophys. Res., 99*, 15,005, 1994b.
Richards, P. G., D. G. Torr, M. J. Buonsanto, and D. P. Sipler, *J. Geophys. Res., 99*, 23,359, 1994c.
Richards, P. G., D. G. Torr, M. E. Hagan, and M. J. Buonsanto, submitted to *J. Geophys. Res., 99*, August, 1994d.
Schunk, R. W., *Planet. Space Sci., 23*, 437, 1975.
Schunk, R. W., and A. F. Nagy, *Rev. Geophys., 16*, 355, 1978.
Schunk, R. W., and A. F. Nagy, *Rev. of Geophys. Space Phys., 18*, 4, 813, 1980.
St.-Maurice, J.-P., and R. W. Schunk, *Planet. Space Sci., 25*, 907, 1976.
Strickland, D. J., J. R. Jasperse, and J. A. Whalen, *J. Geophys. Res., 88*, 8051, 1983.
Torr, M. R., D. G. Torr, P. G. Richards, and S. P. Yung, *J. Geophys. Res., 95*, 21,147, 1990.
Torr, M. R., D. G. Torr, T. Chang, P. G. Richards, W. Swift, and N. Li, *J. Geophys. Res., 99*, in press, 1994.
Young, E. R., P. G. Richards, and D. G. Torr, *J. Comput. Phys., 38*, 141, 1980.
Young, E. R., D. G. Torr, P. Richards, and A. F. Nagy, *Planet. Space Sci., 28*, 881, 1980.

A Coupled Thermosphere-Ionosphere Model (CTIM)

T. J. Fuller-Rowell[1], D. Rees[2], S. Quegan[3], R. J. Moffett[3],
M. V. Codrescu[1], and G. H. Millward[1]

[1]CIRES, University of Colorado/NOAA Space Environment Center,
325 Broadway, Boulder, Colorado 80303, USA

[2]Atmospheric Physics Laboratory, Department of Physics and Astronomy,
University College London, 67-73 Riding House Street,
London W1P 7PP, UK

[3]Upper Atmosphere Modelling Group, School of Mathematics and Statistics,
University of Sheffield, Sheffield S3 7RH, UK

1. Introduction

The Coupled Thermosphere-Ionosphere Model (CTIM) has evolved from the union of two independently-developed physical models. The first is a global, non-linear, time-dependent neutral thermospheric model developed by *Fuller-Rowell and Rees* [1980; 1983], and the second is a mid- and high-latitude ionospheric convection model developed by *Quegan et al.* [1982]. Since that time, the code has been used to understand a range of physical processes in the upper atmosphere. Much of the insight into the physics that has led to significant advances in the field has come from analysis of the coupling between the neutral and plasma environment. It is the recognition of this aspect that has been the impetus for the further coupling of the model with the plasmasphere, as described in the accompanying report in this handbook by *Millward et al.* [1996].

The thermosphere/ionosphere system is highly variable, and responds distinctly to the major driving forces from the magnetosphere, sun and lower atmosphere. These sources include tides, gravity waves and planetary waves propagating from the lower atmosphere, auroral precipitation and convective electric field from the magnetosphere, and radiation from the sun. These variable driving forces, the feed-back mechanisms between the thermosphere and the ionosphere, and the non-linear response of the thermosphere [*Fuller-Rowell and Rees*, 1984], combine to cause complex variations. In view of this complexity, numerical models have gained wide acceptance as a means of investigating and understanding the behavior, and interactions between the thermosphere and ionosphere. If numerical/computation models are in basic agreement with observations, they provide a useful tool to analyze the dominant physical processes.

It is not feasible to present here a comprehensive review of thermospheric observations, nor of the historical development of numerical models of the thermosphere and ionosphere. A brief review of some of the major milestones will, however, be given. More comprehensive reviews and bibliographies can be found in *Roble* [1983], *Hernandez and Killeen* [1988], *Schunk* [1987], *Hedin* [1988], *Oliver et al.* [1988], *Prölss et al.* [1988], *Moffett and Quegan* [1983], and references therein.

The earliest theoretical global model of thermospheric dynamics was that of *Kohl and King* [1967]. It was derived by calculating pressure gradients from empirical thermospheric density models, and used a globally-uniform ionosphere to compute the ion drag term. The computations used considerable simplifications of the full Navier-Stokes equations. It proved successful in determining upper thermospheric winds (300 km), as driven by solar EUV, although it included none of the relevant physics of solar heating, IR cooling, or thermal transport and conduction. Several amendments and improvements were made during the following five years. The next major advances in numerical modeling were made by introducing the physics of solar UV/EUV heating of the thermosphere, and in the development of harmonic models. Such models were presented by *Mayr and Volland* [1972], *Creekmore et al.* [1975], *Harris and Mayr* [1975], and by *Blum and Harris* [1974].

To obtain a stable numerical solution, and to remain within acceptable computer processing requirements, the early models neglected or simplified some of the major terms of the energy and momentum equations, such as non-linear or advection terms. These early studies did not have the benefit of the more recent descriptions of the major physical processes and driving forces affecting the thermosphere, such as EUV heating efficiencies, magnetospheric particle precipitation, and plasma convection.

Reviews of the early modeling work can be found in *Cole* [1971], *Fedder and Banks*, [1972], *Creekmore et al.* [1975], *Straus et al.* [1975], *Blum and Harris*, [1974], and *Dickinson et al.* [1975]. Some of the early theoretical models, including the two-dimensional models of *Richmond and Matsushita* [1975], *Richmond* [1979], and *Dickinson et al.* [1975], produced results which were very important for the later development of three dimensional and time-dependent General Circulation Models (GCM) [*Fuller-Rowell and Rees*, 1980, 1981; *Dickinson et al.*, 1981, 1984; *Roble et al.*, 1982; and *Roble*, 1983].

In the real thermosphere, tides and gravity waves propagate from sources within the troposphere, stratosphere and mesosphere [*Groves and Forbes*, 1984; *Fesen et al.*, 1986; *Parish et al.*, 1990]. The propagation of these tides, and of planetary wave features associated with lower atmospheric meteorology, causes significant wind and temperature perturbations within the lower thermosphere. Their effects can also be traced in the upper thermosphere where, for example, the amplitude of the post-midnight equatorial temperature and density "bulge" has been ascribed to the propagation of tides of lower atmosphere origin. In thermospheric GCMs, the method of introducing propagating tides or gravity waves is to create a "flexible" lower boundary; in other words, the geopotential height of the lower boundary is made non-uniform [*Fesen et al.*, 1986, 1993; *Parish et al.*, 1990, 1992].

Mayr et al. [1978] made it clear that a self-consistent handling of the interaction between thermospheric composition and wind advection/convection was required to handle major composition change, such as those associated with inter-hemispheric flow during solstice. If composition is assumed to be constant at particular pressure levels, quite large errors in the pole-to-pole temperature gradient and mean meridional winds result. A self-consistent dynamical/compositional treatment was introduced into the GCM codes by *Fuller-Rowell and Rees* [1983] and by *Dickinson et al.* [1984]. Wind-driven diffusion, acting in addition to turbulent mixing in the lower thermosphere, and the diffusive separation of heavy and light species, creates the winter polar maximum of atomic oxygen and helium, and the summer polar maximum of molecular nitrogen and argon [*Hedin*, 1987; 1991]. GCM codes with this treatment can simulate both diurnal and seasonal/latitudinal compositional variations, and the compositional changes induced by geomagnetic activity.

Another major problem is handling the rapid time-dependence of the thermospheric wind response to geomagnetic activity [*Richmond and Matsushita*, 1975; *Richmond*, 1979; *Fuller-Rowell and Rees*, 1981; *Rees and Fuller-Rowell*, 1992]. Even during steady solar and

geomagnetic conditions a time dependence is induced by the diurnal migration of the mapping of the magnetospheric sources into the geographic frame. The true value of non-linear, time-dependent models is realized when simulating severe disturbances associated with geomagnetic storms. During these periods, the magnitude of the magnetospheric energy input is at its maximum and can change rapidly over periods of minutes to hours. Strong wave activity is generated during these times and the importance of transport of energy, momentum, and composition is most apparent.

The diameters of the polar cap and the auroral oval expand and contract under the influence of changing solar wind conditions, with an associated modulation of the electric potential across the polar cap. This modulates ion drift velocities, ion drag and Joule heating. Regions of magnetospheric energetic particle precipitation roughly co-vary with convection patterns [*Foster et al.*, 1986], varying the location and magnitude of the signatures of magnetospheric processes. The thermosphere shows a strong time-dependent response to intense forcing during major geomagnetic disturbances [*Fuller-Rowell et al.*, 1994].

Geomagnetic control of the ionosphere and thermosphere in the polar regions has been demonstrated by observations reported from the Dynamics Explorer spacecraft (DE-2) such as those described by *Hays et al.* [1984], *Killeen et al.* [1983], and *Rees et al.* [1983, 1985a, b].

Early studies with three-dimensional models [*Fuller-Rowell and Rees*, 1980, 1981; *Rees et al.* 1980, *Roble et al.*, 1982] showed that the dynamical response of the thermosphere to the energy and momentum sources associated with geomagnetic forcing could be simulated, to first order, by including simplified models of the polar convection electric field such as those of *Heppner* [1977], as parameterized by *Volland* [1979], and using the global *Chiu* [1975] ionospheric model.

Detailed studies of the GCM simulations, however, showed that the polar thermosphere momentum input and the global energy budgets were not sufficiently enhanced at times of moderate geomagnetic disturbances. The *Chiu* [1975] ionospheric model has no terms reflecting the high latitude ionospheric response to geomagnetic activity, as demonstrated by high latitude rocket and satellite data, particularly within the lower thermosphere, and associated with auroral precipitation.

Solution of the problem required incorporation of a more realistic model of the ionosphere [*Quegan et al.*, 1982] which accounted for the interactions between solar photo-ionization, auroral precipitation, plasma convection and thermospheric chemistry and dynamics. Enhanced polar ionospheric plasma densities increase conductivity and momentum coupling between the convecting ions and neutrals. The resulting enhanced Joule heating adds to the direct particle heating. Simulations of thermospheric wind, temperature and composition structures have been shown to be in good general agreement with both large scale and local thermospheric observations, even during time-dependent geomagnetic disturbances [*Rees et al.*, 1983; 1984a, b; 1985a, b].

The concept of following a magnetic tube containing "frozen-in" plasma in the F-region and topside ionosphere was put on a firm mathematical basis by *Kendall* [1962], *Hanson and Moffett* [1966], *Baxter and Kendall* [1968], *Bramley and Young* [1968], *Sterling et al.* [1969] and *Anderson* [1973]. The complexity of the calculation of plasma continuity, diffusion and thermal balance within a moving flux tube has increased greatly since then, particularly in models of the equatorial and mid-latitude ionosphere (for a recent review, see *Stening* [1992]). The crucial effects of magnetospheric convection [*Knudsen*, 1974] were included in models of the high-latitude ionosphere by *Knudsen et al.* [1977], *Watkins* [1978] and *Sojka et al.* [1981]. *Quegan et al.* [1982] also included H^+ and raised the upper boundary so that their high-latitude model included results for mid-latitudes, including the outer plasmasphere.

The first attempts at computing a self-consistent ionosphere and thermosphere model [*Quegan et al.*, 1982; *Fuller-Rowell et al.*, 1984] were achieved by iterating between a thermospheric code [*Fuller-Rowell and Rees*, 1980] and a separate ionospheric code [*Quegan et al.*, 1982]. These first simulations did not include UT dependence, and was derived for northern polar winter. These simulations were tested extensively by comparison with the wind, temperature and neutral composition data sets from spacecraft such as Dynamics Explorer [*Rees et al.*, 1985a, b], from ground-based facilities such as the incoherent scatter radars [*Rees et al.*, 1983] and from ground-based optical instruments such as Fabry-Perot interferometers located at several high latitude stations [*Rees et al.*, 1984a, b]. Comparisons with data and with empirical models show that the major diurnal, latitudinal and seasonal variations of the middle and low latitude thermosphere, in wind velocity, temperature and density of the major species, can be successfully represented in theoretical models for a wide range of solar and geomagnetic activity levels [*Rees and Fuller-Rowell*, 1987, 1988].

A model illustrating the self-consistent coupling of the two regimes was presented by *Fuller-Rowell et al.* [1987]. This model has since been used for understanding the interaction between thermosphere and ionosphere under a range of circumstances [*Fuller-Rowell et al.*, 1988; *Rees et al.*, 1986, 1988; *Rees and Fuller-Rowell*, 1988; *Fuller-Rowell*, 1990; *Fuller-Rowell et al.*, 1991a, b; *Millward et al.*, 1993a, b; *Fuller-Rowell et al.*, 1994]. The present paper describes the current state of this coupled thermosphere ionosphere model (CTIM).

2. The Coupled Thermosphere-Ionosphere Model

The Coupled Thermosphere-Ionosphere Model (CTIM) has evolved from an integration of a neutral thermospheric code and a high and mid-latitude ionosphere model. The neutral thermospheric model was originally developed by *Fuller-Rowell and Rees* [1980] at University College London (UCL); the ionospheric model originated from Sheffield University [*Quegan et al.*, 1982].

2.1 Thermosphere Model

The thermospheric code simulates the time-dependent structure of the wind vector, temperature and density of the neutral thermosphere by numerically solving the non-linear primitive equations of momentum, energy and continuity. The global atmosphere is divided into a series of elements in geographic latitude, longitude and pressure. Each grid point rotates with the Earth to define a non-inertial frame of reference in a spherical polar coordinate system. The latitude resolution is 2°, longitude resolution 18°, and each longitude slice sweeps through local time with a one minute time step. In the vertical direction the atmosphere is divided into 15 levels in logarithm of pressure from a lower boundary of 1 Pa at 80 km altitude.

The top pressure level varies in altitude with changes in the temperature profile, rising from around 300 km during extremely quiet geomagnetic periods at low solar activity to altitudes in excess of 700 km during disturbed periods at high solar activity. In all cases, the range of pressure levels covers the thermospheric regimes from below the mesopause up to, and including, altitudes where there are only small vertical gradients of neutral velocity and temperature, in the vicinity of the exobase. This altitude range covers the ionospheric E- and F-regions.

The momentum equation is non-linear and the solutions describe the horizontal and vertical advection, i.e. the transport of momentum. The transformation to a non-inertial frame of a rotating spherical atmosphere is complete with the exception that the radial centrifugal component is absorbed within the gravitational acceleration, g (which is assumed constant at 9.5

m s^{-2}). This transformation results in the curvature and Coriolis effects which are fundamental in realistic simulations of atmospheric dynamics. The momentum equation also includes horizontal pressure gradients (described exactly by gradients in the heights of the pressure surfaces), horizontal and vertical viscosity, and ion drag. Similarly, the non-linear energy equation is solved self-consistently with the momentum equation, and it describes the three dimensional advection of energy, and the transfer of energy between internal, kinetic and potential energy. The solutions also describe the horizontal and vertical heat conduction by both molecular and turbulent diffusion, heating by solar UV and EUV radiation, cooling by infrared radiation, and heating due to the ohmic dissipation of ionospheric currents, known as Joule or frictional heating.

The solution of a time-dependent mean mass equation was incorporated into the model by *Fuller-Rowell and Rees* [1983]. This formalism assumed the upper atmosphere could be approximated by two species, atomic oxygen and the sum of molecular nitrogen and oxygen. More recently the major species composition has been improved to include solution of the three major species, O, O_2 and N_2, including chemistry, transport and the mutual diffusion between the species.

The time dependent variables of southward and eastward wind, total energy density, and concentrations of O, O_2 and N_2 are evaluated at each grid point by an explicit time-stepping numerical technique. After each iteration, the vertical wind is derived, together with temperature, density, and heights of pressure surfaces. The parameters can be interpolated to fixed heights for comparison with experimental data.

2.1.1 Equation of Motion

The thermosphere, although a tenuous gas, is still collision dominated and isotropic. The consequence is that the basic equations of fluid dynamics, i.e., the Navier-Stokes expressions, can be applied to the system [*Conrad and Schunk*, 1979]. The nature of the atmospheric response to the many sources can be interpreted by these equations. The equation of motion describing the balance of forces acting on a parcel of neutral gas and the resultant time rate of change of velocity is given by:

$$\frac{D}{Dt}\mathbf{V} = \underbrace{-\frac{1}{\rho}\nabla p}_{\text{pressure gradient}} \underbrace{- 2\Omega \wedge \mathbf{V}}_{\text{Coriolis}} \underbrace{- \nu_{ni}(\mathbf{V}-\mathbf{U})}_{\text{ion drag}} \underbrace{+ \frac{1}{\rho}\nabla(\mu \nabla \mathbf{V})}_{\text{viscosity}}, \qquad (1)$$

where $\mathbf{V}$ is the neutral wind velocity, p the gas pressure, Ω the angular rotation rate of Earth, $\mathbf{U}$ the ion drift velocity, ν_{ni} the neutral-ion collision frequency, ρ gas density, and μ the sum of the molecular and turbulent viscosity coefficient. The four main forces acting on a parcel of gas are pressure, Coriolis, ion drag and viscosity. Pressure gradients are produced by heating from solar radiation or Joule dissipation, or are generated by tidal fields propagating from the lower atmosphere. As the atmosphere is forced into motion the Coriolis force begins to act; this tends to turn the gas in a clockwise sense in the northern hemisphere and anti-clockwise in the south. The ion drag term represents the collisional interaction between the neutral and plasma components. This term can either inhibit the neutral motion or, if an electric field is present to accelerate the ions, can provide a strong source of acceleration, driving winds to high velocity. The final term is viscosity, which acts to smooth gradients in the wind field, particularly over short vertical distances. In the lower thermosphere there is a region of cross-over from turbulent to molecular diffusion, where both are small. Such a region enables steep vertical shear to persist and is partly the cause of the high degree of vertical structure in the lower thermosphere.

The above equation is appropriate for the forces acting on a parcel of gas as it moves with respect to Earth, i.e., the so-called Lagrangian frame of reference. To transform to the Earth's frame, or so-called Eulerian frame, where latitude and longitude are the independent variables, the following transformation is required:

$$\frac{D}{Dt}X = \frac{\partial}{\partial t}X + (V \cdot \nabla)X, \tag{2}$$

where X is any property such as temperature or velocity of the fluid. The partial derivative with respect to time represents the rate of change of X at a fixed point on the Earth, and is related to the total derivative by the advection term. The process of advection simply represents the change of a property of the fluid as a result of transport by the wind field past a fixed location.

We can now express the change in velocity of the two wind components, southward (V_θ) and eastward (V_ϕ), transformed to a pressure coordinate system, by the following equations:

$$\begin{aligned}\frac{\partial}{\partial t}V_\theta = &-\frac{V_\theta}{r}\frac{\partial}{\partial \theta}V_\theta - \frac{V_\phi}{r\sin\theta}\frac{\partial}{\partial \phi}V_\theta - \omega\frac{\partial}{\partial p}V_\theta - \frac{g}{r}\frac{\partial}{\partial \theta}h \\ &+\left(2\Omega + \frac{V\phi}{r\sin\theta}\right)V_\phi\cos\theta + g\frac{\partial}{\partial p}\left[(\mu_m + \mu_T)\frac{p}{H}\frac{\partial}{\partial p}V_\theta\right] - \nu_{ni}(V_\theta - U_\theta),\end{aligned} \tag{3}$$

and

$$\begin{aligned}\frac{\partial}{\partial t}V_\phi = &-\frac{V_\theta}{r}\frac{\partial}{\partial \theta}V_\phi - \frac{V_\phi}{r\sin\theta}\frac{\partial}{\partial \phi}V_\phi - \omega\frac{\partial}{\partial p}V_\phi - \frac{g}{r\sin\theta}\frac{\partial}{\partial \phi}h \\ &-\left(2\Omega + \frac{V_\phi}{r\sin\theta}\right)V_\theta\cos\theta + g\frac{\partial}{\partial p}\left[(\mu_m + \mu_T)\frac{p}{H}\frac{\partial}{\partial p}V_\phi\right] - \nu_{ni}(V_\phi - U_\phi),\end{aligned} \tag{4}$$

where r is the Earth's radius, θ is co-latitude, ϕ is longitude, g is gravitational acceleration, μ_m and μ_T are the molecular and turbulent coefficients of viscosity, h is the height of the pressure surface, H is the scale height, and ω is the vertical wind in the pressure coordinate system, $\omega = dp/dt$.

2.1.2 *Equation of Energy*

A similar equation representing conservation of energy of the system can also be derived. The expression for the time rate of change of energy density, ε (the sum of internal energy, c_pT, and kinetic energy density, $V^2/2$) per unit mass of gas is given by:

$$\begin{aligned}\frac{\partial \varepsilon}{\partial t} = &-V \cdot \nabla_p(\varepsilon + gh) - \omega\frac{\partial}{\partial p}(\varepsilon + gh) + g\frac{\partial}{\partial p}\left[(K_m + K_T)\frac{p}{H}\frac{\partial T}{\partial p}\right] \\ &-g\frac{\partial}{\partial p}\frac{K_T g}{C_p} + (K_m + K_T)\frac{1}{\rho}\left(\frac{1}{r^2}\frac{\partial^2 T}{\partial \theta^2} + \frac{\cot\theta}{r^2}\frac{\partial T}{\partial \theta}\right) \\ &+V_\theta F_\theta + V_\phi F_\phi + (J_\theta E_\theta + J_\phi E_\phi)/\rho + \text{viscous dissipation} \\ &+ \text{solar heating} + \text{radiative cooling},\end{aligned} \tag{5}$$

where F_θ and F_ϕ are the viscosity terms in the θ and ϕ direction from the momentum equations, K_m and K_T are the molecular and turbulent coefficients of heat conduction, C_p is the specific heat at constant pressure, J_θ and J_ϕ are current density in the θ and ϕ directions, and E_θ and E_ϕ are the electric fields in the θ and ϕ directions.

The terms on the right-hand side of the energy equation, which are not described, are, in their respective order, (1) horizontal advection of energy, (2) vertical advection of energy, (3) vertical molecular and turbulent heat conduction, (4) eddy mixing of potential temperature, (5) horizontal molecular and turbulent heat conduction, (6) work done by viscous forces in the θ and ϕ directions from the momentum equation, (7) the sum of Joule heating $(\mathbf{J} \cdot (\mathbf{E} + \mathbf{V} \wedge \mathbf{B}))/\rho$ and the change in kinetic energy density due to ion drag $(\mathbf{V} \cdot (\mathbf{J} \wedge \mathbf{B})/\rho)$.

After the total energy density and horizontal wind vector velocity are evaluated, the temperature of the neutral gas is extracted from $\varepsilon = c_p T + V^2/2$

2.1.3 Equation of State

The relationship between temperature, pressure, and density is given by the general gas law:

$$p = nkT = \frac{\rho RT}{m} = H\rho g. \tag{6}$$

where n is total number density, k is Boltzmann's constant, R is the Universal gas constant, and m is the mean molecular mass.

2.1.4 Equation of Continuity

The continuity equation in the pressure coordinate system is given by:

$$\frac{\partial \omega}{\partial p} = -\nabla_p \cdot \mathbf{V}, \tag{7}$$

which results in the interesting observation that the fluid appears incompressible in the pressure coordinate system although the equations make complete allowance for the compressibility of the real fluid.

2.1.5 Equation of Vertical Velocity

The true velocity is given by:

$$V_z = \left(\frac{\partial h}{\partial t}\right)_p - \frac{\omega}{\rho g}, \tag{8}$$

where $(\partial h/\partial t)_p$ is the rate of change of height of a pressure level.

2.1.6 Equation of Current Density

The current density **J** is defined by:

$$J = \sigma \cdot (E + V \wedge B), \tag{9}$$

where σ is the layer conductivity tensor [*Rishbeth and Garriott*, 1969], and **B** is Earth's magnetic field vector.

2.1.7 Equation of Composition

Using a combination of the generalized diffusion equation [*Chapman and Cowling*, 1970] and the continuity equations, the change in composition of the three-species gas (O, O_2 and N_2) is evaluated self-consistently with the wind and temperature fields. The major species are atomic oxygen, molecular nitrogen and molecular oxygen. Allowance is made for mutual molecular diffusion of the three species, horizontal and vertical advection, turbulent mixing vertically and horizontally, and production and loss mechanisms.

The continuity equation for mass mixing ratio, $\psi_i = n_i m_i/\rho$, of species i is given by:

$$\frac{\partial \psi_i}{\partial t} = \frac{1}{\rho} m_i S_i - \mathbf{V}\cdot\nabla_p \psi_i - \omega \frac{\partial}{\partial p}\psi_i - \frac{1}{\rho}\nabla\cdot(n_i\, m_i\, C_i) + \frac{1}{\rho}\nabla(K_T\, n\, \nabla\, m\, \psi_i), \qquad (10)$$

where m_i is its molecular mass, S_i represents sources and sinks of the species, n_i its number density, and C_i is the diffusion velocity.

The terms on the right-hand side of the continuity equation for the species are, in their respective order, (1) sources and sinks of species, (2) horizontal advection, (3) vertical advection, (4) molecular diffusion, and (5) eddy diffusion.

The diffusion velocities are evaluated from the general diffusion equation for a multi-species gas given by:

$$\frac{1}{n}\sum_{j\neq i}\left(\frac{\psi_j}{m_j D_{ij}}\, n_j\, m_j\, \mathbf{C}_j - \frac{\psi_i}{m_j D_{ij}}\, n_i\, m_i\, \mathbf{C}_i\right) = \nabla\, \psi_i + \frac{\psi_i}{m}\nabla m + \left(1 - \frac{m_i}{m}\right)\frac{\psi_i}{p}\nabla p, \qquad (11)$$

where D_{ij} are the mutual diffusion coefficients between species i and j, and m is the mean molecular mass of the gas. Equation (11) is a system of three coupled equations for the three constituents i = 1, 2, and 3.

Chemical production and loss mechanisms for the major species include dissociation of molecular oxygen by UV and EUV radiation, three body recombination of atomic oxygen, and the reaction of atomic oxygen with OH and HO_2, as described in *Fuller-Rowell* [1984].

2.2 Ionosphere Model

The equations for the neutral thermosphere are solved self-consistently with a high- and mid-latitude ionospheric convection model [*Quegan et al., 1982*]. The ionosphere is computed self-consistently with the thermosphere poleward of 23° latitude in both hemispheres. Traditionally, ionospheric models are evaluated in a Lagrangian system, where the evolution of ion density and temperature of parcels of plasma are computed as they are traced along their convection paths. In the coupled model, the ionospheric Lagrangian frame has been modified to be more compatible with the Eulerian frame by implementing a semi-Lagrangian technique [*Fuller-Rowell et al.*, 1987, 1988]. Adoption of a rotating frame of reference for the ionosphere eliminated the need for a "co-rotation potential."

Transport under the influence of the magnetospheric electric field is explicitly treated, assuming $\mathbf{E} \wedge \mathbf{B}$ drifts and collisions with the neutral particles. The atomic ions H^+ and O^+, and ion temperature are evaluated over the height range from 100 to 10,000 km, including horizontal transport, vertical diffusion and the ion-ion and ion-neutral chemical processes. Below 400 km, the additional contribution from the molecular ion species N_2^+, O_2^+ and NO^+, and the atomic ion N^+ are included.

Universal time effects are accounted for when calculating photoionization; the transforms defined in *Quegan et al.* [1986] are used for this purpose. The formulation of the particle precipitation input is identical to that used in the thermospheric code, and the production of individual ionic species is calculated using the expressions of *Vallance-Jones* [1974].

2.2.1 Equation of Ion Continuity

The rate of change of concentration n_i of species i is

$$\frac{\partial n_i}{\partial t} = P_i - L_i - \nabla \cdot (n_i \mathbf{v}_i), \tag{12}$$

where P_i and L_i are the production and loss rates respectively, and $\mathbf{v}_i$ is the bulk velocity. To a very good approximation in the F-region [*Kendall and Pickering*, 1967; *Schunk*, 1975], $\mathbf{v}_i$ may be resolved as:

$$\mathbf{v}_i = \mathbf{v}_i^{\perp} + \mathbf{v}_i^{\parallel}, \tag{13}$$

where

$$\mathbf{v}_i^{\perp} = \frac{\mathbf{E} \wedge \mathbf{B}}{B^2}; \tag{14}$$

$\mathbf{E}$ being the electric field, and where $\mathbf{v}_i^{\parallel}$ arises from diffusion of ions along the magnetic field lines under the influence of gravity, partial pressure gradient, space-charge electric field, thermal diffusion and collisional drag with the neutral air and other ion species. Thus (12) becomes

$$\frac{dn_i}{dt} = P_i - L_i - n_i \nabla \cdot \mathbf{v}_i^{\perp} - \nabla \cdot (n_i \mathbf{v}_i^{\parallel}), \tag{15}$$

where

$$\frac{d}{dt} = \frac{\partial}{\partial t} + \mathbf{v}_i^{\perp} \cdot \nabla. \tag{16}$$

The loss rate can be written as $\beta_i n_i$ and

$$\nabla \cdot \mathbf{v}_i^{\perp} = \frac{6 v_i^{\perp}(eq) \sin^2\theta (1 + \cos^2\theta)}{r_{eq}(1 + 3\cos^2\theta)^2} \tag{17}$$

for a dipole magnetic field, $v_i^{\perp}$ (eq) being $\left|v_i^{\perp}\right|$ at the magnetic equator. It is straightforward to show that

$$\nabla \cdot (n_i v_i^{\parallel}) = B \frac{\partial}{\partial s} \frac{n_i v_i^{\parallel}}{B}, \tag{18}$$

where s denotes arc-length along the field line.

2.2.2 Equation of Ion Diffusion .

The field-aligned component of ion velocity $v_i^{\parallel}$ is determined from the field-aligned momentum equation. For a mixture of ions, electrons and neutral particles, this takes the form [*St.-Maurice and Schunk*, 1977; *Conrad and Schunk*, 1979]:

$$v_i^{\parallel} = h_{ij} v_j^{\parallel} + h_{in} v_n^{\parallel} - D_i \left[\frac{1}{n_i} \frac{\partial n_i}{\partial s} - \frac{m_i G^{\parallel}}{kT_i} + \frac{1}{T_i} \frac{\partial}{\partial s}(T_i + T_e) + \frac{T_e}{T_i} \frac{1}{n_e} \frac{\partial n_e}{\partial s} + \frac{1}{T_i} \left(\beta_{ij} \frac{\partial T_i}{\partial s} - \beta_{ij}^* \frac{\partial T_j}{\partial s} \right) \right], \tag{19}$$

where h_{ij} and h_{in} are drag coefficients between ion species i and ion species j and between ion species i and neutral particles, respectively, $v_n^{\parallel}$ is the field-aligned component of the neutral air velocity, D_i is the ordinary diffusion coefficient, m_i is ion mass, $G^{\parallel}$ is the field-aligned component of gravity, T_i is the temperature of ion species i, T_e is electron temperature and β_{ij} and β_{ij}^* are dimensionless thermal diffusion coefficients. $v_i^{\parallel}$ can be written as:

$$n_i v_i^{\parallel} = X_i n_i - Y_i \frac{\partial n_i}{\partial s}. \tag{20}$$

Equations (15) and (19) can now be solved as a pair of coupled first order equations by using a finite difference scheme, to give densities and field aligned velocities for the ions O^+ and H^+.

2.2.3 Equation of Ion Temperature

The ion temperature is calculated under the assumption of thermal balance between heat gained from the electron gas and from ion-neutral frictional heating, and heat lost to the neutral gas. Therefore we have:

$$3k\, \nu_{ie}(T_e - T_i) + \sum_n \frac{m_i m_n \nu_{in}}{m_i + m_n} \left| v_i - v_n \right|^2 = \sum_n \frac{m_i \nu_{in}}{m_i + m_n}\, 3k(T_i - T_n). \tag{21}$$

2.2.4 Molecular Ions

At each time-step, the concentrations of the molecular ions N_2^+, O_2^+ and NO^+, and the atomic ion N^+ are calculated, under the assumption of chemical equilibrium. The calculation of the molecular ions takes into account the chemistry of the odd nitrogen species. Profiles of $N(^2D)$, $N(^4S)$, and NO are evaluated assuming a balance between vertical diffusion and chemistry at each location. The creation of nitric oxide occurs through the local dissociation of molecular nitrogen into $N(^2D)$ and $N(^4S)$ by solar and auroral particle sources, which are the

precursors of NO. The ion-neutral and neutral-neutral equations used to calculate the molecular ion concentrations are given in Table 1 and 2, respectively.

2.2.5 Parameters

Neutral thermospheric parameters of eddy diffusion, and molecular and turbulent viscosity and heat conduction are as described in *Fuller-Rowell and Rees* [1980]. Mutual diffusion coefficients are assumed to be symmetric and are taken from the expressions by *Colegrove et al.* [1966]. Ion-neutral collision frequencies are given by the expressions in the work of *Schunk and Walker* [1973] with the exception of the O-O^+ collision frequency which is taken from *Salah* [1993]. Neutral gas heating efficiencies for absorption of solar EUV are taken from *Roble et al.* [1987] and infrared cooling is parameterized as described in *Fuller-Rowell* [1984]. The parameterization of empirical inputs of electron temperature at high latitudes is described by *Quegan et al.* [1982].

3. Common Inputs

The magnetospheric input to the model is based on the statistical models of auroral precipitation and electric fields described by *Fuller-Rowell and Evans* [1987] and *Foster et al.* [1986], respectively. Both inputs are keyed to a hemispheric power index (PI), based on the TIROS/NOAA auroral particle measurements, and are mutually consistent in this respect. The magnitudes of the electric fields are increased by 30% above the original model values due to statistical smoothing. The PI index runs from 1 to 10 to cover very quiet to storm levels of geomagnetic activity; the relationship between PI and K_p can be found in *Foster et al.* [1986]. Equatorward of the auroral oval a soft mid-latitude background electron precipitation has been added to the TIROS/NOAA auroral model at all latitudes and local times. The spectrum of this additional particle source is assumed to be Maxwellian with an energy flux of 0.05mW m^{-2} and a mean energy of 50 eV.

Alternative electric field and auroral precipitation models can easily be incorporated into the model. Simulations have also been performed with *Heppner and Maynard* [1987] electric field patterns, which have a dependence on the y-component of the Interplanetary Magnetic Field (IMF), and with auroral precipitation based on DMSP observations [*Hardy et al.*, 1985]. The model is also able to accept theoretically-generated convection and precipitation, for instance, as modeled by the RICE University Magnetospheric Convection Model [*Wolf et al.*, 1991], or those assimilated from experimental data such as the time-dependent maps from AMIE [*Richmond*, 1992].

The (2,2), (2,3), (2,4), (2,5), and (1,1) propagating tidal modes are imposed at 97 km altitude [*Fuller-Rowell et al.*, 1991b; *Salah et al.*, 1995] with a prescribed amplitude and phase. Ionization rates from the EUV flux are evaluated from the *Hinteregger et al.* [1981] reference spectra for high and low solar activity based on the Atmospheric Explorer (AE) measurements.

4. Sample Simulations

The output from the model includes, for the neutral atmosphere, the global specification of the three component wind vector, temperature, the number density of the three major species O, O_2 and N_2, total density, and the densities on the minor species $N(^2D)$, $N(^4S)$, and NO. For the ionosphere, the coverage is global except for a strip 23° either side of the geographic equator, and includes the H^+ and O^+ densities and ion temperature to an altitude of 10,000 km, with the

TABLE 1: Ion-Neutral Reactions Included in the Global Model

Reaction	Rate Constant
$N_2^+ + O \rightarrow N(^2D) + NO^+$	$k_1 = 1.4 \times 10^{-16}(300/T_R)^{0.44}$ m^3 s^{-1} ($T_R < 1500$°K) $= 5.2 \times 10^{-17}(T_R/300.)^{0.2}$ m^3 s^{-1} ($T_R > 1500$°K)
$NO^+ + e^- \rightarrow N(^2D) + O$ (80%) $\rightarrow N(^4S) + O$ (20%)	$k_2 = 4.2 \times 10^{-13}(300./T_e)^{0.85}$ m^3 s^{-1}
$N_2^+ + e^- \rightarrow N(^4S) + N(^4S)$ (10%) $\rightarrow N(^4S) + N(^2D)$ (90%)	$k_3 = 1.8 \times 10^{-13}(T_e/300.)^{-0.39}$ m^3 s^{-1}
$N^+ + O_2 \rightarrow NO^+ + O$	$k_4 = 2.0 \times 10^{-16}$ m^3 s^{-1}
$N^+ + O_2 \rightarrow O_2^+ + N(^4S)$	$k_5 = 4.0 \times 10^{-16}$ m^3 s^{-1}
$N^+ + O \rightarrow O^+ + N$	$k_6 = 1.0 \times 10^{-18}$ m^3 s^{-1}
$O_2^+ + e^- \rightarrow O + O$	$k_7 = 1.6 \times 10^{-13}(300./T_e)^{0.55}$ m^3 s^{-1} ($T_e > 1200$°K) $= 2.7 \times 10^{-13}(300./T_e)^{0.7}$ m^3 s^{-1} ($T_e < 1200$°K)
$O_2^+ + N(^4S) \rightarrow NO + O$	$k_8 = 1.2 \times 10^{-16}$ m^3 s^{-1}
$O_2^+ + NO \rightarrow NO^+ + O_2$	$k_9 = 4.4 \times 10^{-16}$ m^3 s^{-1}
$O^+ + O_2 \rightarrow O_2^+ + O$	$k_{10} = 2.82 \times 10^{-17} - 7.74 \times 10^{-18}(T_1/300.) + 1.073 \times 10^{-18}(T_1/300.)^2$ $- 5.17 \times 10^{-20}(T_1/300.)^3 + 9.65 \times 10^{-22}(T_1/300.)^4$ m^3 s^{-1}
$O^+ + N_2 \rightarrow NO^+ + N(^4S)$	$k_{11} = 1.533 \times 10^{-18} - 5.92 \times 10^{-19}(T_2/300.) + 8.6 \times 10^{-20}$ $\cdot (T_2/300.)^2$ m^3 s^{-1} $300.°K < T_2 < 1700$°K $= 2.73 \times 10^{-18} - 1.155 \times 10^{-18}(T_2/300.) + 1.483 \times 10^{-19}$ $\cdot (T_2/300.)^2$ m^3 s^{-1} $1700.°K < T_2 < 6000$°K
$NO^+ + O_2 \rightarrow O_2^+ + N_2$	$k_{12} = 5.1 \times 10^{-17}$ m^3 s^{-1}
$NO + h\nu_{Lyman\alpha} \rightarrow NO^+ + e^-$	See Fuller-Rowell (1993)

$T_1 = 0.667\ T_i + 0.333\ T_n$; T_i is ion temperature; $T_2 = 0.6363\ T_i + 0.3637\ T_n$; T_n is neutral temperature; T_e is electron temperature; and $T_R = (T_i + T_n)/2$.

TABLE 2: Neutral-Neutral Reactions Included in the Global Model

Reaction	Rate Constant
$O_2 + h\nu \rightarrow O + O$	R.G. Roble (private communication, 1983)
$O + O + M \rightarrow O_2 + M$	$k_2 = 2.7 \times 10^{-46} \exp(710/T)$ m^6 s^{-1}
$O + OH \rightarrow O_2 + H$	$k_3 = 4.2 \times 10^{-17}$ m^3 s^{-1}
$O + HO_2 \rightarrow O_2 + OH$	$k_4 = 3.5 \times 10^{-17}$ m^3 s^{-1}
$O + O \rightarrow O_2 + h\nu$	$k_5 = 1.0 \times 10^{-26}$ m^3 s^{-1}
$N(^2D) + O_2 \rightarrow NO + O$	$k_6 = 5.0 \times 10^{-18}$ m^3 s^{-1}
$N(^4S) + O_2 \rightarrow NO + O$	$k_7 = 4.4 \times 10^{-18} \exp(3220/T)$ m^3 s^{-1}
$N(^2D) + O \rightarrow N(^4S) + O$	$k_8 = 4.5 \times 10^{-19}$ m^3 s^{-1}
$N(^4S) + NO \rightarrow N_2 + O$	$k_9 = 3.4 \times 10^{-17}$ m^3 s^{-1}
$N(^2D) + e^- \rightarrow N(^4S) + e^-$	$k_{10} = 3.6 \times 10^{-16} (T_e/300)^{0.5}$ m^3 s^{-1}
$N(^2D) + NO \rightarrow N_2 + O$	$k_{11} = 7.0 \times 10^{-17}$ m^3 s^{-1}
$N(^2D) \rightarrow N(^4S) + h\nu$	$k_{12} = 1.06 \times 10^{-5}$ s^{-1}
$NO + h\nu \rightarrow N(^4S) + O$	See Fuller-Rowell (1993)
$NO + h\nu_{Lyman\alpha} \rightarrow NO^+ + e^-$	See Fuller-Rowell (1993)

addition on the molecular ions species N_2^+, O_2^+ and NO^+, and the atomic ion N^+ to an altitude of approximately 400 km. The following figures are a sample of some of these parameters to illustrate the scope of the model output.

Figures 1 and 2 compare the neutral temperature and composition from the model with the empirical description of MSIS [*Hedin*, 1987; 1991]. Figure 1 shows the global neutral temperature distribution for January at 300 km altitude and moderate solar activity ($F_{10.7} = 120$); part (a) shows the CTIM model specification, and part (b) that from MSIS for the same conditions. Both are for quiet geomagnetic conditions with an A_p of 5 for MSIS, and TIROS activity level 5 for CTIM. CTIM has been run until the results are diurnally reproducible. The main features of the two models agree very well. The seasonal distribution is clear in the latitude structure with high summer (southern) hemisphere temperatures and a minimum at winter mid-latitudes. In this simulation the winter Joule heating rate has been increased by a factor-of-two in CTIM. This scaling is necessary to shift the minimum temperature in the polar regions to winter mid-latitudes. The justification is based on the neglect of variability in the electric field patterns [*Codrescu et al.*, 1995]. Superimposed on the latitude gradient is a diurnal variation with maximum temperature occurring in the late afternoon and minimum just before dawn. The patterns agree both qualitatively and quantitatively.

Figure 2 illustrates the mean molecular mass from CTIM and MSIS for the same conditions as Figure 1. The mean mass distribution departs from diffusive equilibrium by wind driven transport. The circulation from summer to winter causes upwelling in the summer hemisphere and downwelling in the winter hemisphere. The upwelling transports molecular rich gas from lower altitudes increasing the mean molecular mass. Downwelling in winter has the reverse effect. The distribution is also affected by horizontal transport of species by the wind field. The enhanced magnetospheric forcing in the winter polar region causes the minimum to move from the winter pole to winter mid latitudes.

Figure 3 depicts a polar view of the neutral wind and temperature distribution for the same conditions. The region poleward of 40° N is shown at an altitude of 300 km and at 18 UT. The response of the neutral wind to ion drag, induced by high latitude ion convection, is clearly seen. For these fairly modest levels of auroral or geomagnetic activity winds approach 400 m/s. The figure shows the well observed facet where dusk sector auroral oval winds respond more easily to ion drag than those at dawn. This feature has been explained as an inertial oscillation, where a balance between the Coriolis force and curvature constrains the neutral gas within the auroral oval in the dusk sector [*Fuller-Rowell*, 1984, 1985; *Fuller-Rowell and Rees*, 1984, *Fuller-Rowell et al.*, 1984].

An example of the ionospheric response at a mid-latitude site, for the same northern winter simulation, can be seen in Figure 4. Part (a) and (b) shows the diurnal variation of N_mF_2 and h_mF_2, respectively, from a site equivalent to Millstone Hill incoherent scatter observatory near 40° north latitude in the American sector. The simulation of height and number density of the ionospheric F2 peak compare favorably with mid-winter data [*Sojka et al.*, 1995]. The simulated meridional wind along the magnetic meridian, for this site, is also shown for completeness in part (c). The magnitudes and diurnal variation of the wind agree well with observations [*Hagan*, 1993].

The real value of CTIM becomes apparent when simulating time-dependent phenomena such as the dynamic response to a large increase in the magnetospheric source, commonly known as a geomagnetic storm. The increase in Joule and particle heating during these times causes large-scale gravity waves to propagate globally, and interact with those from the opposite hemisphere. An example of the change in meridional wind from a simulated geomagnetic storm in December, lasting 12 hours, is shown in Figure 5a. The figure shows the deviation of the

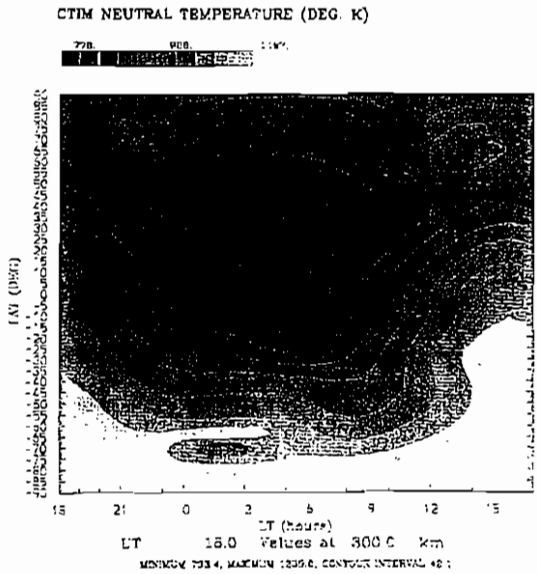

Figure 1a. Global temperature distribution as specified by CTIM for January, 300 km altitude, moderate solar activity ($F_{10.7}$ = 120), and quiet geomagnetic conditions (TIROS/NOAA activity level 5).

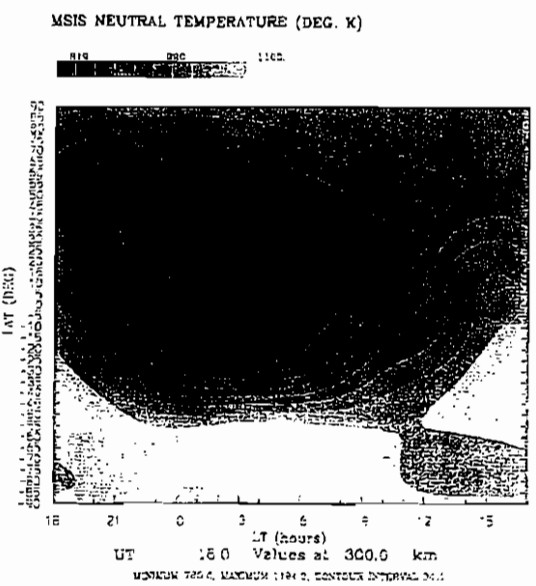

Figure 1b. Global temperature distribution as specified by MSIS, for January, 300 km altitude, moderate solar activity ($F_{10.7}$ = 120), and quiet geomagnetic conditions (A_p 5).

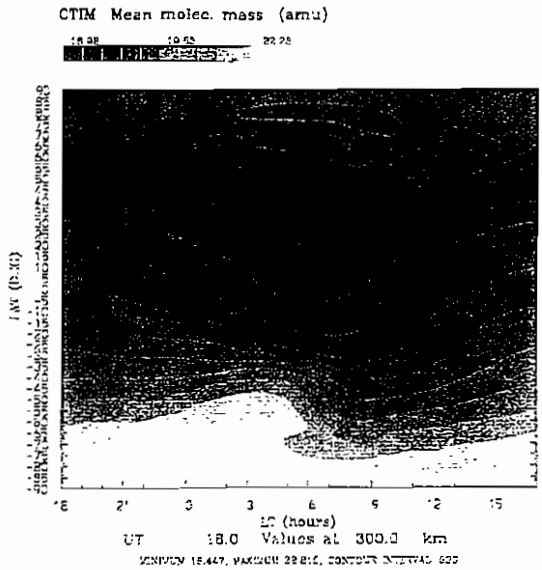

Figure 2a. Global mean molecular mass distribution as specified by CTIM and for January, 300 km altitude, moderate solar activity ($F_{10.7}$ = 120), and quiet geomagnetic conditions (TIROS/NOAA activity level 5).

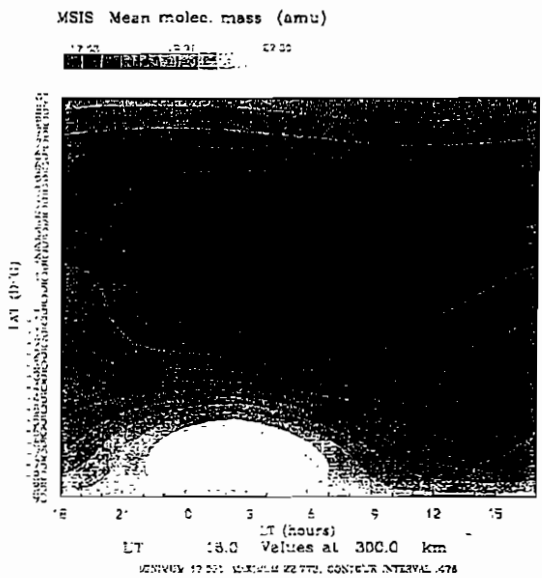

Figure 2b. Global mean molecular mass distribution as specified by MSIS, for January, 300 km altitude, moderate solar activity ($F_{10.7}$ = 120), and quiet geomagnetic conditions (A_p 5).

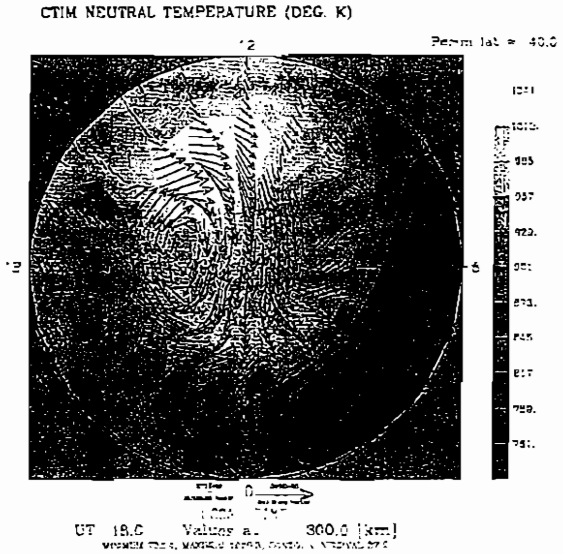

Figure 3. Neutral wind and temperature from 40° N to the pole, at 18 UT and 300 km altitude. The conditions are the same as Figures 1 and 2.

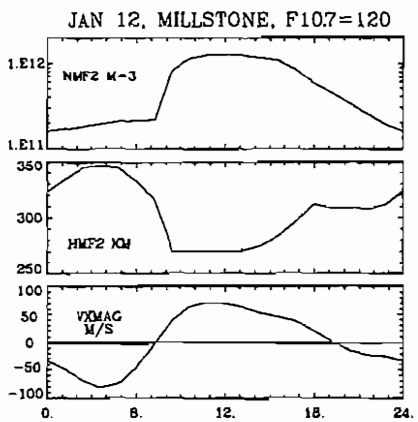

Figure 4. Ionospheric and neutral wind response at the mid-latitude site of Millstone Hill (40° N in the American sector) for the same northern winter simulation depicted in Figures 1 and 2. The figure shows the local time variation of (a) the ionospheric F2 peak density (N_mF_2), and (b) its height (h_mF_2), and (c) the neutral wind along the magnetic meridian at 300 km altitude.

wind from a quiet control run, positive southward, at pressure level 12, from 70° south latitude to 70° north, and at longitude 0° E. The characteristic double surge and interhemispheric penetration of the wind and wave field has been discussed extensively by *Fuller-Rowell et al.* [1994, 1995].

The wind surges from the polar regions causing a wind divergence, and upwelling, which drives molecular-rich gas upward. The horizontal winds, particularly the prevailing circulation from summer to winter hemisphere, subsequently carry the gas equatorward. This is shown in Figure 5b. The figure shows the change in mean molecular mass for a storm occurring in June, at pressure level 12, near 300 km altitude in the upper thermosphere, and at a longitude 270° E. The mean mass increase in the polar regions penetrates to the summer mid- and low- latitudes, carried by the prevailing seasonal summer-to-winter circulation. The altered neutral composition, increases the loss rate of O^+ ions, and is the cause of the "negative phase" that is a characteristic of the summer ionospheric response. The summer mid-latitude plasma densities decrease sharply in response to the composition change. In winter, the prevailing seasonal interhemispheric flow makes it difficult for the polar increase in mean mass to penetrate significantly equatorward; this explains the rare occurrence of a "negative phase" in winter mid-latitudes [*Fuller-Rowell et al.*, 1995].

5. Conclusion

The Coupled Thermosphere Ionosphere Model (CTIM) has been used as a research tool for many years. It is extremely satisfying when a computer code can simulate observations, but it should be recognized that this is not the goal of numerical modeling. One can never completely validate a model, and one can never prove the cause of a particular observation through computer modeling. The purpose of this modeling is to help understand the physics of a complex system, the upper atmosphere, which includes the close coupled between neutral dynamics, energy budget, composition, and plasma parameters. The upper atmosphere, when driven hard by the solar and magnetospheric sources, exhibits a number of non-linear characteristics. It is not always easy to predict the outcome of such a system. In these cases, numerical models can help to guide us, or provide the tools to discover some interesting interaction, that perhaps is not intuitive. Subsequent analysis of model output, by careful dissection of the processes involved, can give us the insight to begin to understand the system. In doing so, we build a picture in our minds of how the atmosphere "works". A model can never get to the point of proving a theory, but once we understand and appreciate the limitations of numerical modeling, they become invaluable tools to help us in research. The CTIM model described in this report is available for use by the science community and collaborations with the authors would be most welcome.

6. References

Anderson, D. N., *Planet. Space Sci., 21*, 409, 1973.
Baxter, R. G. and P. C. Kendall, *Proc. Roy. Soc. London, A304*, 171, 1968.
Blum, P. W. and I. Harris, *J. Atmos. Terr. Phys., 36*, 967-978, 1974.
Bramley, E. N. and M. Young, *J. Atmos. Terr. Phys., 30*, 99, 1968.
Chapman, S. C. and T. G. Cowling, *The Mathematical Theory of Non-Uniform Gases*, Cambridge University Press, 1970.
Chiu, Y. T., *J. Atmos. Terr. Phys., 37*, 1563-1570, 1975.
Codrescu, M. V., T. J. Fuller-Rowell, and J. C. Foster, *Geophys. Res., Lett.*, submitted, 1995.

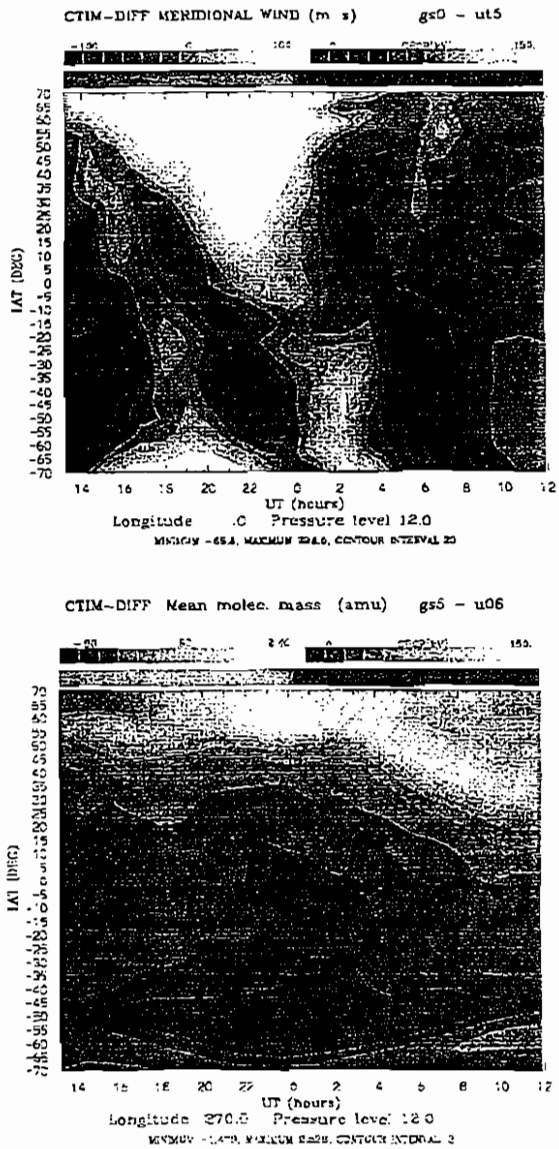

Figure 5. The response of the change in (a) meridional wind, and (b) mean molecular mass to a modeled geomagnetic storm. The region ± 70° latitude is shown at pressure level 12 in the upper thermosphere, near 300 km altitude. The winds are taken from longitude 0° E during a 12 hour storm in December. The mean mass is extracted from longitude 270° E during a storm simulated in June. The gray scale immediately above each figure shows the UT period when the cross polar cap potential is elevated above background; the magnitude of the increase is shown in the gray scale labeled CPCP(kV).

Cole, K. D., *Planet. Space Sci., 19*, 59-75, 1971.
Colgrove, F. D., F. S. Johnson, and W. B. Hanson, *J. Geophys. Res., 71*, 2227-2236, 1966.
Conrad, J. R. and R. W. Schunk, *J. Geophys. Res., 84*, 811-822, 1979.
Creekmore, S. P., J. M. Straus, R. M. Harris, B. K. Ching, and Y. T. Chiu, *J. Atmos. Terr. Phys., 37*, 491-515, 1975.
Dickinson, R. E., E. C. Ridley, and R. G. Roble, *J. Atmos. Terr. Phys., 32*, 1737-1754, 1975.
Dickinson, R. E., E. C. Ridley, and R. G. Roble, *J. Geophys. Res., 86*, 1499-1512, 1981.
Dickinson, R. E., E. C. Ridley, and R. G. Roble, *J. Atmos. Terr. Phys., 41*, 205-209, 1984.
Fedder, J. A., and P. M. Banks, *J. Geophys. Res., 77*, 2328-2340, 1972.
Fesen, C., R. G. Roble, R. D. Ridley, *J. Geophys. Res., 91*, 4471-4489, 1986.
Fesen, C., R. G. Roble, R. D. Ridley, *J. Geophys. Res., 98*, 7805-7820, 1993.
Foster, J. C., J. M. Holt, R. G. Musgrove, and D. S. Evans, *Geophys. Res. Lett., 13*, 656-659, 1986.
Fuller-Rowell, T. J., *J. Geophys. Res., 89*, 2971-2990, 1984.
Fuller-Rowell, T. J., *Adv. Space Res., 10*, 153-166, 1990.
Fuller-Rowell, T. J. and D. S. Evans, *J. Geophys. Res., 92*, 7606-7618, 1987.
Fuller-Rowell, T. J. and D. Rees, *J. Atmos. Sci., 37*, 2545-2567, 1980.
Fuller-Rowell, T. J. and D. Rees, *J. Atmos. Terr. Phys., 43*, 701-721, 1981.
Fuller-Rowell, T. J. and D. Rees, *Planet. Space Sci., 31*, 1209-1222, 1983.
Fuller-Rowell, T. J. and D. Rees, *Planet. Space Sci., 32*, 69-85, 1984.
Fuller-Rowell, T. J., S. Quegan, D. Rees, G. J. Bailey, and R. J. Moffett, *Planet. Space Sci., 32*, 469-480, 1984.
Fuller-Rowell, T. J., S. Quegan, D. Rees, R. J. Moffett, G. J. Bailey, *J. Geophys. Res., 92*, 7744-7748, 1987.
Fuller-Rowell, T. J., S. Quegan, D. Rees, R. J. Moffett, G. J. Bailey, *Pure and Applied Geophys., 127*, 189-217, 1988.
Fuller-Rowell, T. J., D. Rees, S. Quegan, R. J. Moffett, *J. Atmos. Terr. Phys., 53*, 529-540, 1991a.
Fuller-Rowell, T. J., D. Rees, H. F. Parish, T. S. Virdi, P. J. S. Williams, and R. G. Johnson, *J. Geophys. Res., 96*, 1181-1202, 1991b.
Fuller-Rowell, T. J., M. V. Codrescu, R. J. Moffett, and S. Quegan, *J. Geophys. Res., 99*, 3893-3914, 1994.
Fuller-Rowell, T. J., M. V. Codrescu, R. J. Moffett, and S. Quegan, *J. Geophys. Res., 100*, in press, 1995.
Groves, G. V. and J. M. Forbes, *Planet. Space Sci., 32*, 447-456, 1984.
Hagen, M. E., *J. Geophys. Res., 98*, 3731-3740, 1993.
Hanson, W. B. and R. J. Moffett, *J. Geophys. Res., 71*, 5559, 1966.
Hardy, D., M. S. Gussenhoven, and E. Holeman, *J. Geophys. Res., 90*, 4229-4248, 1985.
Harris, I. and H. G. Mayr, *J. Geophys. Res., 80*, 3925-3933, 1975.
Hays, P. B., T. L. Killeen, N. W. Spencer, L. E. Wharton, R. G. Roble, B. A. Emery, T. J. Fuller-Rowell, D. Rees, L. A. Frank, J. D. Craven, *J. Geophys. Res., 89*, 5547-5612, 1984.
Hedin, A. E., *Adv. Space Res., 8*, 9-26, 1988.
Hedin, A. E., *J. Geophys. Res., 92*, 4649-4662, 1987.
Hedin, A. E., et al., *J. Geophys. Res., 96*, 7657-7688, 1991.
Heppner, J. P., *J. Geophys. Res., 82*, 1115-1125, 1977.
Heppner, J. P. and N. C. Maynard, *J. Geophys. Res., 92*, 4467-4489, 1987.
Hernandez, G. and T. L. Killeen, *Adv. Space Res., 8*, 149-214, 1988.
Hinteregger, H. E., K. Fukui, and B. R. Gilson, *Geophys. Res. Lett., 8*, 1147-1150, 1981.
Kendall, P. C., *J. Atmos. Terr. Phys., 24*, 805, 1962.
Kendall, P. C. and W. M. Pickering, *Planet. Space Sci., 15*, 825, 1967.
Killeen, T. L., P. B. Hays, N. W. Spencer, and L. E. Wharton, *Adv. Space Res., 2*, 133-136, 1983.

Knudsen, W. C., *J. Geophys. Res., 79*, 1046, 1974.
Knudsen, W. C., P. M. Banks, J. D. Winningham, and D. M. Klumpar, *J. Geophys. Res., 82*, 4784, 1977.
Kohl, M. and J. W. King, *J. Atmos. Terr. Phys., 29*, 1045-1062, 1967.
Mayr, H. G., I. Harris, and N. W. Spencer, *Rev. Geophys. and Space Phys., 16*, 539-565, 1978.
Mayr, H. G. and H. Volland, *J. Geophys. Res., 77*, 6774-6790, 1972.
Millward, G. H., S. Quegan, R. J. Moffett, T. J. Fuller-Rowell, and D. Rees, *Planet. Space Sci., 41*, 45-56, 1993a.
Millward, G. H., R. J. Moffett, S. Quegan, and T. J. Fuller-Rowell, *J. Geophys. Res., 98*, 19173-19179, 1993b.
Millward, G. H., R. J. Moffett, S. Quegan, and T. J. Fuller-Rowell, STEP Handbook, this issue, 1996.
Moffett, R. J. and S. Quegan, *J. Atmos. Terr. Phys., 45*, 315-343, 1983.
Oliver, W. L., D. Alcayde, and P. Bauer, *Adv. Space Res., 8*, 119-148, 1988.
Parish, H., T. J. Fuller-Rowell, D. Rees, T. S. Virdi, and P. J. S. Williams, *Adv. Space Res., 10*, 215-224, 1990.
Parish, H., T. J. Fuller-Rowell, D. Rees, *Adv. Space Res., 12*, 117-135, 1992.
Prolss, G. W., M. Roemer, and J. W. Slowey, *Adv. Space Res., 8*, 215-262, 1988.
Quegan, S., G. J. Bailey, R. J. Moffett, R. A. Heelis, T. J. Fuller-Rowell, D. Rees, and R. W. Spiro, *J. Atmos. Terr. Phys., 44*, 619-640, 1982.
Quegan, S., G. J. Bailey, R. J. Moffett, and L. C. Wilkinson, *J. Atmos. Terr. Phys., 48*, 25-40, 1986.
Rees, D. and T. J. Fuller-Rowell, *Adv. Space Res., 7*, 27-38, 1987.
Rees, D. and T. J. Fuller-Rowell, *Adv. Space Res., 8*, 27-106, 1988.
Rees, D. and T. J. Fuller-Rowell, *Adv. Space Res., 12*, 69-87, 1992.
Rees, D., T. J. Fuller-Rowell, and R. W. Smith, *Planet Space Sci., 28*, 919-932, 1980.
Rees, D., T. J. Fuller-Rowell, R. Gordon, T. L. Killeen, P. B. Hays, L. E. Wharton, and N. W. Spencer, *Planet Space Sci., 31*, 1299-1314, 1983.
Rees, D., N. Lloyd, P. J. Charleton, M. Carlson, J. Murdin, and I. Haggstrom, *J. Atmos. Terr. Phys., 46*, 545-564, 1984a.
Rees, D., R. W. Smith, P. J. Charleton, F. G. McCormac, N. Lloyd, and Ake Steen, *Planet. Space Sci., 32*, 667-684, 1984b.
Rees, D., T. J. Fuller-Rowell, M. F. Smith, R. Gordon, T. L. Killeen, P. B. Hays, N. W. Spencer, L. E. Wharton, and N. C. Maynard, *Planet. Space Sci., 33*, 425-456, 1985a.
Rees, D., R. Gordon, T. J. Fuller-Rowell, M. F. Smith, G. R. Carignan, T. L. Killeen, P. B. Hays, N. W. Spencer, *Planet. Space Sci., 33*, 617-666, 1985b.
Rees, D., T. J. Fuller-Rowell, R. Gordon, M. F. Smith, J. P. Heppner, N. C. Maynard, N. W. Spencer, L. E. Wharton, P. B. Hays, and T. L. Killeen, *Planet. Space Sci., 34*, 1-40, 1986.
Rees, D., T. J. Fuller-Rowell, S. Quegan, D. Rees, R. J. Moffett, G. J. Bailey, *J. Atmos. Terr. Phys., 50*, 903-930, 1988.
Richmond, A. D., *J. Geophys. Res., 84*, 1880-1890, 1979.
Richmond, A. D., *Adv. Space Res., 12*, (6)59-(6)68, 1992.
Richmond, A. D. and S. Matsushita, *J. Geophys. Res., 80*, 2839-2850, 1975.
Rishbeth, H. and O. K. Garriott, *Introduction to Ionospheric Physics*, Academic Press, 1969.
Roble, R. G., *Rev. Geophys. Space Sci., 21*, 217-233, 1983.
Roble, R. G., R. E. Dickinson, and E. C. Ridley, *J. Geophys. Res., 87*, 1599-1614, 1982.
Roble, R. G., E. C. Ridley, and R. E. Dickinson, *J. Geophys. Res., 92*, 8745-8758, 1987.
Salah, J. E., *Geophys. Res. Lett., 20*, 1543-1546, 1993.
Salah, J. E. et al., *J. Geophys. Res.*, submitted, 1995.
Schunk, R. W., *Planet. Space Sci., 23*, 437, 1975.
Schunk, R. W., *Physica Scripta, 18*, 256-275, 1987.
Schunk, R. W. and J. C. G. Walker, *Planet. Space Sci., 21*, 1875-1896, 1973.

Sojka, J. J., W. J. Raitt, and R. W. Schunk, *J. Geophys. Res., 86*, 609, 1981.
Sojka, J. J. et al., *J. Geophys. Res.*, submitted, 1995.
Stening, R. J., *J. Atmos. Terr. Phys., 54*, 1387, 1992.
Sterling, D. L., W. B. Hanson, R. J. Moffett, and R. G. Baxter, *Radio Sci., 4*, 1005, 1969.
St.-Maurice, J.-P. and R. W. Schunk, *Planet. Space Sci., 25*, 907, 1977.
Straus, J. M., S. P. Creekmore, R. M. Harris, B. K. Ching, and Y. T. Chiu, *J. Atmos. Terr. Phys., 37*, 1245-1253, 1975.
Vallance-Jones, A., *Aurora*, Reidel Publishing, 97, 1974.
Volland, H., *J. Atmos. Terr. Phys., 41*, 853-866, 1979.
Watkins, B. J., *Planet. Space Sci., 26*, 559, 1978.
Wolf, R. A., R. W. Spiro, and F. J. Rich, *J. Atmos. Terr. Phys., 53*, 817, 1991.

A Coupled Thermosphere-Ionosphere-Plasmasphere Model (CTIP)

G. H. Millward[1,2], R. J. Moffett[1], S. Quegan[1], and T. J. Fuller-Rowell[2]

[1]Upper Atmosphere Modeling Group, School of Mathematics and Statistics
University of Sheffield, Sheffield S3 7RH, United Kingdom

[2]CIRES, University of Colorado/NOAA, Space Environment Laboratory,
325 Broadway, Boulder, CO 80303

1. Introduction

This report details a three-dimensional model of the terrestrial mid- and low-latitude ionosphere and plasmasphere, developed at Sheffield University between 1989 and 1993, and forming part of the PhD studies of *Millward* [1993]. The aim of the work was to implement this new model into the UCL/Sheffield coupled model (CTIM) as a major enhancement, thus yielding a global three-dimensional model of the thermosphere, ionosphere and plasmasphere. As such, this report forms an extension to that of *Fuller-Rowell et al.* [1996, this issue] which describes the thermosphere and high-latitude ionosphere models.

The approach taken for the ionosphere and plasmasphere component of CTIP is to solve the coupled equations of continuity, momentum and energy balance along a closed flux-tube to yield parameters such as ion density, field-aligned velocity and temperature. A 'global' model is achieved simply by solving these equations along many flux-tubes concurrently. (The term 'global' here means that we are modeling the mid- and low-latitude ionosphere/plasmasphere at all latitudes and longitudes, though not at high latitudes where the 'coupled model' relies on a separate, open flux-tube model.) Each flux-tube is subject to a normalized $\mathbf{E} \times \mathbf{B}$ drift, modified such that over a 24-hour period each flux-tube returns to its original starting point geographically. This approximation requires slight modifications to values of $\mathbf{E} \times \mathbf{B}$ drift which are taken from the empirical, quiet-time model of *Richmond et al.* [1980]. The passage of ionospheric parameters to the thermosphere part of the model (and vice-versa) is achieved by a complex interpolation procedure.

2. The CTIP Model – History and Development

The CTIP model is the concise name given to a non-linear, coupled thermosphere-ionosphere-plasmasphere model. The model consists of three distinct components which run concurrently and are fully coupled with respect to energy, momentum, and continuity. The program incorporates: (a) A global thermosphere model; (b) A high-latitude ionosphere model, and; (c) A mid and low-latitude ionosphere/plasmasphere model; with the third of these models the recent enhancement which is the subject here. The coupled model is probably best considered as a global thermospheric model upon which increasingly sophisticated descriptions of the ionosphere have been self-consistently incorporated. The reason for considering things in this way (rather than a global ionospheric model with a self-consistent thermosphere) is that the original thermospheric model forms the basis for the present coupled model in terms of global structure. Both ionospheric models originated as descriptions of the plasma within a single flux-tube and did not provide global coverage.

The thermospheric model was described originally by *Fuller-Rowell and Rees* [1980], *Rees et al.* [1980] and, more fully, in the PhD thesis of *Fuller-Rowell* [1981]. At that stage, the

ionospheric densities at high latitudes were computed using an empirical ionospheric model [*Chiu*, 1975]. Subsequent work was concerned with the thermospheric response to a geomagnetic substorm [*Fuller-Rowell and Rees*, 1981; 1984] and with developing a consistent description of the conservation of mean molecular mass for a two-constituent thermosphere [*Fuller-Rowell and Rees*, 1983], which had been absent from earlier model versions. The storm simulations were achieved by increasing the magnitude of the cross-polar cap potential within the model of the convection electric field and also enhancing the E-region ion densities as provided by the Chiu model. The limitation imposed by using an empirical ionospheric model in describing dynamic conditions at high latitudes was removed by inclusion of a fully dynamic ionospheric model [*Quegan*, 1982; *Quegan et al.*, 1982]. Initially, the coupling between the two models was very limited with only one or two iterations between the two, allowing each to come to steady state in between. The effects of this limited coupled ionosphere/thermosphere system were assessed by *Fuller-Rowell et al.* [1984]. A full coupling of the two models followed, yielding initial results on the ionosphere/thermosphere interaction for solstice conditions [*Fuller-Rowell et al.*, 1987], an assessment of seasonal and universal time effects [*Fuller-Rowell et al.*, 1988; *Rees et al.*, 1988] and simulations of the sub-auroral F-region trough [*Fuller-Rowell et al.*, 1991]. More recently, the model has been used to study the coupled ionosphere and thermosphere for conditions of northward IMF [*Rees et al.*, 1994], the response to geomagnetic storms [*Fuller-Rowell et al.*, 1994] and the response to short-lived enhancements in the convection electric field [*Millward*, 1994, *Millward et al.*, 1993a,b]. A full description of the thermospheric and high-latitude ionospheric models is given in this issue by *Fuller-Rowell et al.* [1996].

The model of the Earth's mid- and low-latitude plasmasphere, presented here as an enhancement to the coupled model, is based on the model of *Bailey* [1983]. In this model, the densities, temperatures and velocities are calculated for the ions O^+ and H^+ constrained to a single flux-tube with the Earth's magnetic field approximated by a centered (or tilted) dipole. Recent developments of this model were documented in detail by *Bailey and Sellek* [1990], and a full description is given in this issue by *Bailey and Balan* [1995]. The form of the model, developed here as an enhancement to the coupled model, owes much to work by *Rippeth* [1992], in which a more sophisticated eccentric dipole approximation to the Earth's magnetic field was developed [*Rippeth*, 1992; *Bailey et al.*, 1993]. The method for solving both diffusion and energy equations is also based on the work of *Rippeth* [1992] which is itself different from the techniques used by *Bailey* [1983] and instead originates with *Quegan* [1982].

3. Modeling the Mid- and Low-Latitude Ionosphere

Prior to the work documented here, the coupled model resorted to using an empirical model of the ionosphere for coverage at low latitudes [*Chiu*, 1975], with the Sheffield high-latitude ionospheric model tentatively used at mid-latitudes, as well as high latitudes, thus providing global ionospheric coverage. The basic problem with extending the ionospheric model, developed for use at high latitudes, down to the equator is due to the nature of the geomagnetic field. At high latitudes the geomagnetic field lines are open to the solar wind and deviate little from straight lines up to high altitudes. Moving equatorward, however, the field lines become increasingly curved within the ionosphere. Also, flux-tubes at mid and low latitudes are closed, coupling the two hemispheres. Now, while this can be ignored, to a certain extent, at mid-latitudes, the equatorial ionosphere can only be modeled by fully including the interhemispheric coupling and properly treating the magnetic field, which becomes horizontal in this region.

The new model of the mid- and low-latitude ionosphere, discussed here, is different from that used at high latitudes in that we have adopted a Lagrangian framework in which to work (i.e., a framework in which individual flux-tubes are followed). To produce a global model of the ionosphere, many individual flux-tubes are computed concurrently, with individual tubes defined by magnetic longitude (which is constant along a tube) and L value, which determines

the equatorial crossing height (relative to the center of the dipole) in units of the Earth's radius [*McIlwain*, 1961].

4. Eccentric Dipole Magnetic Field Model

The orientation of the many flux-tubes in the global model is determined by the magnetic field model used. For the global ionospheric model (and also for the coupled model as a whole), we use an eccentric dipole approximation to the Earth's magnetic field as given by the International Geomagnetic Reference Field (IGRF). An eccentric dipole magnetic field is as close to the true field (IGRF) as is possible while still requiring the field to be dipolar. The dipole has an axis inclined at an angle to the Earth's rotational axis and also the center of the dipole is offset from the center of the Earth. Such a model automatically produces the correct offsets for the geographic and magnetic poles, which are different in the two hemispheres.

4.1 Dipole (p,q) Coordinates

The reader may be wondering why we bother to use a dipole approximation to the magnetic field at all, in preference to the IGRF, when the latter contains several important anomalies in which the field differs markedly from the dipole structure. The reason for using a dipole configuration is that the model can then be described by a simple coordinate system which would not be possible if the empirical IGRF magnetic field data were to form the model's basis. The coordinate system used transforms the spherical polar coordinates in the magnetic frame (r, θ, ϕ), as defined in section 4.3, to the dipole coordinates (p, q, ϕ) according to the equations

$$p = \frac{r_m}{r_0} \frac{1}{\sin^2 \theta_m} \tag{1}$$

$$q = \left[\frac{r_0}{r_m} \right]^2 \cos \theta_m \tag{2}$$

In this system of coordinates, p has a constant value for every point along a given field line and is identical to L value. The q coordinate is orthogonal to p. A point on a given field line, which is under the influence of an $\mathbf{E} \times \mathbf{B}$ drift, will maintain a constant q value although the values of r and θ will change. Use of a dipole structure means that the motion of the flux-tube (in terms of computations within the model) is straightforward. For an electric field defined at an altitude of (say) 300 km, the $\mathbf{E} \times \mathbf{B}$ drift of a point on the flux-tube nearest to 300 km will yield a new value for p and thus a recalculation of all the coordinates on the flux-tube as a whole. In practice, the adoption of an eccentric dipole structure as opposed to a simpler centered dipole produces a number of problems. Under $\mathbf{E} \times \mathbf{B}$ drift, the flux-tube can do two things: move outward or inward to a larger or smaller L value, or move east or west relative to co-rotation. The problem which occurs with both these motions (but is more obvious for a flux-tube which is expanding - i.e., moving poleward) is that points on the flux-tube initially located at the base height (130 km) move upward to higher altitudes. In order that the base height for the flux-tube remain at the original height, more points then have to be added to the bottom of the flux-tube. For a centered dipole structure, this process happens by the same amount in each hemisphere. The extra complication with an eccentric structure is that $\mathbf{E} \times \mathbf{B}$ drift can produce different motions (relative to fixed geographic altitude) for the two ends of the flux-tube. In addition to this, the east-west motion discussed above itself produces the same problem. With the eccentric dipole, the axis does not pass through the geographic center of the Earth, but is offset by about 500 km. Motion of the tube to the east or west means that the flux-tube moves vertically up or down relative to the Earth without changing its form, and thus again extra points may be needed at the feet of the flux-tube to maintain a constant base height. In the model, this process is achieved by making sure that there are enough spare points available so that any $\mathbf{E} \times$

B drifts occurring in the subsequent run will not use up all the points on the tube, thus ensuring that the base height remains constant.

4.2 Transforming From (p, q) to (r, θ) Coordinates

For given values of r_m and θ_m, the values of p and q are given by equations (1) and (2). Performing the inverse transformation is slightly more complicated, requiring numerical methods. Eliminating θ_m from the equations (1) and (2) (and dropping the 'm' subscript) gives

$$q^2\left(\frac{r}{r_0}\right)^4+\frac{1}{p}\left(\frac{r}{r_0}\right)-1=0 \tag{3}$$

which is readily solved using the Newton-Raphson numerical method. For point k on the field line, an initial guess for the value of r_k is the value of r_{k+1}, already calculated. In this way, all the values of r_k can be found by starting at the equator (for which $r_k = r_o p$) and moving poleward to each end of the tube.

4.3 Transforming From Geographic to Magnetic Coordinates

Critical to the modeling are transformations between geographic and magnetic coordinates. Both are described using a spherical polar coordinate system (r, θ, ϕ). The geographic coordinate system has an origin at the physical center of the Earth. A radial coordinate (r_g) is given by the distance of a given point from the Earth's center. The 'co-latitude' angle (θ_g) is the angle formed by the radial vector and the N-S rotational axis of the Earth. Measured in degrees, θ_g is zero at the North pole, 90 at the equator and 180 at the South pole. The longitude (ϕ_g) is then measured relative to an assumed origin at the Greenwich meridian, a positive value being eastward from Greenwich. An equivalent system is used to describe coordinates in the magnetic frame. The dipole magnetic field has a center and an axis passing through the north and south magnetic poles. From this, magnetic radial (r_m) and co-latitude (θ_m) coordinates are given. As with the geographic system, the magnetic longitude (ϕ_m) has to be defined relative to a zero meridian defined as lying in the plane which contains both the magnetic axis and the geographic South pole. Having defined both coordinate systems, the next step is to define transformations from one to the other. A transformation from geographic (r_g, θ_g, ϕ_g) to magnetic (r_m, θ_m, ϕ_m) proceeds in two stages. Firstly, a rotational transformation is performed about the Earth's center to give an axis with the same orientation as that of the required eccentric dipole. Such a coordinate system is known as 'centered dipole' or 'tilted dipole,' a general point in this coordinate system being given by (r_{cd}, θ', ϕ'). By definition, $r_{cd} = r_g$. A second transitional transformation is then required moving the center of the dipole away from the Earth's center. *Fraser-Smith* [1987] has given the form of the transformations used in the model.

The rotation from geographic coordinates to centered dipole coordinates proceeds via considerations of the spherical triangle formed by the north geographic pole, the north 'CD' pole and a general point P, all lying on the Earth's surface. The situation is shown in Figures 1 and 2. Applying the sine rule to the spherical triangle in Figure 2, we obtain

$$\frac{\sin\theta_g}{\sin(180°-\phi')}=\frac{\sin\theta_n}{\sin(-\psi)}=\frac{\sin\theta'}{\sin(\phi_g-\phi_n)} \tag{4}$$

where θ_n and ϕ_n are, respectively, the coaltitude and longitude of the centered dipole north pole in geographic coordinates and are calculated below. The cosine rule is also used and gives

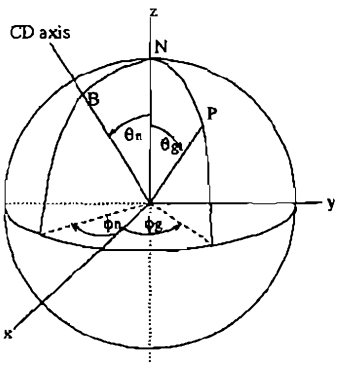

Figure 1. The geographic spherical polar coordinate system (r_g, θ_g, ϕ_g) shown relative to the cartesian system (x, y, z). The centered dipole axis crosses the Earth's surface at point B and P is a general point.

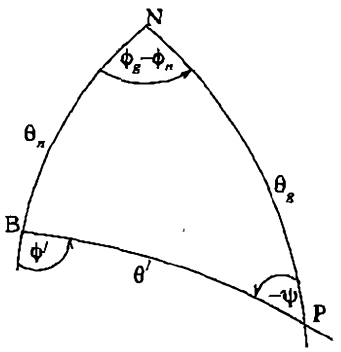

Figure 2. The spherical triangle drawn on the Earth's surface used to convert between geographic and centered dipole spherical polar coordinates. N represents the north pole, B is the centered dipole pole and P is a general point.

$$
\begin{aligned}
\cos\theta_n &= \cos\theta_g \cos\theta' + \sin\theta_g \sin\theta' \cos(-\psi) \\
\cos\theta' &= \cos\theta_n \cos\theta_g + \sin\theta_n \sin\theta_g \cos(\phi_g - \phi_n) \\
\cos\theta_g &= \cos\theta_n \cos\theta' + \sin\theta_n \sin\theta' \cos(180° - \phi')
\end{aligned}
\tag{5}
$$

Equations (4) and (5) yield the transformations:

$$
\begin{aligned}
\theta' &= \cos^{-1}[\cos\theta_n \cos\theta_g + \sin\theta_n \sin\theta_g \cos(\phi_g - \phi_n)] \\
\phi' &= \cos^{-1}[-(\cos\theta_g - \cos\theta_n \cos\theta') / \sin\theta_n \sin\theta'] \\
\phi' &= \sin^{-1}[\sin\theta_g \sin(\phi_g - \phi_n) / \sin\theta']
\end{aligned}
\tag{6}
$$

The two equations for ϕ' avoid the ambiguity in angle that occurs when an inverse sine or cosine is evaluated in the angular range -180° to +180°. The inverse transformations, from centered dipole coordinates to geographic, are given by

$$\theta_g = \cos^{-1}[\cos\theta_n \cos\theta' + \sin\theta_n \sin\theta' \cos(180° - \phi')]$$
$$\phi_g = \phi_n + \cos^{-1}[\cos\theta' - \cos\theta_n \cos\theta_g)/\sin\theta_n \sin\theta_g] \qquad (7)$$
$$\phi_g = \phi_n + \sin^{-1}[\sin\theta' \sin\phi'/\sin\theta_g]$$

The second part of the transformation involves a translation from centered dipole to eccentric dipole (magnetic) coordinates. If the location of the eccentric dipole in centered dipole cartesian coordinates is (x'_0, y'_0, z'_0) and of a general point P is (x', y', z') then

$$x' = r_g \sin\theta' \cos\phi' = r_m \sin\theta_m \cos\phi_m + x'_0$$
$$y' = r_g \sin\theta' \sin\phi' = r_m \sin\theta_m \sin\phi_m + y'_0 \qquad (8)$$
$$z' = r_g \cos\theta' \qquad = r_m \cos\theta_m + z'_0$$

From these equations, the transformation from centered dipole to eccentric dipole coordinates becomes

$$r_m = ((r_g \sin\theta' \cos\phi' - x'_0)^2 + (r_g \sin\theta' \sin\phi' - y'_0)^2 + (r_g \cos\theta' - z'_0)^2)^{\frac{1}{2}}$$
$$\theta_m = \tan^{-1}\left(\frac{\{(r_g \sin\theta' \cos\phi' - x'_0)^2 + (r_g \sin\theta' \sin\phi' - y'_0)^2\}^{\frac{1}{2}}}{(r_g \cos\theta' - z'_0)}\right) \qquad (9)$$
$$\phi_m = \tan^{-1}\left(\frac{r_g \sin\theta' \sin\phi' - y'_0}{r_g \sin\theta' \cos\phi' - x'_0}\right)$$

The inverse transformations from eccentric dipole to centered dipole are given by

$$r_{cd} = ((r_m \sin\theta_m \cos\phi_m + x'_0)^2 + (r_m \sin\theta_m \sin\phi_m + y'_0)^2 + (r_m \cos\theta_m + z'_0)^2)^{\frac{1}{2}}$$
$$\theta' = \tan^{-1}\left(\frac{\{(r_m \sin\theta_m \cos\phi_m + x'_0)^2 + (r_m \sin\theta_m \sin\phi_m + y'_0)^2\}^{\frac{1}{2}}}{(r_m \cos\theta_m + z'_0)}\right) \qquad (10)$$
$$\phi' = \tan^{-1}\left(\frac{r_m \sin\theta_m \sin\phi_m + y'_0}{r_m \sin\theta_m \cos\phi_m + x'_0}\right)$$

Transformations from geographic coordinates (r_g, θ_g, ϕ_g) to magnetic coordinates (r_m, θ_m, ϕ_m) are accomplished via centered dipole coordinates using equations (6) and (9), while equations (7) and (10) do the opposite. We still, however, require the coordinates of the centered dipole north pole (θ_n, ϕ_n) and the cartesian offset of the eccentric dipole relative to the centered dipole (x'_0, y'_0, z'_0). These are obtained when we consider the mathematically idealized dipole approximation to the Earth's geomagnetic field.

4.4 The Direction of the Magnetic Field

For a dipole magnetic field, the components of the field in the directions r_m, θ_m and ϕ_m can be found using

$$\bar{B} = -\nabla\left[\frac{-B_0 r_0^3}{r_m^2}\cos\theta_m\right] \tag{11}$$

In spherical polar coordinates, ∇ is given by

$$\nabla = \vec{e_{r_m}}\frac{\partial}{\partial r_m} + \vec{e_{\theta_m}}\frac{1}{r_m}\frac{\partial}{\partial \theta_m} + \vec{e_{\phi_m}}\frac{1}{r_m \sin\theta_m}\frac{\partial}{\partial \phi_m} \tag{12}$$

where $\vec{e_{r_m}}$, $\vec{e_{\theta_m}}$ and $\vec{e_{\phi_m}}$ denote unit vectors in the three respective directions. The components of $\vec{B}$ are, therefore, given by

$$\begin{aligned} B_{r_m} &= -2B_0\cos\theta_m\left(\frac{r_0}{r_m}\right)^3 \\ B_{\theta_m} &= -B_0\sin\theta_m\left(\frac{r_0}{r_m}\right)^3 \\ B_{\phi_m} &= 0 \end{aligned} \tag{13}$$

with the magnitude of the field given by

$$B = B_0\sqrt{3\cos^2\theta_m + 1}\left(\frac{r_0}{r_m}\right)^3 \tag{14}$$

The unit vector $\vec{e_{\parallel}}$, aligned along the magnetic field, is defined to be positive in the direction of increasing s (from north to south) and, therefore, in the opposite direction to the magnetic field vector. In the magnetic frame, $\vec{e_{\parallel}}$ can be defined as

$$\vec{e_{\parallel}} = a_{r_m}\vec{e_{r_m}} + a_{\theta_m}\vec{e_{\theta_m}} + a_{\phi_m}\vec{e_{\phi_m}} \tag{15}$$

where

$$\begin{aligned} a_{r_m} &= -\frac{B_{r_m}}{B} = \frac{2\cos\theta_m}{\sqrt{3\cos^2\theta_m + 1}} \\ a_{\theta_m} &= -\frac{B_{\theta_m}}{B} = \frac{\sin\theta_m}{\sqrt{3\cos^2\theta_m + 1}} \\ a_{\phi_m} &= 0 \end{aligned} \tag{16}$$

To find the component of the unit vector in the geographic frame, we must first transform to eccentric dipole cartesian coordinates i.e.,

$$
\begin{aligned}
a_x &= a_{r_m} \sin\theta_m \cos\phi_m + a_{\theta_m} \cos\theta_m \cos\phi_m \\
a_y &= a_{r_m} \sin\theta_m \sin\phi_m + a_{\theta_m} \cos\theta_m \sin\phi_m \\
a_z &= a_{r_m} \cos\theta_m - a_{\theta_m} \sin\theta_m
\end{aligned} \tag{17}
$$

The transformation from eccentric dipole to centered dipole coordinates involves only a translation and, therefore, the directions a_x, a_y, and a_z are the same in both frames. Converting to centered dipole polar coordinates we have

$$
\begin{aligned}
a_{r'} &= a_x \sin\theta' \cos\phi' + a_y \sin\theta' \sin\phi' + a_z \cos\theta' \\
a_{\theta'} &= a_x \cos\theta' \cos\phi' + a_y \cos\theta' \sin\phi' - a_z \sin\theta' \\
a_{\phi'} &= -a_x \sin\phi' + a_y \cos\phi'
\end{aligned} \tag{18}
$$

The final conversion, from centered dipole polar coordinates to geographic polar coordinates involves only a rotation. Thus, the radial vector is the same in both frame i.e.,

$$
a_{r_g} = a_{r'} \tag{19}
$$

and a_{θ_g} and a_{ϕ_g} are found using the spherical triangle in Figure 2

$$
\begin{aligned}
a_{\theta_g} &= a_{\theta'} \cos\Omega + a_{\phi'} \sin\Omega \\
a_{\theta_g} &= a_{\theta'} \cos\Omega + a_{\phi'} \sin\Omega
\end{aligned} \tag{20}
$$

where

$$
\begin{aligned}
\sin\Omega &= -\frac{\sin\theta_n \sin(\phi_g - \phi_n)}{\sin\theta'} \\
\cos\Omega &= \frac{\cos\theta'(\cos\theta_n - \cos\theta_g)}{\sin\theta' \sin\theta_g}
\end{aligned} \tag{21}
$$

For a vector such as the neutral wind with components u_r, u_θ, u_ϕ, defined in the geographic frame, the component along the field line is given by

$$
u_{\parallel} = a_{r_g} u_r + a_{\theta_g} u_\theta + a_{\phi_g} u_\phi \tag{22}
$$

4.5 Orientation of the Dipole

In the absence of currents, the geomagnetic field can be represented by a scalar potential γ where $\bar{B} = \nabla\gamma$ since $\bar{B}$ satisfies $\nabla \times \bar{B} = 0$. A spherical harmonic expansion of γ is thus possible and can be written in the form

$$
\gamma = r_e \sum_{n=1}^{\infty} \sum_{m=0}^{n} \left(\frac{r_0}{r_g}\right)^{n+1} P_n^m(\cos\theta_g)(g_n^m \cos m\phi_g + h_n^m \sin m\phi_g) \tag{23}
$$

where r_0 is the radius of the Earth, P_n^m are the Schmidt normalized Legendre functions and g_n^m and h_n^m are the Gauss coefficients. These coefficients have been calculated for nine separate magnetic field models covering the years 1945–1985 and are collectively referred to as the International Geomagnetic Reference Field (IGRF) which is published by the International Association for Geomagnetism and Aeronomy (IAGA); the data has been tabulated by *Barraclough* [1985] and *Barker et al.* [1986]. The first eight coefficients for 1985 are given in Table 1.

Table 1: The first eight Gauss coefficients (nT) from the 1985 IGRF [*Barker et al.*, 1986].

n	m	g_n^m	h_n^m
1	0	-29877	
1	1	-1903	5497
2	0	2073	
2	1	3045	-2191
2	2	1691	-309

For a full description of the centered dipole magnetic field, the first three coefficients are required in the expansion of γ; while for the eccentric dipole, the first eight are needed. For the centered dipole description we have

$$\gamma = r_e\left(\frac{r_e}{r_g}\right)^2\left(g_1^0\cos\theta_g + (g_1^1\cos\phi_g + h_1^1\sin\phi_g)\sin\theta_g\right) \tag{24}$$

In terms of dipole coordinates the scalar potential is given by

$$\gamma = -\frac{B_0 r_e^3}{r_g^2}\cos\theta' \tag{25}$$

which, using the transformation in equation (7), can be written

$$\gamma = -\frac{r_e^3}{r_g^2}B_0(\cos\theta_n\cos\theta_g + \sin\theta_n\sin\theta_g(\cos\phi_g\cos\phi_n + \sin\phi_g\sin\phi_n)) \tag{26}$$

The reference field B_0 is defined by the dipole moment M as

$$B_0 = \frac{\mu_0 M}{4\pi r_e^3} \tag{27}$$

Eliminating γ from equations (24) and (26) gives

$$B_0 = \sqrt{(g_1^0)^2 + (g_1^1)^2 + (h_1^1)^2}$$
$$\cos\theta_n = -g_1^0 / B_0 \tag{28}$$
$$\tan\phi_n = h_1^1 / g_1^1$$

Substituting the 1985 IGRF values from Table 1 into the above equations gives

$$B_0 = 30438\text{nT}$$
$$M = 7.865 \times 10^{22}\,\text{Am}^2$$
$$\theta_n = 11.02^\circ$$
$$\phi_n = -70.91^\circ$$

The eccentric dipole is fully described by the scalar potential γ if the first eight Gauss coefficients (i.e., up to second order) are used. These second order terms were found by *Schmidt* [1934] to be at a minimum in the spherical harmonic representation when the center of the eccentric dipole is located, relative to the geographic center of the Earth, at cartesian coordinates (x_0, y_0, z_0) where

$$x_0 = r_e(L_1 - g_1^1 E) / 3B_0^2$$
$$y_0 = r_e(L_2 - h_1^1 E) / 3B_0^2 \tag{29}$$
$$z_0 = r_e(L_0 - g_1^0 E) / 3B_0^2$$

and

$$L_0 = 2g_1^0 g_2^0 + \sqrt{3}(g_1^1 g_2^1 + h_1^1 h_2^1)$$
$$L_1 = -g_1^1 g_2^0 + \sqrt{3}(g_1^0 g_2^1 + g_1^1 g_2^2 + h_1^1 h_2^2)$$
$$L_2 = -h_1^1 g_2^0 + \sqrt{3}(g_1^0 h_2^1 - h_1^1 g_2^2 + g_1^1 h_2^2) \tag{30}$$
$$E = (Lo g_1^0 + L1 g_1^1 + L2 h_1^1) / 4B_0^2$$

The eccentric dipole has the same orientation and the same dipole moment as the centered dipole and B_0 is thus given by equation (28). For the coefficients given in Table 1, the offset is

$$x_0 = -391.8\text{ km}$$
$$y_0 = 257.6\text{ km}$$
$$z_0 = 178.9\text{ km}$$

The geographic spherical polar coordinates of the offset (d_o, θ_o, ϕ_o) are

$$d_0 = \sqrt{x_0^2 + y_0^2 + z_0^2}$$
$$\theta_0 = \cos^{-1}(z_0 / d_0) \tag{31}$$
$$\phi_0 = \tan^{-1}(y_0 / x0)$$

and the values given above

$$d_0 = 501.9 \text{ km}$$

$$\theta_0 = 69.33^\circ$$

$$\phi_0 = 146.68^\circ$$

The coordinates of the center of the eccentric dipole relative to the centered dipole (x_0', y_0', z_0'), which are required for equations (9) and (10), are defined according to spherical polar coordinates as

$$\begin{aligned} x_0' &= d_0 \sin\theta_0' \cos\phi_0' \\ y_0' &= d_0 \sin\theta_0' \cos\phi_0' \\ z_0' &= d_0 \cos\theta_0' \end{aligned} \tag{32}$$

The coordinates (θ_0', ϕ_0') can be found from (θ_0, ϕ_0) by using equation (6).

5. Field Line Distribution of Points

Each separate flux-tube within the model consists of a finite, one dimensional grid of points aligned along the dipole magnetic field and linking the northern and southern hemispheres. This section gives details of the calculation of the distribution of individual points along a given tube.

The first procedure in establishing a grid of points along the flux-tube is to find the q values for the northern and southern ends of the flux-tube. The base height for all the tubes in the model is 130 km and, thus, to find the two q-values corresponding to the two end points we need to find the equivalent magnetic coordinates. We begin by defining the magnetic longitude (ϕ_m) and L value of a tube. The problem now is to find the values of the remaining magnetic coordinates of the base points r_{m_b} and θ_{m_b}. Firstly, an initial guess of the value of r_{m_b} is made by making r_{m_b} equal to r_{g_b}. For this value of r_{m_b}, θ_{m_b} is given by equation (1). This gives a complete set of magnetic coordinates $(r_{m_b}, \theta_{m_b}, \phi_m)$ from which accompanying geographic coordinates are calculated using equations (7) and (10). The geographic radial value calculated this way $(r_{calc.})$ differs from the required base value (r_{g_b}). For a difference $\Delta r = r_{calc.} - r_{g_b}$, a second estimate of r_{m_b} is made $(r_{m_b}^{2nd} = r_{m_b}^{1st} - \Delta r)$. An iteration procedure then follows the steps outlined above until the calculated $r_{calc.}$ equals the required r_{g_b} (to within, say, 1 km). The number of iteration steps required for this process is small (usually less than 5) and we quickly arrive at the magnetic coordinates for the end of the flux-tube. The q value for the end point of the tube is then given by equation (2). This procedure has then to be repeated for the southern hemisphere. Thus, we finally end up with two q values, referred to as q_{max}, for the two ends of the flux-tube.

Having calculated the q values for the two ends of the flux-tube, the next step is to define all points along the flux-tube. Using a constant increment in q (i.e., $q_i = q_{i-1} + c$) is unsatisfactory because this produces a closer spacing of points (in terms of their separation along the flux-tube) toward the top of the tube (i.e., as $q \rightarrow 0$). On the contrary, a higher density of points is required toward the ends of the flux-tube (in the ionosphere) with fewer points for the plasmasphere. A pragmatic solution is to define another variable x given by

$$x = \frac{\sinh \gamma q}{\sinh \gamma q_{max}} \tag{33}$$

and then define points along the flux-tube using

$$x_i = x_{i-1} + c \tag{34}$$

where c is a constant increment, γ is a constant and q_{max} is given, for each hemisphere, by the technique outlined above. At the ends of the flux-tube, x has values of +1 and −1 (north and south respectively) and a value of 0 at the center of the tube (where $q = 0$). If we require a flux-tube to have N points in total, with $(N - 1)/2$ points in each hemisphere (and one at the center) then

$$c = \frac{2}{N-1} \tag{35}$$

For each hemisphere, consecutive values of x are calculated (moving upwards along the flux-tube) using equation (34) and the corresponding q-values using equation (33). The constant γ controls the distribution of points, with a larger value of γ producing a correspondingly larger density of points at lower altitudes. At present, a value of 5 is used for γ.

Each field line parameter in the model consists of an array of size 401 (with the array number increasing in the direction N → S). Points along the field line are allocated to this array such that the 'central' point (with $q = 0$) is located at address 201 in the array. The base points for northern and southern hemispheres are located at $I\,N$ and $I\,S$, respectively. Thus, in the array, the field line runs from $I\,N$ in the north to $I\,S$ in the south with array locations $1 - I\,N$ and $I\,S - 401$ unused. The situation is shown diagramatically in Figure 3.

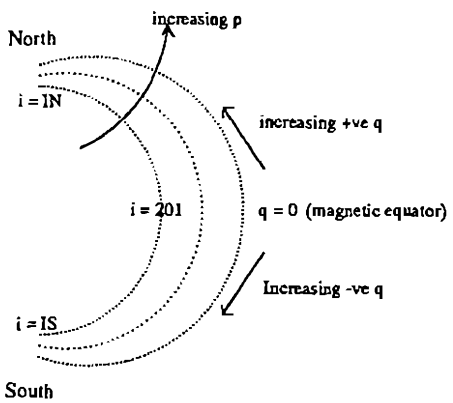

Figure 3. Geomagnetic field lines as constructed in the model.

6. More Than One Flux Tube

A global model requires that a large number of flux-tubes are followed concurrently in order to provide resolution in latitude, longitude and height. The model described here consists of 300 separate tubes. These 300 flux-tubes are arranged as 20 'bunches' of 15, each 'bunch' initially having the same magnetic longitude. The bunches are separated by 18° magnetic longitude, this being the same resolution used for (geographic) longitudes on the neutral grid. The 15 tubes within each bunch are spaced in L value to provide resolution in latitude (and height). The tubes are initially spaced in L value as follows:

- The first tube ($il = 1$) has an L value of 3.0.
- The next three tubes ($il = 2, 3, 4$) have successively smaller L values such that the resolution, in geographic latitude, of the northern hemisphere base points, is roughly 10°.
- The remaining 11 flux-tubes have successively smaller L values such that the maximum crossing height provides a 40 km vertical resolution. The outermost of these tubes ($il = 5$) has a crossing height of about 600 km with the innermost one ($il = 15$) about 200 km.

Table 2 gives the L value, the geographic crossing height ($r_g(max)$), and the latitudes of the base of the flux-tubes in the northern and southern hemispheres ($\theta_g(N)$ and $\theta_g(S)$, respectively) for a typical 'bunch' of 15 flux-tubes. Figure 4 plots all of the grid points for a typical 'bunch' of 15 flux-tubes, in the altitude/latitude plane. The figure shows clearly the high density of flux-tubes required near the equator in order to produce a satisfactory vertical profile of ionization as input to the thermosphere code. Figure 5 plots, in the (a) magnetic and (b) geographic latitude/longitude plane, typical positions of the base heights of all 300 flux-tubes, a total of 600 points. Figure 5(b) clearly shows the global form of the eccentric dipole magnetic field on the surface of the Earth.

Table 2. Initial values of L value, geographic crossing height and the position, in latitude, of the two end points of the tube for a typical 'bunch' of 15 flux-tubes.

il	L	$r_g(max)$	$\theta_g(N)$	$\theta_g(S)$
1	3.000	12450.5	46.4	–64.6
2	2.000	6081.6	36.0	–54.1
3	1.508	2948.1	25.5	–43.3
4	1.246	1284.0	14.7	–32.4
5	1.140	612.6	6.9	–24.5
6	1.134	572.6	6.3	–23.9
7	1.128	532.7	5.6	–23.2
8	1.122	492.8	4.9	–22.5
9	1.115	452.8	4.2	–21.7
10	1.109	412.9	3.4	–20.9
11	1.103	373.0	2.5	–20.1
12	1.096	333.1	1.6	–19.1
13	1.090	293.2	0.5	–18.0
14	1.084	253.2	–0.7	–16.8
15	1.078	213.3	–2.1	–15.4

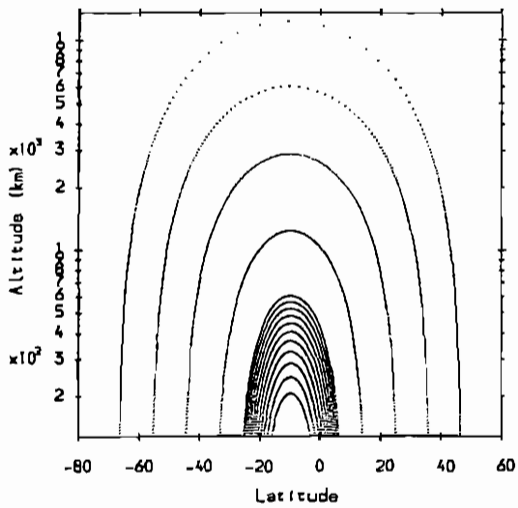

Figure 4. Grid points for a 'bunch' of 15 flux-tubes (with magnetic longitude 0 degrees), plotted in the altitude/latitude plane.

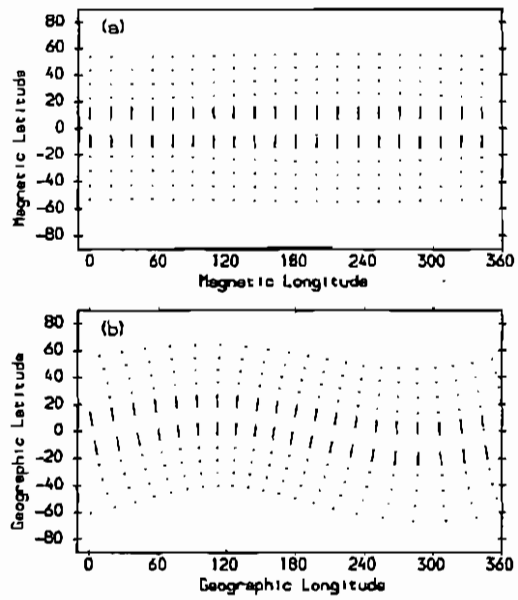

Figure 5. The positions of the 'feet' (130 km) of all the flux-tubes (prior to drifting) plotted in (a) magnetic coordinates, (b) geographic coordinates.

7. $\vec{E} \times \vec{B}$ Drift

The flux-tubes move under the effect of electric fields with a velocity given by

$$\vec{v_{em}} = \frac{\vec{E} \times \vec{B}}{B^2} \tag{36}$$

The velocity $\vec{v_{em}}$ is assumed to be completely decoupled from the field aligned velocities of the ions ($v_{||}$) which are the result of winds, diffusion and space-charge electric fields. The resultant vector velocity of ions in the flux-tube is given by $\vec{v_i} = \vec{v_{em}} + \vec{v_{||}}$. All the electric field models available are externally applied, from empirical or analytical models. At mid- and low latitudes, the electric field in the model comes from an empirical model of the mid-latitude and low-latitude electric field resulting from the dynamo action of E-region winds [*Richmond*, 1976; *Richmond et al.*, 1980].

The velocity due to $\mathbf{E} \times \mathbf{B}$ drift, $\vec{v_{em}}$, can be split into two components

$$\vec{v_{em}} = \vec{v_{\perp}} + \vec{v_{\phi}} \tag{37}$$

where $\vec{v_{\perp}}$ is in the magnetic meridional plane (positive for a flux-tube moving 'outward') and $\vec{v_{\phi}}$ is in the magnetic zonal direction (positive eastward and additional to co-rotation). The Richmond electric field model produces values of $v_{\perp}$ and v_{ϕ} at an altitude of 300 km for given values of θ_m and ϕ_m. In this case, the technique used for calculating the $\mathbf{E} \times \mathbf{B}$ drift for a flux-tube is firstly to find the point on the tube (in the magnetic northern hemisphere) that is nearest to 300 km (geographic) and then using the accompanying values of θ_m and ϕ_m to acquire values for $v_{\perp}$and v_{ϕ}. For a dipole magntic field the values of $v_{\perp}$ and v_{ϕ} at the magnetic equator are given by

$$v_{\perp}^{eq} = v_{\perp} \frac{\sqrt{1+3\cos^2\theta_m}}{\sin^3\theta_m} \tag{38}$$

and

$$v_{\phi}^{eq} = \frac{v_{\phi}}{\sin^3\theta_m} \tag{39}$$

For a time step of Δt, the new value of r_{eq}, the equatorial radial distance of the magnetic field line (defined as $r_{eq} = L \times r_o$), is given by

$$r_{eq} \rightarrow r_{eq} + v_{\perp}^{eq} \Delta t \tag{40}$$

and the new magnetic longitude is given by

$$\phi_m \rightarrow \phi_m + \frac{v_{\phi}^{eq} \Delta t}{r_{eq}} \tag{41}$$

Values for $v_{\perp}$ and v_{ϕ} at all points along the flux-tube can also be calculated using equations (38) and (39).

7.1 Normalizing the Electric Field

A significant problem is encountered when allowing the many flux-tubes to move under the influence of $\mathbf{E} \times \mathbf{B}$ drift. After a series of computations (in which the results from a given run are used as input to the following run) it is found that the tubes have acquired a net drift, moving away from their starting positions and adversely affecting the spatial resolution of the model. The solution, presently employed, is to alter the values of $\mathbf{E} \times \mathbf{B}$ drift such that, over a 24 hour simulation, each flux-tube returns exactly to its starting position. It has been found that only small changes in the values of $v_\perp$, as given by the Richmond model, are required to achieve this. In contrast the "east-west" velocity v_ϕ cannot be normalized in this way, and at present is set to zero at all times.

7.2 The Divergence of $\vec{v_{em}}$

The divergence of $\vec{v_{em}}$ is an important term which appears in the continuity equation (equations (52) and (53)) and also the energy balance equation (117). It is given by

$$\begin{aligned}\nabla \cdot \vec{v_{em}} &= \nabla \cdot \left(\frac{\vec{E} \times \vec{B}}{B^2} \right) \\ &= \frac{1}{B^2} \nabla \cdot (\vec{E} \times \vec{B}) + (\vec{E} \times \vec{B}) \cdot \nabla \left(\frac{1}{B^2} \right) \\ &= \frac{1}{B^2} (\vec{B} \cdot \nabla \times \vec{E} - \vec{E} \cdot \nabla \times \vec{B}) + (\vec{E} \times \vec{B}) \cdot \left(-2 \frac{\nabla B}{B^3} \right)\end{aligned} \tag{42}$$

Taking $\nabla \times \vec{E} = 0$ (i.e., $\vec{E} = -\nabla \Phi$) and also (for a dipole magnetic field) $\nabla \times \vec{B} = 0$, we get

$$\nabla \cdot \vec{v_{em}} = -2 \vec{v_{em}} \cdot \frac{\nabla B}{B} \tag{43}$$

Now, since the magnetic flux density B is independent of magnetic longitude, we can write

$$\begin{aligned}\vec{v_{em}} \cdot \nabla B &= \vec{v_\perp} \cdot \nabla B \\ &= \left| \vec{v_\perp} \right| \left[\cos I \frac{\partial}{\partial r} - \sin I \frac{\partial}{\partial \theta} \right] \frac{B_o (1 + 3\cos^2 \theta)^{\frac{1}{2}}}{r^3}\end{aligned} \tag{44}$$

which gives

$$\vec{v_\perp} \cdot \nabla B = - \frac{3 v_\perp^{eq} \sin^4 \theta (1 + \cos^2 \theta)}{r^4 (1 + 3\cos^2 \theta)^{\frac{3}{2}}} \tag{45}$$

and, using equation (43),

$$\nabla \cdot \vec{v_{em}} = \frac{6 v_\perp^{eq} \sin^2 \theta (1 + \cos^2 \theta)}{r_{eq} (1 + 3\cos^2 \theta)^2} \tag{46}$$

which is the form used in the model.

8. Ion Densities and Velocities: The Diffusion Equation

Having looked in detail at the mathematical description of the model structure, we now turn to the equations of continuity, momentum and energy balance, solved along each field line to give the densities and field-aligned velocities of ions O^+ and H^+ and the temperatures for both of these ions and the electrons. (The densities of molecular ions NO^+ and O_2^+ are calculated separately within CTIP using a simpler scheme which assumes chemical equilibrium.) The form of the equations used, and the solution procedures, originate with work by *Bailey and Sellek* [1990], *Rippeth* [1992] and *Quegan* [1982]. We begin by looking at the diffusion equation for the ions O^+ and H^+, before moving on to the energy balance equations for O^+, H^+ and e^-.

8.1 The Continuity Equation

Continuity considerations require that the rate of change of density for the i^{th} ion is given by

$$\frac{\partial N_i}{\partial t} = P_i - L_i - \nabla \cdot (N_i \vec{v_i}) \tag{47}$$

where N_i is the ion density, $\vec{v_i}$ is the vector velocity, P_i and L_i are the rates of production and loss, respectively, and $\partial/\partial t$ indicates a partial derivative with respect to time. The ion velocity $\vec{v_i}$ consists of two completely de-coupled components, $\vec{v_\perp}$ perpendicular and $\vec{v_\parallel}$ parallel to the direction of the magnetic field. For a frame moving with the Hall ($\mathbf{E} \times \mathbf{B}$) drift $\vec{v_\perp}$, we have

$$\frac{dN_i}{dt} = \frac{\partial N_i}{\partial t} + \vec{v_\perp} \cdot \nabla N_i \tag{48}$$

The third term on the right-hand side of equation (47) can be expanded as

$$\nabla \cdot (N_i \vec{v_i}) = N_i \nabla \cdot \vec{v_\perp} + \vec{v_\perp} \cdot \nabla N_i + \nabla \cdot (N_i \vec{v_\parallel}) \tag{49}$$

By definition $\vec{v}_\parallel$ is in the direction of the magnetic field, and thus using $\nabla \cdot \vec{B} = 0$, we have

$$\nabla \cdot (N_i \vec{v_\parallel}) = \nabla \cdot \left(N_i v_\parallel \frac{\vec{B}}{B} \right) = \vec{B} \cdot \nabla \left(\frac{N_i v_\parallel}{B} \right) = B \frac{\partial}{\partial s} \left(\frac{N_i v_\parallel}{B} \right) \tag{50}$$

where $\partial/\partial s$ denotes a differential along the field line. Also, the loss rate L_i is proportional to the ion density N_i, i.e.,

$$L_i = \beta N_i \tag{51}$$

with the loss coefficient β for ions O^+ and H^+ being given in section 9.4. We can, therefore, define a variable α_i as

$$\alpha_i = \beta - \nabla \cdot \vec{v_\perp} \tag{52}$$

with the divergence of $\vec{v_\perp}$ as given in section 7.2 (equation 46). Finally, this gives

$$\frac{dN_i}{dt} = P_i - \alpha_i N_i - B \frac{\partial}{\partial s} \left(\frac{N_i v_\parallel}{B} \right) \tag{53}$$

8.2 The Momentum Equation

A rearrangement of the momentum equation for the i^{th} ion, as given by *Moffett et al.* [1989] (and the simplification of considering two ion species) gives the form of the field-aligned ion velocity used in the model:

$$\begin{aligned} v_{\parallel} &= h_{ij} v_j + h_{in} v_n \\ &-D_i \left[\frac{1}{N_i} \frac{\partial N_i}{\partial s} + \frac{T_e}{T_i N_e} \frac{\partial N_e}{\partial s} - \frac{m_i}{kT_i} g_{\parallel} \right. \\ &\left. + \frac{1}{T_i} \left(\frac{\partial}{\partial s}(T_e + T_i) + \beta_i \frac{\partial T_i}{\partial s} - \beta_{ij} \frac{\partial T_j}{\partial s} \right) \right] \end{aligned} \tag{54}$$

The terms on the right-hand side of equation (54) are due to the effects of: (1) collisions between ions i and j; (2) collisions between ions i and the neutral gas; (3) the partial pressure gradient of the i^{th} ion constituent; (4) the partial pressure gradient of the electron gas; (5) the field-aligned component of gravity; and (6) terms due to the effects of thermal diffusion resulting from field-aligned temperature gradients.

The drag coefficient, h_{ij}, for momentum transfer between ion j and ion i is given by

$$h_{ij} = \frac{\nu_{ij}(1 - \Delta_{ij})}{\nu_{ij}(1 - \Delta_{ij}) + \nu_{in}} \tag{55}$$

and similarly,

$$h_{in} = \frac{\nu_{in}}{\nu_{ij}(1 - \Delta_{ij}) + \nu_{in}} \tag{56}$$

is the drag coefficient for momentum transfer between the ion i and the neutral gas. The collision frequencies ν_{in} and ν_{ij} are given in section 9.2. The coefficients β_i and β_{ij} are thermal diffusion coefficients, with Δ_{ij} being a diffusion correction factor due to thermal diffusion. All are given in section 9.3. The diffusion coefficient D_i is given by

$$D_i = \frac{kT_i}{m_i} \frac{1}{\nu_{ij}(1 - \Delta_{ij}) + \nu_{in}} \tag{57}$$

Equation (54) can be written as

$$N_i v_{\parallel} = -X_i N_i - Y_i \frac{\partial N_i}{\partial s} \tag{58}$$

where

$$X_i = -(h_{ij}v_j + h_{in}v_n) + D_i\left[\frac{T_e}{T_i N_e}\frac{\partial N_j}{\partial s} - \frac{m_i}{kT_i}g_{\|} + \frac{1}{T_i}\left(\frac{\partial}{\partial s}(T_e + T_i) + \beta_i\frac{\partial T_i}{\partial s} - \beta_{ij}\frac{\partial T_j}{\partial s}\right)\right] \tag{59}$$

and

$$Y_i = D_i\left(1 + \frac{N_i}{N_e}\frac{T_e}{T_i}\right) \tag{60}$$

using the assumption that the total electrical charge is zero and, therefore,

$$N_e = N_i + N_j \tag{61}$$

9. Solving the Diffusion Equation

In order to solve the transport equations, it is convenient to transform into the (p, q) coordinate system (as defined in section 4.1). For the dipole field, $\partial/\partial s$ and $\partial/\partial q$ are related by

$$\frac{\partial}{\partial s} = -r_0^2\frac{\sqrt{(1+3\cos^2\theta_m)}}{r_m^3}\frac{\partial}{\partial q} = \eta\frac{\partial}{\partial q} \tag{62}$$

and also

$$B = B_o r_o^3\frac{\sqrt{(1+3\cos^2\theta_m)}}{r_m^3} = -B_o r_o \eta \tag{63}$$

The continuity equation now becomes

$$\frac{dN_i}{dt} = P_i - \alpha_i N_i - \eta^2\frac{\partial}{\partial q}\left(\frac{N_i v_{\|}}{\eta}\right) \tag{64}$$

and the momentum equation

$$N_i v_{\|} = -X_i N_i - \eta Y_i\frac{\partial N_i}{\partial q} \tag{65}$$

Clearly equations (64) and (65) can be combined directly by eliminating the flux term $N_i v_{\|}$ to produce the diffusion equation. However, this results in a second order equation in q for which it is difficult to construct a finite difference scheme that is flux preserving (i.e., conservative). Instead, the technique employed here is to solve the continuity and momentum equations as a pair of first order equations by using a finite difference scheme.

9.1 The Finite Difference Scheme

A central difference technique is used to discretize both the diffusion and momentum equations. If we write the ion flux at the k^{th} point along the flux-tube as

$$\phi_k = \frac{N_k v_k}{\eta_k} \tag{66}$$

where we have now dropped all the previous subscripts, then from equation (65) the flux at the point $k+\frac{1}{2}$ can be defined in terms of the points on either side (i.e., points k and $k+1$) as

$$\phi_{k+\frac{1}{2}} = -\frac{1}{2}\left[\frac{X_{k+1}N_{k+1}}{\eta_{k+1}} + \frac{X_k N_k}{\eta_k}\right] - \frac{1}{2}(Y_{k+1}+Y_k)\frac{(N_{k+1}-N_k)}{d_k} \tag{67}$$

where $d_k = q_{k+1} - q_k$. Similarly, the flux at the point $k-\frac{1}{2}$ is given by

$$\phi_{k-\frac{1}{2}} = -\frac{1}{2}\left[\frac{X_k N_k}{\eta_k} + \frac{X_{k-1}N_{k-1}}{\eta_{k-1}}\right] - \frac{1}{2}(Y_k+Y_{k-1})\frac{(N_k-N_{k-1})}{d_{k-1}} \tag{68}$$

The continuity equation at the point k can be written as

$$\left[\frac{dN}{dt}\right]_k = P_k - \alpha_k N_k - \eta_k^2 \frac{(\phi_{k+\frac{1}{2}} - \phi_{k-\frac{1}{2}})}{\frac{1}{2}(d_k + d_{k-1})} \tag{69}$$

All of the terms in equations (67), (68) and (69) are to be evaluated at a time step j. Thus, in what follows, a general term written A_k is equivalent to A_k^j. Any terms evaluated at the previous time step will be explicitly labeled as such (e.g. A_k^{j-1}). The differential on the left-hand side of equation (69) is written as a backward difference (i.e., in terms of the previous time step)

$$\left[\frac{dN}{dt}\right]_k = \frac{N_k - N_k^{j-1}}{\Delta t} \tag{70}$$

where Δt represents the time step used by the model. The flux terms at points $k+\frac{1}{2}$ and $k-\frac{1}{2}$, given by equations (67) and (68) are now substituted into the continuity equation (69). Rearranging the resulting equation to gather terms in N_{k-1}, N_k and N_{k+1} on the right-hand side, while leaving all other terms on the left-hand side, gives

$$-P_k - \frac{N_k^{j-1}}{\Delta t} = N_{k-1}\left[\frac{\eta_k^2}{(d_{k-1}+d_k)}\left(\frac{(Y_{k-1}+Y_k)}{d_{k-1}} - \frac{X_{k-1}}{\eta_{k-1}}\right)\right]$$
$$+N_k\left[-\frac{\eta_k^2}{(d_{k-1}+d_k)}\left(\frac{(Y_{k-1}+Y_k)}{d_{k-1}} + \frac{(Y_k+Y_{k+1})}{d_k}\right) - \alpha_k - \frac{1}{\Delta t}\right] \quad (71)$$
$$+N_{k+1}\left[\frac{\eta_k^2}{(d_{k-1}+d_k)}\left(\frac{(Y_k+Y_{k+1})}{d_k} + \frac{X_{k+1}}{\eta_{k+1}}\right)\right]$$

which can be simplified to

$$S_k N_{k-1} + T_k N_k + U_k N_{k+1} = W_k \quad (72)$$

where

$$S_k = \left[\frac{\eta_k^2}{(d_{k-1}+d_k)}\left(\frac{(Y_{k-1}+Y_k)}{d_{k-1}} - \frac{X_{k-1}}{\eta_{k-1}}\right)\right]$$
$$T_k = \left[-\frac{\eta_k^2}{(d_{k-1}+d_k)}\left(\frac{(Y_{k-1}+Y_k)}{d_{k-1}} + \frac{(Y_k+Y_{k+1})}{d_k}\right) - \alpha_k - \frac{1}{\Delta t}\right]$$
$$U_k = \left[\frac{\eta_k^2}{(d_{k-1}+d_k)}\left(\frac{(Y_k+Y_{k+1})}{d_k} + \frac{X_{k+1}}{\eta_{k+1}}\right)\right] \quad (73)$$
$$W_k = -P_k - \frac{N_k^{j-1}}{\Delta t}$$

Equation (72) can now be solved. If we have (say) a flux-tube containing n points, with point 1 at the base of the tube in the northern hemisphere and point n similarly in the southern hemisphere, then evaluating equation (72) at all points from 2 to $n-1$ gives a set of simultaneous equations

$$\begin{aligned}
S_2N_1 + T_2N_2 + U_2N_3 &= W_2 \\
S_3N_2 + T_3N_3 + U_3N_4 &= W_3 \\
S_4N_3 + T_4N_4 + U_4N_5 &= W_4 \\
&\cdots\cdots \\
S_{n-2}N_{n-3} + T_{n-2}N_{n-2} + U_{n-2}N_{n-1} &= W_{n-2} \\
S_{n-1}N_{n-2} + T_{n-1}N_{n-1} + U_{n-1}N_n &= W_{n-1}
\end{aligned} \quad (74)$$

This set of equations has a tridiagonal structure. All of the coefficients S, T, U and W are known for every point along the flux-tube and all that is required to solve these equations are the values of N_1 and N_n which form boundary conditions. Since both points are at low altitudes, a reasonable assumption is for the densities to be given by chemical equilibrium. Setting the flux term in equation (47) to zero and rearranging gives

$$N_1 = \frac{P_1 + N_1^{j-1}/\Delta t}{\beta_1 + 1/\Delta t}$$
$$N_n = \frac{P_n + N_n^{j-1}/\Delta t}{\beta_n + 1/\Delta t} \tag{75}$$

To solve all equations (74), we start with the first one (for $k = 2$). Since we know N_1 from equation (75), we have N_2 in terms of N_3. We can now eliminate N_2 from the second equation, leaving N_3 in terms of N_4. Again, N_3 can be eliminated from the third equation leaving N_4 in terms of N_5. Thus, we move 'upward' along the tube until we reach the 'top.' At the second before last equation, we have N_{n-2} in terms of N_{n-1}. As before, we can eliminate N_{n-2} from the last equation to give N_{n-1} in terms of N_n. Since N_n is given by the boundary conditions (equation 75), the last equation can now be used to calculate N_{n-1}. Knowing N_{n-1} gives us N_{n-2} and thus we now work our way back 'down' the tube calculating every value of N_k. The field-aligned velocity can now be calculated using equation (65). In the finite difference scheme, this gives

$$v_k = -X_k - \frac{\eta_k Y_k}{N_k}\frac{(N_{k+1} - N_k)}{d_k} \tag{76}$$

9.2 Collision Frequencies

The collision frequencies (in units s^{-1}) for the transfer of momentum between the ions and the neutrals are from *Raitt et al.* [1975] and are given by

$$\begin{aligned} \nu_{O^+n} &= 3.42\times10^{-17}[\mathrm{O}]T^{\frac{1}{2}}(1.04 - 0.67\log_{10}T)^2 \\ &+ 6.82\times10^{-16}[\mathrm{N_2}] \\ &+ 6.66\times10^{-16}[\mathrm{O_2}] \end{aligned} \tag{77}$$

and

$$\begin{aligned} \nu_{H^+n} &= 2.0\times10^{-16}[\mathrm{H}]T^{\frac{1}{2}}(1.0 - 0.082\log_{10}T)^2 \\ &+ 6.61\times10^{-17}[\mathrm{O}]T_i^{\frac{1}{2}}(1.0 - 0.047\log_{10}T_i)^2 \\ &+ 3.36\times10^{-15}[\mathrm{N_2}] \\ &+ 3.20\times10^{-15}[\mathrm{O_2}] \end{aligned} \tag{78}$$

where $T = (T_i + T_n)/2$ and the terms in square brackets indicate the number densities of the respective constituents. The frequency of collisions between ions i and j is given by [*Schunk and Nagy*, 1980]

$$\nu_{ij} = 1.27 n_j \frac{\sqrt{A_{ij}}}{A_i T_{ij}^{\frac{3}{2}}} \tag{79}$$

where A_i gives the mass of ion i in a.m.u. and the reduced mass and reduced temperature are given, respectively, by

$$A_{ij} = \frac{A_i A_j}{A_i + A_j} \tag{80}$$

$$T_{ij} = \frac{m_i T_j + m_j T_i}{m_i + m_j} \tag{81}$$

where m_i is the mass (in kg).

9.3 Thermal Diffusion Coefficients

The thermal diffusion coefficients are taken from equations given by *Quegan et al.* [1981] for the two major ion cases. These are given by

$$\beta_i = \frac{15}{8}\frac{A_{ij}}{A_i}\frac{T_i}{T_{ij}}\frac{\nu_{ij}(\nu_i' - \nu_{ji}')}{(\nu_i'\nu_j' - \nu_{ij}'\nu_{ji}')} \tag{82}$$

$$\beta_{ji}^* = \frac{n_i}{n_j}\beta_i \tag{83}$$

$$\nu_i' = \nu_{ii} + \frac{5}{4}\nu_{ij}\left(D_{ij}^{(1)} + \frac{3}{2}\frac{A_{ij}}{A_i}\frac{T_i}{T_{ij}}\right) \tag{84}$$

$$\nu_{ij}' = \frac{5}{4}\left[D_{ij}^{(4)} + \frac{3}{2}\frac{A_{ij}}{A_i}\frac{T_i}{T_{ij}}\right] \tag{85}$$

$$D_{ij}^{(1)} = 3\left(\frac{A_{ij}}{A_j}\frac{T_j}{T_{ij}}\right)^2 - B_{ij}^{(1)} - \frac{B_{ij}^{(3)}}{5} + \frac{A_{ij}}{(A_i + A_j)}\frac{T_j}{T_{ij}}\left(\frac{8}{5} - \frac{3}{2}\frac{T_i}{T_{ij}}\right) \tag{86}$$

$$D_{ij}^{(4)} = 3\left(\frac{A_{ij}}{A_i}\frac{T_j}{T_{ij}}\right)^2 - B_{ij}^{(2)} - \frac{B_{ij}^{(3)}}{5} + \frac{A_{ij}}{(A_i + A_j)}\frac{T_i}{T_{ij}}\left(\frac{8}{5}\frac{A_j}{A_i} + \frac{3}{2}\frac{T_j}{T_{ij}}\right) \tag{87}$$

$$B_{ij}^{(1)} = -\frac{1}{5}\frac{A_{ij}^2}{A_i(A_i + A_j)}\frac{(T_j - T_i)}{T_{ij}}\left(4 + 3\frac{A_i}{A_j}\frac{T_j}{T_{ij}}\right) \tag{88}$$

$$B_{ij}^{(2)} = \frac{1}{5}\frac{A_{ij}^2}{A_i(A_i + A_j)}\frac{(T_j - T_i)}{T_{ij}}\left(4 - 3\frac{T_j}{T_{ij}}\right) \tag{89}$$

$$B_{ij}^{(3)} = \left(\frac{A_{ij}}{A_i}\right)\left[1 + 3\left(\frac{A_{ij}}{A_j}\right)^2\left(\frac{T_j - T_i}{T_{ij}}\right)^2\right] \tag{90}$$

The diffusion correction factor is given by

$$\Delta_{ij} = \Delta_{ji} = \frac{2}{5}(C_{ij}\beta_i + C_{ji}\beta_j) \tag{91}$$

where

$$C_{ij} = \frac{5}{2} - \frac{A_{ij}}{A_j}\left[\frac{5}{2}\frac{T_j}{T_{ij}} + \frac{A_j}{A_i}\frac{T_{ij}}{T_i} - \frac{(T_j - T_i)}{T_i}y_{ij}\right] \tag{92}$$

and

$$y_{ij} = \frac{A_{ij}}{A_i}\left[4 - 5\frac{T_i}{T_{ij}} - 3\frac{A_{ij}}{A_j}\frac{T_j - T_i}{T_{ij}}\right] \tag{93}$$

9.4 Production and Loss Processes

The photoionization production rate for the ion O^+ is given by

$$P_{\text{photo}}(O^+) = \sum_{\lambda}\Phi(\lambda)\sigma^i(\lambda)[O]\times\exp\left[-\sum_j \sigma_j^a(\lambda)n_j H_j Ch_j(\chi)\right] \tag{94}$$

where the summation Σ_λ is over the wavelength range of the ionizing radiation and Σ_j denotes a summation over the neutral gases O, O_2 and N_2. The solar EUV radiation flux intensities, $\Phi(\lambda)$, are taken from *Schunk and Nagy* [1978], as are the ionization and absorption cross sections (σ^i and σ^a, respectively). The Chapman grazing incidence function, $Ch_j(\chi)$, for the j^{th} neutral gas, as approximated by *Rishbeth and Garriott* [1969], is given by

$$Ch(\chi) = \left(\frac{1}{2}\pi x\sin\chi\right)^{\frac{1}{2}}\exp\left(\frac{1}{2}x\cos^2\chi\right)\left[1 \pm \mathbf{erf}\left(\frac{1}{2}x\cos^2\chi\right)^{\frac{1}{2}}\right] \tag{95}$$

where χ is the solar zenith angle, **erf** is the error function, the $\pm$ refers to $\chi > 90°$ or $\chi < 90°$, respectively, and x denotes the ratio of the geocentric height to the scale height i.e.,

$$x = \frac{r_g}{H} \tag{96}$$

For the O^+ ion the main chemical loss processes are due to the two reactions

$$O^+ + N_2 \rightarrow NO^+ + N \tag{97}$$

with reaction rate k_1, and

$$O^+ + O_2 \rightarrow O_2^+ + O \tag{98}$$

with reaction rate k_2. For ions O^+ and H^+, the reversible reaction

$$O + H^+ \leftrightarrow O^+ + H \tag{99}$$

provides both a source and loss term for each ion. The rate of chemical production of O^+ is given by

$$P_{chem}(O^+) = k_4[O][H^+] + 1.0 \times 10^{10}[O] \tag{100}$$

with the terms in square brackets indicating the number density of the respective constituents. The second term on the right-hand side of equation (100) provides a small amount of production for O^+ to prevent $N(O^+)$ from going negative at night. For the H^+ ion, chemical production is given by

$$P_{chem}(H^+) = k_3[H][O^+] \tag{101}$$

The rate coefficients k_3 and k_4 are defined in the next section. This equation is the only production source of H^+ in the model since it is much larger than any production due to the photoionization of atomic hydrogen. The production term for O^+ as used in the continuity equation (47) is thus given by

$$P = P_{photo}(O^+) + P_{chem}(O^+) \tag{102}$$

and for the H^+ ion is given by

$$P = P_{chem}(H^+) \tag{103}$$

The loss coefficient for O^+, as used in equations (51) and (52), is given by

$$\beta(O^+) = (k_1[N_2] + k_2[O_2] + k_3[H]) \tag{104}$$

and for H^+ is given by

$$\beta(H^+) = k_4[O] \tag{105}$$

9.5 Chemical Reaction Rates

The reaction rates for chemical loss of O^+, due to reactions with N_2 and O_2, in units of m^3 s^{-1}, are taken from *Torr and Torr* [1979] and are given by

$$k_1 = 1.533 \times 10^{-18} - 5.920 \times 10^{-19}\left(\frac{T_{eff}}{300}\right) + 8.600 \times 10^{-20}\left(\frac{T_{eff}}{300}\right)^2$$

for ($300K \leq T_{eff} \leq 1700K$) and

$$k_1 = 2.730\times10^{-18} - 1.155\times10^{-18}\left(\frac{T_{\text{eff}}}{300}\right) + 1.483\times10^{-19}\left(\frac{T_{\text{eff}}}{300}\right)^2 \tag{106}$$

for ($1700K < T_{\text{eff}}$).

$$k_2 = 2.820\times10^{-17} - 7.740\times10^{-18}\left(\frac{T_{\text{eff}}}{300}\right) + 1.073\times10^{-18}\left(\frac{T_{\text{eff}}}{300}\right)^2 - 5.170\times10^{-20}\left(\frac{T_{\text{eff}}}{300}\right)^3 + 9.650\times10^{-22}\left(\frac{T_{\text{eff}}}{300}\right)^4 \tag{107}$$

The effective temperature is given by

$$T_{\text{eff}} = \frac{M_n}{M(\text{O}^+)+M_n}\left(\frac{M(\text{O}^+)}{3k}\left|\vec{V}_i - \vec{V}_n\right|^2 + T_i + T_n\right) + T_n \tag{108}$$

where $M_n \equiv M(\text{N}_2)$ in equation (106) and $M_n \equiv M(\text{O}_2)$ in equation (107).

The rate coefficients k_3 and k_4 (m^3s^{-1}), for the reversible charge exchange reaction between oxygen and hydrogen, are taken from *Raitt et al.* [1975], and are given by

$$k_3 = 2.5\times10^{-17}\sqrt{T_n} \tag{109}$$

$$k_4 = 2.5\times10^{-17}\sqrt{T(\text{H}^+)}\,/\,1.125 \tag{110}$$

10. Ion Temperatures: The Energy Balance Equation

We now move on to calculating the temperatures of the two ion species and the electron gas by solving the coupled energy balance equations. For the i^{th} constituent (where i is O^+, H^+ or e), the energy balance equation is given by

$$\frac{3}{2}kN_i\frac{DT_i}{Dt} = Q_i - kN_iT_i\nabla\cdot\vec{v_i} + \nabla\cdot(\kappa_i\nabla T_i) + F_{in} \tag{111}$$

where Q_i gives the heating rate (positive or negative) due to collisional interactions with other ion or neutral species, the second and third terms on the right-hand side are due to adiabatic heating/cooling and thermal conductivity, respectively (where κ_i is the thermal conductivity), and F_{in}, the term due to frictional heating of the ions by the neutrals, is given by

$$F_{in} = \sum_n \frac{m_i m_n}{m_i + m_n} \nu_{in} N_i \left| \vec{v_i} - \vec{v_n} \right|^2 \tag{112}$$

When the frictional heating, F_{in}, is large, the ion temperature becomes anisotropic. This feature is not included in the CTIP model although calculations of temperature anisotropy have been performed by *Moffett et al.* [1993] using a modified version of the SUPIM code which is described by *Bailey and Balan* [1996, this issue]. The differential $(DT_i/Dt)$is given by

$$\frac{DT_i}{Dt} = \frac{\partial T_i}{\partial t} + \vec{v_i} \cdot \nabla T_i \tag{113}$$

where the partial derivative is defined for a stationary (Eulerian) frame. The second term on the right-hand side expresses the conversion between heat energy and work energy. Also, for a tube of plasma undergoing $\mathbf{E} \times \mathbf{B}$ drift, the differential in the moving (Lagrangian) frame is given by

$$\frac{dT_i}{dt} = \frac{\partial T_i}{\partial t} + \vec{v_\perp} \cdot \nabla T_i \tag{114}$$

and therefore,

$$\frac{dT_i}{dt} = \frac{DT_i}{Dt} - \vec{v_\parallel} \cdot \nabla T_i \tag{115}$$

Since thermal conduction occurs primarily along the flux-tube we can write

$$\nabla T_i \approx \frac{\partial T_i}{\partial s} \tag{116}$$

Using equation (62) to write the field line differentials in q coordinates, equation (111) now becomes

$$\begin{aligned} \frac{3}{2} k N_i \frac{dT_i}{dt} = Q_i - k N_i T_i \left[\eta^2 \frac{\partial}{\partial q} \left(\frac{v_\parallel}{\eta} \right) + \nabla \cdot \vec{v_\perp} \right] \\ + \eta^2 \frac{\partial}{\partial q} \left(\kappa_i \frac{\partial T_i}{\partial q} \right) + F_{in} - \frac{3}{2} k N_i v_\parallel \eta \frac{\partial T_i}{\partial q} \end{aligned} \tag{117}$$

11. Solving the Energy Balance Equation

The energy balance equation is solved by using finite difference techniques similar to those used to solve the diffusion equation. If we define the heat flow vector ψ as

$$\psi = \kappa \frac{\partial T}{\partial q} \tag{118}$$

where we have now dropped the i subscripts, then this can be written as a forward difference for the k^{th} q step as

$$\psi_k = \kappa_k \frac{T_{k+1} - T_k}{d_k} \tag{119}$$

Expressing both the time and q derivatives as backward differences, we can write equation (117) as

$$\begin{aligned} \frac{3}{2} kN_k \frac{(T_k - T_k^{j-1})}{\Delta t} = Q_k - kN_k T_k^{j-1} \left[\eta_k^2 \frac{\partial}{\partial q} \left(\frac{v_k^{\parallel}}{\eta_k} \right) + \nabla \cdot v_{\perp} \right] \\ + \eta_k^2 \frac{(\psi_k - \psi_{k-1})}{d_{k-1}} + F_k \\ - \frac{3}{2} kN_k v_k^{\parallel} \eta_k \frac{(T_k - T_{k-1})}{d_{k-1}} \end{aligned} \tag{120}$$

As with the diffusion equation, the superscript $j-1$ indicates values taken at the previous time step. The second term on the right-hand side contains T_k^{j-1} instead of T_k $(=T_k^j)$. The reason for this is that the term

$$\frac{\partial}{\partial q} \left(\frac{v_k^{\parallel}}{\eta_k} \right),$$

calculated at the present time step j, was shown by *Bailey and Sellek* (private communication) to produce instabilities. Following the method of *Bailey and Sellek* [1990], the term

$$\eta_k^2 \frac{\partial}{\partial q} \left(\frac{v_k^{\parallel}}{\eta_k} \right) + \nabla \cdot v_{\perp} \tag{121}$$

is taken as a coefficient of T_k^{j-1}. Substituting equation (119) into equation (120) and collecting terms in T_{k-1}, T_k and T_{k+1} on the right-hand side we produce the tridiagonal set of equations given by

$$A_k T_{k-1} + B_k T_k + C_k T_{k+1} = D_k \tag{122}$$

where

$$A_k = \left[\frac{\eta_k^2 \kappa_{k-1}}{d_{k-1}^2} + \frac{3}{2} k N_k v_k^{\parallel} \frac{\eta_k}{d_{k-1}}\right]$$

$$B_k = \left[-S_k - \frac{\eta_k^2}{d_{k-1}}\left(\frac{\kappa_k}{d_k} + \frac{\kappa_{k-1}}{d_{k-1}}\right) - \frac{3}{2} k N_k \left(v_k^{\parallel} \frac{\eta_k}{d_{k-1}} + \frac{1}{\Delta t}\right)\right]$$

$$C_k = \left[\frac{\eta_k^2 \kappa_k}{d_k d_{k-1}}\right] \tag{123}$$

$$D_k = k N_k T_k^{j-1}\left[\eta_k^2 \frac{\partial}{\partial q}\left(\frac{v_k^{\parallel}}{\eta_k}\right) + \nabla \cdot v_{\perp} - \frac{3}{2\Delta t}\right] - R_k - F_k$$

Here, the heating rate Q_k has been written as

$$Q_k = R_k - S_k T_k \tag{124}$$

a linear function of T_k. In several cases, however, the heating rates are non-linear functions of T.

11.1 Non-Linear Heating Rates

The heating rates for each constituent are, in several cases, non-linear functions of T (as shown in section 12) and, therefore, do not obey equation (124). In this case, non-linear functions are forced into the form given in equation (124) by evaluating other powers of T at the previous time step. For instance, if a heating rate is given by the (hypothetical) equation

$$Q_k = a_k \frac{(z_k - T_k)}{(b_k + c_k T_k^{1.5})} \tag{125}$$

then the term $T_k^{1.5}$ would be evaluated from the previous time step, i.e., $(T_k^{j-1})^{1.5}$. Thus, in this case, the coefficients R_k and S_k would be given by

$$R_k = a_k \frac{z_k}{(b_k + c_k (T_k^{j-1})^{1.5})}$$

$$S_k = a_k \frac{1}{(b_k + c_k (T_k^{j-1})^{1.5})}$$

The temperature at every point along the field line can now be solved using the same technique as outlined for the ion density in the equation (74). At the ends of the flux-tube (at points 1 and n) the temperature change is assumed to be due to the heating rate Q alone i.e.,

$$T_1 = T_1^{j-1} + \frac{2}{3} Q_1 \frac{\Delta t}{k N_1}$$

$$T_n = T_n^{j-1} + \frac{2}{3} Q_n \frac{\Delta t}{k N_n} \tag{126}$$

12. Heating Rates

All the ion and electron heating rates are given in units of $eVm^{-3}s^{-1}$.

12.1 Ion Heating Rates

The heating rate for the i^{th} ion (where i represents either O^+ or H^+) is given by the sum of heating rates due to ion-electron collisions, ion-ion collisions and elastic and non-elastic collisions with the neutrals, i.e.,

$$Q_i = Q_{ie} + Q_{ij} + Q_{in}^{el} + Q_{in} \tag{127}$$

where each term can have a positive (heating) or negative (cooling) influence. The heating rates due to ion-electron collisions and ion-ion collisions are given by

$$Q_{ie} = 7.7 \times 10^{-12} N_e N_i \frac{(T_e - T_i)}{A_i T_e^{1.5}} \tag{128}$$

and

$$Q_{ij} = 3.3 \times 10^{-10} N_i N_j \frac{(T_i - T_j)}{A_i A_j \left[\frac{T_i}{A_i} + \frac{T_j}{A_j}\right]^{1.5}} \tag{129}$$

respectively, the equations having been taken from *Banks and Kockarts* [1973]. The heating rates for the O^+ and H^+ ions due to elastic and inelastic collisions with neutrals are taken from *Bailey and Sellek* [1990] and are given by

$$\begin{aligned} Q_{O^+n}^{el} = {} & [O^+](T_n - T_{O^+}) \times \\ & (2.1 \times 10^{-21}[O]\sqrt{T_{O^+} + T_n} \\ & + 5.8 \times 10^{-20}[O_2] + 6.6 \times 10^{-20}[N_2] \\ & + 2.8 \times 10^{-20}[He] + 3.3 \times 10^{-20}[H]) \end{aligned} \tag{130}$$

$$\begin{aligned} Q_{H^+n}^{el} = {} & [H^+](T_n - T_{H^+}) \times \\ & (1.4 \times 10^{-20}[H]\sqrt{T_{H^+} + T_n} \\ & + 3.5 \times 10^{-20}[O] + 3.1 \times 10^{-20}[N_2] \\ & + 2.8 \times 10^{-20}[O_2] + 0.5 \times 10^{-20}[He]) \end{aligned} \tag{131}$$

$$Q_{H^+O} = 3.4 \times 10^{-21}\left(\frac{9}{8}[H][O^+]T_n^{1.5} - [O][H^+]T_{H^+}^{1.5}\right) \tag{132}$$

$$Q_{O^+H} = 3.8 \times 10^{-21}\left(\frac{8}{9}[O][H^+]T_n\sqrt{T_{H^+}} - [H][O^+]T_{O^+}\right) \tag{133}$$

12.2 Electron Heating Rates

The electron heating rate is given by the sum of the heating rates due to photoelectrons, ion-electron collisions, rotational and vibrational heating

$$Q_e = Q_{\text{phe}} + \sum_i Q_{ei} + Q_{en}^{\text{rot}} + Q_{en}^{\text{vib}} + Q_{en}^{\text{f}} \tag{134}$$

where the term $Q_{ei} = -Q_{ie}$. Energetic photoelectrons are created during the photoionization of the neutral gases and go on to heat the ambient electron gas. At lower altitudes, most of the photoelectron heat is distributed locally. At higher altitudes, the more energetic electrons are able to propagate along the magnetic field lines heating the gas further afield with observable effects in the opposite hemisphere. In the model, for altitudes of less than 300 km, the photoelectron heating rate is given by

$$Q_{\text{phe}} = \varepsilon P_{\text{photo}}(O^+) \tag{135}$$

where $P_{\text{photo}}(O^+)$, the photoionization rate for O^+, is given in section 9.4. The electron heating efficiency ε, from *Swartz and Nisbet* [1972], is given by the empirical relationship

$$\varepsilon = \exp-(12.75 + 6.941x + 1.66x^2 + 0.08034x^3 + 0.001996x^4) \tag{136}$$

where

$$x = \log_e\left(\frac{N_e}{[O_2] + [N_2] + 0.1[O]}\right) \tag{137}$$

For altitudes greater than 300 km, Q_{phe} is given by

$$Q_{\text{phe}} = N_e q_0 \frac{B}{B_0} \exp-\left(C \int N_e ds\right) \tag{138}$$

where q_0 is the heat input per electron at 300 km, B_0 is the magnetic field strength at 300 km and the constant C is taken to be $3 \times 10^{-18} m^2$ [in line with *Nisbet*, 1968; *Bauer et al.*, 1970; *Bailey and Sellek*, 1990; *Rippeth*, 1992].

The rotational heat transfer rate is given by *Dalgarno et al.* [1968] and *Mentzoni and Rao* [1963] as

$$Q_{en}^{\text{rot}} = N_e \frac{(T_n - T_e)}{\sqrt{T_e}} (7.0 \times 10^{-20}[O_2] + 2.8 \times 10^{-20}[N_2]) \tag{139}$$

The vibrational heat transfer rate for electrons comes from an approximation by *Williams and McDonald* [1987] and is given by

$$\begin{aligned} Q_{en}^{\text{vib}} = {} & 6.5 \times 10^{-28} N_e [N_2](T_n - 310)^2 (T_n - T_e) \\ & \times \exp[0.0023(T_e - T_n)] \end{aligned} \tag{140}$$

The fine structure heat transfer rate, from *Hoegy* [1976], is given by

$$Q_{en}^{f} = -8.629\times10^{-12}\frac{N_e[O]}{Z}\sum_{i=1}^{3}A_iC_iT_e^{(B_i-0.5)} \times\left\{\varepsilon(E_{xi}-D_{xi})+5.91\times10^{-9}(T_e-T_n) \times\left[(1+B_i)D_{xi}+\left(\frac{E_i}{T_e}+1+B_i\right)E_{xi}\right]\right\} \quad (141)$$

where

$$\varepsilon_1 = 0.02 \qquad \varepsilon_2 = 0.028 \qquad \varepsilon_3 = 0.008$$
$$A_1 = 7.883\times10^{-6} \qquad A_2 = 9.466\times10^{-6} \qquad A_3 = 1.037\times10^{-8}$$
$$B_1 = 1.021 \qquad B_2 = 0.8458 \qquad B_3 = 1.633$$
$$C_1 = 1.009 \qquad C_2 = 0.9444 \qquad C_3 = 1.466$$
$$E_1 = 228 \qquad E_2 = 326 \qquad E_3 = 98$$
$$D_{x1} = \exp\left(-\frac{E_1}{T_1}\right) \qquad D_{x2} = \exp\left(-\frac{E_2}{T_0}\right) \qquad D_{x3} = D_{x2}$$
$$E_{x1} = \exp\left(-\frac{E_1}{T_e}\right) \qquad E_{x2} = \exp\left(-\frac{E_2}{T_e}\right) \qquad E_{x3} = \exp\left(-\frac{E_3}{T_e}-\frac{E_1}{T_1}\right)$$

$$Z = 5+3\exp\left(-\frac{E_1}{T_n}\right)+\exp\left(-\frac{E_2}{T_n}\right)$$

12.3 Thermal Conductivities

The thermal conductivity for the i^{th} ion (in units of $eVm^{-1}s^{-1}K^{-1}$) is given by *Banks and Kockarts* [1973]

$$\kappa_i = 4.6\times10^{6}\frac{N_i}{N_e}\frac{T_i^{2.5}}{A_i^{0.5}} \quad (142)$$

where A_i is the ion mass in a.m.u. The thermal conductivity for the electrons is given by *Schunk and Nagy* [1978]

$$\kappa_e = \frac{7.7\times10^{7}T_e^{2.5}}{\left[1+\frac{3.22\times10^{4}T_e^{2}}{N_e}(q(O)[O]+q(N_2)[N_2]+q(O_2)[O_2])\right]} \quad (143)$$

where

$$q(\mathrm{O}) = 1.1\times10^{-16}(1+5.7\times10^{-4}T_e)$$
$$q(\mathrm{N_2}) = 2.82\times10^{-17}T_e^{0.5}(1-1.21\times10^{-4}T_e) \qquad (144)$$
$$q(\mathrm{O_2}) = 2.2\times10^{-16}(1+3.6\times10^{-2}T_e^{0.5})$$

13. Results

This section contains sample results obtained using the full ionosphere-thermosphere-plasmasphere model (CTIP). The results come from three separate simulations of the upper atmosphere for conditions of moderately high solar activity ($F_{10.7}$ = 165): June solstice, September equinox, and December solstice. For each of these dates, results are presented showing a global snapshot of N_mF_2 at 04:00 and 16:00 UT. In each of Figures 6 to 11, contours of N_mF_2 are plotted against geographic latitude (–90 – +90 degrees) and geographic longitude (0-360 degrees). The contour spacing is 1×10^{11}m^{-3} on all plots with bold contours, labeled 1, 2 and 3, signifying electron densities of 0.5, 1.0 and 1.5×10^{12}m^{-3}, respectively.

All of the figures reveal evidence of the equatorial ionization (Appleton) anomaly. Figure 10 shows clearly a double peaked structure, with maxima located at around 180 degrees longitude and latitudes of –15 and +15 degrees latitude, respectively. The six figures also reveal many variations in the form of the anomaly. For instance, in Figures 7 and 11, the Appleton anomaly can be seen clearly on the nightside (120 - 180 degrees longitude), whereas this feature is much less distinct at equinox (Figure 9), which instead reveals a broad tongue of relatively high density extending virtually until dawn. Another clear result is the difference between the form of the anomaly at the June and December solstices. Both Figures 6 and 7 reveal a dayside anomaly with a much larger southern peak than northern peak, although the northern peak becomes much more pronounced at later local times. For December solstice (Figures 10 and 11), the exact opposite is true. In between, at the equinox, the northern and southern peaks are of similar magnitude, reflecting the much larger symmetry seen generally at this time (Figures 8 and 9).

The results also reveal seasonal anomalies in daytime N_mF_2 at mid latitudes. A clear 'winter anomaly' can be seen in both hemispheres with daytime N_mF_2 larger in winter than summer. The results also give evidence for a semi-annual variation, with daytime N_mF_2 larger at the equinox than in both winter and summer, for certain locations [*Moffett et al.*, 1994]. Recent results are shown in Figure 12, which plots local noon N_mF_2 against day number for longitude 270 degrees. The ten panels show model results for latitudes –90 to +90 with a resolution of 20 degrees. The results show a seasonal variation in noon N_mF_2 for latitudes 50 and 70 degrees, with larger values seen in winter than summer (winter anomaly). In contrast, latitudes –50 and –70 degrees show semi-annual variations in N_mF_2 with maxima near to the equinoxes and minima at the solstices. The physical cause of this semi-annual variation is the subject of continuing model studies.

Samples of plasmasphere results are shown in Figures 13 and 14. Equatorial H^+ density profiles are shown in Figure 13 up to an altitude of roughly 12,000 km, at four local times and four different times of the year: Day 1 (solid curve), day 84 (dashed curve), day 200 (dot-dashed curve), and day 280 (dotted curve). The figure shows peak H^+ densities at between 1000 and 2000 km, with larger values during the day and at the equinoxes (the peak values are noticeably smaller at December solstice than at June solstice). The field-aligned velocity (positive in the direction north to south) is plotted in Figure 14 for the same conditions as in Figure 13. Large velocities at around 1000 km can be seen at 6 LT and 18.5 LT for days 1 and 200 (roughly December and June solstices). For day 1, the velocity at this altitude is in the direction of south to north, at both dawn and dusk. Likewise, the velocity for day 200 is in the direction north to south at both local times.

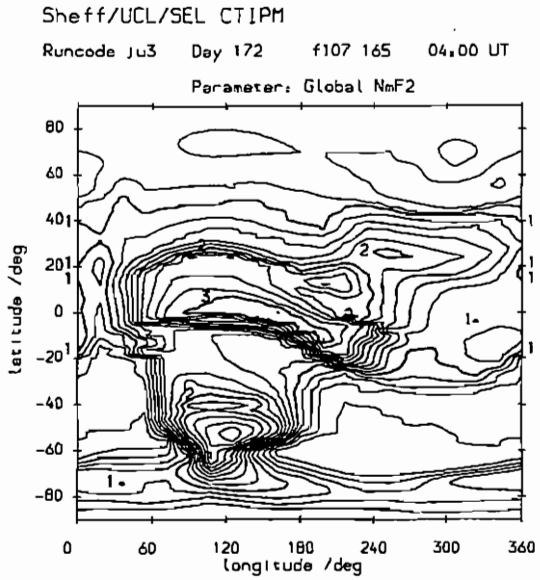

Figure 6. Global N_mF_2 for June Solstice, 04:00 UT.

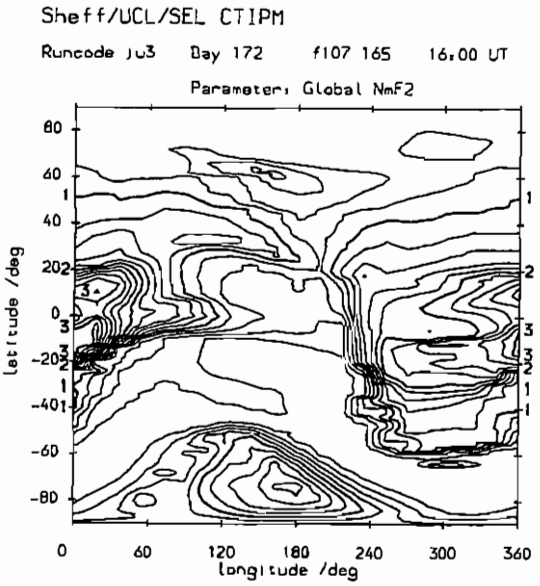

Figure 7. Global N_mF_2 for June Solstice, 16:00 UT.

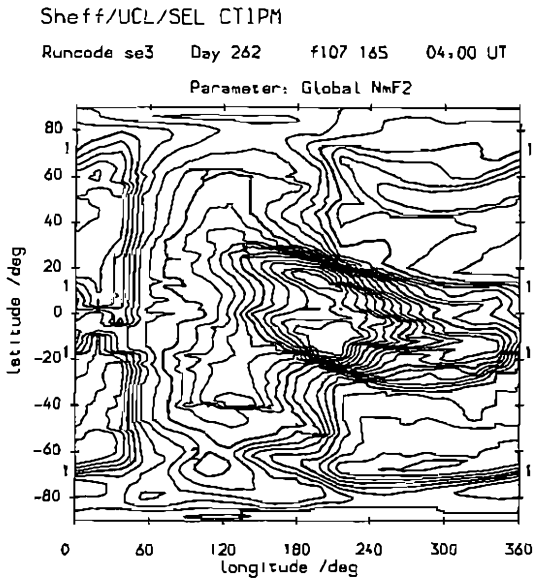

Figure 8. Global N_mF_2 for September Equinox, 04:00 UT.

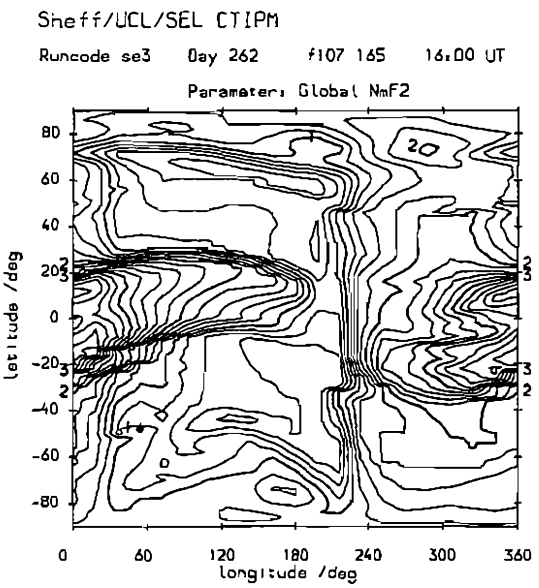

Figure 9. Global N_mF_2 for September Equinox, 16:00 UT.

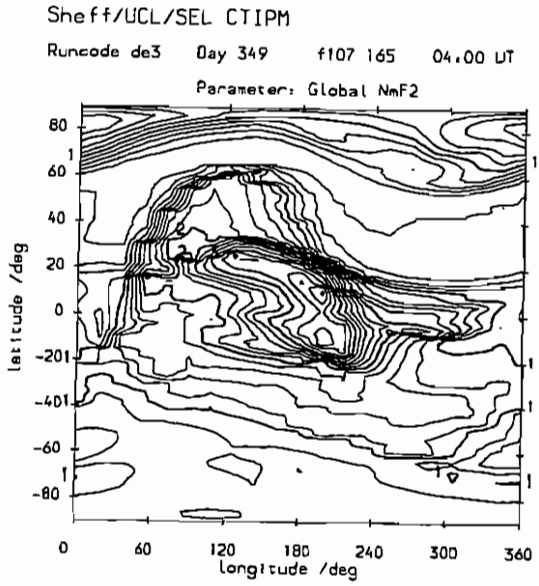

Figure 10. Global N_mF_2 for December Solstice, 04:00 UT.

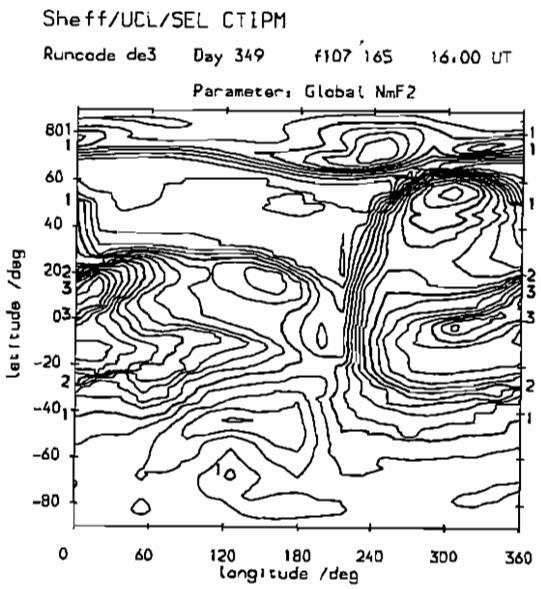

Figure 11. Global N_mF_2 for December Solstice, 16:00 UT.

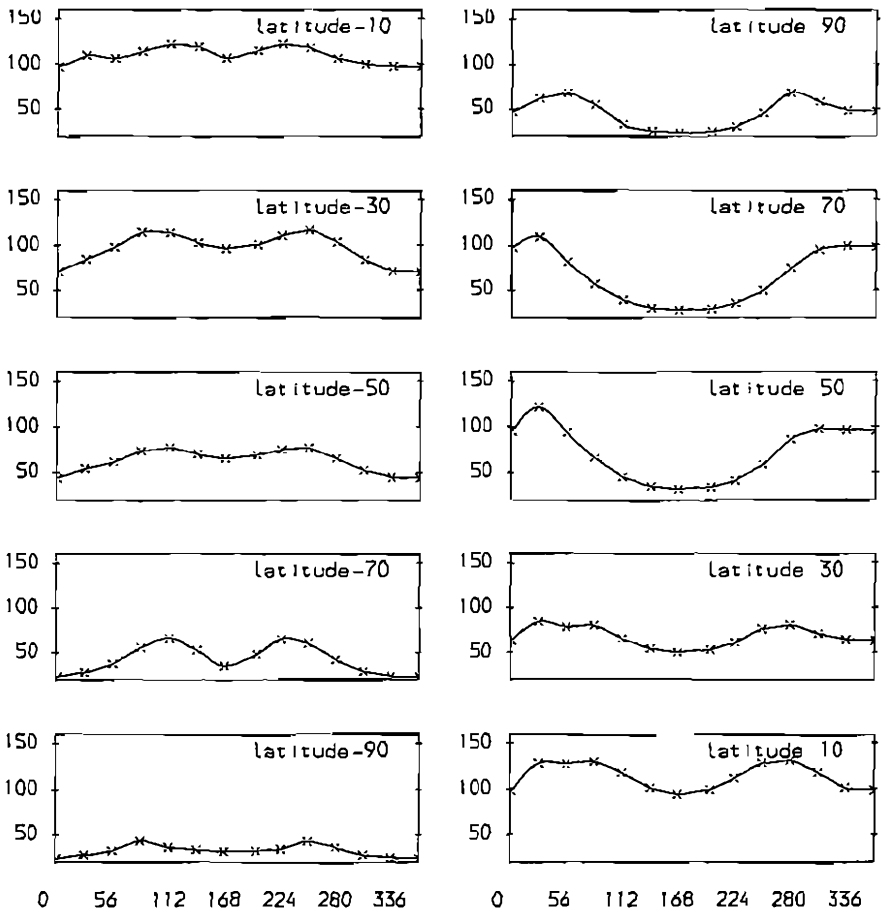

Figure 12. Local Noon N_mF_2 (in units of $10^{10}m^{-3}$) plotted against day number (1 - 365) for longitude 270 degrees. The ten panels show model results for latitudes -90 to +90 with a resolution of 20 degrees. All simulations are for fairly high solar activity ($F_{10.7}$ - 165). The results show a seasonal variation in noon N_mF_2 for latitudes 50 and 70 degrees with larger values seen in winter than summer (winter anomaly). In contrast, latitudes -50 and -70 degrees show semi-annual variations in N_mF_2 with maxima near to the equinoxes and minima at the solstices. The physical cause of this semi-annual variation is the subject of continuing model studies.

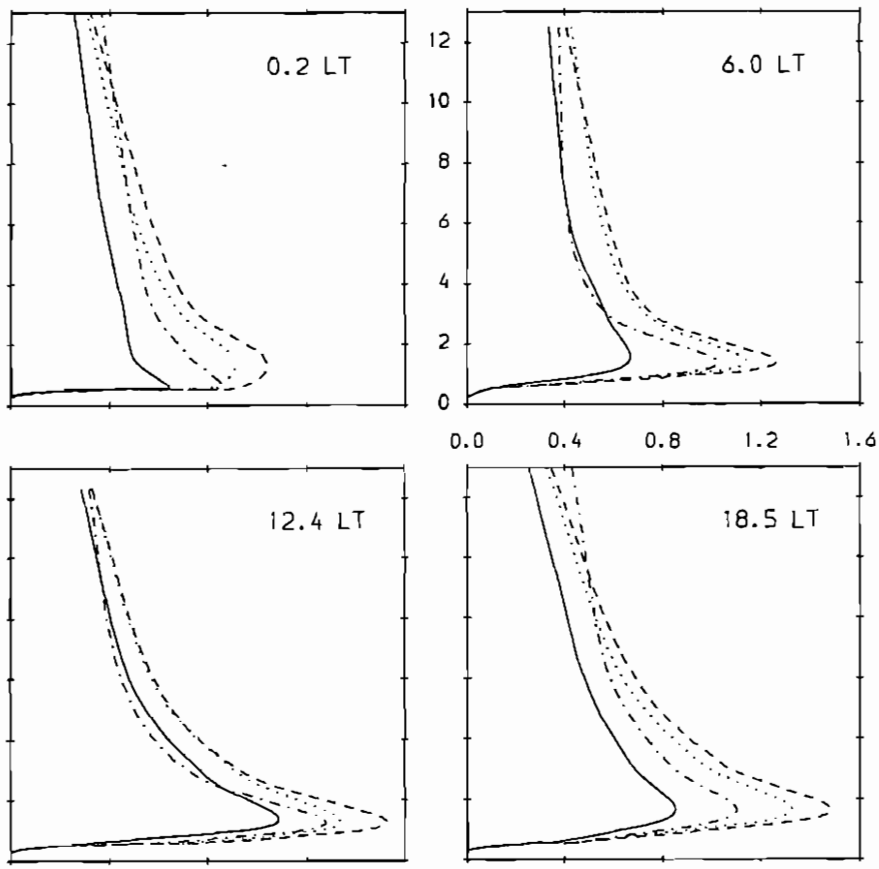

Figure 13. Equatorial H^+ density profiles at UT 12:25 and local times of 0.2, 6.0, 12.4 and 18.5. The four curves plotted show results from four separate simulations at different times of the year: Day 1 (solid curve), day 84 (dashed curve), day 200 (dot-dashed curve) and day 280 (dotted curve). The top right hand panel gives the scale for all panels and shows hydrogen densities up to 1.6e10m^{-3} (x-axis) and altitudes up to 12,000 km (y-axis). All these results are for fairly high solar activity ($F_{10.7} = 165$).

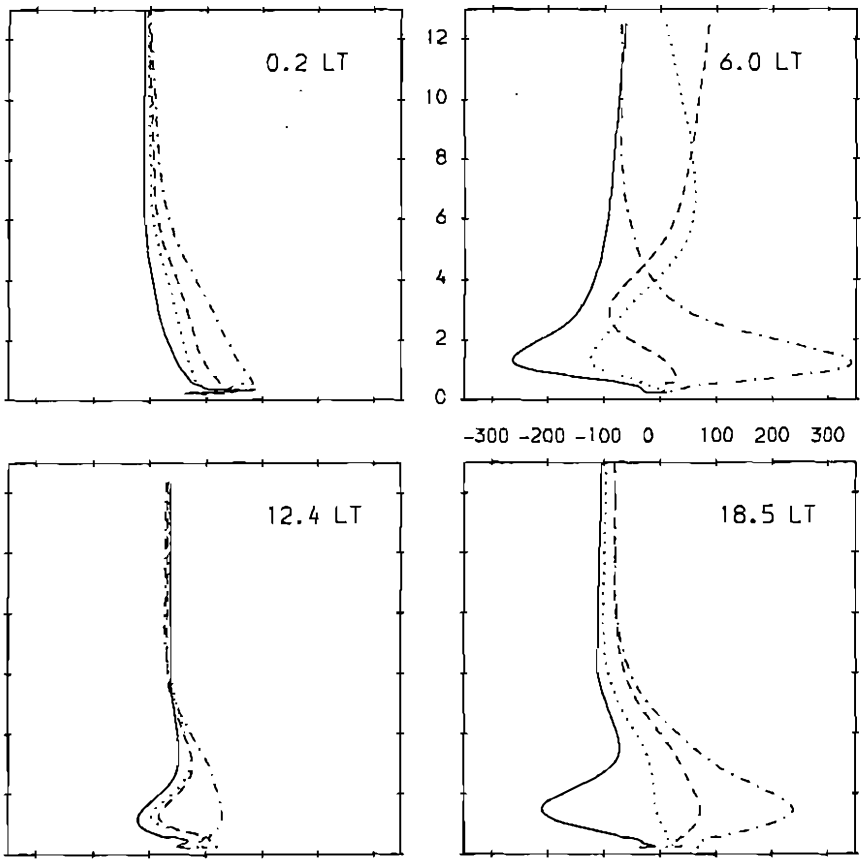

Figure 14. As for Figure 13, but for the field aligned H^+ velocity. Here the scale along the x-axis ranges from -300 to +300 ms^{-1} (positive values are field-aligned in the direction north to south).

14. References

Bailey, G. J., *Planet. Space Sci., 31*, 389, 1983.
Bailey, G. J. and R. Sellek, *Ann. Geophys., 8*, 171, 1990.
Bailey, G. J., R. Sellek, and Y. Rippeth, *Ann. Geophys., 11*, 263, 1993.
Bailey, G. J. and N. Balan, *STEP Handbook on Ionospheric Models* (ed. R. W. Schunk), Utah State University, 1996.
Banks, P. M. and G. Kockarts, *Aeronomy*, Academic Press, New York, 1973.
Barker, F. S., D. R. Barraclough, V. P. Golovkov, P. J. Hood, F. J. Lowes, W. Mundt, N. W. Peddie, Qi Gui-zhong, S. P. Srivastava, R. Witworty, D. E. Winch, T. Yukutake, and D. P. Zidarov, *EOS Trans., AGU, 67*, 523, 1986.
Barraclough, D. R., *Assoc. Geomagn. Aeron. News, 24*, 60, 1985.
Bauer, P., G. Lejeune, and M. Petit, *Planet. Space Sci., 18*, 1447, 1970.
Chiu, Y. T., *J. Atmos. Terr. Phys., 37*, 1563, 1975.
Delgarno, A., M. B. McElroy, M. H. Rees, and J. C. G. Walker, *Planet. Space Sci., 16*, 1371, 1968.
Fraser-Smith, A. C., *Rev. Geophys. Space Phys., 25*, 1, 1987.
Fuller-Rowell, T. J., PhD thesis, University College London, 1981.
Fuller-Rowell, T. J. and D. Rees, *J. Atmos. Sci., 37*, 2545, 1980.
Fuller-Rowell, T. J. and D. Rees, *J. Atmos. Terr. Phys., 43*, 701, 1981.
Fuller-Rowell, T. J. and D. Rees, *Planet. Space Sci., 31*, 1209, 1983.
Fuller-Rowell, T. J. and D. Rees, *Planet. Space Sci., 32*, 69, 1984.
Fuller-Rowell, T. J., S. Quegan, D. Rees, G. J. Bailey, and R. J. Moffett, *Planet. Space Sci., 32*, 469, 1984.
Fuller-Rowell, T. J., D. Rees, S. Quegan, R. J. Moffett, and G. J. Bailey, *J. Geophys. Res., 92*, 7744, 1987.
Fuller-Rowell, T. J., D. Rees, S. Quegan, R. J. Moffett, and G. J. Bailey, *Pure and Appl. Geophys., 127*, 189, 1988.
Fuller-Rowell, T. J., D. Rees, S. Quegan, and R. J. Moffett, *J. Atmos. Terr. Phys., 53*, 529, 1991.
Fuller-Rowell, T. J., M. V. Codrescu, R. J. Moffett, and S. Quegan, *J. Geophys. Res., 99*, 3893, 1994.
Fuller-Rowell, T. J., R. J. Moffett, S. Quegan, D. Rees, M. V. Codrescu, and G. H. Millward, *STEP Handbook on Ionospheric Models* (ed. R. W. Schunk), Utah State University, 1996.
Hoegy, W. R., *Geophys. Res. Lett., 3*, 541, 1976.
McIlwain, C. E., *J. Geophys. Res., 66*, 3681, 1961.
Mentzoni, M. H. and R. V. Rao, *Phys. Rev., 130*, 2312, 1963.
Millward, G. H., PhD Thesis, University of Sheffield, 1993.
Millward, G. H., *Ann. Geophys., 12*, 94, 1994.
Millward, G. H., S. Quegan, R. J. Moffett, T. J. Fuller-Rowell, and D. Rees, *Planet. Space Sci., 41*, 45, 1993a.
Millward, G. H., R. J. Moffett, S. Quegan, and T. J. Fuller-Rowell, *J. Geophys. Res., 98*, 19,173, 1993b.
Moffett, R. J., G. J. Bailey, S. Quegan, Y. Rippeth, A. M. Samson, and R. Sellek, *Phil. Trans. R. Soc. Lond., 328*, 255, 1989.
Moffett, R. J., B. Jenkins, and G. J. Bailey, *Ann. Geophys., 11*, 1051, 1993.
Moffett, R. J., G. H. Millward, S. Quegan, A. D. Aylward, and T. J. Fuller-Rowell, *Adv. Space Sci.*, in press, 1994.
Nisbet, J. S., *J. Atmos. Terr. Phys., 30*, 1257, 1968.
Quegan, S., PhD Thesis, University of Sheffield, 1982.
Quegan, S., *Phil. Trans. R. Soc. Lond., 328*, 119, 1989.
Quegan, S., G. J. Bailey, and R. J. Moffett, *Planet. Space Sci., 15*, 851, 1981.

Quegan, S., G. J. Bailey, R. J. Moffett, R. A. Heelis, T. J. Fuller-Rowell, D. Rees, and R. W. Spiro, *J. Atmos. Terr. Phys.*, *44*, 619, 1982.
Raitt, W. J., R. W. Schunk, and P. M. Banks, *Planet. Space Sci.*, *23*, 1103, 1975.
Rees, D., T. J. Fuller-Rowell, and R. W. Smith, *Planet. Space Sci.*, *28*, 919, 1980.
Rees, D., T. J. Fuller-Rowell, S. Quegan, R. J. Moffett, and G. J. Bailey, *J. Atmos. Terr. Phys.*, *50*, 903, 1988.
Rees, D., S. Quegan, R. J. Moffett, G. J. Bailey, and T. J. Fuller-Rowell, *J. Atmos. Terr. Phys.*, *56*, 297, 1994.
Richmond, A. D., *J. Geophys. Res.*, *81*, 1447, 1976.
Richmond, A. D., M. Blanc, B. A. Emery, R. H. Wand, B. G. Fejer, R. F. Woodman, S. Ganguly, P. Amayenc, R. A. Behnke, C. Calderon, and J. V. Evans, *J. Geophys. Res.*, *85*, 4658, 1980.
Rippeth, Y., PhD Thesis, University of Sheffield, 1992.
Rishbeth, H. and O. K. Garriott, *Introduction to Ionospheric Physics*, Academic Press, 138, 1969.
Schmidt, A., *Gerlands Beitr. Geophys.*, *41*, 346, 1934.
Schunk, R. W. and A. F. Nagy, *Rev. Geophys. Space Phys.*, *16*, 355, 1978.
Schunk, R. W. and A. F. Nagy, *Rev. Geophys. Space Phys.*, *18*, 813, 1980.
Swartz, W. E. and J. S. Nisbet, *J. Geophys. Res.*, *77*, 6259, 1972.
Torr, D. G., and M. R. Torr, *J. Atmos. Terr. Phys.*, *41*, 797, 1979.
Williams, P. J. S., and J. N. McDonald, *J. Atmos. Terr. Phys.*, *49*, 873, 1987.

The NCAR Thermosphere-Ionosphere-Mesosphere-Electrodynamics General Circulation Model (TIME-GCM)

R. G. Roble

High Altitude Observatory, National Center for Atmospheric Research,
P.O. Box 3000, Boulder, CO 80307

1. Introduction

The NCAR thermosphere-ionosphere-mesosphere-electrodynamics general circulation model (TIME-GCM) describes the three-dimensional time-dependent temperature and compositional structure, dynamics and electrodynamics of the coupled upper stratosphere, mesosphere, thermosphere and ionosphere between 30 and 500 km altitude. The model is a first-principles numerical model and it is driven by a time-dependent specification of solar EUV and UV spectral irradiance, and magnetic conjugate auroral particle precipitation and ionospheric convection patterns at the upper boundary of the model. At the lower boundary of the model, the geopotential height fields and temperatures along the 10 mb constant pressure surface near 30 km are specified as well as the mass mixing ratio of long-lived chemical species. This model is the culmination of nearly 20 years of model development and it combines all of the main features of our previous models, the TGCM, TIGCM, and TIE-GCM, that are described in the next section. The various models reside on the NCAR CRAY-YMP-8-64 and they have been used by a large number of students and colleagues for numerical experiments and comparisons of model simulations with satellite and ground-based data. This paper gives a brief overall description of the model, its capability, and characteristic features.

2. TGCM, TIGCM and TIE-GCM History

2.1 TGCM.

The NCAR TIME-GCM is the latest in a series of three-dimensional general circulation models of the Earth's upper atmosphere that have been developed during the past decade. The original thermosphere general circulation model (TGCM) was described by *Dickinson et al.* [1981]. An extension of the model to include couplings between dynamics and composition was described by *Dickinson et al.* [1984]. *Fesen et al.* [1986] and *Forbes et al.* [1993] included a coupling of the semi-diurnal and diurnal upward propagating tides from the middle atmosphere into the model. Empirical models of high latitude ion convection and auroral particle precipitation used in the TGCM were described by *Roble et al.* [1982] and *Roble and Ridley* [1987].

2.2 TIGCM.

Roble et al. [1987] developed a self-consistent aeronomic scheme for the coupled thermosphere and ionosphere system, tested it in a global average model, and then incorporated it into a new TIGCM [*Roble et al.*, 1988]. This model calculates global distributions of neutral gas temperature, winds, mass mixing ratios of the major constituents, N_2, O_2 and O, and the mass mixing ratio of the minor neutral gas constituents, $N(^2D)$, $N(^4S)$, NO, He, and Ar. The interactive Eulerian model of the ionosphere solves for global distributions of electron and ion temperatures, O^+, O_2^+ NO^+, N_2^+, N^+ and electron number densities. Mutual couplings between

the thermosphere and ionosphere occur at each model time step and at each point of the geographic grid. Both the TGCM and TIGCM have an effective 5° latitude by longitude grid with 25 constant pressure surfaces in the vertical between approximately 95 and 500 km altitude, with a vertical resolution of 2 grid points per scale height and a model time step of 5 minutes.

The TIGCM used empirical models to represent electric fields and ion drift within the model, but recently *Richmond and Roble* [1987] and *Richmond et al.* [1992] extended the TIGCM to include self-consistent electrodynamic interactions between the thermosphere and ionosphere. This thermosphere-ionosphere-electrodynamics general circulation model (TIE-GCM) calculates the dynamo effects of winds and uses the resultant electric fields and currents to calculate neutral and plasma dynamics at each model time step and each point on the geographic grid. The TIE-GCM is internally self-consistent and requires only the specification of external boundary conditions, such as the solar EUV and UV spectral irradiance, auroral particle precipitation, and ion convection pattern within the polar caps and the upward propagating tides and other disturbances from the middle atmosphere.

2.3 TIME-GCM.

The above models were designed to study upper thermosphere and F-region ionospheric dynamics. The scientific motivation for the development of a new model that couples the mesosphere and upper stratosphere with the thermosphere and ionosphere is twofold: (1) to determine how deep into the atmosphere the effects of solar and auroral variability penetrate; and (2) to determine how physical, chemical and dynamic processes in the lower atmosphere affect the structure, dynamics and electrodynamics of the thermosphere and ionosphere.

Similar to the procedure used by *Roble et al.* [1987] to develop and test a self-consistent aeronomic scheme for the TIGCM, *Roble* [1995] developed and tested a self-consistent aeronomic scheme that operated between 30 and 500 km and used that model to examine the global mean structure of the upper atmosphere before inclusion into the TIME-GCM. The additional physical and chemical processes that were included in the model were described by *Roble and Ridley* [1994] and *Roble* [1995] and are briefly summarized as follows:

- The overall chemistry used in the model is given in Table 1 of *Roble* [1995]. For the mesosphere, it is essentially the same as that described by *Allen et al.* [1984] and *Brasseur and Solomon* [1986] using the JPL-90 [*DeMore et al.*, 1990] reaction and photoabsorption rates.

- The major species transport equation for N_2, O_2 and O, described by *Dickinson et al.* [1984], for the thermosphere is still solved over the entire grid, but now for $O_x = (O + O_3)$ instead of O.

- The minor species transport equation that solved for $N(^4S)$ and NO in the thermosphere is also extended downward and used to solve for the mass mixing ratio of the long-lived species H_2O, H_2, CH_4, CO and CO_2, as well as for the families $HO_x = (H + HO_2 + OH)$ and $NO_X = (NO + NO_2)$. $N(^4S)$ is still solved as an individual species because it does not photochemically partition in the thermosphere. All species are calculated over the entire altitude grid and includes reactions with ion chemistry and EUV photodissociation in the thermosphere. Even though the model extends into the upper stratosphere (to resolve the stratopause), stratospheric chemistry is limited and excludes species such as Cl_x, N_2O, NO_3, N_2O_5, etc. It is assumed that the effect of these species can be crudely accounted for by specifying lower boundary mixing ratios obtained from a more complete chemical/dynamic model of the stratosphere.

- The family species distributions are photochemically partioned and distributions of $O(^1D)$, $N(^2D)$, H_2O_2, $O_2(^1\Delta_g)$, and $O_2(^1\Sigma_g)$ are obtained assuming photochemical equilibrium.

- The lower boundary conditions for the long-lived species are obtained from the 2D chemical/dynamic model of *Garcia and Solomon* [1994]. The latitudinal variation of the mass mixing ratio along the 10 mb constant pressure surface is specified with no assumed longitudinal variations, but varies with time throughout the year. At the upper boundary, diffusive equilibrium is assumed for all long-lived species except for H where exospheric escape is specified. The total escape flux includes Jean's thermal escape, $H\text{-}H^+$ charge exchange and the polar wind, using equation 4 of *Liu and Donahue* [1974], uniformly around the globe.

- The CO_2 LTE and non-LTE 15 μm radiational cooling parameterization of *Fomichev et al.* [1993] and the O_3 9.6 μm cooling parameterization of *Fomichev and Shved* [1985] are used to calculate IR cooling rates at each point on the grid and at every time step. A CO_2-O relaxation rate of 4×10^{-12} cm^{-2} s^{-1} is used.

- Solar photodissociation and heating rates are determined at each time step using the calculated composition and solar flux model of *Rottman et al.* [1986]. Chemical heating rates are determined using the procedure of *Mlynczak and Solomon* [1992].

- The ion chemistry in the F-region has been upgraded to include metastable ion species and is now the same as that given in Table 1 of *Torr et al.* [1990]. The six ion chemical scheme of *Mitra and Rowe* [1972] is used for the D-region.

- At the present time, dynamic lower boundary conditions along the 10 mb surface are obtained by using either (1) tidal theory, or (2) data from the NMC daily analyses. For tidal theory only the diurnal and semi-diurnal migrating tides and a zonally symmetric annual tide is used to specify couplings with the atmosphere below 10 mb. The zonally symmetric annual tide is based on the geopotential heights from the empirical model of *Fleming et al.* [1988]. There are no planetary waves or other disturbing features included for these tidal theory simulations. The model vertical resolution is 2 grid points per scale height and appears adequate to resolve the diurnal tide.

  The TIME-GCM lower boundary forcing can also accept the NMC data analysis on the 10 mb constant pressure surface to specify the geopotential heights and temperatures along the lower boundary. The NMC analysis is daily and the TIME-GCM linearly interpolates between daily values for intermediate time values. This procedure gives the planetary wave structure at the lower boundary but the diurnal tidal amplitude and phase and subgrid-scale gravity wave energy density still need to be specified at the lower boundary of the model. At the same time that time variations of NMC data are used, time dependent solar EUV and UV spectral irradiance and auroral forcings are also introduced for the day being simulated to give as realistic simulation of the period under investigation as possible. The solar EUV and UV special irradiance are related to the solar F10.7 values using the empirical model described by *Roble* [1995]. Ionospheric convection cross-polar cap potential drop and auroral particle precipitation patterns are based on empirical relations with Kp values. With this new procedure the model can be used to realistically simulate any period between January 1977 and the present. This procedure is being tested by comparing model simulations with observations.

- The subgrid scale gravity wave drag parameterization used in the model is the scheme developed by *Fritts and Lu* [1993]. It is applied at each spatial grid point and at every model time step. It is assumed that the upward directed gravity wave energy flux is isotropic along the 10 mb and has a latitudinal distribution that is consistent with the measurements of *Fetzer and Gille* [1994]. The magnitude of the energy flux at 10 mb is an adjustable parameter that is varied in such a manner to achieve reasonable agreement between the calculated and observed climatology of the upper stratosphere, mesosphere and thermosphere.

The TIME-GCM has the same 5 degree latitude by longitude grid used by the other TGCMs, but now has 45 constant pressure surfaces in the vertical at two grid points per scale height resolution extending approximately between 30 and 500 km. The model time step is typically 6 minutes.

3. Mathematical Formulation

The TIME-GCM solves the primitive equations of dynamic meteorology but the model has been adapted to include processes appropriate for the mesosphere, thermosphere and ionosphere. The basic model derives from the NCAR third generation, fourth order general circulation model (GCM) of lower atmosphere meteorology described by *Washington and Williamson* [1977]. The basic equations are in log pressure coordinates and are an expanded version of the primitive equations presented by *Holton* [1975]. The initial equations of the TGCM have been described by *Dickinson et al.* [1981] and by *Killeen and Roble* [1984]. The equations for the coupling of composition with dynamics has been described by *Dickinson et al.* [1984]. The incorporation of semi-diurnal and diurnal tidal components from the lower atmosphere into the model has been described by *Fesen et al.* [1986] and *Forbes et al.* [1993]. High latitude ion convection inputs have been described by *Roble et al.* [1982] and auroral particle precipitation and ion convection inputs have been described by *Roble and Ridley* [1987].

Roble et al. [1987] designed a self-consistent aeronomic scheme, tested it in a globally averaged model of the coupled thermosphere-ionosphere system and then implemented that scheme into the TIGCM [*Roble et al.*, 1988]. This TIGCM included a Eulerian model of the ionosphere with mutual interactions occurring between the thermosphere and ionosphere at each point of the geographic grid and each model time step. The electrodynamic drifts for this model, however, were still specified using empirical models of the high latitude [*Heelis et al.*, 1982] and low latitude [*Richmond et al.*, 1980] ion convection. The model also calculated the minor neutral constituent mass mixing ratios for NO, $N(^4S)$ and $N(^2D)$. The ion and neutral chemical reactions and physical and chemical processes within the model were also described in detail by *Roble et al.* [1987, 1988].

Richmond et al. [1992] made the next major model improvement by designing and incorporating interactive electrodynamics within a new model, the TIE-GCM. This model eliminated the need for non-interacting empirical models of ion drift by solving directly for the ion drifts using the TIE-GCM calculated neutral winds and ionospheric electrical conductivity. The calculated electric field and ion drift are then used in the calculation of ionospheric structure and also used to specify the ion drag and Joule heating acting on the neutral gas. The dynamo calculation is made in geomagnetic coordinates and transformed to geographic coordinates for the calculation of ionospheric structure and neutral dynamics. The magnetic coordinate system and dynamo equations used in the TIE-GCM and TIME-GCM have been recently described by *Richmond* [1995].

The aeronomy in the current version of the TIME-GCM has been described by *Roble and Ridley* [1994] and *Roble* [1995].

4. Model Inputs

The TIME-GCM uses a 59 wavelength parameterization of the spectral solar irradiance from 0.1 to 200 nm in the EUV and UV as described by *Roble* [1995]. This empirical model requires the specification of the solar F10.7 and 81 day average of the solar F10.7, to determine the spectral irradiance in the 59 wavelength interval. For the TIME-GCM the UV spectral irradiance is determined from the empirical model of *Rottman et al.* [1986] that is also based on solar F10.7.

The auroral inputs into the TIME-GCM include energetic electron auroral particle precipitation using the model of *Fuller-Rowell and Evans* [1987] with ionization rate as described by *Roble and Ridley* [1987] and an ionospheric convection model as described by *Roble et al.* [1982] and *Roble and Ridley* [1987]. These auroral inputs are specified in geomagnetic coordinates and then transformed into geographic coordinates for the TIME-GCM run. All auroral inputs are time-dependent and can be used to specify upper atmosphere auroral inputs for a wide variety of time-dependent geomagnetic disturbances. Both the TIE-GCM and TIME-GCM can also accept time-dependent output from the Assimilative Mapping of Ionospheric Electrodynamics (AMIE) technique of *Richmond and Kamide* [1988].

The TIME-GCM also requires the specification of the diurnal tidal amplitude and phase at the lower boundary at 10 mb near 30 km. In addition, the model can also utilize NMC 10 mb daily analyses for lower boundary forcing of large-scale planetary waves.

5. Model Outputs

The model solves for the neutral, electron and ion temperature profiles as well as for the compositional profiles of $O_x = (O + O_3)$, O_2, and N_2 coupled through major species diffusion equations. It also includes, as minor species with transport and appropriate photochemistry, $N(^4S)$, $NO_x = (NO + NO_2)$, H_2O, H_2, CH_4, CO, CO_2, and $HO_x = (H + OH + HO_2)$, and in photochemical equilibrium with the above (including O_x, NO_x, and HO_x family partitioning) O, O_3, NO, NO_2, $N(^2D)$, $O(^1D)$, $O_2(^1\Sigma_g)$, $O_2(^1\Delta_g)$, OH, H, HO_2, and H_2O_2. The distribution of the passive tracers He and Ar are also calculated. The model also includes appropriate F-, E-, D-region and upper stratospheric ion chemistry.

These quantities are calculated at every 5-minute time step and at each point of the geographic 5 degrees latitude by longitude grid at 45 constant pressure surfaces, at a vertical grid resolution of 2 grid points per scale height over and approximate altitude range of 30 to 500 km.

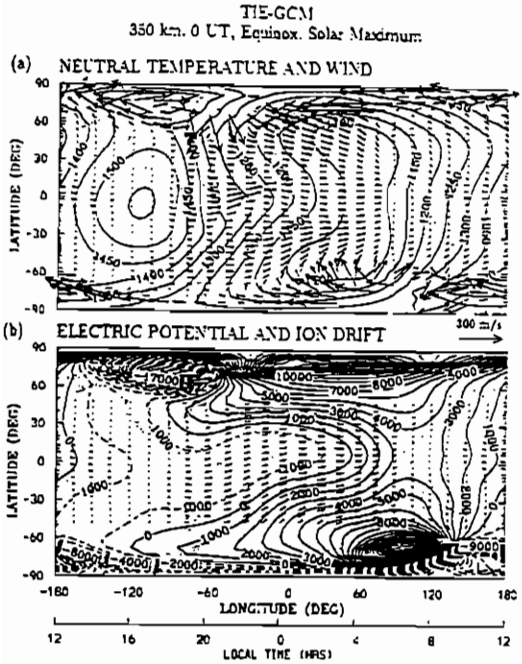

Figure 1.

These output fields are written as history tapes to the NCAR mass store system and there is a large variety of different processors developed to plot output fields. Figures 1 through 4 present some of the model outputs as derived from the history tapes. Figure 1 shows contours of neutral gas temperature and vectors of wind in (a) and contours of electric potential and vectors of ion drift in (b) from a TIE-GCM simulation of solar cycle maximum equinox conditions. These are global maps on a constant pressure surface near 300 km. Figure 2 shows a zonally averaged latitudinal distribution of neutral gas temperature for December solstice solar cycle minimum conditions from 30 to 110 km as derived from the TIME-GCM. Figure 3 shows contours of electron density calculated over the Arecibo Observatory for equinox solar cycle minimum conditions using a station processor. Figure 4 shows the meridional winds from 30 to 400 km calculated along the 17.5° N latitude circle for equinox solar cycle minimum

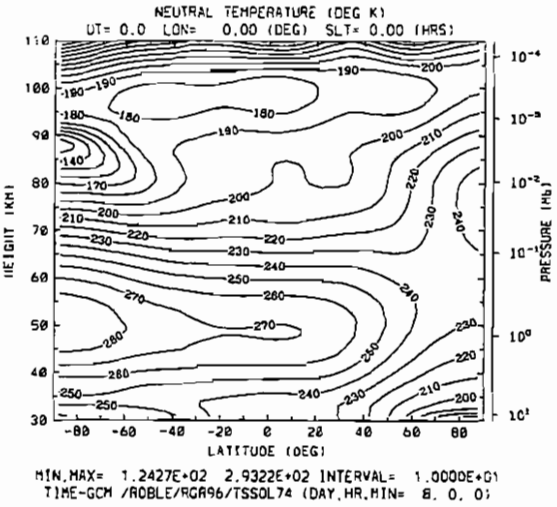

Figure 2

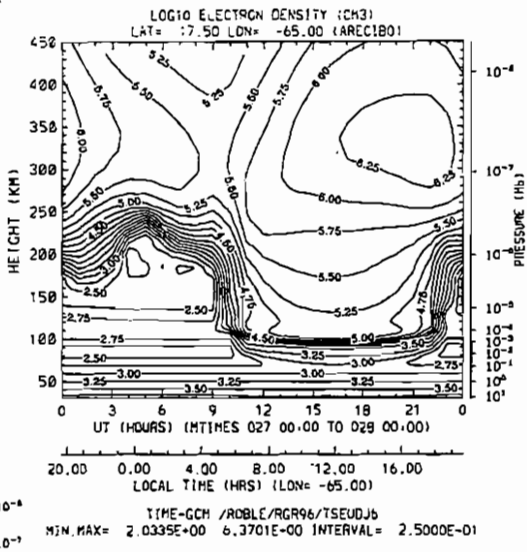

Figure 3

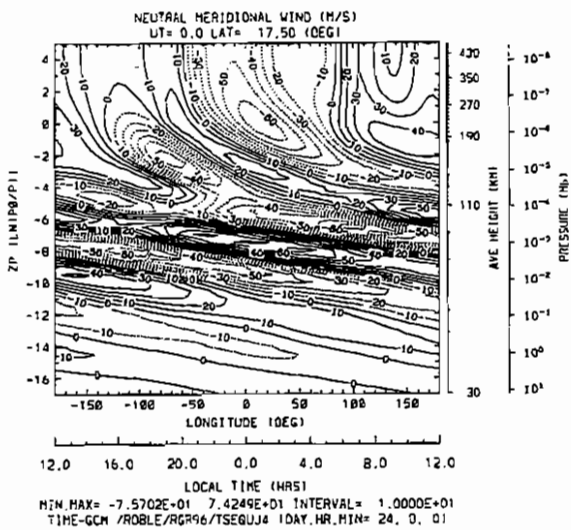

Figure 4

conditions. These are just samples of the many processors that have been developed over the years to examine model output.

6. Model Uncertainties and Limitations

The model has been designed to study global phenomena. Its 5 degree latitude and longitude grid can resolve only the large-scale features of the upper atmosphere and subgrid scale phenomena such as gravity wave propagation and breaking, etc., have to be parameterized. Also there are many uncertainties associated with chemical reaction rates, branching rates, radiative transfer parameterizations, etc., that must be considered in evaluating any model run.

7. Model Availability

All of the models described above run on the NCAR CRAY YMP-8-64 and utilizes the NCAR mass store system to store history tapes of model output. A typical TIME-GCM history is 42 megabytes per history and a typical recording frequency for histories is every 12 hours of model run time, but can be as frequent as 1 hour for special runs used to compare measurements made by ground-based stations or satellites with model output. The model is not transportable and our typical mode of operation is for a potential user to request a run and histories are stored on the NCAR mass store system. The user can then either request various data histories, station data or global plots, or obtain an NCAR computer account (requires an NSF sponsored contract or a direct purchase of NCAR computer time) and use our various processors locally or remotely. A possible mode of data transfer is through the CEDAR data base.

8. References

Allen, M., J. I. Lunine, and Y. L. Yung, The vertical distribution of ozone in the mesosphere and lower thermosphere, *J. Geophys. Res., 89*, 4841-4872, 1984.

Brasseur, G. and S. Solomon, *Aeronomy of the Middle Atmosphere*, pp. 441, D. Reidel, Hingham, MA, 1986.

DeMore, W. B., et al., Chemical kinetics and photochemical data for used in stratospheric modeling, Evaluation Number 9, *JPL-Publication 90-1*, NASA-JPL, Pasadena, CA, 1990.

Dickinson, R. E., E. C. Ridley, and R. G. Roble, A three-dimensional general circulation model of the thermosphere, *J. Geophys. Res., 86*, 1499-1512, 1981.

Dickinson, R. E., E. C. Ridley, and R. G. Roble, Thermospheric general circulation with coupled dynamics and composition, *J. Atmos. Sci., 41*, 205-219, 1984.

Fesen, C. G., R. E. Dickenson, and R. G. Roble, Simulation of thermospheric tides at equinox with the National Center for Atmospheric Research thermospheric general circulation model, *J. Geophys. Res., 91*, 4471-4489, 1986.

Fetzer, E. J. and J. C. Gille, Gravity wave variance in LIMS temperatures, Part 1, Variability and comparison with background winds, *J. Atmos. Sci., 51*, 2461-2483, 1994.

Fleming, E. R., S. Chandra, M. R. Shoeberl, and J. J. Barnett, Monthly mean global climatology of temperature, wind, geopotential height, and pressure for 0-120 km, *NASA Technical Memorandum 100697*, February, 1988.

Fomichev, V. I. and G. M. Shved, Parameterization of the radiative flux divergence in the 9.6 μm O_3 band, *J. Atmos. Terr. Phys., 47*, 1037-1049, 1985.

Formichev, V. I. A. A. Kutepov, R. A. Akmaev, and G. M. Shved, Parameterization of the 15 μm CO_2 band cooling in the middle atmosphere (15-115 km), *J. Atmos. Terr. Phys., 55*, 7-18, 1993.

Forbes, J. M., R. G. Roble, and C. G. Fesen, Acceleration, heating and compositional mixing of the thermosphere due to upward propagating tides, *J. Geophys. Res., 98*, 311-321, 1993.

Fritts, D. C. and W. Lu, Spectral estimates of gravity wave energy and momentum fluxes, II, Parameterization of wave forcing and variability, *J. Geophys. Res.*, in press, 1993.

Fuller-Rowell, T. J. and D. S. Evans, Height-integrated Pedersen and Hall conductivity patterns inferred from TIROS-NOAA satellite data, *J. Geophys. Res., 92*, 7606-7618, 1987.

Garcia, R. R. and S. Solomon, A new numerical model of the middle atmosphere, 2, Ozone and related species, *J. Geophys. Res., 99*, 12937-12952, 1994.

Heelis, R. A., J. K. Lowell, and R. W. Spiro, A model of the high-latitude ionospheric convection pattern, *J. Geophys. Res., 87*, 6339-6345, 1982.

Holton, J. R., The dynamic meteorology of the stratosphere and mesosphere, *Meteorol. Monogr. No. 37*, Am. Meteorol. Soc., Boston, MA, 1975.

Killeen, T. L. and R. G. Roble, An analysis of the high-latitude thermospheric wind pattern calculated by a thermospheric general circulation model, I, Momentum forcing, *J. Geophys. Res., 89*, 7509-7522, 1984.

Liu, S. C. and T. M. Donahue, Mesospheric hydrogen related to exospheric escape mechanism, *J. Atmos. Sci., 31*, 1466-1470, 1974.

Mitra, A. P. and J. N. Rowe, Ionospheric effects of solar flares, VI, Changes in D-region ion chemistry during solar flares, *J. Atmos. Terr. Phys., 34*, 795-806, 1972.

Mlynczak, M. G. and S. Solomon, A detailed evaluation of the heating efficiency in the middle atmosphere, *J. Geophys. Res., 98*, 10517-10541, 1993.

Richmond, A. D., Ionospheric electrodynamics using magnetic apex coordinates, *J. Geomagn. Geoelectr.*, in press, 1995.

Richmond, A. D. and Y. Kamide, Mapping electrodynamic features of the high-latitude ionosphere from localized observations: Technique, *J. Geophys. Res., 93*, 5741-5759, 1988.

Richmond, A. D. and R. G. Roble, Electrodynamic effects of thermospheric winds from the NCAR thermospheric general circulation model, *J. Geophys. Res., 92*, 12365-12376, 1987.

Richmond, A. D., E. C. Ridley, and R. G. Roble, A thermosphere/ionosphere general circulation model with coupled electrodynamics, *Geophys. Res. Lett., 19*, 601-604, 1992.

Richmond, A. D., M. Blanc, B. A. Emery, R. H. Wand, B. G. Fejer, R. F. Woodman, S. Ganguly, P. Amayenc, R. A. Behnke, C. Calderon, and J. V. Evans, An empirical model of quiet-day ionospheric electric fields at middle and low latitudes, *J. Geophys. Res., 85*, 4658-4664, 1980.

Roble, R. G., Energetics of the mesosphere and thermosphere, in *The Upper Mesosphere and Lower Thermosphere: A Review of Experiment and Theory, Geophys. Mono., 87*, 1-21, 1995.

Roble, R. G. and E. C. Ridley, An auroral model for the NCAR thermospheric general circulation model (TGCM), *Annales. Geophysicae, 5A*, (6), 369-382, 1987.

Roble, R. G. and E. C. Ridley, A thermosphere-ionosphere-mesosphere-electrodynamics general circulation model (TIME-GCM): Equinox solar cycle minimum simulations (30-500 km), *Geophys. Res. Lett., 21*, 417-420, 1994.

Roble, R. G., R. E. Dickinson, and E. C. Ridley, Global circulation and temperature structure of the thermosphere with high latitude convection, *J. Geophys. Res., 87*, 1599-1614, 1982.

Roble, R. G., E. C. Ridley, and R. E. Dickinson, On the global mean structure of the thermosphere, *J. Geophys. Res., 92*, 8745-8758, 1987.

Roble, R. G., E. C. Ridley, A. D. Richmond, and R. E. Richmond, A coupled thermosphere and ionosphere general circulation model, *Geophys. Res. Lett., 15*, 1325-1328, 1988.

Rottman, G. J., et al., WMO, atmospheric ozone, assessment of our understanding of processes controlling its present distributions and change, *Report No. 16, World Meteorological Organization Global Ozone Research and Monitoring Project*, Vol. 1, Washington, DC, 1986.

Torr, M. R., D. G. Torr, P. G. Richards, and S. P. Yung, Mid- and low-latitude model of thermospheric emissions, 1, $O^+(^2P)$ 7320 Å and $N_2(^2P)$ 3371 Å, *J. Geophys. Res., 95*, 21147-21168, 1990.

Washington, W. M. and D. L. Williamson, A description of the NCAR global circulation models, in *Methods in Computational Physics, Vol. 17, General Circulation Models of the Atmosphere* (J. Chang, ed.), Academic Press, 111-172, 1977.

USU Electrodynamic Model of the Ionosphere

L. Zhu

Center for Atmospheric and Space Sciences
Utah State University, Logan, UT 84322-4405

1. Introduction

The USU electrodynamic model of the ionosphere describes the large-scale electrodynamics in the high-latitude ionospheric regions. By assuming the ionospheric process under study is in a steady state or a quasi-steady state, the model solves the Ohm's law and the current continuity equation in a global MLT-MLAT coordinate system so as to obtain self-consistency between the ionospheric conductivity, field-aligned current, ionospheric horizontal current, and convection electric field. The model outputs cover the ionospheric regions from 50° to 90° of magnetic latitude with a spatial resolution of tens of kilometers in both MLT and MLAT directions. The model includes the effect of the inclination of the geomagnetic field.

2. Model Formulation

The ionosphere is treated as a two-dimensional slab with an integrated conductivity. The relationship between the ionospheric electric field **E** and the ionospheric height-integrated current density **i** can be expressed by Ohm's law

$$\mathbf{i} = \sigma \cdot \mathbf{E} \tag{1}$$

where

$$\sigma = \begin{pmatrix} \Sigma_{\theta\theta} & \Sigma_{\theta\phi} \\ \Sigma_{\phi\theta} & \Sigma_{\phi\phi} \end{pmatrix} \tag{2}$$

is a 2×2 tensor representing the anisotropic height-integrated conductivity in the ionosphere in which θ denotes colatitude and ϕ denotes longitude. The elements of the tensor are

$$\Sigma_{\theta\theta} \simeq \frac{\Sigma_P}{\sin^2 I} \quad \Sigma_{\theta\phi} \simeq \frac{\Sigma_H}{\sin I} \quad \Sigma_{\phi\theta} = -\Sigma_{\theta\phi} \quad \Sigma_{\phi\phi} \simeq \Sigma_P \tag{3}$$

where I is the inclination angle of the geomagnetic field with respect to the horizontal ionosphere, Σ_H and Σ_P are the height-integrated Hall and Pedersen conductivities, respectively.

The current continuity equation can be expressed as

$$\nabla \cdot \mathbf{i} = j_{\parallel} \sin I \tag{4}$$

where $j_{\parallel}$ is the field-aligned current density, and

$$\sin I = \frac{2\cos\theta}{(1+3\cos^2\theta)^{1/2}}. \tag{5}$$

By inserting equation (1) into equation (4), we obtain

$$\nabla\cdot(\sigma\cdot\mathbf{E}) = j_{\parallel}\sin I. \tag{6}$$

By using $\nabla\times\mathbf{E}=0$, equation (6) can be rewritten in terms of the potential Φ as,

$$\nabla\cdot(\sigma\cdot\nabla\Phi) = -j_{\parallel}\sin I, \tag{7}$$

When the field-aligned current associated with a plasma convection pattern flows into the ionosphere, it must connect to the ionospheric Hall and/or Pedersen currents. For different convection patterns and various ionospheric conductivity distributions, the closure feature can be significantly different. To analyze the closure characteristics of the field-aligned and horizontal currents for various convection patterns and conductivity conditions, one needs to decompose equation (6). In a polar coordinate system, equation (6) can be rewritten as

$$\frac{1}{\sin I}\nabla\cdot(\sigma\cdot\mathbf{E}) = (j_{\parallel H} + j_{\parallel P1} + j_{\parallel P2}) = j_{\parallel} \tag{8}$$

where

$$j_{\parallel H} = \frac{1}{\sin I}\left[E_\phi\frac{\partial\Sigma_{\theta\phi}}{\partial r} + \frac{E_\theta}{r}\frac{\partial\Sigma_{\phi\theta}}{\partial\phi}\right] \tag{9}$$

$$j_{\parallel P1} = \frac{1}{\sin I}\left[E_\theta\frac{\partial\Sigma_{\theta\theta}}{\partial r} + \frac{E_\phi}{r}\frac{\partial\Sigma_{\phi\phi}}{\partial\phi}\right] \tag{10}$$

$$j_{\parallel P2} = \frac{1}{\sin I}\left[\Sigma_{\theta\theta}\frac{E_\theta}{r} + \Sigma_{\theta\theta}\frac{\partial E_\theta}{\partial r} + \frac{\Sigma_{\phi\phi}}{r}\frac{\partial E_\phi}{\partial\phi}\right] \tag{11}$$

In equations (9), (10), and (11), r is the radial distance from the pole, and E_θ and E_ϕ are the latitudinal and longitudinal components of the ionospheric electric field, respectively. An inspection of these equations shows that $j_{\parallel H}$ comes from the contribution of the Hall current, and $j_{\parallel P1}$ and $j_{\parallel P2}$ come from the contribution of the Pedersen current. The major difference between the terms $j_{\parallel P1}$ and $j_{\parallel P2}$ is that the former is mainly determined by the gradient of the Pedersen conductance and the latter is mainly determined by the divergence of the electric field. Equations (8) to (11) are the working equations solved in the model.

The ionosphere in our simulation is modeled by computational grids on a polar coordinate system in which the radial dimension measures the geomagnetic latitude from 50° to 90° and the azimuthal dimension measures the longitude (or MLT). The grid size can vary from 20 km to 500 km in both directions.

3. Model Inputs and Outputs

The basic electrodynamical quantities in the ionosphere are field-aligned current, ionospheric conductivity, and convection electric field. The model has been formulated with

various operation modes and it can take the 2-D distributions of any two of the above basic quantities as the model inputs to start the modeling. These inputs can be either theoretical ones or observational ones.

The outputs of the model can be 2-D distributions of the field-aligned current, ionospheric height-integrated conductivity, convection electric field, ionospheric horizontal current, Joule heating rate, and the components of the field-aligned current. The last one is particularly useful for studying the current closure feature in the ionosphere.

In the following, we show an example of the applications of the USU electrodynamic model of the ionosphere. In this case, we studied the large-scale features of the ionospheric electrodynamics during northward IMF periods [*Zhu et al., 1991*]. The large-scale convection patterns are adopted from the *Heppner-Maynard* convection model [1987], which is an empirical model based on the DE 2 satellite data. Figure 1 shows the Heppner-Maynard convection pattern for strongly northward IMF with a negative B_y. The left plot of Figure 1 shows the potential distribution of the convection field and the right plot shows the calculated electric field from the USU model.

The height-integrated Hall and Pedersen conductivities in our modeling are obtained from the ionospheric conductivity model developed by *Rasmussen and Schunk* [1987]. This model calculates ion densities in the *E* and lower *F* regions by numerically solving the chemical reaction equations for N_2^+, O_2^+, O^+, and NO^+. The ion densities are then used to calculate the Hall and Pedersen conductivities.

Figure 2 shows the case in which the ionospheric conductivity is appropriate for winter time, quiet aurora, and solar maximum conditions. The top left panel of Figure 2a shows the integrated Hall conductivity in which the ionization effects of EUV radiation, auroral precipitation, starlight, and resonantly scattered radiation have been included. The top-right panel of Figure 2a shows the field-aligned current distribution associated with the Heppner-Maynard distorted two-cell convection pattern for $B_y < 0$. The dashed lines are for upward field-aligned currents, and the solid lines are for downward field-aligned currents. The Region 1 and 2 current systems can be seen in the plot. The most important thing to note is the existence of the NBZ current in the polar cap.

The bottom left panel of Figure 2a shows the ionospheric horizontal current. Instead of the strong westward and eastward electrojets in the evening-midnight sector, which are typical for a southward IMF condition, the strong shear between an eastward and a westward current can be seen in the noon sector. The bottom right panel of Figure 2a shows the distribution of $j_{\|H}$, which reflects the contribution of the divergence of the Hall current. The left panel of Figure 2b shows the distribution of the Joule heating rate, in which a strong heating can be seen on the dayside. The right panel of Figure 2b shows the distribution of the sum of $j_{\|P1}$ and $j_{\|P2}$, which reflects the contribution of the divergence of the Pedersen current. As can be seen, the contribution of the Hall current to the field-aligned current is very small compared to that of the Pedersen current, especially on the dayside. This suggests that the field-aligned current during northward IMF is mainly closed by the Pedersen current.

4. Model Uncertainties and Limitations

The model can be used to study the large-scale electrodynamical features of steady state or quasi-steady state ionospheric processes. It is not appropriate for the study of transient ionospheric processes when the magnetosphere-ionosphere coupling and the ionosphere-thermosphere coupling are still in a dynamical time-varying fashion.

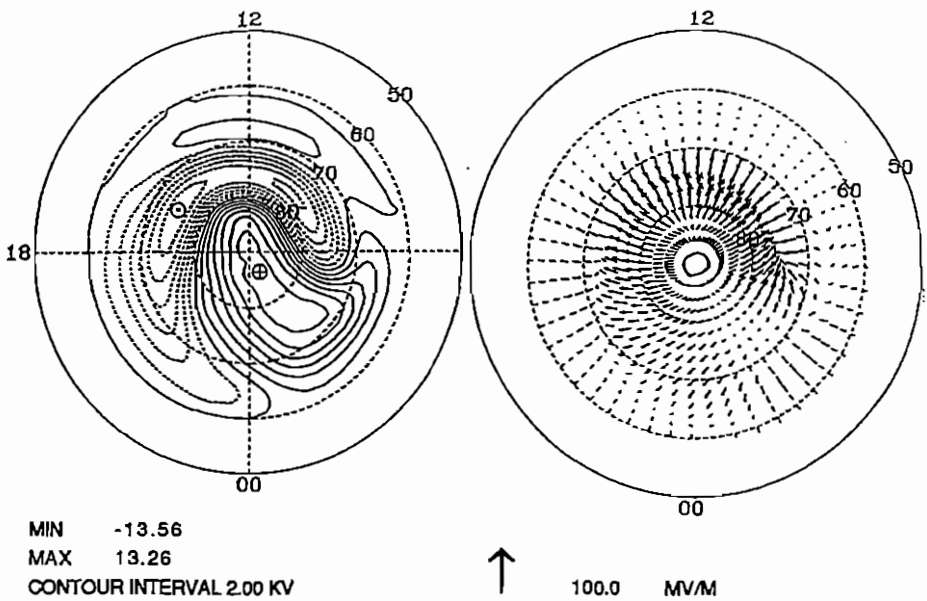

Figure 1. Electric potential and electric field distributions for strongly northward IMF with a negative B_y from the *Heppner and Maynard* [1987] convection model. From *Zhu et al.* [1991].

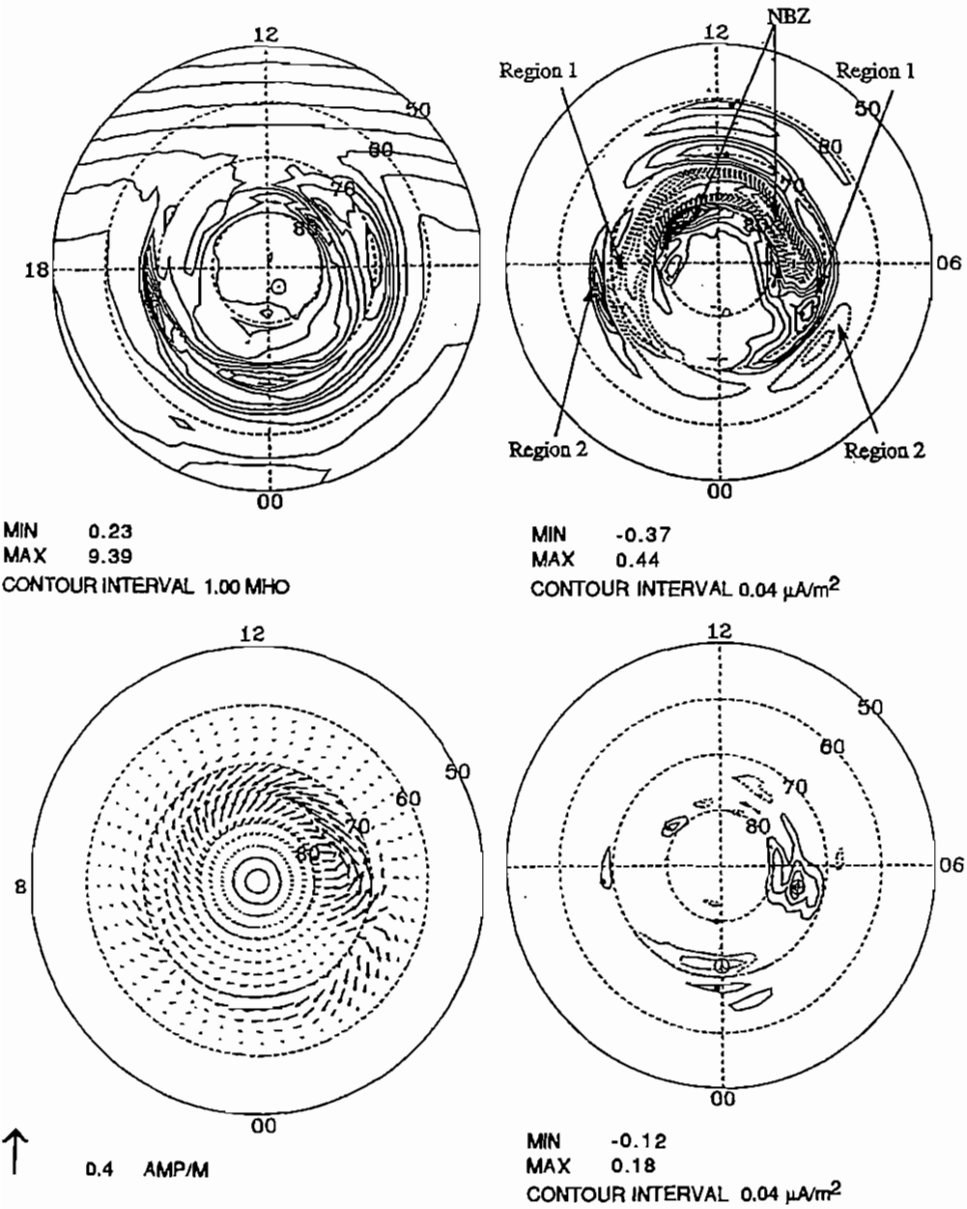

Figure 2a. Input ionospheric Hall conductance for winter, quiet aurora, and solar maximum (top, left panel), total field-aligned current (top, right panel), ionospheric horizontal current (bottom, left panel), and the field-aligned current connecting to the Hall current (bottom, right panel). In the plots of field-aligned current, the dashed lines denote the upward field-aligned currents and the solid lines denote the downward field-aligned currents. From *Zhu et al.* [1991].

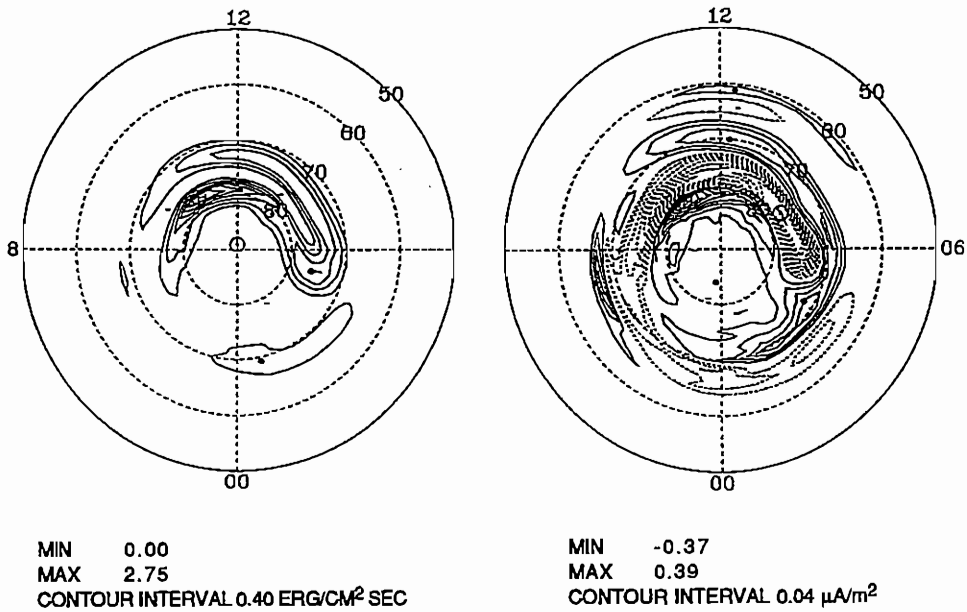

Figure 2b. The continuation of the case shown in Figure 2a, which shows the distribution of Joule heating rate (left panel) and the field-aligned current connecting to the Pedersen current (right panel). From *Zhu et al.* [1991].

The greatest uncertainty in the modeling by using the USU electrodynamic model of the ionosphere is related to the uncertainty in the adopted observational inputs. Even though the model can mathematically make all the inputs and outputs satisfy Ohm's law and current continuity equations, in reality an inconsistency between the observational inputs always exists. This is because self-consistent, simultaneous, 2-D distributions of the ionospheric electrodynamic quantities (for example, convection field and conductivity) are hard to obtain due to the limitation of the observational capability. For theoretical modeling with the USU electrodynamic model, the uncertainty can be minimal. The self-consistency of the model inputs can be achieved through a treatment of time-dependent M-I coupling or an iteration process [*Zhu et al.*, 1993].

5. Model Availability

The model developers are willing to collaborate with interested scientists on both theoretical or model-observation comparison studies.

6. References

Heppner, J. P. and N. C. Maynard, *J. Geophys. Res.*, *92*, 4467, 1987.
Rasmussen, C. E. and R. W. Schunk, *J. Geophys. Res.*, *92*, 4491, 1987.
Zhu, L., R. W. Schunk, and J. J. Sojka, *J. Geophys. Res.*, *96*, 19397, 1991.
Zhu, L., J. J. Sojka, R. W. Schunk, and D. J. Crain, *J. Geophys. Res.*, *98*, 6139, 1993.